High Velocity Clouds

and the

Milky Way Halo

Christopher Thom

BSc (Hons)

A dissertation presented in fulfillment
of the requirements for the degree of
Doctor of Philosophy
Swinburne University Of Technology

February, 2006



Hofstadter's Law: It always takes longer than you expect, even when you take into account Hofstadter's Law.

— *Douglas Hofstadter*

TELESCOPE, *n.* A device having a relation to the eye similar to that of the telephone to the ear, enabling distant objects to plague us with a multitude of needless details. Luckily it is unprovided with a bell summoning us to the sacrifice.

— *Ambrose Bierce*, "The Devil's Dictionary"

ABSTRACT

This thesis presents an exploration of stars and gas in the halo of our Galaxy. A sample of 8321 field horizontal branch (FHB) stars was selected from the Hamburg/ESO Survey. The stars make excellent tracers of the Milky Way halo, and we studied the kinematics of a subset of the HES FHB stars, comparing their velocity dispersions to those predicted by several models. Since these stars are intrinsically luminous, hot and numerous they make ideal probes of the distances to high-velocity clouds (HVCs) — clouds of neutral hydrogen gas whose distances are largely unknown and which do not fit simple models of Galaxy rotation. A catalogue of stars which align with the HVCs was developed. High resolution spectroscopy of 16 such HVC probes with the Magellan telescope has yielded a remarkably tight distance constraint to complex WB. This is one of only a handful of such distance limits so far established. Lower distance limits were set for several other clouds. Finally, we have suggested that some of the HVCs may be associated with the accretion onto the Milky Way of the Sagittarius dwarf galaxy.

ACKNOWLEDGEMENTS

The path to preparing a Ph.D. thesis is a long, often circuitous, intensely rewarding, and sometimes painful one — somewhat like a journey to Ithaca. During my four years, I have made many friends, both at home and abroad. The support of those new friends, and some old ones, my collaborators, along with that of my parents, has been crucial.

My supervisor Brad Gibson, has shown great support throughout my candidature; for my travels, I owe him much. Of equal importance, his knowledge of *exactly* the right time to partake of a warming glass of red, or quiet single malt, is not to be understated. Time spent with the rest of my supervisory team has been equally rewarding. Norbert Christlieb has spent much time explaining the complexities of stellar astrophysics. My first visit to Bergedorf was somewhat daunting; Norbert's good sense of humour made return visits a pleasure.

I have had the privilege to spend several seasons in and around Turku, visiting Tuorla Observatory and my supervisor Chris Flynn. Chris and his wife Leena welcomed me into their home, provided a limitless supply of enthusiasm, and showed me much of the Finnish countryside I would otherwise have missed. Kiitos! I'd also like to thank Janne and Mari, for showing me the younger side of Turku and Helsinki. My Finnish experiences were much more pleasant for all of your company. During the latter stages of my Ph.D. a most fruitful collaboration with Mary Putman developed. Mary's support, knowledge and enthusiasm made her a joy to work with. She also introduced me to the funky town that is Ann Arbor, and put many things in perspective with good advice.

Upon first arriving in Melbourne, I made many friends very quickly. The speed with which I was accepted made the transition to a new place an easy one. Annie Hughes quickly became a great friend and confidant. To you and the rest of the David St crowd, thank you. Special mention is due to my perennial partners in crime, Steve and Daisuke. Always to be relied upon for a night out in Melbourne, with far ranging conversations, from the technical to girls to philosophy — thank you for dragging me to places I didn't want to go, and following me to places you didn't want to; there'll always be time for just one more. To the rest of the Melbourne crowd, in particular yesh, asha, gaz, mikey, sar, willem, chris P and james — thank you all for your ready friendship. Thanks are also due to Ruth: a good housemate, but an even better travelling buddy.

One summer a girl from Canberra came to play. I quickly discovered that Kath and I shared an affinity for many things. I'm glad she came, and that, through her, I also had the pleasure of meeting Brij. Thank you both for recipes, G&Ts, evenings at the Brunswick Green, and generally making life bearable. On my first ever observing run, an insane German girl with whom I shared a supervisor introduced me to the horribly complex telescope I was expected to operate. I quickly realised that neither were as scary as they seemed, and Anna quickly became one of my closest friends — someone upon whom I could rely. Your support when I needed it most will not be forgotten Anna, nor will your endless supply of bizarre German sayings. At this juncture, it would be remiss of me not to thank Kait. Thank you for putting the pieces back together again, the advice I didn't want to hear, and for all the fabulous and bizarre postcards. To my parents: thank you for your support throughout, especially immediately after the operation. Without it, I could never have made it this far.

Finally, in the final months of my Ph.D., when I least expected it, I found immense support in a newfound friend. You showed me your town, reminded me why I was excited by science, and made my dim world a little brighter every day. Thank you Marla.

DECLARATION

This thesis contains no material which has been accepted for any other degree or diploma, except where due reference is made in the text. To the best of my knowledge, it contains no material previously published or written by another person except where due reference is made in the text of the thesis.

Christopher Thom

February, 2006

PUBLICATIONS

The following publications have arisen from the work presented in this thesis:

- Thom, C., Putman, M. E., Gibson, B. K., Christlieb, N., Flynn, C., Beers, T. C., Wilhelm, R., & Lee, Y. S., 2006, ApJ, 638, L97
  The Galactic Nature of High Velocity Cloud Complex WB

- Thom, C., Gibson, B. K. & Christlieb, N., 2005b, ApJS, 161, 147
  A Catalog of Field Horizontal Branch Stars Aligned With High-Velocity Clouds

- Thom, C., Flynn, C., Bessell, M. S., Beers, T. C., Hänninen, J., James, D., Christlieb, N., Holmberg, J. & Gibson, B. K., 2005a, MNRAS, 360, 354
  Kinematics of the Galactic halo from Horizontal Branch stars in the Hamburg/ESO Survey

- Christlieb, N., Beers, T. C., Thom, C., Wilhelm, R., Rossi, S., Flynn, C., Wisotzki, L., & Reimers, D., 2005, A&A, 431, 143
  The stellar content of the Hamburg/ESO survey. III. Field horizontal-branch stars in the Galaxy

- Putman, M.E., Thom, C., Gibson, B. K., Staveley-Smith, L., 2004, ApJ, 603, L77
  The Gaseous Trail of the Sagittarius Dwarf Galaxy

CONTENTS

1 Introduction **1**
- 1.1 The High-Velocity Clouds . . . 1
- 1.2 HVC Distances . . . 3
  - 1.2.1 Stellar Absorption Lines . . . 3
  - 1.2.2 Other Distance Estimates . . . 5

2 Stellar Selection **7**
- 2.1 Introduction . . . 7
- 2.2 The Hamburg/ESO Survey . . . 8
- 2.3 Selection . . . 9
- 2.4 Results . . . 9
  - 2.4.1 Contamination . . . 10

3 Halo Kinematics **13**
- 3.1 Introduction . . . 13
- 3.2 Sample and Observations . . . 15
  - 3.2.1 Radial Velocities and Selection . . . 16
- 3.3 Kinematic Models . . . 17
- 3.4 Final Sample and Velocity Dispersion . . . 19
- 3.5 Results and Analysis . . . 21
  - 3.5.1 Outer Halo Comparison . . . 21
  - 3.5.2 Discussion . . . 22
- 3.6 Summary and Conclusions . . . 23

4 FHB Stars aligned with HVCs **25**
- 4.1 Introduction . . . 25
- 4.2 Stellar selection and Matching . . . 28
  - 4.2.1 The Hamburg/ESO Survey . . . 29
  - 4.2.2 Spectrum Extraction . . . 29
  - 4.2.3 Moment Maps . . . 30
  - 4.2.4 Cloud Matching and the Magellanic Stream . . . 31
  - 4.2.5 Stellar Velocities . . . 32
  - 4.2.6 Optical Detections . . . 33
- 4.3 The Catalogue . . . 35

4.4 Conclusion 35

5 The Galactic Nature of Complex WB 37
5.1 Introduction 37
5.2 Observations and Data 38
5.3 Results 40
5.3.1 HE1048+0231 40
5.3.2 HE1138−1303 43
5.4 Discussion 43

6 Lower Distance Limits to HVCs 45
6.1 Introduction 45
6.2 Observations and Data 45
6.2.1 Optical Data 46
6.2.2 Radio Data 47
6.2.3 Equivalent Widths 48
6.2.4 Non-detections 50
6.3 Optical and Radio Spectra 51
6.4 Discussion of Sightlines 60
6.4.1 Wannier Clouds - Complex WA 60
6.4.2 Wannier Clouds - Complex WD 61
6.4.3 CHVC 786 62
6.4.4 Population “EN” 64
6.4.5 HVC 283 64
6.4.6 Magellanic Stream 66
6.4.7 Magellanic Stream — Leading Arm 67
6.5 Discussion of Complexes 68
6.5.1 Wannier Clouds 68
6.5.2 HVC 283 69
6.5.3 CHVC 786 69
6.5.4 Magellanic Stream 69
6.6 Concluding Remarks 69

7 The Gaseous Trail of the Sgr Dwarf 71
7.1 Introduction 71
7.2 Observations 72
7.3 Results 73
7.4 Discussion 75
7.5 Overview 77

8 Conclusions 79
8.1 Summary 79
8.2 Future Directions 80
8.2.1 HVC Distances 80

8.2.2 Compact HVCs 80
8.2.3 The Wannier Clouds and Complex WB 81
8.2.4 Connection to IVC gas 81
8.2.5 Gas Associated with the Sgr Stream 82
8.2.6 Magellanic Stream 82
8.2.7 The Larger Picture 82

References **83**

Appendices **91**

A FHB/HVC Catalogue **93**

B FHB/HVC Spectra and Column Density Maps **103**

LIST OF FIGURES

2.1 HES FHB selection boundary 10
2.2 Distance distribution of HES FHB stars 11

3.1 Radial velocity differences 14
3.2 Radial velocity correlation 15
3.3 Sky distribution of FHB stars 20
3.4 Histogram of FHB distances 20
3.5 Model comparisons for measures $\sigma_{\rm LOS}$ 21
3.6 Comparison of Sirko et al. (2004a) data to model 22
3.7 SLFC and isothermal model predictions 24

4.1 Example H I spectrum 27
4.2 Example column density map 28
4.3 Example H I spectrum with peak flux inside the $|v_{\rm LSR}| \geq 90\,{\rm km\,s^{-1}}$ boundary 32
4.4 Example medium resolution spectrum of an FHB star 33

5.1 Complex WB H I column density map 40
5.2 HE $1048+0231$ and HE $1138-1303$ spectral stacks 41

6.1 Example of the continuum fitting process 49
6.2 Radio/Optical stacks for HE 0046−3255 and HE 0056−3330 52
6.3 Radio/Optical stacks for HE 0502−2528 and HE 0504−2509 53
6.4 Radio/Optical stacks for HE 0932−0404 and HE 1004−0516 54
6.5 Radio/Optical stacks for HE 1045−2550 and HE 1125−3030 55
6.6 Radio/Optical stacks for HE 1318−2555 and HE 1319−3034 56
6.7 Radio/Optical stacks for HE 2155−2243 and HE 2200−2222 57
6.8 Radio/Optical stacks for HE 2304−3858 and HE 2340+0149 58
6.9 CHVC 786 63
6.10 HVC 283 65

7.1 Aitoff plot of gas along the Sgr orbit 73
7.2 Channel maps of HVCs along the Sgr orbit 75

LIST OF TABLES

3.1 Definition of fields 23

4.1 MS Boxes 30
4.2 Stellar velocity comparisons 34

5.1 Basic parameters of HVC probes 39

6.1 Magellan probes — Cloud alignments 46
6.2 Magellan probes — fundamental data 47
6.3 H I data for all probes 48
6.4 Equivalent width errors 50
6.5 Non-detection equivalent widths 59
6.6 Summary of HVC distance limits and masses quantities 68

A.1 Catalogue of FHB stars aligned with HVCs. 94

CHAPTER 1

INTRODUCTION

1.1 The High-Velocity Clouds

In 1963, Muller et al. published the first paper on neutral hydrogen moving with velocities inconsistent with the differential rotation of the Galactic system (Muller et al., 1963). These clouds, which came to be known as high-velocity clouds (HVCs) due to their identifying characteristic, have been a source of debate ever since. Are the HVCs a tracer of important physical processes, or are they merely unimportant flotsam which can tell us little?

In practical terms, HVCs are usually defined by their velocity in the Local Standard of Rest (LSR) frame, with $|v_{\rm LSR}| > 90 - 100\,{\rm km\,s^{-1}}$ being the most widely used definition (see Wakker & van Woerden, 1997, for a review). They can also be defined in terms of their "deviation velocity" — the degree to which they deviate from Galactic rotation models (Wakker, 1991; de Heij et al., 2002b). The primary unknown property of HVCs is their distance. Since they do not co-rotate with the Galaxy, we cannot, by definition, apply a model of Galactic rotation to obtain a kinematic distance. Many attempts, using a variety of methods, have been made to determine or constrain HVC distances, with mixed success. The range of possible distances has led to a plethora of models attempting to explain their existence; Oort (1966) was the first to discuss many of them. Some progress has been made in the last decade, but only recently have the resources become available to address the problem in a systematic fashion. The Hubble Space Telescope (*HST*) and Far Ultraviolet Spectroscopic Explorer (*FUSE*) satellites have allowed great strides to be made in our knowledge of the metal content of the gas, but detailed knowledge of the distances still remains scarce.

Spitzer (1956) was the first to propose the idea of a hot $\sim 10^6$ K halo surrounding the Milky Way. Attempting to explain both the observed soft X-ray background and absorption by O VI gas towards young stars (e.g. York, 1974), Shapiro & Field (1976) suggested a "galactic fountain" mechanism. Bregman (1980) later linked this process to the formation of the HVCs. The Galactic fountain model considers gas that has been expelled from the disk by supernova explosions. If this gas is bound, it must remain in a corona surrounding the Galaxy. Thermal instabilities cause the hot gas to cool, which then returns to the disk. Gas in such a fountain would be expected to reach heights of $\sim 5 - 10\,{\rm kpc}$

above the disk (Wakker, 1990; de Avillez, 2000), and would explain some of the observed high-velocity H I clouds. Since it is material ejected from the disk, we would expect that its metal content is a significant fraction of the solar value. These two pieces of information are key observables for this theory.

The Milky Way halo shows clear evidence of accretion events in recent history, both in stars and gas. The Large and Small Magellanic Clouds are currently being shredded in the potential of the Milky Way, giving rise to the Magellanic Stream (Mathewson et al., 1974). The Sagittarius (Ibata et al., 1994; Majewski et al., 2003) and Monocerous (Newberg et al., 2002) stellar streams show further evidence of dwarf galaxies that have been accreted onto the Milky Way. With such accretion comes gas, and it has been suggested that some subset of the high-velocity clouds are related to accretion events. Certainly this is the case for the Magellanic Stream (e.g. Putman et al., 2003b), one of the dominant structures in the Southern, radio sky. Indeed, some of the clouds studied in this thesis are associated with the Magellanic Stream (see Chaps 6 & 7).

If one studies a simple, closed-box, prescription of the chemical evolution of the Galaxy, it is difficult to reproduce the observed metallicity distribution function (MDF) of nearby G-dwarf stars (Pagel & Patchett, 1975) — this is the so-called "G-dwarf problem". The reason is that, under the simple assumptions made, all the gas initially in the system quickly collapses to form stars. Since they form early, there is a preponderance of metal-poor stars, of which the low-mass specimens (i.e. the G-dwarfs) remain to be observed today. To fix this overproduction problem, chemical evolution models generally allow the formation of the disk to occur more slowly (e.g. Chiappini et al., 1997). Such an evolution requires the input of further star formation fuel. The HVCs have been cited as a potential source of this necessary gas (e.g. Tosi, 1988; Alibés et al., 2001). This gas would be relatively metal-poor (~ 0.1 solar). It has been suggested that complex C, a large HVC in the northern sky, represents such star formation fuel (Wakker et al., 1999), but this interpretation is uncertain, as abundance variations in complex C have been observed (Gibson et al., 2001; Collins et al., 2003).

With the launch in 1999 of the *FUSE* satellite, it has become possible to obtain much higher resolution UV spectra towards hot stars and background extragalactic sources, such as quasars. Some $\sim 85\%$ of the sight-lines studied with *FUSE* show local absorption in the O VI line, indicating the presence of a diffuse ($10^{-4} - 10^{-5}\,\mathrm{cm}^{-3}$), hot ($\sim 10^6\,\mathrm{K}$) and extended ($\gtrsim 70\,\mathrm{kpc}$) halo around the Galaxy (Sembach et al., 2003), although the location of these O VI absorbers has been disputed (Nicastro et al., 2003). Motivated by improving the treatment of gas cooling in dark matter simulations, Maller & Bullock (2004) proposed a multi-phase formulation of gas cooling within the "cooling radius" of galaxies. Their prescription describes the formation of warm $\sim 10^4\,\mathrm{K}$ gas clouds, pressure-supported by a hot gas background. The formation of these clouds follows from fragmentary cooling processes. Thus, galaxy formation would be fuelled by the infall of gas clouds condensing out of a hot halo. Such clouds are predicted to have a circum-Galactic distance distribution ($\lesssim 150\,\mathrm{kpc}$) and typical total masses of order $5 \times 10^6\,\mathrm{M}_\odot$. Such clouds are broadly consistent with the observed properties of HVCs, and this scenario might offer a plausible

explanation for the origin of some clouds.

Several authors have considered the case that the HVCs are very distant inhabitants of the Local Group (up to ~ 1 Mpc) (e.g. Oort, 1966; Verschuur, 1969; Arp, 1985; Blitz et al., 1999; Braun & Burton, 1999). Simulations of hierarchical structure formation predict that the local universe should contain $\sim 5 - 10\times$ more dark matter halos than are observed (Klypin et al., 1999); this is the "missing satellite" problem of CDM. One suggestion has been that the HVCs are not local objects, but occupy a much larger range of distances, and may be the baryonic content of the missing dark matter halos. Blitz et al. (1999) argued that a subset of HVCs lie at such large distance, based on arguments that the Local Group standard of rest is a more natural frame for describing the HVC kinematics. Braun & Burton (1999) suggested that it was only the "Compact" HVCs — those that are isolated and smaller than 2° FWHM — that form this distant population. This stance was further refined by de Heij et al. (2002a) to suggest that the CHVCs reside in extended halos around the Milky Way and M 31.

1.2 HVC Distances

1.2.1 Stellar Absorption Lines

Various methods have been used in attempts to derive distances to HVCs. Most rely on model predictions or strong assumptions. The only method which yields direct distances, free of such model-dependence, is stellar absorption line spectroscopy. The process is relatively simple — one observes the spectrum of a star which is aligned with the HVC gas. If a doppler-shifted absorption line at the velocity of the gas is seen, the star must be behind the clouds, and an upper distance limit is set. If no absorption is seen, and we are confident that it should have been were the star located behind the cloud, then a lower distance limit is set.

The requirements of this method restrict the choice of stellar targets. We would like the stars to be distant, so as to maximise our chances of detecting HVC absorption. Further, we must be able to obtain the stellar distances with relative ease. Hot stars are clearly desirable; since we seek absorption lines of intervening gas, we would like to limit the possibility of confusion with intrinsic stellar metal lines. Attempts at absorption line work have been mostly made using hot O- and B-stars in the UV. RR Lyrae variables and Blue Horizontal Branch stars, observed in the optical, are also promising targets, especially since they are numerous and intrinsically luminous.

While the technique is relatively straightforward, the difficulty of its application is attested to by the paucity of HVC absorption detections. Soon after the discovery of HVCs several attempts were made to detect Na I and Ca II in absorption. Prata & Wallerstein (1967) failed to detect HVC gas in absorption, while Kepner (1968) presented the first catalogue of early-type stars useful for such absorption line work. Others have also tried in vain

to detect the HVCs in absorption (e.g. Hulsbosch, 1971; York et al., 1986; Smoker et al., 2004).

A few HVC detections toward stars exist. Bates et al. (1990) detected the HVC $100 - 7 + 100$[1] in the spectrum of the B9 Iab star 4 Lac using the *IUE* satellite. The detection in various species (O I, Mg I, Mg II. Fe II and Al II) places an upper limit of 1.2 kpc on the cloud. Also taking advantage of the strength of metal resonance lines in the UV, Sembach et al. (1991) detected high velocity absorption lines toward the O-star HD 156359 using *IUE*. By analogy with other positive velocity "Wannier Clouds" (complexes WA – WD) in the 3rd and 4th Galactic quadrants, Wakker (2001) classified many small clouds in this region as "complex WE". At 11 kpc, the detection towards this star places the complex a modest $\lesssim 3$ kpc below the disk, in the inner halo of the Galaxy, with a mass of less than $2 \times 10^5\,\mathrm{M}_\odot$.

Richter et al. (1999) made the first detection of an HVC ($279 - 33 + 120$) in molecular hydrogen (H_2). Using the *ORFEUS* satellite, they detected molecular gas in the line of sight towards HD 269546, in the Large Magellanic Cloud (LMC). This detection places an upper limit to the cloud of 50 kpc (i.e. the assumed distance to the LMC). Bluhm et al. (2001) also measured the H_2 in this and other lines of sight, yielding log(N) = 15.6 and $N(\mathrm{H_2})/N(\mathrm{H\,I}) = 3 \times 10^{-6}$ (Wakker, 2001). Both Richter et al. and Bluhm et al. suggested that this gas originates either in the Milky Way or LMC — it is not extra-Galactic.

Of the major HVC complexes, the properties of which are summarised by Wakker & van Woerden (1991), only complexes A and M have been detected in stellar absorption. Danly et al. (1993) detected HVC absorption by complex M towards the B-star BD $+38^\circ\,2182$. The derived z-height is $z < 4.4$ kpc, setting a mass limit of $< 6 \times 10^4\,\mathrm{M}_\odot$. The abundances of complex M follow more closely a disk, rather than halo, depletion pattern (Wakker, 2001) and there is evidence that complex M is linked to the intermediate velocity "IV Arch"; some parts of complex M have also been classified as intermediate velocity clouds (Kuntz & Danly, 1996; Ryans et al., 1997), consistent with closer distances.

One of the most well-studied of all HVC complexes is complex A in the northern hemisphere, first surveyed by Hulsbosch & Raimond (1966) and Hulsbosch (1968). van Woerden et al. (1999) detected the cloud in Ca II H and K absorption in the spectrum of RR Lyrae star AD UMa. Detections toward RR Lyraes requires observations to be carefully timed, so as to observe the star at its brightest phase. Variable stellar absorption lines must also be taken into account. However, the variability provides very accurate distances, and the ability to observe them at large distances makes them attractive targets in the optical. Both upper and lower distance limits were derived for complex A ($4 < d < 10$ kpc), a range which was later revised to the more restrictive $8 < d < 10$ kpc (Wakker et al., 2003). At $3 < z < 7$ kpc above the Galactic plane, the total gas mass of the cloud is $10^5 - 10^6\,\mathrm{M}_\odot$.

[1] This oft-used nomenclature for individual clouds is based on Galactic longitude, latitude and LSR velocity.

1.2.2 Other Distance Estimates

Attempts to constrain the distances to the HVCs have been made using other, indirect methods. All of these depend on either model predictions, or the assumption of similarity between external systems and the Milky Way or Local Group. Nevertheless, they can provide useful insights, and the predictions of several of these methods is converging on a scenario in which the HVCs are mostly Galactic or circum-Galactic objects, located within ~ 150 kpc, and probably within ~ 50 kpc. We summarise some of these indirect arguments here.

Cohen (1981) made a study of the H I stream in the anticentre direction first surveyed in the 1970s (van Kuilenburg, 1972). He argued that this stream, later dubbed the "Cohen stream", is close to the solar neighbourhood ($100-300$ pc), based on the coincidence with a parallel stream at much lower velocities. Thus the Cohen stream would be impacting with the local disk gas. In a series of studies of the anticentre clouds (including Cohen's stream) Tamanaha (1994, 1995, 1996, 1997) made high spatial- and velocity-resolution observations of the area, and proposed a collisional origin for this gas. In his model, the high velocity gas in Cohen's stream is a remnant of a collision between very high velocity and lower velocity gas (Tamanaha, 1995). Lack of optical absorption places the gas further than 350 pc away (Tamanaha, 1996).

Pisano et al. (2004) used the Parkes telescope to perform deep searches for HVCs in Local Group analogues. They chose 3 loose groups, which have similar characteristics to the Local Group (i.e. only large spirals, separated by $\gtrsim 100$ kpc, spread over ~ 1 Mpc). They failed to detect any HVC analogues in the inter-group region, down to a mass limit of $4 \times 10^5\,\mathrm{M}_\odot$. They concluded that any undetected HI clouds should lie within 150 kpc of the spiral galaxies, and not at megaparsec distances. Zwaan & Briggs (2000) arrived at the same conclusion using a similar, but less sensitive, search in the Arecibo H I Strip Survey.

Thilker et al. (2004) have recently detected HVC analogues in the halo of M31. They found at least 20 individual H I clouds out to a projected distance of 50 kpc around M31. A subset of these clouds were the focus of follow-up, higher resolution observations using the Westerbork Synthesis Radio Telescope (WSRT) (Westmeier et al., 2005b). They resolved 16 individual clouds with typical masses $10^5\,\mathrm{M}_\odot$, with some of those possibly dominated by extra, unseen mass (dark matter, ionised gas etc). A tidal origin is suggested for many of these M31 clouds.

It has been suggested that the compact HVCs (CHVCs) are a subset of the HVC phenomenon; that they are distant, dark-matter dominated objects (de Heij et al., 2002a). Westmeier et al. (2005a) have observed several CHVCs using the Effelsberg telescope. With its $9'$ beam, the spatial resolution gives a reasonably accurate account of the gas structure. They found almost universal evidence of interactions between these small clouds and an ambient medium — head-tail structures, bow-shocks and ram-pressure interactions. These interactions imply that the CHVCs lie within 100 kpc of the Galaxy.

Quilis & Moore (2001) also studied the head-tail structure of HVCs, performing numerical simulations of clouds moving through a diffuse medium. They predicted that a density of at least $10^{-4}\,\mathrm{cm}^{-3}$ is required to produce the observed cloud structures, and suggested that such clouds must be either very close, based on observations that a large number of clouds show such structure. It should be noted, however, that distant ($\sim 300\,\mathrm{kpc}$), dark-matter dominated objects were also permitted by their simulations.

A distribution within 100 kpc of the Galaxy agrees well with the results that have been obtained using Hα. Tufte et al. (2002) used the Wisconsin H-Alpha Mapper (WHAM) to map several HVCs in the Hα line. Detection of Hα emission suggests that the clouds are being illuminated by UV photons escaping from the disk, placing the clouds within the Galactic halo. Putman et al. (2003a) performed deep Hα spectroscopy on a much larger sample of HVCs of varying morphologies (from CHVCs to the Magellanic Stream). Their results suggested that the HVCs are within $\sim 40\,\mathrm{kpc}$, under the assumption of a particular photo-ionisation model. It is worthwhile noting that these authors find that this particular model cannot accurately describe the high Hα emission seen in the Magellanic Stream. When a sizeable number of HVC distances are accurately known, it should be possible to invert this technique, and constrain the models.

The *FUSE* satellite has made tremendous work in the area of HVC metallicities since it was launched, and some observations have also been used to indirectly constrain HVC distances. Collins et al. (2003) used observations of O VI and other transitions to suggest that the hot gas is created at shock fronts in gas clumps falling onto the Galactic plane. Fox et al. (2004) used similar observations to suggest that highly ionised absorption in sightlines towards complex C is created at the interface of the neutral/warm gas and a hot ambient medium in the halo or Local Group.

The primary aim of this thesis is to extend the number of HVCs that have direct, absorption line distance limits. We have used Field Horizontal Branch (FHB) stars for this work, since they are numerous, distant, luminous and hot. Chapter 2 outlines the selection procedures that were used to select FHB candidates from the vast database of the Hamburg/ESO survey. We study the kinematics of a subset of these stars in Chapter 3. Chapter 4 outlines the process of selecting those FHB stars which are useful as HVC probes. The successful application of the absorption line technique, and the resulting distance limit to HVC complex WB are the subject of Chapter 5, while Chapter 6 outlines some preliminary results derived from those probes which did not exhibit absorption. Chapter 7 presents work which suggests a connection between several HVC complexes and the Sagittarius stellar stream.

CHAPTER 2

STELLAR SELECTION

Summary
This chapter is based on Christlieb, N., Beers, T. C., Thom, C., Wilhelm, R., Rossi, S., Flynn, C., Wisotzki, L., & Reimers, D., 2005, A&A, 431, 143. The main product of this paper is the compilation of a large sample of field horizontal branch star candidates. This sample is estimated to have $\lesssim 16\%$ contamination by other, higher-gravity stars and is the base sample on which the majority of this thesis is built. The paper has been rewritten in abridged form for inclusion here, giving a mostly qualitative description of the stellar selections. Complete details may be found in the published work, and references therein. My contribution to this work was the screening by eye of some 10,000+ individual spectra, rejecting noise artefacts and inappropriate objects, and testing/verification of the catalogue. In consultation with my primary supervisor, I estimate approximately one third of the work included in the final paper may be attributed to my efforts.

2.1 Introduction

While the basic components of the Galaxy are well established — disk, bulge and halo — we require more detailed knowledge of the Galaxy's constituents if we are to accurately describe its formation and evolution. Recently, it has become clear that the halo contains many structures which are the result of merger activity, such as the Sagittarius Stream (Ibata et al., 1994; Majewski et al., 2003) and Monocerous Stream (Newberg et al., 2002; Yanny et al., 2003a). This meshes well with the predictions of hierarchical formation models, in which the Galaxy accretes dwarf satellites over time. To further our knowledge of the Galactic Halo, a census of the chemical and kinematic properties of halo stars is desirable.

Field horizontal branch (FHB) stars provide excellent tracers of the Halo, since their intrinsic luminosities mean they may be found at large distances. Further, their distances may be readily obtained. One immediate application of a sample of FHB stars is to obtain a mass estimate of the Galaxy (e.g. Norris & Hawkins, 1991; Wilkinson & Evans, 1999).

Previous catalogues of FHBs have come from objective prism surveys, such as the HK Survey of Beers and collaborators (e.g. Beers et al., 1996). The HK survey is magnitude-limited to $B \simeq 15.5$, with a corresponding distance limit of $\sim 10\,$kpc. The Hamburg/ESO

Survey (Wisotzki et al., 1996, 2000, HES), with its deeper limiting magnitude of $B \simeq 18.0$ can reach greater distances (~ 30 kpc).

One of the main issues in selecting FHB stars is the contamination of stars in the same colour range with higher surface gravities (i.e. main-sequence A-type stars). These stars are much closer and therefore less interesting in terms of studying the halo. In a magnitude-limited sample such as the HES, some $\sim 50\%$ of stars with colours in the same range as the FHB stars are, in fact, of lower luminosity (see, e.g. Norris & Hawkins, 1991; Wilhelm et al., 1999b). It is also likely that the majority of the "blue metal poor" stars of Preston et al. (1994) are also blue stragglers (Preston & Sneden, 2000). Separation of the higher-gravity A-type stars has been attempted on the basis of broadband UBV colours alone (e.g. Sommer-Larsen et al., 1989; Preston et al., 1991) or Strömgren photometry (e.g. Philip, 1967). More robust measures also employ spectroscopic parameters, such as the width of the Balmer lines at a given depth (e.g Flynn et al., 1994), or the Balmer line profiles and Ca II K equivalent width (Wilhelm et al., 1999a). Clewley et al. (2002) have described a method that attempts this differentiation based solely on good quality, medium-resolution spectroscopy.

Here we have attempted to select a *clean* sample of the FHB stars; that is, we are more interested in low pollution of main-sequence stars in our sample, than a large number of stars. Follow-up observations of a subset of these stars demonstrate that we are able to select a large, clean sample of FHB stars, without the need for extensive follow-up observations.

2.2 The Hamburg/ESO Survey

The Hamburg/ESO Survey (HES) is a survey of the southern extra-Galactic sky, originally designed to detect quasars (Wisotzki et al., 1996). It is an objective prism survey conducted with the ESO Schmidt telescope. The magnitude range covered is $12.5 \lesssim B_j \lesssim 17.5$ with a seeing-limited spectral resolution of ~ 10 Å at Ca II K. The digitised spectra typically cover a range $3200 < \lambda < 5200$ Å. The entire HES database consists of some ~ 4 million spectra and the spectral resolution is such that it may successfully be exploited to identify interesting classes of stars, such as white dwarfs (Christlieb et al., 2001b), high-latitude carbon stars (Christlieb et al., 2001a), extremely metal-poor stars (e.g. Christlieb et al., 2002; Frebel et al., 2005; Frebel, 2006) and FHB stars (Christlieb et al., 2005). Further details are available elsewhere (e.g. Wisotzki et al., 1996, 2000; Christlieb et al., 2001b).

2.3 Selection

Selection of the FHB candidates in the HES follows a two-step procedure. First we selected stars in the colour range $-0.2 < B-V < 0.3$ and $-0.3 < U-B < 0.5$. The $B-V$ cut selects stars in the temperature range $7000\,K \lesssim \mathrm{T_{eff}} \lesssim 10,000\,K$. The $U-B$ limits were chosen so as to keep the number of DA white dwarfs to a minimum (see Christlieb et al., 2001b, for details).

The second stage is to apply to those stars meeting the colour selection, an automated classification routine. A sample of 228 HES stars were analysed using the method of Wilhelm et al. (1999a). This allowed us to define a classification boundary in the two-dimensional parameter space of the Strömgren index $c_1 = (u-v) - (b-v)$, which measures the strength of the Balmer jump, versus the sum of the equivalent widths of the Balmer lines $\mathrm{H}\beta + \mathrm{H}\gamma + \mathrm{H}\delta$, separating stars into two classes: "FHB" or "A" star. In the temperature range of interest, the strength of the Balmer jump is a good surface gravity indicator. Lower surface gravity stars will have a lower electron pressure, and hence lower continuous opacity. In these stars, the Balmer and Paschen continuum opacities then contribute a greater fraction of the total opacity, resulting in a stronger Balmer jump. Conversely, higher gravity main-sequence stars have a less pronounced Balmer jump. By choosing an appropriate classification boundary, we can control the contamination of the final sample. We refer the interested reader to Christlieb et al. (2001b), who have described extensively the details and statistics of choosing this selection boundary. Fig. 2.1 shows this process when applied to the 228 stars in the learning sample. The quadratic boundary in the c_1 vs Balmer sum space is evident in the right panel of this figure. Note that while the number of true FHB stars that have been incorrectly classed as main-sequence stars is high (37 out of 228), the number of true main-sequence stars classed as FHBs (i.e. those that would contaminate the final sample) is relatively low (12 out of 228). In other words, we have sacrificed *completeness* in order to ensure a *clean* sample.

2.4 Results

Having defined the appropriate selection criteria, they were then applied to the 329 plates of the Hamburg/ESO Survey currently used for studying stars (i.e. some ~ 4 million spectra). After the colour cuts and automated selection, it remained only to exclude spurious objects, such as plate artefacts, overlapping spectra etc, which could not be rejected by simple means. More than 10,000 spectra were screened by eye to remove spurious identifications, resulting in 9335 stars in our sample. Refinements to the classification algorithm further reduced this to a final sample of 8321 stars identified as FHB stars. The full catalogue of stars is available through CDS as catalogue J/A+A/431/143.

To determine the distances and the distance distribution, we first assumed that all stars in the catalogue were *bona fide* FHB stars. While not strictly true (since there will be some contamination), this will only have a significant effect on the distance distribution if the

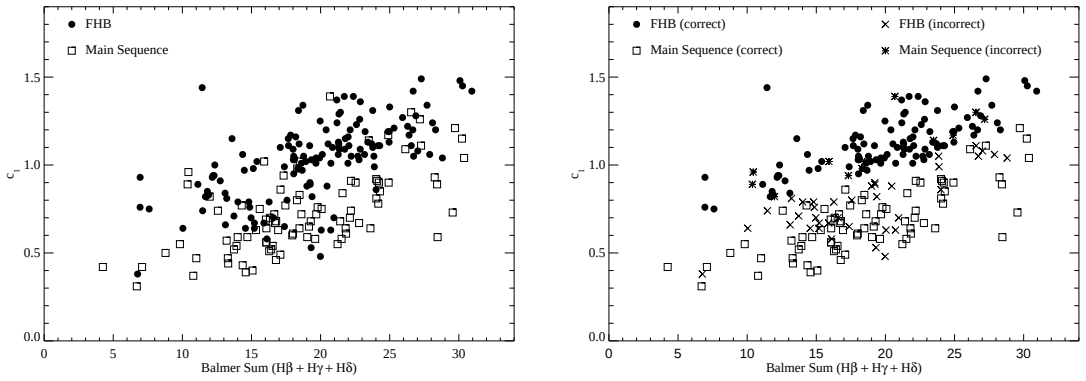


Figure 2.1: Illustration of the HES automated selection criteria, as applied to the 228 HES stars in the training sample. **Left panel:** The learning sample before automatic classification is applied. The types indicated are the ones that have been pre-determined. **Right panel:** The results of the automated classification. Circles and crosses show the *bona fide* FHB stars which have been correctly and incorrectly classified, respectively. Squares and asterisks show the main-sequence stars which have been correctly and incorrectly classified, respectively.

contamination rate is high, and the magnitude distribution is significantly different from the FHB stars. We used the dust maps of Schlegel et al. (1998) to estimate the reddening, applying the empirical correction of Beers et al. (2002) when the reddening exceeded $E(B-V) > 0.1$ mag. The average reddening of the sample was $E(B-V) = 0.046$, and hence the correction has a negligible effect on the distance distribution when compared to the expected photometric accuracy of $\sim 0.2 - 0.3$ mag.

To calculate the distances, we require the absolute magnitude, M_v, which is given by

$$M_v = 0.19\,([\text{Fe/H}] + 1.5) + 0.68 \tag{2.1}$$

The form of this relation — which was derived specifically for RR Lyraes — is given by Clementini et al. (1995). We adopted a zero-point which was informed by an analysis of FHB stars for which parallaxes are available from *Hipparcos* (Gratton, 1998). Since Equation 2.1 was derived for RR Lyrae variables, a correction must be applied to account for the variation between FHB and RR Lyrae absolute magnitudes as a function of $B-V$. This is taken from Preston et al. (1991). Since [Fe/H] is not available for all stars in the HES, we assumed [Fe/H] $= -1.9$, the average value determined by Wilhelm et al. (1999b). The de-reddened apparent magnitudes were then used to calculate the distance moduli. Fig. 2.2 shows the distribution of distances. The average distance is 10 kpc.

2.4.1 Contamination

From the final HES FHB catalogue, 125 stars — which were not part of the original learning sample — were observed at moderate spectral resolution with the CTIO 4 m and

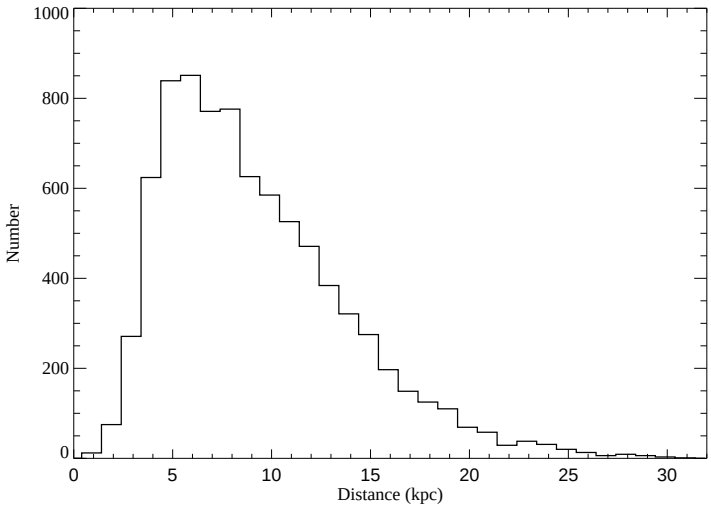


Figure 2.2: Distance distribution of stars in the HES FHB catalogue. The mean distance of the final sample is 10 kpc.

ESO 3.6 m telescopes. The spectra have $S/N > 20$ per pixel at Ca II K. They were reduced in *IRAF* in the usual fashion, using the standard optimal extraction technique. UBV photometry was obtained at the ESO–Danish 1.5 m telescope during November 1998 and November 2000.

The UBV colours, Ca II K equivalent widths, and Balmer line profiles for all stars were compared to synthetic spectra using the methods described by Wilhelm et al. (1999a). These techniques yield effective temperatures, surface gravities and metallicities accurate to ± 250 K, ± 0.14 dex and ± 0.12 dex respectively, allowing us to independently classify the stars and test the accuracy of the selection criteria. This resulted in 103 stars classified as FHB, 5 as FHB/A (either "FHB" or "A" stars), 17 classified as A-stars. Thus we can be confident that our sample has, at most, only $\sim 16\%$ contamination.

Acknowledgements
We thank A. Frebel for technical help and careful proof-reading. T.C.B. acknowledges partial support from grants AST 00-98508 and AST 00-98548, and PHY 02-16783, Physics Frontier Centers/JINA: Joint Institute for Nuclear Astrophysics, awarded by the US National Science Foundation. S.R. thanks the Brazilian Institutions FAPESP and CNPq for partial financial support.

CHAPTER 3

HALO KINEMATICS

Summary
This chapter has been published as Thom, C., Flynn, C., Bessell, M. S., Beers, T. C., Hänninen, J., James, D., Christlieb, N., Holmberg, J. & Gibson, B. K., 2005a, MNRAS, 360, 354. It has been altered only to maintain stylistic consistency. Copyright for the article is held by The Royal Astronomical Society and it is reproduced here with permission. In this chapter we examine the kinematics of 530 stars, selected from the catalogue presented in the previous chapter. We compare the measured velocity dispersions to two models. We find that we are unable to differentiate between a physically motivated model, and an isothermal one, although we do not include the well-constrained solar neighbourhood values. We suggest that additional observations towards the Galactic centre might help to differentiate between the two models.

3.1 Introduction

The stellar halo only comprises about 1 % of the luminous mass of the Galaxy and is composed of very old, metal-poor stars. In spite of this, the present-day dynamical and chemical state of the stellar halo has exerted considerable influence in shaping our understanding of the formation of large disk galaxies such as the Milky Way, particularly in its very early stages.

Large samples of field horizontal branch stars (FHBs) in the Galactic halo are excellent "test particles" for studies of halo kinematics (e.g. Sommer-Larsen et al., 1994, 1997; Sirko et al., 2004b); tracing the mass (Beers et al., 2004) and the merger history (Kinman et al., 1994; Brown et al., 2004) of the Milky Way. Their intrinsic brightness and the relative ease with which distances can be obtained, together with their relatively clean spectra, also make them ideal probes of distances to high-velocity clouds (e.g. Schwarz et al. 1995; Thom et al. 2005; Chapter 4).

The HK survey of Beers and collaborators (e.g. Beers et al., 1985, 1992) has identified $\sim 12,000$ candidate Horizontal Branch stars, of which about half are expected to be on the Horizontal Branch; the other half appear to be a mixture of A-type main-sequence stars and halo blue stragglers (Beers et al., 1988, 1996). More recently, several groups have reported large and clean samples of Horizontal Branch stars. The Hamburg/ESO

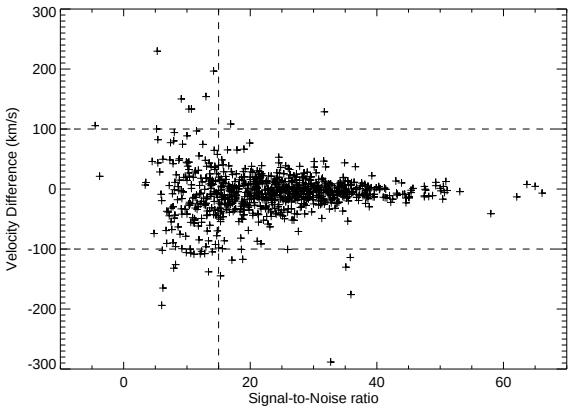


Figure 3.1: Radial velocity differences, as measured using the Hδ and Hγ lines, versus Signal-to-Noise ratio of the spectra, for our sample stars. The vertical and horizontal lines indicate the adopted $S/N > 15$ and $|v_{\rm diff}| < 100\,{\rm km\,s^{-1}}$ limits, respectively (see text).

survey (HES), originally designed to identify low-luminosity quasars, has been shown to contain a remarkable sample of interesting stars, including 8321 FHBs. This sample has a contamination level by non-FHBs (mostly high-gravity A-type stars) of less than 16 % (Christlieb et al., 2005). A subset of these stars is used here to constrain models of halo kinematics.

The Sloan Digital Sky Survey (SDSS), although primarily designed for extragalactic studies, has also revealed a large sample of 1170 Horizontal Branch stars at distances up to $\sim 100\,$kpc (Sirko et al., 2004a). From this sample Sirko et al. (2004b) measured an isotropic velocity ellipsoid for the outer halo. This result contrasts with halo stars in the solar neighbourhood, which show an ellipsoid elongated in the radial direction (Chiba & Beers, 2000; Gould, 2003, 2004).

Wilhelm et al. (1999a) have described a technique for separating Horizontal Branch stars from higher gravity A stars on the basis of broadband *UBV* colours and medium-resolution spectroscopy. Clewley et al. (2002, 2004) explored similar techniques based on broadband colours and medium-resolution spectroscopy, and also presented a method relying solely on medium resolution spectroscopy. They used this method to identify ~ 100 stars at distances of $> 30\,$kpc with the aim of providing better constraints on the mass of the Milky Way.

Brown et al. (2004) used the full *2MASS* point-source catalogue to select close to 100,000 objects, of which they expect 47 % to be on the Blue Horizontal Branch. They find an absence of structure in the inner halo (the sample has distance $d < 9\,$kpc), concluding that there have been no major accretion events in the inner halo over the past few Gyrs.

Here we present the results of a programme to obtain radial velocities (RVs), and study the kinematics, of more than 500 FHB stars selected from the HES catalogue. We wish

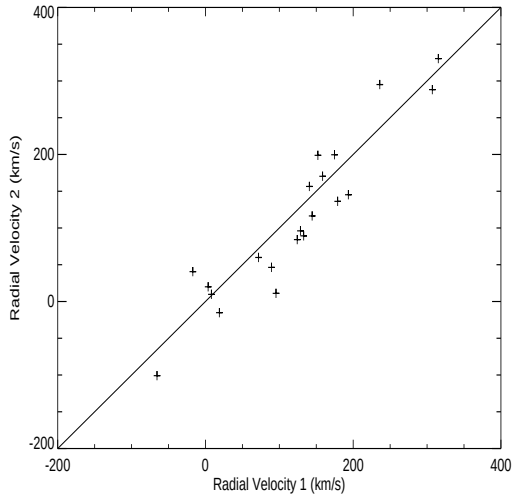


Figure 3.2: RV1 versus RV2 for the 21 stars with repeated measurements. The solid line is the one-to-one correspondence.

to test specifically the predictions of the Sommer-Larsen et al. (1994) (hereafter, SLFC) model, as refined by Sommer-Larsen et al. (1997). In the SLFC model, the velocity ellipsoid of the halo changes from radially-dominated orbits to tangentially-dominated orbits as one proceeds from the inner to the outer halo. We attempt to distinguish between this model and the simpler isothermal halo model, which specifies an isotropic distribution of stellar orbits, independent of Galactocentric radius, in the outer halo. Section 3.2 presents the sample and observations. It also includes details on the radial velocity measurements and selection criteria. Section 3.3 discusses the models which we wish to test. Section 3.4 details the final sample selection, division into fields, and calculation of the line-of-sight velocity dispersions, $\sigma_{\rm LOS}$. Section 3.5 presents the major results and analysis. A summary and conclusions are provided in Section 3.6.

3.2 Sample and Observations

Our sample of stars was drawn from the Christlieb et al. (2005) catalogue of FHB stars selected from the Hamburg/ESO survey. As part of a large programme of follow-up observations of the stellar content of the HES and HK surveys, over 1100 FHB stars were observed at the UK Schmidt Telescope (UKST)[1], using the six degree field (6dF) fibre-fed spectrograph. The 6dF instrument allows one to observe up to 150 objects simultaneously across the 6° field of the Schmidt telescope, obtaining spectra at 2 Å resolution. More than forty nights of observations took place between April 2001 and April 2003. Integration

[1]The UKST is operated and supported by the Anglo-Australian Observatory, on behalf of the astronomical communities of Australia and the UK

times were typically 4–5 times $2700\,\mathrm{s}$ per field, depending on observing conditions.

The targets were, in most cases, selected by HES field number, with roughly equal numbers of fibres used for metal-poor candidates and FHB stars. The data were reduced using the *Figaro* and *6dfdr* software packages, the latter being written specifically to handle the fibre data from the 6dF instrument. This process yielded *FITS* files containing the reduced spectra of all 150 fibres. These files were separated, with one spectrum per file and assigned a unique name based on the star name, field number, and date of observation. A hand-screening process was then used to exclude obvious problems and artefacts.

Catalogues of FHB stars may contain a significant fraction of contaminants — higher surface gravity A-type stars which fall within the colour range of the survey (in the case of the HES, $-0.2 < B - V < 0.3$). Since the HES FHB candidates have been shown to have a much lower level of contamination from higher-gravity stars ($< 16\,\%$; Christlieb et al., 2005), as compared to the HK survey ($\sim 50\,\%$; Beers et al., 1996), we considered only the HES stars in our observations. We made no attempt to separate the potential contaminants from the true FHB stars, judging that a $\sim 16\,\%$ level is acceptable for our present purpose. While it is, in principle, possible to further refine the classification, using the spectroscopic method of Clewley et al. (2002) would result in a sample clean to about the $\sim 12\,\%$ level and hence nothing would be gained. Since systematic, accurate photometry is not available, methods based on this are not applicable. Conversely, we have no way of obtaining RVs from the objective prism of the HES, but can measure velocities in the 6df spectra, since the S/N requirements for RVs are less stringent than those for classification.

3.2.1 Radial Velocities and Selection

Sersic profiles were fit to the Hγ and Hδ Balmer lines, as described by Clewley et al. (2002). Due to changes in the spectrograph settings over the long observing period, these were the only two prominent lines common to all spectra. We rejected any star for which we could not obtain a radial velocity measurement in both lines. We also noticed large systematic discrepancies ($> 150\,\mathrm{km\,s^{-1}}$) between the measurements of RV from the Hγ and Hδ lines in some stars. These stars were noted to be concentrated in one field (HES field 573), hence all stars in this field were rejected. One star was also rejected due to difficulties with sky subtraction. This left a total of 827 stars.

We sought to combine the velocity measurements from the two lines into an average value, but we first used the difference in the measurements of the two lines to provide an internal consistency check on the radial velocities. Fig. 3.1 shows a plot of the difference between the Hδ and Hγ line, versus signal-to-noise ratio. We applied cuts, retaining all stars with measurement difference less than $100\,\mathrm{km\,s^{-1}}$ and S/N greater than 15, as shown in Fig. 3.1. An average RV was then computed from all available measurements. Heliocentric corrections were calculated using the IRAF task *rvcorrect*. This selection yielded 636 RV measurements.

Twenty-one stars in our sample were observed at more than a single epoch and thus enable a further check on the measurements. The correlation between the two average RVs for these stars is shown in Fig. 3.2. The difference between these two measurements for a given star — the range of measurements — provides an estimate of the standard deviation of the underlying error distribution (Pearson, 1926; Tippett, 1925). This distribution will be normally distributed with $\mu = RV$ and $\sigma =$ error in the measurement. Applying a correction factor of 1.12838 (see Table X of Tippett 1925) to the absolute value of the range, we obtain a mean statistical velocity error of $30\,\mathrm{km\,s^{-1}}$. This agrees well with the assumption of Gaussian errors, under which we obtain $27\,\mathrm{km\,s^{-1}}$, dividing the standard deviation of the velocity differences by $\sqrt{2}$. We therefore adopt $30\,\mathrm{km\,s^{-1}}$ as the formal error on our radial velocity measurements. To definitively characterise the error on a single RV measurement would require many repeated velocity measurements of the same star. For the analysis, the two RV measurements were combined into a single entry by averaging the two independent RVs, weighted by the S/N in the respective spectra, yielding RVs for 615 unique stars.

3.3 Kinematic Models

The density distribution of the stellar halo follows a power-law, $R^{-\alpha}$, with Galactocentric radius, R. The value of α has been the subject of many studies, using RR Lyrae stars, halo giants, and Blue Horizontal Branch (BHB) stars (e.g. Preston et al., 1991; Kinman et al., 1994; Sluis & Arnold, 1998; Morrison et al., 2000). Most of these converge on a value of $\alpha \approx 3.0-3.5$. In contrast, Robin et al. (2000) find a lower value consistent with the range $\alpha = 2.0-2.75$, whilst noting significant degeneracy between α and the flattening parameter c/a. This contrasts with the density distribution of the Galactic dark halo, which follows R^{-2} (i.e. the isothermal case expected from a flat rotation curve), at least in the outer parts where it dominates over the luminous matter.

Stars in the halo of the Milky Way are drawn from a population with a total dispersion on the order of $200\,\mathrm{km\,s^{-1}}$, i.e. they have velocities needed to maintain equilibrium with the Galactic gravitational potential. In the stellar halo, this velocity is directed roughly equally into three components, resulting in a system with little bulk rotation and thus mainly "pressure support" against gravitational collapse.

The three components of the stellar halo's velocity ellipsoid have been measured accurately in the solar neighbourhood, for stars within roughly 1 kpc of the Sun, to be $\sigma = (\sigma_R, \sigma_\theta, \sigma_\phi) \approx (140, 100, 100)\,\mathrm{km\,s^{-1}}$ (Chiba & Beers, 2000; Gould, 2003), where we have adopted a spherical coordinate system (R, θ, ϕ) around the Galactic centre. This determination is based on stars for which all three components of the space velocity can be measured via both radial line-of-sight velocities and proper motions. Beyond a few kpc from the Sun, usually only the radial velocity can be measured (a situation which will change dramatically when the ESA GAIA mission is completed; Perryman 2002), and special techniques are required to reconstruct the three components of the velocity

ellipsoid. One can either propose and fit data to models of the velocity ellipsoid as a function of position in the Galaxy — as performed by Sommer-Larsen et al. (1997) for some ~ 700 stars — or attempt to recover the three components directly (Sirko et al., 2004b).

The velocity ellipsoid of the stellar halo is a consequence of its density profile and the total matter distribution in the Galaxy. Let us assume that the 3-D dispersion of the velocity distribution is isothermal (i.e. it has the same magnitude in all three components), and that the density falls off like $R^{-\alpha}$. It then follows, for a Galactic potential dominated by a dark halo with a flat rotation curve (characterised by constant circular velocity V_0) that $\sigma = V_0/\sqrt{\alpha}$. For the Milky Way, $V_0 \approx 220\ \mathrm{km\,s^{-1}}$, and thus $\sigma \approx 120\,\mathrm{km\,s^{-1}}$ for each component (Binney & Tremaine, 1987). The total velocity dispersion is then of order $\sqrt{3}\sigma \approx 200\,\mathrm{km\,s^{-1}}$.

The stellar halo is clearly not isothermal in the vicinity of the Sun (the component of the velocity dispersion in the radial direction is $\sim 40\%$ larger than the two other components of the velocity ellipsoid); nevertheless, the total velocity dispersion is of order $200\,\mathrm{km\,s^{-1}}$.

What is the velocity dispersion like elsewhere in the halo? SLFC and Sirko et al. (2004b) have attempted a reconstruction from radial velocities of distant halo stars. SLFC proposed a model for the velocity dispersion $\sigma(R, \theta, \phi)$ as a function of Galactocentric radius R alone; the model permitted sharp deviations from isothermal behaviour (such as is seen in the solar neighbourhood) and was fit to both the local and distant halo stars. This model was subsequently refined using a much larger sample of about ~ 700 distant halo stars by Sommer-Larsen et al. (1997). It was found that the radial anisotropy ($\sigma_R > \sigma_{\phi,\theta}$) seen near the Sun persists into the inner halo ($R < 8\,\mathrm{kpc}$), changing to tangential anisotropy in the outer halo (roughly $R > 15-20\,\mathrm{kpc}$). Sirko et al. (2004b) present an ostensibly opposing view; from radial velocities of 1170 halo stars found in the SDSS, they found that the velocities of (distant) halo stars are very close indeed to isothermal $(\sigma_R, \sigma_\theta, \sigma_\phi) = (101.4 \pm 2.8, 97.7 \pm 16.4, 107.4 \pm 16.6)\,\mathrm{km\,s^{-1}}$. The Sirko et al. study is essentially of the outer halo, where the SLFC model is not yet well constrained, hence the ostensible contradiction with the non-isothermal model of SLFC is, as those authors argued, probably not significant.

We treat the halo's kinematics statistically, characterised by the velocity ellipsoid alone; i.e. we explicitly ignore substructure, such as dissolving satellites or other features in density and/or velocity space. From the point of view of halo substructure, the halo can be divided into inner and outer regions. The inner halo is that part which is within $\sim 15\,\mathrm{kpc}$ radius from the Galactic centre. In this region, the relevant dynamical timescales are expected to be considerably shorter than the age of the Galaxy. This expectation is borne out by the lack of detected substructure (e.g. Brown et al., 2004). Thus, in the inner halo, the stellar population appears likely to be fairly well mixed, with a smooth density distribution. There is additional evidence that this is the case in the solar neighbourhood, based on an analysis of 4588 sub-dwarfs (Gould, 2003, 2004). In the outer halo, beyond some 20 kpc or so, dynamical timescales approach the age of the Galaxy. In these regions it has long been suspected that the halo would contain the debris of dissolving satellite

galaxies; this is now well established (e.g. Majewski 1994; Ibata et al. 1994; Lynden-Bell & Lynden-Bell 1995; Morrison et al. 2000). While the outer halo is undoubtedly quite lumpy, most of the stellar halo's mass, and most of that part probed via our data, is in the well mixed inner halo. Additional tests of this assertion will be the subject of a forthcoming study.

3.4 Final Sample and Velocity Dispersion

We analysed the kinematics of our stars following the methodology of SLFC. This involved dividing the sample into regions on the sky in which there are sufficient stars to measure $\sigma_{\rm LOS}$ for two distance bins along the line of sight. The stars in each field were split evenly into the two distance bins. The requirement we applied, that each bin should have at least twenty stars, forced us to exclude all stars with Galactic latitude $b < 0^{\circ}$. This left us with a total of 530 stars with which to study the kinematics of the Galactic halo. The distribution on the sky of all 530 FHB stars in our final sample is shown in Fig. 3.3. The average distance to the stars is 6.7 kpc; the distance distribution is shown in Fig. 3.4.

In calculating the velocity dispersion along the line-of-sight ($\sigma_{\rm LOS}$) we excluded the upper and lower 5 % the data, in order to protect these numbers from the adverse effects of outliers. The result is adjusted by a factor of $\frac{1}{0.789}$ to recover the true standard deviation of the original distribution, a process described in detail by Morrison et al. (1990). The $\sigma_{\rm LOS}$ were corrected for a $30\,{\rm km\,s^{-1}}$ velocity measurement error by subtraction in quadrature and then compared to the model predictions. We have consistently used velocities in a heliocentric frame throughout the calculations, with the corresponding distance. Since the model predictions are made in a galactocentric frame, a projection factor was applied to recover the appropriate line-of-sight value.

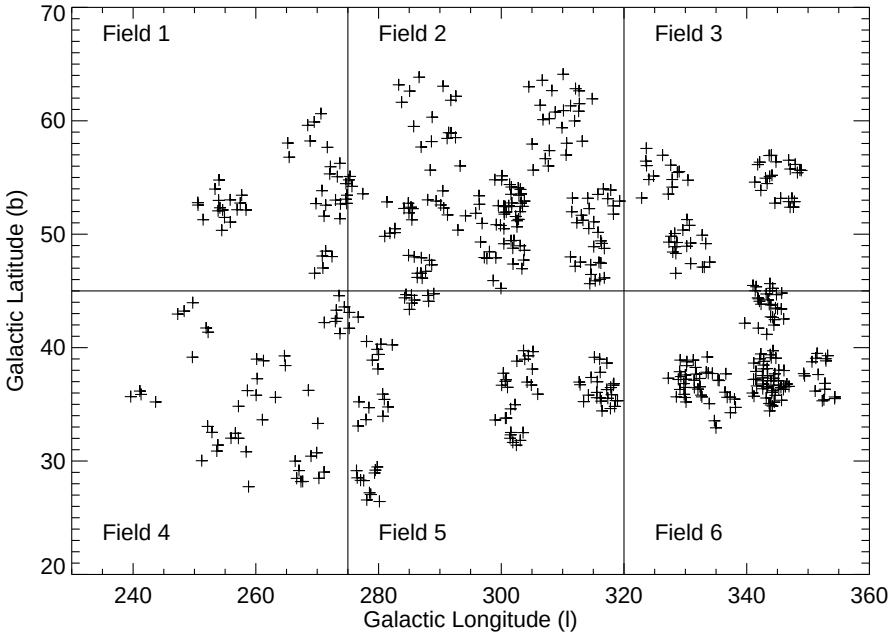


Figure 3.3: Sky distribution of all 530 stars in 6 northern fields.

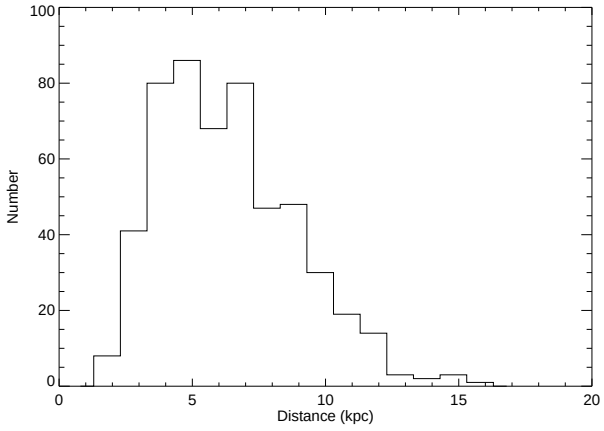


Figure 3.4: Histogram of heliocentric distances for the final sample of 530 stars.

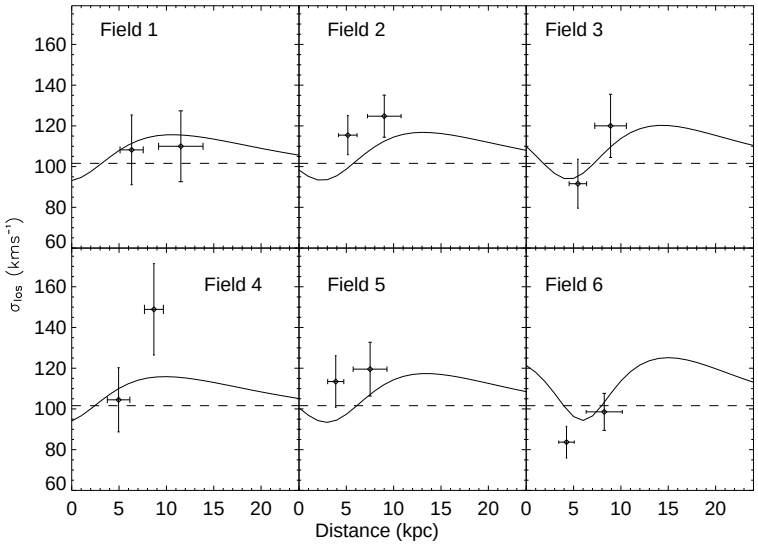


Figure 3.5: Comparison of measured $\sigma_{\rm LOS}$ to the two models. The horizontal dashed line shows an isothermal model with the value measured by Sirko et al.. The solid line is the line-of-sight velocity dispersion predicted by the SLFC model for the average line-of-sight of the field. The error bars show the 1σ errors.

3.5 Results and Analysis

Table 3.5.1, in addition to listing the fields, shows the observed velocity dispersions and the 1σ errors. These have been used to test both an isothermal, isotropic halo with velocity dispersion of $101.6\,{\rm km\,s^{-1}}$ (i.e. the value observed by Sirko et al. (2004b)) and the predictions of the SLFC model. Fig. 3.5 shows this comparison for all six northern fields. The SLFC predictions are shown as the solid line, while the isothermal model is the horizontal dashed line. Visual inspection leads us to conclude that both models fit the data equally well; a χ^2 analysis confirms this view. Both models arise from predictions rather than fits to the data, and hence have no free parameters. For the twelve $\sigma_{\rm LOS}$ in the six fields we measured a reduced χ^2 of 1.31 and 1.85 for the SLFC and isothermal models respectively, with 12 degrees of freedom each. Since this is not a statistically significant difference, both must be regarded as fitting the data equally well.

3.5.1 Outer Halo Comparison

Sirko et al. (2004a) have provided a similar sample of 1170 FHB stars in the outer halo (distances up to $\sim 100\,$kpc). From this sample they derive an estimate of the isothermal velocity dispersion of $101.6\,{\rm km\,s^{-1}}$. We have analysed their data in the same manner as above (see their Table 3 for distances and heliocentric red-shift). The results are shown in Fig. 3.6. At the distance of the Sirko data, both models predict similar line-of-sight

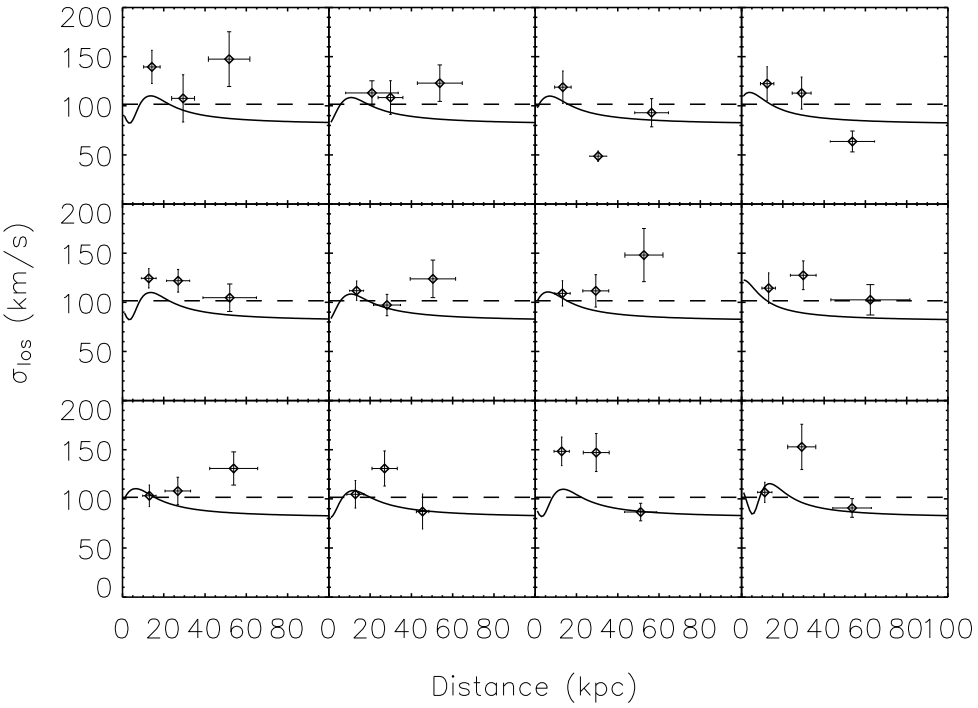


Figure 3.6: Comparison of Sirko et al. (2004a) data $\sigma_{\rm LOS}$ to the models fit by Sirko et al. (dashed lines) and SLFC (solid lines). Velocities are heliocentric and distances are in kpc.

velocity dispersions. Therefore these data are not an effective test of the SLFC model. These data, divided into nine fields and three distance bins per field, fit both models equally well. The reduced χ^2 statistics for the two models are 2.37 and 2.19 for the SLFC and isothermal models respectively, for 35 degrees of freedom, excluding the obvious outlier in panel 3 (third from left, top row in Fig. 3.6). This data point is likely caused by the Sagittarius stream (Ibata et al., 1994), as noted by Sirko et al.. Again, the difference in χ^2 is not statistically significant.

3.5.2 Discussion

It is clear that neither this sample of inner Galactic halo stars, nor the outer halo sample of Sirko et al. (2004a), permit us to distinguish between the two competing models. It is worth emphasising here that the SLFC model is a physically realisable system (Flynn et al., 1996), whereas the isothermal model cannot account for the locally observed halo velocity dispersion anisotropy. Where then should we look in order to best discriminate between these two models?

We have used the model of SLFC to determine regions on the sky where the two models

Field	BLC (l, b)	TRC (l, b)	Num	Dist (kpc)	$\sigma_{\rm LOS}$ $\rm km\,s^{-1}$
Field 1	(220,45)	(275,70)	22	6.3 ± 1.2	108 ± 17
			22	11.5 ± 2.3	110 ± 17
Field 2	(275,45)	(320,70)	78	5.2 ± 1.0	115 ± 10
			79	9.0 ± 1.8	125 ± 10
Field 3	(320,45)	(360,70)	31	5.5 ± 0.9	92 ± 12
			32	8.9 ± 1.7	120 ± 15
Field 4	(220,20)	(275,45)	24	5.0 ± 1.2	104 ± 16
			24	8.7 ± 1.0	149 ± 22
Field 5	(275,20)	(320,45)	44	3.9 ± 0.8	113 ± 13
			45	7.5 ± 1.8	120 ± 13
Field 6	(320,20)	(360,45)	64	4.3 ± 0.8	84 ± 8
			65	8.2 ± 1.9	98 ± 9

Table 3.1: Definition of fields in Galactic co-ordinates, showing Bottom Left Corner (BLC), Top Right Corner (TRC), number of stars, distance and $\sigma_{\rm LOS}$ of stars in field. Errors are 1σ.

differ in their predictions of $\sigma_{\rm LOS}$ by more than $30\,\rm km\,s^{-1}$. This area is restricted to lines-of-sight toward the Galactic centre and at low Galactic latitude. Along these lines of sight one might expect a clear signature of the SLFC model, as demonstrated in Fig. 3.7. A survey of 500 FHB stars at $(l, b) = (340 \text{ to } 20; -30 \text{ to } +30)$ with distance bins centred at 4, 8 and 13 kpc would provide a good discriminant between the models. This effect may also be seen in Field 6 of Fig. 3.5, which is the closest the bulge.

3.6 Summary and Conclusions

Line of sight velocities have been measured for a sample of 530 FHB stars in the inner Galactic halo, with an average heliocentric distance of 6.7 kpc. We have used these velocities to test the velocity dispersions predicted by the Sommer-Larsen et al. (1994) halo model, and compared with those predicted by an isothermal model. The former model allows for marked anisotropies to account for the well-constrained parameters of the local Galactic halo. These new data are equally well described by both models. We also compared the model predictions to the sample of 1170 FHB stars in the outer Galactic halo, as published by Sirko et al. (2004a). We confirm their findings that both models fit these data equally well.

We suggest that the best place on the sky to differentiate these two models is towards the Galactic bulge and at low galactic latitudes; we propose that future efforts concentrate on the more challenging task of recovering clean samples of halo FHB stars at low galactic latitudes.

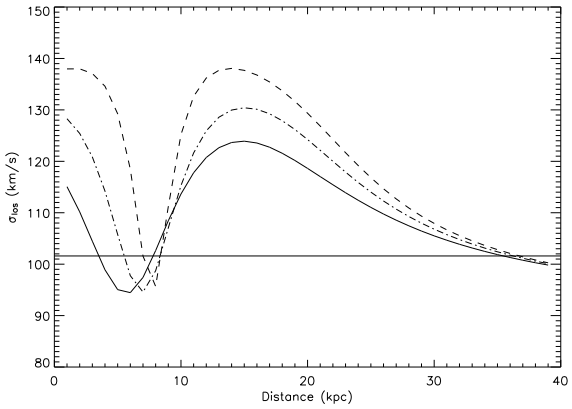


Figure 3.7: Difference between the SLFC and isothermal model predictions in the direction of the Galactic centre. Dashed, dot-dashed and solid curves are drawn for lines-of-sight at $(l, b) = (0, 15), (0, 30), (0, 45)$ respectively. For comparison, the solid line shows the constant velocity dispersion measured in the Sirko sample.

Acknowledgements
We thank the UKST staff for their support during the observations. We also thank Lee Clewley and collaborators, who kindly provided the Sersic profile fitting code.

CT would like to thank Tuorla Observatory for its support during an extended stay, and Hamburger Sternwarte for support during several visits. CF thanks the Academy of Finland and the ANTARES program for its support of space based research. BKG, CF, and CT acknowledge the financial support of the Australian Research Council and its Discovery and Linkage International programs.

T.C.B. acknowledges partial support from grants AST 00-98508, AST 00-98549, and AST 04-06784, as well as from grant PHY 02-16783; Physics Frontier Center/Joint Institute for Nuclear Astrophysics (JINA), awarded by the U.S. National Science Foundation. We are also grateful to Michigan State University for providing partial financial support for the UK Schmidt Telescope during the time the data presented herein were gathered.

CHAPTER 4

FHB STARS ALIGNED WITH HVCS

Summary
This chapter has been published as Thom, C., Gibson, B. K. & Christlieb, N., 2005b, ApJS, 161, 147. It has been modified in style only, for presentation here. Copyright for the published article resides with the American Astronomical Society and it is reproduced here with permission. We present a catalogue 430 Field Horizontal Branch (FHB) stars, selected from the sample of FHB stars presented in (Christlieb et al., 2005, see also Chapter 2), which fortuitously align with high column density neutral hydrogen (H I) high-velocity cloud (HVC) gas. These stars are ideal candidates for absorption-line studies of HVCs, a subject to which we will progress in the following chapters. This chapter details the selection of appropriate lines of sight. Appendix A shows the full FHB/HVC catalogue, while H I spectra and column density maps of all lines of sight are shown in Appendix B.

4.1 Introduction

Discovered by Muller et al. (1963) over 40 years ago, high-velocity clouds (HVCs) are H I clouds with velocities that do not conform to simple models of Galactic rotation (e.g. Wakker & van Woerden, 1997, and references therein). Since their discovery, HVC distances (and origins) have been the source of much debate, with various scenarios suggested. Shapiro & Field (1976) proposed the existence of a "Galactic Fountain" to explain the observed soft X-ray background and O VI absorption lines. This process, in which hot gas is driven up into the halo by supernovae and stellar winds, which then condenses and falls back onto the disk, was linked by Bregman (1980) to the HVCs (see also de Avillez, 2000). Others have suggested they may be the result of tidal disruption of satellite galaxies, e.g. the Magellanic Stream (Putman et al., 2003b). Perhaps they are the infalling source of star formation fuel long required by chemical evolution models (e.g. Fenner & Gibson, 2003)? Oort (1966) first suggested that some subset of HVCs may be at much larger distances, being the remnants of the galaxy formation process (a suggestion revived by Blitz et al., 1999). Other authors have proposed that the smaller, isolated Compact HVCs (CHVCs) may be explained under this scenario (e.g. de Heij et al., 2002a), suggesting that such objects may also be observable around M31 with sen-

sitive H I observations. Subsequent observations toward M31 have successfully detected HVC-analogs (Thilker et al., 2004), whilst others have failed to find them in searches of Local Group analogues (Pisano et al., 2004).

It is clear that to establish a definitive theory describing HVCs the largely unknown distances are a key element. Many physical properties scale with the distance; physical size ($\propto d$), mass ($\propto d^2$), density ($\propto d^{-1}$) and pressure ($\propto d^{-1}$) for example. Since HVCs do not conform to models of Galactic rotation, we cannot use those models to derive distances from their observed velocities. Hence another method is required. A distance limit may be set by high-resolution absorption spectroscopy (Danly et al., 1993; Schwarz et al., 1995; van Woerden et al., 1999). If a star is located behind the HVC, the stellar spectrum should contain the imprint of the HVC at the (known) velocity of the cloud. A sufficiently high resolution spectrum should be able to resolve such features. Detection of these absorption lines indicates the star is behind the cloud, and an upper distance limit is set, namely the distance to the star.

The interpretation of non-detections is more challenging and is succinctly summarised by Wakker & van Woerden (1997) (see their Fig. 4). Several possibilities must be taken into account before one can be convinced that the lack of an optical HVC absorption feature indicates that the star is in front of the HVC, and sets a significant lower distance limit. HVCs have been shown to have large column density variations over small (arcmin) angular scales (e.g. Wakker & Schwarz, 1991). Since HVCs are usually identified in H I surveys with large beam sizes, high-resolution (interferometric) radio imaging is necessary, to ensure the line of sight does not pass through a "sucker hole" in the cloud, missing the expected high column density gas. If the alignment is favourable, we also require sufficiently high metallicity intervening gas (a typical value for HVCs is $\sim 0.1 - 0.3$ solar; see Wakker, 2001); clearly if this is not the case, there will be no metal ions to create an absorption line. Further, knowledge of the gas metallicity comes from other lines-of-sight, so we must assume that there are no abundance variations within the cloud.

Optical absorption line studies are often conducted using the Ca II H and K resonance lines ($\lambda\lambda 3968.469$ Å and 3933.663 Å respectively). These two resonance lines have high oscillator strengths and thus should be easily detectable. Prata & Wallerstein (1967) were the first to specifically target the HVCs (unsuccessfully) using absorption line studies, with Kepner (1968) producing the first catalogue of early-type stars aligned with HVCs. Despite almost 40 years of efforts by various groups, only a handful of stellar absorption line studies have successfully detected HVC absorption features[1], providing firm upper limits. van Woerden et al. (1999) detected HVC "Chain A" in Ca II absorption in the optical spectrum of the RR Lyrae star AD UMa, giving a maximum distance of 10 kpc. A few years earlier, Danly et al. (1993) used the *IUE* satellite to detect the HVC Complex M in the UV resonance lines O I, C II and Si II toward the early-type star BD $+38^\circ 2182$, limiting the HVC to $z < 4.4$ kpc.

[1]There is also a large body of ultraviolet absorption line detections against stellar and extra-galactic sources. These ionised high-velocity clouds in some cases align with H I HVCs, in some cases not. See e.g. Sembach et al. (2003) for details.

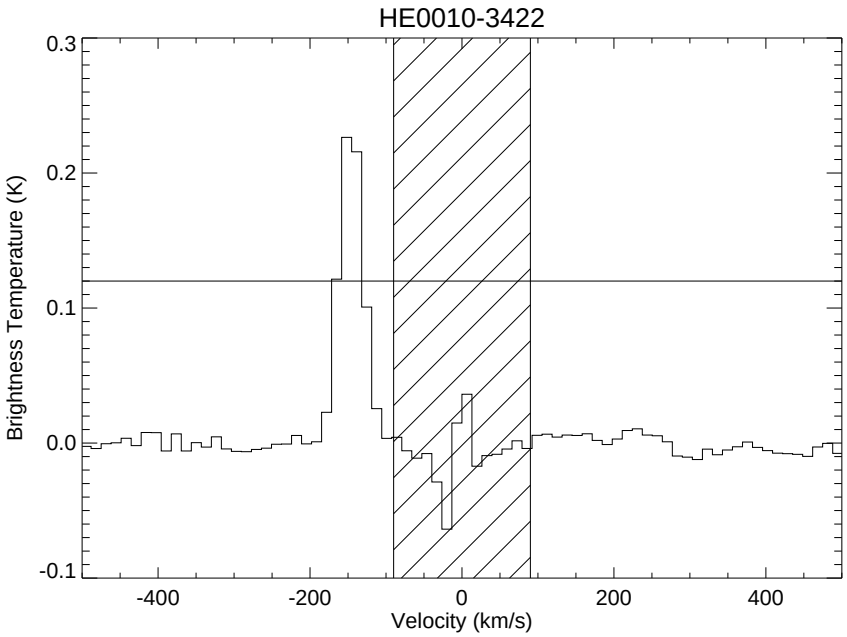


Figure 4.1: An example H I spectrum of a stellar line of sight meeting the selection criteria. The horizontal line shows the brightness temperature cut-off, while the shaded region indicates velocity selection criteria. Note that the HIPASS data are unreliable in the vicinity of the Galactic emission near $0\,\mathrm{km\,s^{-1}}$. The HIPASS spectra were extracted spatially averaging a 3x3 box around the closest pixel to the specified coordinate. The column density map around this line of sight is shown in Fig. 4.2

Field Horizontal Branch (FHB) stars are valuable probes for distance determination work, for two primary reasons: (i) Their intrinsic luminosity means that sufficiently high signal-to-noise optical spectra can be obtained for distant halo FHB stars ($d \geq 20$ kpc), meaning they can act as useful and interesting discriminators of the various origin scenarios, and (ii) Being hot stars, their spectra are relatively free of intrinsic absorption features, making the detection and interpretation of the HVC absorption features relatively straightforward. Previous authors have also successfully employed RR Lyrae stars (van Woerden et al., 1999) or bright B-stars in the ultraviolet (Danly et al., 1993) and optical (Smoker et al., 2004).

Here we present a table of 430 FHB stars which align with H I gas at high velocities, and the associated H I spectra and moment maps. These stars are ideal for high-resolution optical spectroscopy and distance determinations. Section 4.2 gives the details about the selection of HVC distance probes from the HES FHB catalogue of Christlieb et al. (2005, hereafter C05). The catalogue of HVC distance probes is presented in Section 4.3. A brief conclusion is given in Section 4.4. The full catalogue plus H I spectra and summed intensity moment maps towards each star in the catalogue are presented in the online edition.

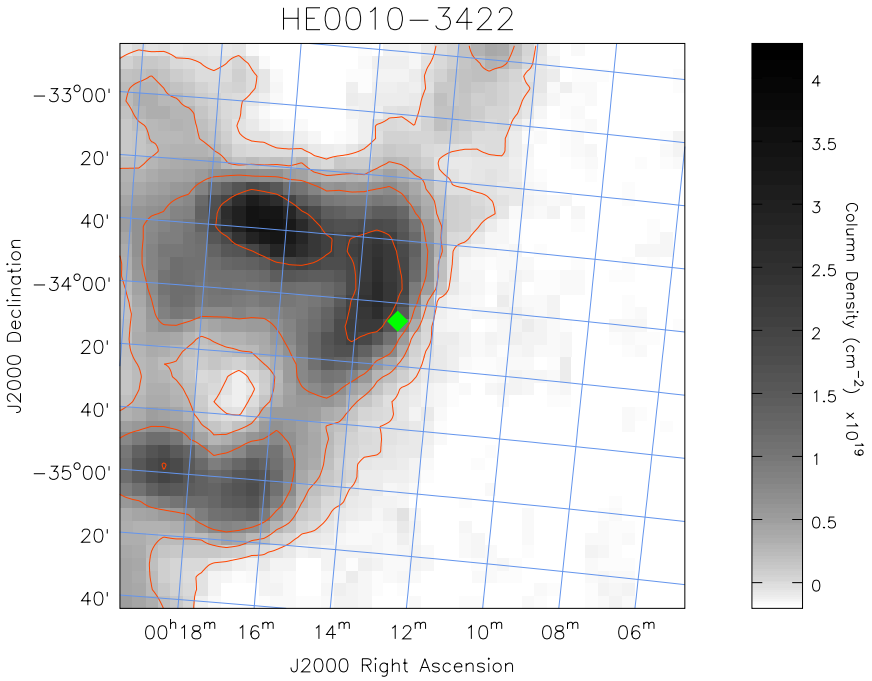


Figure 4.2: An example column density map of the region around the line of sight in Fig. 4.1. The stellar position is indicated by the green diamond. Neutral hydrogen contours are drawn in orange at 2.0×10^{18}, 5.0×10^{18}, 1.0×10^{19}, 2.5×10^{19}, 5.0×10^{19} and 1.0×10^{20}cm^{-2}

4.2 Stellar selection and Matching

We have taken as our input sample, the C05 catalogue of 8321 FHB stars selected from the Hamburg/ESO Survey, which has been shown to have contamination from high-gravity main-sequence stars of $< 16\%$. For each stellar line of sight, an H I spectrum was extracted from the H I Parkes[2] All-Sky Survey (HIPASS; Barnes et al., 2001; Putman et al., 2002, hereafter P02) and any emission above a threshold of 0.15 Jy/Beam at high velocities ($|v_{\rm LSR}| \geq 90\,{\rm km\,s^{-1}}$) identified. This threshold corresponds to a brightness temperature threshold of 0.12 K for the Parkes Multibeam used for the HIPASS survey (e.g. Putman et al., 2003b) and is set by the level at which Ca II absorption lines are expected to be detectable in optical spectra (see Sec 4.2.6). All lines-of-sight meeting these criteria were then screened by eye to reject obvious problems. In all cases, these were due to the wings of emission features well below the $|v_{\rm LSR}| \geq 90\,{\rm km\,s^{-1}}$ limit extending outside this range above the level of 0.12 K. H I moment maps were created from the HIPASS data cubes around each line of sight, and the positions were matched against several HVC catalogues.

[2]The Parkes telescope is part of the Australia Telescope which is funded by the Commonwealth of Australia for operation as a National Facility managed by CSIRO.

4.2.1 The Hamburg/ESO Survey

We briefly review the salient points of the HES, while a fuller description of the survey and its stellar products may be found elsewhere (e.g. Wisotzki et al., 1996, C05). Originally a survey for bright quasars, the HES is an objective prism survey which covers a large fraction of the southern extra-galactic sky ($\delta < +2.5^\circ; |b| \gtrsim 30^\circ$) to a limiting magnitude of $B \lesssim 18.0$. As well as finding quasars, it has also become a valuable resource for identifying many different classes of interesting stars; e.g. Carbon stars (Christlieb et al., 2001a), White Dwarfs (Christlieb et al., 2001b), metal-poor halo stars (e.g. Christlieb, 2003) and FHB stars (C05). Selection of the FHB stars was made first on the basis of a colour cut. The second step involved automated selection criteria based on the summed Balmer line equivalent widths and the Strömgren c_1 index. This process resulted in 8321 stars, which have been shown to have a contamination from, e.g. higher surface gravity A-stars, of $< 16\%$. See C05 for further details.

4.2.2 Spectrum Extraction

To identify stars aligned with HVCs, HIPASS H I spectra for all stellar lines-of-sight were first extracted from the HIPASS HVC cubes. These cubes were produced from the HIPASS data by P02 using the *MINMED5* bandpass calibration, which recovers much of the extended emission lost in the original HIPASS bandpass calibration; since the survey was originally designed for point sources, this loss was not a critical issue. Nevertheless, when emission extends spatially to fill more than $\sim 6^\circ$ of a full HIPASS 8° declination scan, the calibration will not be accurate e.g. for data close to the Galactic plane (see Putman et al., 2003b, for details).

The *miriad* task *mbspect* was used to extract the spectra, averaging spatially over a 3x3 pixel box (approximately the HIPASS beam size of 15.5′; HIPASS pixels are 4′). *mbspect* uses the nearest pixel to the specified coordinate. All spectra containing emission above the level of $0.12\,\mathrm{K}$ at velocities $|v_{\mathrm{LSR}}| \geq 90\,\mathrm{km\,s^{-1}}$ were automatically flagged. An example of such a spectrum is shown[3] in Fig. 4.1. We plot only the velocity range $-500 - +500\,\mathrm{km\,s^{-1}}$ since this is the range occupied by nearly all Galactic HVCs[4]. The associated moment map is shown in Fig. 4.2 (see Section 4.2.3 for details).

To create the final FHB/HVC catalogue, the spectra for these 430 lines of sight were then visually inspected to reject obvious noise artefacts. In some cases, the peak flux was at an absolute velocity less than the enforced $90\,\mathrm{km\,s^{-1}}$ limit, while significant emission was still present outside this range. In these cases, stars were retained if the channel(s) outside the $90\,\mathrm{km\,s^{-1}}$ boundary had a flux comparable to the peak value. Fig. 4.3 shows an example of such a case. In these cases, the peak emission with $|v_{\mathrm{LSR}}| \geq 90\,\mathrm{km\,s^{-1}}$ was

[3]Similar figures are provided for all probes in Table A.1 in Appendix B.

[4]Note that Thilker et al. (2004) have found HVCs associated with M31 at velocities more negative than the $-500\,\mathrm{km\,s^{-1}}$ limit.

Region	l (deg)	b (deg)	$v_{\rm LSR}$ ($\rm km\,s^{-1}$)
1	—	$b \leq -70$	$-300 \leq v \leq 300$
2	$270 \leq l \leq 315$	$-70 \leq b \leq -20$	$70 \leq v \leq 400$
3	$315 \leq l \leq 345$	$-70 \leq b \leq -50$	$70 \leq v \leq 200$
4	$45 \leq l \leq 110$	$-70 \leq b \leq -60$	$-320 \leq v \leq -130$
5	$65 \leq l \leq 110$	$-60 \leq b \leq -48$	$-390 \leq v \leq -200$
6	$65 \leq l \leq 110$	$-48 \leq b \leq -33$	$-390 \leq v \leq -250$

Table 4.1: Lines-of-sight in these regions, with velocities consistent with the limits specified, are flagged as associated with the Magellanic Stream.

recorded.

During screening, it was noted that some spectra contained multiple high-velocity emission components. In cases where these were not immediately identifiable as the same cloud, a separate entry in Table A.1 was recorded. These multiple components were flagged in the catalogue and separate moment maps produced. Obviously, separate H I spectra are not required, although the spectra are repeated for completeness. In all but a few cases, these doubles are flagged as associated with the Magellanic Stream (see Section 4.2.4). HE 1008−0438 also aligns by chance with the galaxy HIPASS J1010-04. The star HE 0053−3740 was found to align with a Sculptor Group galaxy and was excluded. HE 0056−4043 shows a noise spike at $\sim -410\,\rm km\,s^{-1}$ which is evident in the HIPASS data cubes.

4.2.3 Moment Maps

In order to visualise the spatial locations of the stars with respect to the gas, summed-intensity moment maps of a region approximately $3^\circ \times 3^\circ$ centred around each probe were created. Moment maps were generated by summing the velocity channel containing the peak flux outside the $|v_{\rm LSR}| \geq 90\,\rm km\,s^{-1}$ boundary and the two adjacent channels. This summed width equates to 39.6 $\rm km\,s^{-1}$, which is approximately the 36 $\rm km\,s^{-1}$ median FWHM of the HIPASS HVCs (P02) (note, though, that this median is almost certainly an overestimate of the true value and a product of the coarse velocity resolution of the HIPASS data). Maps were converted to column densities using the relation $N(\rm H\,I) = 1.823 \times 10^{18} \int T_b dv$ (Dickey & Lockman, 1990). Onto these moment maps, contours were drawn at H I column densities of 2.0×10^{18}, 5.0×10^{18}, 1.0×10^{19}, 2.5×10^{19}, 5.0×10^{19} and 1.0×10^{20} $\rm cm^{-2}$. The positions of the FHB stars are marked by a green diamond in the centres of these images, one example of which is shown[5] in Fig. 4.2.

[5]Similar figures are provided for all probes in Table A.1 in Appendix B.

4.2.4 Cloud Matching and the Magellanic Stream

One of the most prominent features in the southern radio sky at 21 cm is the Magellanic Stream (MS). We wanted to differentiate the entries that probe gas possibly associated with the Stream, from those probing other HVCs. In this vein we follow the spatial and kinematic regions defined in Figs. 5 and 7 respectively of Putman et al. (2003b). Table 4.2.3 shows the regions we adopt as being associated with the Stream. Probes within these regions are flagged in the catalogue. Note that exact definitions of which clouds clouds are associated with the Stream are difficult and somewhat subjective — the definitions here should be considered as a guide only. Further, there is some overlap between the Stream as defined here and the Sculptor group of galaxies. Despite this attempted flagging, some of the CHVCs and semi-compact HVCs catalogued by P02 and de Heij et al. (2002b, hereafter D02) are also flagged as Stream-related. Since their origin has been proposed to be quite different from that of the large complexes, and given the imperfect nature of the MS flagging, these probes may prove quite interesting and are not excluded from Table A.1.

Using the HVC catalogues published by PO2, D02 and Wakker & van Woerden (1991, hereafter WvW91) we have attempted to identify which clouds are associated with each detection. From P02, we use both the tables of HVCs, plus their table of XHVCs — clouds which have emission at high velocities, but which clearly link to emission at lower deviation velocities[6]. Since clouds have arbitrary shapes, this is a difficult process.

In general, the optimal solution to the problem of associating stellar lines-of-sight with individual clouds would be to obtain component lists for all clouds in the desired catalogue (i.e. which pixels make up a particular cloud). Unfortunately, such lists are not available for the catalogues we searched, so another strategy was required.

From the tables of HVCs and XHVCs reported in P02, we took a position and angular size. Assuming a circular cloud, we found all clouds which encompass the stellar position. We then required that the velocity measured in the HIPASS spectrum and the velocity of the cloud differ by no more than the FWHM of the cloud. For the few cases where multiple clouds met these criteria, the data cubes were examined and it was immediately apparent which was the correct entry.

The D02 catalogue is very similar in structure; indeed, the same algorithm was used by P02 to create the HIPASS catalogue. The one exception is that D02 do not publish the size of individual clouds, based on the number of associated pixels, as do P02. They do, however, provide the major and minor axes of an ellipse which is fit to half the peak flux level. We used the major axis length to search a circular area around the reported cloud position. To avoid associating some clouds with large fractions of the sky (i.e. some clouds have major axes up to $\sim 165^{\circ}$), we limited the search radius to 10 deg. The same FWHM velocity criteria as above were also applied.

[6]Deviation velocity is the degree to which a velocity deviates from the maximum allowed by Galactic rotation in that direction (Wakker, 1991).

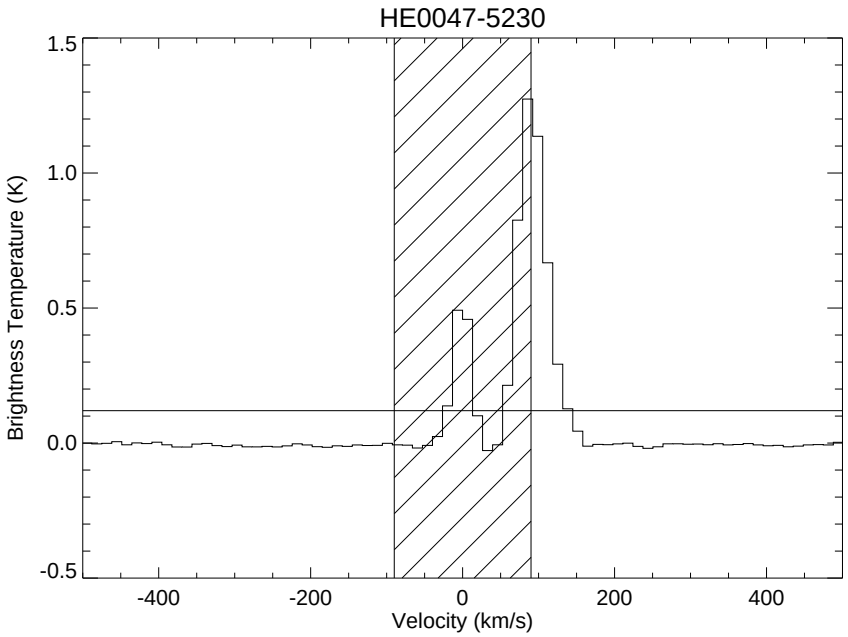


Figure 4.3: Example H I spectrum of a stellar line of sight with peak flux inside the $|v_{\rm LSR}| \geq 90\,{\rm km\,s^{-1}}$ boundary. Note the clean separation from the Galactic emission at low velocity.

For the clouds in the catalogue of WvW91 the same process was repeated. Since those authors do not tabulate the FWHM for individual clouds, we assumed a FWHM of $36\,{\rm km\,s^{-1}}$, based on the global properties of the HIPASS HVCs listed in Table 2 of P02.

4.2.5 Stellar Velocities

It will be difficult or impossible to detect HVC absorption features in high resolution optical spectra if the velocity of the gas and stellar radial velocity (RV) are too close. In this case, stellar absorption will dominate the spectrum and the HVC feature will be lost. As part of a separate program, we have obtained medium-resolution spectra of 18 stars in our catalogue using the double-beam spectrograph on the SSO 2.3 m telescope. An example of such a spectrum is shown in Fig. 4.4. Note the general lack of metal absorption lines, with the exception of the stellar Ca II K line at 3933.663 Å. From these spectra we obtained radial velocities by fitting Sersic profiles to the Hβ, Hγ and Hδ Balmer lines. Table 4.2.6 lists the average stellar RV corrected to the Local Standard of Rest (LSR) frame, along with the H I velocity and the absolute difference of the two. Clearly, the greater the difference between the stellar and HVC features, the easier a detection will be and we suggest that a velocity difference of greater than $\sim 50\,{\rm km\,s^{-1}}$ will be needed. Such observations must be of sufficient resolution (i.e. R = 40000 – 60000, corresponding to $\sim 7.5 - 5\,{\rm km\,s^{-1}}$ at Ca II K) to resolve the separation between the HVC, stellar and

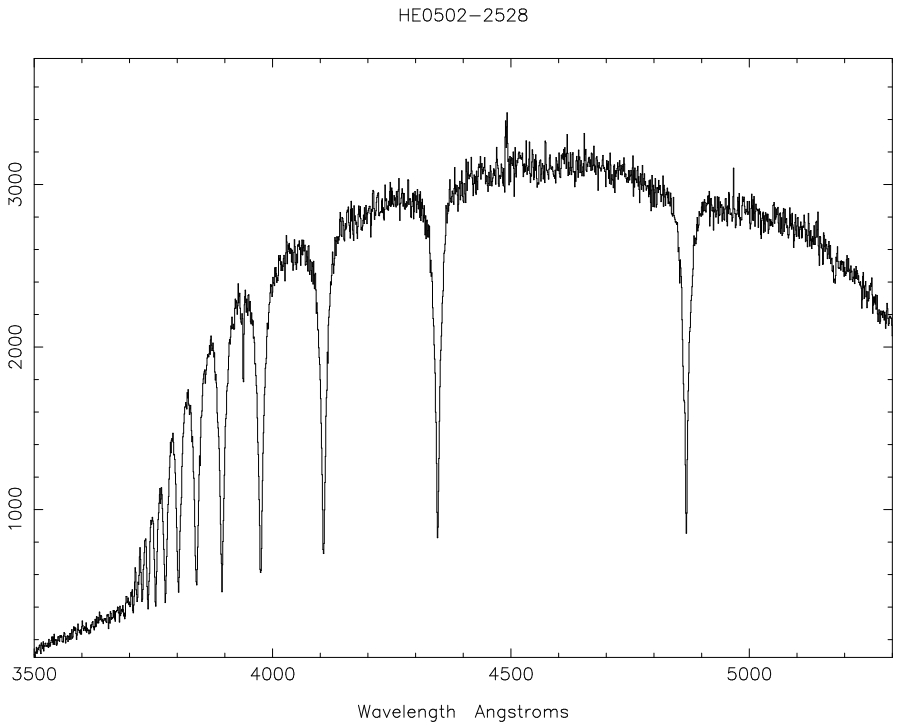


Figure 4.4: Medium resolution spectrum of the FHB star HE 0502−2528. Note the general lack of metal absorption lines, which could confuse the interpretation of any potential HVC.

disk absorption features.

We have performed a simple simulation to estimate, to first-order, the percentage of halo stars that are expected to have velocities within $50\,\mathrm{km\,s^{-1}}$ of an HVC. Stars in the halo are drawn from a population with a total dispersion of $\sigma \simeq 200\,\mathrm{km\,s^{-1}}$ (see Sec. 3.3). Assuming an isotropic distribution of velocities, a single projection (e.g. the line of sight component) will then follow a Gaussian distribution with $\sigma_{LOS} \simeq 200/\sqrt{3} \simeq 120\,\mathrm{km\,s^{-1}}$. We randomly generated stellar velocities according to such a distribution. For each of these velocities, we also generated a random HVC velocity using the HIPASS HVC velocity distribution (e.g. Fig. 10 of Putman et al., 2002). Comparing these two velocities, we find that they are within $50\,\mathrm{km\,s^{-1}}$ of each other $\sim 13\,\%$ of the time. It should be noted, however, that this is a global average; clearly HVCs with lower velocities will have, on average, a chance velocity alignment more often, while very high velocity HVCs will suffer such problems less than the average.

4.2.6 Optical Detections

In order to detect an absorption line in the optical, there must be a sufficient number of absorbing atoms along the line of sight. Assuming an optically thin gas, Savage & Sem-

HE name	Radial Velocity ($\mathrm{km\,s^{-1}}$)	$v_{\rm LSR}$ ($\mathrm{km\,s^{-1}}$)	v_{diff} ($\mathrm{km\,s^{-1}}$)
HE 0003−5248	+058	+112	−054
HE 0046−3255	−012	+112	−124
HE 0056−3330	+113	−191	+304
HE 0157−5126	+047	+165	−118
HE 0420−5405	+070	+099	−029
HE 0502−2528	+370	+099	+271
HE 0504−2509	+066	+112	−046
HE 0506−2530	+204	+125	+079
HE 0932−0404	+257	+152	+105
HE 1004−0516	+219	+112	+107
HE 1027−2625	+261	+218	+043
HE 1045−2550	+125	+178	−053
HE 1318−2555	−035	+112	−147
HE 1323−2511	+182	+112	+070
HE 2155−2243	−098	−139	+041
HE 2200−2222	+141	−099	+240
HE 2242−6106	+094	+112	−018
HE 2304−3858	−038	−112	+074

Table 4.2: Stellar velocity comparisons for stars with medium resolution optical observations. Listed are the LSR stellar and H I velocities. A minimum separation of 50 $\mathrm{km\,s^{-1}}$ is suggested for a star to be useful for high resolution optical observations. Stellar radial velocities have been corrected to the LSR frame using the IRAF task *rvcorrect*, which assumes a solar motion of 20 $\mathrm{km\,s^{-1}}$ towards α = 18:00:00, δ = 30:00:00 (B1900).

bach (1996) give a relation between the column density N and the equivalent width of the absorption line W_λ. Since an H I column density can be measured from the HIPASS spectra by integrating over the HVC emission line, if the ratio of Ca II ions to H I atoms, $N(\mathrm{Ca\ II})/N(\mathrm{H\ I})$ is known, we can predict the equivalent width of the Ca II absorption features. It should be noted that an accurate determination of $N(\mathrm{Ca\ II})/N(\mathrm{H\ I})$is important, since this quantity can vary by up to 2 orders of magnitude from cloud to cloud (Wakker, 2001)[7]. For the lowest column density features in Table A.1, the expected equivalent width is ~ 20 mÅ, which should be detectable using large telescopes in a reasonable amount of time.

[7]However Wakker & Mathis (2000) show a relation between the Ca II abundance and column density with much less variation at a given column density.

4.3 The Catalogue

After these selection criteria were applied, we had a total of 430 stars probing sufficiently dense HVC gas. These stars are listed in Table A.1. The table contains the following columns: Column (1) gives the running number. Column (2) indicates the HES name of the star. Multiple components in a single line of sight have separate entries and are numbered. Columns (3) and (4) list the right ascension and declination (J2000) of the stellar probe, with Columns (5) and (6) showing the corresponding Galactic coordinates of the star. The large gap between RA $\sim$ 13:30 – 21:30 is due to the HES avoidance of the Galactic plane. Column (7) gives the HES B magnitude, which is accurate to $\sim 0.2 - 0.3$ mag (Wisotzki et al., 2000). The distance to the star (in kpc) is shown in column (8) and is taken directly from C05. Briefly, the distance was derived by those authors by estimating the absolute magnitude $M_{\rm v}$ from the $B-V$ colour. A metallicity correction was applied based on an assumed average halo metallicity and the distance moduli computed. For any higher gravity A-star contaminants, this distance will be incorrect. The peak brightness temperature (in K) is shown in column (9); P02 quote a 5σ sensitivity of 0.04 K. Column (10) shows the H I column density along the line of sight, which was measured from the moment maps. The LSR velocity ($\rm km\,s^{-1}$) of the peak H I emission outside the $|v_{\rm LSR}| \geq 90\,\rm km\,s^{-1}$ zone is given in column (11). This is the velocity of the HIPASS channel containing the peak flux — no attempt at profile fitting was made. The HIPASS velocity resolution is 26.4 $\rm km\,s^{-1}$ after Hanning smoothing. An asterisk in column (12) indicates an association with the Magellanic Stream, (see Sec. 4.2.4). The matches to the P02 HVCs and XHVCs, the WvW91 HVCs and the D02 HVCs are given in columns (13), (14), (15) and (16) respectively. For the P02 and D02 catalogues, the original nomenclature classifying the cloud (e.g. HVC, CHVC, HVC: etc) has been retained.

4.4 Conclusion

We have presented a catalogue of FHB stars, selected from the Hamburg/ESO Survey, that fortuitously align with high-velocity H I gas. These stars should make ideal candidates for echelle spectroscopy. Such observations offer the possibility of detecting the doppler-shifted absorption features in the spectrum, placing an upper limit on the distance to the HVC. In a similar fashion, non-detections place lower limits on the distance. Distance limits will help to resolve the question of the origins of HVCs and their role in the formation and evolution of Galaxies.

Acknowledgements
The financial support of the Australian Research Council, through its Discovery Project and Linkage International Award schemes, is gratefully acknowledged. We thank W. Butler Burton, the scientific editor responsible for the manuscript at The Astrophysical Journal. His extensive and insightful comments greatly improved the manuscript .

CHAPTER 5

THE GALACTIC NATURE OF HIGH VELOCITY CLOUD COMPLEX WB

Summary
This chapter has been published as Thom, C., Putman, M. E., Gibson, B. K., Christlieb, N., Flynn, C., Beers, T. C., Wilhelm, R., & Lee, Y. S., 2006, ApJ, 638, L97. It has been modified in style only for presentation here. Copyright for the published article resides with the American Astronomical Society and it is reproduced here with permission. In this chapter we present the results of echelle spectroscopy of two stars, selected from the FHB/HVC catalogue presented in the previous chapter. We have detected absorption lines from the High Velocity Cloud complex WB in the spectrum of the star HE $1048+0231$. This detection sets an upper distance limit to the cloud of $8.8^{+2.3}_{-1.3}$ kpc. Non-detection (at $> 3\sigma$ confidence) in the star HE $1138-1303$ at 7.7 ± 0.2 kpc sets a probable lower limit. This distance bracket implies that complex WB has a probable Galactic or circum-Galactic origin.

5.1 Introduction

High-velocity clouds (HVCs) are clouds of neutral hydrogen (H I) gas with velocities that are inconsistent with a simple model of differential Galactic rotation. Since a kinematic distance cannot be derived, the exact location and nature of the HVCs has been the topic of much speculation. Determination of the distances to HVCs is vitally important, as such measurements can constrain their likely origins, and establish their physical parameters, many of which scale with distance.

The HVCs have been ascribed to many different origins, from local Galactic processes, to distant proto-galaxies. Shapiro & Field (1976) were the first to suggest the existence of a Galactic Fountain, in which supernovae drive hot gas into the halo, which then condenses and returns to the disk (e.g. Bregman, 1980). Extra-Galactic origins have been discussed almost since the discovery of HVCs (Oort, 1966). Blitz et al. (1999) have inspired vigorous debate by reviving and further refining this scenario, noting that it naturally explains the kinematics of clouds towards the bary- and anti-Barycentre of the Local Group. They suggested that these distant HVCs could be dark-matter dominated objects, which some

have claimed might be the solution to the "satellite problem" of Cold Dark Matter simulations (namely, that many more dark matter haloes are predicted to exist than satellite galaxies observed, e.g. Klypin et al., 1999).

Despite many years of effort, few HVCs have been detected in absorption against stellar probes. Of the traditional complexes, only M and A have been detected (Danly et al., 1993; van Woerden et al., 1999). Several other smaller clouds have also been detected in the spectra of background stars (e.g. Bates et al., 1990; Sembach et al., 1991). Wakker (2001) provides a much more comprehensive summary.

Wannier et al. (1972) were the first to report on the positive velocity clouds in the third and fourth Galactic quadrants. Fainter than the traditional negative velocity complexes such as A and C, they were divided into four separate complexes WA – WD (Wakker & van Woerden, 1991, hereafter WvW91). These complexes span a wide range of position and velocity space, comprising a total of 64 clouds in the WvW91 catalogue, with mostly moderate deviation velocities[1]. complex WB ($l = 225 - 265°$; $b = 0 - 60°$) is composed of 29 separate clouds, with a total H I mass M(H I) $= 0.236\, S\, d^2 \sim 6.5 \times 10^3\, d^2\, \mathrm{M}_\odot$, where S is the integrated flux (in Jy Beam^{-1}) and d is the distance (in kpc). Robertson et al. (1991) have observed the Wannier Clouds in absorption towards the Seyfert galaxy PKS 0837–12. Along this line of sight they derive a $N(\mathrm{Ca\ II})/N(\mathrm{H\ I})$ ratio of 160×10^{-9}. Using a higher resolution H I spectrum, Wakker (2001) revised this value upwards to 280×10^{-9}. Both sets of authors note the anomalously high calcium abundance (one of the highest measured for any HVC), while Robertson et al. concluded that a distance is necessary to discern between the various possible explanations they offered.

The Wannier clouds, along with the extreme positive velocity clouds (population EP) lie in the direction of the Local Group anti-Barycentre. They are explicitly included in the Blitz et al. (1999) scenario as being very distant and undergoing infall towards the Local Group Barycentre. Thus a confirmed upper limit on the distance would stand in opposition to this suggestion and may have broader consequences for the HVCs as a whole.

5.2 Observations and Data

As part of a program to bracket the distances to many HVCs, we have obtained echelle spectra of two stars: HE $1048 + 0231$ (which is aligned with WW 35) and HE $1138 - 1303$ (WW 62). Both stars were drawn from our catalogue of Field Horizontal Branch stars aligned with HVC gas (Thom et al., 2005); Fig. 5.1 shows their alignment with the HVC gas. Basic information for both lines of sight is listed in Table 5.1. Results for other targets in this program will be reported in a future paper.

The stars HE $1048 + 0231$ and HE $1138 - 1303$ were observed in excellent conditions on 2005 April 01 and 2005 March 31 respectively, using the MIKE spectrograph (Bernstein

[1]Deviation velocity is the amount by which a velocity deviates from allowed Galactic rotation velocities (Wakker, 1991).

	HE $1048+0231$	HE $1138-1303$
Stellar properties		
RA,DEC (J2000)	10:50:52.5 +02:15:19	11:41:14.8 −13:20:17
(l,b) (deg)	(248.517, +51.911)	(277.905, +46.098)
Magnitude [V_0, $(B-V)_0$]	16.51 ± 0.03; 0.00	14.87 ± 0.01; 0.40
Distance (kpc)	$8.8^{+2.3}_{-1.3}$	7.7 ± 0.2
Exp time (s)	10×1800	3×1800
Signal-to-noise (pix^{-1})	60	90
HVC properties		
N(H I) ($\times 10^{19}$ cm^{-2})	1.64 ± 0.31	1.73 ± 0.33
v_{LSR} (km s^{-1})	96	110
W_λ (mÅ):		
Ca II K (order 90)	116.2 ± 4.6	$\sigma(W_\lambda) = 3.4$
Ca II K (order 91)	112.9 ± 4.1	$\sigma(W_\lambda) = 3.9$
Ca II H	69.5 ± 7.2	$\sigma(W_\lambda) = 3.3$
Na I D_1	31.0 ± 7.0	$\sigma(W_\lambda) = 4.4$
Na I D_2	51.3 ± 7.7	$\sigma(W_\lambda) = 5.0$

Table 5.1: Magnitudes have been corrected for dust extinction using the maps of Schlegel et al. (1998). Distance errors are computed based on the variation of atmospheric parameters (obtained from photometric errors).

et al., 2003) mounted on the Magellan Clay 6.5ṁ telescope. Spectra covering the range 3350 – 9500 Å with resolving power (as measured from arc lines) R $= 40,000$ at 4000 Å and R $= 31,000$ at 5900 Å were obtained. The data were reduced using the MIKE *redux* package[2] and corrected from a heliocentric to Local Standard of Rest (LSR) frame for comparison with H I emission data.

H I emission data were obtained from two sources. First we used the H I spectra presented in Thom et al. (2005), which was taken from the H I Parkes All-Sky Survey. These data were reduced in such a way as to be sensitive to extended emission (Putman et al., 2003b). Secondly, to estimate the column density along the line of sight, we obtained higher velocity resolution (but poorer spatial resolution) data from the Leiden/Argentine/Bonn (LAB) survey (Kalberla et al., 2005).

Accurate UBV photometry was obtained with the WIYN 0.9 m telescope between 2005 November 20 – 22, with Landolt standards obtained at the same time. The data were reduced in the usual fashion using *IRAF* and aperture photometry was performed. The results are listed in Table 5.1.

[2]See http://web.mit.edu/˜burles/www/MIKE/

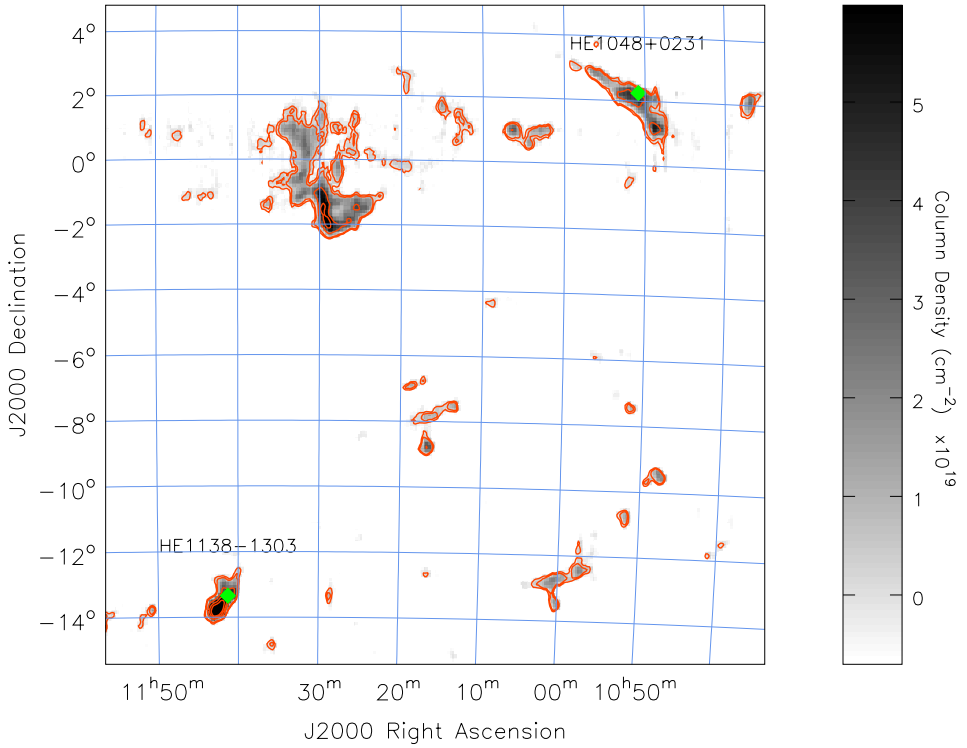


Figure 5.1: HIPASS column density map showing region around both sight lines (not the whole of complex WB). The labelled green diamonds indicate the positions of the stars. Contours are drawn at 8.0×10^{18}, 1.0×10^{19}, 2.0×10^{19} and 3.0×10^{19} cm^{-2}.

5.3 Results

5.3.1 HE1048+0231

In the spectrum of HE $1048 + 0231$ we detect a clear signature of absorption, shown in Fig. 5.2 (left panel). We plot the optical absorption and H I emission spectra aligned in velocity space. Both lines of the Na I doublet, the Ca II H and K lines, and the HIPASS and LAB H I spectra are shown. Note that two separate Ca II K spectra are shown, since this line falls onto two adjacent echelle orders, allowing us to confirm in one order what is seen in the other. Significant HVC absorption ($> 3\sigma$) was detected in all of these lines. Since the same absorption structure is seen at the same velocity of several different species, we can reject the possibility that these are intrinsic stellar features. The shaded region indicates the boundary of lower velocities ($|v_{\rm LSR}| \leq 90\,{\rm km\,s^{-1}}$) where HIPASS data are unreliable, while the vertical line shows the HVC velocity ($|v_{\rm LSR}| = 96\,{\rm km\,s^{-1}}$).

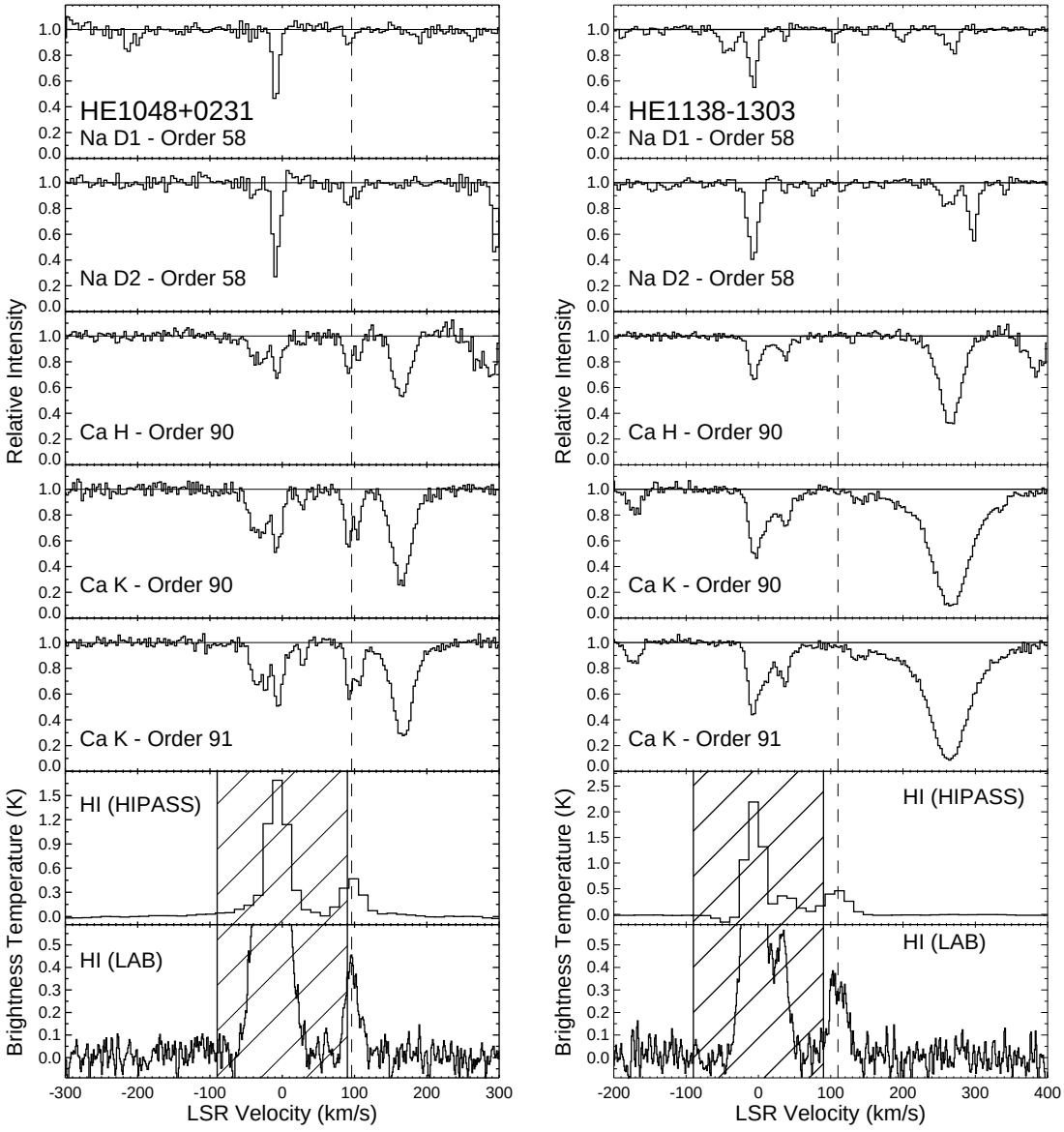


Figure 5.2: Optical and radio spectra along the line of sight towards HE $1048+0231$ (left panel) and HE $1138-1303$ (right panel). For HE $1048+0231$, both Ca II lines, and at least one Na I line, show the same absorption structure. The large absorption line at $\sim 170\,\mathrm{km\,s^{-1}}$ is the intrinsic stellar Ca II line, while the complex absorption near $0\,\mathrm{km\,s^{-1}}$ is due to local gas. For HE $1138-1303$, no such HVC absorption is present; the absorption line at $\sim 140\,\mathrm{km\,s^{-1}}$ near Ca II K is an intrinsic Ti II line. The shaded region in the H I spectra show the limit of low velocity gas; below this the HIPASS data are expected to be unreliable. The dashed vertical line is drawn at the velocity of the HVC, as measured in the LAB spectrum (see § 5.3.1).

Equivalent widths (EWs) and errors were derived following the method outlined in Sembach & Savage (1992, hereafter SS92). Legendre polynomials (order $2-5$) were fit to the local continuum regions ($|v_{\rm LSR}| < 1000\,{\rm km\,s^{-1}}$), with an F-test determining the appropriate polynomial order. EWs were measured by direct integration of the normalised spectra in the range $78-115\,{\rm km\,s^{-1}}$, as determined from the Ca II K absorption. EW errors due to both intensity variations and continuum placement were added in quadrature[3]. The results are listed in Table 5.1. Note that the EWs of the Ca II K and Ca II H are in the expected $\sim 2:1$ ratio (at the limit of the range permitted by the errors), as is the EW ratio of Na I D_2 to Na I D_1.

In order to disentangle the complex absorption structure, multiple Gaussians were fit to the HVC absorption features. Averaging over the 5 separate spectral regions, we determined line centres of 91.5 and 105.2 $\rm km\,s^{-1}$. A multi-component Gaussian decomposition was attempted for the HVC emission seen in the LAB spectrum, but the data did not support more than a single component, c entered at $96\,{\rm km\,s^{-1}}$. We conclude that beam smearing is a significant problem — the H I data have a spatial resolution of 40′(Kalberla et al., 2005). The HIPASS data, while having higher spatial resolution, have a much coarser velocity sampling, and were no help in this regard. This multiple absorption is indicative of either two distinct, spatially aligned clouds, or two components of the same cloud with a large kinematic separation. Higher resolution data are required to fully disentangle the possibilities.

Averaging over the two Ca II K measurements, we obtained N(Ca II)= $1.32 \pm 0.05 \times 10^{12}$ cm^{-2}, assuming a linear relation between equivalent width and column density (e.g. Savage & Sembach, 1996). The corresponding total H I column density (from the LAB data) is N(H I)= $1.64 \pm 0.31 \times 10^{19}$ cm^{-2}, where we have again assumed the optically thin case (since the H I brightness temperature is low, this assumption is valid; Dickey & Lockman, 1990). Combining these two values yields a Ca II to H I ratio of N(Ca II)/N(H I)= $81 \pm 16 \times 10^{-9}$. The solar Ca II abundance is $A_\odot = 2.2 \times 10^{-6}$ (Anders & Grevesse, 1989), yielding an abundance of 0.04 solar. Note that ionisation effects (which are difficult to estimate) have not been taken into account.

We attempted to confirm the low surface gravity nature of HE $1048+0231$ using the method of Wilhelm et al. (1999a). We derived stellar parameters in the range $T_{\rm eff} = 9350-9750$ K, $\log g = 3.5-4.25$, with an associated distance $d = 8.8^{+2.3}_{-1.3}$ kpc. Note that these values place HE $1048+0231$ on the main-sequence, with a colour consistent with spectral type A0. The uncertainty in $\log g$ (and hence the distance) is due mainly to the degeneracy of $U-B$ in this temperature range.

[3] Full details are given in Sec. 6.2.3.

5.3.2 HE1138−1303

The star HE $1138-1303$ is aligned with cloud WW 62. While not originally classified as part of complex WB, its position and velocity strongly suggest an association. Note also that in this region, the complexes WA and WB inhabit similar parts of position and velocity space (c.f. Figs. 1j and 1k of WvW91). The interpretation of the optical spectrum of HE $1138-1303$ (Fig. 5.2, right panel) is less certain than that of HE $1048+0231$. The same methods as described above and in SS92 were applied, with the results given in Table 5.1. Integration was performed in the range $92-127\,\mathrm{km\,s^{-1}}$ (± 1.5 the Gaussian σ determined from the LAB spectrum). No significant absorption near Ca II H or K was detected. There is a single-pixel feature at the location of the Na I D_1 line which yields an EW of $W_\lambda(\text{Na I } D_1) = 9.3 \pm 4.4\,\text{mÅ}$. Around Na I D_2 there is an unidentified absorption feature with $W_\lambda(\text{Na I } D_2) = 12.1 \pm 5.0\,\text{mÅ}$. Neither of these are statistically significant detections, nor are their locations correlated. Together with the lack of Ca II K absorption, we conclude that there is no evidence of HVC absorption towards HE $1138-1303$.

The interpretation of the lack of observed HVC absorption in the direction of HE 1138-1303 requires some caution (see comments by Wakker, 2001). We first assumed that beam-smearing would contribute a factor of two reduction in the H I column density along the sight line. This is not unreasonable, since HVCs exhibit column density variations on arcminute scales (e.g. Wakker & Schwarz, 1991). Further reductions in the expected equivalent width were applied to account for possible variations due to depletion ($2.5\times$) and ionisation ($2\times$). Taking these factors into account, we would then expect to observe a Ca II K EW of $\sim 12\,\text{mÅ}$. The measured error in these orders is $\sim 3.4\,\text{mÅ}$, giving a ratio of $W_{\lambda,expected}/\sigma(W_\lambda) \sim 3.5$, i.e. we expect to see HVC absorption with at least 3σ confidence (or more, since it is unlikely that all the above factors would be perfectly correlated).

We also performed a stellar parameter analysis for HE $1138-1303$. The results suggested stellar parameters $T_{\text{eff}} = 6000\,\text{K}$, $\log g = 2.0$ (i.e. on the Horizontal Branch), at a distance of $\sim 7.7 \pm 0.2\,\text{kpc}$. These parameters are near the limits of the models, so the errors are likely to be somewhat underestimated.

5.4 Discussion

The upper distance limit we obtain places WB firmly inside the halo of the Milky Way. The non-detection towards HE $1138-1303$ sets a probable lower limit. Although a scenario in which the two clouds are physically disjoint is not excluded, it is unlikely given the location and kinematics of the gas. A distance of $7.7\,\text{kpc} < \text{d} < 8.8\,\text{kpc}$ implies a total H I mass of $3.8\times10^5\,\text{M}_\odot < \text{M}_{\text{H I}} < 4.9\times10^5\,\text{M}_\odot$ for the entire complex. We measured a Ca II abundance $N(\text{Ca II})/N(\text{H I}) = 81 \pm 16 \times 10^{-9}\,\text{cm}^{-2}$ (~ 0.04 solar) which is about a factor of four less than that seen towards PKS 0837–120 (280×10^{-9}; Wakker, 2001), $\sim 35^\circ$ away from HE $1048+0231$.

Since the H I data have poor spatial resolution (in the case of the LAB) and poor velocity resolution (HIPASS), we cannot resolve individual cloud structures; the H I column density estimates are likely to be accurate only to a factor of two. While the broad characteristics of the H I and optical data match, we cannot resolve any condensations within the cloud, which are suggested by the multiple absorption components seen in the optical data. Higher resolution interferometric or large single-dish data (e.g. ALFA at Arecibo), with good velocity resolution, are thus crucial.

In the Galactic rest frame, the measured velocity of complex WB ($96\,\mathrm{km\,s^{-1}}$) implies that the complex is in-falling with $v_{\mathrm{GSR}} = -30\,\mathrm{km\,s^{-1}}$. A maximum distance of 9 kpc places complex WB 7 kpc above the disk of the Milky Way, some 12 kpc from the Galactic centre. Both fountain and infalling gas interpretations are consistent with the data. Under an infall scenario, the anomalously high $N(\mathrm{Ca\ II})/N(\mathrm{H\ I})$ measurement might be explained in terms of low depletion due to low dust content or hydrogen ionisation (which has not been taken into account here). If the gas is closer to the disk, then complex WB may be fountain gas returning to the disk. The Ca II abundance is not implausible since Ca II does not accurately trace the total gas metallicity, although a more accurate metallicity estimate would be very helpful for this discussion.

The distance bracket towards complex WB is an important step towards the final goal of determining the distances to a large sample of High Velocity Clouds. It is one of only a few upper distance limits to HVCs, and the first direct limit towards a cloud that was predicted to be very distant by the Blitz et al. (1999) model. Our results add to the growing body of evidence that the High Velocity Clouds are much more likely to belong to a Galactic or circum-Galactic population, rather than a distant, extra-Galactic one.

Acknowledgements
We are grateful to Rebecca Bernstein, Ian Thompson and Steve Shectman for help with the MIKE spectrograph. We thank Scott Burles and Jason Prochaska for help with the MIKE redux package. Thanks to Peter Kalberla for providing the LAB survey data before publication. Nathan DeLee participated in the WIYN observations, for which we are grateful. We would like to thank Tuorla Observatory for its support, and acknowledges travel support from the ANSTO AMRF Programme. The financial support of the Australian Research Council is greatly appreciated. TCB acknowledges partial support NSF grants AST 04-06784 and PHY 02-16783.

CHAPTER 6

LOWER DISTANCE LIMITS TO HIGH VELOCITY CLOUDS

Summary
This chapter presents the results of echelle spectroscopy of 14 stars selected from our FHB/HVC catalogue (see Chapter 4). Unlike the previous chapter, none of these observations show evidence of HVC absorption features. We use this lack of absorption to set lower distance limits to several clouds.

6.1 Introduction

Having presented the results of an HVC detection in Chapter 5, we now turn our attention to the remaining Magellan data. We follow the same methodology as for the complex WB data presented in the previous chapter. A more detailed discussion of the techniques we employed is presented. The optical and radio observations and data are first described, along with the analysis procedures. We then summarise the pertinent information about all sightlines. Radio/Optical spectra are presented for all lines of sight. Interpretations of the sight lines are given in Section 6.4, grouped by cloud/complex where appropriate. A summary table is given. We conclude with a discussion of the results and their implications.

6.2 Observations and Data

We observed a total of 16 stars at high resolution with the Magellan telescope, two of which were presented in the previous chapter. The remaining 14 will be discussed here. These stars were chosen from our catalogue of FHB stars aligned with HVCs (Thom et al., 2005, hereafter T05cat; see also Chapter 4). The clouds with which the stars are aligned are given in Table 6.1; positions, magnitudes, radial velocities and distances for the stars are listed in Table 6.2. The distances to the stars were taken directly from (Christlieb et al., 2005). Under the assumption that photometric error in the HES magnitudes ($\sim 0.2 - 0.3$ mag) is the dominant source of error, the distances are accurate to $\sim 15\%$. This

HE name	P02	Complex	WvW91	D02
HE 0046−3255	HVC1550	MS	—	—
HE 0056−3330	HVC1292	EN	WW 561	CHVC?873
HE 0502−2528	:HVC648	—	—	CHVC786
HE 0504−2509	:HVC648	—	—	CHVC786
HE 0932−0404	HVC714	WA	WW 91	HVC809
HE 1004−0516	HVC777	WA	WW 91	HVC819
HE 1045−2550	HVC1105	MS/LA*	WW 163	CHVC866
HE 1125−3030	—	WD	WW 164	—
HE 1318−2555	XHVC135	WD*	—	—
HE 1319−3034	XHVC134	WD*	WW 154	—
HE 2155−2243	HVC283	—	—	CHVC:64
HE 2200−2222	HVC283	—	—	HVC45
HE 2304−3858	CHVC1976	MS	WW 548	—
HE 2340+0149	—	MS*	—	HVC322

Table 6.1: Alignment of stellar probes with various catalogued clouds. Complexes are those defined by WvW91. An "*" in this column indicates that this association has been made here (see below), but not indicated in the original catalogue, where applicable. The original nomenclature of the D02 and P02 catalogues has been retained. Note that HE 1045−2550 is associated with gas in the Leading Arm of the Magellanic Stream.

does not include systematic errors. More accurate photometry (with better understood errors, including systematics) is currently being sought.

6.2.1 Optical Data

Echelle Spectroscopy

High resolution echelle spectroscopy was obtained for all lines of sight with the Magellan Clay telescope and the Magellan Inamori Kyocera Echelle (MIKE) spectrograph (Bernstein et al., 2003) during two separate observing runs: 2004 September 28 – 30 and 2005 March 30 – April 01. Two instrument configurations were used. For the 2004 September run, and 2005 March 30, the $0.7'' \times 2'' \times 2$ slit pair was used. The separation of the two slits is $1''$. With the CCD binned $\times 2$ in the dispersion direction, we obtained spectra with a resolution of $\sim$ 40,000 at 4000 Å and $\sim$ 32,000 at 5900 Å. Targets were observed in pairs of exposures, with the star in the top slit for the first exposure, then in the bottom for the second. This "A-B" observing strategy allows a well defined sky spectrum (the seeing was $< 1.2''$ at all times for these four nights). Raw data were bias-subtracted, using a 128×128 overscan strip. Multiple flat field exposures of a rapidly rotating B star (for the blue side) or the quartz lamp with a diffuser slide (for the red arm) were combined. Bias correction, flat fielding, image pair combination and sky subtraction were accomplished

HE name	RA (J2000)	DEC (J2000)	l (deg)	b (deg)	Mag	S/N	RV ($\mathrm{km\,s^{-1}}$)	Dist (kpc)
HE 0046−3255	00:49:15.4	−32:39:35	307.68	−84.45	16.1	34	-003.7 ± 1.5	10.9
HE 0056−3330	00:59:14.6	−33:14:41	288.00	−83.66	16.2	50	$+138.9 \pm 1.2$	11.7
HE 0502−2528	05:04:58.1	−25:24:47	226.67	−33.77	16.5	40	$+442.9 \pm 1.2$	12.8
HE 0504−2509	05:07:00.6	−25:05:07	226.46	−33.23	15.3	100	$+083.7 \pm 1.5$	7.5
HE 0932−0404	09:34:56.9	−04:17:50	238.72	+33.14	14.9	70	$+270.2 \pm 0.9$	5.8
HE 1004−0516	10:07:17.1	−05:31:05	246.15	+38.63	14.8	80	$+246.4 \pm 0.4$	5.7
HE 1045−2550	10:47:56.3	−26:06:10	271.12	+29.03	14.3	90	$+155.4 \pm 2.8$	3.8
HE 1125−3030	11:27:38.6	−30:46:52	282.43	+28.73	16.7	40	$+230.8 \pm 2.8$	13.2
HE 1318−2555	13:21:28.0	−26:11:14	311.29	+36.20	14.5	50	-033.7 ± 1.7	4.9
HE 1319−3034	13:22:00.1	−30:50:08	310.63	+31.58	15.5	60	$+143.3 \pm 0.8$	7.0
HE 2155−2243	21:58:39.9	−22:29:29	029.92	−50.71	15.3	100	-105.2 ± 1.2	6.2
HE 2200−2222	22:02:54.8	−22:08:06	030.90	−51.55	16.4	65	$+126.9 \pm 1.3$	10.4
HE 2304−3858	23:07:26.3	−38:41:52	358.27	−65.42	16.4	70	-023.6 ± 1.7	9.8
HE 2340+0149	23:43:24.0	+02:06:30	090.97	−56.48	17.6	35	-336.7 ± 1.4	20.8

Table 6.2: Fundamental data for stars observed with Magellan. Magnitudes are HES survey magnitudes, taken from (Christlieb et al., 2005); distances are from the same source and are based on HES magnitudes. S/N indicates the signal-to-noise ratio in the continuum about the Ca II K line in the Magellan data. Radial velocities are in a *heliocentric* frame and are measured from the positions of metal lines in Magellan spectra (in most cases more than 20 lines have been used). RV errors are 1σ.

using a Fortran programme written by Steve Shectman. The resulting images were extracted using *iraf* in the usual way. Spectra were corrected to the Local Standard of Rest (LSR) reference frame.

For the nights of 2005 March 31 – April 01, stars were observed through a single $0.7'' \times 5''$ slit. As for previous data, the CCD was binned $\times 2$ in the dispersion direction. These data were reduced using the MIKE *redux* idl package[1]. This package is a full reduction pipeline, producing wavelength calibrated final spectra suitable for analysis. These data were also corrected into the LSR frame for comparison with radio data.

6.2.2 Radio Data

H I spectra were obtained from several locations. In the first instance, HIPASS spectra were available for all sightlines from our catalogue (T05cat); it was on this basis that stars were identified as aligned with HVC gas. The HIPASS data have good spatial resolution (14.3′) but poor velocity resolution ($26.4\,\mathrm{km\,s^{-1}}$) (Putman et al., 2003b, hereafter P03). For most lines of sight, spectra were also available from the all-sky LAB survey (Kalberla et al., 2005). The LAB survey data have much better velocity resolution ($1.9\,\mathrm{km\,s^{-1}}$), but a much coarser spatial resolution ($35' - 40'$). A few of the sightlines were towards the Compact HVCs studied by Westmeier (2003) and these higher resolution (9′; $2\,\mathrm{km\,s^{-1}}$) data were made available.

The first step in characterising the HVC features (or lack thereof) in the optical is to

[1] See http://web.mit.edu/~burles/www/MIKE/

HE name	Centre $\mathrm{km\,s^{-1}}$	FWHM $\mathrm{km\,s^{-1}}$	σ $\mathrm{km\,s^{-1}}$	Min $\mathrm{km\,s^{-1}}$	Max $\mathrm{km\,s^{-1}}$	N(H I) $\mathrm{cm^{-2}}$	Source	Notes
HE 0046−3255	111.0	33.5	14.3	89.6	132.4	2.66 ± 0.36	LAB	
HE 0056−3330	−191.0	20.0	8.5	−203.7	−178.3	2.20 ± 0.01	HIPASS	#1
HE 0502−2528	102.0	17.1	7.3	91.1	112.9	0.75 ± 0.02	LAB	
HE 0504−2509	116.6	16.6	7.0	106.0	127.1	1.35 ± 0.62	Effelsberg	
HE 0932−0404	158.1	25.1	10.7	142.1	174.1	1.17 ± 0.27	LAB	
HE 1004−0516	115.6	25.4	10.8	99.4	131.8	2.00 ± 0.30	LAB	
HE 1045−2550	184.9	22.4	9.5	170.6	199.2	3.62 ± 0.17	LAB	
	183.5	18.2	7.7	171.9	195.1	4.93 ± 0.51	Effelsberg	
HE 1125−3030	109.3	31.8	13.5	89.0	129.6	1.56 ± 0.33	LAB	
HE 1318−2555	107.0	21.1	9.0	93.6	120.4	0.87 ± 0.17	LAB	
HE 1319−3034	91.8	38.1	13.5	80.0	112.1	1.86 ± 0.26	LAB	#2
HE 2155−2243	−128.3	37.4	15.9	−152.1	−104.5	3.48 ± 0.48	LAB	#3
	−137.8	32.9	14.0	−158.8	−116.8	7.77 ± 1.10	Effelsberg	
HE 2200−2222	−98.4	33.2	14.1	−119.5	−77.3	2.25 ± 0.39	LAB	#4
HE 2304−3858	−112.1	28.1	11.9	−130.0	−94.2	1.39 ± 0.25	LAB	#3
HE 2340+0149	−312.9	27.8	11.8	−330.6	−295.2	1.74 ± 0.32	LAB	

Table 6.3: Summary of available H I data for all lines of sight. *Notes:* #1 — A FWHM of $20\,\mathrm{km\,s^{-1}}$ was chosen arbitrarily, based on a $\sim 7000\,\mathrm{K}$ temperature, since the HIPASS data do not adequately resolve the emission. #2 — Minimum limit chosen in order to avoid contamination with Galactic emission. #3 — Profile would probably support more than a single component Gaussian model. #4 — This line of sight is just outside the bounds of the Effelsberg data. $N(\mathrm{H\,I})$ errors are 1σ statistical errors only, and do not account for systematic effects such as beam smearing or H I fine scale structure; column densities are probably only accurate to a factor of 2.

determine the properties of the HVC emission from the H I data. To determine the line centre, width and limits of integration, we fit a single Gaussian component to the H I spectrum using the idl *xgaussfit* routine. The limits of the line region were chosen to be $\pm 1.5\sigma$ from the line centre. These limits include all significant H I emission. H I column densities were then obtained by directly integrating the H I spectra between the determined limits, and applying the well-known relation

$$N(\mathrm{H\,I}) = 1.823 \times 10^{18} \int T_b dv \tag{6.1}$$

assuming that all profiles are optically thin (e.g. Dickey & Lockman, 1990). Table 6.3 summarises these results.

6.2.3 Equivalent Widths

In order to calculate the equivalent widths of detected absorption lines, and detection limits for non-detections, we applied the method described in Sembach & Savage (1992, hereafter SS92; see their Appendix A). A qualitative description is given here, while full details of the techniques are described elsewhere (Sembach & Savage, 1992; Press et al., 1992; Bevington & Robinson, 2003).

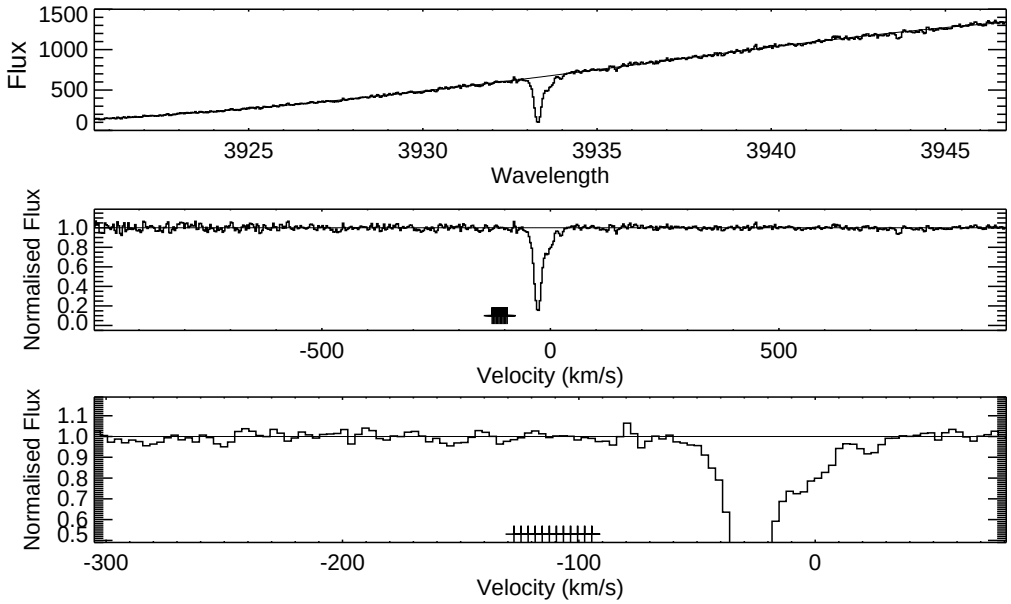


Figure 6.1: Example of the continuum fitting process, to the spectrum of HE 2304−3858. The top panel shows the original data, with the continuum fit. The middle panel shows the same spectral region (now in $\mathrm{km\,s^{-1}}$), normalised by the continuum fit. The bottom panel shows a region $\pm 175\,\mathrm{km\,s^{-1}}$ about the HVC position. The "+" symbols indicate the expected location of the HVC absorption line.

After the optical data were reduced and corrected into the desired reference frame (in this case, LSR), we considered a small spectral region — typically $\pm 1000\,\mathrm{km\,s^{-1}}$ — around the Ca II H and K and Na I $D_{1,2}$ lines. We selected line-free regions of continuum by eye, and fit Legendre polynomials to the continuum region. We used the idl function *lmfit* for this process, which performs a Levenberg-Marquart minimisation to determine the appropriate polynomial. If the data were reduced using the idl *redux* pipeline, the errors computed by the pipeline were supplied to the *lmfit* routine, otherwise we assumed simple Poisson statistics for the errors. The continuum fit was performed for all polynomial orders in the range 2 – 5; the computed χ^2 values were then used in an F-test to determine successively whether the next highest order was statistically significant (i.e. whether the coefficient of the newly added polynomial term differs from zero). With the continuum determined, we then normalised the spectrum, and integrated over the line region determined from the H I data. In some cases, these equivalent widths were adversely affected by the wings of another line (e.g. a Balmer line in the case of Ca II H, or an intrinsic stellar line). Fig. 6.1 illustrates this process. The top panel shows the original spectrum, with the continuum fit overlayed. The middle panel shows the resulting normalised spectrum. The bottom panel shows a region $\pm 175\,\mathrm{km\,s^{-1}}$ around the expected position of the line.

To calculate the errors in the equivalent widths, we added error estimates from intensity fluctuations and continuum placement errors in quadrature. The intensity errors were ob-

HE name	Ca II K (order 90)	Ca II K (order 91)	Ca II H	Na I D_1	Na I D_2
HE 0046−3255	5.3	5.2	9.4	6.0	5.6
HE 0056−3330	5.4	3.3	4.6	4.3	4.5
HE 0502−2528	4.1	3.3	2.9	3.9	4.1
HE 0504−2509	1.2	2.2	1.6	2.5	2.7
HE 0932−0404	2.1	2.5	4.2	4.3	4.3
HE 1004−0516	2.6	2.6	2.2	2.7	2.7
HE 1045−2550	1.7	1.8	4.8	3.0	3.1
HE 1125−3030	8.0	9.2	9.7	5.8	5.7
HE 1318−2555	3.5	4.3	3.8	3.6	3.3
HE 1319−3034	2.8	2.9	4.4	5.1	5.2
HE 2155−2243	2.5	1.7	4.1	3.5	3.4
HE 2200−2222	3.7	2.4	3.9	5.2	5.6
HE 2304−3858	2.9	2.1	3.9	4.7	5.0
HE 2340+0149	11.4	4.8	4.8	5.8	6.1

Table 6.4: Error in the equivalent width measurements for each line of sight, in each order and line. These errors combine both statistical (Poisson) error and the continuum placement error.

tained simply following SS92. To calculate the continuum placement errors, we adopted a slightly different approach to those authors. Since we had a good *a priori* estimate of the errors of the flux at each wavelength point, we used these to constrain the continuum fit, instead of setting all the errors to 1.0. We do not, therefore, compute the "reduced" error matrix ($\hat{E}$); rather, the "true" error matrix ($\sigma^2_{a_{hk}}$) is returned from the *lmfit* function.

This process was performed for each sight line, in each of 5 spectral regions: Ca II K (once each for orders 90 and 91), Ca II H, and the Na I $D_{1,2}$ lines. Results of these calculations are shown in Table 6.4.

6.2.4 Non-detections

If no HVC absorption features were seen, we would like to be sure that we should have seen them, were they present. To do this, we compared the error in the equivalent width, with the expected equivalent width. To calculate the expected equivalent width, we took the abundance [i.e. $N(\text{Ca II})/N(\text{H I})$] either from previous measurements, or we obtained it from the relation provided by Wakker & Mathis (2000), namely

$$N(\text{Ca II})/N(\text{H I}) = -0.78[log(N(\text{H I})) - 19.5] - 7.76 \tag{6.2}$$

Multiplying by $N(\text{H I})$ then gives $N(\text{Ca II})$, which is related to the equivalent width through the formula (e.g. Cowie & Songaila, 1986)

$$N = 1.13 \times 10^{17} \frac{\text{W}_\lambda}{f\lambda^2} \tag{6.3}$$

where W_λ is given in mÅ, N in cm^{-2}, λ in Å, and f is the unitless oscillator strength taken from Morton (2003, 2004).

In order to determine whether the lack of discernible absorption is significant several factors must be taken into account (Wakker, 2001). This was done under the pessimistic assumption that they will all act to decrease the expected absorption. Thus, several "safety factors" must be included in the calculation.

Our H I column density estimates are, for the most part, taken from data with poor spatial resolution (30′ for the LAB survey, 13′ for HIPASS, 9′ for Effelsberg). Comparison of single-dish and interferometric maps has shown that HVCs exhibit variations in column density on arcminute scales (Wakker & Schwarz, 1991). Thus an uncertainty of $2\times$ is included to account for H I small-scale structure. The gas-phase abundance in an HVC varies, as both dust depletion and ionisation vary. A factor of $2.5\times$ is included to account for depletion variations; the ionisation uncertainty requires a further reduction of $2\times$. Finally, since there is evidence of abundance variations across a given cloud (e.g. Gibson et al., 2001), a further $2\times$ reduction must be included if we assumed the abundance, rather than measured it directly. Thus, for all lines of sight, the expected EW is reduced by a $10-20\times$ before comparing to the measured EW error. If we then have $\mathrm{W}_{\lambda,safety} \gtrsim \sigma(\mathrm{W}_\lambda)$ then we consider the star to set a lower distance limit to the HVC. If $\mathrm{W}_{\lambda,safety} > 3\sigma(\mathrm{W}_\lambda)$, we consider this a strong limit. In performing such an analysis, we have attempted to quantify all the effects which could act against us detecting an absorption line. These assumptions are quite *pessimistic*, since it is unlikely that all such effects would act together to decrease the strength of an absorption line. Eliminating the need for such guesswork is clearly the desired route; in this vein, we are attempting to obtain better column density estimates in order to more reliably interpret the optical data.

6.3 Optical and Radio Spectra

For each of the 14 lines of sight, Figs. 6.2 – 6.8 show the optical spectrum around the Ca II H and K and Na I $\mathrm{D}_{1,2}$ lines, aligned in velocity space. We also include the relevant H I spectrum in the same region. Clear HVC emission can be seen for all lines of sight. Lower distance limits were derived for some of the clouds, based on the expected strength of the Ca II K line, which is the most likely to be detected. In a few cases, no conclusions can be made. Each line of sight is discussed below.

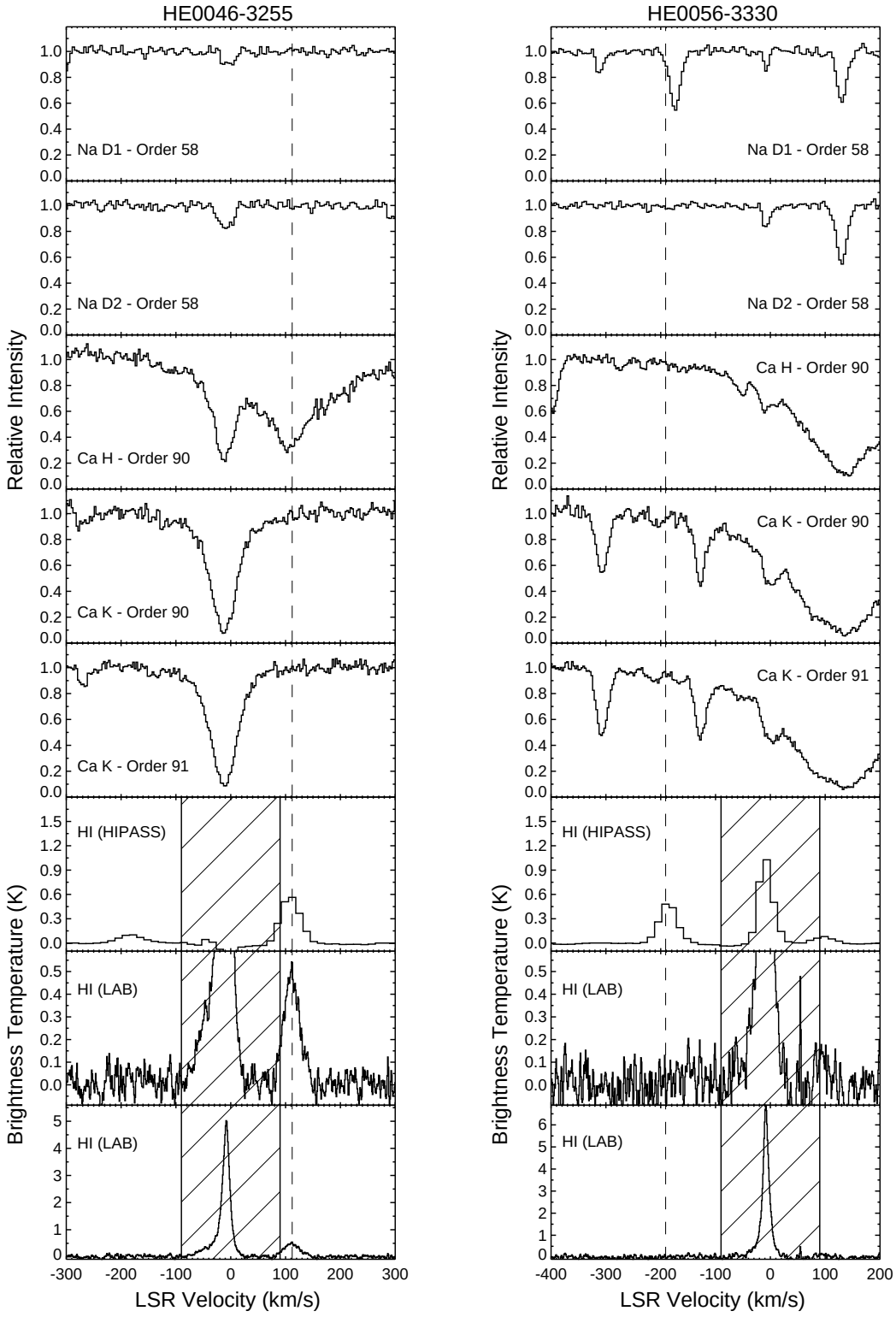


Figure 6.2: Left panel: HE 0046−3255. Right panel: HE 0056−3330

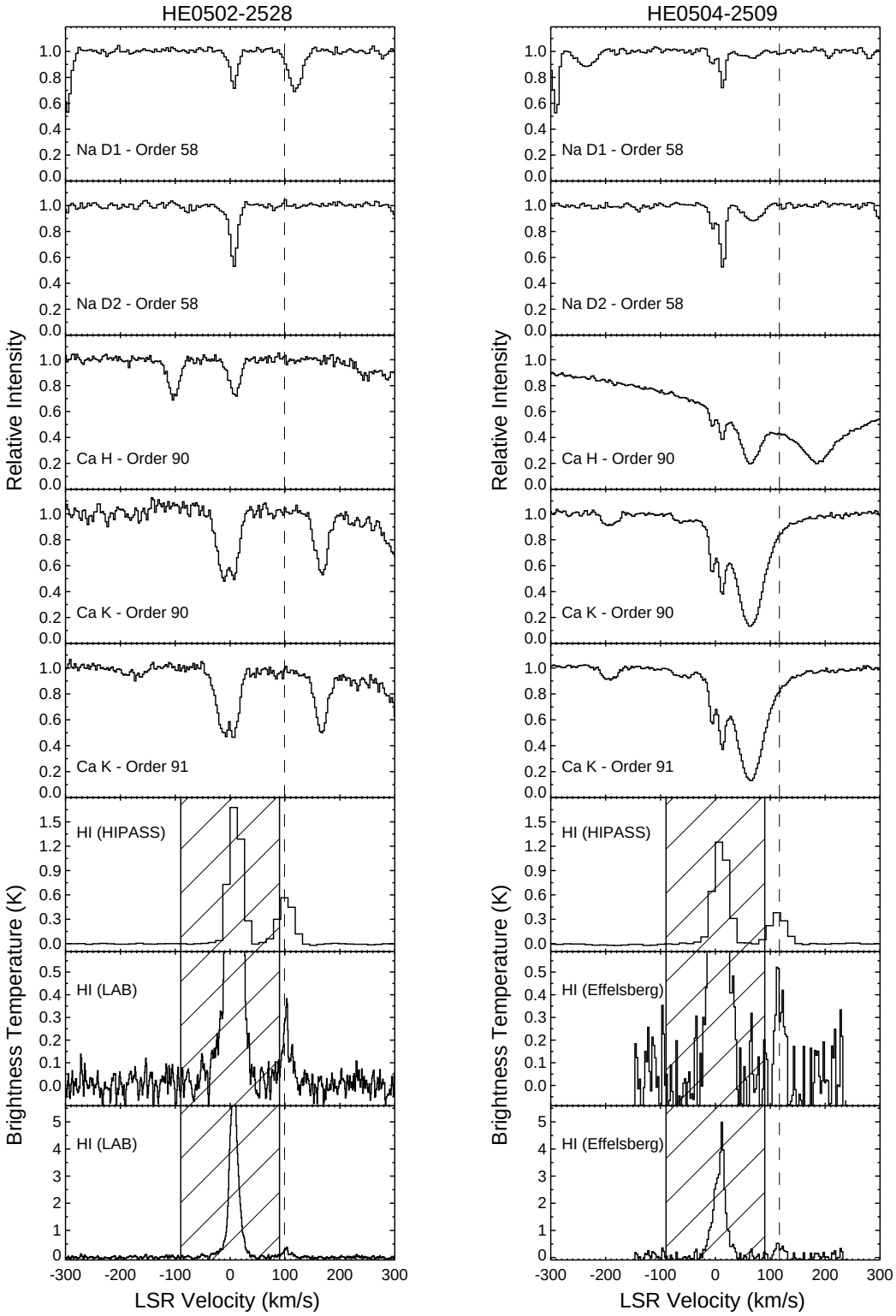


Figure 6.3: Left panel: HE 0502−2528. Right panel: HE 0504−2509

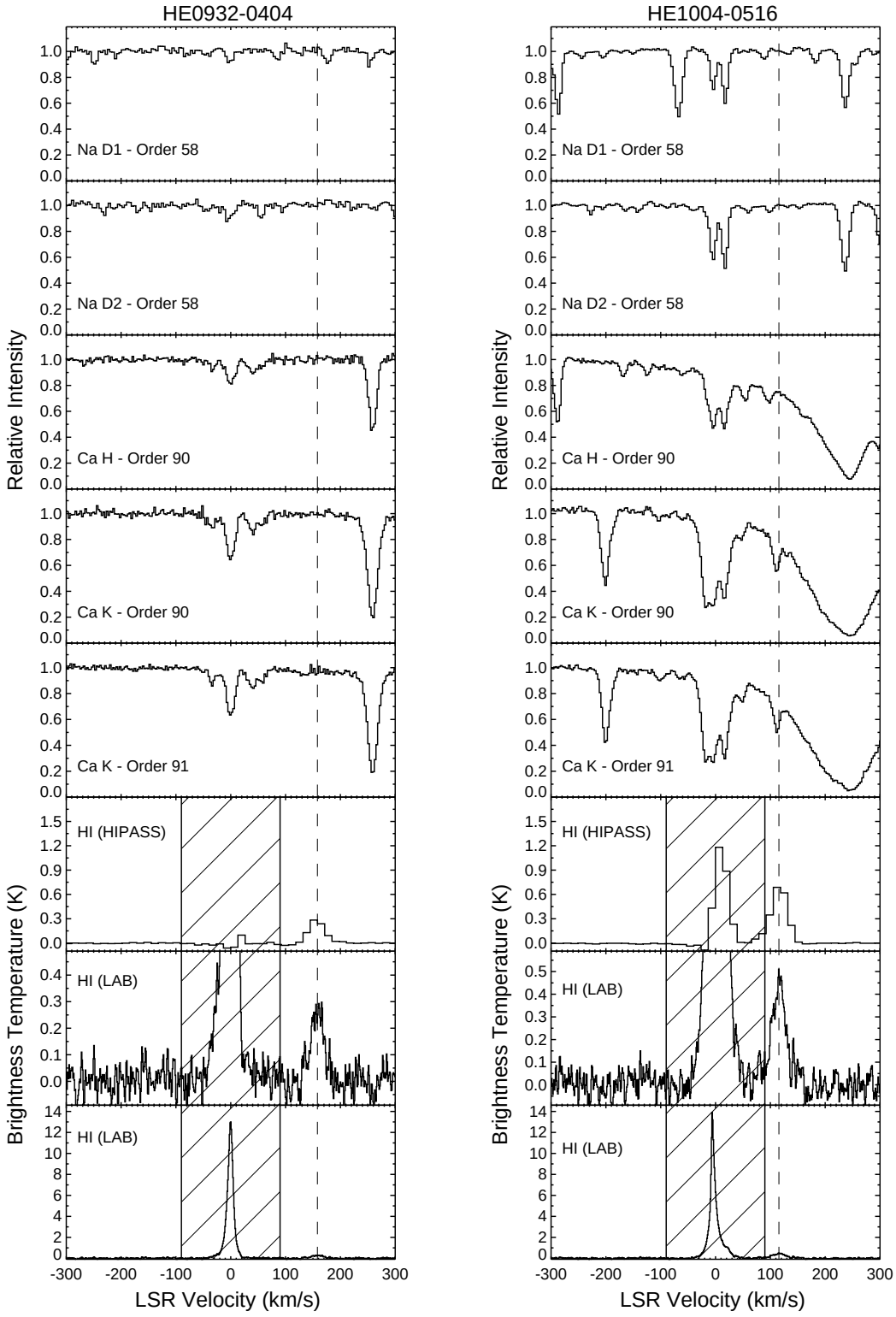


Figure 6.4: Left panel: HE 0932−0404. Right panel: HE 1004−0516

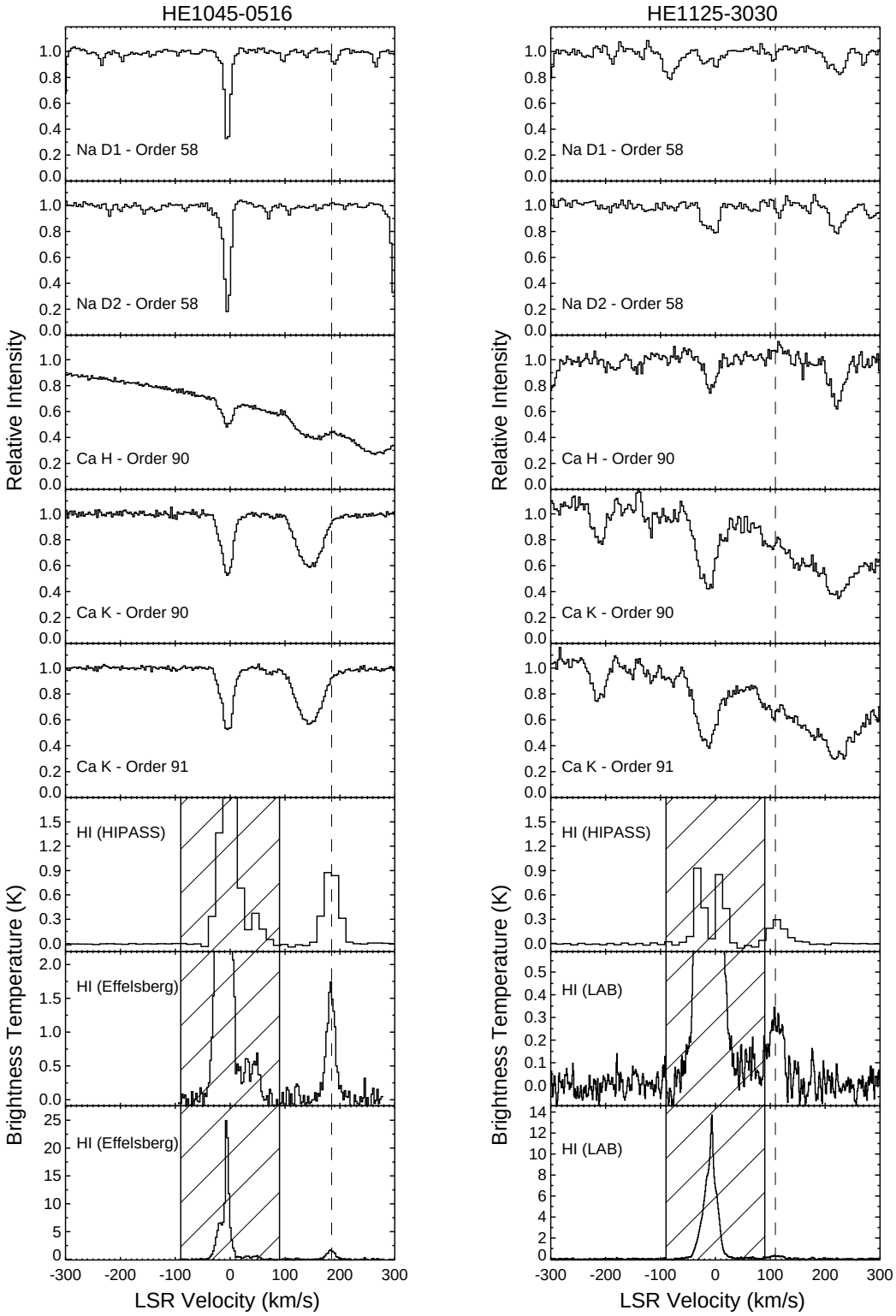


Figure 6.5: Left panel: HE 1045−2550 Right panel: HE 1125−3030

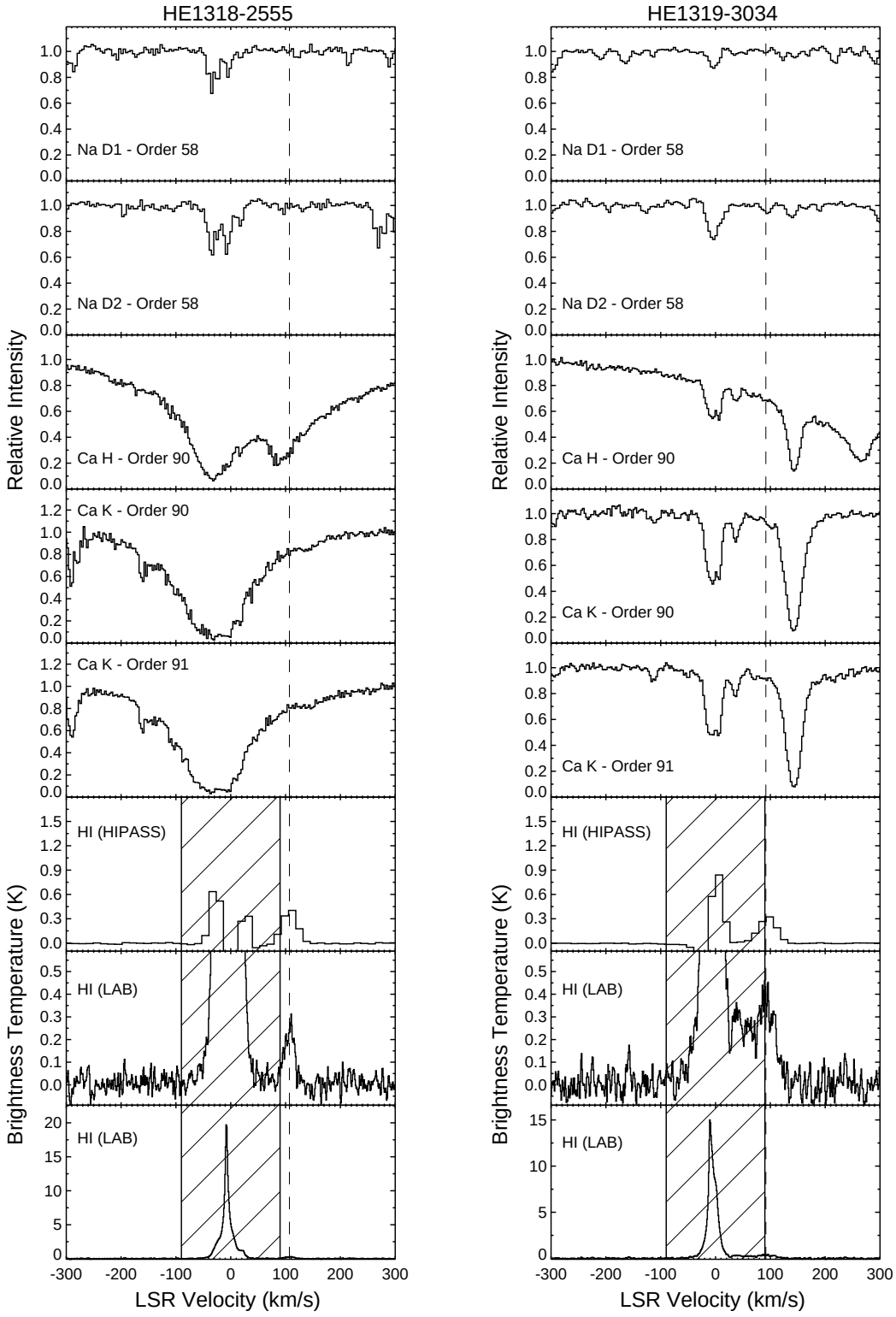


Figure 6.6: Left panel: HE 1318−2555. Right panel: HE 1319−3034

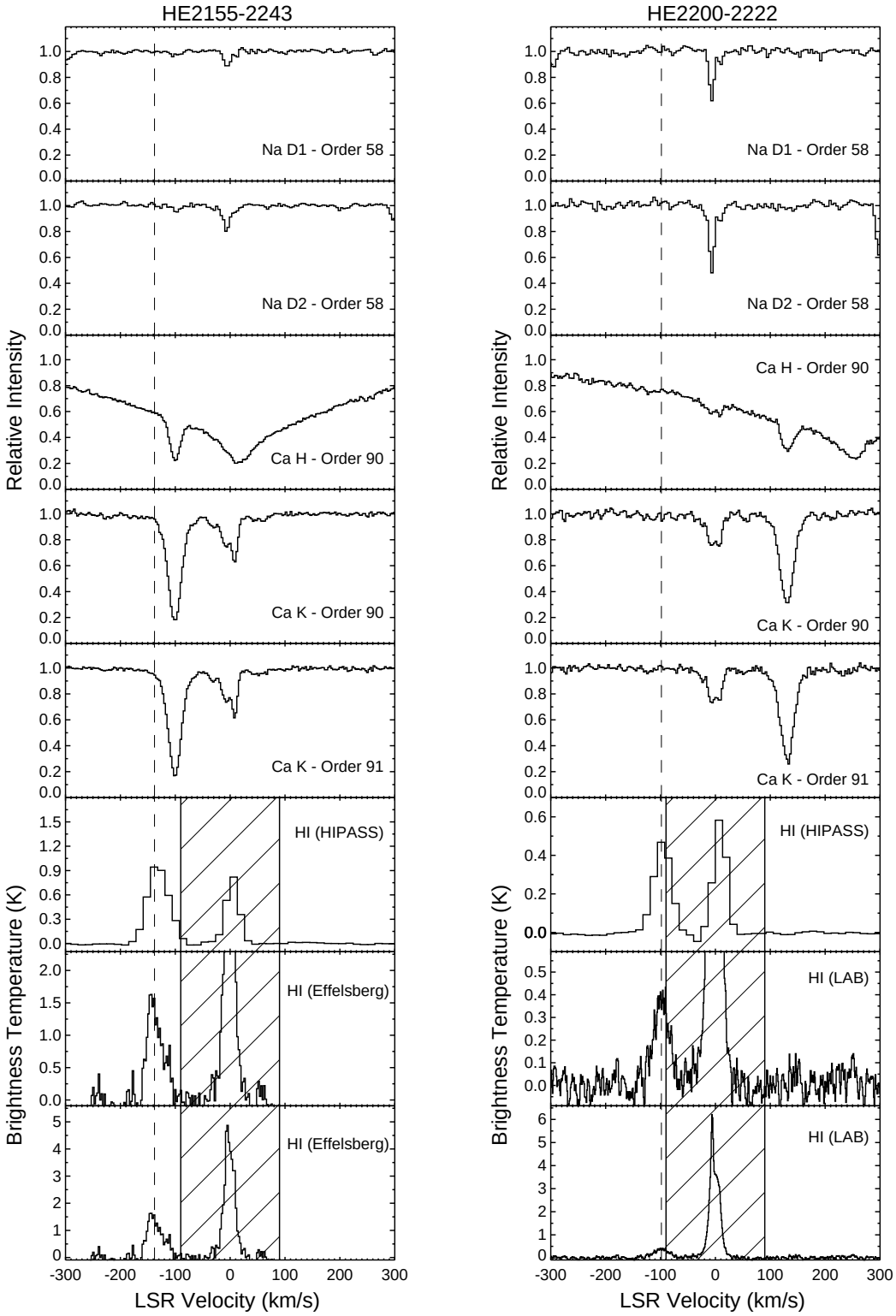


Figure 6.7: Left panel: HE 2155−2243. Right panel: HE 2200−2222

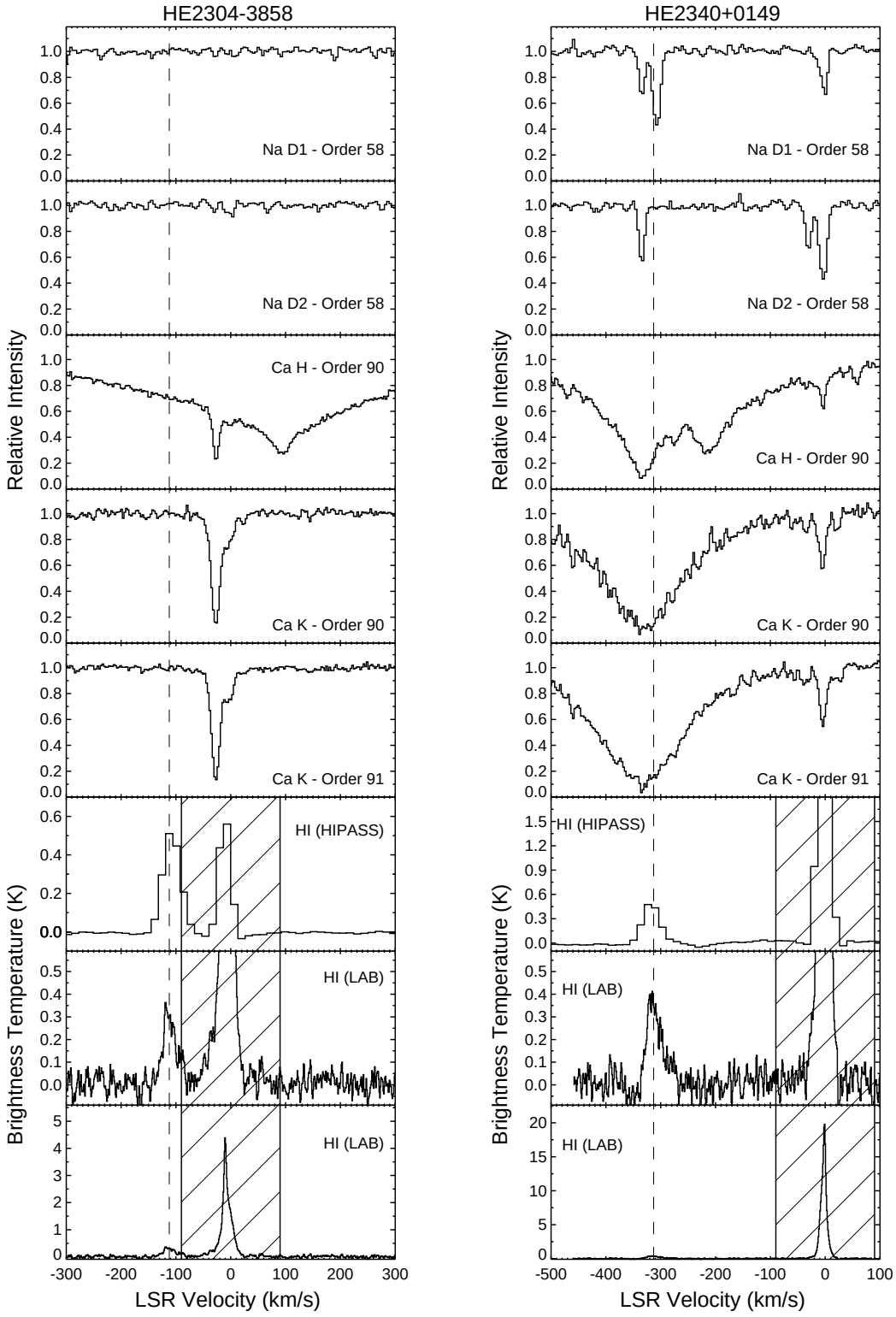


Figure 6.8: Left panel: HE 2304−3858. Right panel: HE 2340+0149

Probe	Dist kpc	Cmpx	Flg	N(H I) 10^{19} cm^{-2}	N(Ca II)/N(H I) 10^{-9}	N(Ca II) 10^{11} cm^{-2}	Safety Factor	$W_{\lambda,expected}$ mÅ	$W_{\lambda,safety}$ mÅ	$\sigma(W_\lambda)$ mÅ	ratio	ref
HE 0046−3255	10.9	MS		2.66	27	0.72	10	62.6	6.3	5.2	1.2	SY80
					20	0.53	20	46.1	2.3	5.2	0.4	WM00
HE 0056−3330	11.7	EN	*	2.20	23	0.51	20	44.3	2.2	3.3	—	WM00
HE 0502−2528	12.8	—		0.75	53	0.40	20	34.8	1.7	2.9	0.6	WM00
HE 0504−2509	7.5	—		1.35	34	0.46	20	40.0	2.0	1.2	1.7	WM00
HE 0932−0404	5.8	WA		1.17	81	0.95	20	82.6	4.1	2.1	2.0	T06
					38	0.44	20	38.2	1.9	2.1	0.9	WM00
HE 1004−0516	5.7	WA	*	2.00	81	1.62	20	140.8	7.0	2.6	—	T06
			*		25	0.50	20	43.4	2.2	2.6	—	WM00
Ca II H					81	1.62	20	70.3	3.5	2.6	1.4	T06
HE 1045−2550	3.8	LA*		4.93	27	1.33	10	115.6	11.6	1.7	6.8	SY80
					12	0.61	20	53.0	2.7	1.7	1.6	WM00
HE 1125−3030	13.2	WD	*	1.56	81	1.26	20	109.5	5.5	8.0	—	T06
			*		30	0.47	20	40.8	2.0	8.0	—	WM00
HE 1318−2555	4.9	WD*		0.87	81	0.70	20	60.8	3.0	3.5	0.9	T06
					48	0.41	20	35.6	1.8	3.5	0.5	WM00
HE 1319−3034	7.0	WD*	*	1.86	81	1.51	20	131.2	6.6	2.8	2.4	T06
			*		26	0.49	20	42.6	2.1	2.8	0.8	WM00
HE 2155−2243	6.2	—		7.77	9	0.67	20	58.2	2.9	1.7	1.7	WM00
HE 2200−2222	10.4	—		2.25	23	0.51	20	44.3	2.2	2.4	0.9	WM00
HE 2304−3858	9.8	MS		1.39	27	0.38	10	33.0	3.3	2.1	1.6	SY80
					33	0.46	20	40.0	2.0	2.1	1.0	WM00
HE 2340+0149	20.8	MS*	*	1.74	27	0.47	10	40.8	4.1	4.8	—	SY80
			*		28	0.48	20	41.7	2.1	4.8	—	WM00

Table 6.5: Comparison of the EWs from the Magellan data. A "*" in the Complex column indicates that this assignment has been made here. The flag column indicates those lines of sight about which no conclusions can be made. See text for details. The ratio column represents the ratio $W_{\lambda,safety}/\sigma(W_\lambda)$; values greater than 1 represent significant non-detection; values greater than 3 are considered to set strong lower limits. The reference column gives the reference for N(Ca II)/N(H I): WM00 — Wakker & Mathis (2000); SY80 — Songaila & York (1980); T06 — Thom et al. (2006).

6.4 Discussion of Sightlines

Table 6.5 compares, for each cloud, the expected equivalent width with the error in the EW measurements. For some clouds, we have used measurements of the $N(\text{Ca II})/N(\text{H I})$ ratio from other sightlines as a guide. For all lines of sight, we also perform the same calculation using an abundance inferred from the H I column density, using the relation of Wakker & Mathis (2000) (see Eqn 6.2).

6.4.1 Wannier Clouds - Complex WA

HE 0932−0404

Towards HE 0932−0404 there is clearly no optical absorption associated with the HVC, WW 91. The H I column density along this line of sight is $1.17 \pm 0.27\,\text{cm}^{-2}$, as measured from the nearest LAB spectrum to the line of sight. Complex WA, of which WW 91 is a member, occupies a similar region, both spatially and kinematically, as complex WB. It is quite possible that all the Wannier complexes (we report on complex WA, complex WB and complex WD here) have similar origins, given their overlap in position- and velocity-space. Therefore, we used the measured Ca II abundance of complex WB to guide our expectations for all these clouds. There are two measurements for this cloud: HE $1048+0231$ yields a Ca II to H I ratio of 81×10^{-9} (T06), while Wakker (2001) measured a much higher 280×10^{-9} towards PKS 0837−12. Conservatively, we adopt the lower value, while noting that this is rather high compared to other HVCs. Since we have assumed a constant Ca II abundance across all the Wannier complexes, a safety factor of $2\times$ is included to account for possible variations. The failure to detect HVC absorption implies a lower distance limit of 6 kpc.

HE 1004−0516

The spectrum of HE 1004−0516 shows a very clear absorption line in the Ca II K orders. In the stellar rest frame, this line is at 3932.0 Å, with a strength of 53 mÅ. If it were really caused by HVC absorption, we would expect to see a line at Ca II H with $W_\lambda \sim 26$ mÅ, since the Ca II K and Ca II H oscillator strengths are in a 2:1 ratio. This is clearly seen, for example, in the spectrum of HE 1048+0231 (see Fig. 5.2). No such line is seen here. Further, a line list from the Vienna Atomic Line Database (Kupka et al., 2000, hereafter VALD) shows a Ti II line at 3932.02 Å. This same identification also appears in the NIST database[2]. This is a common ion in FHB stars, and we therefore identify this line not as an HVC feature, but intrinsic to the star. Since the Ti line is at almost the precise velocity of a putative HVC feature, there is no possibility to use Ca II K to set a convincing non-detection.

[2] see http://physics.nist.gov/PhysRefData/ASD/index.html

Any Ca II H absorption line due to the HVC would be approximately half the strength of the Ca II K line. Nevertheless, we use it in order to determine whether any meaningful conclusions can be drawn about the distance to complex WA. The two lines redward of the HVC velocity near Ca II H are identified as Fe I lines. No HVC absorption in Ca II H is seen. The line of sight column density towards HE 1004−0516 is $2.00 \pm 0.30 \times 10^{19}$ cm^{-2}. For an assumed ratio $N(\text{Ca II})/N(\text{H I}) = 81 \times 10^{-9}$, we would therefore expect W$_\lambda$(Ca II H) = 70 mÅ. Applying the same safety factors as above reduces this to W$_\lambda$(Ca II H)$_{expected} = 3.5$ mÅ. The error in the Ca II H spectral region is 2.2 mÅ. We conclude that the non-detection in Ca II H sets a weak lower distance limit to complex WA of 5.7 kpc.

6.4.2 Wannier Clouds - Complex WD

HE 1125−3030

HE 1125−3030 aligns with gas in cloud WW 164, which forms part of the Wannier cloud complex WD. The interpretation of the optical spectrum of this star is somewhat difficult, due to a confluence of factors. Firstly, the spectrum is rather noisy. The position of the expected HVC feature is also part of the broad line wing of the stellar absorption feature. In both Ca II K orders, there appears to be an absorption feature just redward of the HVC velocity. The feature is not present in the Ca II H line, although it is weak enough that we would probably not expect to see it. In the stellar rest frame, the line is at 3932 Å and a line list from VALD indicates this to be the position of a Ti II line. Either side of the HVC position in the Na I D$_1$ and Na I D$_2$ spectra are two small features. Neither are identified by VALD, but both appear genuine (i.e. not noise). Their velocity alignment indicates that they are unlikely to be HVC related. We thus conclude that there is no evidence of HVC absorption. Due to the noise in the spectrum ($8 - 9$ mÅ at Ca II K) we cannot set any meaningful lower distance limits - higher quality data are required. Given the distance of this star (13 kpc) and the well-established distance limit to complex WB, this would be valuable, possibly allowing us to determine whether the Wannier Clouds all have the same origins, or are separate objects.

HE 1318−2555

HE 1318−2555 aligns with the cloud XHVC135. Although catalogued as "XHVC" by P02 (meaning that the HVC gas links with gas at $|v_{dev}| < 60\,\mathrm{km\,s^{-1}}$), it is clearly separated from any galactic emission. Following the definition of D02, the deviation velocity at this point is $94\,\mathrm{km\,s^{-1}}$. This gas is close, both spatially and kinematically to clouds in complex WD (it lies only $6 - 8^\circ$ away from large bulk of WW 154), and is very likely part of this complex.

The position of the HVC absorption lies on the very edge of the broad stellar absorption in the Ca II K spectral region. No HVC absorption is detected, but the error in the EW mea-

surements is slightly larger than the predicted EW when the safety factors are considered. We cannot, therefore, place any significant limits on complex WD.

HE 1319−3034

The star HE 1319−3034 offers little possibility to further constrain complex WD. The spectrum is noisy enough that its interpretation is difficult. Certainly there are not the obvious, strong, HVC absorption features seen in HE 1048+0231, but the Ca II K line in order 91 shows a definite absorption line just redwards of the HVC position. This interpretation is complicated, however, by the lack of an obvious corresponding feature in order 90. It is strong enough (~ 12 mÅ) not to be immediately dismissed as noise. Corrected to the stellar rest frame, the feature is centred at 3933.1 Å and there are no nearby metal lines in the VALD line list. The Na I D_2 spectral region shows and absorption line at the exact velocity of the HVC. This line is also real (i.e. not noise, with a strength of 26 mÅ at 5888.98 Å in the stellar rest frame) and unidentified. For these reasons, we cannot derive any meaningful conclusions as to the distance of complex WD.

The failure to derive any meaningful lower distance limits to complex WD is disappointing. This is an area that would benefit highly from additional, high quality data. Distance indications for this complex would help determine whether the Wannier clouds can be treated as a single entity, or whether they are distinct objects with different histories and properties.

6.4.3 CHVC 786

The two stars HE 0502−2528 and HE 0504−2509 lie very close to one another, and both align with the CHVC 786 in the D02 catalogue. P02 classify this cloud as semi-compact :HVC 648. Fig. 6.9 shows a column density map of the region with the locations of the two stars marked; its classification as a Compact HVC seems borne out. The cloud shows a distinct head-tail structure, which is probably an indication of an interaction with an ambient medium.

This HVC was also observed by Tobias Westmeier with the Effelsberg 100 m radio telescope near Bonn (Westmeier, 2003). Unfortunately, there were problems with the calibration in 3 pointings, one of which was the sightline towards HE 0502−2528, so Effelsberg data are only available for HE 0504−2509. LAB data are available for the HE 0502−2528 sightline.

HE 0502−2528

The optical spectrum of HE 0502−2528 shows no indication of HVC absorption. The only anomaly is the large absorption line just redward of the HVC velocity in the Na I D_1 spectrum. This line is the stellar Na I D_2 absorption line, which has been doppler shifted

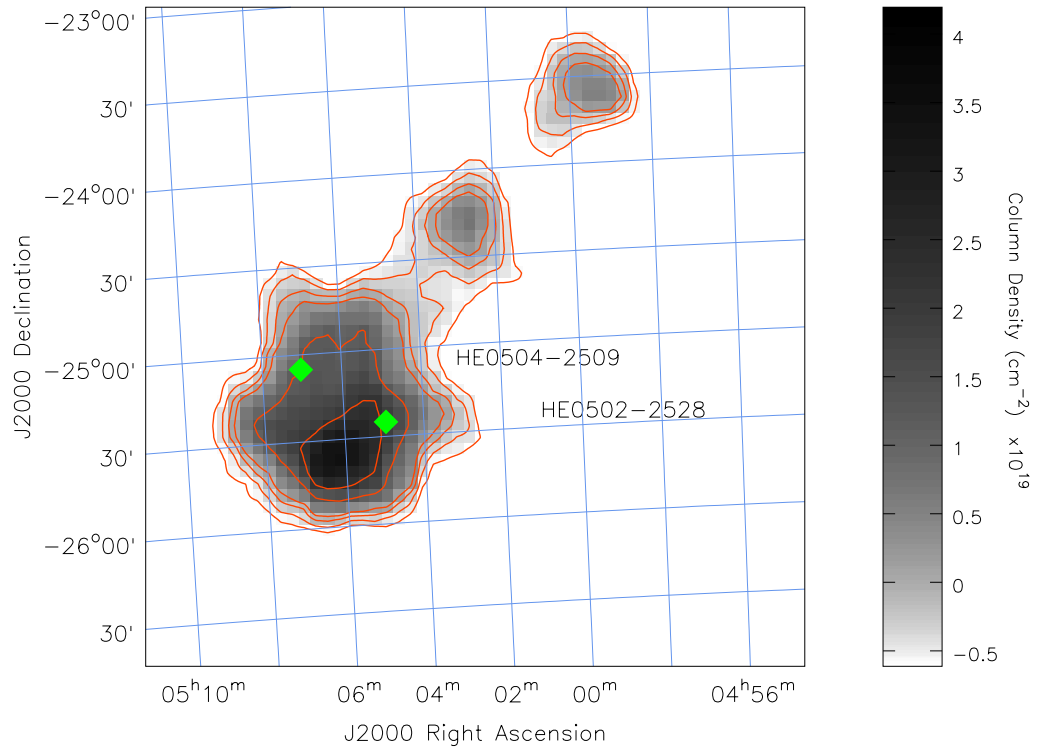


Figure 6.9: H I column density map of CHVC786 from HIPASS data. The greyscale and contour lines represent column density. Contours are drawn at $3 \times 10^{18}, 5 \times 10^{18}, 7.5 \times 10^{18}, 1.0 \times 10^{19}, 2 \times 10^{19}$ and 3.0×10^{19} cm^{-2}. The positions of the two probes are marked with green diamonds.

into this region by the large stellar radial velocity ($442.9 \pm 1.2\,\mathrm{km\,s^{-1}}$). The H I column density along this line of sight is quite low, as measured by the LAB survey, resulting in a low expected EW and consequent inability to set meaningful limits.

There is, however, evidence that beam-smearing is important. If we compare the spatial positions of HE 0502−2528 and HE 0504−2509, the HIPASS column density map indicates that HE 0502−2528 has a *higher* column density than HE 0504−2509. However, the LAB column density for HE 0502−2528 is lower than that of HE 0504−2509, which has been measured at better spatial resolution with Effelsberg. This fact suggests that a better column density determination (i.e. with higher spatial resolution) is necessary to interpret the non-detection. Further Effelsberg observations are currently scheduled.

HE 0504−2509

The quality of the optical spectrum of HE 0504−2509 is excellent, especially in the blue orders. This spectrum is another one in which the HVC position lies on the edge of the

stellar Ca II K line wing. Nevertheless, we should expect to see any absorption lines from the HVC, as demonstrated by the clear absorption caused by local disk gas. No such absorption is seen and a weak lower limit to the cloud of $d > 7.5$ kpc is set.

6.4.4 Population "EN"

HE 0056−3330

HE 0056−3330 aligns with an HVC catalogued as HVC 1292 by P02, and CHVC? 873 by D02. This is cloud WW 561 in the catalogue of Wakker & van Woerden (1991). The cloud itself is small and compact, hence the possible CHVC designation by D02. HIPASS data show many small separate clouds in this region, which collectively form "Population EN" at extreme negative velocities. Despite being in the same region as the MS, they are clearly separated kinematically from the main body of the stream. Due to the small, faint nature of the clouds, they do not appear in the LAB survey, probably as a result of beam-smearing. We must rely on HIPASS for H I data.

The optical spectrum of HE 0056−3330 is difficult to interpret. No HVC absorption appears at the velocity measured in the H I data. Slightly bluewards there does appear to be a broad absorption line in both Ca II K orders. Note also the very broad stellar Ca II K absorption line. Shifted into the rest frame, this small absorption line appears at 3929.25 Å. The VALD line list indicates two Fe I lines at 3929.12 and 3929.21 Å, which could both contribute. If this absorption line is real, we suggest that it is intrinsically stellar. We do not believe that meaningful lower limits can be set based on the low data quality and line confusion.

6.4.5 HVC 283

HE 2155−2243

The line of sight towards HE 2155−2243 is coincident with HVC 283 in the P02 catalogue. This cloud is also classified as semi-compact HVC in the D02 catalogue (CHVC: 64). The cloud was observed at higher spatial resolution with the Effelsberg telescope by Westmeier (2003). The core appears quite compact, but the HIPASS cubes reveal low intensity gas extended in a filamentary structure, which could have been smeared out in the lower resolution LDS survey used by D02. This is clearly shown in Fig. 6.10. The extended structure is also apparent in the Effelsberg map. Thus the compact or semi-compact label does not apply.

The non-detection towards HE 2155−2243 is quite clear. As with HE 1045−2550, the HVC position lies at the very edge of the stellar absorption line, but there is no evidence of any HVC absorption. The H I spectra from both the LAB survey, and the higher resolution Effelsberg map, show a lopsided, multi-component structure. We might expect to see this

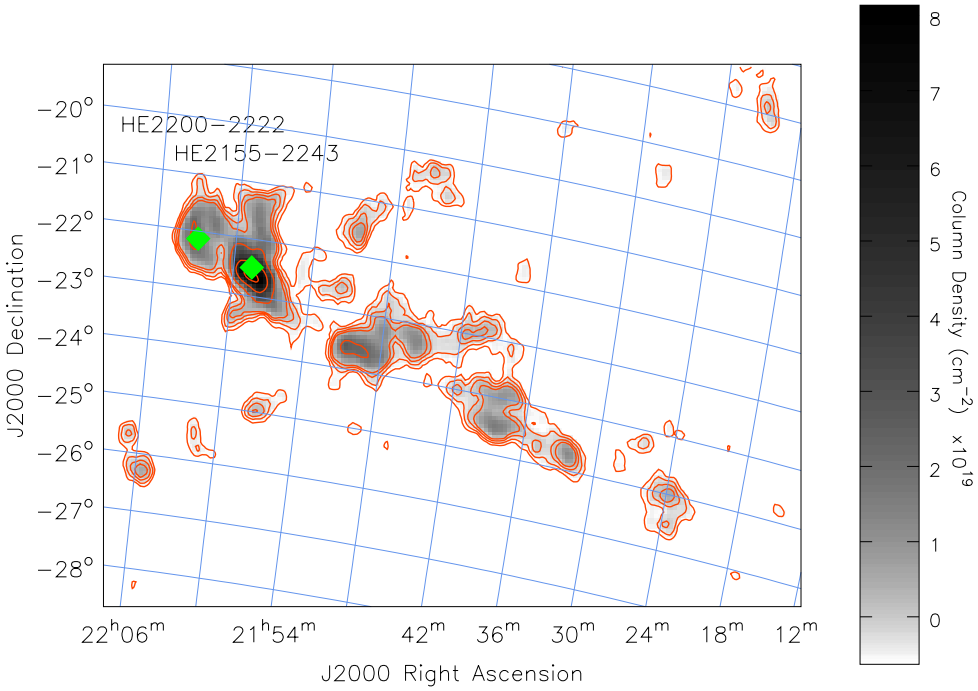


Figure 6.10: H I column density map of HVC 283 from HIPASS data. The greyscale and contour lines represent column density. Contours are drawn at $3 \times 10^{18}, 5 \times 10^{18}, 7.5 \times 10^{18}, 1.0 \times 10^{19}, 2.5 \times 10^{19}, 5.0 \times 10^{19}$ and 7.5×10^{19} cm^{-2}. The positions of HE 2155−2243 and HE 2200−2222 are marked as the green diamonds and labelled.

profile reflected in any HVC absorption, not unlike HE 1048+0231. The failure to detect the expected HVC absorption sets a lower distance limit of 6 kpc.

HE 2200−2222

HE 2200−2222 aligns with the same cloud as the previous star, HE 2155−2243. D02 list two separate clouds, but the HIPASS data show that this is a single structure. There is no credible evidence of optical absorption in the spectrum of HE 2200−2222; the 2-pixel dip in the Ca II K order 91 spectrum is noise. In the LAB spectrum we measure an H I column density of $2.25 \pm 0.39 \times 10^{19}$ cm^{-2}. For this column density, the WM00 relation predicts $N(\text{Ca II})/N(\text{H I}) = 23 \times 10^{-9}$, a factor of 3 higher than for HE 2155−2243. Variations in $N(\text{Ca II})/N(\text{H I})$ of up to a factor of 5 have been observed (Wakker, 2001), so such a predicted variation is not physically invalid. The resulting expected EW, combined with the good quality of the optical spectrum, allows us to set a lower distance limit of 10 kpc.

Since these lower limits are all conservative (i.e. they give the case of an unlucky con-

fluence of events, all conspiring to lower the strength of any optical absorption), it is therefore even more unlikely to occur twice in a single cloud. This suggests that the cloud is at least as distant as 6 kpc, and possibly more distant than HE2200−2222, at 10 kpc.

6.4.6 Magellanic Stream

There are several stars aligned with HVCs that are part of the Magellanic Stream. In considering these, we have adopted the $N(\text{Ca II})/N(\text{H I})$ ratio measured along the line of sight towards Fairall 9 (27×10^{-9}; Songaila & York 1980, hereafter SY80; Wakker 2001).

HE 0046−3255 — HVC 1550

HE 0046−3255 is aligned with the cloud HVC 1550 in the P02 catalogue. Approximately 6° from the South Galactic Pole, it is very likely part of the Magellanic Stream (MS II). The lack of HVC absorption is fairly clear. The strong H I column density ($2.66 \pm 0.36\,\text{cm}^{-2}$) means we should expect to see a significant absorption line — some 63 mÅ before safety factors are considered. Despite the comparatively low quality optical data (S/N $\sim$ 35 at Ca II K), we can set a lower limit to the cloud of $d > 11$ kpc.

HE 2304−3858 — WW 548

There is no evidence of HVC absorption in the spectrum of HE 2304−3858, which aligns with cloud WW 548. WvW91 list this cloud as belonging to the Stream. The star has only a very modest RV ($-24\,\text{km s}^{-1}$), and the intrinsic Ca II K absorption line blends with the absorption line due to the local disk gas. The Ca II H order shows the same profile, blended with the broad Balmer line. No absorption (local or stellar) is visible in the Na I D orders. A modest absorption line is expected for the HVC gas (some 33 mÅ), which is still significantly absent after the safety factors are considered. This lack sets a lower limit of 10 kpc to WW 548.

HE 2340+0149 — HVC 322

HVC 322 is part of the tip of the Magellanic Stream, in the MS V region (see Putman et al., 2003b). There are two competing models which seek to explain the formation of the Magellanic Stream. One involves tidal stripping of the gas from the LMC/SMC, while the other invokes an interaction with a diffuse ambient medium, resulting in gas that is stripped due to ram pressure. The tidal model of the MS produced by Connors et al. (2006) places this gas at around 50 kpc (T. Connors, priv. comm.). Some ram pressure models of the Stream formation predict that the gas should be much closer (e.g. Moore & Davis, 1994, hereafter MD94). The distance to HE 2340+0149 is some 21 kpc, approximately that predicted by MD94 for the MS V region.

The optical spectrum of HE 2340+0149 is an excellent example of why medium-resolution spectroscopy of FHB candidates is desirable. Since the original selection of FHB stars is made on the basis of objective prism spectra (see Christlieb et al., 2005, for details), no radial velocity information was available. In the case of HE 2340+0149, the HVC and stellar radial velocities are almost perfectly matched. Further, the very broad stellar absorption line makes it completely impossible to detect any narrow HVC absorption features. Note also the confluence of the stellar Na I D_1 feature, with the galactic absorption at Na I D_2. No distance limits may be set using this star as a background/foreground probe.

We also considered a scenario in which the star is embedded in the gas. Might this be the long-sought detection of an HVC with stellar content? Many searches have been made for stellar content in HVCs (e.g. Simon & Blitz, 2002; Davies et al., 2002; Hopp et al., 2003; Siegel et al., 2005), all unsuccessful. In order to pursue this model, however, a more accurate stellar distance is required — the 21 kpc distance noted above is based on the HES photometry. More accurate photometry is currently being obtained. This will allow more accurate stellar models to be computed, improving the distance estimate.

6.4.7 Magellanic Stream — Leading Arm

HE 1045−2550

The line of sight towards HE 1045−2550 lies less than a degree from the catalogued cloud WW 163 in the WvW91 catalogue, HVC 1105 in the P02 catalogue, and CHVC 866 as determined by D02. The HIPASS column density map from T05cat (Fig. B.290) reveals a complex and extended structure probably inconsistent with it being a CHVC. WvW91 associate the cloud with Population EP — "extreme positive velocity clouds outside the MS". Putman et al. (1998) later discovered the Leading Arm of the Magellanic Stream — gas which leads the Magellanic Clouds and has been removed by tidal forces. WW 163 is part of this leading arm, and can be clearly seen in the MS maps of Brüns et al. (2005). Note that the Wannier Clouds also occupy this part of position-velocity space.

LAB data for this line of sight indicate a column density of $3.62 \pm 0.17 \times 10^{19}\,\mathrm{cm}^{-2}$. Higher resolution ($9'$) observations were obtained at Effelsberg by Tobias Westmeier (Westmeier, 2003). The column density from the Effelsberg data, measured in the closest spectrum to the line of sight, is $4.93 \pm 0.05 \times 10^{20}\,\mathrm{cm}^{-2}$.

The optical data for this star show no sign of an HVC detection. The position of the expected HVC feature in Ca II K lies on the very edge of the stellar Ca II K line. Since the absorption in the line wing is small at this point, we would not expect it to mask HVC features of the strength expected ($> 100\,$mÅ, before safety considerations are made). In the Na I D_1 line there is a small absorption line ($\sim 25\,$mÅ) which is not identified in any line list. If this were real, however, we would expect to see a corresponding feature with twice the strength in Na I D_2. Since we do not, we exclude the possibility that this line is

HVC related. The quality of the optical data is excellent and we can set a strong lower distance limit to the gas, $d > 3.8$ kpc.

6.5 Discussion of Complexes

For convenience, the distance limits to the individual clouds from above are summarised in Table 6.6. Mass limits were computed using the relation

$$\mathrm{M(H\,I)} = 0.236\, S\, d^2 \tag{6.4}$$

where S is the total observed flux in Jy $\mathrm{km\,s^{-1}}$ and d is the distance in kpc.

Cloud	Dist Limit (kpc)	S (Jy. $\mathrm{km\,s^{-1}}$)	$\mathrm{M_{H\,I}}$ ($\mathrm{M_\odot}$)	Probe
Complex WA	> 5.8 kpc	5.1×10^3	$> 4.0 \times 10^4$	HE 0932−0404
	> 5.7 kpc	5.1×10^3	$> 3.9 \times 10^4$	HE 1004−0516
Complex WB	$8 - 9$ kpc	2.7×10^4	$4 - 5 \times 10^5$	HE 1048+0231
	—	—	—	HE 1138−1303
HVC283	> 6.2 kpc	6.2×10^2	$> 5.6 \times 10^3$	HE 2155−2243
	> 10.4 kpc	6.2×10^2	$> 1.6 \times 10^4$	HE 2200−2222
CHVC786	> 7.5 kpc	2.3×10^2	$> 3.0 \times 10^3$	HE 0504−2509
MS — HVC1550	> 10.9 kpc	2.3×10^2	$> 6.5 \times 10^3$	HE 0046−3255
MS — WW 548	> 9.8 kpc	1.6×10^2	$> 3.6 \times 10^3$	HE 2304−3858
MS/LA — WW 163	> 3.8 kpc	5.1×10^3	$> 1.7 \times 10^4$	HE 1045−2550

Table 6.6: Summary of distance limits and implied mass limits of the constrained HVCs. We have included the results for complex WB from the previous chapter for completeness. The mass limits listed here are for entire complexes, assuming the distance limit to the individual clouds is generally applicable, except in the case of the Magellanic Stream, where the limits apply to individual clouds only.

6.5.1 Wannier Clouds

Towards complex WA we fail to detect absorption in the lines of sight toward both HE 0932−0404 and HE 1004−0516. While these stars only set weak lower limits, failure to detect absorption towards both stars strengthens the conclusion that the gas is more distant than the stars. A distance limit of 6 kpc sets a z-height limit of $z \gtrsim 3$ kpc. These results are consistent with, and extend the limits of Smoker et al. (2004), who found weak z-height limits of 1400 pc and 2470 pc for two stars in the WA/WB region. If the two complexes are linked physically, then all these limits are consistent with the limits found for complex WB. The latter complex consists of $5 \times 10^5\,\mathrm{M_\odot}$ of H I, while complex WA

has $> 4 \times 10^4\,\mathrm{M}_\odot$. If complex WA is physically connected to complex WB and at the same distance (9 kpc), its mass would be $\sim 10^5\,\mathrm{M}_\odot$.

6.5.2 HVC 283

HE 2155−2243 sets a lower distance limit to HVC 283 of 6 kpc ($z \gtrsim 5$ kpc), while HE 2200−2222 sets a rather weak limit of 10 kpc ($z \gtrsim 8$ kpc). Since these lines of sight are towards the highest column density regions in the cloud, they offer the best possibility of setting firm lower limits. Higher quality data for HE 2200−2222 would be ideal for this purpose. The line of sight towards this cloud is in the first galactic quadrant, and if a distance of 10 kpc is accurate, this would be only 4.5 kpc from the galactic centre. In a galactocentric frame, this cloud has velocity $v_{\mathrm{GSR}} = -69\,\mathrm{km\,s^{-1}}$. In the inner galaxy, it would be hard to reconcile this cloud with fountain models, given its height and assumed position. We tentatively suggest that this cloud is falling into the galaxy, although a more detailed study is required.

6.5.3 CHVC 786

The lower limit of $d \gtrsim 8$ kpc for this compact HVC places it more than 4 kpc below the disk. There is some evidence of an interaction of the cloud with the surrounding medium. Effelsberg observations may help in this regard, as well as potentially making the interpretation of the HE 0502−2528 line of sight more significant. At 8 kpc, the cloud contains $> 3 \times 10^3\,\mathrm{M}_\odot$ of H I.

6.5.4 Magellanic Stream

No meaningful conclusions about the Stream are possible, given that the lower limits are not very restrictive, and the canonical distance to the Stream is of order 50 kpc. We note, however, that the case of HE 2340+0149 is intriguing, and deserving of more study. If a more accurate distance can be determined, and if this distance is consistent with the currently estimated $\sim$ 20 kpc, then this star may be more interesting for constraining Stream formation models, as well as any potential star-gas association.

6.6 Concluding Remarks

We have set lower limits to several high-velocity clouds and complexes. Care must be taken, however, not to over-interpret the results. The distances are inaccurate (probably $\sim 15\%$ random error) due to the inaccuracies in the HES photometry. Note also that this does *not* account for possible systematic errors. We stress that magnitude errors as

large as $0.2 - 0.3$ mag (as expected from the HES survey) are large enough to render the classification method of Wilhelm et al. (1999a) essentially useless; with such data, only statistical classification of large samples is possible. Incorrectly identifying a star's luminosity class will result in a totally incorrect distance. To counter these problems, more accurate photometry is currently being obtained. The method of Wilhelm et al. (1999a) will allow much more precise determinations of $T_{\rm eff}$, $\log g$ and [Fe/H] for all the stars. Detailed stellar abundance analyses should also be possible, further refining the results. In tandem, higher resolution H I measurements are being sought (e.g. with Effelsberg, Arecibo), in order to better interpret the lack of absorption along the lines of sight.

Acknowledgements
We are grateful for the help received from Rebecca Bernstein, Ian Thompson and Steve Shectman on the MIKE spectrograph. Steve Shectman kindly gave us his A-B mode reduction code. Thanks are due to Jason Prochaska for extensive help with, and development of, the MIKE *redux* pipeline.

CHAPTER 7

THE GASEOUS TRAIL OF THE SAGITTARIUS DWARF GALAXY

Summary

This chapter is based on Putman, M.E., Thom, C., Gibson, B. K., Staveley-Smith, L., 2004, ApJ, 603, L77. It has been modified in style only for presentation here. Copyright for the published article resides with the American Astronomical Society and it is reproduced here with permission. My contribution to this work was in the reduction of the northern HIPASS data, as well as the data conversion, and generation of the column density map and overlays. This corresponded to $\sim 40\%$ of the total effort. The major result of the paper is the suggestion that several HVCs are the gaseous component of Sagittarius Stream. The gas occupies roughly the same position and velocity as stars identified as coming from the Sgr dwarf galaxy. If the associated, the gas was likely stripped from the main body of the galaxy on its last passage through the diffuse outer Galactic disk.

7.1 Introduction

Evidence for the process which formed our Galaxy is found throughout our Galaxy's halo as trails of stars and gas (e.g. Yanny et al., 2003b; Putman et al., 2003b, hereafter P03). These Galactic building blocks are currently accreting satellites, and the Sagittarius dwarf galaxy (hereafter Sgr dwarf) is one of the closest examples of this process (Ibata et al., 1994). The evidence continues to accumulate that contiguous streams of leading and trailing stellar debris are being pulled from the Sgr dwarf as it spirals into the Milky Way (e.g. Newberg et al., 2003; Majewski et al., 2003, hereafter M03). The stars associated with the Sgr dwarf span a wide range of ages, with the youngest population between 0.5 – 2 Gyr old (Layden & Sarajedini 2000; Dolphin 2002; M03). This indicates that within the past Gyr, the Sgr dwarf was forming stars and had a source of star formation fuel.

Neutral hydrogen is a principal source of star formation fuel for a galaxy. Galaxies which contain H I are commonly currently forming stars (e.g. Lee et al., 2002) and those without detectable H I tend to have primarily an older stellar population and thus appear to have exhausted their star formation fuel (e.g. Gavazzi et al., 2002). This is evident in the dwarf galaxies of the Local Group. The stars in the Local Group dwarfs vary from being almost

entirely ancient ($>$ 10 Gyr; e.g., Ursa Minor) to a number of systems which are actively forming stars (e.g. WLM, Phoenix, LMC). The H I content of the dwarfs is summarised by Mateo (1998), Grebel et al. (2003) and Bouchard et al. (2003). The majority of the Local Group galaxies with H I have formed stars within the past 2 Gyr and those with no evidence for recent star formation do not contain detectable H I (e.g. Mateo, 1998; Dolphin, 2002).

Pointed H I observations of the central region of the Sgr dwarf (α, δ = 19^h 00^m, -30° $25'$ (J2000); $l, b = 6^\circ, -15^\circ$) indicate that our closest satellite galaxy does not currently contain a significant amount of star formation fuel ($M_{H\,I} < 1.5 \times 10^4$ $M_\odot$ (3σ Koribalski et al., 1994). The search for H I associated with the Sgr dwarf was continued by Burton & Lockman (1999); but they also found no associated gas over 18 deg^2 between $b = -13^\circ$ to -18.5° with limits of $M_{H\,I} < 7 \times 10^3$ $M_\odot$ (3σ detection limit). These results are surprising considering the Sgr dwarf was forming stars within the last Gyr. Since the orbital period of the Sgr dwarf is approximately 0.7 Gyr (Ibata & Lewis, 1998), one might expect to find this fuel stripped along the dwarfs orbit, possibly at a similar location to the stellar trail. The trailing stellar tidal tail of the Sgr dwarf has recently been found to extend for over 150° across the South Galactic Hemisphere with a mean distance between 20 to 40 kpc from the Sun (M03). Here we present H I data from HIPASS (H I Parkes All-Sky Survey[1]) along the entire Sgr dwarf galaxy orbit to investigate the possibility that a gaseous Sgr trail is also present. The gas detected represents a potential method of tracing the history, make-up, and classification of the Sgr dwarf galaxy, as well as the construction of our Galaxy.

7.2 Observations

The neutral hydrogen data are from the H I Parkes All-Sky Survey (HIPASS) reduced with the MINMED5 method (P03). HIPASS is a survey for H I in the Southern sky, extending from the South celestial pole to $\delta = +25^\circ$, over velocities from -1280 to $+12700$ km s^{-1} (Barnes et al., 2001). The survey utilised the 64 m Parkes radio telescope, with a focal–plane array of 13 beams arranged in a hexagonal grid, to scan the sky in 8° zones of declination with Nyquist sampling. The MINMED5 reduced HIPASS data has a spatial resolution of 15.5′ and a spectral resolution, after Hanning smoothing, of 26.4 km s^{-1}. The survey was completed with a repetitive scanning procedure which provides source confirmation, mitigates diurnal influences, and aids interference excision. For extended sources, the RMS noise is 10 mJy beam^{-1} (beam area 243 arcmin^2), corresponding to a brightness temperature sensitivity of 8 mK. The northern extension of the survey, from $+2^\circ$ to $+25^\circ$, was only recently completed and is presented for the first time here. The noise in these cubes is slightly elevated compared to the southern data (11 mK vs. 8 mK). This may be due to a combination of low zenith angles during these observations and an

[1]The Parkes Telescope is part of the Australia Telescope which is funded by the Commonwealth of Australia for operation as a National Facility managed by CSIRO.

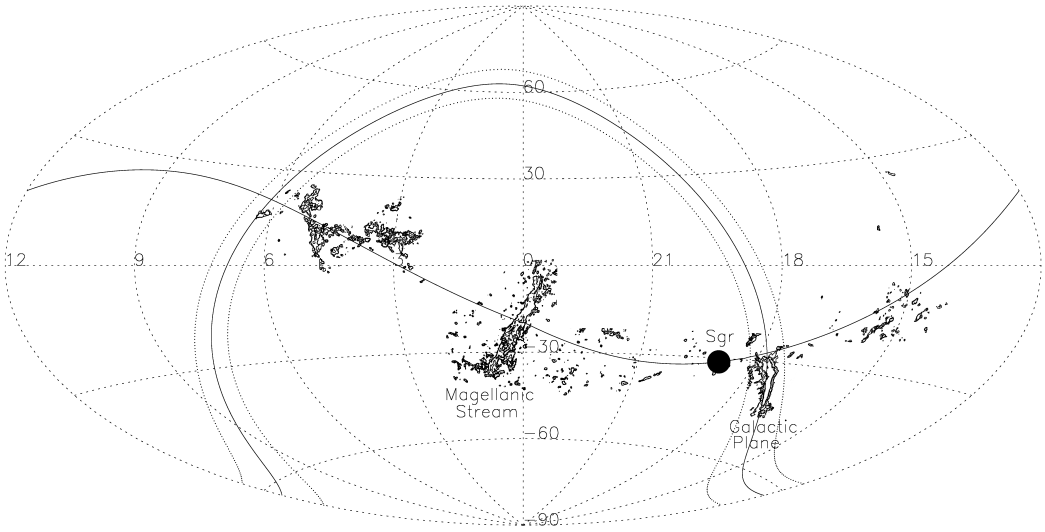


Figure 7.1: The negative high-velocity H I (~ -85 to $-400\,\mathrm{km\,s^{-1}}$; LSR) along the orbit of the Sgr dwarf galaxy in Celestial coordinates. The current position of the Sgr dwarf is shown by the solid point, and the orbit of the Sgr dwarf (Ibata & Lewis 1998) is plotted as the solid line through this point. The negative velocity gas attributed to the Magellanic Stream and Galactic Plane gas at the Galactic Centre is labelled. $b = 0^\circ$ is indicated by the solid line through the labelled Galactic Plane gas, with the two dotted lines on each side representing $b = +5^\circ$ and -5°. The negative velocity carbon stars extend from approximately $\alpha, \delta = 0^h, -20^\circ$ to $12^h, 20^\circ$ along the Sgr orbit (Ibata et al. 2001). Contours represent column density levels of 0.5, 1.0, 5.0, and 10.0 $\times 10^{19}$ cm^{-2}.

inability to avoid solar interference as effectively. Integrated intensity maps of the high positive and negative velocity gas (generally $|\mathrm{v_{lsr}}| > 80\,\mathrm{km\,s^{-1}}$, as long as the gas was clearly separate from Galactic emission) were made for the 24 deg^2 cubes which lie along the Sgr orbit. The positive velocity cubes had very little emission in them, so we concentrated on the negative velocity cubes. The noise at the edges of the negative velocity maps were blanked within AIPS and the images were then read into IDL to create the map of the entire orbit shown in Fig. 7.3. At 20 – 40 kpc the MINMED5 reduced HIPASS data has a sensitivity to clouds of gas with $\mathrm{M_{H\,I}} > 80 - 320\ \mathrm{M_\odot}$ ($\Delta v = 25\,\mathrm{km\,s^{-1}}; 3\sigma$).

7.3 Results

The large scale H I map which includes all of the high negative velocity gas along the orbit of the Sgr dwarf is shown in Fig. 7.3. This plot is in Celestial coordinates as it depicts the main features found along the orbit better than Galactic coordinates. The Galactic Plane, the orbit of the Sgr dwarf (Ibata & Lewis, 1998), and the current position of the

Sgr dwarf are shown. The stream of M giants presented by M03 has quite a broad width (typically several degrees) along this orbit. The orbit of the Sgr dwarf crosses the Galactic Plane at $\ell \sim 185^\circ$ and $\ell \sim 0^\circ$ which corresponds to approximately $(\alpha, \delta) = 6^h$, 25° and 18^h, -30°, respectively. At the Galactic Centre high negative and positive velocity gas is present, thus we have labelled the negative velocity H I emission within $\pm 5^\circ$ of the Galactic plane at that location. The Sgr orbit crosses the Magellanic Stream (labelled) at the South Galactic Pole or $(\alpha, \delta) = 0^h, -15^\circ$. The majority of the Sgr dwarf orbit does not have both stars and H I gas at high negative velocities, with the exception of the H I gas between $\alpha = 3 - 4.5$ h and $\delta = 0 - 30^\circ$, or $\ell \approx 155 - 195^\circ$ and $b \approx -5 - -50^\circ$. A close up of the velocity distribution of these H I clouds in Galactic coordinates is shown in the channel maps of Fig. 7.3. The M giants of the Sgr stellar stream fill a large percentage of the region shown Fig. 7.3. This high velocity H I gas was previously identified as part of the Anticenter complexes (ACHV and ACVHV; Wakker & van Woerden, 1991) and was discovered almost 40 years ago, but its relationship to the Sgr dwarf was not previously noted. There are some small negative velocity clouds along the Sgr dwarf orbit, but besides the labelled gas in Fig. 7.3, the only other substantial complex of negative velocity gas along the orbit of the Sgr dwarf is in a region which has predominantly positive velocity stars (Ibata et al., 2001). This is the group of high-velocity clouds known as Complex L at $\alpha \approx 15.25$ h, $\delta \approx -19.5^\circ$. The amount of high positive velocity gas along the orbit of the Sgr dwarf is very limited, and not correlated with the position of the positive velocity stars along the Sgr stellar stream.

Fig. 7.3 shows the gas along the orbit of the Sgr dwarf between $\alpha = 2 - 5.5$ h and $\delta = 0 - 30^\circ$ in Galactic coordinates over the velocity range of -380 to $-85\,\mathrm{km\,s^{-1}}$ (LSR). The emission extending from -380 to $-180\,\mathrm{km\,s^{-1}}$ at $b < -20^\circ$ is orientated along the orbit of the Sgr dwarf and is completely isolated from gas which merges with lower velocity emission. This complex of gas would amount to $\mathrm{M}_{HI} = 4.3 \times 10^6$ $\mathrm{M}_\odot$ at 36 kpc, the approximate distance to the stars in the Sgr stream. Other emission which appears in the channel maps include a distinct filament beginning at $b = -10^\circ$ in the velocity range of -245 to $-75\,\mathrm{km\,s^{-1}}$ that would have a mass of 5.4×10^6 $\mathrm{M}_\odot$ at 36 kpc. The gas in both complexes has peak column densities on the order of 10^{20} cm^{-2} at the 15.5′ resolution of HIPASS and extends to the column density limits of the data ($5\sigma \sim 3 \times 10^{18}$ cm^{-2}; $\Delta v = 25\,\mathrm{km\,s^{-1}}$). There is also a population of clouds appearing at $-125\,\mathrm{km\,s^{-1}}$ that merge into intermediate velocity emission and are not included in Fig. 7.3 for this reason. The distance of 36 kpc was adopted based on the continuous stellar trail presented in M03 at those distances and the matching distance of a population of carbon stars (Ibata et al., 2001). The carbon stars associated with the Sgr dwarf at this position have velocities between -140 to $-160\,\mathrm{km\,s^{-1}}$ (LSR Dinescu et al., 2002; Totten & Irwin, 1998; Green et al., 1994).

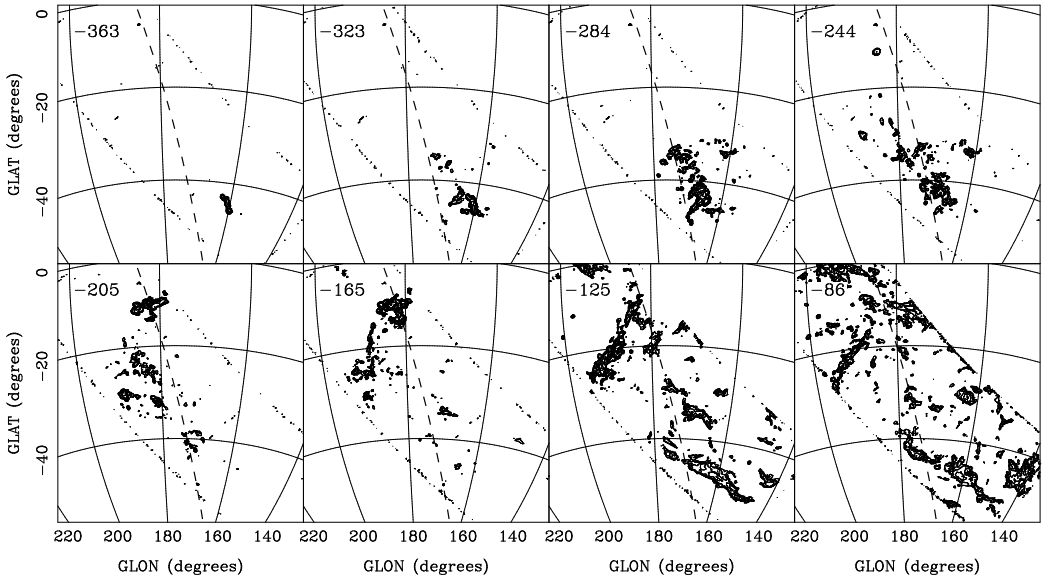


Figure 7.2: Channel maps of the H I clouds found along the trailing stellar stream of the Sgr dwarf in Galactic coordinates with v_{LSR} labelled in the upper left corner. The M giants (M03) extend across this region in a $\sim$15° band along the orbit of the Sgr dwarf (dashed line; (Ibata & Lewis, 1998)). Contours are 0.055, 0.11, 0.22, 0.44, 0.88, and 1.8 K.

7.4 Discussion

The present orbit of the Sgr dwarf is estimated to be 0.7 Gyr (Ibata & Lewis, 1998). Using this orbit, the core of the Sgr dwarf was at the position of the H I complex presented here approximately 0.2 – 0.3 Gyr ago. It would make sense if the gas was part of the Sgr dwarf 0.3 – 0.7 Gyr ago considering the age of part of the Sgr dwarf stellar population (0.5 – 2 Gyr Layden & Sarajedini, 2000; Dolphin, 2002, M03). Not surprisingly star formation surveys find that those galaxies which are actively forming stars also contain substantial amounts of star formation fuel in the form of neutral hydrogen (Lee et al. 2002 (KISS); Meurer et al., in preparation (SINGG)). This paper addresses the issue of when and how the star formation fuel of the Sgr dwarf was stripped from the galaxy.

The gas between -380 and $-180\,\mathrm{km\,s^{-1}}$ at $b < -20°$ in Fig. 7.3 is the gas we propose was most likely once part of the Sgr dwarf, as it follows the orbit of the Sgr dwarf and is completely isolated from lower velocity emission that may have a relation to disk gas

(e.g. Tamanaha, 1995). This gas lies at a position where the Sgr dwarf would have passed through the extreme edge of the Galactic disk, and at this position the Sgr dwarf stellar debris is approximately $40 - 50$ kpc from the Galactic Centre (M03). We have adopted 45 kpc as the typical distance from the Galactic Centre at the position of the bulk of the gas. This distance is significantly beyond the typical radius quoted for our Galaxy ($\sim$26 kpc), however it is possible that an extended ionised disk exists for our Galaxy (e.g. Savage et al., 2003), as found in other systems (Maloney, 1993; Bland-Hawthorn et al., 1997; Steidel et al., 2002) . The passage through an extended disk of our Galaxy, in addition to the tidal forces already obviously at work as evident from the stellar tidal stream, might have been enough to disrupt the H I in the core of the galaxy and cause the dwarf to lose all remaining star formation fuel. The gas will be stripped from a galaxy if $\rho_{IGM} v^2 > \sigma^2 \rho_{gas}/3$ (Mori & Burkert, 2000; Gunn & Gott, 1972). We can use this equation to estimate the density needed at the edge of the disk to strip the gas from the core of the Sgr dwarf. We use a tangential velocity of $280\,\mathrm{km\,s^{-1}}$ for the Sgr dwarf and a velocity dispersion of $11.4\,\mathrm{km\,s^{-1}}$ (Ibata & Lewis, 1998). If the column densities and size of the H I distribution in the core of the Sgr dwarf were on the order of 5×10^{20} cm^{-2} (averaged over the core) and 1 kpc, the typical ρ_{gas} is 0.16 cm^{-3}. An extended disk density greater than 3×10^{-4} cm^{-3} is then needed to strip the gas via ram pressure stripping. Based on previous estimates of the density of the Galactic halo, this density would be easily achieved in the plane of Galaxy, 20 kpc from the currently observed edge of the disk. Examples of estimates for the density of the Galactic halo which are consistent with $\sim 10^{-4}$ cm^{-3} at distances of 50 kpc and more include: explaining the existence of head-tail clouds which can be associated with the Magellanic Stream (Quilis & Moore, 2001); the confinement of the tip of the Magellanic Stream (Stanimirović et al., 2002) ; the O VI high-velocity absorption line results (Sembach et al., 2003); and the diffuse X-ray emission (Wang & McCray, 1993) and dispersion measures for LMC pulsars (Taylor et al., 1993) when the ionised medium is extended over $\sim$100 kpc.

Stripping gas from a Galactic satellite by passing it through the edge of the Galaxy's disk was proposed as a possible solution for the origin of the Magellanic Stream by Moore & Davis (1994, hereafter MD94). They invoked an extended ionised disk at 65 kpc from the Galactic Centre with column densities $< 10^{19}$ cm^{-2} to strip gas from the satellite galaxy. The stripped gas initially has its speed reduced, but the decelerated gas falls to a lower orbit and subsequently attains a higher angular velocity. In order to reproduce the properties and distribution of the Magellanic Stream, MD94 induce a braking effect on the gas with a diffuse medium in the halo, preventing it from rapidly falling into the Galactic potential. Though the H I trail of the Sgr dwarf has a very different structure from the Magellanic Stream, parallels can be made between the MD94 model and the stripping of the Sgr H I clouds. Both of the systems have similar impact velocities and have gas at similar distances from their cores (roughly 50 – 60 kpc) with similar column densities and velocities. The gas along the Sgr dwarf orbit has slightly higher negative velocities than the carbon stars with velocity determinations in this region and this may be due to the gas falling into a slightly lower orbit than the stars. The exact predicted position and velocity

of the gas relative to the stars will be addressed in a future simulation paper.

At 36 kpc from the sun the H I gas between -380 and $-180\,\mathrm{km\,s^{-1}}$ at $b < -20^\circ$ has a mass of 4.3×10^6 $M_\odot$. If the filament extending from $b = -10$ to -25° and $v_{\rm LSR} = -245$ to $-85\,\mathrm{km\,s^{-1}}$ is included as once being part of the Sgr dwarf, the total H I mass goes up to 9.7×10^6 $M_\odot$. A typical total H I mass for a dwarf galaxy is on the order of 10^{7-8} $M_\odot$ Grebel et al. (2003), so 10^{6-7} $M_\odot$ of gas originally being associated with the dwarf is certainly plausible and may represent anywhere from the majority to 10% of the Sgr dwarf's original H I mass. Using a total Sgr dwarf mass of 5×10^8 $M_\odot$ (M03), this gas represents 1 – 2% of its total mass. The Sgr dwarf most likely originally had more than 10^{6-7} $M_\odot$ of neutral hydrogen associated with it, as the outer gaseous component would have been the first thing stripped (e.g. Mihos, 2001; Yoshizawa & Noguchi, 2003). This outer gas would have had column densities between $10^{18} - 10^{19}$ cm^{-2} and has most likely either already dispersed or been ionised, although remnants of this gas may be present as small HVCs along the Sgr dwarf orbit. Since there is currently no H I associated with the core of the Sgr dwarf (Koribalski et al., 1994), and the dwarf has stars which are 0.5 – 2 Gyr old, the H I gas presented here most likely represents the high column density gas from the core of the Sgr dwarf which was finally stripped when the dwarf passed through the higher density medium in the extended Galactic disk. This is supported by the relatively high peak column densities of the H I gas currently ($\sim 10^{20}$ cm^{-2}). For the Sgr H I gas to survive for 0.2 – 0.3 Gyr (the time since the last passage of the core Sgr dwarf), not to mention the Magellanic Stream which is thought to be > 0.5 Gyr old, the gas should either be confined by an existing halo medium or associated with significant amounts of dark matter.

7.5 Overview

Our Galaxy's halo is made up of numerous streams of satellite debris which trace its formation. The association of H I gas with the Sagittarius dwarf galaxy emphasises the number of dynamical processes occurring within the Galactic halo. In this paper we find $4 - 10 \times 10^6$ $M_\odot$ of H I gas along the orbit of the Sgr dwarf. This is approximately 1 – 2% of the total mass of the dwarf, 10 – 20 times lower than the H I mass of the Magellanic Stream, and approximately the same H I mass as the Leading Arm of the Magellanic System (P03). We argue this H I was the last gas stripped from the core of the Sgr dwarf ~ 0.2 – 0.3 Gyr ago due to its passage through the extended Galactic disk with densities $> 10^{-4}$ cm^{-3}. This is supported by the agreement in the spatial distribution of the gas and stars along the Sgr orbit, both components having high negative velocities, the location of the gas relative to the plane of our Galaxy, the relatively high column densities of the H I gas, and the star formation history of the Sgr dwarf. The association of H I gas with the Sgr stellar stream suggests that the dwarf spheroidal classification for the Sagittarius galaxy may need to be reconsidered. It also suggests that slightly offset H I and stellar streams may be a common feature of disrupted satellites in the Galactic halo. With

the accretion of this Sgr H I stream, the Magellanic Stream (P03), Complex C (Wakker et al., 1999), and possibly other HVCs, there is ample fuel for our Galaxy's continuing star formation and understanding the distribution of stellar metallicities (i.e. the G-dwarf problem is not a problem). Determining the metallicity, distance, and ionisation properties of the H I gas presented here will aid in confirming if this H I gas was indeed stripped from the Sgr dwarf during its current orbit. Since we propose this is the last gas from the core of the Sgr dwarf, we will also look for molecular gas and dust associated with these clouds. A future simulation paper will address the exact spatial and velocity distribution expected for gas stripped from the Sgr dwarf.

Acknowledgements
We would like to thank Phil Maloney, Steve Majewski and Geraint Lewis for useful discussions. We also thank the referee for many useful comments. M.E.P. acknowledges support by NASA through Hubble Fellowship grant HST-HF-01132.01 awarded by the Space Telescope Science Institute, which is operated by AURA Inc. under NASA contract NAS 5-26555. B.K.G. acknowledges the support of the Australian Research Council, through its Large Research Grant and Discovery Project schemes.

CHAPTER 8

CONCLUSIONS

8.1 Summary

The main aim of this thesis has been the use of field Horizontal Branch stars in the Hamburg/ESO Survey as probes of the gaseous Milky Way halo. In Chapter 2 and we described how these 8321 FHB stars were selected from more than 4 million spectra in the HES database. With an emphasis on low contamination by higher-gravity A-type stars, tests show this sample to be polluted at the $\lesssim 16\%$ level. Since this sample is relatively clean, we can study the kinematics of these predominantly halo stars without concern that small levels of contamination will adversely affect our results. When transformed to a GSR velocity frame, there is no evidence of a cold component in the sample, moving with disk-like velocities — a further demonstration that the sample is mostly comprised of stars following random orbits. The kinematics of 530 of these FHB stars were compared with two models of the halo velocity dispersion in Chapter 3. We found, somewhat surprisingly, that we could not distinguish between a physically motivated and isothermal model of the velocity ellipsoid, in the regions we survey. Comparing the two models, we suggest regions close to the centre of the galaxy as worthy of further analysis if one wishes to separate the two models.

Having established a large sample of halo stars, covering the whole southern sky away from the disk, we then progressed to the main thrust of the thesis. Chapter 4 details the identification of the HES FHB stars which align with HVC gas. 430 were identified as potentially useful for distance determinations. Having identified useful stars, we then observed 16 of these using Magellan/MIKE, obtaining good quality echelle spectra. Data on two of these, HE $1048+0231$ and HE $1138-1303$, were presented in Chapter 5. These two stars place a tight distance constraint on complex WB. The rest of the Magellan data were presented in Chapter 6, in which we use the non-detections of HVC gas to set lower distance limits.

Finally, in Chapter 7 we present the suggestion that some HVCs are gas that has been stripped from the Sagittarius dwarf galaxy. This gas follows the same orbit as the stellar stream, and has similar velocities as the stellar component of the Sgr stream. We suggest that this gas was stripped from the main part of the Sgr dwarf on its last passage through the diffuse, outer Milky Way disk.

8.2 Future Directions

It is natural that a Ph.D thesis should propose more questions than it answers. Many such questions have arisen out of this work, and below I highlight some of those which naturally follow.

8.2.1 HVC Distances

After more than 40 years of effort, only about half a dozen HVCs have been observed in stellar absorption, setting upper distance limits. We still lack a clear picture of exactly where the HVCs are. It is clear the vast majority of HVCs do not lie within ~ 1 kpc or so. Recent evidence suggests there is no substantial population of clouds at very large distances ($\gtrsim 150$ kpc). Yet the space between these extremes is large. To build a comprehensive picture of the relation of HVCs to the Galaxy, detailed knowledge of their distances is an integral part.

Past attempts to obtain distances using stellar absorption have been limited by the size of the available telescopes. Modern large telescopes now offer the possibility of obtaining echelle spectra of stars that are up to 50 kpc away in a reasonable amount of time (and it is amusing to speculate how such advances will be viewed in another 40 years); no longer are we restricted to observing local, hot stars. In parallel to the depths which may be reached with telescopes such as Magellan, VLT, Keck etc, large-scale surveys are also yielding more and more distant halo tracers which are suitable as background sources. The Hamburg/ESO Survey, Sloan Digital Sky Survey and targeted searches are revealing HB stars out to $\sim 50 - 100$ kpc (e.g. Sirko et al., 2004a; Clewley et al., 2004). Surveys expected to start operation in the next few years, such as the Stromlo Southern Sky Survey, are expected to probe to the very edges of the stellar halo over the whole sky. All the requirements are now in place to address the HVC distance issue in a systematic fashion. Such a pursuit is by no means easy. To observe 50 – 100 (say) stars aligned with HVCs, would require several hundred hours of 8m-class telescope time. Convincing a TAC to allocate such an amount of time remains a significant challenge.

8.2.2 Compact HVCs

It is important to note that more than 20 compact or semi-compact HVCs are included in our FHB/HVC catalogue. It is still a matter of debate whether the CHVCs and the HVCs are drawn from the same population, or whether they are distinct. Such observations were made in the context of dark-matter dominated models (Braun & Burton, 1999; de Heij et al., 2002a). Establishing the distances, and with them the physical conditions, of the CHVCs would go a long way to answering this question. Recent studies place the CHVCs with the Milky Way halo (Westmeier et al., 2005a), yet by definition they are isolated; many will be distinct from the large clouds and complexes. Where do they

originate? Are they stable? Are they confined, and if so, by what?

8.2.3 The Wannier Clouds and Complex WB

The detection and subsequent distance bracket for complex WB is surely the outstanding result of this work, but many questions remain. The first of these is to confirm the classification (and hence distance estimates) of HE $1048+0231$ and HE $1138-1303$ with additional photometry. Using the $T_{\rm eff}$ and $\log g$ obtained from the methods of Wilhelm et al. (1999a), we can perform an analysis of the metal abundance of the two stars. This abundance can then be fed back into the distance relations, further refining the distance. The stars may also prove chemically interesting in their own right.

Having affirmed the distance to complex WB, we can then progress to study the other clouds in this region. Is all the gas in this region of position-velocity space connected, or is it physically disjoint? What is the relation to the intermediate-velocity gas in this region? There appears to be a smooth kinematic connection of high- and intermediate-velocity gas in this region. Perhaps all these clouds share a similar origin? Certainly knowledge of the metallicity of the gas in this region would be a boon — preliminary results of *FUSE* observations towards several extra-Galactic sightlines in this region were presented at the recent AAS meeting in Washington (Ojalvo & Wakker, 2005). The metallicity aspect may prove to be quite important, given the anomalously high Ca II abundances measured in these clouds (Robertson et al., 1991; Thom et al., 2006). What is the cause of these large values?

8.2.4 Connection to IVC gas

Related to the nature of the Wannier clouds is the association of the HVC gas with intermediate-velocity gas. The positive velocity clouds in this region show smooth kinematic links to intermediate velocity emission. Is this link physical, and if so, what does it imply for the HVC-IVC gas as a whole? Perhaps this is gas on the last stages of infall onto the disk and has been slowed by drag forces? Or perhaps all this gas is linked to fountain-like flows? Several of the Magellan spectra show a clear detection absorption at intermediate velocities. Caution is required for their interpretation, however, since the HIPASS data are unreliable in this velocity regime — they have not been corrected for stray radiation. Optical spectra from the VLT and AAT telescopes (which have not been discussed here) also show absorption at intermediate velocities towards clouds in this region. Interestingly, these same stars show no hint of absorption by high-velocity gas. Further work in this area will be aided by the Galactic All-Sky Survey (GASS; McClure-Griffiths et al., 2006) with the Parkes telescope, which is currently more than 50% complete. This survey is designed to study the regime of the disk-halo interface, has much higher velocity resolution than the HIPASS survey, and also has the requisite stray-radiation corrections.

8.2.5 Gas Associated with the Sgr Stream

In Chapter 7 we suggested that some high-velocity clouds with similar positions and velocities to the stellar stream were physically related; that the gas was also stripped from the Sgr dwarf. It is apparent that the stars and gas will follow different kinematics when no longer bound to the host galaxy. While the stars might have little change to their velocities, can we expect the gas to follow a similar ballistic path? Perhaps the action of a diffuse halo medium will brake the clouds? It is not immediately obvious how such clouds would react, and numerical simulations would be helpful to resolve these questions.

8.2.6 Magellanic Stream

The most prominent HVC is the Magellanic Stream (Mathewson et al., 1974); it is well known that this gas has been stripped from the Magellanic clouds as they interact with the Milky Way. Two competing scenarios attempt to explain the features of the Stream: a ram-pressure stripping model (e.g. Moore & Davis, 1994; Mastropietro et al., 2005), and a tidal disruption model (e.g. Gardiner & Noguchi, 1996; Yoshizawa & Noguchi, 2003; Connors et al., 2006). Since the two scenarios involve fundamentally different processes, they predict different physical locations for the Stream gas. Distance limits from stars in the $30 - 40$ kpc range may help to distinguish between the correct model, providing important constraints for simulations of the Stream. In Chapter 6, we identified the star HE 2340+0149 as possibly associated with Stream gas. This is an obvious place to start when pursuing further investigations. Of critical importance is a precise classification of the star, in order to determine accurately the stellar distance. Further observations would be required to assess whether the star is associated with the gas, or this is merely a chance coincidence.

8.2.7 The Larger Picture

Recent observations of O VI with *FUSE* show local ionised gas with a covering fraction of $\sim 85\%$ (Sembach et al., 2003). Some of this O VI emission is coincident with the neutral hydrogen HVCs and is probably a result of HVC interaction with an ambient medium (e.g. Fox et al., 2004), but much of the O VI has no neutral counterpart, a fact taken as evidence of a hot, low density corona around the Galaxy (Sembach et al., 2003). Such a hot corona has been recently detected around the quiescent spiral NGC 5746 (Pedersen et al., 2005). Maller & Bullock (2004) suggest a mechanism relating this hot and neutral gas through cooling and accretion. All this work, including the nature of the HVCs, is a facet of more fundamental questions: *how does gas get into galaxies?* What is the relationship between the hot and cool gas? How do they affect the formation and evolution of galaxies? Answering these questions is, ultimately, the goal towards which we are working.

BIBLIOGRAPHY

Alibés, A., Labay, J., & Canal, R. 2001, A&A, 370, 1103

Anders, E. & Grevesse, N. 1989, Geochim. Cosmochim. Acta, 53, 197

Arp, H. 1985, AJ, 90, 1012

Barnes, D. G., Staveley-Smith, L., de Blok, W. J. G., Oosterloo, T., Stewart, I. M., Wright, A. E., Banks, G. D., Bhathal, R., Boyce, P. J., Calabretta, M. R., Disney, M. J., Drinkwater, M. J., Ekers, R. D., Freeman, K. C., Gibson, B. K., Green, A. J., Haynes, R. F., te Lintel Hekkert, P., Henning, P. A., Jerjen, H., Juraszek, S., Kesteven, M. J., Kilborn, V. A., Knezek, P. M., Koribalski, B., Kraan-Korteweg, R. C., Malin, D. F., Marquarding, M., Minchin, R. F., Mould, J. R., Price, R. M., Putman, M. E., Ryder, S. D., Sadler, E. M., Schröder, A., Stootman, F., Webster, R. L., Wilson, W. E., & Ye, T. 2001, MNRAS, 322, 486

Bates, B., Catney, M. G., & Keenan, F. P. 1990, MNRAS, 242, 267

Beers, T. C., Chiba, M., Sakamoto, T., Wilhelm, R., Allende Prieto, C., Sommer-Larsen, J., Newberg, H. J., Yanny, B., Marsteller, B., & Pier, J. R. 2004, in IAU Symposium, 195

Beers, T. C., Drilling, J. S., Rossi, S., Chiba, M., Rhee, J., Führmeister, B., Norris, J. E., & von Hippel, T. 2002, AJ, 124, 931

Beers, T. C., Preston, G. W., & Shectman, S. A. 1985, AJ, 90, 2089

—. 1988, ApJS, 67, 461

—. 1992, AJ, 103, 1987

Beers, T. C., Wilhelm, R., Doinidis, S. P., & Mattson, C. J. 1996, ApJS, 103, 433

Bernstein, R., Shectman, S. A., Gunnels, S. M., Mochnacki, S., & Athey, A. E. 2003, in Proc. SPIE, Vol. 4841, 1694

Bevington, P. R. & Robinson, D. K. 2003, Data reduction and error analysis for the physical sciences (Data reduction and error analysis for the physical sciences, 3rd ed., by Philip R. Bevington, and Keith D. Robinson. Boston, MA: McGraw-Hill, ISBN 0-07-247227-8, 2003.)

Binney, J. & Tremaine, S. 1987, Galactic dynamics (Princeton, NJ, Princeton University Press, 1987, 747 p.)

Bland-Hawthorn, J., Freeman, K. C., & Quinn, P. J. 1997, ApJ, 490, 143

Blitz, L., Spergel, D. N., Teuben, P. J., Hartmann, D., & Burton, W. B. 1999, ApJ, 514, 818

Bluhm, H., de Boer, K. S., Marggraf, O., & Richter, P. 2001, A&A, 367, 299

Bouchard, A., Carignan, C., & Mashchenko, S. 2003, AJ, 126, 1295

Braun, R. & Burton, W. B. 1999, A&A, 341, 437

Bregman, J. N. 1980, ApJ, 236, 577

Brown, W. R., Geller, M. J., Kenyon, S. J., Beers, T. C., Kurtz, M. J., & Roll, J. B. 2004, AJ, 127, 1555

Brüns, C., Kerp, J., Staveley-Smith, L., Mebold, U., Putman, M. E., Haynes, R. F., Kalberla, P. M. W., Muller, E., & Filipovic, M. D. 2005, A&A, 432, 45

Burton, W. B. & Lockman, F. J. 1999, A&A, 349, 7

Chiappini, C., Matteucci, F., & Gratton, R. 1997, ApJ, 477, 765

Chiba, M. & Beers, T. C. 2000, AJ, 119, 2843

Christlieb, N. 2003, Rev. Mod. Astron., 16, 191, astro-ph/0308016

Christlieb, N., Beers, T. C., Thom, C., Wilhelm, R., Rossi, S., Flynn, C., Wisotzki, L., & Reimers, D. 2005, A&A, 431, 143

Christlieb, N., Bessell, M., Beers, T., Gustafsson, B., Korn, A., Barklem, P., Karlsson, T., Mizuno-Wiedner, M., & Rossi, S. 2002, Nature, 419, 904

Christlieb, N., Green, P., Wisotzki, L., & Reimers, D. 2001a, A&A, 375, 366

Christlieb, N., Wisotzki, L., Reimers, D., Homeier, D., Koester, D., & Heber, U. 2001b, A&A, 366, 898

Clementini, G., Carretta, E., Gratton, R., Merighi, R., Mould, J. R., & McCarthy, J. K. 1995, AJ, 110, 2319

Clewley, L., Warren, S. J., Hewett, P. C., Norris, J. E., & Evans, N. W. 2004, MNRAS, 352, 285

Clewley, L., Warren, S. J., Hewett, P. C., Norris, J. E., Peterson, R. C., & Evans, N. W. 2002, MNRAS, 337, 87

Cohen, R. J. 1981, MNRAS, 196, 835

Collins, J. A., Shull, J. M., & Giroux, M. L. 2003, ApJ, 585, 336

Connors, T. W., Kawata, D., & Gibson, B. K. 2006, MNRAS, submitted (astro-ph/0508390)

Cowie, L. L. & Songaila, A. 1986, ARA&A, 24, 499

Danly, L., Albert, C. E., & Kuntz, K. D. 1993, ApJ, 416, L29+

Davies, J., Sabatini, S., Davies, L., Linder, S., Roberts, S., Smith, R., & Evans, R. 2002, MNRAS, 336, 155

de Avillez, M. A. 2000, Ap&SS, 272, 23

de Heij, V., Braun, R., & Burton, W. B. 2002a, A&A, 392, 417

—. 2002b, A&A, 391, 159

Dickey, J. M. & Lockman, F. J. 1990, ARA&A, 28, 215

Dinescu, D. I., Majewski, S. R., Girard, T. M., Méndez, R. A., Sandage, A., Siegel, M. H., Kunkel, W. E., Subasavage, J. P., & Ostheimer, J. 2002, ApJ, 575, L67

Dolphin, A. E. 2002, MNRAS, 332, 91

Fenner, Y. & Gibson, B. K. 2003, Publ. Astr. Soc. Aus., 20, 189

Flynn, C., Sommer-Larsen, J., & Christensen, P. R. 1994, MNRAS, 267, 77

—. 1996, MNRAS, 281, 1027

Fox, A. J., Savage, B. D., Wakker, B. P., Richter, P., Sembach, K. R., & Tripp, T. M. 2004, ApJ, 602, 738

Frebel, A., Aoki, W., Christlieb, N., Ando, H., Asplund, M., Barklem, P. S., Beers, T. C., Eriksson, K., Fechner, C., Fujimoto, M. Y., Honda, S., Kajino, T., Minezaki, T., Nomoto, K., Norris, J. E., Ryan, S. G., Takada-Hidai, M., Tsangarides, S., & Yoshii, Y. 2005, Nature, 434, 871

Frebel, A., e. a. 2006, in preparation

Gardiner, L. T. & Noguchi, M. 1996, MNRAS, 278, 191

Gavazzi, G., Bonfanti, C., Sanvito, G., Boselli, A., & Scodeggio, M. 2002, ApJ, 576, 135

Gibson, B. K., Giroux, M. L., Penton, S. V., Stocke, J. T., Shull, J. M., & Tumlinson, J. 2001, AJ, 122, 3280

Gould, A. 2003, ApJ, 583, 765

—. 2004, ApJ, 607, 653

Gratton, R. G. 1998, MNRAS, 296, 739

Grebel, E. K., Gallagher, J. S., & Harbeck, D. 2003, AJ, 125, 1926

Green, P. J., Margon, B., Anderson, S. F., & Cook, K. H. 1994, ApJ, 434, 319

Gunn, J. E. & Gott, J. R. I. 1972, ApJ, 176, 1

Hopp, U., Schulte-Ladbeck, R. E., & Kerp, J. 2003, MNRAS, 339, 33

Hulsbosch, A. N. M. 1968, Bull. Astron. Inst. Netherlands, 20, 33

—. 1971, A&A, 14, 489

Hulsbosch, A. N. M. & Raimond, E. 1966, Bull. Astron. Inst. Netherlands, 18, 413

Ibata, R., Lewis, G. F., Irwin, M., Totten, E., & Quinn, T. 2001, ApJ, 551, 294

Ibata, R. A., Gilmore, G., & Irwin, M. J. 1994, Nature, 370, 194

Ibata, R. A. & Lewis, G. F. 1998, ApJ, 500, 575

Kalberla, P. M. W., Burton, W. B., Hartmann, D., Arnal, E. M., Bajaja, E., Morras, R., & Pöppel, W. G. L. 2005, A&A, 440, 775

Kepner, M. E. 1968, Bull. Astron. Inst. Netherlands, 20, 98

Kinman, T. D., Suntzeff, N. B., & Kraft, R. P. 1994, AJ, 108, 1722

Klypin, A., Kravtsov, A. V., Valenzuela, O., & Prada, F. 1999, ApJ, 522, 82

Koribalski, B., Johnston, S., & Otrupcek, R. 1994, MNRAS, 270, L43+

Kuntz, K. D. & Danly, L. 1996, ApJ, 457, 703

Kupka, F. G., Ryabchikova, T. A., Piskunov, N. E., Stempels, H. C., & Weiss, W. W. 2000, Baltic Astronomy, 9, 590

Layden, A. C. & Sarajedini, A. 2000, AJ, 119, 1760

Lee, J. C., Salzer, J. J., Impey, C., Thuan, T. X., & Gronwall, C. 2002, AJ, 124, 3088

Lynden-Bell, D. & Lynden-Bell, R. M. 1995, MNRAS, 275, 429

Majewski, S. R. 1994, ApJ, 431, L17

Majewski, S. R., Skrutskie, M. F., Weinberg, M. D., & Ostheimer, J. C. 2003, ApJ, 599, 1082

Maller, A. H. & Bullock, J. S. 2004, MNRAS, 355, 694

Maloney, P. 1993, ApJ, 414, 41

Mastropietro, C., Moore, B., Mayer, L., Wadsley, J., & Stadel, J. 2005, MNRAS, 363, 509

Mateo, M. L. 1998, ARA&A, 36, 435

Mathewson, D. S., Cleary, M. N., & Murray, J. D. 1974, ApJ, 190, 291

McClure-Griffiths, N. M., Ford, A., Pisano, D. J., Gibson, B. K., Staveley-Smith, L., Calabretta, M. R., Dedes, L., & Kalberla, P. M. W. 2006, ApJ, 638, 196

Mihos, J. C. 2001, ApJ, 550, 94

Moore, B. & Davis, M. 1994, MNRAS, 270, 209

Mori, M. & Burkert, A. 2000, ApJ, 538, 559

Morrison, H. L., Flynn, C., & Freeman, K. C. 1990, AJ, 100, 1191

Morrison, H. L., Mateo, M., Olszewski, E. W., Harding, P., Dohm-Palmer, R. C., Freeman, K. C., Norris, J. E., & Morita, M. 2000, AJ, 119, 2254

Morton, D. C. 2003, ApJS, 149, 205

—. 2004, ApJS, 151, 403

Muller, C. A., Oort, J. H., & Raimond, E. 1963, Comptes Rendus de l'Académie des Sciences Paris, 257, 1661

Newberg, H. J., Yanny, B., Grebel, E. K., Hennessy, G., Ivezić, Ž., Martinez-Delgado, D., Odenkirchen, M., Rix, H.-W., Brinkmann, J., Lamb, D. Q., Schneider, D. P., & York, D. G. 2003, ApJ, 596, L191

Newberg, H. J., Yanny, B., Rockosi, C., Grebel, E. K., Rix, H.-W., Brinkmann, J., Csabai, I., Hennessy, G., Hindsley, R. B., Ibata, R., Ivezić, Z., Lamb, D., Nash, E. T., Odenkirchen, M., Rave, H. A., Schneider, D. P., Smith, J. A., Stolte, A., & York, D. G. 2002, ApJ, 569, 245

Nicastro, F., Zezas, A., Elvis, M., Mathur, S., Fiore, F., Cecchi-Pestellini, C., Burke, D., Drake, J., & Casella, P. 2003, Nature, 421, 719

Norris, J. E. & Hawkins, M. R. S. 1991, ApJ, 380, 104

Ojalvo, I. & Wakker, B. 2005, American Astronomical Society Meeting Abstracts, 207,

Oort, J. H. 1966, Bull. Astron. Inst. Netherlands, 18, 421

Pagel, B. E. J. & Patchett, B. E. 1975, MNRAS, 172, 13

Pearson, E. 1926, Biometrika, 18, 173

Pedersen, K., Rasmussen, J., Sommer-Larsen, J., Toft, S., Benson, A., & Bower, R. 2005, New Astronomy, in press (astro

Perryman, M. A. C. 2002, Ap&SS, 280, 1

Philip, A. G. D. 1967, ApJ, 148, L143+

Pisano, D. J., Barnes, D. G., Gibson, B. K., Staveley-Smith, L., Freeman, K. C., & Kilborn, V. A. 2004, ApJ, 610, L17

Prata, S. & Wallerstein, G. 1967, PASP, 79, 202

Press, W. H., Teukolsky, S. A., Vetterling, W. T., & Flannery, B. P. 1992, Numerical recipes in FORTRAN. The art of scientific computing (Cambridge: University Press, —c1992, 2nd ed.)

Preston, G. W., Beers, T. C., & Shectman, S. A. 1994, AJ, 108, 538

Preston, G. W., Shectman, S. A., & Beers, T. C. 1991, ApJ, 375, 121

Preston, G. W. & Sneden, C. 2000, AJ, 120, 1014

Putman, M. E., Bland-Hawthorn, J., Veilleux, S., Gibson, B. K., Freeman, K. C., & Maloney, P. R. 2003a, ApJ, 597, 948

Putman, M. E., de Heij, V., Staveley-Smith, L., Braun, R., Freeman, K. C., Gibson, B. K., Burton, W. B., Barnes, D. G., Banks, G. D., Bhathal, R., de Blok, W. J. G., Boyce, P. J., Disney, M. J., Drinkwater, M. J., Ekers, R. D., Henning, P. A., Jerjen, H., Kilborn, V. A., Knezek, P. M., Koribalski, B., Malin, D. F., Marquarding, M., Minchin, R. F., Mould, J. R., Oosterloo, T., Price, R. M., Ryder, S. D., Sadler, E. M., Stewart, I., Stootman, F., Webster, R. L., & Wright, A. E. 2002, AJ, 123, 873

Putman, M. E., Gibson, B. K., Staveley-Smith, L., Banks, G., Barnes, D. G., Bhatal, R., Disney, M. J., Ekers, R. D., Freeman, K. C., Haynes, R. F., Henning, P., Jerjen, H., Kilborn, V., Koribalski, B., Knezek, P., Malin, D. F., Mould, J. R., Oosterloo, T., Price, R. M., Ryder, S. D., Sadler, E. M., Stewart, I., Stootman, F., Vaile, R. A., Webster, R. L., & Wright, A. E. 1998, Nature, 394, 752

Putman, M. E., Staveley-Smith, L., Freeman, K. C., Gibson, B. K., & Barnes, D. G. 2003b, ApJ, 586, 170

Quilis, V. & Moore, B. 2001, ApJ, 555, L95

Richter, P., de Boer, K. S., Widmann, H., Kappelmann, N., Gringel, W., Grewing, M., & Barnstedt, J. 1999, Nature, 402, 386

Robertson, J. G., Schwarz, U. J., van Woerden, H., Murray, J. D., Morton, D. C., & Hulsbosch, A. N. M. 1991, MNRAS, 248, 508

Robin, A. C., Reylé, C., & Crézé, M. 2000, A&A, 359, 103

Ryans, R. S. I., Keenan, F. P., Sembach, K. R., & Davies, R. D. 1997, MNRAS, 289, 83

Savage, B. D. & Sembach, K. R. 1996, ARA&A, 34, 279

Savage, B. D., Sembach, K. R., Wakker, B. P., Richter, P., Meade, M., Jenkins, E. B., Shull, J. M., Moos, H. W., & Sonneborn, G. 2003, ApJS, 146, 125

Schlegel, D. J., Finkbeiner, D. P., & Davis, M. 1998, ApJ, 500, 525

Schwarz, U. J., Wakker, B. P., & van Woerden, H. 1995, A&A, 302, 364

Sembach, K. R. & Savage, B. D. 1992, ApJS, 83, 147

Sembach, K. R., Savage, B. D., & Massa, D. 1991, ApJ, 372, 81

Sembach, K. R., Wakker, B. P., Savage, B. D., Richter, P., Meade, M., Shull, J. M., Jenkins, E. B., Sonneborn, G., & Moos, H. W. 2003, ApJS, 146, 165

Shapiro, P. R. & Field, G. B. 1976, ApJ, 205, 762

Siegel, M. H., Majewski, S. R., Gallart, C., Sohn, S. T., Kunkel, W. E., & Braun, R. 2005, ApJ, 623, 181

Simon, J. D. & Blitz, L. 2002, ApJ, 574, 726

Sirko, E., Goodman, J., Knapp, G. R., Brinkmann, J., Ivezić, Ž., Knerr, E. J., Schlegel, D., Schneider, D. P., & York, D. G. 2004a, AJ, 127, 899

—. 2004b, AJ, 127, 914

Sluis, A. P. N. & Arnold, R. A. 1998, MNRAS, 297, 732

Smoker, J. V., Lynn, B. B., Rolleston, W. R. J., Kay, H. R. M., Bajaja, E., Poppel, W. G. L., Keenan, F. P., Kalberla, P. M. W., Mooney, C. J., Dufton, P. L., & Ryans, R. S. I. 2004, MNRAS, 352, 1279

Sommer-Larsen, J., Beers, T. C., Flynn, C., Wilhelm, R., & Christensen, P. R. 1997, ApJ, 481, 775

Sommer-Larsen, J., Christensen, P. R., & Carter, D. 1989, MNRAS, 238, 225

Sommer-Larsen, J., Flynn, C., & Christensen, P. R. 1994, MNRAS, 271, 94

Songaila, A. & York, D. G. 1980, ApJ, 242, 976

Spitzer, L. J. 1956, ApJ, 124, 20

Stanimirović, S., Dickey, J. M., Krčo, M., & Brooks, A. M. 2002, ApJ, 576, 773

Steidel, C. C., Kollmeier, J. A., Shapley, A. E., Churchill, C. W., Dickinson, M., & Pettini, M. 2002, ApJ, 570, 526

Tamanaha, C. M. 1994, ApJ, 433, 648

—. 1995, ApJ, 450, 638

—. 1996, ApJS, 104, 81

—. 1997, ApJS, 109, 139

Taylor, J. H., Manchester, R. N., & Lyne, A. G. 1993, ApJS, 88, 529

Thilker, D. A., Braun, R., Walterbos, R. A. M., Corbelli, E., Lockman, F. J., Murphy, E., & Maddalena, R. 2004, ApJ, 601, L39

Thom, C., Gibson, B. K., & Christlieb, N. 2005, ApJS, 161, 147

Thom, C., Putman, M. E., Gibson, B. K., Christlieb, N., Flynn, C., Beers, T. C., Wilhelm, R., & Lee, Y. S. 2006, ApJL, 638, L97

Tippett, L. 1925, Biometrika, 17, 364

Tosi, M. 1988, A&A, 197, 47

Totten, E. J. & Irwin, M. J. 1998, MNRAS, 294, 1

Tufte, S. L., Wilson, J. D., Madsen, G. J., Haffner, L. M., & Reynolds, R. J. 2002, ApJ, 572, L153

van Kuilenburg, J. 1972, A&AS, 5, 1

van Woerden, H., Schwarz, U. J., Peletier, R. F., Wakker, B. P., & Kalberla, P. M. W. 1999, Nature, 400, 138

Verschuur, G. L. 1969, ApJ, 156, 771

Wakker, B. P. 1990, PhD thesis, Univ. Gröningen

—. 1991, A&A, 250, 499

—. 2001, ApJS, 136, 463

Wakker, B. P., Howk, J. C., Savage, B. D., van Woerden, H., Tufte, S. L., Schwarz, U. J., Benjamin, R., Reynolds, R. J., Peletier, R. F., & Kalberla, P. M. W. 1999, Nature, 402, 388

Wakker, B. P. & Mathis, J. S. 2000, ApJ, 544, L107

Wakker, B. P., Savage, B. D., Sembach, K. R., Richter, P., Meade, M., Jenkins, E. B., Shull, J. M., Ake, T. B., Blair, W. P., Dixon, W. V., Friedman, S. D., Green, J. C., Green, R. F., Kruk, J. W., Moos, H. W., Murphy, E. M., Oegerle, W. R., Sahnow, D. J., Sonneborn, G., Wilkinson, E., & York, D. G. 2003, ApJS, 146, 1

Wakker, B. P. & Schwarz, U. J. 1991, A&A, 250, 484

Wakker, B. P. & van Woerden, H. 1991, A&A, 250, 509

—. 1997, ARA&A, 35, 217

Wang, Q. D. & McCray, R. 1993, ApJ, 409, L37

Wannier, P., Wrixon, G. T., & Wilson, R. W. 1972, A&A, 18, 224

Westmeier, T. 2003, Master's thesis, Bonn

Westmeier, T., Brüns, C., & Kerp, J. 2005a, A&A, 432, 937

Westmeier, T., Braun, R., & Thilker, D. 2005b, A&A, 436, 101

Wilhelm, R., Beers, T. C., & Gray, R. O. 1999a, AJ, 117, 2308

Wilhelm, R., Beers, T. C., Sommer-Larsen, J., Pier, J. R., Layden, A. C., Flynn, C., Rossi, S., & Christensen, P. R. 1999b, AJ, 117, 2329

Wilkinson, M. I. & Evans, N. W. 1999, MNRAS, 310, 645

Wisotzki, L., Christlieb, N., Bade, N., Beckmann, V., Köhler, T., Vanelle, C., & Reimers, D. 2000, A&A, 358, 77

Wisotzki, L., Köhler, T., Groote, D., & Reimers, D. 1996, A&AS, 115, 227

Yanny, B., Newberg, H. J., Grebel, E. K., Kent, S., Odenkirchen, M., Rockosi, C. M., Schlegel, D., Subbarao, M., Brinkmann, J., Fukugita, M., Ivezic, Ž., Lamb, D. Q., Schneider, D. P., & York, D. G. 2003a, ApJ, 588, 824

—. 2003b, ApJ, 588, 824

York, D. G. 1974, ApJ, 193, L127

York, D. G., Burks, G. S., & Gibney, T. B. 1986, AJ, 91, 354

Yoshizawa, A. M. & Noguchi, M. 2003, MNRAS, 339, 1135

Zwaan, M. A. & Briggs, F. H. 2000, ApJ, 530, L61

APPENDIX A

FHB/HVC CATALOGUE

Table A.1. Catalogue of FHB stars aligned with HVCs.

Num	HEname	RA (J2000)	DEC (J2000)	l (deg)	b (deg)	B mag (mag)	Distance (kpc)	T_b (K)	N(H I) (cm^{-2})	v_{LSR} $km\ s^{-1}$	MS Flag	HVC	XHVC	WvW91	de Heij
001	HE 2357−0242	00 00 03.1	-02 25 49	94.27	-62.418	17.9	24.4	0.18	1.1e+19	-310	—	CHVC#505	—	WvW#542	CHVC:#341
002	HE 2357−1617	00 00 08.1	-16 00 37	73.38	-73.724	16.1	10.1	0.30	1.9e+19	-191	*	—	—	—	HVC#243
003	HE 2357−2211	00 00 10.4	-21 55 15	54.23	-77.244	18.3	29.8	0.36	1.9e+19	-112	*	—	XHVC#25	—	HVC#261
004	HE 2358−6115	00 00 37.1	-60 59 04	313.67	-55.071	15.9	10.2	0.30	1.9e+19	+152	*	—	—	—	—
005	HE 2358−1813	00 00 49.2	-17 57 15	68.48	-75.167	15.0	6.7	0.39	2.3e+19	-152	*	—	—	—	—
006	HE 2358−0339	00 01 29.2	-03 23 02	94.09	-63.427	14.0	3.7	0.21	1.3e+19	-310	—	CHVC#505	—	WvW#542	CHVC:#341
007	HE 2359−1320	00 01 44.9	-13 04 04	80.91	-71.766	16.7	13.8	0.19	1.2e+19	-257	*	HVC#481	—	—	—
008	HE 2359−4258	00 02 08.5	-42 42 14	332.52	-71.485	13.9	4.0	0.20	1.0e+19	+099	*	—	XHVC#150	—	—
009	HE 2359−2257	00 02 13.2	-22 40 20	52.02	-77.997	16.0	10.4	0.25	1.4e+19	-112	*	—	XHVC#25	—	HVC#261
010	HE 0000−5241	00 02 37.7	-52 24 24	319.50	-63.129	16.2	7.8	0.33	2.0e+19	+099	*	HVC#1659	—	WvW#543	—
011	HE 0000−2022	00 03 02.4	-20 06 04	62.75	-76.890	17.0	15.9	0.34	2.1e+19	-139	*	—	XHVC#25	—	HVC#261
012	HE 0000−4238	00 03 02.7	-42 22 09	332.73	-71.854	16.7	11.6	0.76	4.6e+19	+099	*	—	XHVC#150	—	—
013	HE 0000−1818	00 03 25.1	-18 02 15	69.84	-75.681	15.4	6.8	0.48	3.2e+19	-191	*	—	—	—	HVC#243
014	HE 0000−6026	00 03 29.4	-60 09 33	313.57	-55.971	18.0	23.7	0.27	1.6e+19	+152	*	—	—	—	—
015	HE 0001−6021	00 03 39.2	-60 04 25	313.59	-56.053	14.4	5.2	0.20	1.0e+19	+152	*	—	—	—	—
016	HE 0001−6121	00 03 58.5	-61 04 19	312.95	-55.122	17.4	18.3	0.30	2.0e+19	+152	*	—	—	—	—
017	HE 0001−4300	00 04 00.7	-42 43 57	331.59	-71.661	14.9	6.6	0.98	5.9e+19	+099	*	—	XHVC#150	—	—
018	HE 0003−3451	00 05 45.0	-34 34 45	352.87	-77.701	16.7	14.7	0.31	2.1e+19	+112	*	—	XHVC#181	—	—
019	HE 0003−2305	00 06 14.2	-22 48 56	53.30	-78.899	14.8	5.7	1.02	6.5e+19	-125	*	—	XHVC#25	—	HVC#261
020	HE 0003−5248	00 06 17.9	-52 31 41	318.26	-63.245	15.8	9.5	0.34	2.2e+19	+112	*	HVC#1659	—	WvW#543	—
021	HE 0004−2027	00 06 49.3	-20 11 12	64.78	-77.667	16.8	14.4	0.43	2.8e+19	-152	*	—	—	—	—
022	HE 0004−5813	00 07 02.1	-57 56 35	314.12	-58.214	16.4	7.0	0.24	1.4e+19	+125	*	HVC#1630	—	—	—
023	HE 0004−5251	00 07 28.0	-52 34 24	317.86	-63.266	15.8	9.5	0.16	9.3e+18	+099	*	HVC#1659	—	WvW#543	—
024	HE 0005−2140	00 07 41.5	-21 23 34	60.50	-78.519	17.3	18.5	0.20	1.2e+19	-139	*	—	XHVC#25	—	HVC#261
025	HE 0005−2116	00 08 15.4	-20 59 52	62.51	-78.400	14.8	6.1	0.52	3.3e+19	-139	*	—	XHVC#25	—	HVC#261
026	HE 0006−3510	00 08 47.2	-34 53 33	349.93	-78.021	16.4	12.6	0.22	1.4e+19	+099	*	—	XHVC#181	—	—
027	HE 0006−1506	00 09 07.3	-14 49 27	82.13	-74.242	16.7	14.6	0.19	1.3e+19	-257	*	CHVC#484	—	—	—
028	HE 0006−6119	00 09 10.8	-61 02 29	311.91	-55.347	16.9	11.9	0.50	3.2e+19	+165	*	—	—	—	—
029	HE 0006−2349	00 09 11.6	-23 33 10	51.15	-79.816	16.3	11.5	0.49	3.1e+19	-112	*	—	XHVC#25	—	HVC#261
030	HE 0007−2441	00 09 56.0	-24 24 43	46.84	-80.271	16.3	12.0	1.21	7.4e+19	-112	*	—	XHVC#25	—	HVC#261
031	HE 0009−2437	00 11 39.2	-24 21 09	47.94	-80.627	17.3	18.4	0.93	5.8e+19	-112	*	—	XHVC#25	—	HVC#261
032	HE 0009−2048	00 11 53.7	-20 32 05	66.94	-78.826	16.5	13.3	0.57	3.5e+19	-139	*	—	XHVC#25	—	HVC#261
033	HE 0009−2321	00 12 15.0	-23 04 33	55.34	-80.257	17.3	19.0	0.23	1.4e+19	-139	*	—	XHVC#25	—	HVC#261
034	HE 0010−3422	00 12 55.8	-34 05 45	350.49	-79.196	15.6	8.5	0.23	1.3e+19	-152	*	—	—	—	—
035	HE 0010−6130_1	00 13 06.3	-61 13 53	311.02	-55.291	18.0	26.3	0.31	1.8e+19	+099	*	—	—	—	—
036	HE 0010−6130_2	00 13 06.3	-61 13 53	311.02	-55.291	18.0	26.3	0.26	1.9e+19	+165	*	—	—	—	—
037	HE 0010−6137	00 13 22.5	-61 21 17	310.91	-55.183	17.3	11.2	0.47	3.1e+19	+112	*	—	—	—	—
038	HE 0011−2119	00 13 37.7	-21 02 46	66.10	-79.456	17.1	13.1	0.85	5.4e+19	-139	*	—	XHVC#25	—	HVC#261
039	HE 0011−5316	00 14 00.7	-53 00 13	315.47	-63.205	15.3	7.7	0.35	2.0e+19	+112	*	:HVC#1620	—	WvW#543	—
040	HE 0011−2233	00 14 26.3	-22 16 26	60.95	-80.301	13.5	3.3	0.50	3.0e+19	-139	*	—	XHVC#25	—	HVC#261
041	HE 0012−4904	00 15 11.0	-48 47 29	318.48	-67.237	15.8	9.3	0.18	1.0e+19	+125	*	HVC#1642	—	—	—
042	HE 0013−2823	00 16 02.8	-28 06 29	23.77	-82.105	17.0	16.7	0.27	1.5e+19	-112	*	—	XHVC#25	—	—
043	HE 0013−3436	00 16 07.0	-34 20 15	347.22	-79.546	16.2	11.6	0.20	1.2e+19	-125	*	—	XHVC#180	—	—
044	HE 0013−2434	00 16 22.9	-24 18 19	50.66	-81.625	16.2	8.8	0.71	4.5e+19	-112	*	—	XHVC#25	—	HVC#261
045	HE 0014−2748	00 16 40.1	-27 31 47	27.96	-82.273	16.2	10.7	0.20	1.1e+19	-125	*	—	XHVC#25	—	—
046	HE 0014−3922	00 16 54.5	-39 06 01	331.78	-76.032	16.4	12.4	0.75	4.0e+19	+178	*	—	—	—	—
047	HE 0015−2516	00 17 35.2	-24 59 48	46.71	-82.117	15.6	8.8	1.14	6.5e+19	-112	*	—	XHVC#25	—	HVC#261
048	HE 0015−6134	00 18 11.4	-61 17 36	309.95	-55.384	17.6	12.3	0.16	8.5e+18	+165	*	—	—	—	—
049	HE 0016−6000	00 18 55.7	-59 43 29	310.44	-56.936	17.5	10.5	0.14	8.3e+18	+165	*	HVC#1564	—	—	—
050	HE 0017−2800	00 20 30.2	-27 43 51	26.14	-83.116	15.4	6.0	0.71	4.4e+19	-099	*	—	XHVC#25	—	—

Table A.1

Num	HEname	RA (J2000)	DEC (J2000)	l (deg)	b (deg)	B mag (mag)	Distance (kpc)	T_b (K)	N(H I) (cm^{-2})	v_{LSR} $km\ s^{-1}$	MS Flag	HVC	XHVC	WvW91	de Heij
051	HE 0021−2810	00 23 53.5	-27 53 35	24.21	-83.853	15.5	7.0	0.59	3.3e+19	-099	*	—	XHVC#25	—	—
052	HE 0022−2216	00 24 53.6	-22 00 01	71.86	-82.087	17.0	12.4	0.26	1.5e+19	-125	*	—	XHVC#25	—	HVC#261
053	HE 0046−5241	00 49 08.3	-52 24 54	303.75	-64.711	17.3	11.9	0.87	5.4e+19	+099	*	—	XHVC#112	—	—
054	HE 0046−3255	00 49 15.4	-32 39 35	307.68	-84.452	16.1	10.9	0.46	2.9e+19	+112	*	HVC#1550	—	—	—
055	HE 0047−5309	00 49 44.9	-52 53 36	303.52	-64.232	17.1	10.6	1.27	7.2e+19	+099	*	—	XHVC#112	—	—
056	HE 0047−5230	00 49 49.8	-52 14 13	303.51	-64.889	15.9	9.8	1.12	7.4e+19	+098	*	—	XHVC#112	—	—
057	HE 0050−5602	00 52 43.5	-55 45 44	302.55	-61.375	14.8	6.0	0.15	7.2e+18	+152	*	—	—	—	—
058	HE 0050−5414	00 52 43.6	-53 58 09	302.51	-63.165	15.4	7.7	1.26	7.4e+19	+125	*	—	XHVC#112	—	—
059	HE 0050−5153	00 52 54.8	-51 37 29	302.38	-65.506	17.2	18.0	0.79	5.0e+19	+099	*	—	XHVC#112	—	—
060	HE 0051−5603	00 53 28.4	-55 47 12	302.33	-61.343	17.3	19.4	0.14	7.5e+18	+152	*	—	—	—	—
061	HE 0051−5231	00 53 59.8	-52 15 39	302.01	-64.868	17.2	12.8	1.99	1.2e+20	+099	*	—	XHVC#112	—	—
062	HE 0052−5031	00 54 57.3	-50 15 27	301.50	-66.865	16.7	14.5	2.44	1.4e+20	+099	*	—	XHVC#112	—	—
063	HE 0053−5032	00 55 20.1	-50 16 35	301.35	-66.849	15.5	8.4	2.76	1.6e+20	+099	*	—	XHVC#112	—	—
064	HE 0053−5442	00 55 49.6	-54 25 48	301.54	-62.692	14.9	6.3	1.19	7.4e+19	+138	*	—	XHVC#112	—	—
065	HE 0053−4119	00 56 06.6	-41 03 30	299.28	-76.047	15.0	6.3	0.38	2.5e+19	+165	*	—	XHVC#117	—	—
066	HE 0054−5314	00 56 33.8	-52 58 32	301.16	-64.145	16.7	14.4	2.02	1.2e+20	+099	*	—	XHVC#112	—	—
067	HE 0057−6131	00 59 10.6	-61 15 06	301.27	-55.854	17.7	21.5	0.20	1.2e+19	+218	*	—	—	WvW#493	—
068	HE 0056−3330	00 59 14.6	-33 14 41	288.00	-83.669	16.2	11.7	0.39	2.7e+19	-191	*	HVC#1292	—	WvW#561	CHVC?#873
069	HE 0056−4043	00 59 16.3	-40 27 25	296.50	-76.571	15.1	6.2	0.16	1.0e+19	+152	*	—	XHVC#117	—	—
070	HE 0057−5846	00 59 29.0	-58 30 01	300.91	-58.606	15.7	9.0	0.23	1.4e+19	+099	*	—	—	—	—
071	HE 0057−5323	01 00 10.0	-53 07 31	299.95	-63.950	14.3	4.6	0.40	2.2e+19	+112	*	—	XHVC#112	—	—
072	HE 0058−5316	01 01 09.3	-53 00 49	299.59	-64.054	16.0	10.1	0.24	1.4e+19	+112	*	—	XHVC#112	—	—
073	HE 0059−5957	01 01 17.1	-59 41 50	300.63	-57.394	16.5	10.5	0.22	1.3e+19	+178	*	—	—	WvW#493	—
074	HE 0059−6218	01 01 23.6	-62 02 22	300.89	-55.057	15.6	8.5	0.36	2.2e+19	+165	*	—	—	WvW#531	—
075	HE 0059−5841_1	01 01 26.5	-58 24 58	300.41	-58.661	16.1	9.4	0.17	1.1e+19	+178	*	—	—	WvW#493	—
076	HE 0059−5841_2	01 01 26.5	-58 24 58	300.41	-58.661	16.1	9.4	0.16	9.5e+18	+112	*	—	—	—	—
077	HE 0059−6005	01 01 34.8	-59 49 26	300.58	-57.261	16.5	11.2	0.48	2.8e+19	+178	*	—	—	WvW#493	—
078	HE 0059−5952	01 01 49.1	-59 35 55	300.49	-57.482	17.3	17.3	0.16	8.8e+18	+178	*	—	—	WvW#493	—
079	HE 0059−6056_1	01 01 55.1	-60 40 41	300.61	-56.403	16.3	11.8	0.44	2.5e+19	+125	*	—	—	WvW#531	—
080	HE 0059−6056_2	01 01 55.1	-60 40 41	300.61	-56.403	16.3	11.8	0.33	2.0e+19	+191	*	—	—	WvW#493	—
081	HE 0100−6006	01 02 05.4	-59 50 09	300.46	-57.244	17.0	13.2	0.43	2.6e+19	+178	*	—	—	WvW#493	—
082	HE 0059−2003	01 02 17.6	-19 46 55	142.21	-82.243	15.9	10.2	0.16	9.9e+18	-231	*	CHVC#534	—	—	CHVC:#500
083	HE 0100−6024	01 02 56.9	-60 08 32	300.31	-56.939	15.7	8.8	0.21	1.2e+19	+178	*	—	—	WvW#493	—
084	HE 0102−6012	01 04 08.5	-59 56 02	300.00	-57.120	17.6	21.8	0.20	1.2e+19	+178	*	—	—	WvW#493	—
085	HE 0102−6019	01 04 18.9	-60 03 13	299.98	-57.004	18.2	28.1	0.18	1.0e+19	+178	*	—	—	WvW#493	—
086	HE 0103−4830	01 05 57.1	-48 14 01	296.27	-68.710	15.4	8.3	0.25	1.3e+19	+112	*	—	XHVC#112	—	—
087	HE 0103−2031	01 06 05.7	-20 15 48	149.74	-82.361	16.8	15.1	0.16	8.6e+18	-257	*	CHVC#538	—	—	CHVC#523
088	HE 0104−6204	01 06 48.2	-61 48 17	299.75	-55.234	17.0	16.1	1.24	8.1e+19	+204	*	—	—	WvW#493	—
089	HE 0106−5926	01 08 04.5	-59 10 03	298.93	-57.832	15.1	6.1	0.15	7.4e+18	+191	*	—	—	WvW#493	—
090	HE 0106−4913	01 08 18.6	-48 57 56	295.55	-67.925	15.3	7.9	1.10	6.3e+19	+125	*	—	XHVC#112	—	—
091	HE 0106−5921	01 08 42.6	-59 06 01	298.76	-57.898	17.9	24.6	0.41	2.2e+19	+191	*	—	—	WvW#493	—
092	HE 0107−4802	01 09 23.0	-47 46 16	294.47	-69.060	16.8	15.4	0.55	3.2e+19	+112	*	—	XHVC#112	—	—
093	HE 0107−5651	01 09 37.9	-56 35 06	297.86	-60.360	15.5	8.2	0.29	1.8e+19	+178	*	—	—	WvW#493	—
094	HE 0107−4835	01 09 38.1	-48 19 53	294.66	-68.506	16.2	11.6	0.34	1.8e+19	+125	*	—	XHVC#112	—	—
095	HE 0107−5736	01 09 47.3	-57 20 35	298.04	-59.616	17.0	15.8	0.62	3.7e+19	+178	*	—	—	WvW#493	—
096	HE 0108−5451	01 10 44.4	-54 35 38	296.91	-62.319	15.5	8.5	0.13	6.5e+18	+165	*	—	XHVC#112	—	—
097	HE 0108−3554	01 11 18.0	-35 38 53	277.74	-80.495	16.3	11.2	0.50	3.0e+19	-112	*	—	XHVC#88	—	—
098	HE 0109−5743	01 11 21.9	-57 27 50	297.66	-59.466	17.1	12.8	0.61	3.7e+19	+178	*	—	—	WvW#493	—
099	HE 0110−6122_1	01 12 10.2	-61 06 24	298.47	-55.843	18.0	25.8	1.00	5.9e+19	+218	*	—	—	WvW#493	—
100	HE 0110−6122_2	01 12 10.2	-61 06 24	298.47	-55.843	18.0	25.8	0.35	1.9e+19	+138	*	—	—	WvW#529	—

Table A.1

Num	HEname	RA (J2000)	DEC (J2000)	l (deg)	b (deg)	B mag (mag)	Distance (kpc)	T_b (K)	$N(\mathrm{H\ I})$ (cm^{-2})	v_{LSR} $\mathrm{km\ s}^{-1}$	MS Flag	HVC	XHVC	WvW91	de Heij
101	HE 0110−6119_1	01 12 28.1	-61 03 16	298.40	-55.898	16.6	13.0	1.12	6.6e+19	+218	*	—	—	WvW#493	—
102	HE 0110−6119_2	01 12 28.1	-61 03 16	298.40	-55.898	16.6	13.0	0.27	1.5e+19	+138	*	—	—	WvW#529	—
103	HE 0111−6057	01 13 08.0	-60 41 13	298.15	-56.241	15.3	7.3	0.79	4.6e+19	+204	*	—	—	WvW#493	—
104	HE 0112−6108	01 14 10.6	-60 52 10	297.98	-56.045	17.1	17.2	0.70	4.1e+19	+204	*	—	—	WvW#493	—
105	HE 0112−5650	01 14 42.1	-56 34 15	296.47	-60.272	16.9	15.7	0.17	1.0e+19	+178	*	—	—	WvW#493	—
106	HE 0112−5748	01 14 48.0	-57 32 47	296.79	-59.305	16.2	8.9	0.60	3.6e+19	+178	*	—	—	WvW#493	—
107	HE 0112−4915	01 15 01.9	-48 59 56	292.71	-67.662	16.1	9.3	0.14	8.3e+18	+125	*	—	XHVC#112	—	—
108	HE 0113−5547	01 15 09.0	-55 31 33	295.94	-61.284	17.1	16.3	0.29	1.7e+19	+165	*	—	XHVC#112	—	—
109	HE 0113−3543	01 15 54.6	-35 27 29	272.36	-80.171	15.8	8.5	0.18	1.2e+19	-139	*	—	XHVC#88	—	—
110	HE 0114−5929	01 16 50.1	-59 14 05	296.87	-57.598	15.3	7.2	0.43	2.5e+19	+204	*	—	—	WvW#493	—
111	HE 0115−5947	01 17 07.8	-59 31 54	296.91	-57.302	14.3	4.6	0.39	2.3e+19	+218	*	—	—	WvW#493	—
112	HE 0115−6049	01 17 19.2	-60 33 59	297.21	-56.276	16.7	14.6	0.21	1.0e+19	+138	*	—	—	WvW#529	—
113	HE 0115−5929	01 17 35.9	-59 13 32	296.69	-57.599	15.2	7.2	0.35	1.9e+19	+204	*	—	—	WvW#493	—
114	HE 0115−4825	01 17 40.8	-48 09 17	291.00	-68.363	14.5	4.9	0.26	1.6e+19	+152	*	—	XHVC#112	—	—
115	HE 0115−6119_1	01 17 42.7	-61 03 32	297.28	-55.787	17.7	15.7	0.28	1.5e+19	+138	*	—	—	WvW#529	—
116	HE 0115−6119_2	01 17 42.7	-61 03 32	297.28	-55.787	17.7	15.7	0.13	7.0e+18	+204	*	—	—	WvW#493	—
117	HE 0117−5523	01 19 02.2	-55 07 41	294.64	-61.559	16.7	14.8	0.20	9.0e+18	+178	*	—	—	WvW#493	—
118	HE 0119−5856	01 21 15.8	-58 41 07	295.62	-58.026	17.3	19.0	0.41	2.2e+19	+204	*	—	—	WvW#493	—
119	HE 0119−5825	01 21 19.8	-58 09 30	295.38	-58.537	16.6	13.8	0.72	4.5e+19	+191	*	—	—	WvW#493	—
120	HE 0119+0050	01 21 47.4	+01 05 58	138.66	-60.847	15.3	7.3	0.20	1.1e+19	-112	—	—	—	—	—
121	HE 0120−5933_1	01 22 01.4	-59 17 40	295.69	-57.405	16.9	15.2	0.23	9.0e+18	+204	*	—	—	WvW#493	—
122	HE 0120−5933_2	01 22 01.4	-59 17 40	295.69	-57.405	16.9	15.2	0.20	1.1e+19	+152	*	—	—	WvW#531	—
123	HE 0120−5909	01 22 11.4	-58 54 13	295.49	-57.783	17.7	21.0	0.30	1.7e+19	+204	*	—	—	WvW#493	—
124	HE 0120−5829	01 22 12.8	-58 14 07	295.20	-58.435	16.6	10.3	0.75	4.6e+19	+191	*	—	—	WvW#493	—
125	HE 0121−5609	01 23 08.0	-55 53 55	293.85	-60.676	17.3	19.4	2.73	1.6e+20	+191	*	—	—	WvW#493	—
126	HE 0121−5943	01 23 36.3	-59 28 06	295.40	-57.192	15.6	8.7	0.74	5.0e+19	+191	*	—	—	WvW#493	—
127	HE 0122−5821	01 24 04.3	-58 05 48	294.68	-58.512	17.2	16.2	0.93	6.0e+19	+191	*	—	—	WvW#493	—
128	HE 0123−5952_1	01 25 00.2	-59 37 01	295.14	-57.001	16.8	14.9	0.72	4.5e+19	+204	*	—	—	WvW#493	—
129	HE 0123−5952_2	01 25 00.2	-59 37 01	295.14	-57.001	16.8	14.9	0.71	4.6e+19	+152	*	—	—	WvW#531	—
130	HE 0123−6212_1	01 25 09.6	-61 57 20	296.08	-54.720	16.6	12.1	1.88	1.1e+20	+138	*	—	—	WvW#529	—
131	HE 0123−6212_2	01 25 09.6	-61 57 20	296.08	-54.720	16.6	12.1	0.25	1.5e+19	+191	*	—	—	WvW#493	—
132	HE 0123−2449	01 26 12.4	-24 34 14	196.76	-81.778	16.1	11.0	0.35	2.5e+19	-178	*	CHVC#586	—	—	HVC#726
133	HE 0124−6212	01 26 20.8	-61 57 11	295.84	-54.691	15.6	8.6	1.47	7.9e+19	+138	*	—	—	WvW#529	—
134	HE 0124−5709	01 26 25.6	-56 53 39	293.49	-59.593	17.3	17.6	0.34	2.1e+19	+165	*	—	—	—	—
135	HE 0125−6004_1	01 27 35.4	-59 49 18	294.66	-56.729	16.6	13.3	0.58	3.6e+19	+152	*	—	—	WvW#531	—
136	HE 0125−6004_2	01 27 35.4	-59 49 18	294.66	-56.729	16.6	13.3	0.44	2.6e+19	+204	*	—	—	WvW#493	—
137	HE 0125−5801	01 27 39.9	-57 45 42	293.63	-58.712	17.9	24.7	0.56	3.3e+19	+152	*	—	—	—	—
138	HE 0127−6143	01 28 52.4	-61 28 14	295.13	-55.096	17.4	19.1	0.30	1.7e+19	+218	*	—	—	WvW#493	—
139	HE 0127−5926	01 29 08.0	-59 11 31	294.01	-57.288	17.3	13.0	0.97	5.9e+19	+165	*	—	—	WvW#531	—
140	HE 0128−6016_1	01 30 07.2	-60 00 42	294.19	-56.458	17.0	15.8	0.79	4.8e+19	+152	*	—	—	WvW#531	—
141	HE 0128−6016_2	01 30 07.2	-60 00 42	294.19	-56.458	17.0	15.8	0.77	4.3e+19	+218	*	—	—	WvW#493	—
142	HE 0128−6157	01 30 31.9	-61 41 57	294.90	-54.813	16.7	14.5	0.35	2.1e+19	+218	*	—	—	WvW#493	—
143	HE 0129−5848_1	01 31 26.2	-58 33 32	293.14	-57.803	16.4	10.1	1.46	9.9e+19	+178	*	—	—	WvW#493	—
144	HE 0129−5848_2	01 31 26.2	-58 33 32	293.14	-57.803	16.4	10.1	0.53	3.4e+19	+112	*	—	—	WvW#529	—
145	HE 0129−6213	01 31 44.1	-61 57 45	294.79	-54.520	15.9	8.8	0.22	1.1e+19	+204	*	—	—	WvW#493	—
146	HE 0131−6214	01 33 05.0	-61 58 45	294.53	-54.470	17.0	15.9	0.37	2.4e+19	+204	*	—	—	WvW#493	—
147	HE 0131−6209	01 33 25.2	-61 54 28	294.43	-54.525	16.6	11.0	0.37	2.2e+19	+204	*	—	—	WvW#493	—
148	HE 0131−5757	01 33 48.2	-57 42 24	292.09	-58.520	16.7	14.7	0.75	4.6e+19	+152	*	—	—	—	—
149	HE 0132−6112	01 34 39.8	-60 57 25	293.71	-55.393	17.9	24.5	0.46	2.8e+19	+178	*	—	—	WvW#493	—
150	HE 0133−5750	01 35 03.1	-57 35 21	291.72	-58.585	15.8	7.1	0.38	2.4e+19	+152	*	—	—	—	—

Table A.1

Num	HEname	RA (J2000)	DEC (J2000)	l (deg)	b (deg)	B mag (mag)	Distance (kpc)	T_b (K)	$N(\mathrm{H\,I})$ (cm^{-2})	v_{LSR} $\mathrm{km\,s}^{-1}$	MS Flag	HVC	XHVC	WvW91	de Heij
151	HE 0134−5925_1	01 36 38.6	-59 10 11	292.30	-57.020	15.8	8.4	1.20	6.8e+19	+178	*	:HVC#1317	—	WvW#493	—
152	HE 0134−5925_2	01 36 38.6	-59 10 11	292.30	-57.020	15.8	8.4	0.55	3.4e+19	+112	*	—	—	WvW#529	—
153	HE 0135−5945	01 37 38.9	-59 29 48	292.27	-56.665	17.7	23.0	1.86	1.1e+20	+178	*	:HVC#1317	—	WvW#493	—
154	HE 0136−6057_1	01 37 50.6	-60 42 45	292.93	-55.517	16.4	12.7	1.01	5.8e+19	+099	*	—	—	WvW#529	—
155	HE 0136−6057_2	01 37 50.6	-60 42 45	292.93	-55.517	16.4	12.7	0.84	4.9e+19	+165	*	—	—	WvW#531	—
156	HE 0136−6103_1	01 38 24.4	-60 48 29	292.87	-55.396	17.1	17.3	1.21	6.5e+19	+099	*	—	—	WvW#529	—
157	HE 0136−6103_2	01 38 24.4	-60 48 29	292.87	-55.396	17.1	17.3	0.73	4.3e+19	+165	*	—	—	WvW#531	—
158	HE 0136−5830	01 38 29.9	-58 15 23	291.32	-57.805	17.4	14.9	0.47	3.1e+19	+231	*	:HVC#1317	—	WvW#493	—
159	HE 0136−6131_1	01 38 42.6	-61 16 14	293.06	-54.949	18.0	9.8	0.75	4.5e+19	+178	*	—	—	WvW#493	—
160	HE 0136−6131_2	01 38 42.6	-61 16 14	293.06	-54.949	18.0	9.8	0.61	3.9e+19	+112	*	—	—	WvW#529	—
161	HE 0137−6108_1	01 38 50.5	-60 53 42	292.83	-55.298	17.4	18.4	1.29	7.3e+19	+099	*	—	—	WvW#529	—
162	HE 0137−6108_2	01 38 50.5	-60 53 42	292.83	-55.298	17.4	18.4	0.65	3.9e+19	+165	*	—	—	WvW#531	—
163	HE 0137−5835	01 39 29.5	-58 20 46	291.15	-57.671	17.4	16.3	0.39	2.3e+19	+231	*	:HVC#1317	—	WvW#493	—
164	HE 0139−6129_1	01 41 19.5	-61 14 37	292.53	-54.870	17.4	19.7	0.68	3.8e+19	+165	*	—	—	—	—
165	HE 0139−6129_2	01 41 19.5	-61 14 37	292.53	-54.870	17.4	19.7	0.55	3.2e+19	+112	*	—	—	WvW#529	—
166	HE 0142−6029	01 44 27.3	-60 14 25	291.29	-55.670	18.2	28.9	1.51	8.4e+19	+178	*	:HVC#1317	—	WvW#493	—
167	HE 0143−6107	01 44 48.8	-60 52 17	291.62	-55.077	17.7	23.1	0.98	5.7e+19	+178	*	—	—	WvW#493	—
168	HE 0143−6023	01 45 25.5	-60 08 53	291.03	-55.729	15.6	8.6	1.24	7.4e+19	+178	*	:HVC#1317	—	WvW#493	—
169	HE 0143−4608	01 45 51.8	-45 53 02	276.57	-68.362	15.2	6.7	0.43	2.6e+19	+191	*	:HVC#1186	—	WvW#493	—
170	HE 0146−5140	01 48 30.5	-51 26 03	282.86	-63.412	16.4	11.2	0.24	1.5e+19	+125	*	HVC#1293	XHVC#112	—	—
171	HE 0146−3306	01 48 36.5	-32 51 40	241.25	-76.385	16.9	15.9	0.20	1.1e+19	-099	*	HVC#739	—	—	—
172	HE 0147−6119	01 49 03.5	-61 04 12	290.91	-54.694	16.9	15.7	0.81	4.7e+19	+178	*	—	—	WvW#493	—
173	HE 0148−6040	01 50 18.6	-60 25 58	290.24	-55.223	16.1	9.8	0.15	8.8e+18	+231	*	:HVC#1317	—	WvW#493	—
174	HE 0154−6143	01 56 08.4	-61 28 36	289.86	-53.984	17.3	14.7	0.26	1.5e+19	+231	*	—	—	WvW#493	—
175	HE 0154−6115	01 56 27.1	-61 00 58	289.47	-54.386	17.5	20.6	0.21	1.3e+19	+231	*	—	—	WvW#493	—
176	HE 0156−5844	01 58 06.4	-58 30 10	287.16	-56.544	17.9	25.3	0.40	2.8e+19	+218	*	:HVC#1317	—	WvW#493	—
177	HE 0157−5126	01 59 30.8	-51 11 56	279.36	-62.702	14.7	5.9	0.13	9.3e+18	+165	*	HVC#1223	—	—	—
178	HE 0158−2916	02 00 37.6	-29 02 27	224.12	-74.636	16.2	11.4	0.12	8.0e+18	-178	*	:HVC#635	—	—	—
179	HE 0159−5839	02 00 50.1	-58 24 51	286.52	-56.456	16.7	10.6	0.20	1.0e+19	+204	*	:HVC#1317	—	WvW#493	—
180	HE 0204−5925	02 06 01.5	-59 10 54	286.14	-55.455	16.4	9.3	0.17	1.1e+19	+204	*	:HVC#1317	—	WvW#493	—
181	HE 0206−5802	02 07 44.8	-57 48 30	284.54	-56.519	17.5	13.2	0.34	2.2e+19	+218	*	:HVC#1317	—	WvW#493	—
182	HE 0207−5752	02 08 48.5	-57 37 58	284.15	-56.586	15.6	8.7	0.26	1.6e+19	+218	*	:HVC#1317	—	WvW#493	—
183	HE 0207−5941	02 09 06.7	-59 27 18	285.79	-55.019	17.8	23.1	0.25	1.5e+19	+204	*	:HVC#1317	—	WvW#493	—
184	HE 0208−6009	02 09 57.3	-59 55 00	286.05	-54.563	16.5	10.5	0.28	1.6e+19	+204	*	:HVC#1317	—	WvW#493	—
185	HE 0209−5643	02 11 14.6	-56 29 29	282.49	-57.368	17.5	19.5	0.18	1.1e+19	+191	*	:HVC#1317	—	WvW#493	—
186	HE 0210−5947	02 12 16.8	-59 33 04	285.29	-54.726	17.5	19.0	0.57	3.3e+19	+204	*	:HVC#1317	—	WvW#493	—
187	HE 0210−4749	02 12 47.6	-47 35 42	270.50	-64.091	15.6	7.5	0.20	1.2e+19	+138	*	—	—	—	—
188	HE 0211−6031	02 13 00.7	-60 17 21	285.83	-54.056	16.5	12.9	0.25	1.4e+19	+218	*	—	—	WvW#493	—
189	HE 0211−6008	02 13 08.8	-59 54 47	285.46	-54.360	18.1	25.2	0.52	3.1e+19	+204	*	:HVC#1317	—	WvW#493	—
190	HE 0215−6012	02 16 47.7	-59 58 34	284.86	-54.057	17.8	15.9	0.15	8.9e+18	+204	*	—	—	WvW#493	—
191	HE 0217−6045_1	02 18 46.0	-60 32 04	285.04	-53.452	13.4	2.4	0.36	2.1e+19	+112	*	—	—	WvW#522	—
192	HE 0217−6045_2	02 18 46.0	-60 32 04	285.04	-53.452	13.4	2.4	0.13	7.3e+18	+218	*	—	—	WvW#493	—
193	HE 0218−6211_1	02 20 21.2	-61 57 59	286.09	-52.166	17.7	15.2	0.32	2.0e+19	+218	*	—	—	WvW#493	—
194	HE 0218−6211_2	02 20 21.2	-61 57 59	286.09	-52.166	17.7	15.2	0.14	7.8e+18	+152	*	—	—	WvW#519	—
195	HE 0220−5957	02 21 48.3	-59 43 48	283.74	-53.902	16.7	11.3	0.46	2.6e+19	+191	*	—	—	WvW#493	—
196	HE 0221−6221_1	02 22 38.5	-62 08 18	285.88	-51.865	15.8	9.2	0.50	2.9e+19	+152	*	—	—	WvW#519	—
197	HE 0221−6221_2	02 22 38.5	-62 08 18	285.88	-51.865	15.8	9.2	0.13	6.8e+18	+204	*	—	—	WvW#493	—
198	HE 0221−5938	02 23 18.9	-59 24 33	283.16	-54.058	17.6	20.8	0.13	6.8e+18	+191	*	—	—	WvW#493	—
199	HE 0222−6153	02 23 37.5	-61 39 52	285.29	-52.191	17.7	12.5	0.20	1.2e+19	+138	*	—	—	WvW#522	—
200	HE 0222−6115_1	02 23 57.6	-61 01 29	284.63	-52.694	16.7	13.7	0.51	3.2e+19	+191	*	—	—	WvW#493	—

Table A.1

Num	HEname	RA (J2000)	DEC (J2000)	l (deg)	b (deg)	B mag (mag)	Distance (kpc)	T_b (K)	N(H I) (cm^{-2})	v_{LSR} $km\,s^{-1}$	MS Flag	HVC	XHVC	WvW91	de Heij
201	HE 0222−6115_2	02 23 57.6	-61 01 29	284.63	-52.694	16.7	13.7	0.25	1.5e+19	+125	*	—	—	WvW#522	—
202	HE 0222−6105_1	02 23 58.4	-60 52 19	284.48	-52.822	17.6	21.1	0.52	3.3e+19	+191	*	—	—	WvW#493	—
203	HE 0222−6105_2	02 23 58.4	-60 52 19	284.48	-52.822	17.6	21.1	0.25	1.5e+19	+125	*	—	—	WvW#522	—
204	HE 0223−5532	02 25 36.3	-55 19 22	278.23	-57.068	14.1	4.4	0.21	1.5e+19	+191	*	—	—	WvW#493	—
205	HE 0224−5848	02 25 47.7	-58 34 50	281.87	-54.522	16.3	9.3	0.23	1.4e+19	+152	*	—	—	—	—
206	HE 0225−6057	02 26 39.7	-60 43 48	283.91	-52.747	17.1	15.5	0.17	1.1e+19	+191	*	—	—	WvW#493	—
207	HE 0225−5535	02 26 39.8	-55 22 05	278.08	-56.922	15.7	8.9	0.20	1.1e+19	+165	*	—	—	—	—
208	HE 0225−5521	02 27 04.1	-55 07 51	277.71	-57.066	16.4	11.9	0.20	1.2e+19	+165	*	—	—	—	—
209	HE 0227−5359	02 29 35.7	-53 46 25	275.50	-57.812	17.2	18.6	0.49	2.9e+19	+191	*	—	—	WvW#493	—
210	HE 0228−5326	02 29 39.6	-53 13 41	274.77	-58.209	16.0	10.3	0.29	1.6e+19	+191	*	—	—	WvW#493	—
211	HE 0228−5612	02 30 09.4	-55 59 00	278.15	-56.143	14.9	6.2	0.18	8.7e+18	+191	*	—	—	WvW#493	—
212	HE 0229−5503	02 30 38.1	-54 50 34	276.66	-56.939	14.2	4.4	0.39	1.9e+19	+204	*	—	—	WvW#493	—
213	HE 0229−5625	02 31 00.2	-56 12 10	278.25	-55.899	16.4	12.3	0.18	8.8e+18	+191	*	—	—	WvW#493	—
214	HE 0229−5638	02 31 12.6	-56 24 50	278.46	-55.720	17.2	14.9	0.24	1.3e+19	+191	*	—	—	WvW#493	—
215	HE 0231−6150	02 32 19.7	-61 37 06	283.89	-51.626	17.0	15.2	0.21	1.2e+19	+178	*	—	—	WvW#493	—
216	HE 0238−6223	02 39 46.1	-62 10 26	283.35	-50.644	17.5	19.0	0.17	7.7e+18	+191	*	—	—	WvW#493	—
217	HE 0240−5738	02 41 42.7	-57 25 41	277.85	-54.009	14.4	4.8	2.49	1.6e+20	+165	*	—	—	—	—
218	HE 0242−6214	02 43 26.8	-62 02 03	282.70	-50.478	17.4	12.8	0.58	3.5e+19	+191	*	—	—	WvW#493	—
219	HE 0242−5513	02 44 29.3	-55 00 54	274.38	-55.391	15.6	7.4	0.32	2.0e+19	+165	*	—	—	—	—
220	HE 0243−5620	02 44 49.0	-56 07 35	275.75	-54.607	16.0	7.0	0.48	2.8e+19	+165	*	—	—	—	—
221	HE 0243−5740	02 44 56.1	-57 27 47	277.37	-53.671	15.4	6.9	1.94	1.1e+20	+165	*	—	—	—	—
222	HE 0245−5958	02 46 54.4	-59 45 41	279.75	-51.852	17.7	19.4	0.21	1.2e+19	+231	*	—	—	WvW#493	—
223	HE 0246−5718	02 47 35.8	-57 05 56	276.51	-53.661	14.4	4.4	1.04	6.0e+19	+165	*	—	—	—	—
224	HE 0246−5949	02 48 00.1	-59 36 42	279.42	-51.873	16.4	9.6	0.36	2.0e+19	+218	*	—	—	WvW#493	—
225	HE 0247−5623	02 48 42.2	-56 10 47	275.19	-54.170	14.8	6.0	0.60	3.4e+19	+178	*	—	—	WvW#493	—
226	HE 0248−5907	02 49 22.5	-58 55 25	278.43	-52.231	16.7	12.2	0.25	1.5e+19	+231	*	—	—	WvW#493	—
227	HE 0248−5755	02 49 33.6	-57 42 42	276.96	-53.058	14.1	4.2	0.48	3.0e+19	+178	*	—	—	WvW#493	—
228	HE 0248−5955	02 50 07.8	-59 43 29	279.24	-51.606	15.6	7.9	0.30	1.8e+19	+231	*	—	—	WvW#493	—
229	HE 0249−5853	02 50 55.2	-58 41 39	277.93	-52.242	18.0	25.6	0.25	1.5e+19	+231	*	—	—	WvW#493	—
230	HE 0250−6029	02 51 17.7	-60 17 21	279.72	-51.093	16.8	13.4	0.23	1.3e+19	+231	*	—	—	WvW#493	—
231	HE 0250−5948	02 51 34.0	-59 35 57	278.89	-51.553	18.0	20.4	0.19	1.1e+19	+231	*	—	—	WvW#493	—
232	HE 0251−5942	02 52 26.0	-59 30 08	278.66	-51.542	17.1	15.2	0.13	7.5e+18	+231	*	—	—	WvW#493	—
233	HE 0251−5539	02 52 41.6	-55 26 48	273.61	-54.225	15.3	7.6	0.25	1.3e+19	+165	*	—	—	—	—
234	HE 0251−5646	02 53 11.4	-56 34 28	274.99	-53.443	15.9	9.4	0.12	7.4e+18	+178	*	—	—	WvW#493	—
235	HE 0252−5948	02 53 56.2	-59 36 44	278.58	-51.338	16.1	10.8	0.21	1.3e+19	+257	*	—	—	—	—
236	HE 0254−6211	02 55 53.2	-61 59 27	280.99	-49.504	16.3	9.1	0.30	1.9e+19	+231	*	HVC#1206	—	WvW#493	—
237	HE 0255−5825	02 56 30.6	-58 13 36	276.57	-52.022	16.4	10.4	0.28	1.5e+19	+191	*	—	—	WvW#493	—
238	HE 0255−5909_1	02 56 38.6	-58 57 03	277.42	-51.520	15.9	8.7	0.22	1.3e+19	+191	*	—	—	WvW#493	—
239	HE 0255−5909_2	02 56 38.6	-58 57 03	277.42	-51.520	15.9	8.7	0.17	1.0e+19	+257	*	—	—	—	—
240	HE 0255−4429	02 57 31.6	-44 17 19	255.45	-59.481	16.4	12.6	0.13	7.9e+18	+178	—	CHVC#882	—	WvW#493	—
241	HE 0257−5941	02 58 37.5	-59 29 44	277.80	-50.971	15.9	8.7	0.15	8.0e+18	+191	*	HVC#1206	—	WvW#493	—
242	HE 0300−6039	03 01 17.3	-60 27 16	278.57	-50.086	17.1	17.5	0.48	3.2e+19	+270	*	—	—	—	—
243	HE 0300−5946_1	03 01 30.3	-59 34 41	277.51	-50.648	18.2	28.2	0.19	1.3e+19	+270	*	—	—	—	—
244	HE 0300−5946_2	03 01 30.3	-59 34 41	277.51	-50.648	18.2	28.2	0.19	1.2e+19	+204	*	HVC#1206	—	WvW#493	—
245	HE 0304−6056	03 05 26.9	-60 44 48	278.39	-49.512	15.4	7.0	0.28	1.4e+19	+270	*	—	—	—	—
246	HE 0305−6211	03 06 14.6	-61 59 30	279.72	-48.619	17.3	19.3	0.17	8.7e+18	+218	*	HVC#1206	—	WvW#493	—
247	HE 0305−6008	03 06 35.8	-59 56 54	277.30	-49.912	15.2	6.4	0.34	2.0e+19	+270	*	—	—	—	—
248	HE 0306−6057	03 07 15.8	-60 46 12	278.19	-49.326	17.4	14.2	0.16	1.0e+19	+204	*	HVC#1206	—	WvW#493	—
249	HE 0308−5952	03 09 53.6	-59 41 26	276.59	-49.763	16.9	16.1	0.24	1.4e+19	+270	*	—	—	—	—
250	HE 0310−6104	03 11 33.4	-60 52 50	277.81	-48.853	16.1	9.9	0.20	1.3e+19	+218	*	HVC#1206	—	WvW#493	—

Table A.1

Num	HEname	RA (J2000)	DEC (J2000)	l (deg)	b (deg)	B mag (mag)	Distance (kpc)	T_b (K)	N(H I) (cm^{-2})	v_{LSR} $km\,s^{-1}$	MS Flag	HVC	XHVC	WvW91	de Heij
251	HE 0330−6057	03 30 59.3	-60 47 19	275.62	-46.999	17.1	15.7	0.15	8.4e+18	+231	*	HVC#1172	—	WvW#493	—
252	HE 0341−6116	03 42 12.4	-61 06 42	274.98	-45.664	16.5	8.5	0.12	8.0e+18	+257	*	HVC#1157	—	—	—
253	HE 0341−6017	03 42 30.6	-60 07 48	273.73	-46.122	16.1	10.4	0.17	1.1e+19	+297	*	HVC#1143	—	—	—
254	HE 0342−5847	03 43 40.8	-58 38 03	271.72	-46.701	17.8	23.4	0.35	2.1e+19	+323	*	HVC#1103	—	—	—
255	HE 0343−5839	03 44 30.2	-58 29 51	271.47	-46.677	17.1	12.1	0.38	2.2e+19	+323	*	HVC#1103	—	—	—
256	HE 0343−5817	03 44 38.6	-58 07 44	270.98	-46.820	17.7	19.6	0.15	8.1e+18	+323	*	HVC#1103	—	—	—
257	HE 0344−6111	03 45 38.4	-61 02 35	274.60	-45.342	15.4	6.5	0.16	1.0e+19	+244	*	HVC#1157	—	—	—
258	HE 0345−5809	03 46 19.9	-58 00 39	270.68	-46.678	16.3	12.0	0.18	1.0e+19	+323	*	HVC#1103	—	—	—
259	HE 0346−5852	03 47 27.3	-58 43 09	271.50	-46.239	18.0	24.0	0.21	1.2e+19	+323	*	HVC#1103	—	—	—
260	HE 0347−5851	03 48 31.9	-58 42 45	271.41	-46.109	14.6	4.9	0.14	7.6e+18	+323	*	HVC#1103	—	—	—
261	HE 0356−6021_1	03 57 32.5	-60 13 23	272.63	-44.429	17.2	11.9	0.32	1.9e+19	+284	*	HVC#1110	—	—	—
262	HE 0356−6021_2	03 57 32.5	-60 13 23	272.63	-44.429	17.2	11.9	0.27	1.6e+19	+336	*	HVC#1110	—	—	—
263	HE 0357−5941	03 57 56.3	-59 33 21	271.75	-44.659	17.3	12.4	0.20	1.2e+19	+112	*	HVC#1114	—	—	—
264	HE 0401−6011	04 02 14.8	-60 03 13	272.07	-43.959	17.3	18.1	0.12	7.1e+18	+350	*	HVC#1110	—	—	—
265	HE 0406−6039	04 07 13.3	-60 31 59	272.34	-43.202	17.8	20.5	0.13	8.2e+18	+350	*	HVC#1110	—	—	—
266	HE 0408−6034	04 08 50.1	-60 26 31	272.12	-43.059	15.6	8.4	0.14	8.4e+18	+350	*	HVC#1110	—	—	—
267	HE 0408−6130_1	04 09 02.3	-61 22 19	273.28	-42.676	16.4	12.5	0.25	1.4e+19	+349	*	HVC#1110	—	—	—
268	HE 0408−6130_2	04 09 02.3	-61 22 19	273.28	-42.676	16.4	12.5	0.17	1.1e+19	+178	*	—	—	WvW#493	—
269	HE 0415−5409	04 17 03.9	-54 02 33	263.26	-44.038	14.8	6.3	0.39	2.4e+19	+099	—	—	XHVC#74	—	—
270	HE 0419−5332	04 20 34.1	-53 25 36	262.26	-43.680	15.8	8.7	0.20	1.2e+19	+112	—	—	XHVC#74	—	—
271	HE 0420−5405	04 21 48.9	-53 58 08	262.93	-43.378	16.0	10.6	0.54	3.2e+19	+099	—	—	XHVC#74	—	—
272	HE 0421−2813	04 23 38.2	-28 06 35	227.07	-43.371	15.7	7.8	0.15	9.5e+18	+099	—	:HVC#652	—	—	—
273	HE 0426−5353	04 27 57.4	-53 46 37	262.40	-42.535	15.3	7.8	0.14	8.1e+18	+099	—	—	XHVC#74	—	—
274	HE 0427−5420	04 28 21.0	-54 13 30	262.98	-42.382	16.0	10.6	0.16	9.0e+18	+099	—	—	XHVC#74	—	—
275	HE 0502−2528	05 04 58.1	-25 24 47	226.67	-33.772	16.5	12.8	0.46	2.6e+19	+099	—	:HVC#648	—	—	CHVC#786
276	HE 0504−2509	05 07 00.6	-25 05 07	226.46	-33.233	15.3	7.5	0.31	1.8e+19	+112	—	:HVC#648	—	—	CHVC#786
277	HE 0506−2530	05 08 05.4	-25 26 13	226.94	-33.106	15.5	8.2	0.25	1.6e+19	+125	—	:HVC#648	—	—	CHVC#786
278	HE 0932−0346	09 34 50.9	-03 59 25	238.41	+33.301	16.1	8.7	0.18	1.0e+19	+152	—	HVC#714	—	WvW#91	HVC#809
279	HE 0932−0404	09 34 56.9	-04 17 50	238.72	+33.143	14.9	5.8	0.23	1.4e+19	+152	—	HVC#714	—	WvW#91	HVC#809
280	HE 0935−0405	09 38 28.4	-04 19 07	239.37	+33.835	14.9	5.9	0.12	8.0e+18	+165	—	HVC#722	—	WvW#91	HVC#809
281	HE 1001+0057	10 03 36.5	+00 43 03	239.06	+41.878	17.0	16.3	0.30	1.8e+19	+099	—	—	—	—	HVC#808
282	HE 1004−0516	10 07 17.1	-05 31 05	246.15	+38.634	14.8	5.7	0.57	3.4e+19	+112	—	HVC#777	—	WvW#91	HVC#819
283	HE 1008−0438	10 10 33.5	-04 53 21	246.24	+39.664	16.3	10.3	0.53	3.3e+19	+310	—	—	—	—	—
284	HE 1010−1840	10 12 36.3	-18 55 13	258.68	+29.991	16.2	8.4	0.23	1.4e+19	+152	—	—	XHVC#68	WvW#152	HVC#844
285	HE 1011−1920	10 14 18.8	-19 35 27	259.54	+29.742	17.2	13.0	0.19	9.6e+18	+112	—	HVC#949	XHVC#68	WvW#153	HVC#845
286	HE 1015−0543	10 18 25.8	-05 58 09	249.01	+40.371	17.1	13.9	0.15	8.7e+18	+125	—	HVC#807	—	WvW#91	—
287	HE 1027−2625	10 29 29.7	-26 41 15	267.59	+26.281	17.0	12.0	1.47	7.7e+19	+218	—	HVC#1051	—	WvW#176	HVC#863
288	HE 1027−2510	10 29 34.0	-25 25 34	266.79	+27.317	16.2	6.8	0.24	1.2e+19	+099	—	—	XHVC#80	—	—
289	HE 1028−2434	10 30 42.9	-24 49 36	266.64	+27.950	15.6	6.4	0.22	1.4e+19	+178	—	—	—	—	HVC#862
290	HE 1045−2550	10 47 56.3	-26 06 10	271.13	+29.036	14.3	3.8	0.72	4.2e+19	+178	—	HVC#1105	—	WvW#163	CHVC#866
291	HE 1047+0232	10 50 19.9	+02 16 16	248.35	+51.829	15.5	7.7	0.34	2.0e+19	+099	—	—	—	WvW#35	HVC#822
292	HE 1047−1852	10 50 26.4	-19 08 17	267.30	+35.235	16.2	11.1	0.17	9.3e+18	+138	—	HVC#1052	—	WvW#118	HVC#864
293	HE 1048+0231	10 50 52.5	+02 15 19	248.52	+51.911	17.0	16.1	0.39	2.2e+19	+099	—	—	—	WvW#35	HVC#822
294	HE 1048−2639	10 51 08.4	-26 55 11	272.31	+28.706	16.1	5.7	0.33	1.9e+19	+178	—	HVC#1105	—	WvW#163	CHVC#866
295	HE 1049−1900	10 51 36.7	-19 16 18	267.67	+35.271	16.5	11.4	0.20	1.2e+19	+138	—	HVC#1052	—	WvW#118	HVC#864
296	HE 1049+0200	10 51 48.0	+01 44 08	249.38	+51.719	16.1	10.3	0.13	7.0e+18	+099	—	—	—	WvW#35	HVC#822
297	HE 1049−1943	10 51 58.8	-19 59 23	268.23	+34.711	17.4	19.0	0.21	1.2e+19	+138	—	HVC#1052	—	WvW#118	HVC#864
298	HE 1049+0203	10 52 12.5	+01 47 37	249.43	+51.831	15.8	9.2	0.12	6.7e+18	+099	—	—	—	WvW#35	HVC#822
299	HE 1050−1808	10 52 47.2	-18 24 15	267.38	+36.155	15.2	6.5	0.19	1.0e+19	+138	—	HVC#1052	—	WvW#118	HVC#864
300	HE 1051−1709	10 53 40.8	-17 25 34	266.93	+37.081	16.5	10.8	0.15	8.4e+18	+152	—	HVC#1052	—	WvW#118	HVC#864

Table A.1

Num	HEname	RA (J2000)	DEC (J2000)	l (deg)	b (deg)	B mag (mag)	Distance (kpc)	T_b (K)	N(H I) (cm^{-2})	v_{LSR} $\mathrm{km\ s}^{-1}$	MS Flag	HVC	XHVC	WvW91	de Heij
301	HE 1051−2546	10 53 44.8	-26 02 42	272.38	+29.752	16.1	10.1	0.17	9.6e+18	+178	—	HVC#1105	—	WvW#163	—
302	HE 1052−1749	10 54 42.5	-18 05 52	267.64	+36.655	16.8	10.7	0.29	1.7e+19	+138	—	HVC#1052	—	WvW#118	HVC#864
303	HE 1053−2050	10 55 45.3	-21 06 08	269.86	+34.238	16.2	10.5	0.20	1.1e+19	+125	—	HVC#1052	—	WvW#126	HVC#864
304	HE 1054−2513	10 57 24.7	-25 29 19	272.88	+30.650	15.1	6.2	0.13	7.8e+18	+165	—	HVC#1105	—	—	—
305	HE 1100+0124	11 03 07.7	+01 08 29	253.40	+53.267	16.8	14.2	0.14	9.2e+18	+099	—	HVC#869	—	WvW#35	HVC#822
306	HE 1121−3111	11 23 55.9	-31 27 47	281.87	+27.801	17.1	12.8	0.19	8.8e+18	+112	—	—	XHVC#95	WvW#164	—
307	HE 1123−3100	11 26 12.0	-31 17 26	282.31	+28.143	15.4	7.1	0.17	9.6e+18	+112	—	—	XHVC#95	WvW#164	—
308	HE 1125−3030	11 27 38.6	-30 46 52	282.43	+28.732	16.7	13.2	0.24	1.4e+19	+112	—	—	—	WvW#164	—
309	HE 1128−0051	11 31 00.6	-01 08 28	265.30	+55.740	15.2	7.4	0.12	7.4e+18	+112	—	—	XHVC#75	WvW#23	HVC#857
310	HE 1129−0021	11 31 33.9	-00 38 21	265.02	+56.242	15.3	7.7	0.14	8.2e+18	+112	—	HVC#970	XHVC#75	WvW#23	HVC#856
311	HE 1130−1812	11 32 36.3	-18 29 15	278.04	+40.543	15.1	6.9	0.17	1.1e+19	+099	—	HVC#1207	—	—	—
312	HE 1131−2948	11 34 19.7	-30 05 12	283.69	+29.897	15.8	5.2	0.15	9.1e+18	+099	—	—	—	—	—
313	HE 1132−2626	11 34 41.3	-26 42 45	282.42	+33.088	14.8	5.3	0.14	8.5e+18	+152	—	HVC#1296	—	—	HVC#870
314	HE 1135−2457	11 38 21.0	-25 14 22	282.74	+34.753	15.6	7.2	0.15	9.5e+18	+125	—	—	—	—	—
315	HE 1138−1303	11 41 14.8	-13 20 17	277.90	+46.098	15.1	6.7	0.38	2.2e+19	+112	—	—	XHVC#91	WvW#62	CHVC#867
316	HE 1139−1254	11 42 17.7	-13 11 09	278.16	+46.332	15.7	9.0	0.19	1.2e+19	+112	—	—	XHVC#91	WvW#62	CHVC#867
317	HE 1141−1331	11 43 44.7	-13 48 18	278.97	+45.898	15.9	9.7	0.21	1.2e+19	+112	—	—	XHVC#91	WvW#62	CHVC#867
318	HE 1153−2530	11 55 48.7	-25 47 37	287.54	+35.416	15.5	2.7	0.14	7.3e+18	+099	—	HVC#1325	—	—	HVC#874
319	HE 1211−2948	12 13 49.4	-30 05 10	293.33	+32.086	15.0	6.2	0.12	7.2e+18	+138	—	HVC#1382	XHVC#111	—	—
320	HE 1312−3226	13 15 38.2	-32 42 28	308.80	+29.895	16.2	10.4	0.20	1.1e+19	+099	—	—	XHVC#134	WvW#154	—
321	HE 1318−2555	13 21 28.0	-26 11 14	311.29	+36.202	14.5	4.9	0.33	1.9e+19	+112	—	—	XHVC#135	—	—
322	HE 1319−2547	13 21 49.8	-26 03 05	311.41	+36.323	16.6	10.5	0.39	2.2e+19	+112	—	—	XHVC#135	—	—
323	HE 1319−3034	13 22 00.1	-30 50 08	310.63	+31.580	15.5	7.0	0.26	1.6e+19	+099	—	—	XHVC#134	WvW#154	—
324	HE 1321−3146	13 24 32.1	-32 01 52	311.06	+30.325	16.6	11.8	0.39	2.7e+19	+099	—	—	XHVC#134	WvW#154	—
325	HE 1323−2459	13 25 55.5	-25 15 14	312.70	+36.960	14.8	4.4	0.24	1.5e+19	+112	—	—	XHVC#135	—	—
326	HE 1323−2511	13 26 37.8	-25 27 30	312.85	+36.739	14.8	5.1	0.26	1.5e+19	+112	—	—	XHVC#135	—	—
327	HE 2129−0202	21 32 31.5	-01 49 20	52.18	-36.127	16.8	14.3	0.13	7.4e+18	+112	—	CHVC#425	—	—	HVC#162
328	HE 2141−2039	21 44 28.7	-20 25 29	31.44	-46.950	16.3	6.8	0.14	8.3e+18	-178	—	HVC#291	—	—	CHVC#68
329	HE 2153−2323	21 56 32.7	-23 09 24	28.70	-50.416	14.5	4.8	0.25	1.6e+19	-112	—	HVC#283	—	—	HVC#51
330	HE 2155−2133	21 58 25.9	-21 18 47	31.67	-50.320	16.7	11.9	0.20	1.2e+19	-125	—	HVC#283	—	—	HVC#45
331	HE 2155−2243	21 58 39.9	-22 29 29	29.92	-50.711	15.3	6.2	0.77	4.8e+19	-139	—	HVC#283	—	—	CHVC:#64
332	HE 2200−2222	22 02 54.8	-22 08 06	30.90	-51.551	16.4	10.4	0.39	2.3e+19	-099	—	HVC#283	—	—	HVC#45
333	HE 2200−2157	22 03 17.4	-21 42 31	31.59	-51.528	17.7	21.5	0.25	1.5e+19	-099	—	HVC#283	—	—	HVC#45
334	HE 2200−2249	22 03 32.4	-22 35 13	30.26	-51.824	15.7	7.2	0.13	7.7e+18	-099	—	HVC#283	—	—	HVC#45
335	HE 2235−4908	22 38 52.5	-48 52 38	343.54	-56.474	16.2	9.3	0.22	1.4e+19	+099	*	:HVC#1877	—	—	—
336	HE 2236−6040	22 39 26.1	-60 25 07	327.61	-49.916	16.7	14.8	0.17	1.1e+19	+099	—	HVC#1727	—	—	—
337	HE 2242−6106	22 45 48.5	-60 51 02	326.29	-50.207	14.0	3.9	0.22	1.1e+19	+112	*	HVC#1727	—	—	—
338	HE 2247−5811	22 50 18.7	-57 55 22	329.10	-52.619	16.3	12.5	0.15	8.4e+18	+099	*	—	XHVC#147	—	—
339	HE 2248−5733	22 51 17.5	-57 17 54	329.72	-53.132	14.5	5.4	0.21	1.2e+19	+099	*	—	XHVC#147	—	—
340	HE 2249−5740	22 52 46.8	-57 24 30	329.36	-53.204	15.1	6.4	0.49	2.8e+19	+099	*	—	XHVC#147	—	—
341	HE 2251−5755	22 54 18.6	-57 39 02	328.83	-53.197	17.1	16.7	0.50	2.7e+19	+099	*	—	XHVC#147	—	—
342	HE 2252−5943	22 55 25.1	-59 27 39	326.53	-52.025	16.4	12.6	0.20	1.1e+19	+112	*	—	XHVC#147	—	—
343	HE 2253−6056	22 56 35.4	-60 40 07	325.02	-51.258	16.5	12.6	0.20	1.3e+19	+125	*	HVC#1727	XHVC#147	—	—
344	HE 2254−5929	22 57 17.7	-59 13 38	326.52	-52.366	16.2	10.7	0.36	2.1e+19	+112	*	—	XHVC#147	—	—
345	HE 2255−5806	22 58 39.1	-57 50 29	327.92	-53.470	16.7	13.0	0.17	9.7e+18	+152	*	—	XHVC#147	—	—
346	HE 2256−5859	22 59 12.0	-58 43 37	326.80	-52.890	16.8	13.4	0.30	1.7e+19	+138	*	—	XHVC#147	—	—
347	HE 2301−6154	23 04 49.1	-61 38 18	322.80	-51.186	15.9	9.4	0.34	1.8e+19	+099	*	—	—	—	—
348	HE 2302−6140	23 05 35.6	-61 24 04	322.93	-51.422	15.5	7.6	0.60	3.4e+19	+099	*	—	—	—	—
349	HE 2304−3858	23 07 26.3	-38 41 52	358.27	-65.426	16.4	9.8	0.42	2.5e+19	-112	—	CHVC#1976	—	WvW#548	—
350	HE 2305−6146	23 08 24.6	-61 30 00	322.41	-51.551	16.9	16.3	0.56	3.3e+19	+099	*	—	—	—	—

Table A.1

Num	HEname	RA (J2000)	DEC (J2000)	l (deg)	b (deg)	B mag (mag)	Distance (kpc)	T_b (K)	N(H I) (cm^{-2})	v_{LSR} $\mathrm{km\ s}^{-1}$	MS Flag	HVC	XHVC	WvW91	de Heij
351	HE 2307+0131	23 09 46.4	+01 47 55	78.63	-52.111	17.4	18.1	0.19	1.1e+19	-310	—	HVC#476	—	—	HVC#265
352	HE 2307+0125	23 09 58.4	+01 41 38	78.59	-52.227	16.9	14.1	0.15	9.1e+18	-310	—	HVC#476	—	—	HVC#265
353	HE 2308−3256	23 11 37.6	-32 39 58	12.50	-67.736	17.5	20.3	0.16	8.9e+18	-165	—	CHVC#129	—	—	—
354	HE 2310−6214	23 13 08.4	-61 58 36	321.23	-51.523	17.1	16.2	0.16	9.7e+18	+099	*	—	—	—	—
355	HE 2310−6211	23 13 17.4	-61 55 16	321.26	-51.575	15.3	7.2	0.12	7.5e+18	+112	*	—	—	—	—
356	HE 2311−0324	23 13 43.6	-03 08 03	74.48	-56.522	15.0	6.0	0.13	7.8e+18	-257	—	HVC#466	—	—	HVC#246
357	HE 2314−5954	23 17 39.8	-59 37 53	322.81	-53.739	15.1	7.1	0.26	1.7e+19	+112	*	—	—	—	—
358	HE 2316−1007	23 18 54.6	-09 50 38	66.92	-62.175	15.2	7.1	0.13	7.9e+18	-244	—	HVC#448	—	—	—
359	HE 2316−6131	23 19 26.1	-61 15 23	320.93	-52.546	14.2	4.5	0.39	2.4e+19	+099	*	—	—	—	—
360	HE 2317−6206	23 20 22.8	-61 49 34	320.25	-52.132	15.2	7.3	0.53	3.1e+19	+099	*	—	—	—	—
361	HE 2318−6107	23 21 40.8	-60 51 04	320.94	-53.038	15.0	6.6	0.45	2.7e+19	+138	*	—	—	—	—
362	HE 2320−6123	23 23 51.9	-61 07 05	320.33	-52.951	16.8	15.7	0.32	2.0e+19	+152	*	—	—	—	—
363	HE 2322−6108	23 25 02.2	-60 51 31	320.37	-53.256	17.4	20.1	0.34	2.2e+19	+152	*	—	—	—	—
364	HE 2325−0501	23 28 06.5	-04 44 35	77.66	-60.076	17.3	12.1	0.12	7.7e+18	-257	—	HVC#472	—	—	HVC#264
365	HE 2325−0507	23 28 17.2	-04 50 51	77.60	-60.187	16.0	10.0	0.12	7.7e+18	-257	—	HVC#472	—	—	HVC#264
366	HE 2326−0524	23 29 24.0	-05 08 08	77.66	-60.588	16.8	13.4	0.14	8.8e+18	-257	—	—	—	—	HVC#274
367	HE 2328−6123	23 31 05.5	-61 06 27	319.10	-53.439	14.1	4.4	1.88	1.2e+20	+138	*	—	—	—	—
368	HE 2329−5953	23 32 36.7	-59 37 04	320.14	-54.803	16.0	10.4	0.96	5.0e+19	+112	*	—	—	—	—
369	HE 2330−6132	23 33 09.7	-61 15 53	318.61	-53.424	17.0	16.7	0.85	5.5e+19	+138	*	—	—	—	—
370	HE 2330−6046	23 33 45.4	-60 29 52	319.15	-54.122	16.7	14.5	0.51	3.1e+19	+152	*	—	—	—	—
371	HE 2331−6148	23 33 50.8	-61 31 27	318.27	-53.234	16.5	13.3	0.22	1.4e+19	+138	*	—	—	—	—
372	HE 2331−6203	23 34 01.7	-61 46 35	318.03	-53.021	16.3	10.4	0.21	1.4e+19	+125	*	—	—	—	—
373	HE 2332+0132	23 34 46.8	+01 49 18	87.36	-55.663	17.6	16.3	0.13	7.4e+18	-310	—	—	—	—	HVC#322
374	HE 2333−0428	23 36 21.6	-04 11 42	81.65	-60.904	14.8	5.7	0.16	9.3e+18	-257	—	—	—	—	HVC#274
375	HE 2333+0130	23 36 29.3	+01 47 35	87.99	-55.911	15.6	7.8	0.17	9.3e+18	-310	—	—	—	—	HVC#322
376	HE 2334+0131	23 36 55.5	+01 48 31	88.17	-55.950	16.7	13.6	0.17	9.2e+18	-310	—	—	—	—	HVC#322
377	HE 2335−1059	23 37 36.8	-10 42 58	72.77	-66.103	16.5	12.9	0.44	2.8e+19	-218	—	—	—	—	HVC#241
378	HE 2336+0016	23 38 51.8	+00 33 33	87.77	-57.273	16.4	6.5	0.18	1.1e+19	-310	—	—	—	—	HVC#322
379	HE 2337+0028	23 39 38.5	+00 45 32	88.26	-57.206	15.1	6.2	0.17	1.0e+19	-297	—	—	—	—	HVC#322
380	HE 2336−6143	23 39 39.0	-61 26 35	317.32	-53.633	17.3	19.0	0.46	2.7e+19	+165	*	—	—	—	—
381	HE 2338−1029	23 41 04.9	-10 12 27	75.17	-66.314	15.1	5.1	0.12	8.2e+18	-205	—	—	—	—	HVC#241
382	HE 2338−0549	23 41 26.7	-05 32 30	82.15	-62.732	15.5	7.9	0.30	1.9e+19	-244	—	—	—	—	HVC#274
383	HE 2338−1056	23 41 30.3	-10 40 09	74.59	-66.727	17.4	19.4	0.15	8.9e+18	-205	—	—	—	—	HVC#241
384	HE 2339−0015	23 41 37.2	+00 01 22	88.37	-58.082	15.0	6.4	0.21	1.2e+19	-297	—	—	—	—	HVC#322
385	HE 2339−1203	23 41 43.8	-11 47 09	72.71	-67.577	17.3	18.1	0.82	4.9e+19	-218	—	—	—	—	HVC#241
386	HE 2339+0058	23 42 07.0	+01 14 46	89.70	-57.089	17.2	17.3	0.12	7.6e+18	-297	—	—	—	—	HVC#322
387	HE 2339−0720	23 42 07.1	-07 04 02	80.42	-64.061	16.7	14.2	0.51	3.3e+19	-244	—	—	—	—	HVC#274
388	HE 2340+0149	23 43 24.0	+02 06 30	90.97	-56.487	17.6	20.8	0.39	2.3e+19	-323	—	—	—	—	HVC#322
389	HE 2341−0141	23 43 38.4	-01 25 19	87.79	-59.594	15.4	7.2	0.20	1.2e+19	-297	—	—	—	—	HVC#322
390	HE 2342−0855	23 44 43.1	-08 39 01	79.33	-65.704	15.6	6.6	0.30	2.0e+19	-231	—	—	—	—	HVC#274
391	HE 2342−1112	23 44 55.4	-10 55 54	75.74	-67.482	16.2	8.8	0.66	4.1e+19	-218	—	—	—	—	HVC#241
392	HE 2342−0449	23 45 06.6	-04 32 22	85.01	-62.421	16.8	14.2	0.32	2.0e+19	-244	—	—	—	—	HVC#274
393	HE 2342−1057	23 45 10.6	-10 40 24	76.30	-67.339	15.7	9.1	0.66	4.1e+19	-218	—	—	—	—	HVC#241
394	HE 2342−0918	23 45 17.7	-09 01 49	79.03	-66.091	17.2	18.5	0.50	3.3e+19	-231	—	—	—	—	HVC#274
395	HE 2342−0214	23 45 29.5	-01 57 28	88.03	-60.283	15.5	6.5	0.26	1.6e+19	-297	—	—	—	—	—
396	HE 2343−0246	23 45 56.0	-02 30 07	87.66	-60.815	15.5	8.1	0.22	1.3e+19	-284	—	—	—	—	—
397	HE 2343−4650	23 46 35.0	-46 34 08	332.00	-66.730	17.3	18.7	0.14	8.6e+18	+112	*	HVC#1795	—	—	—
398	HE 2344−1441	23 46 35.2	-14 25 18	69.75	-70.265	17.7	20.0	0.25	1.6e+19	-205	*	—	—	—	HVC#208
399	HE 2344−6045	23 46 46.4	-60 28 51	316.73	-54.887	17.5	15.9	0.15	8.5e+18	+112	*	—	—	—	—
400	HE 2345−1504_1	23 47 52.8	-14 48 01	69.54	-70.753	15.8	8.5	0.20	1.2e+19	-205	*	—	—	—	HVC#243

Table A.1

Num	HEname	RA (J2000)	DEC (J2000)	l (deg)	b (deg)	B mag (mag)	Distance (kpc)	T_b (K)	N(H I) (cm^{-2})	v_{LSR} $\mathrm{km\,s}^{-1}$	MS Flag	HVC	XHVC	WvW91	de Heij
401	HE 2345−1504_2	23 47 52.8	-14 48 01	69.54	-70.753	15.8	8.5	0.16	9.5e+18	-152	*	—	—	—	—
402	HE 2345−0933	23 47 55.5	-09 16 28	79.92	-66.682	16.5	10.6	0.24	1.6e+19	-218	—	—	—	—	HVC#274
403	HE 2345−1425	23 48 21.7	-14 08 25	71.23	-70.380	14.8	5.9	0.32	2.0e+19	-205	*	—	—	—	HVC#243
404	HE 2346−1510	23 48 42.1	-14 53 47	69.74	-70.963	17.4	17.4	0.23	1.5e+19	-205	*	—	—	—	HVC#243
405	HE 2346−1450	23 49 24.0	-14 34 11	70.82	-70.867	16.2	11.2	0.33	2.1e+19	-152	*	—	—	—	—
406	HE 2346−1331	23 49 24.8	-13 14 38	73.63	-69.936	16.4	11.6	0.16	1.0e+19	-178	—	—	—	—	HVC#208
407	HE 2347−2057	23 49 44.9	-20 40 31	54.24	-74.519	14.5	4.9	0.16	9.5e+18	-112	*	HVC#426	XHVC#25	—	—
408	HE 2347−1043	23 49 48.2	-10 27 03	78.96	-67.895	17.6	21.1	0.25	1.6e+19	-218	—	—	—	—	HVC#243
409	HE 2347−1453	23 49 52.1	-14 36 39	70.97	-70.972	14.0	3.9	0.38	2.5e+19	-152	*	—	—	—	—
410	HE 2347−1103	23 50 15.0	-10 46 43	78.64	-68.223	15.8	9.1	0.34	2.0e+19	-231	—	—	—	—	HVC#262
411	HE 2348−1633	23 50 48.4	-16 17 02	67.50	-72.252	16.5	11.8	0.20	1.3e+19	-191	*	—	—	—	HVC#208
412	HE 2349−0357	23 52 07.8	-03 41 09	89.22	-62.614	15.8	8.8	0.13	7.5e+18	-297	—	CHVC#493	—	—	HVC#313
413	HE 2349−6038	23 52 21.2	-60 21 22	315.72	-55.283	17.6	17.8	0.16	1.0e+19	+152	*	—	—	—	—
414	HE 2350−6037	23 52 48.3	-60 20 55	315.64	-55.314	18.0	24.7	0.17	1.1e+19	+152	*	—	—	—	—
415	HE 2350−1542	23 53 22.9	-15 25 27	70.94	-72.147	16.1	10.5	0.20	1.3e+19	-178	*	—	—	—	HVC#208
416	HE 2351−1338	23 53 35.7	-13 21 56	75.59	-70.712	17.5	17.9	0.43	2.5e+19	-231	*	—	—	—	HVC#243
417	HE 2351−2213	23 54 13.7	-21 57 01	51.54	-76.016	15.9	9.9	0.21	1.4e+19	-125	*	—	XHVC#25	—	HVC#160
418	HE 2351−2208	23 54 15.0	-21 52 10	51.85	-75.988	17.3	18.1	0.29	1.8e+19	-139	*	—	XHVC#25	—	HVC#160
419	HE 2352−1259	23 54 42.8	-12 42 21	77.51	-70.393	16.0	10.3	0.30	1.9e+19	-218	*	—	—	—	HVC#262
420	HE 2353−1710	23 55 52.0	-16 54 09	68.58	-73.586	16.7	13.4	0.20	1.4e+19	-178	*	—	—	—	HVC#208
421	HE 2353−6113	23 56 17.4	-60 56 20	314.55	-54.937	17.7	22.1	0.57	3.6e+19	+138	*	—	—	—	—
422	HE 2354−1821	23 57 22.4	-18 04 28	66.13	-74.606	16.3	11.7	0.41	2.5e+19	-165	*	—	—	—	HVC#208
423	HE 2355−6109	23 57 46.2	-60 52 41	314.30	-55.059	14.3	4.8	0.29	1.8e+19	+152	*	—	—	—	—
424	HE 2355−1805	23 58 02.6	-17 49 03	67.25	-74.575	17.6	21.5	0.61	3.9e+19	-165	*	—	—	—	HVC#208
425	HE 2355−3401	23 58 06.5	-33 45 10	359.71	-76.754	14.7	5.8	0.16	9.2e+18	+125	*	HVC#1996	—	—	—
426	HE 2355−2017	23 58 10.7	-20 00 38	60.38	-75.890	14.4	4.8	0.15	9.8e+18	-152	*	—	—	—	—
427	HE 2355−1821	23 58 17.9	-18 04 44	66.63	-74.780	17.2	11.4	0.57	3.6e+19	-165	*	—	—	—	HVC#208
428	HE 2355−6053	23 58 26.6	-60 36 45	314.33	-55.339	17.0	17.2	0.12	7.5e+18	+152	*	—	—	—	—
429	HE 2355−3753	23 58 32.9	-37 36 43	346.34	-74.712	16.7	14.4	0.13	8.4e+18	+165	*	CHVC#1893	—	—	—
430	HE 2356−2219	23 58 36.6	-22 02 20	53.04	-76.971	14.6	5.4	0.28	1.5e+19	-112	*	—	XHVC#25	—	HVC#261

Note. — Table A.1 is also published in its entirety in machine-readable form in the electronic edition of the *Astrophysical Journal*.

APPENDIX B

FHB/HVC SPECTRA AND COLUMN DENSITY MAPS

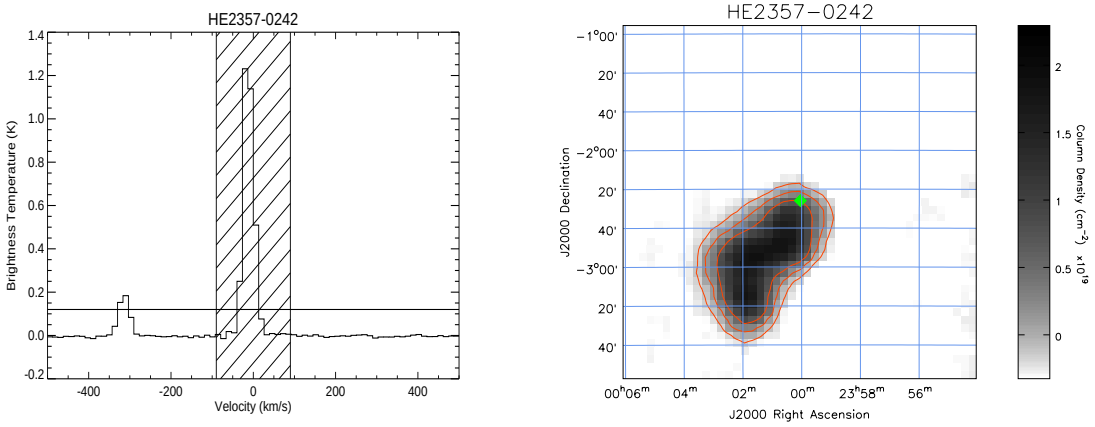


Figure B.1: HE 2357−0242

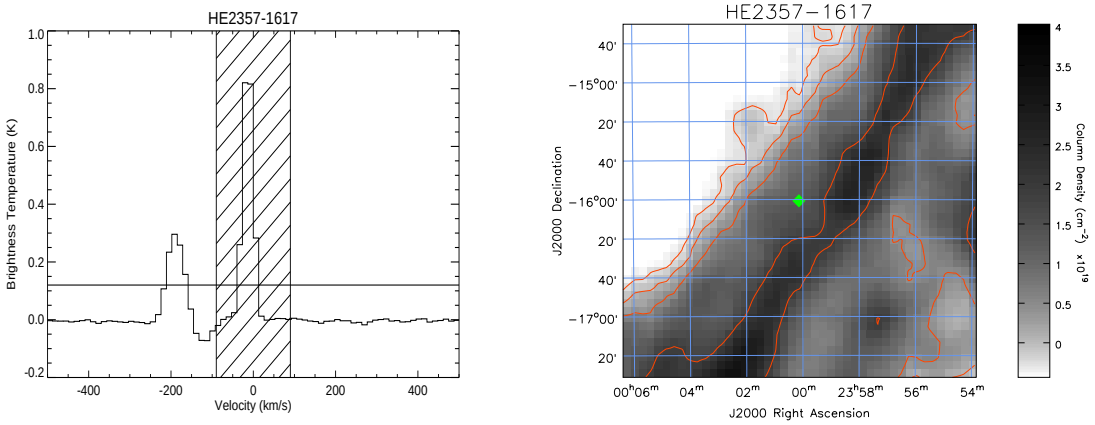


Figure B.2: HE 2357−1617

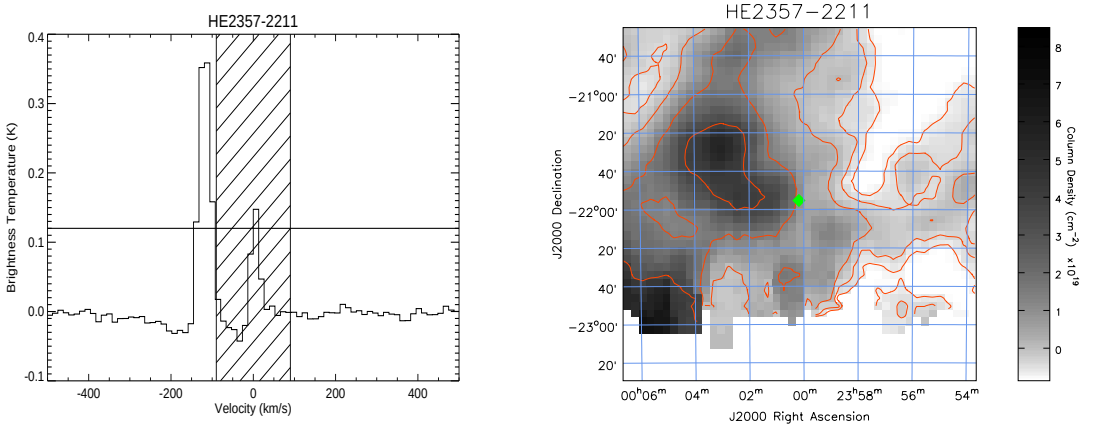


Figure B.3: HE 2357−2211

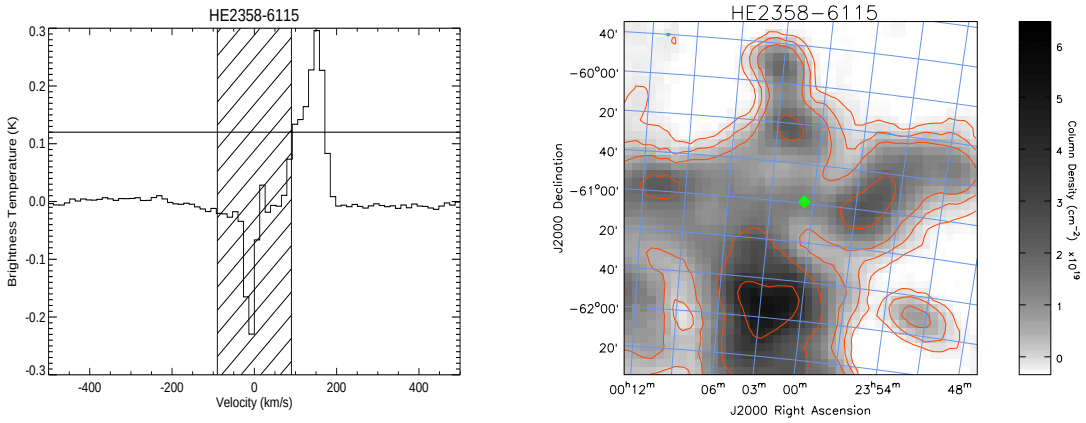


Figure B.4: HE 2358−6115

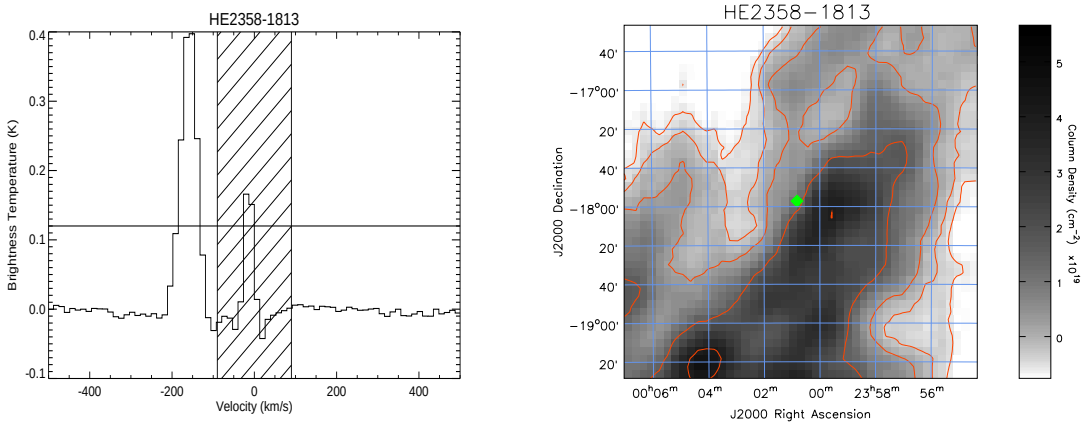


Figure B.5: HE 2358−1813

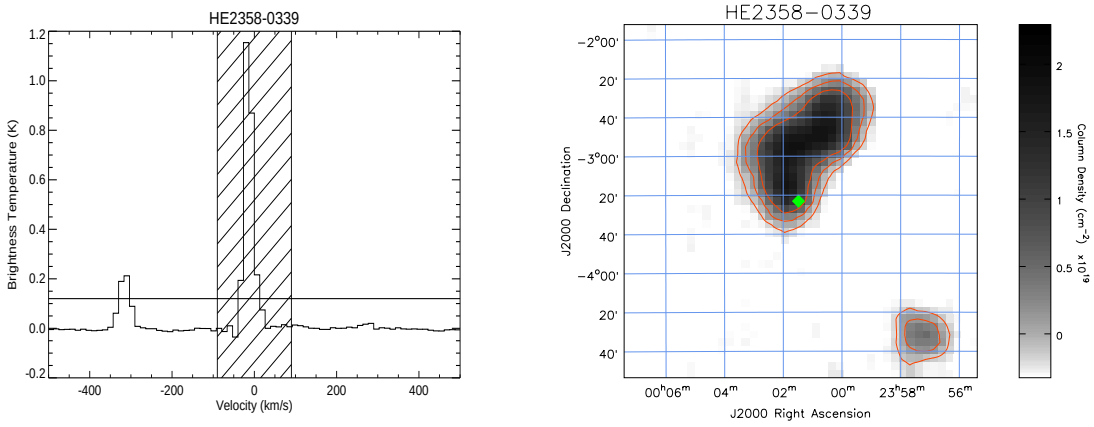


Figure B.6: HE 2358−0339

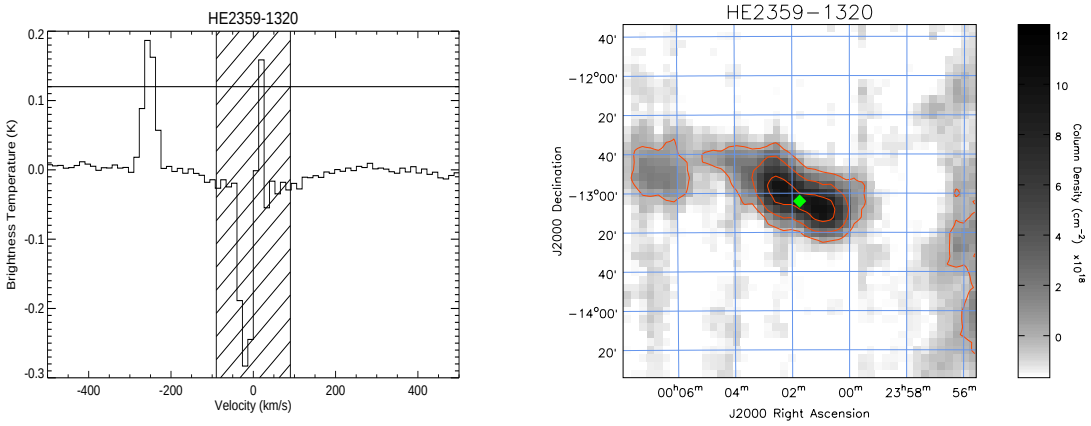


Figure B.7: HE 2359−1320

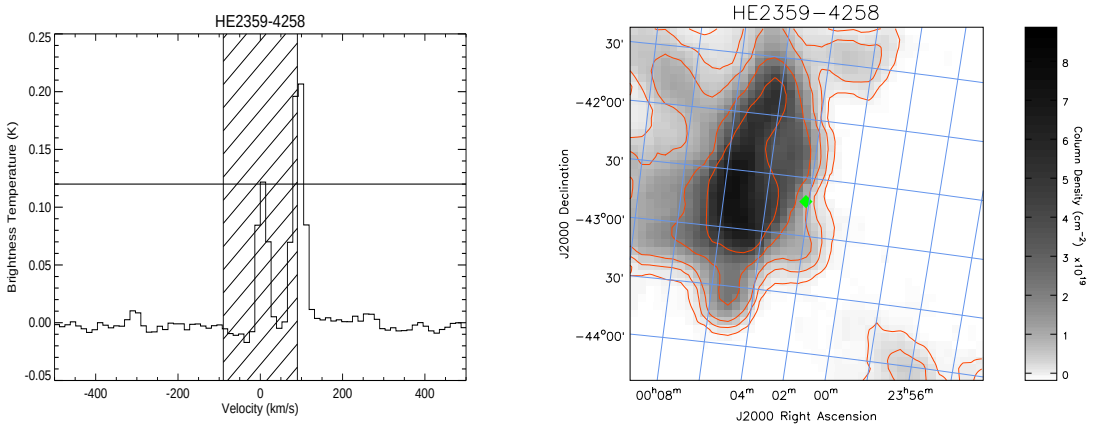


Figure B.8: HE 2359−4258

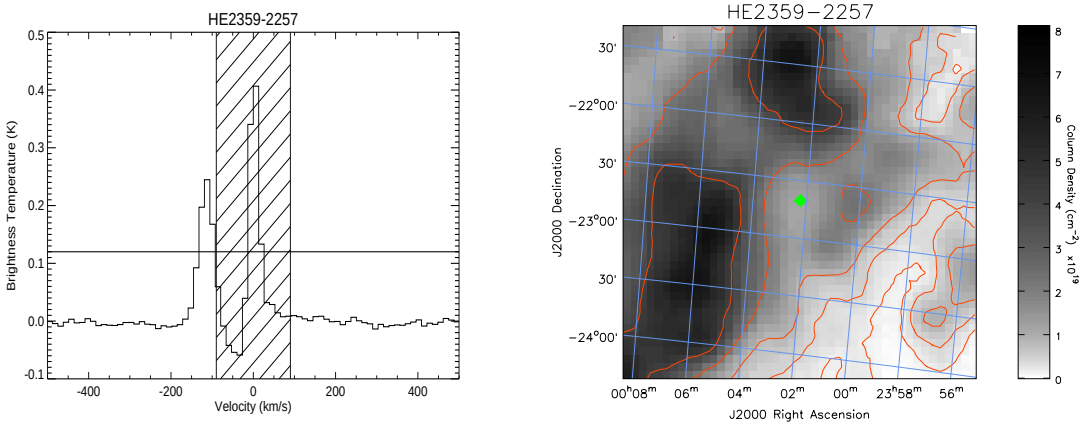


Figure B.9: HE 2359−2257

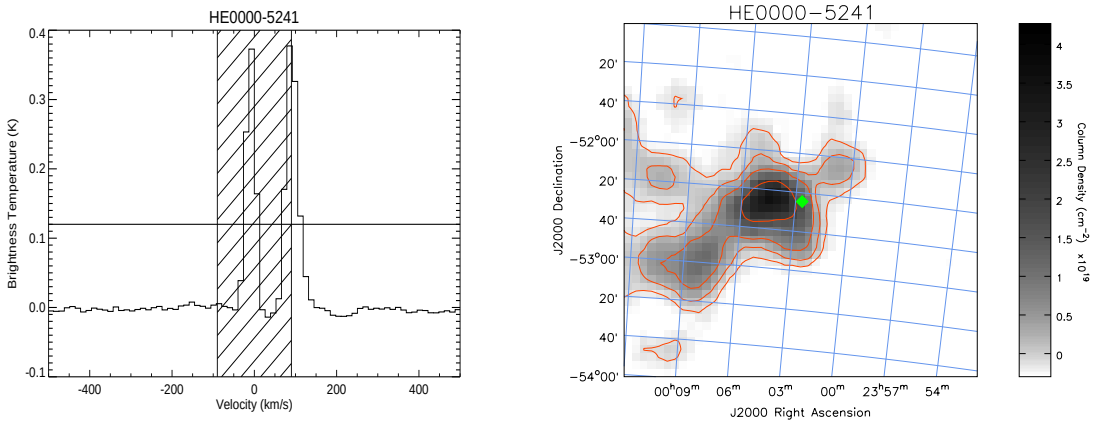


Figure B.10: HE 0000−5241

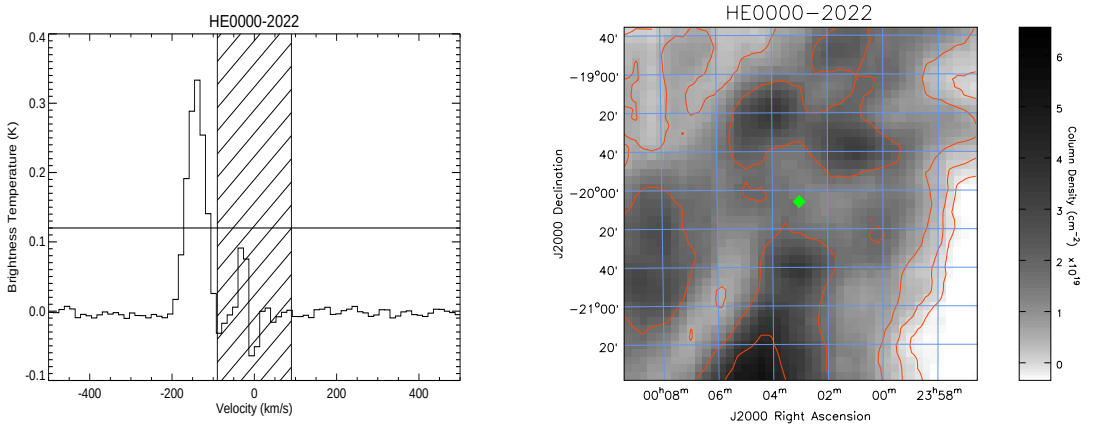


Figure B.11: HE 0000−2022

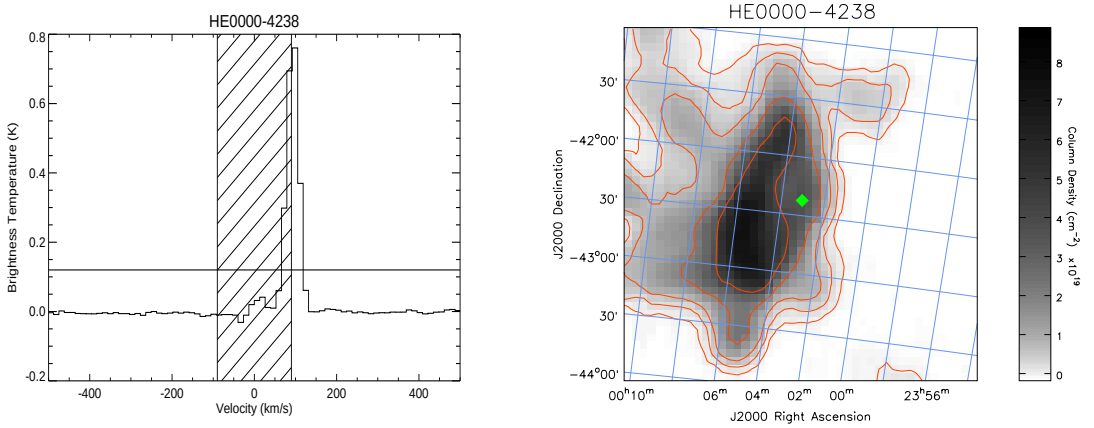


Figure B.12: HE 0000−4238

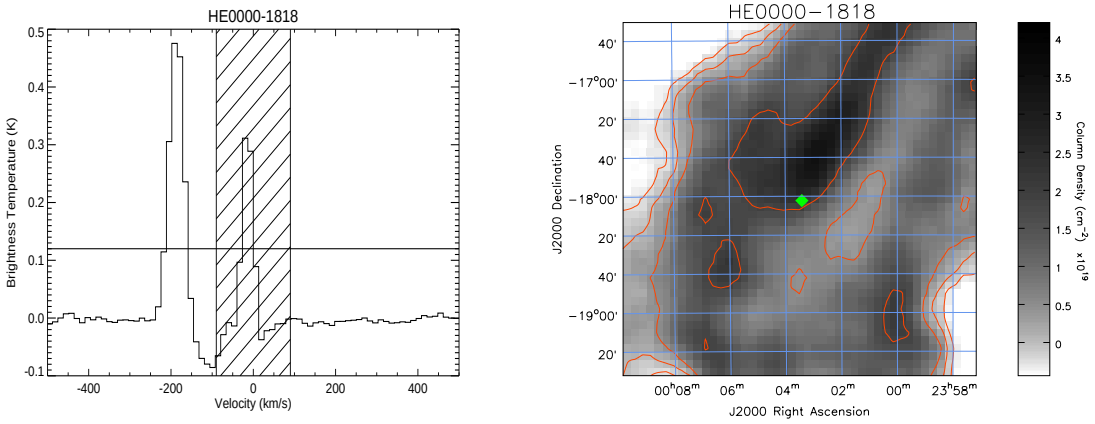


Figure B.13: HE 0000−1818

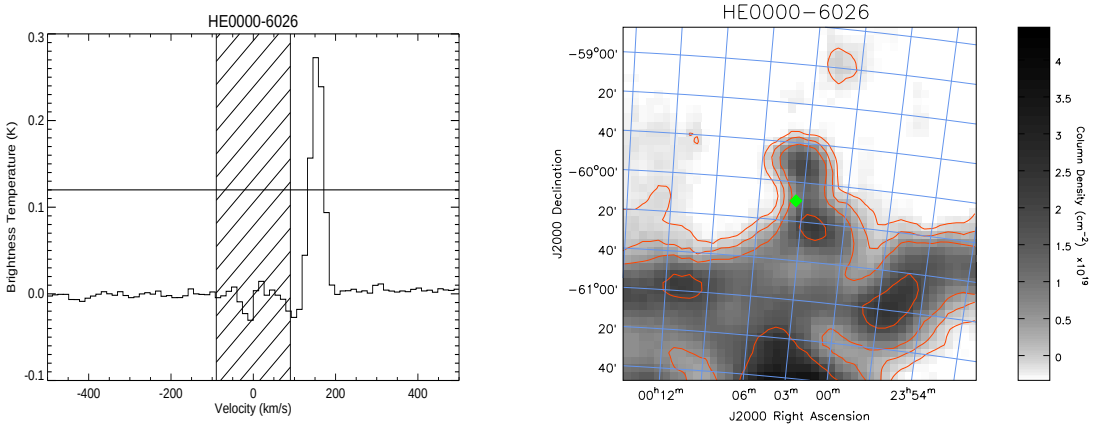


Figure B.14: HE 0000−6026

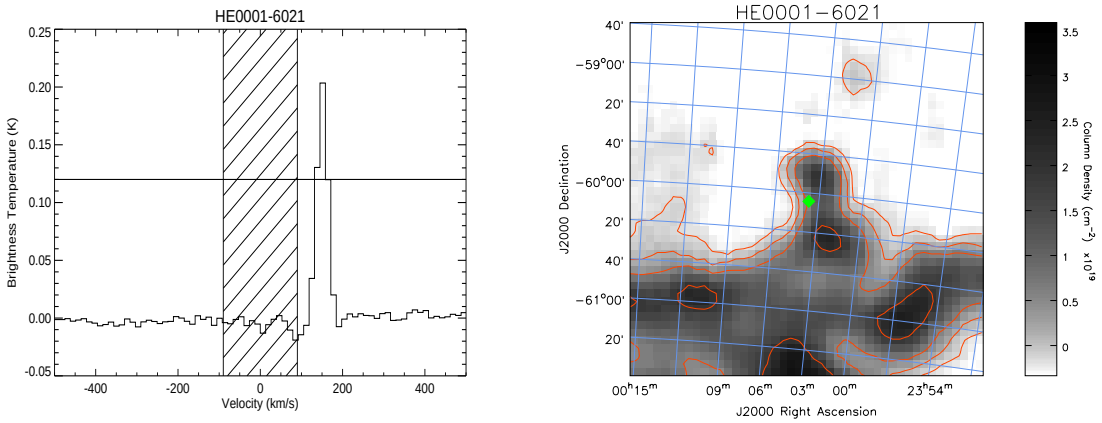


Figure B.15: HE 0001−6021

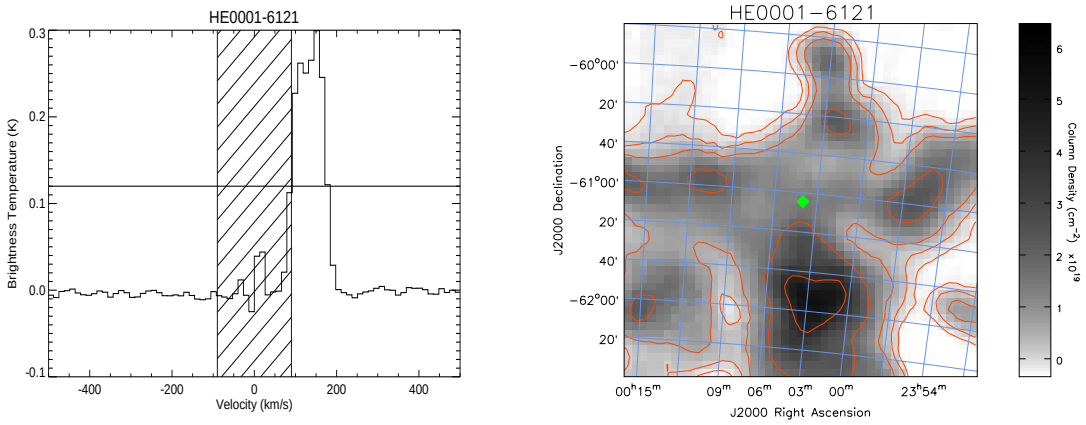


Figure B.16: HE 0001−6121

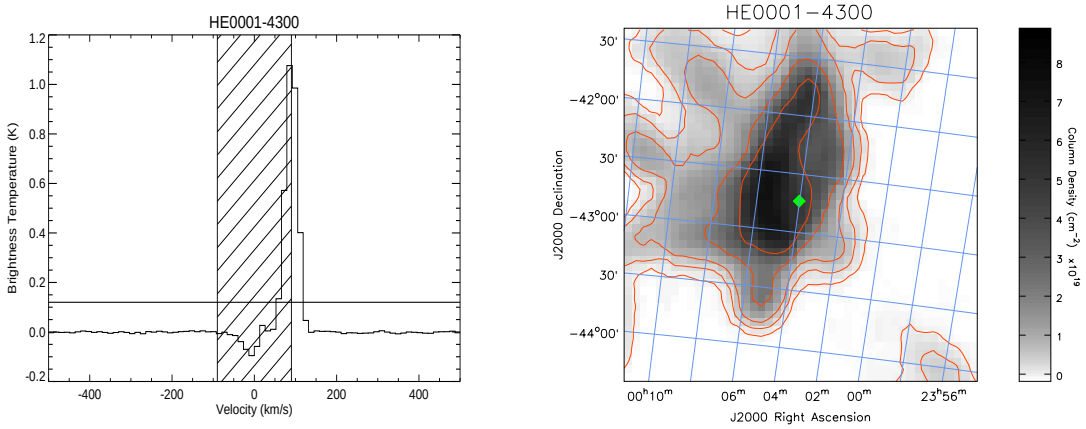


Figure B.17: HE 0001−4300

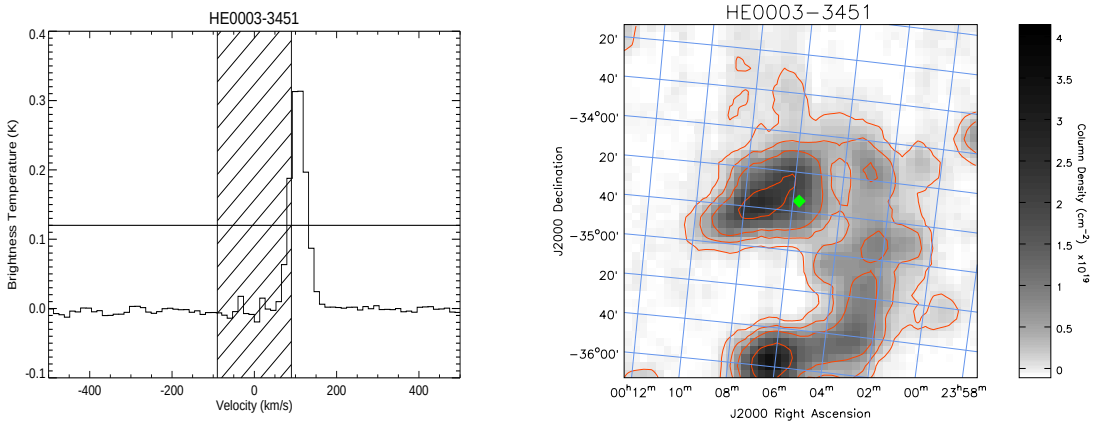
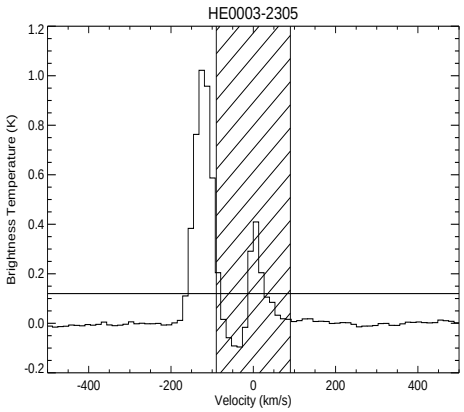


Figure B.18: HE 0003−3451



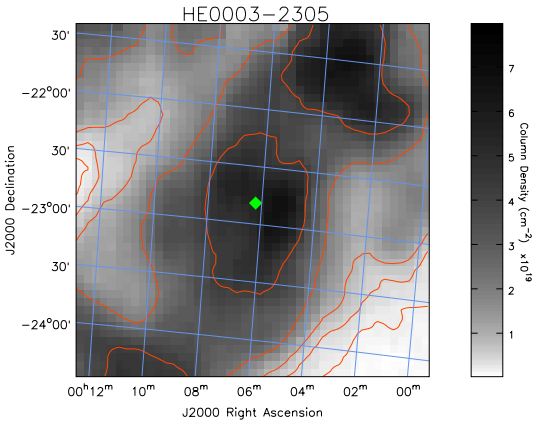
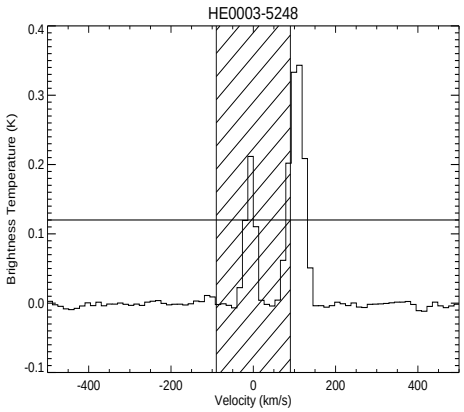


Figure B.19: HE 0003−2305



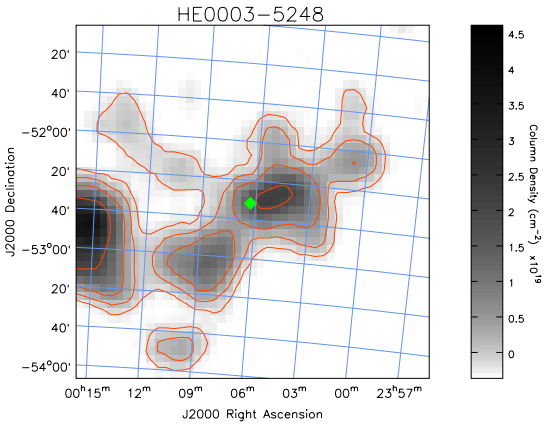
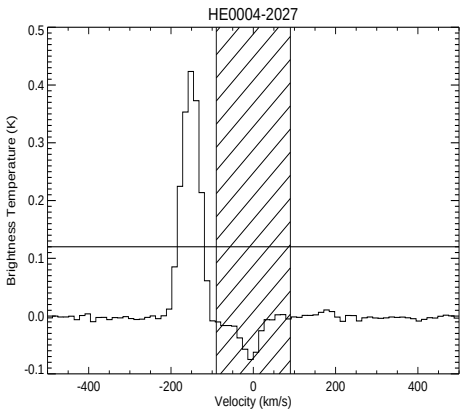


Figure B.20: HE 0003−5248



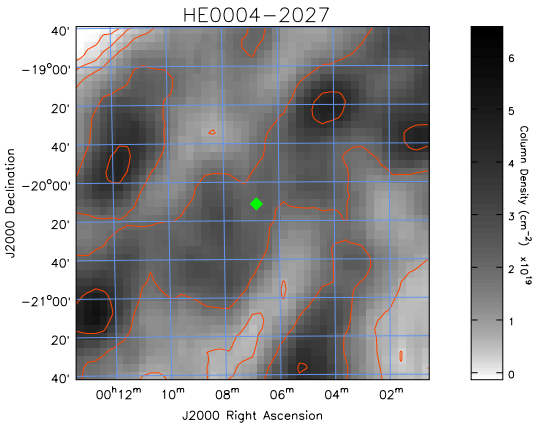


Figure B.21: HE 0004−2027

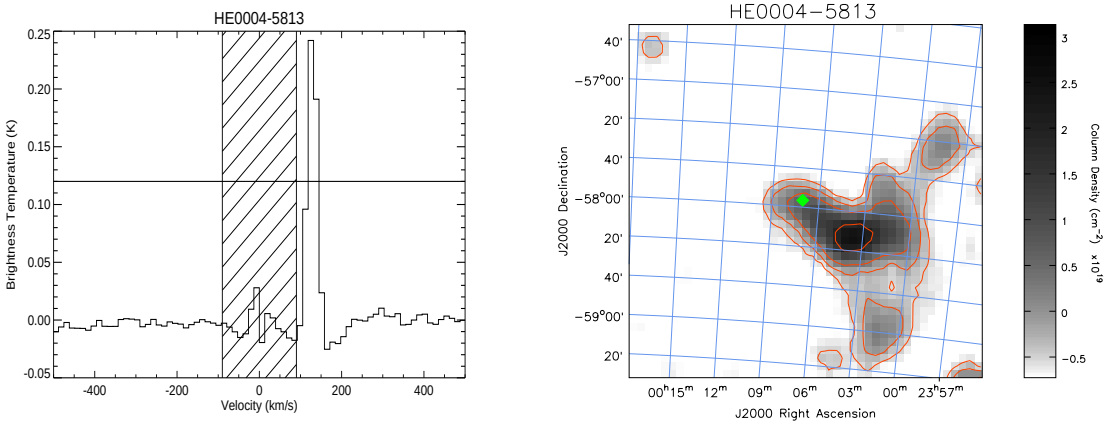


Figure B.22: HE 0004−5813

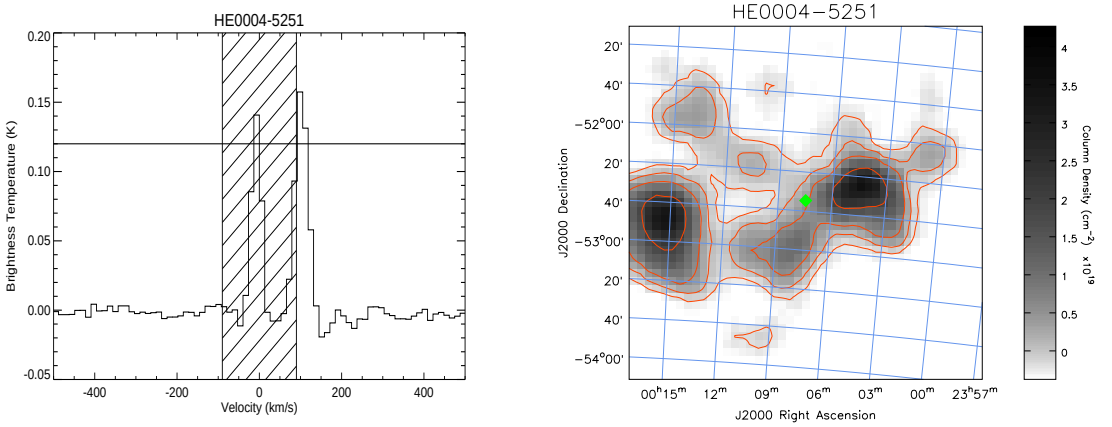


Figure B.23: HE 0004−5251

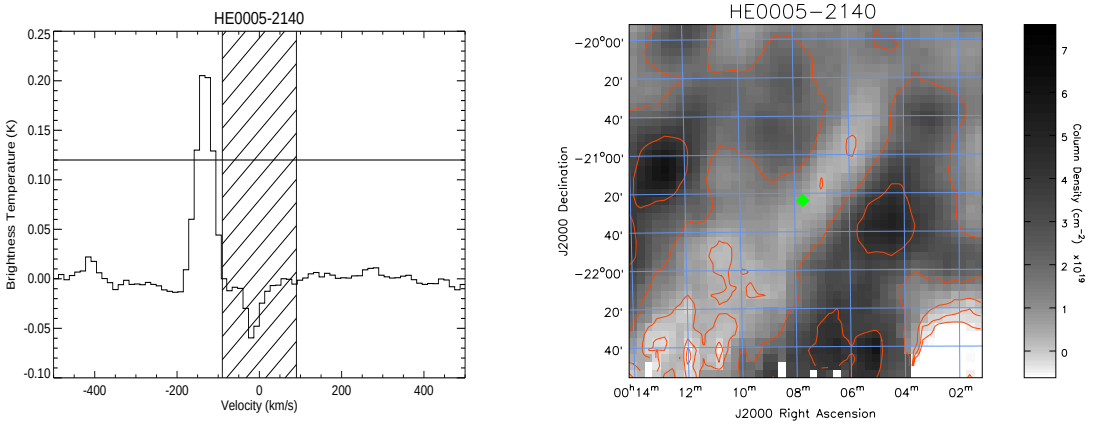


Figure B.24: HE 0005−2140

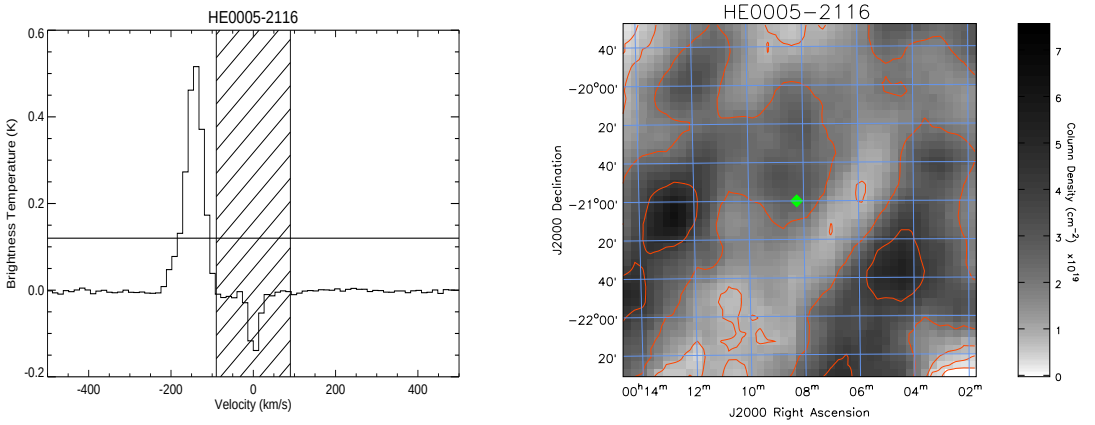


Figure B.25: HE 0005−2116

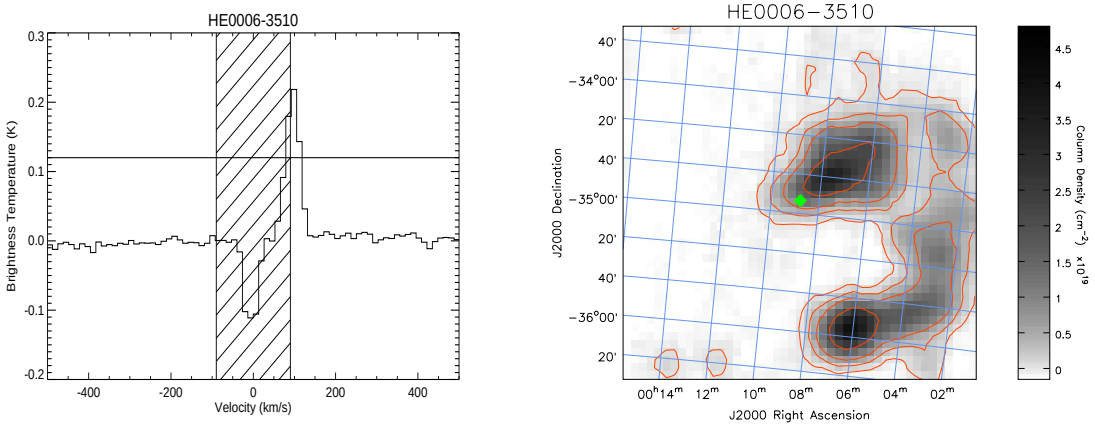


Figure B.26: HE 0006−3510

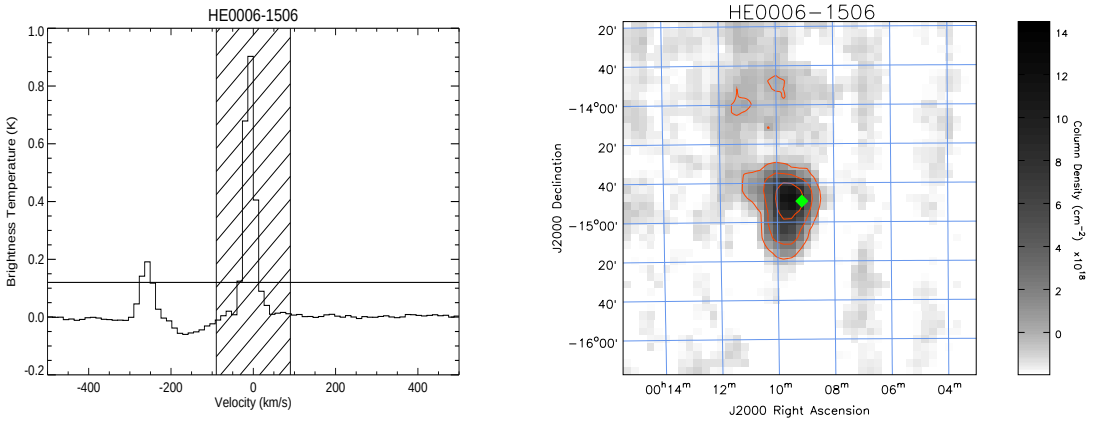


Figure B.27: HE 0006−1506

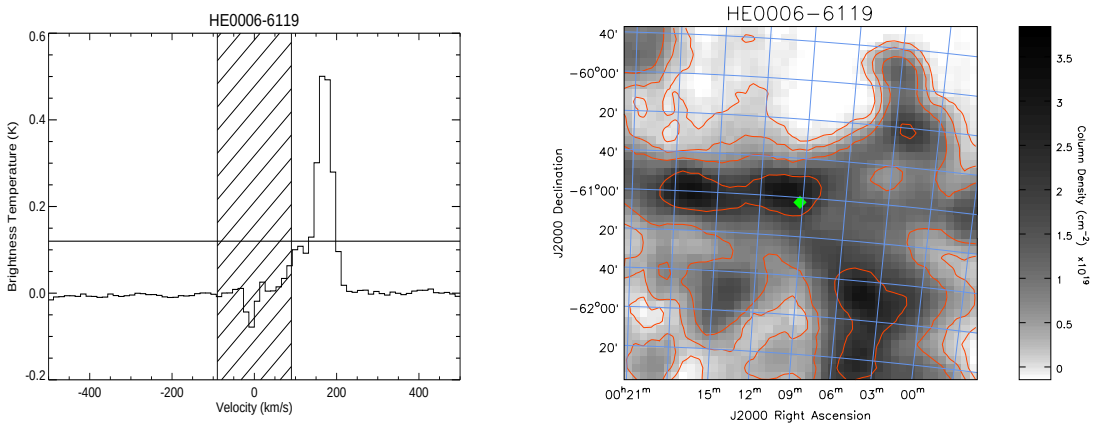


Figure B.28: HE 0006−6119

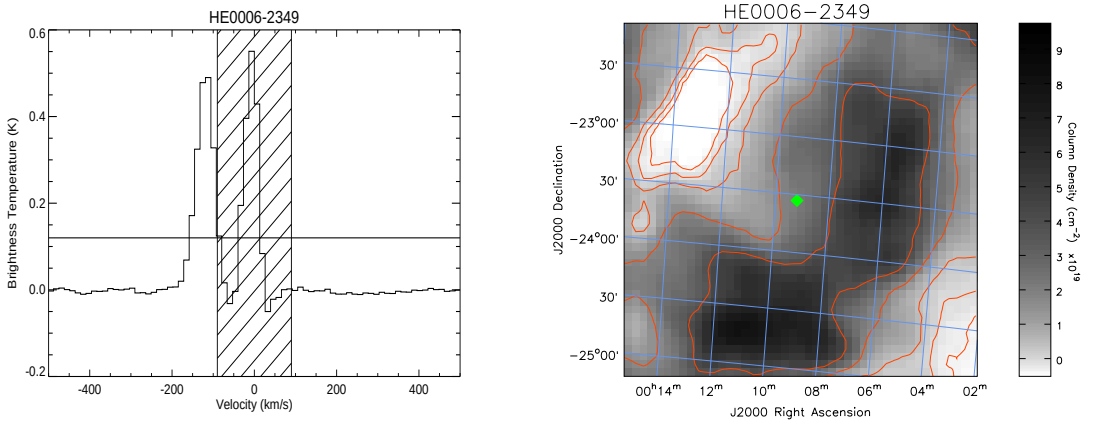


Figure B.29: HE 0006−2349

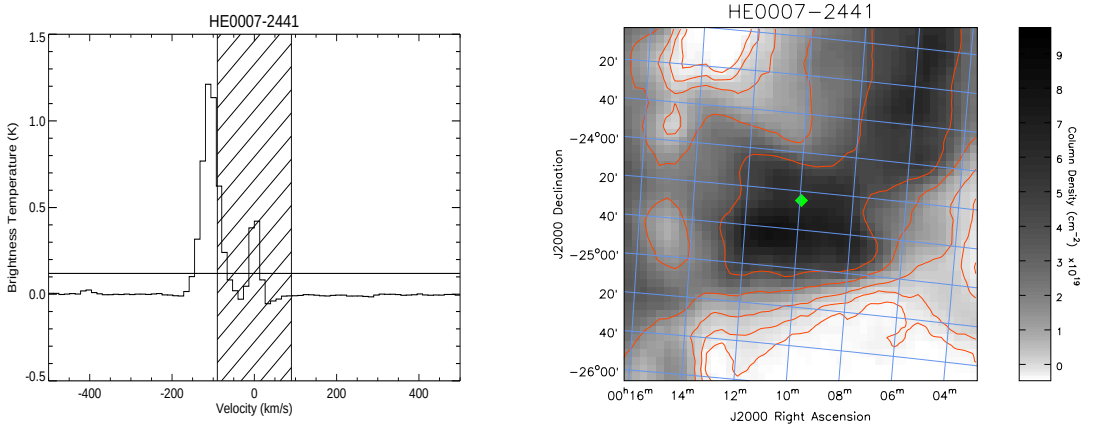


Figure B.30: HE 0007−2441

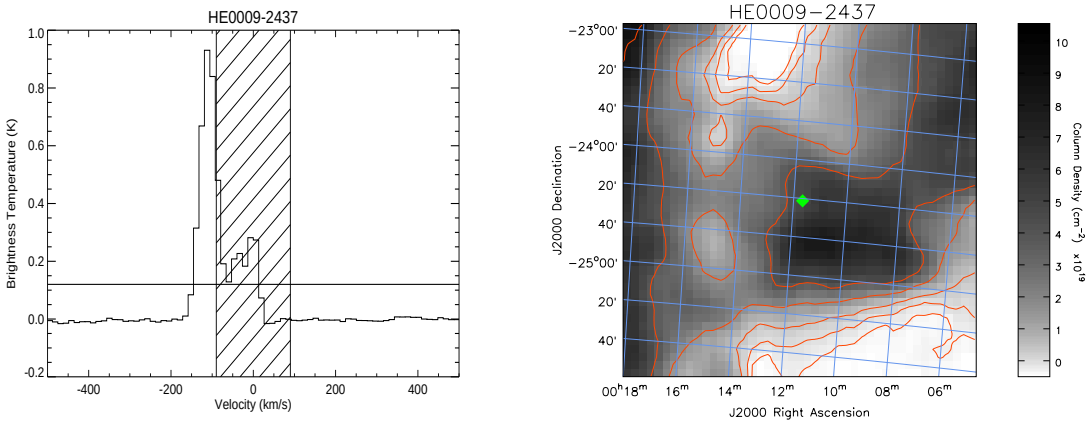


Figure B.31: HE 0009−2437

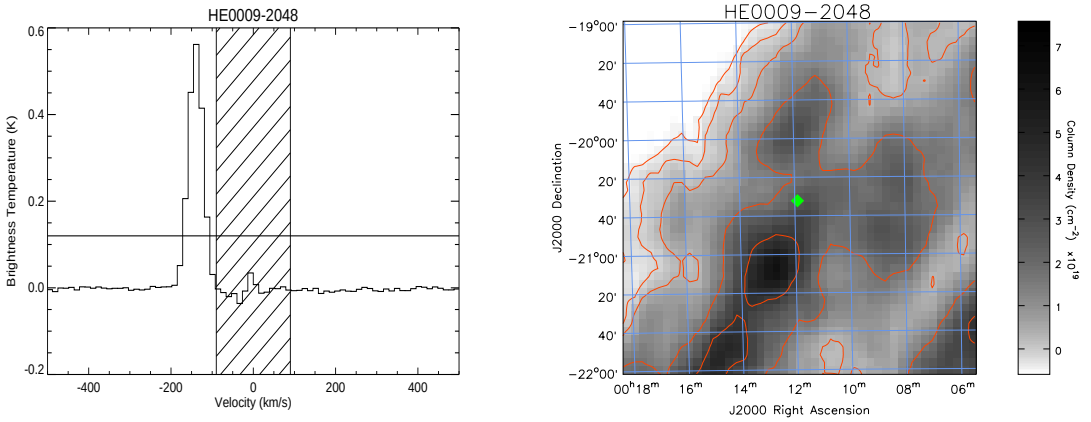


Figure B.32: HE 0009−2048

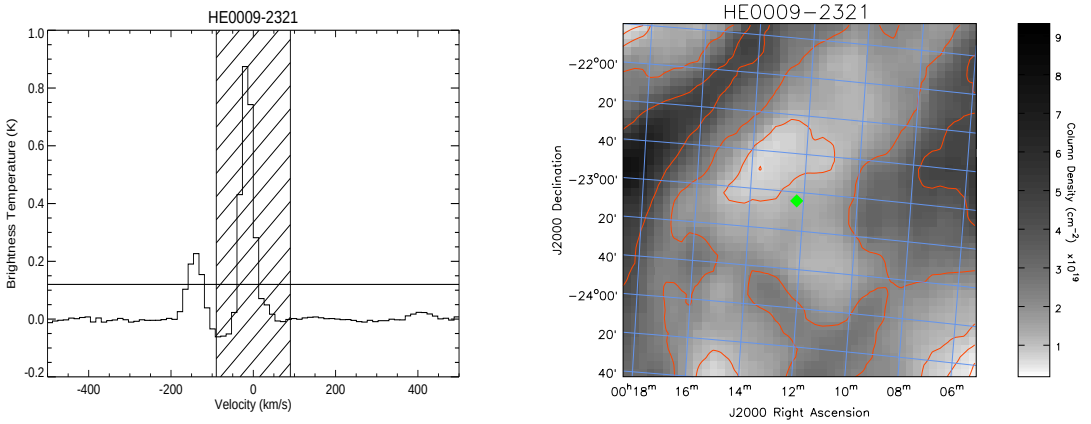


Figure B.33: HE 0009−2321

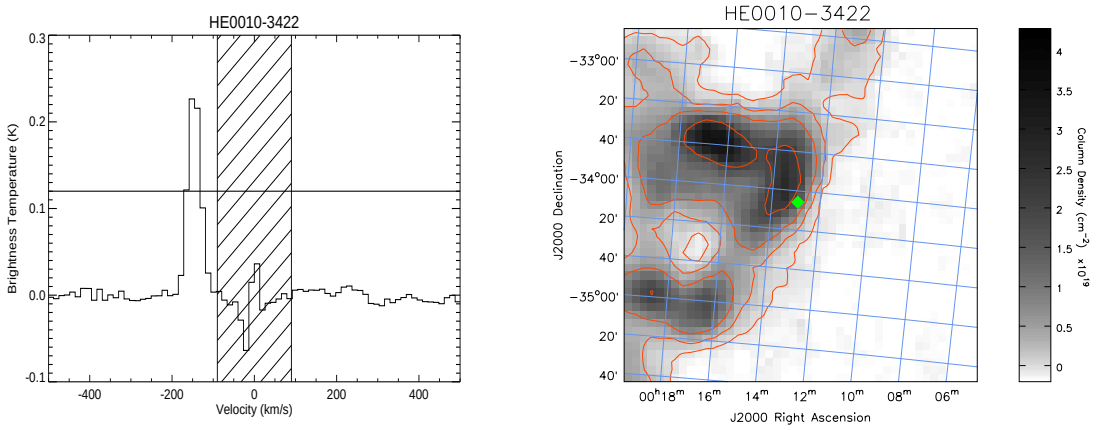


Figure B.34: HE 0010−3422

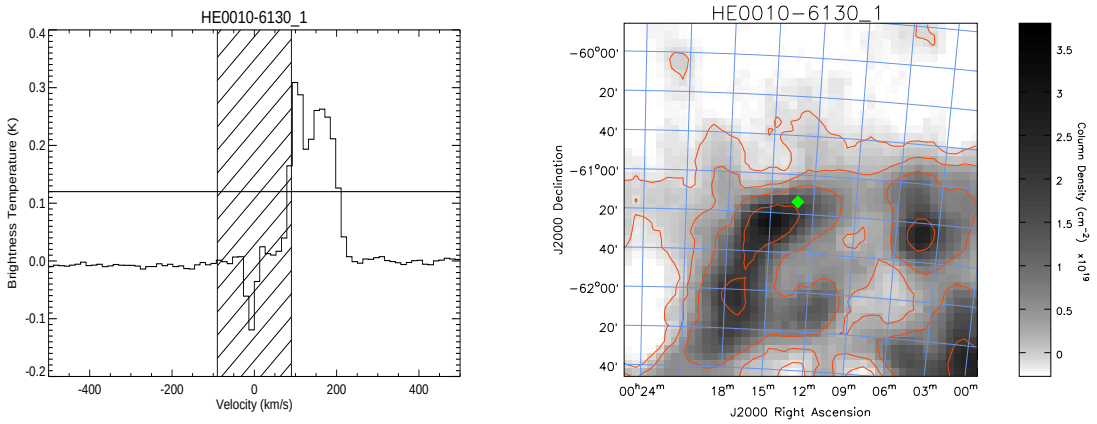


Figure B.35: HE 0010−6130_1

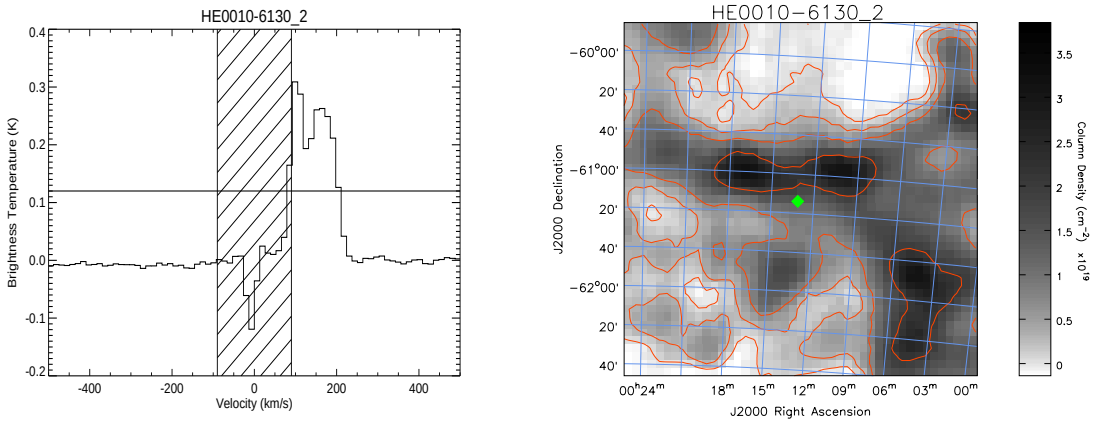
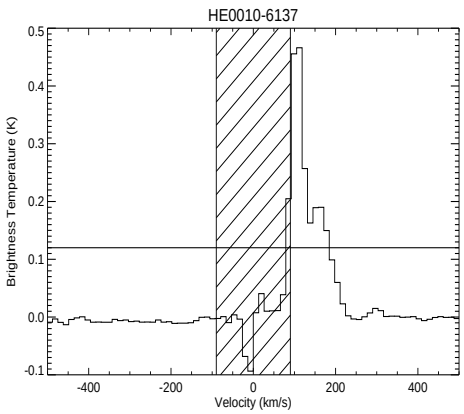


Figure B.36: HE 0010−6130_2



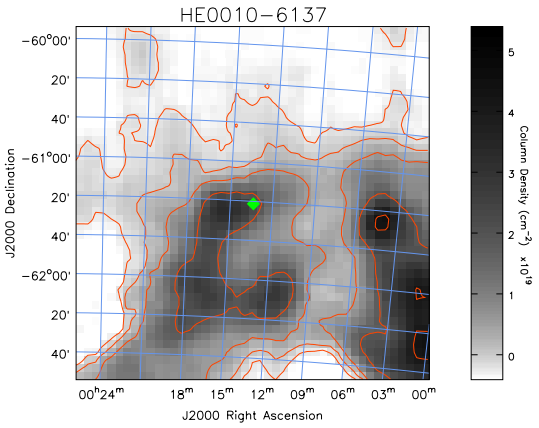
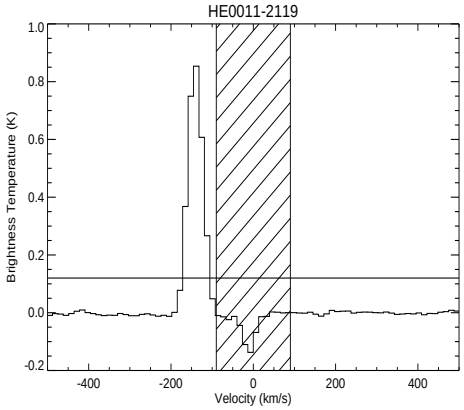


Figure B.37: HE 0010−6137



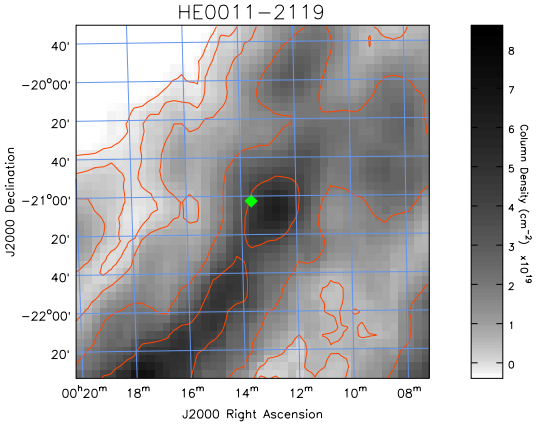
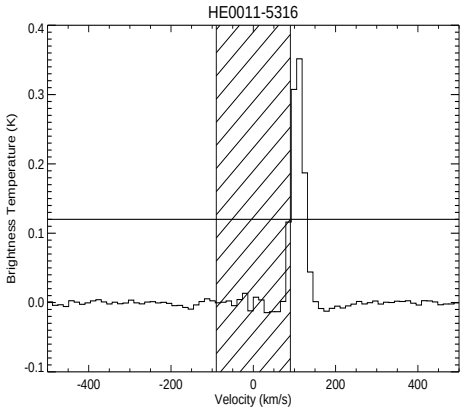


Figure B.38: HE 0011−2119



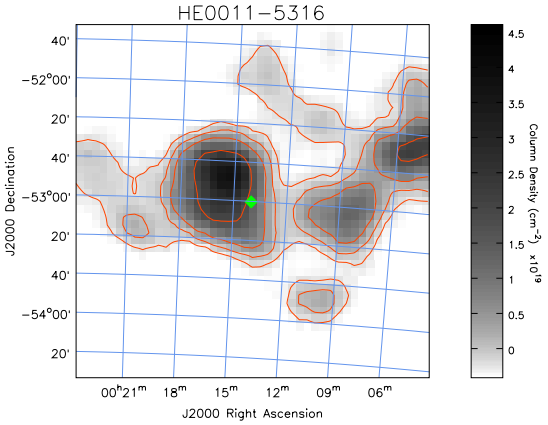


Figure B.39: HE 0011−5316

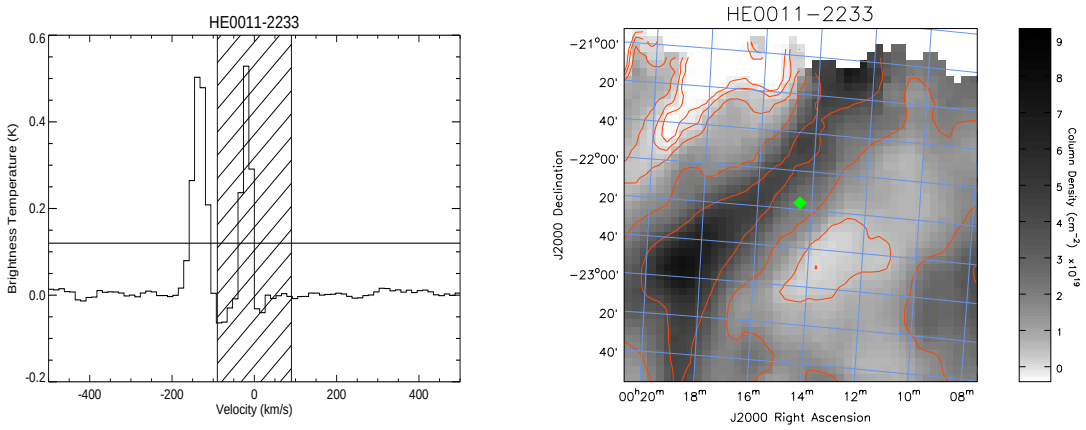


Figure B.40: HE 0011−2233

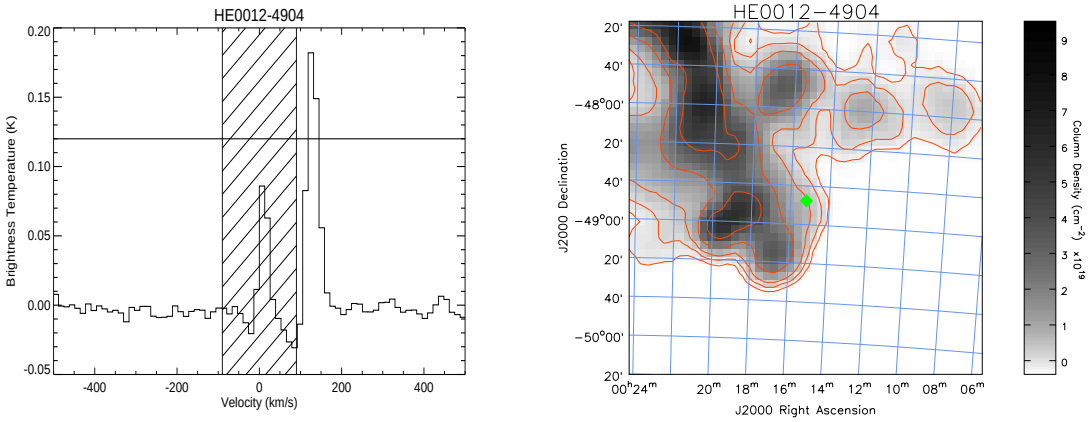


Figure B.41: HE 0012−4904

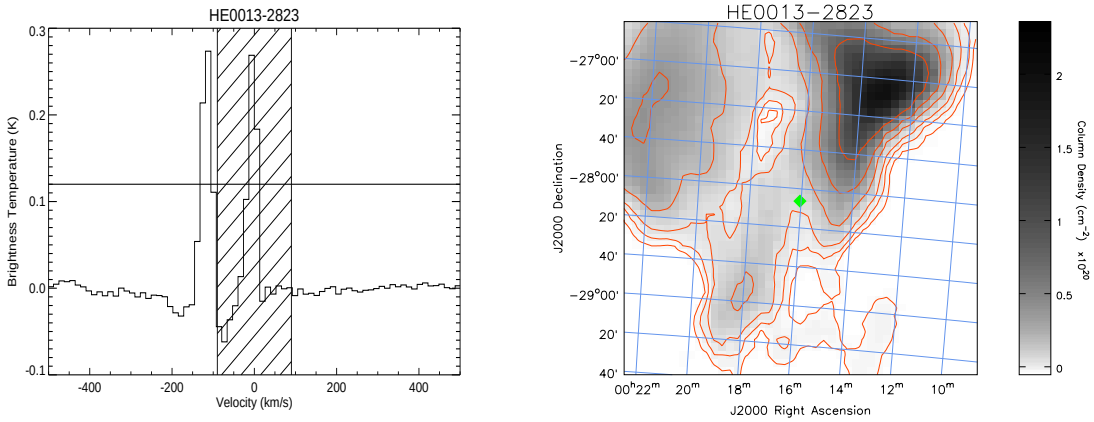
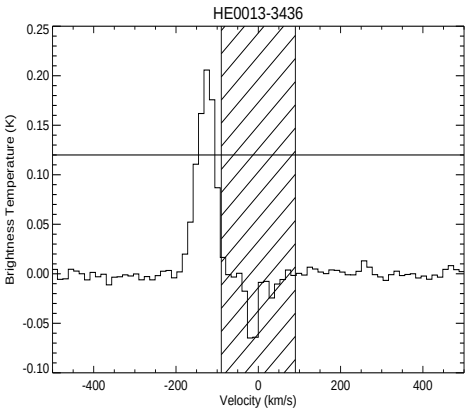


Figure B.42: HE 0013−2823



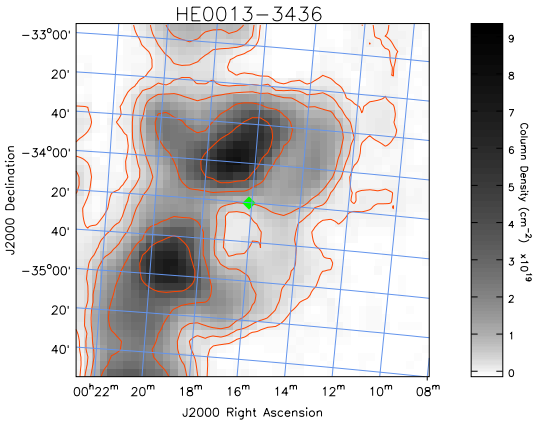
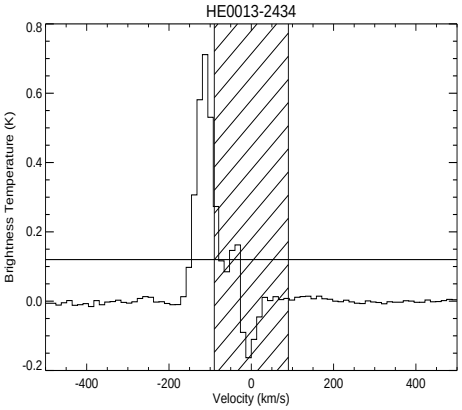


Figure B.43: HE 0013−3436



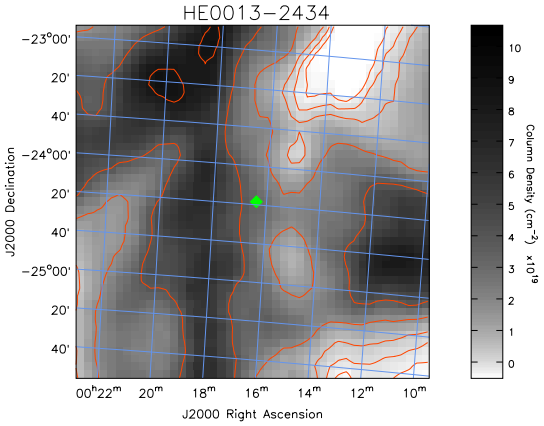
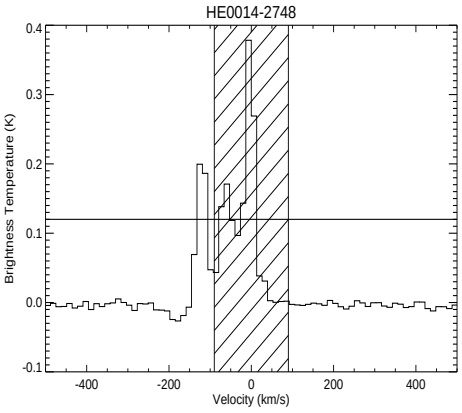


Figure B.44: HE 0013−2434



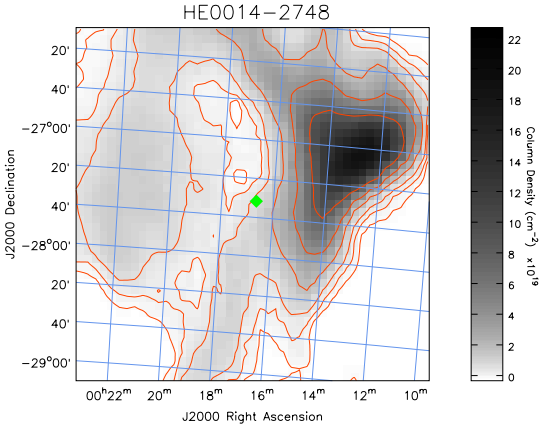


Figure B.45: HE 0014−2748

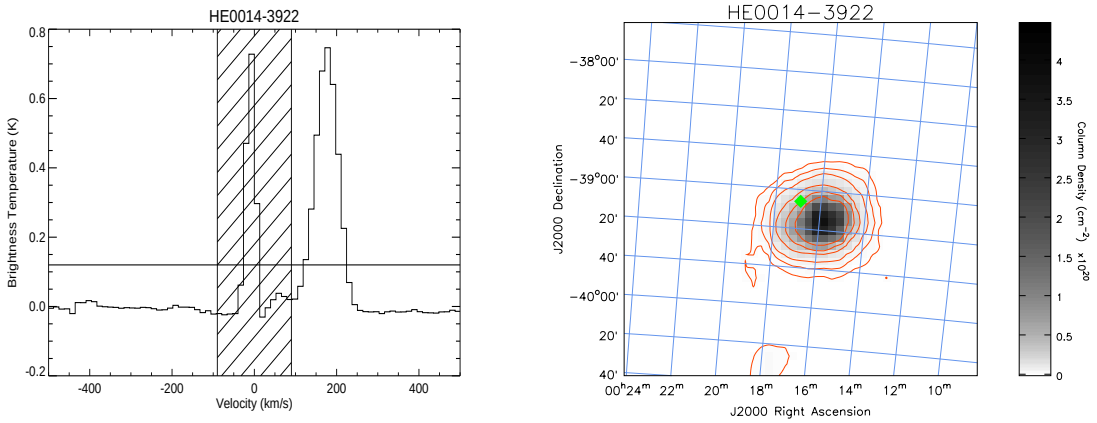


Figure B.46: HE 0014−3922

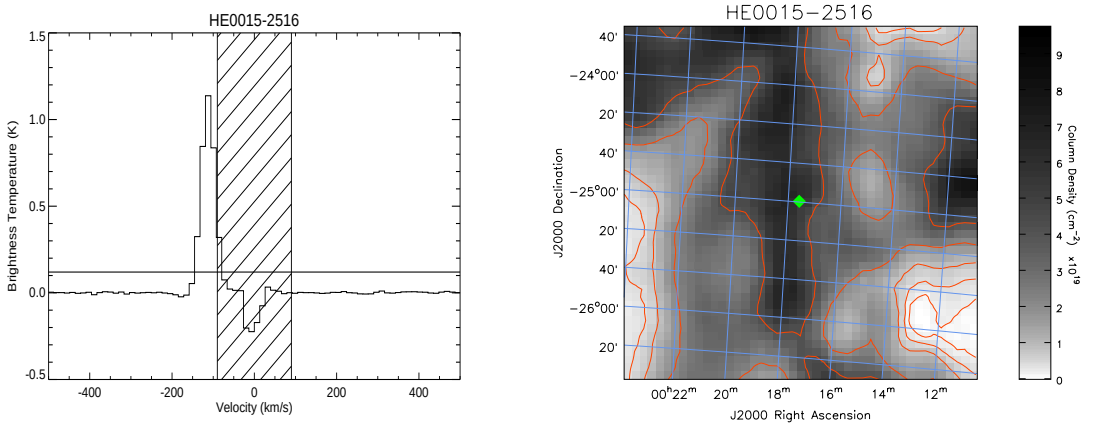


Figure B.47: HE 0015−2516

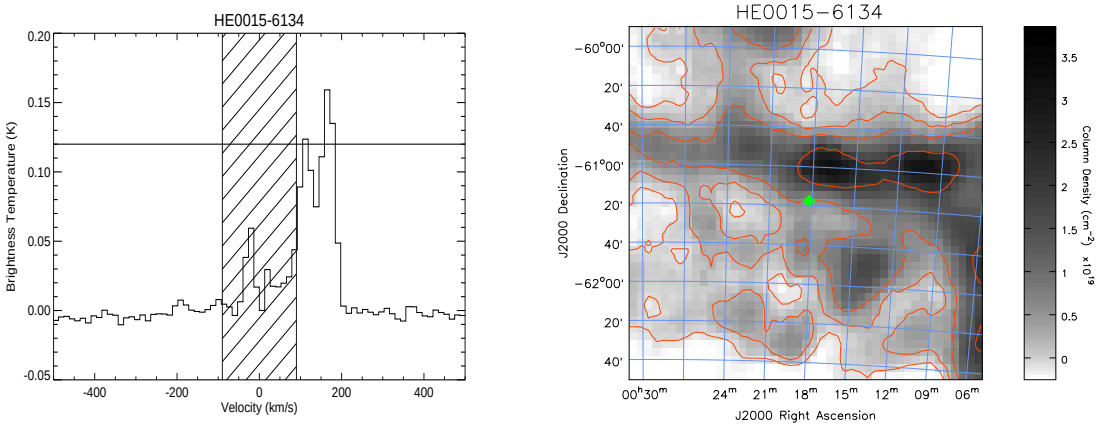


Figure B.48: HE 0015−6134

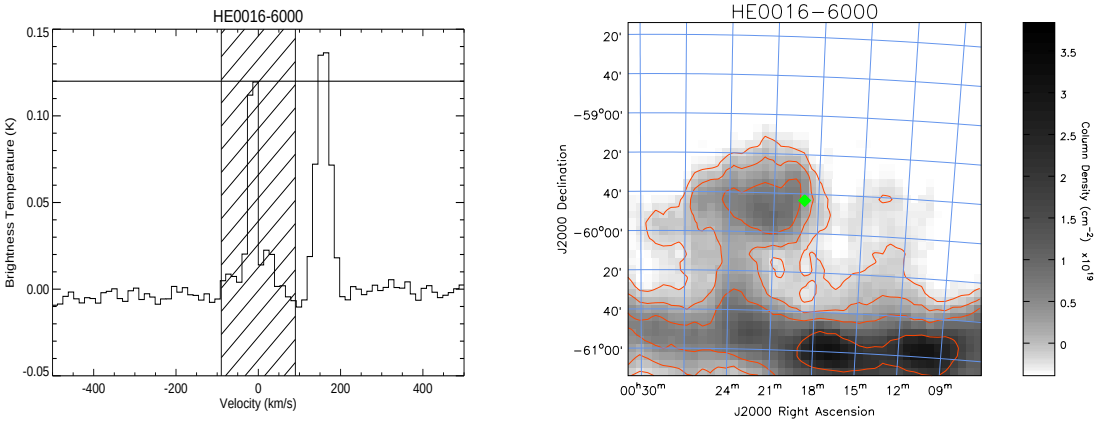


Figure B.49: HE 0016−6000

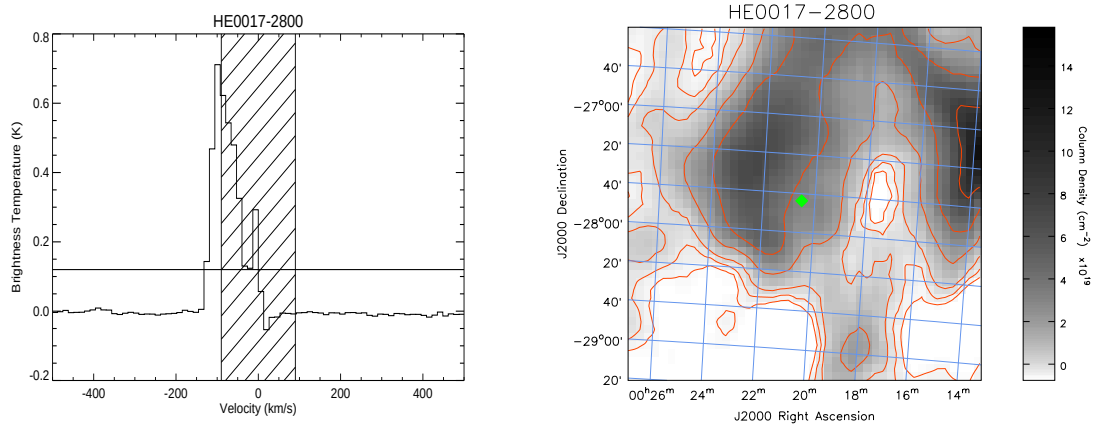


Figure B.50: HE 0017−2800

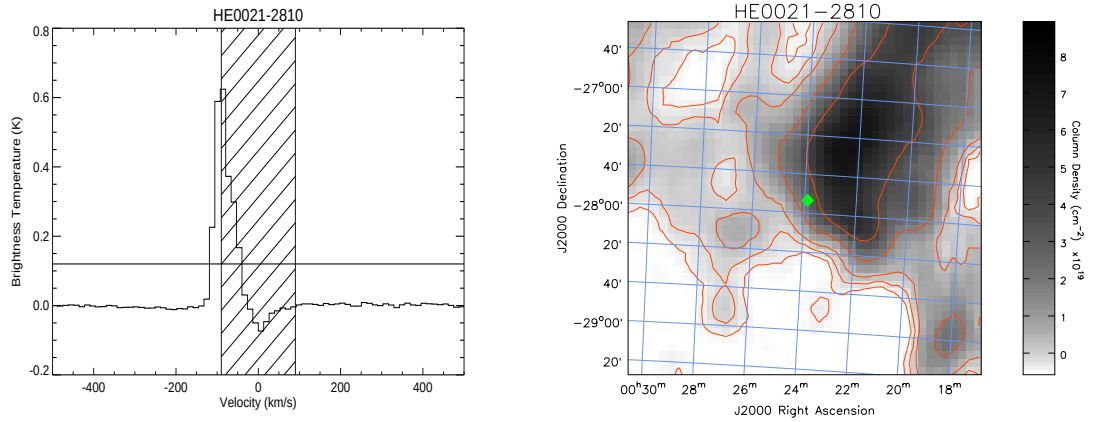


Figure B.51: HE 0021−2810

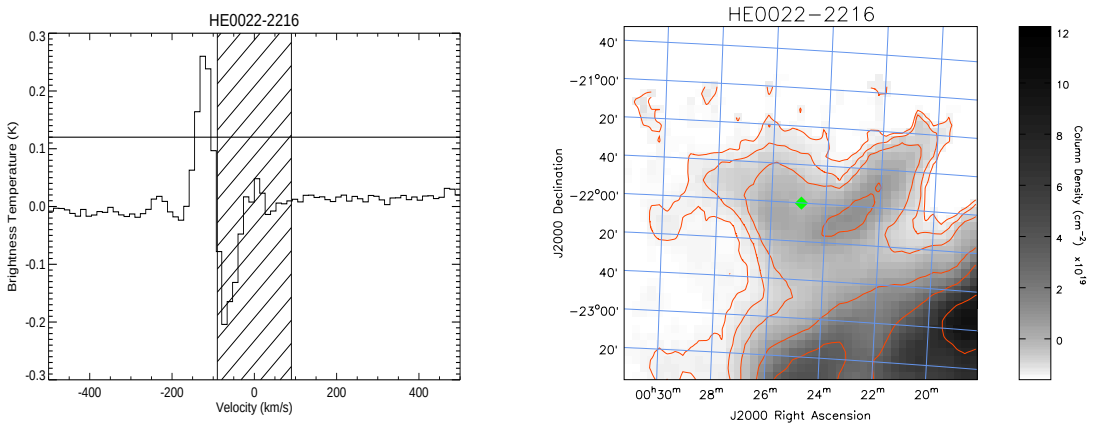


Figure B.52: HE 0022−2216

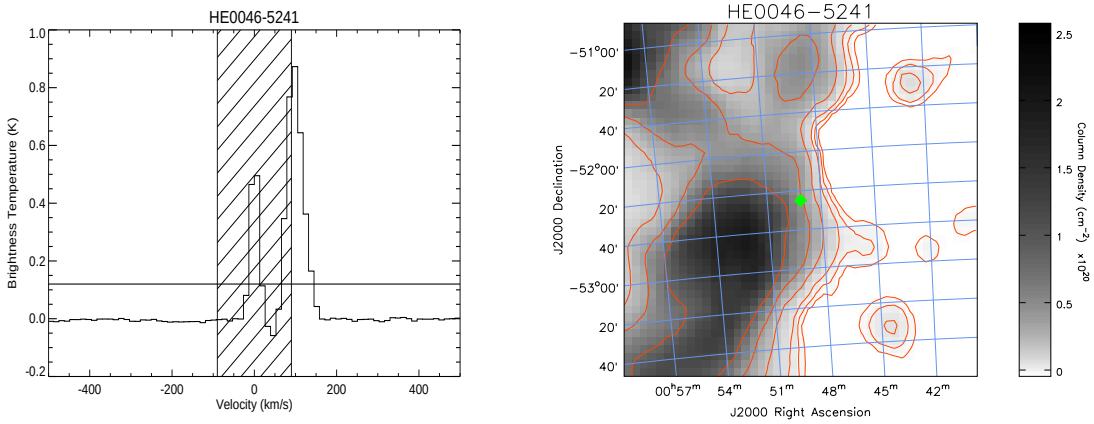


Figure B.53: HE 0046−5241

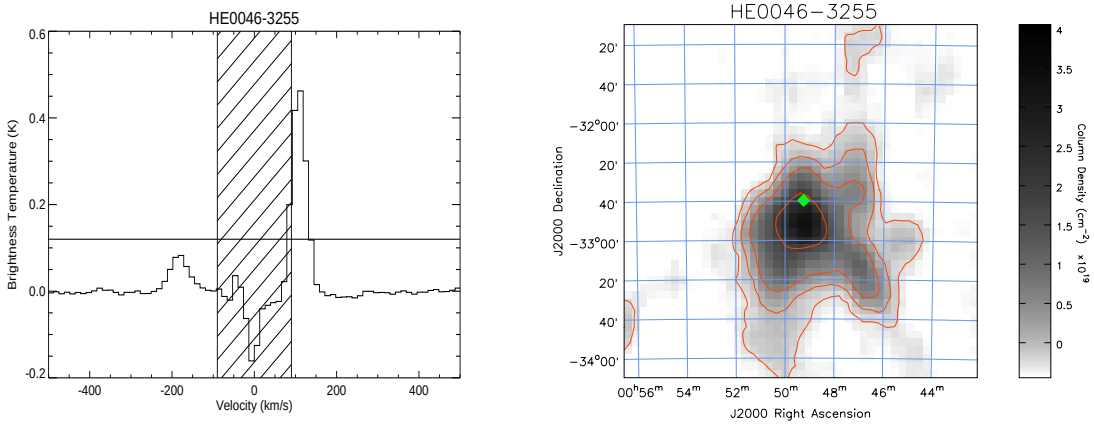


Figure B.54: HE 0046−3255

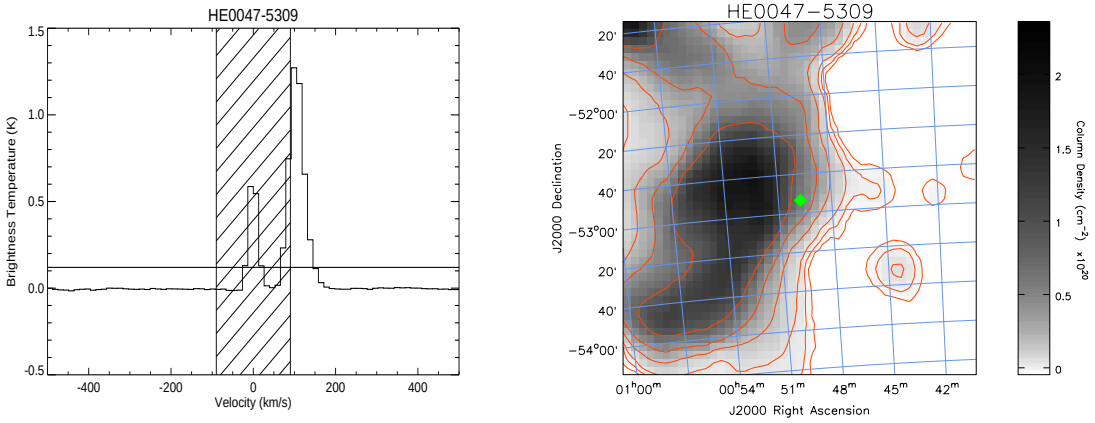


Figure B.55: HE 0047−5309

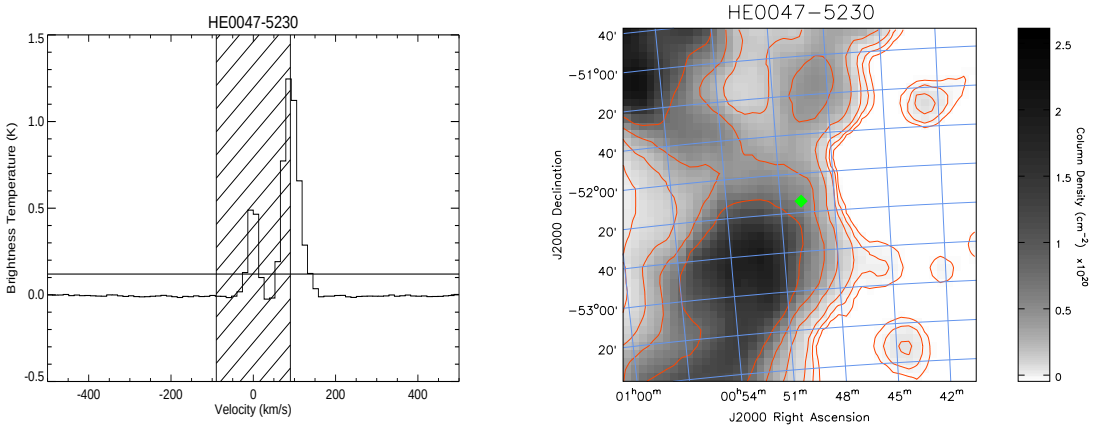


Figure B.56: HE 0047−5230

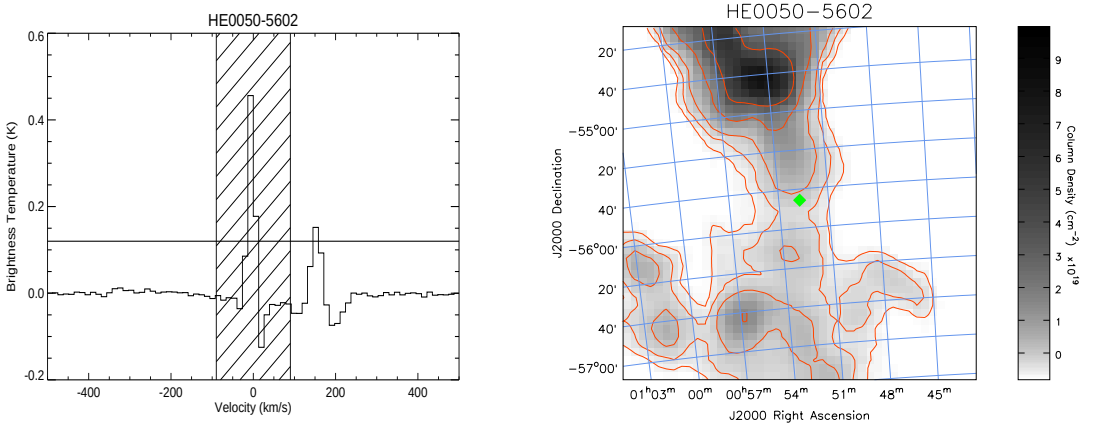


Figure B.57: HE 0050−5602

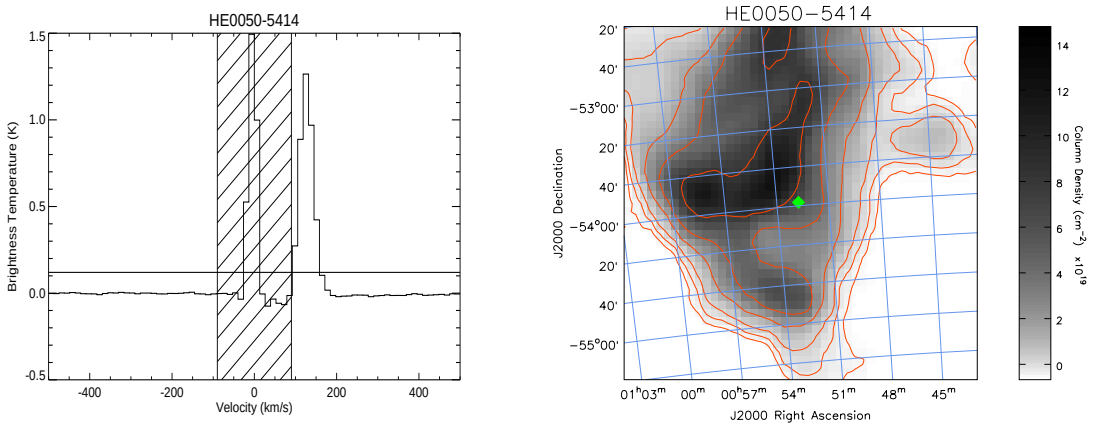


Figure B.58: HE 0050−5414

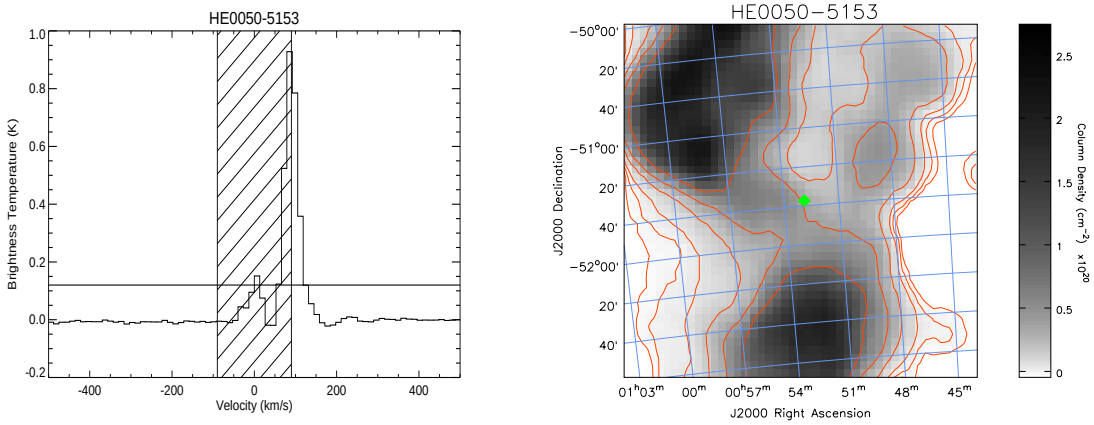


Figure B.59: HE 0050−5153

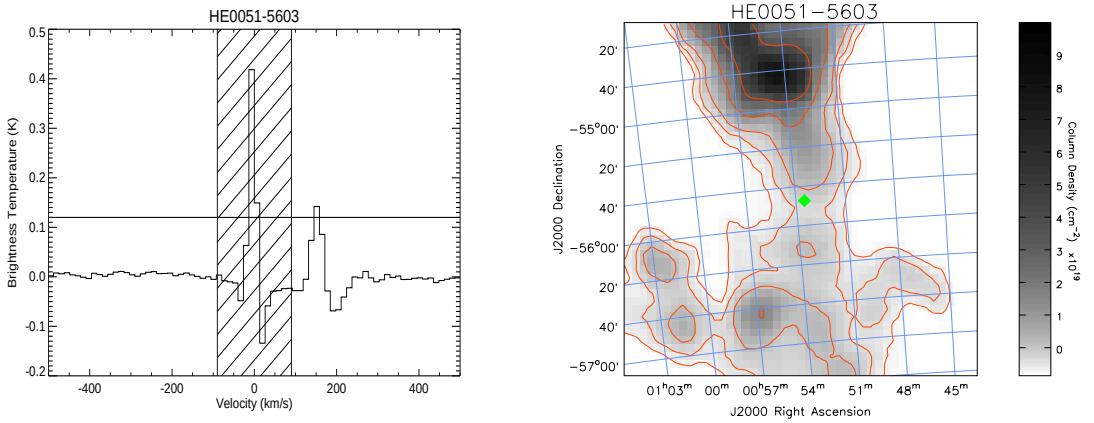
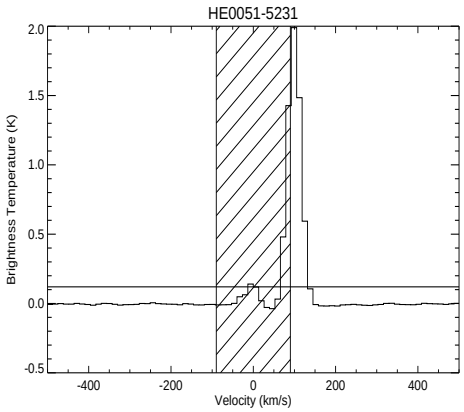


Figure B.60: HE 0051−5603



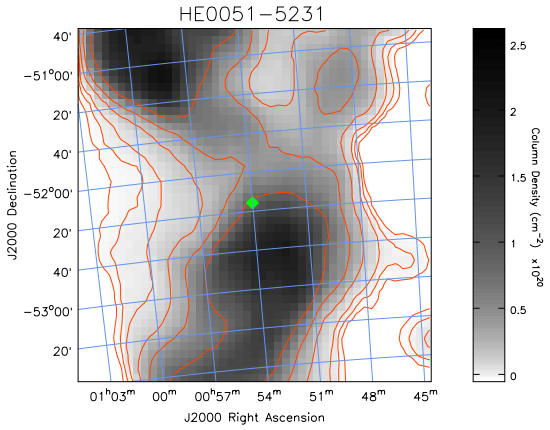
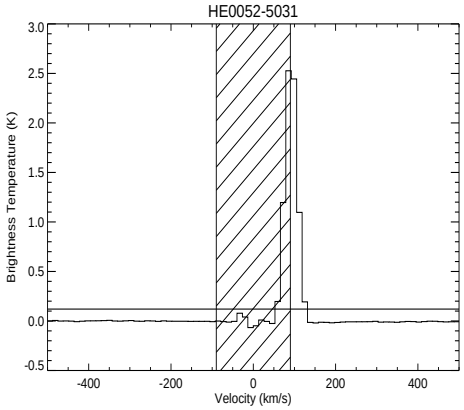


Figure B.61: HE 0051−5231



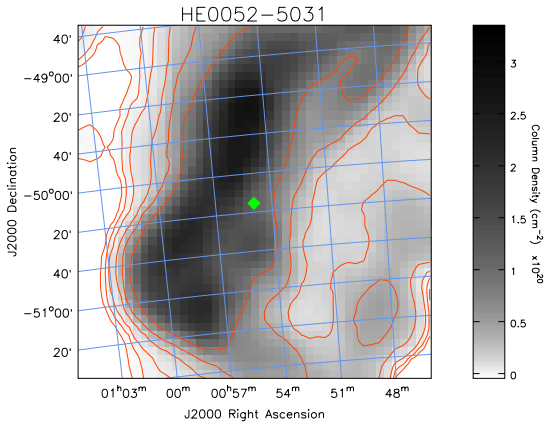
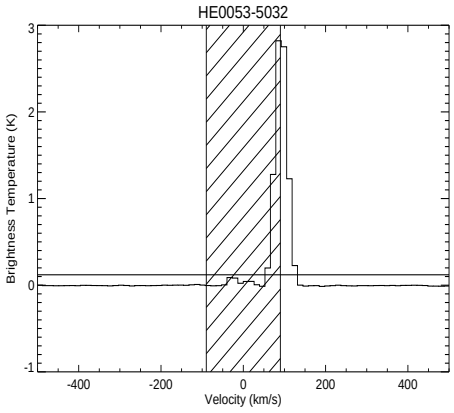


Figure B.62: HE 0052−5031



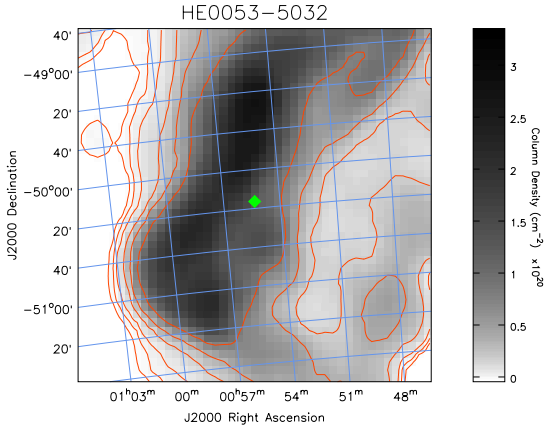


Figure B.63: HE 0053−5032

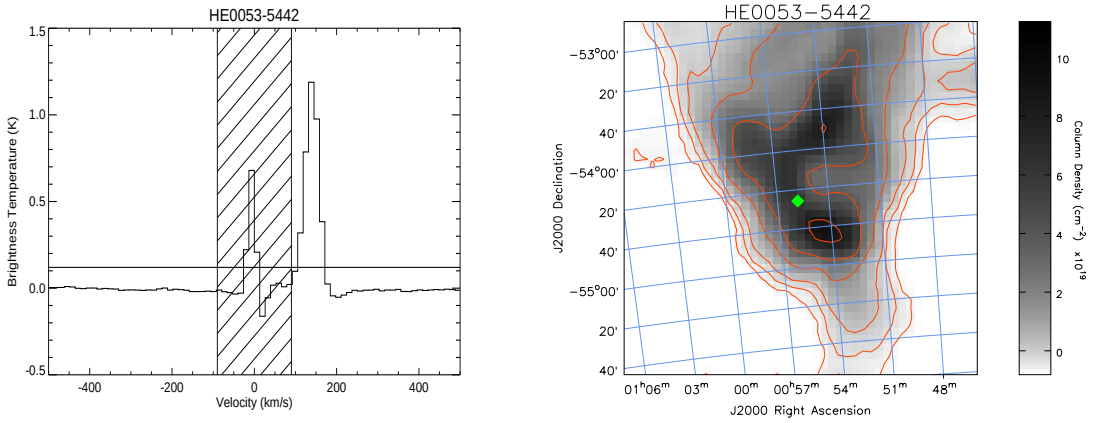


Figure B.64: HE 0053−5442

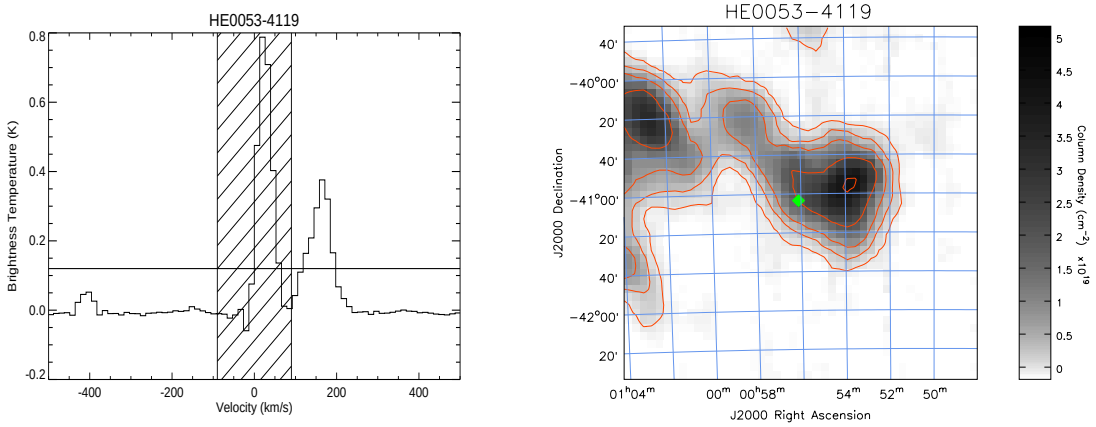


Figure B.65: HE 0053−4119

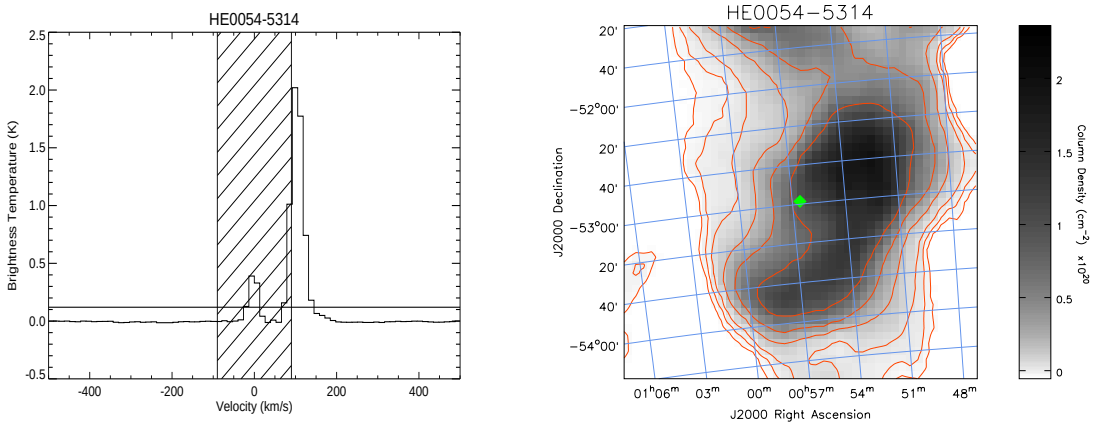


Figure B.66: HE 0054−5314

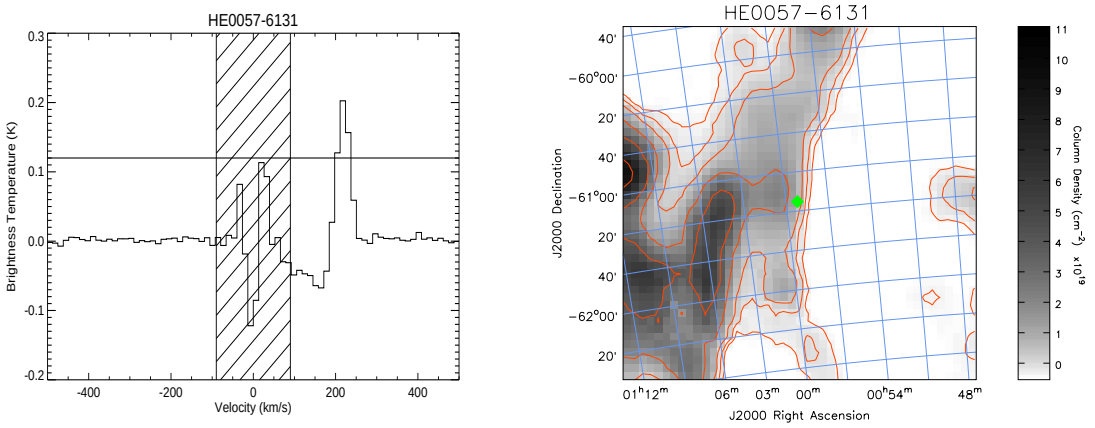


Figure B.67: HE 0057−6131

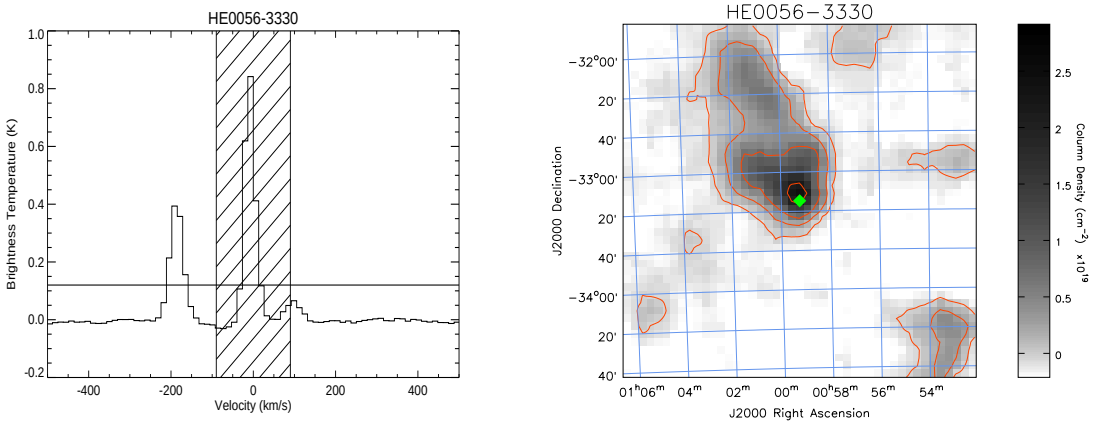


Figure B.68: HE 0056−3330

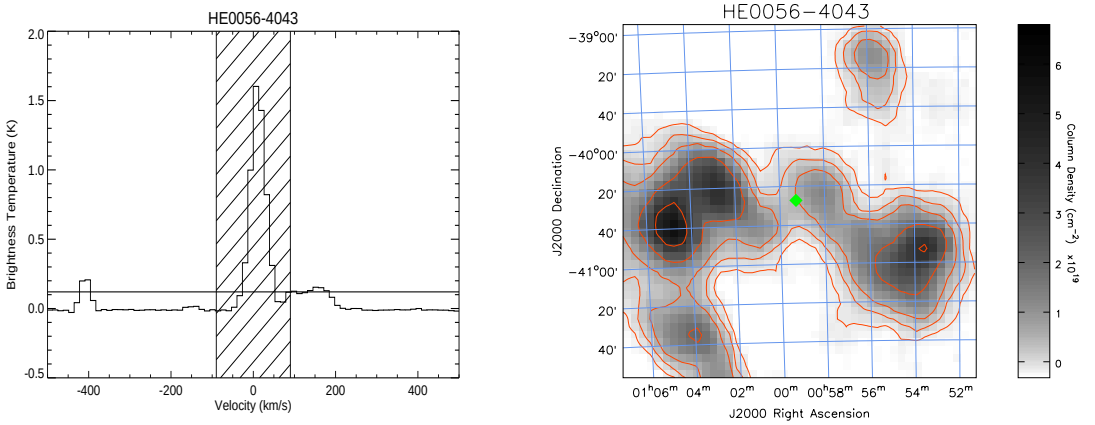


Figure B.69: HE 0056−4043

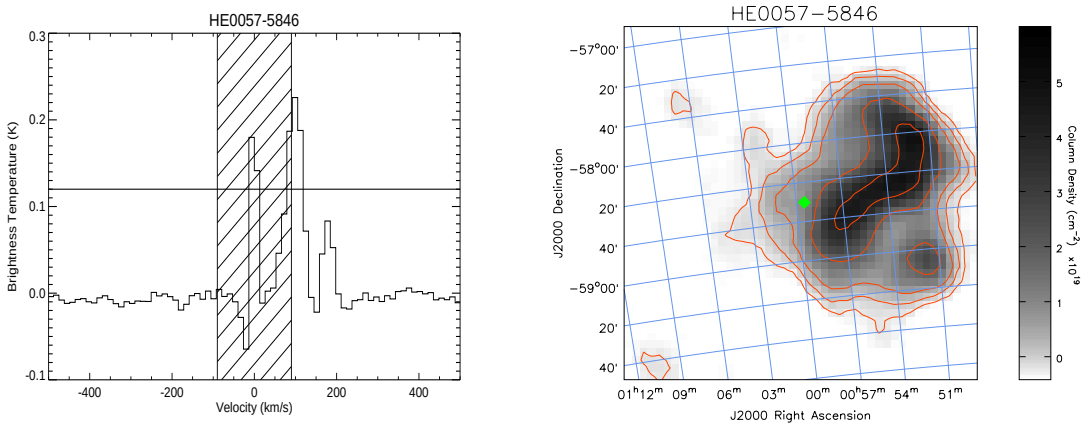


Figure B.70: HE 0057−5846

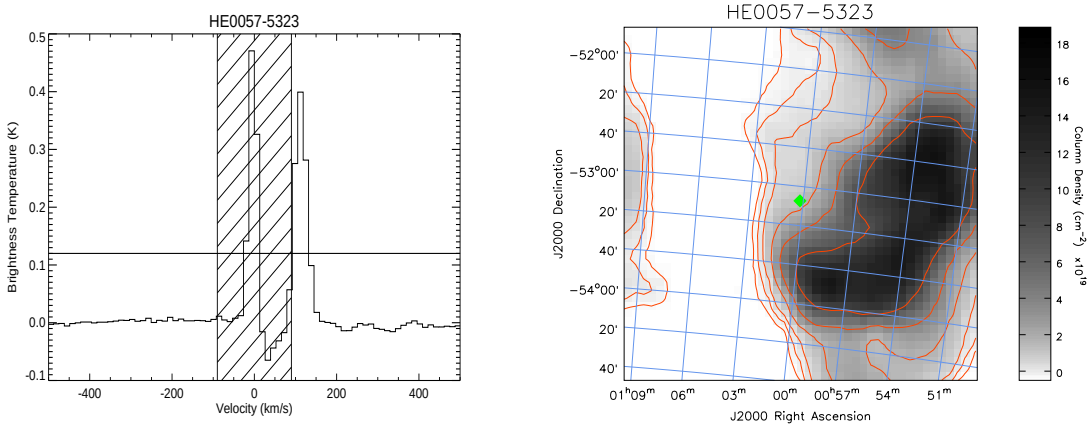


Figure B.71: HE 0057−5323

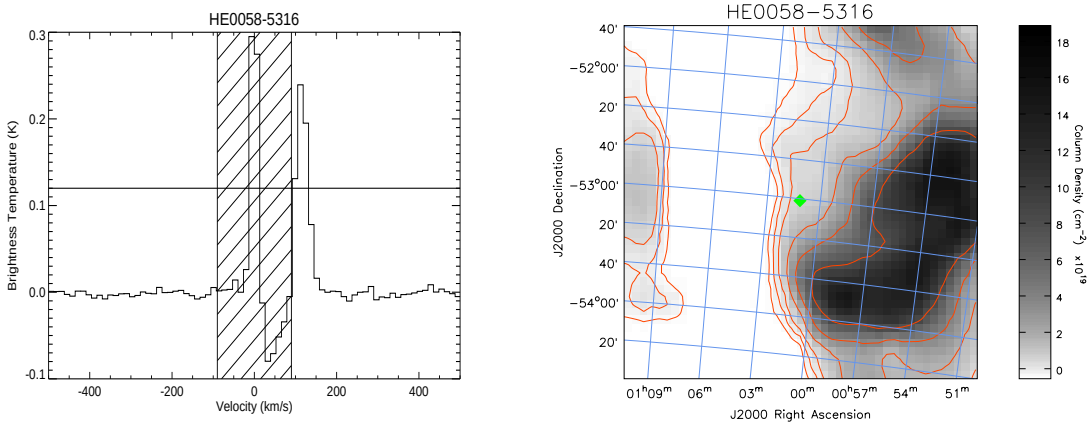


Figure B.72: HE 0058−5316

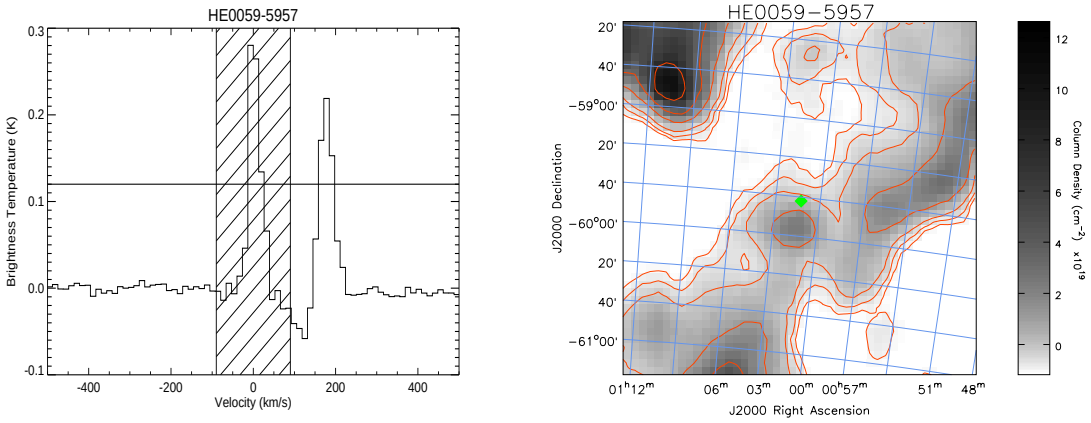


Figure B.73: HE 0059−5957

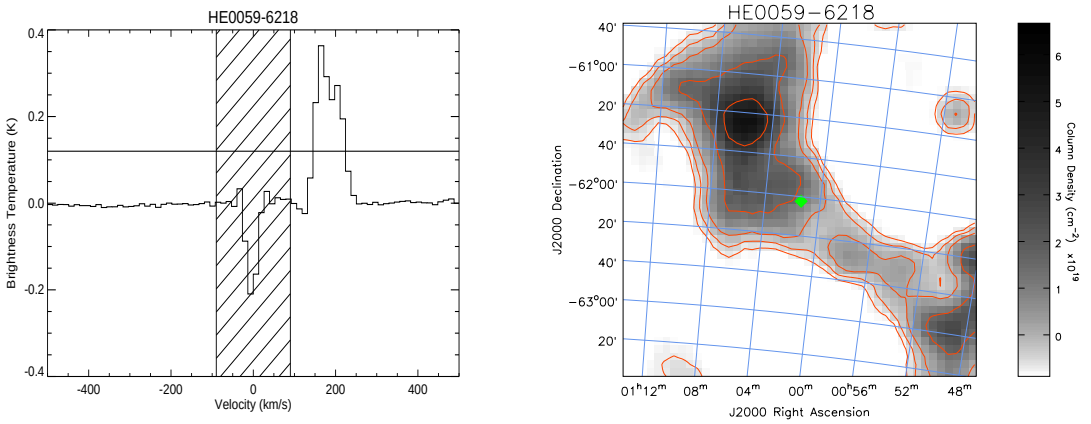


Figure B.74: HE 0059−6218

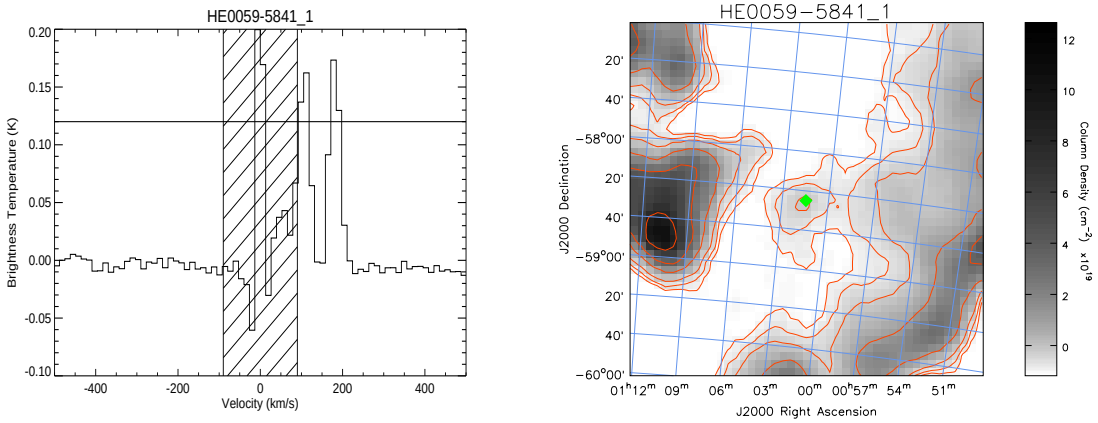


Figure B.75: HE 0059−5841_1

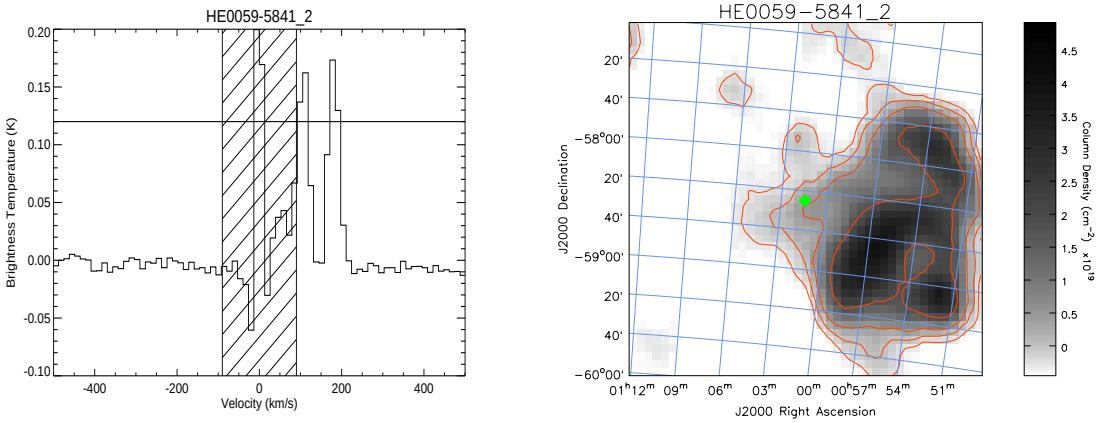


Figure B.76: HE 0059−5841_2

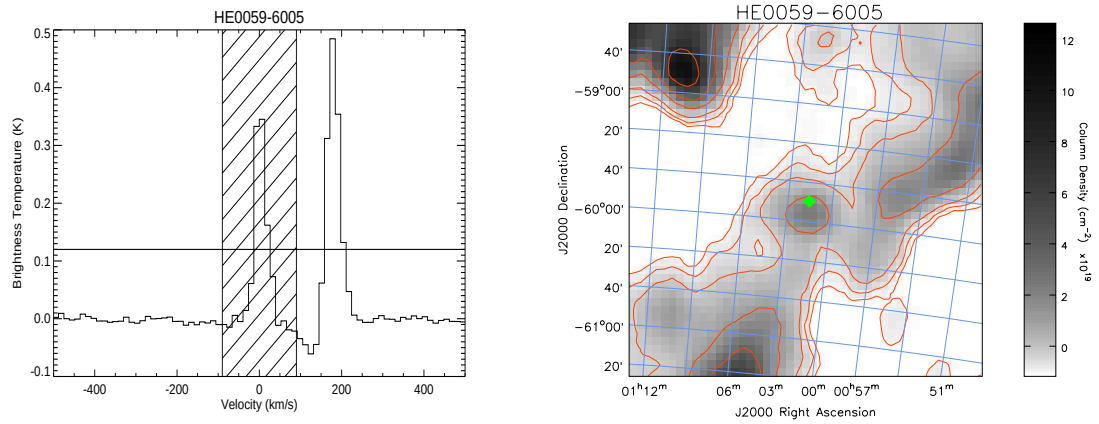


Figure B.77: HE 0059−6005

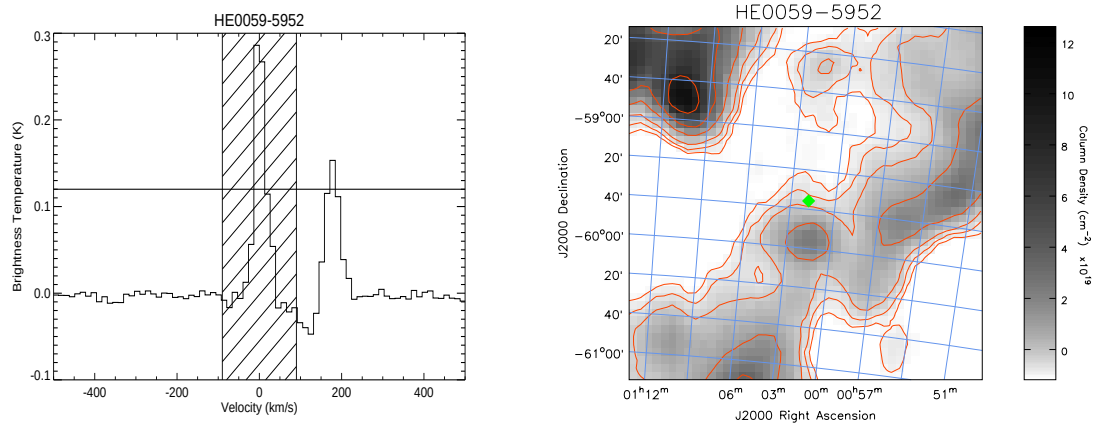


Figure B.78: HE 0059−5952

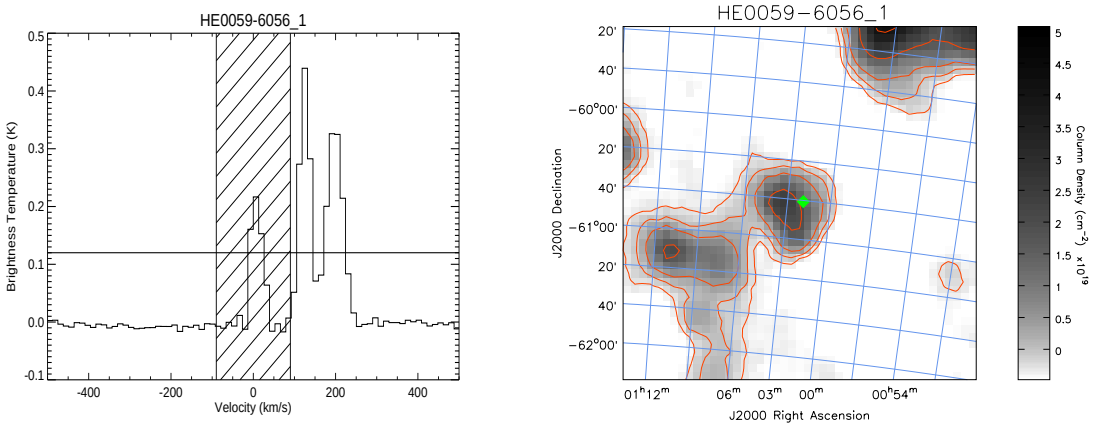


Figure B.79: HE 0059−6056_1

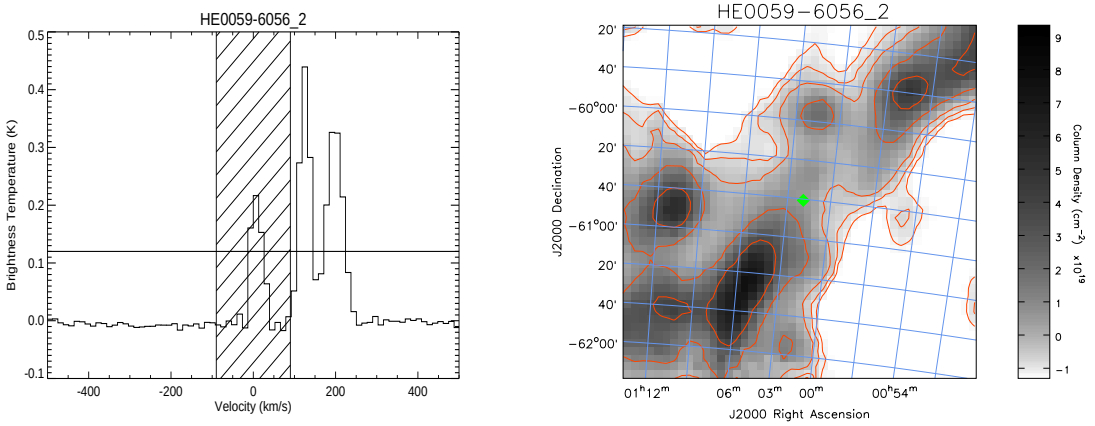


Figure B.80: HE 0059−6056_2

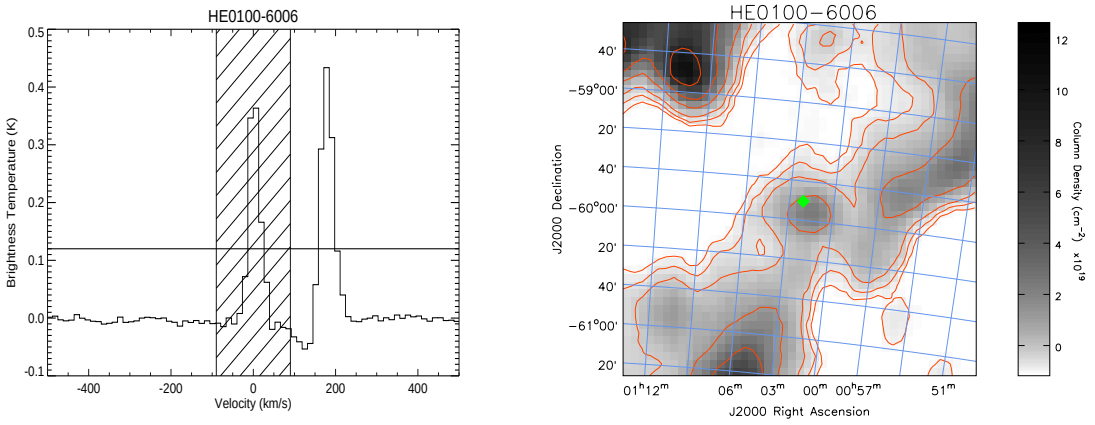


Figure B.81: HE 0100−6006

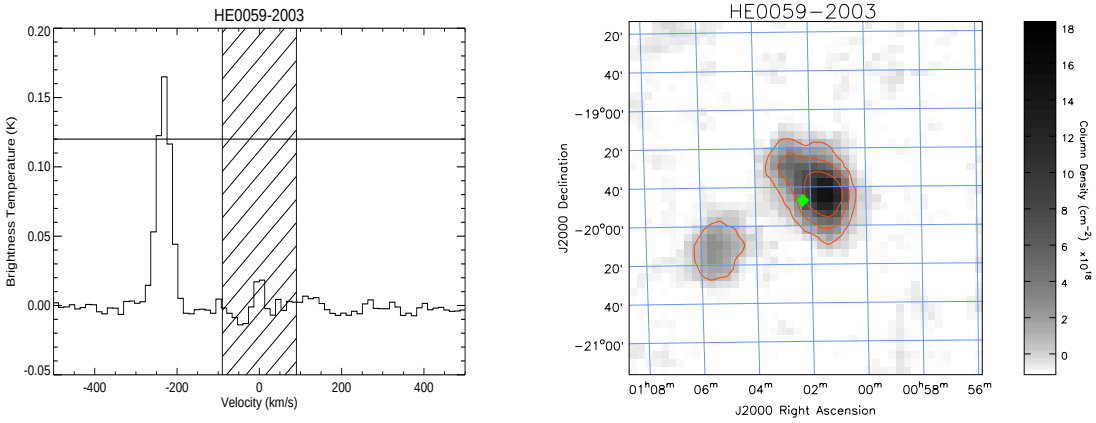


Figure B.82: HE 0059−2003

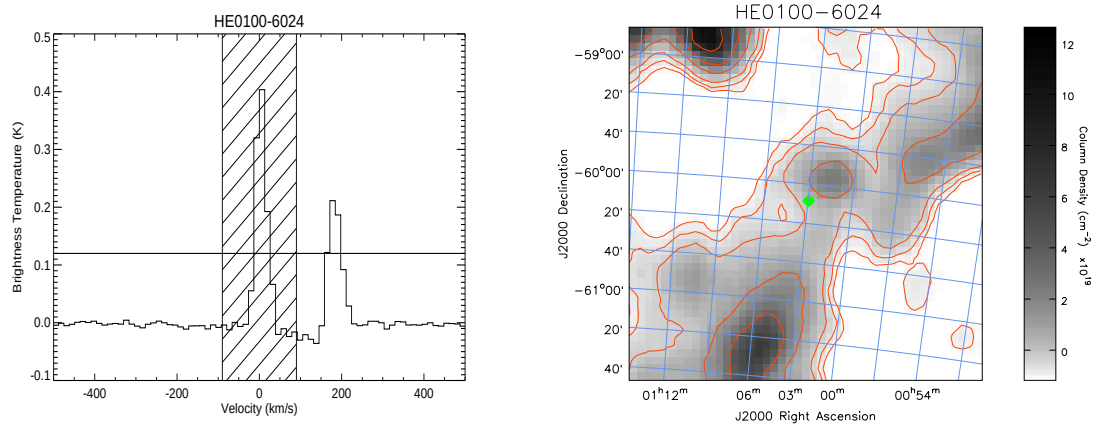


Figure B.83: HE 0100−6024

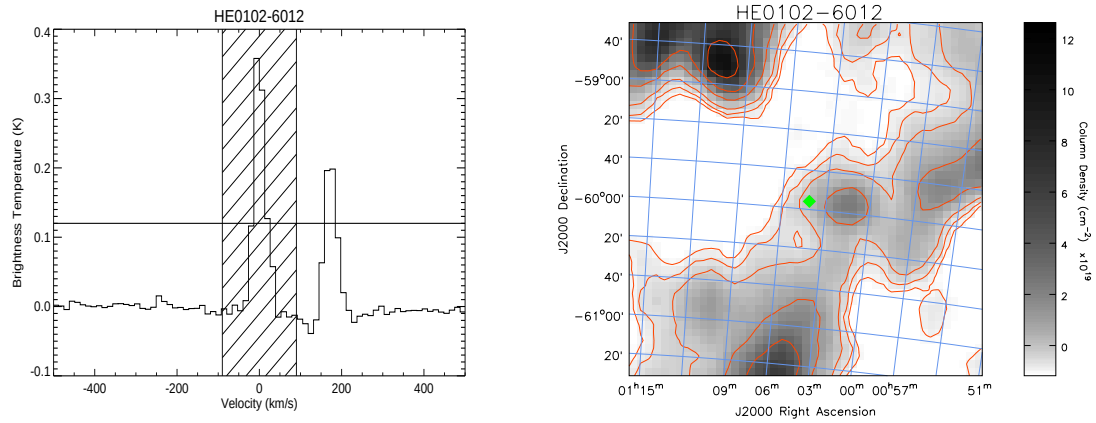
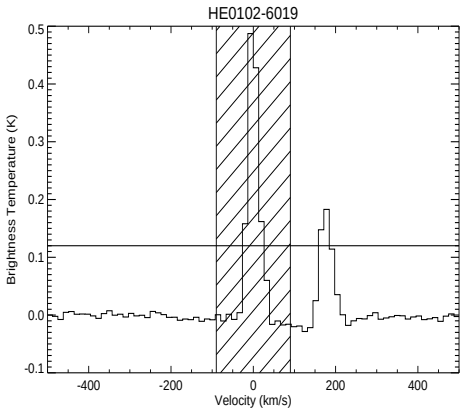


Figure B.84: HE 0102−6012



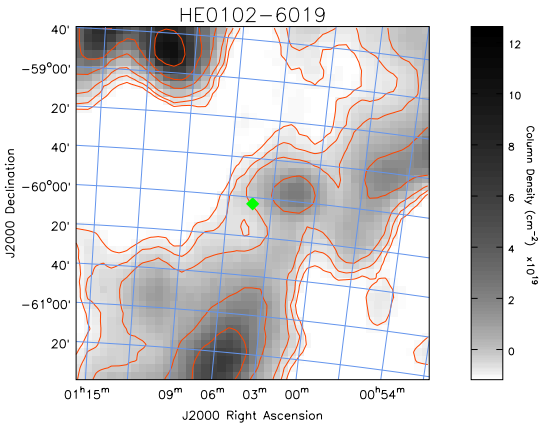
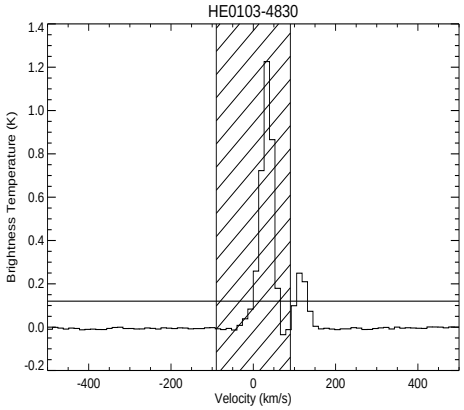


Figure B.85: HE 0102−6019



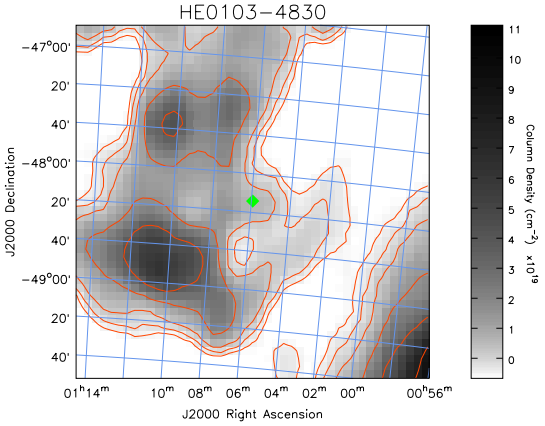
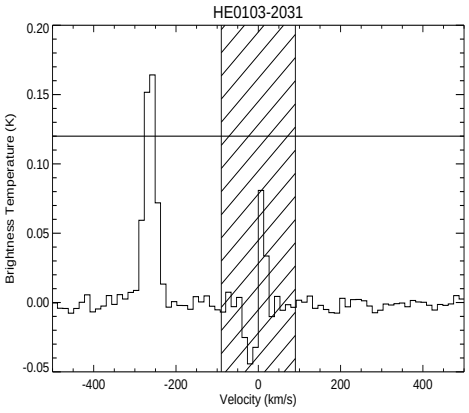


Figure B.86: HE 0103−4830



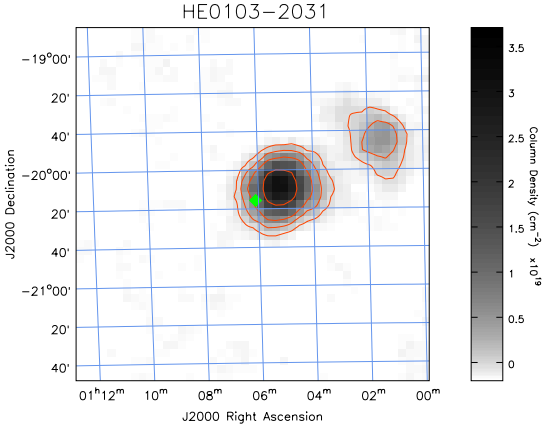


Figure B.87: HE 0103−2031

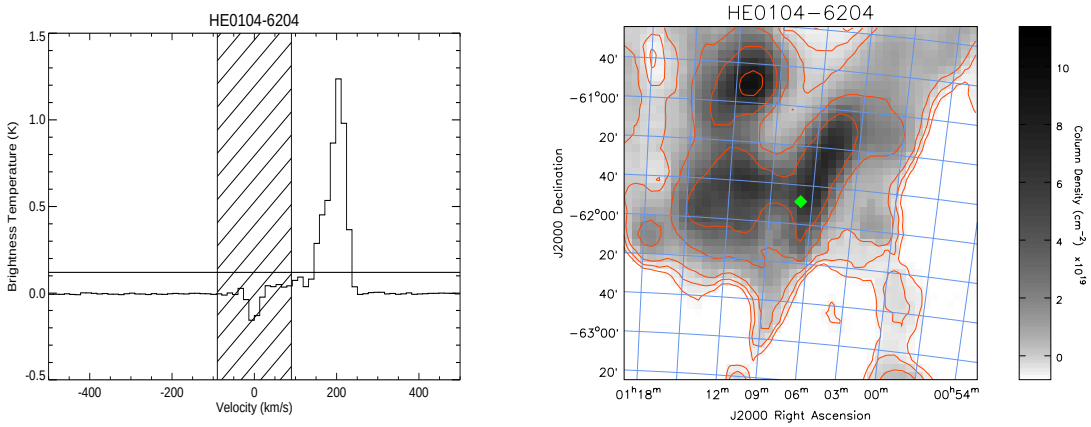


Figure B.88: HE 0104−6204

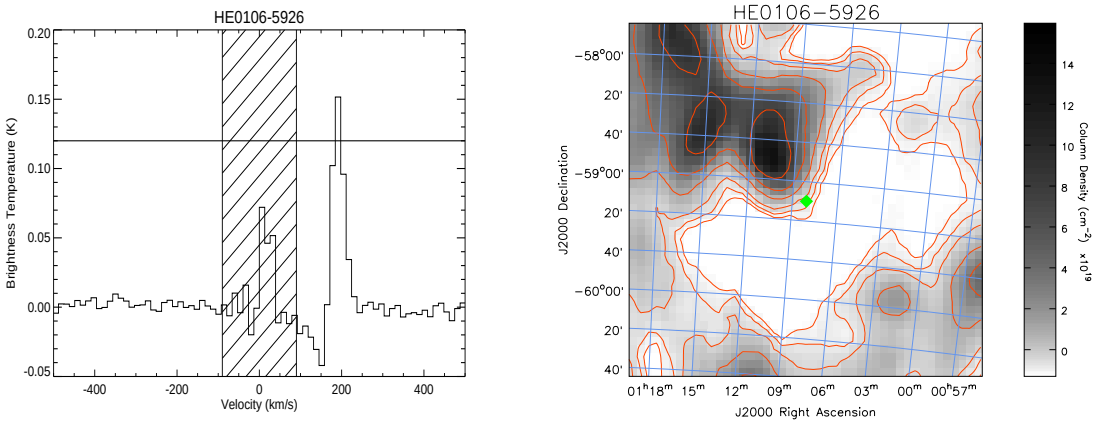


Figure B.89: HE 0106−5926

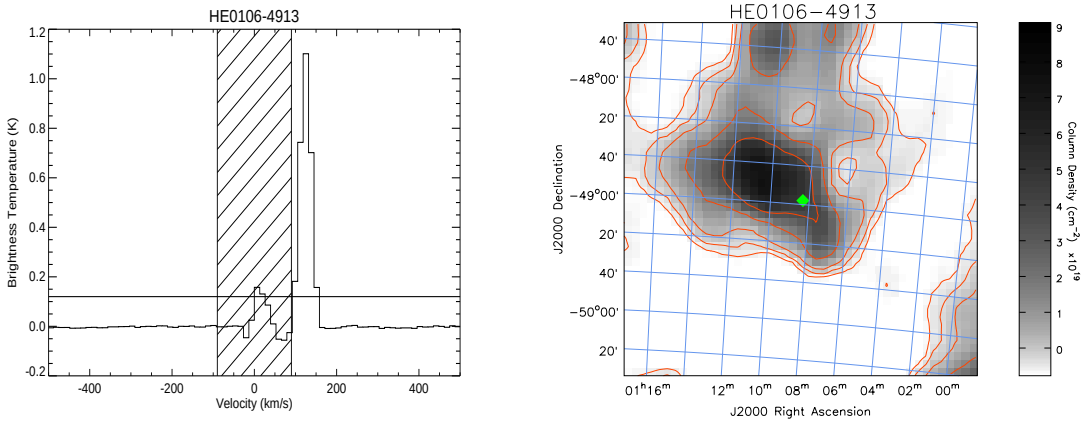


Figure B.90: HE 0106−4913

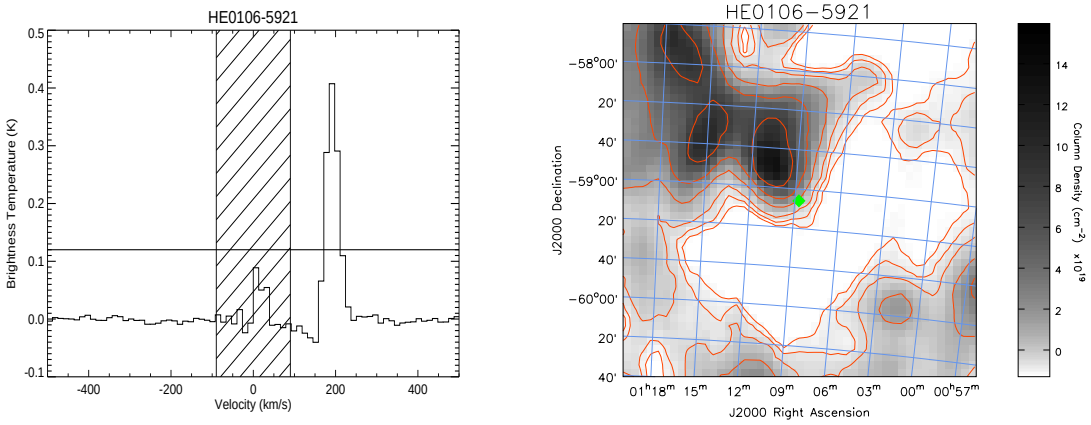


Figure B.91: HE 0106−5921

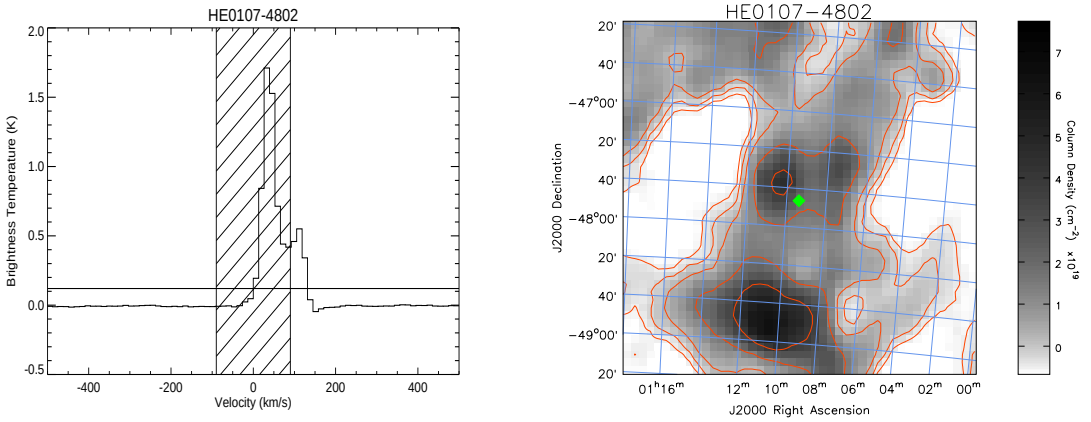


Figure B.92: HE 0107−4802

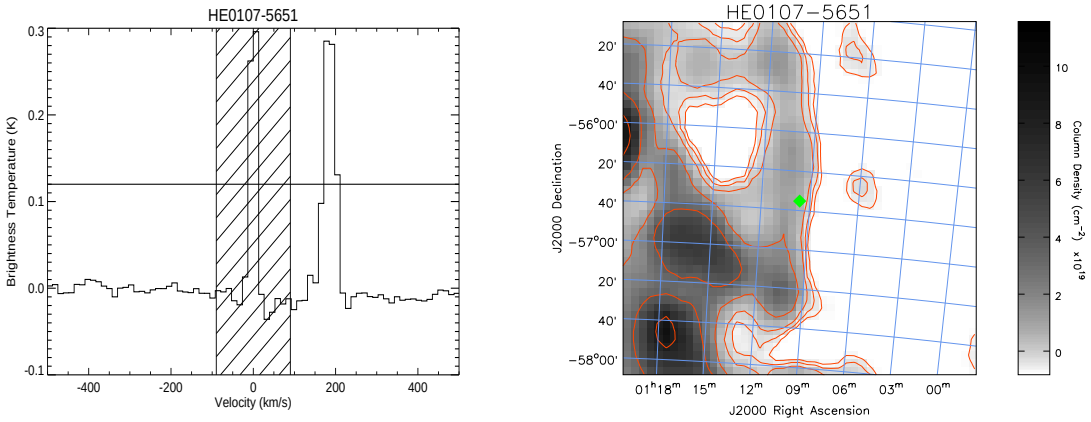


Figure B.93: HE 0107−5651

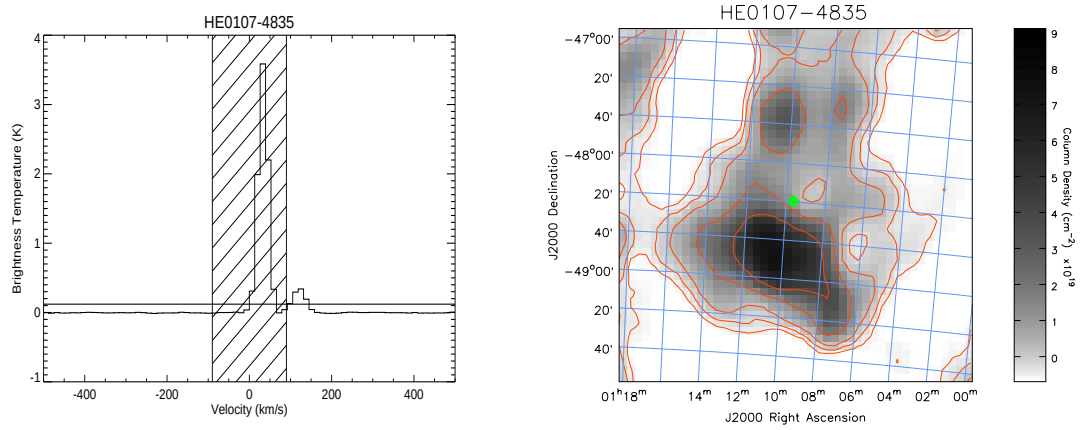


Figure B.94: HE 0107−4835

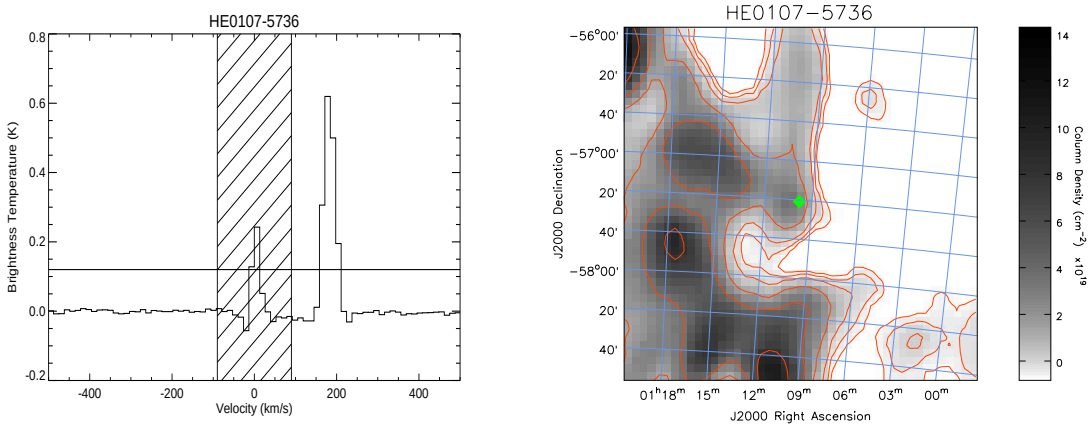


Figure B.95: HE 0107−5736

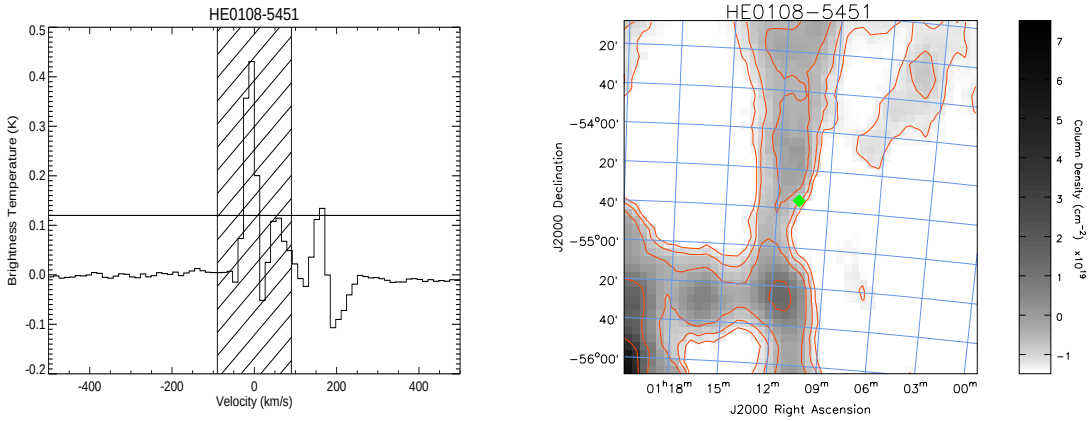


Figure B.96: HE 0108−5451

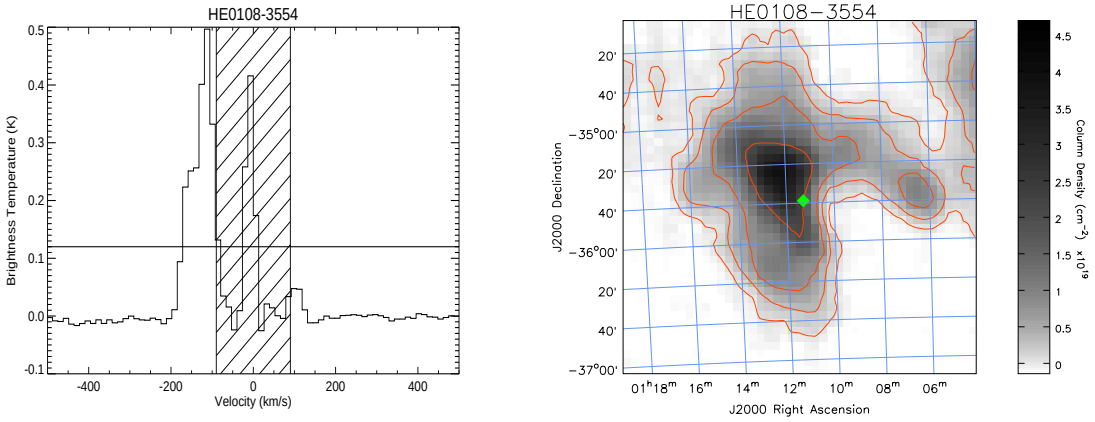


Figure B.97: HE 0108−3554

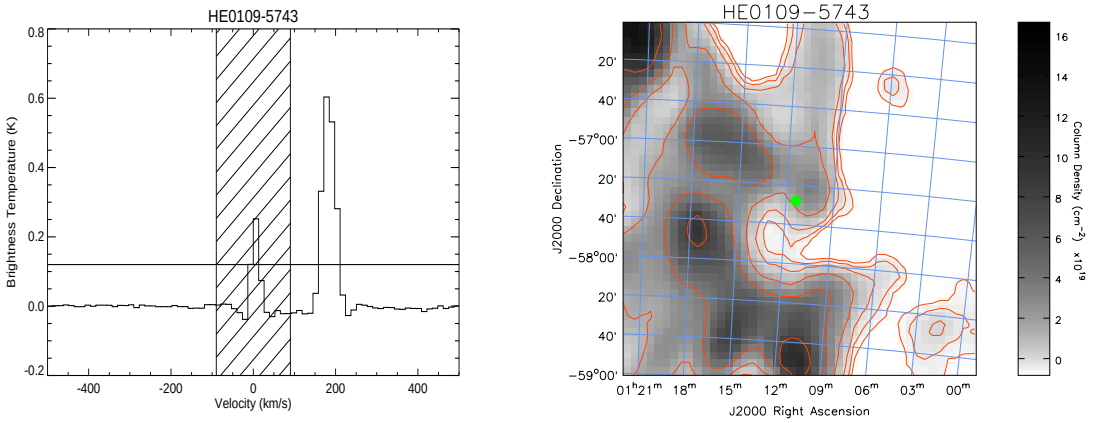


Figure B.98: HE 0109−5743

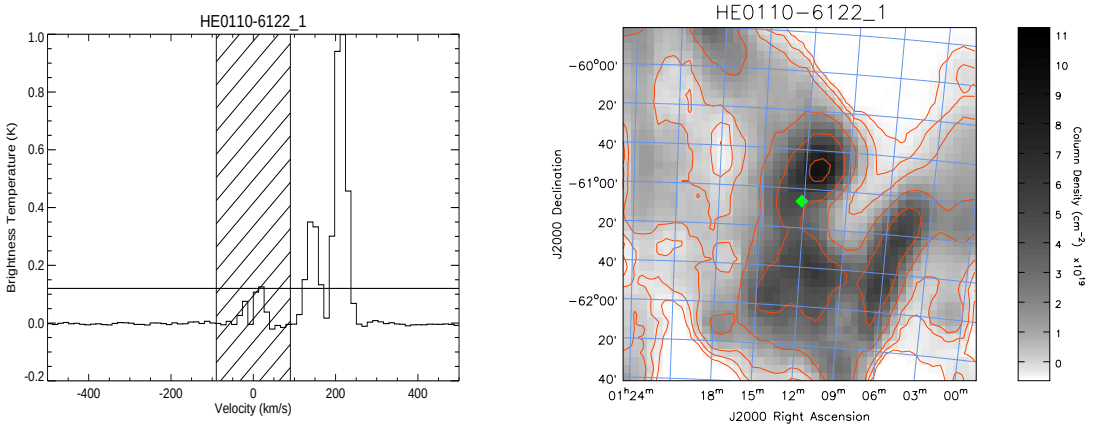


Figure B.99: HE 0110−6122_1

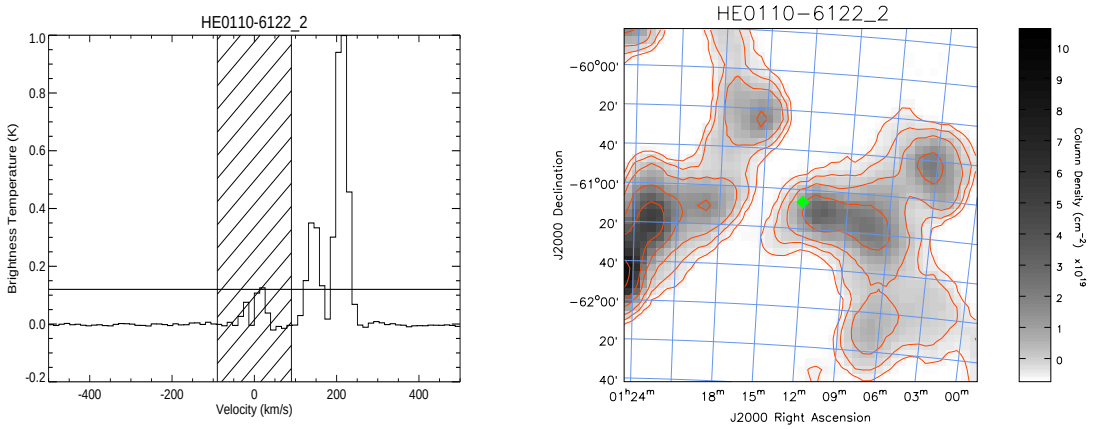


Figure B.100: HE 0110−6122_2

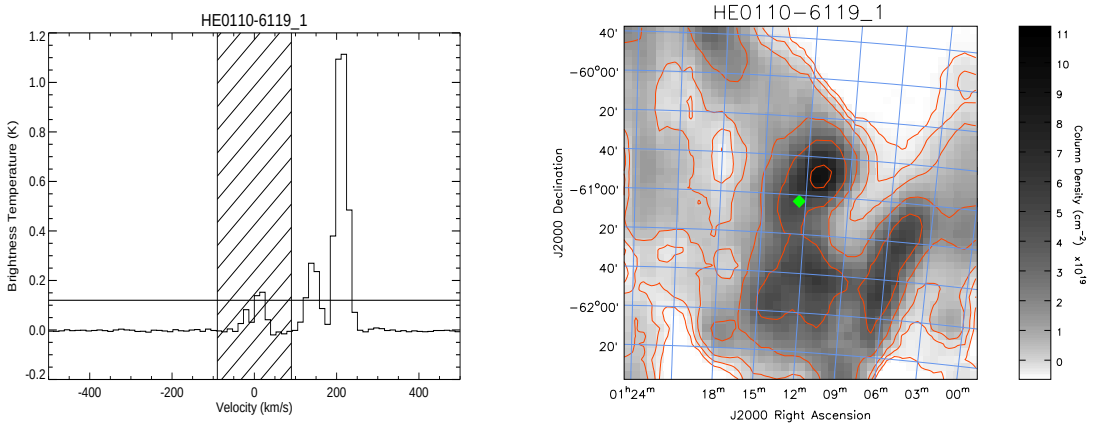


Figure B.101: HE 0110−6119_1

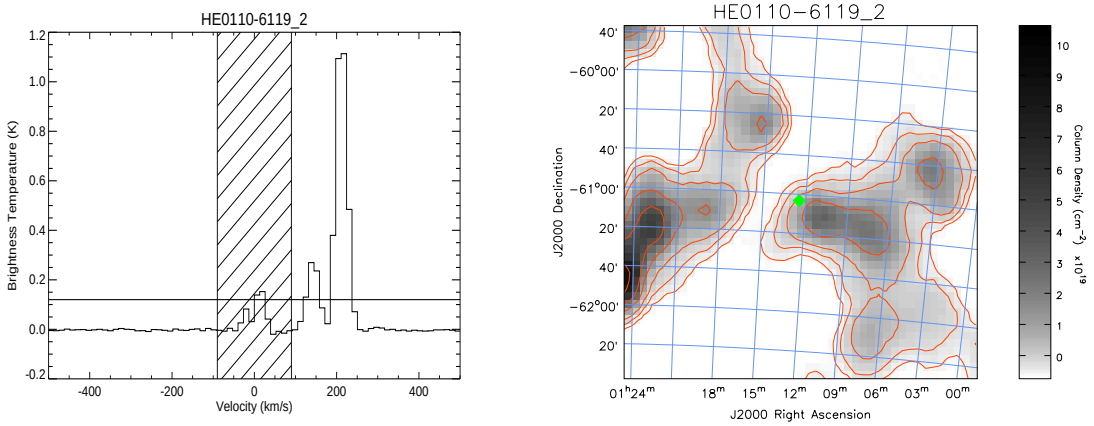


Figure B.102: HE 0110−6119_2

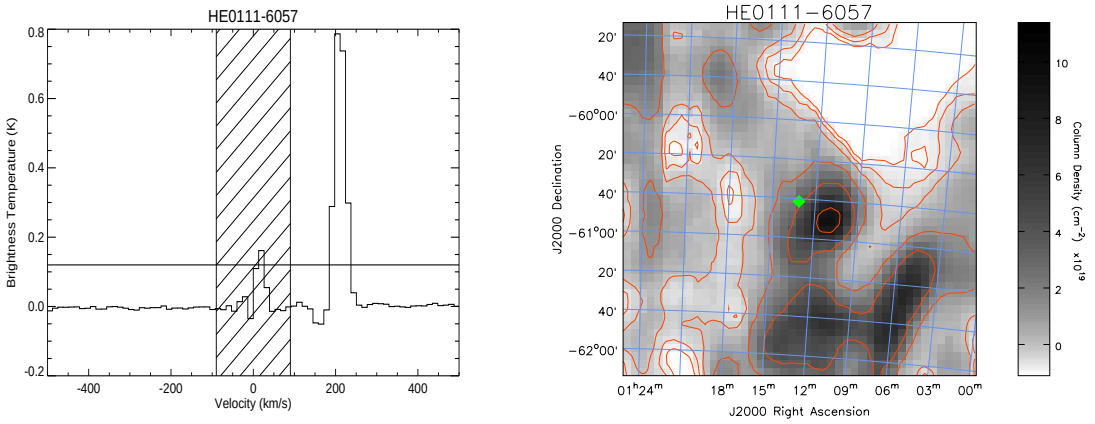


Figure B.103: HE 0111−6057

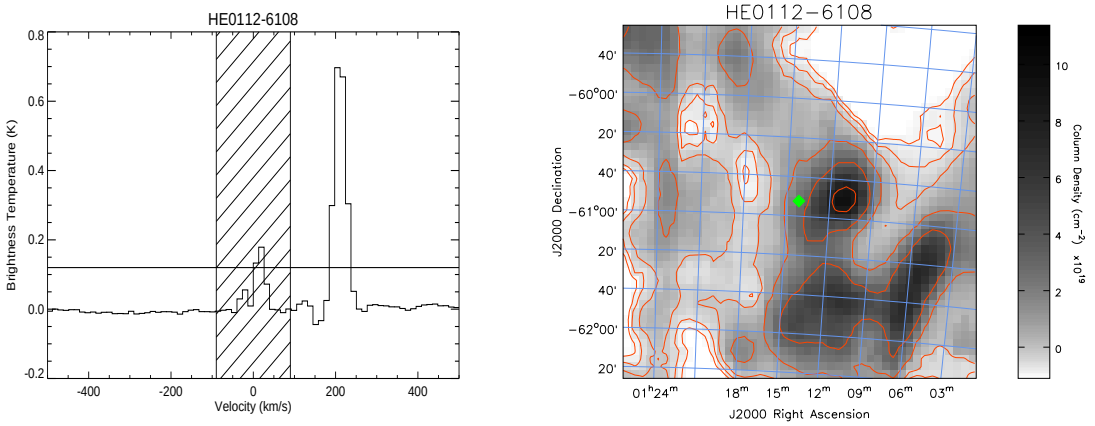


Figure B.104: HE 0112−6108

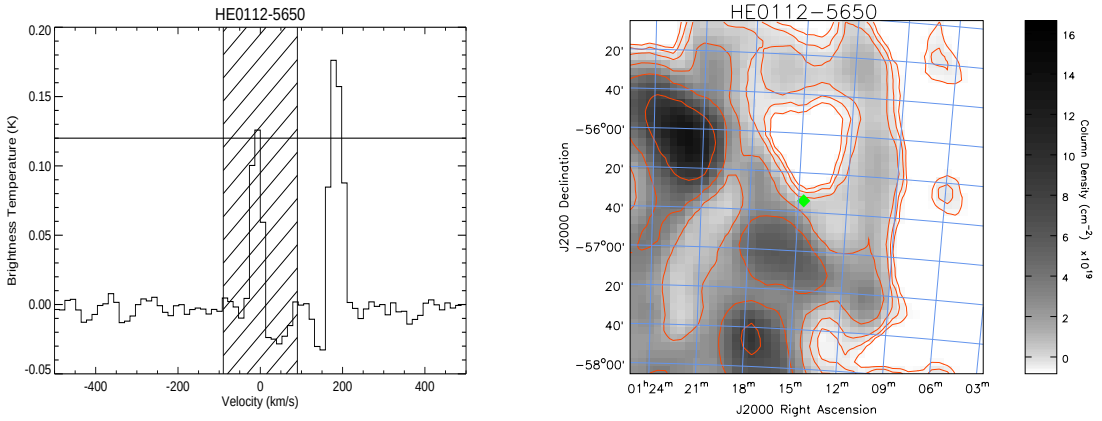


Figure B.105: HE 0112−5650

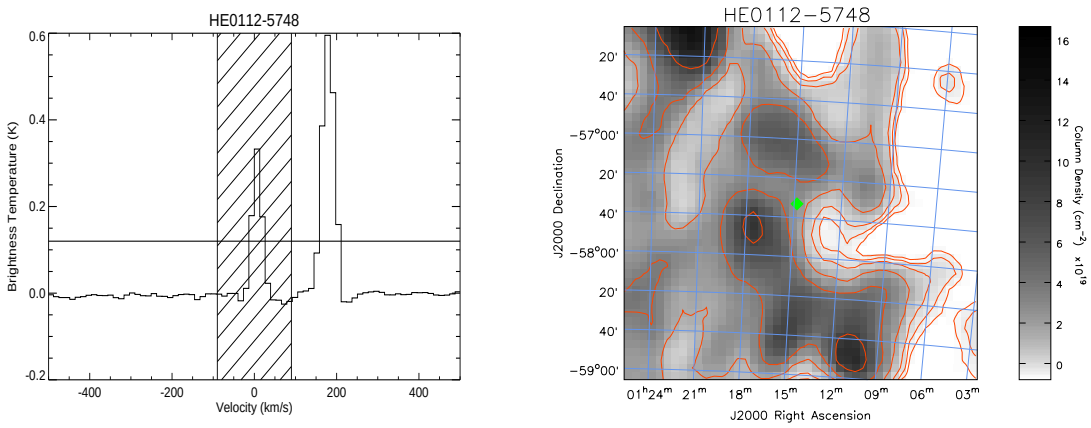


Figure B.106: HE 0112−5748

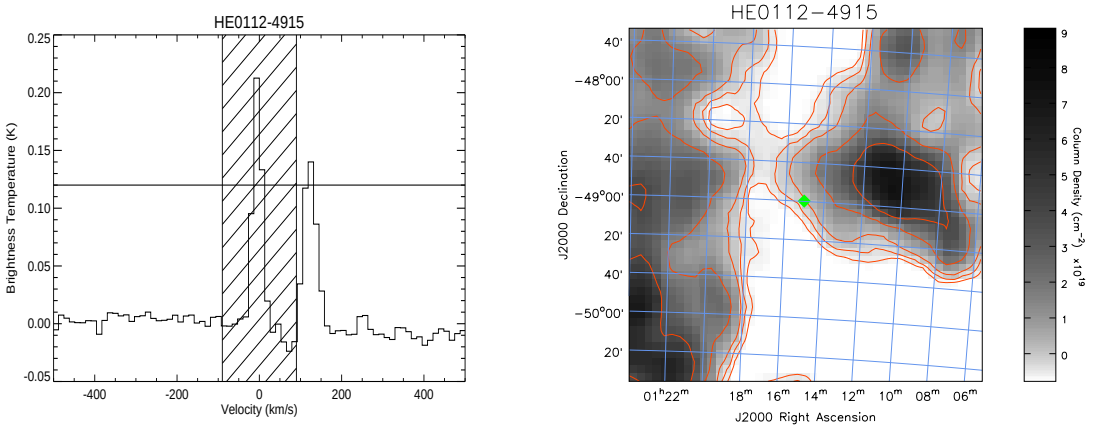


Figure B.107: HE 0112−4915

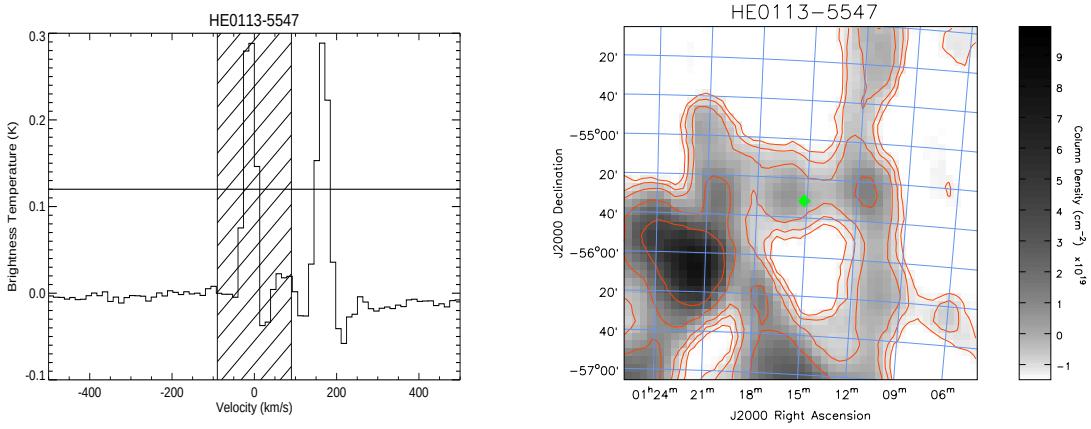


Figure B.108: HE 0113−5547

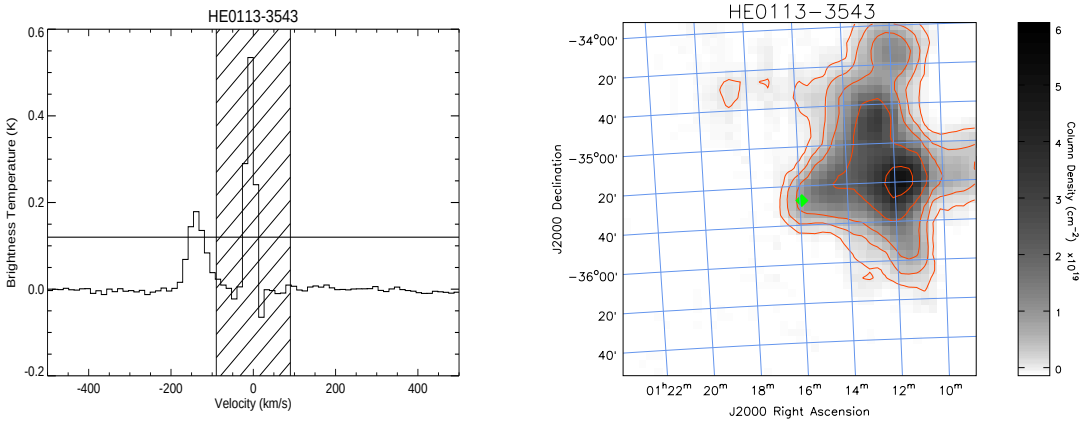


Figure B.109: HE 0113−3543

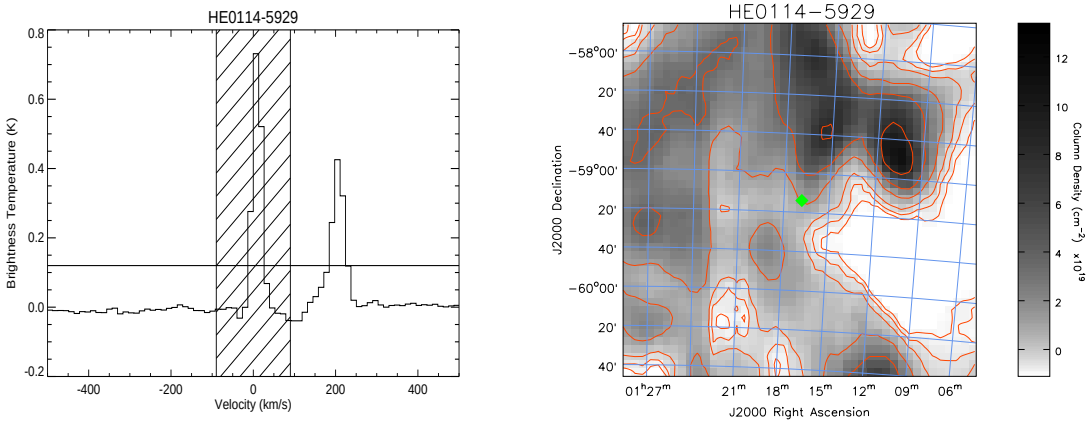


Figure B.110: HE 0114−5929

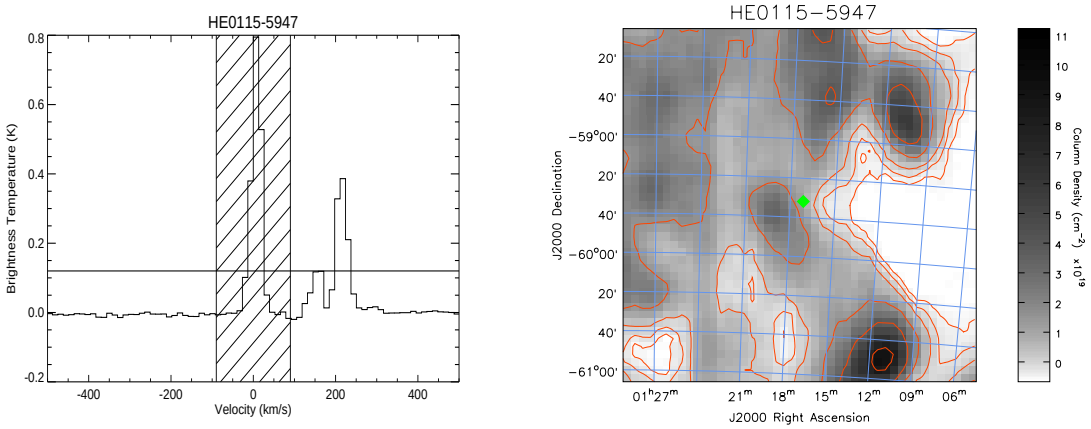


Figure B.111: HE 0115−5947

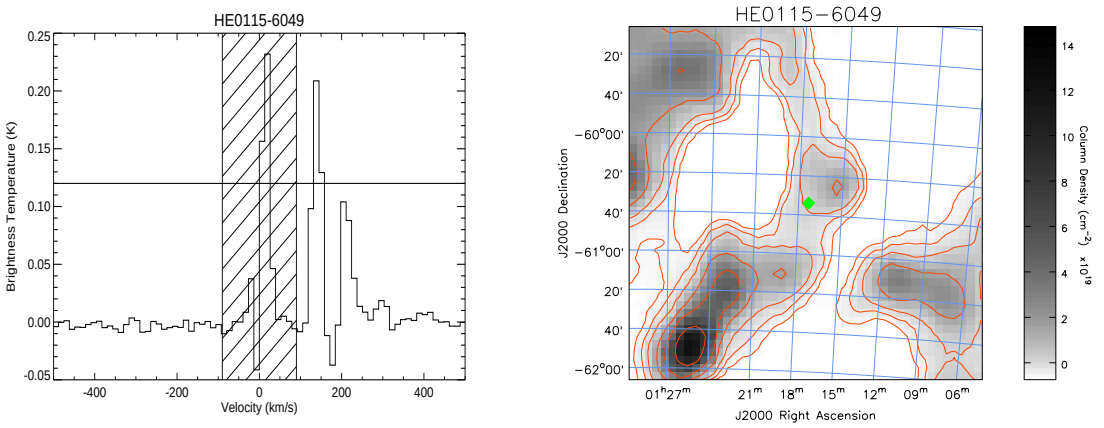


Figure B.112: HE 0115−6049

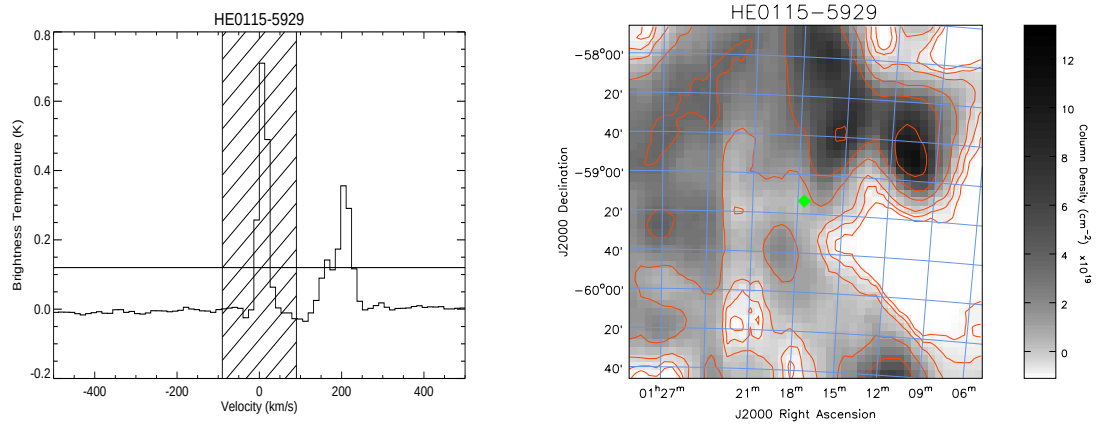


Figure B.113: HE 0115−5929

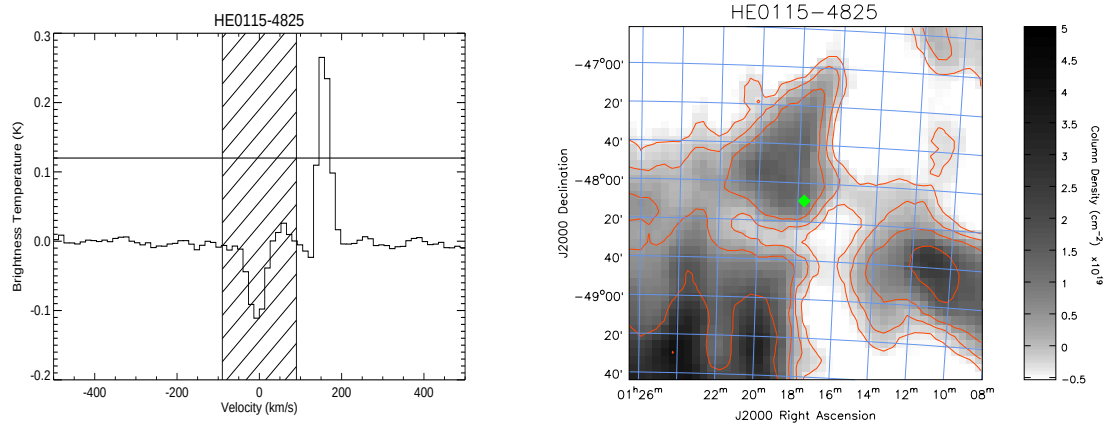
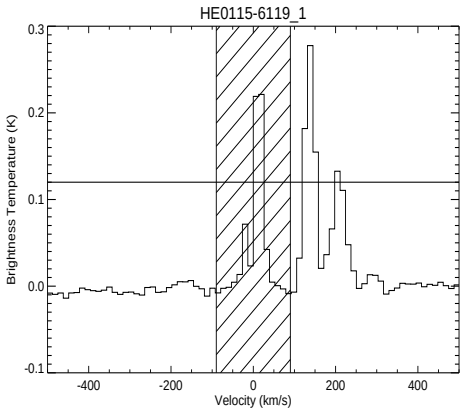


Figure B.114: HE 0115−4825



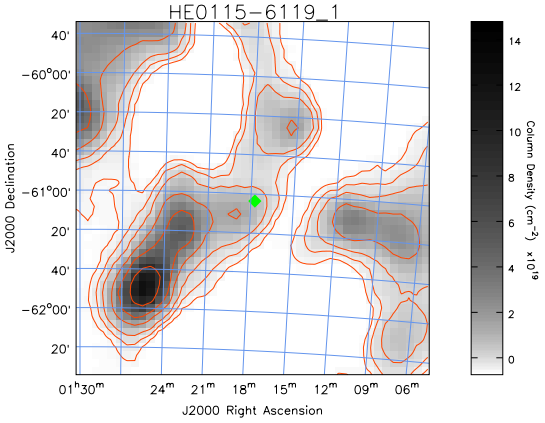
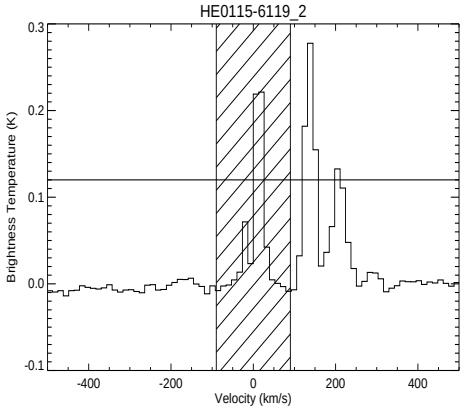


Figure B.115: HE 0115−6119_1



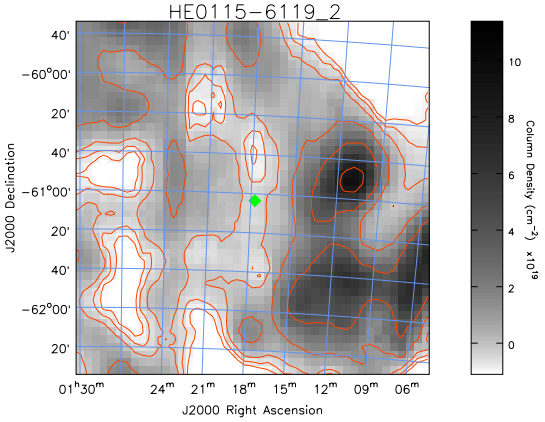
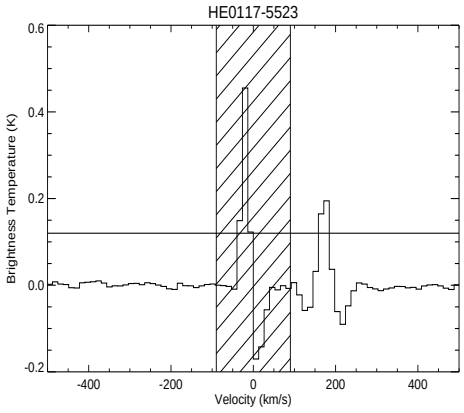


Figure B.116: HE 0115−6119_2



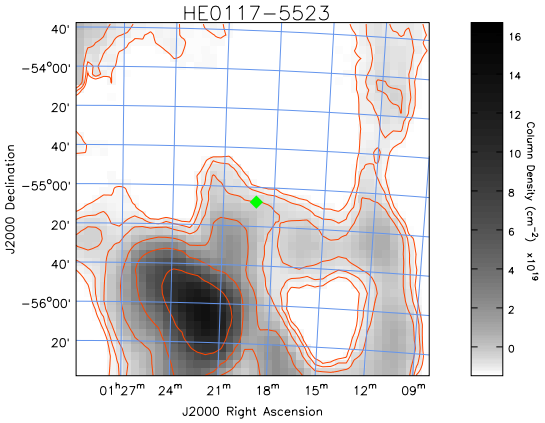


Figure B.117: HE 0117−5523

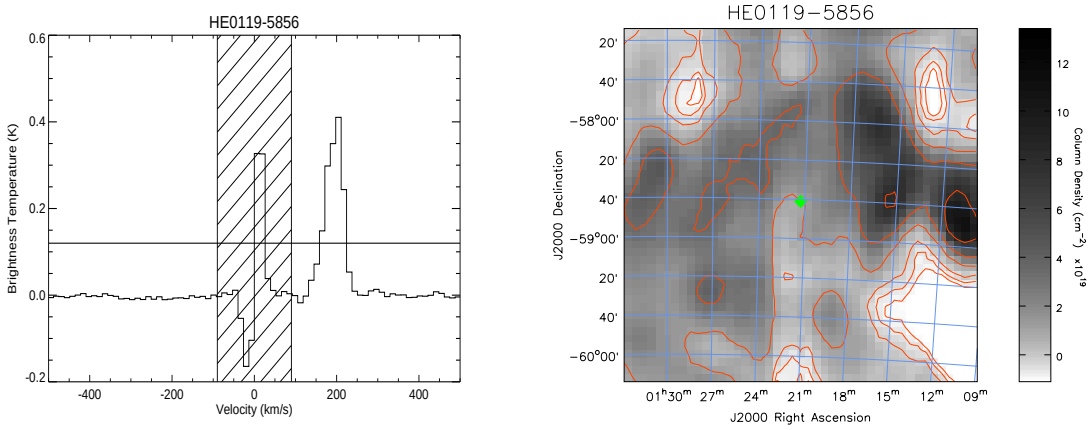


Figure B.118: HE 0119−5856

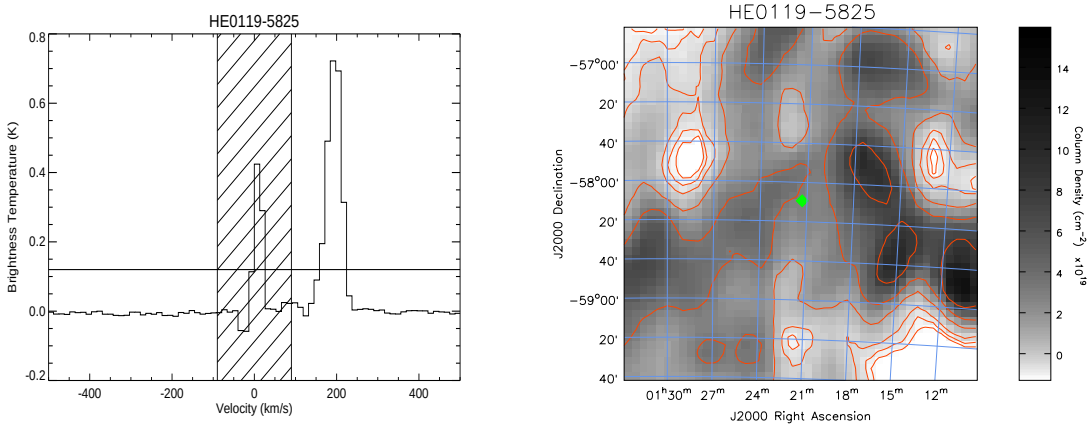


Figure B.119: HE 0119−5825

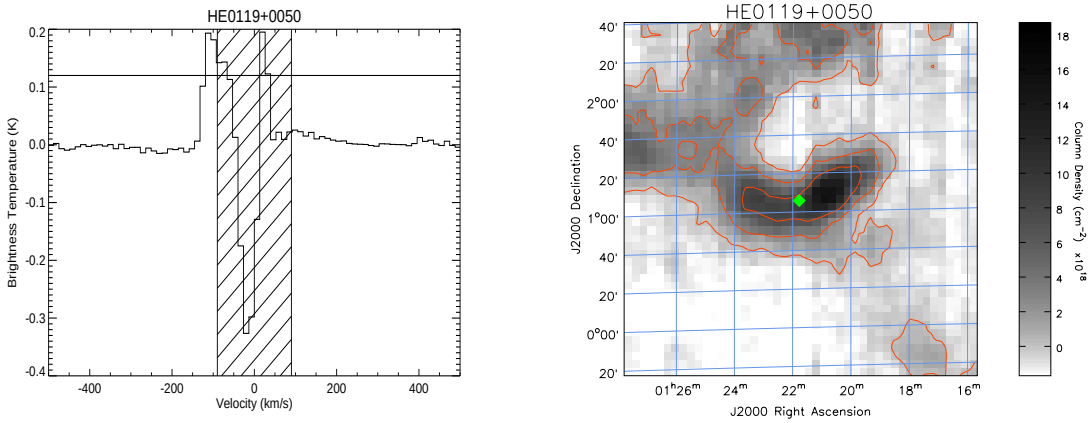


Figure B.120: HE 0119+0050

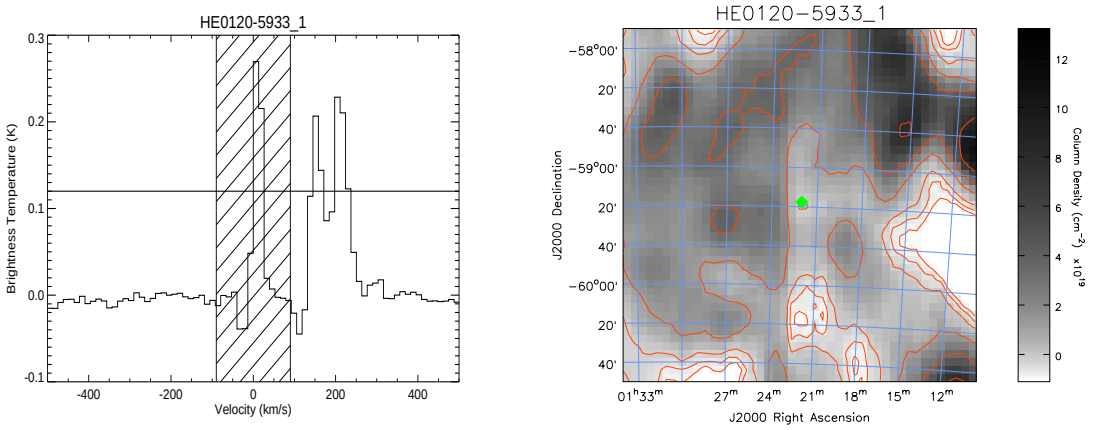


Figure B.121: HE 0120−5933_1

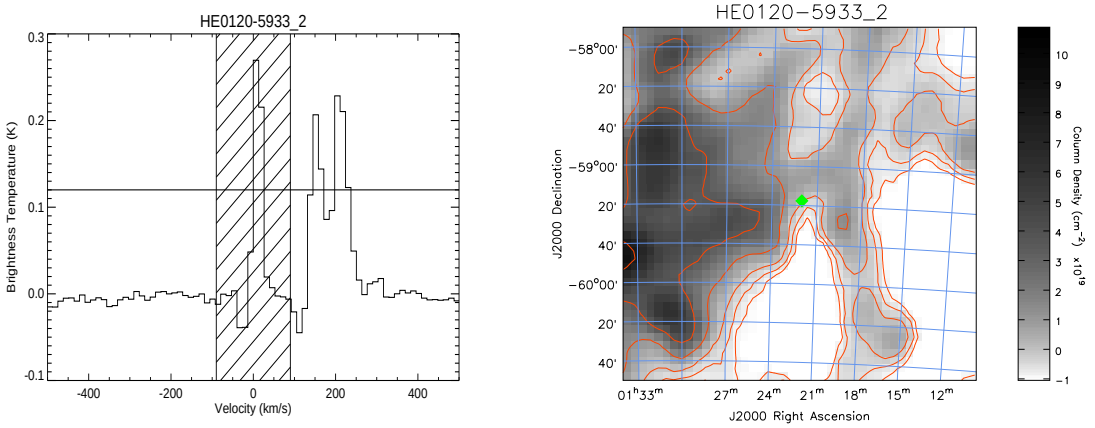


Figure B.122: HE 0120−5933_2

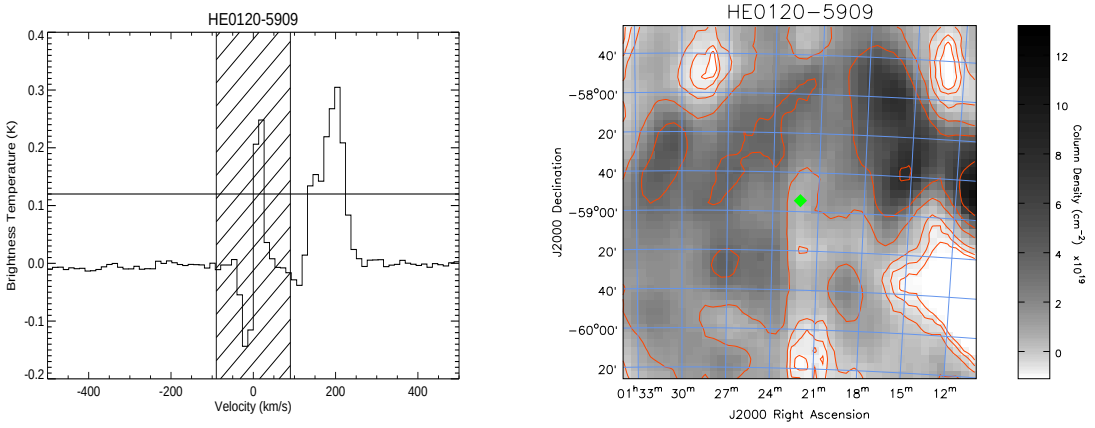


Figure B.123: HE 0120−5909

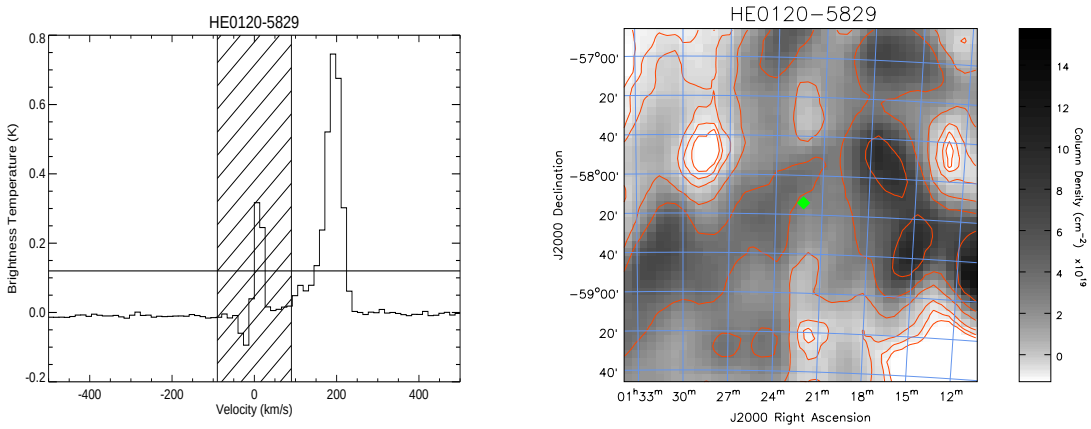


Figure B.124: HE 0120−5829

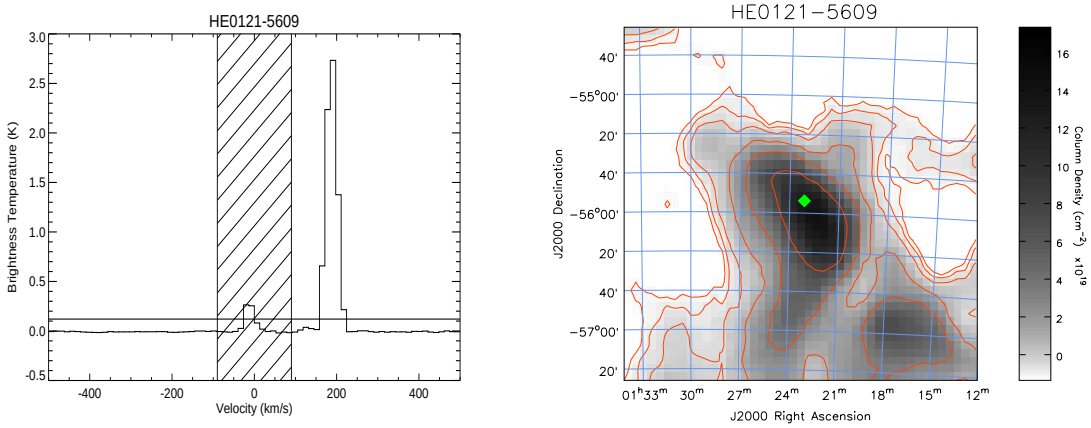


Figure B.125: HE 0121−5609

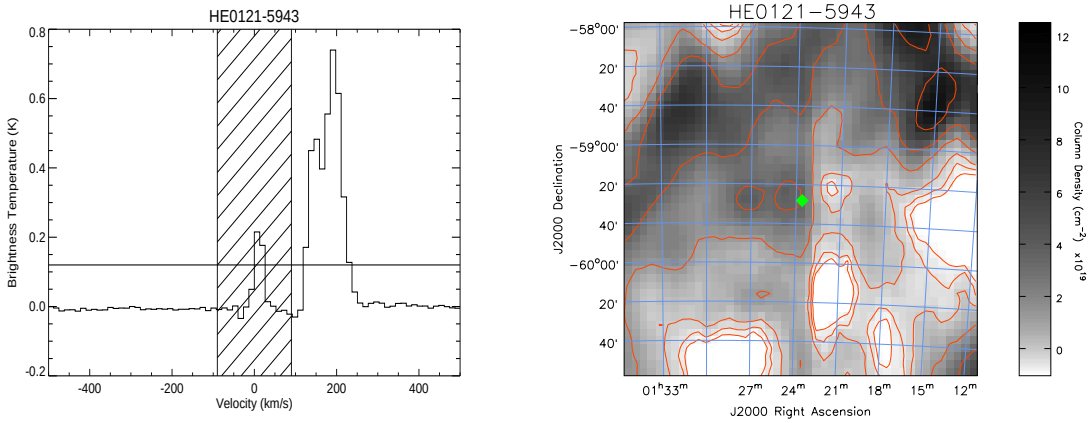


Figure B.126: HE 0121−5943

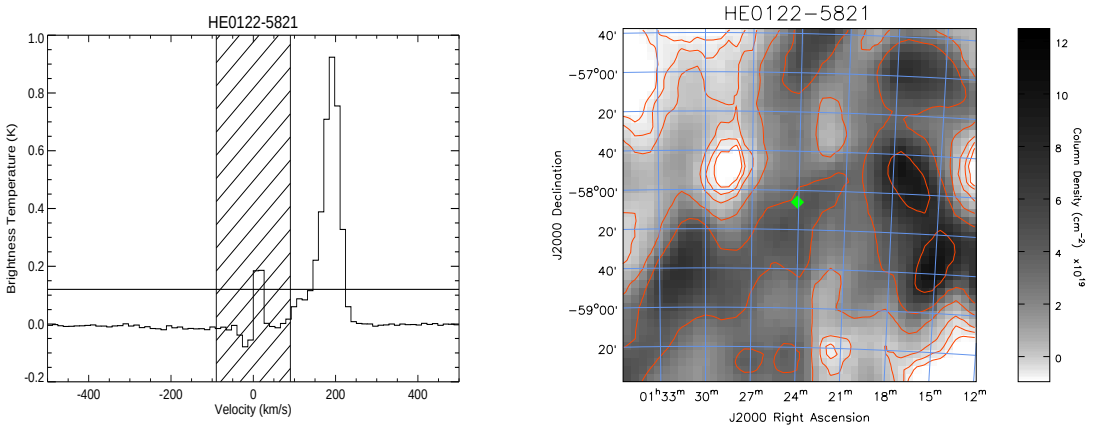


Figure B.127: HE 0122−5821

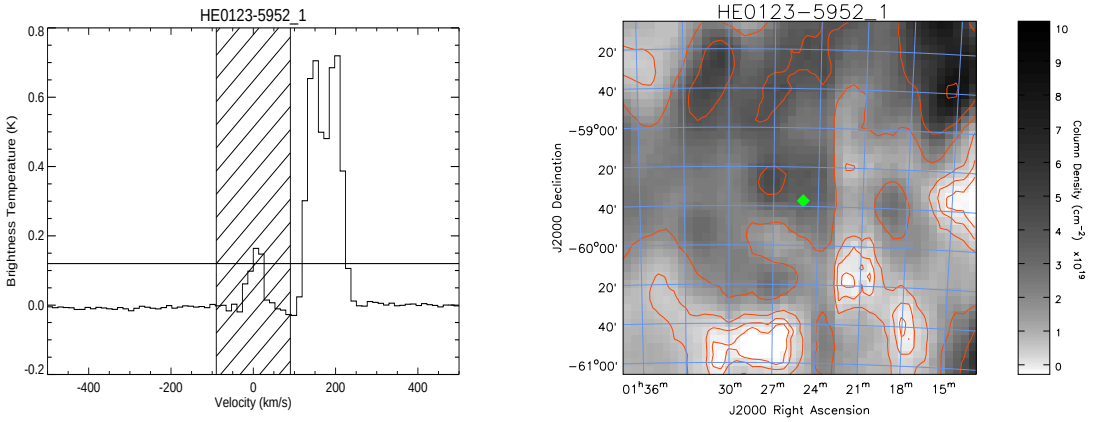


Figure B.128: HE 0123−5952_1

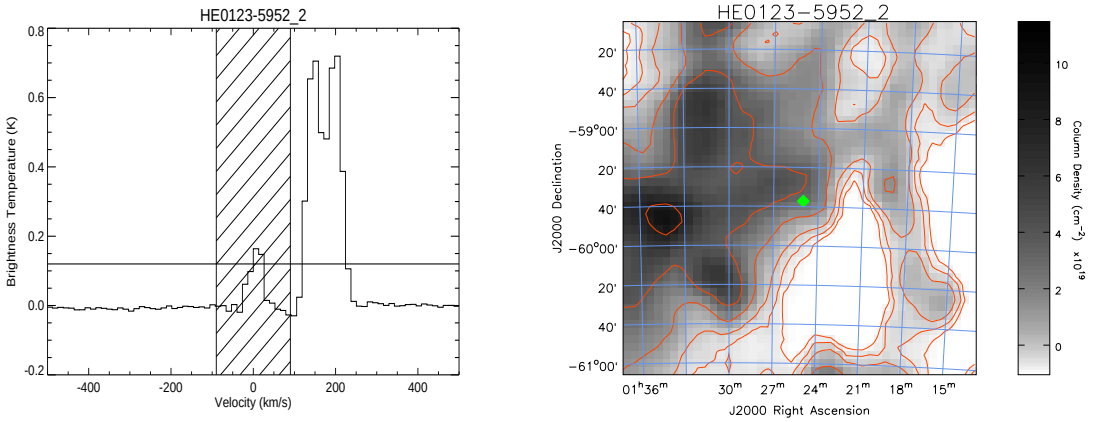


Figure B.129: HE 0123−5952_2

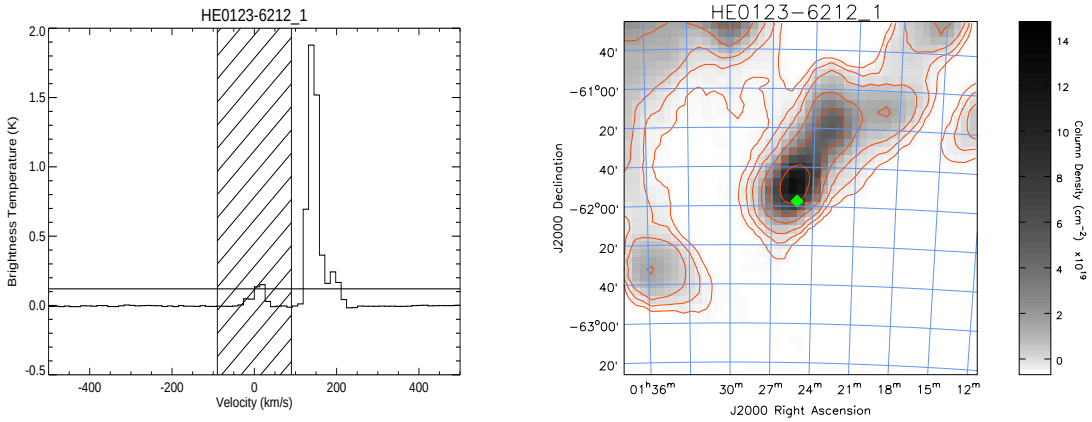


Figure B.130: HE 0123−6212_1

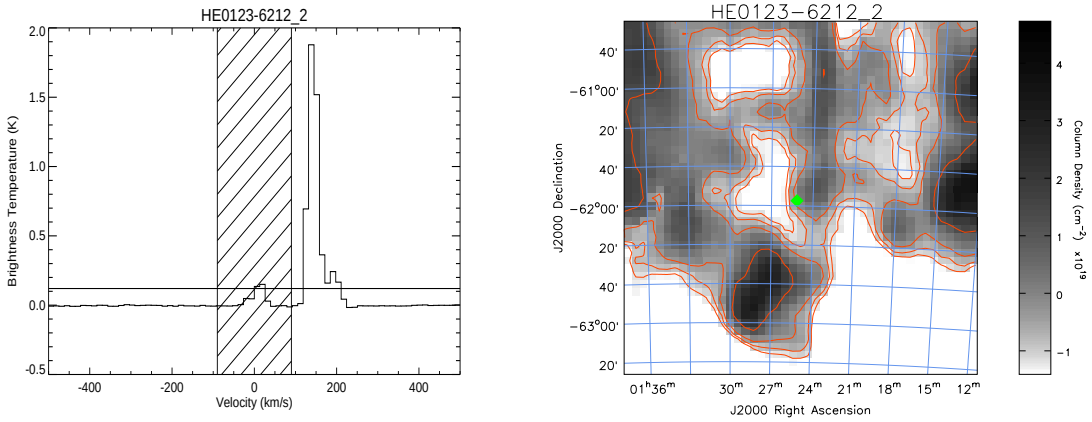


Figure B.131: HE 0123−6212_2

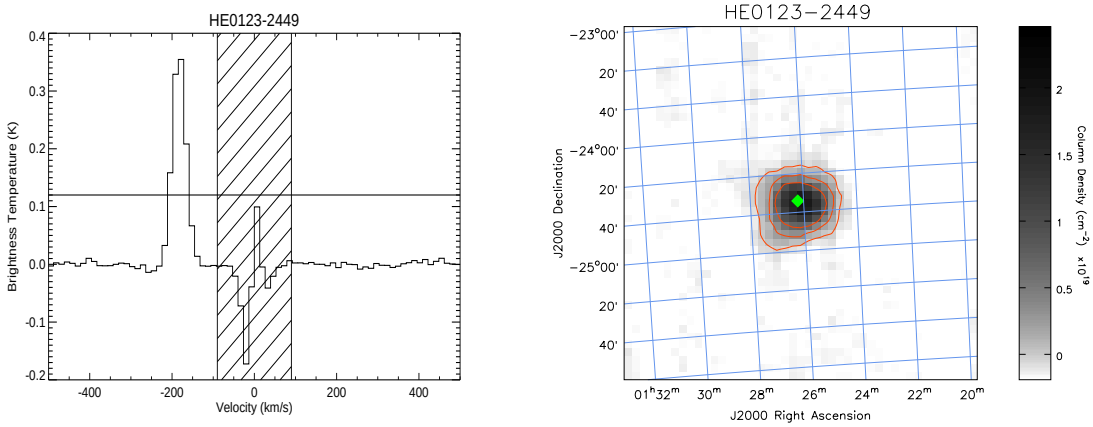


Figure B.132: HE 0123−2449

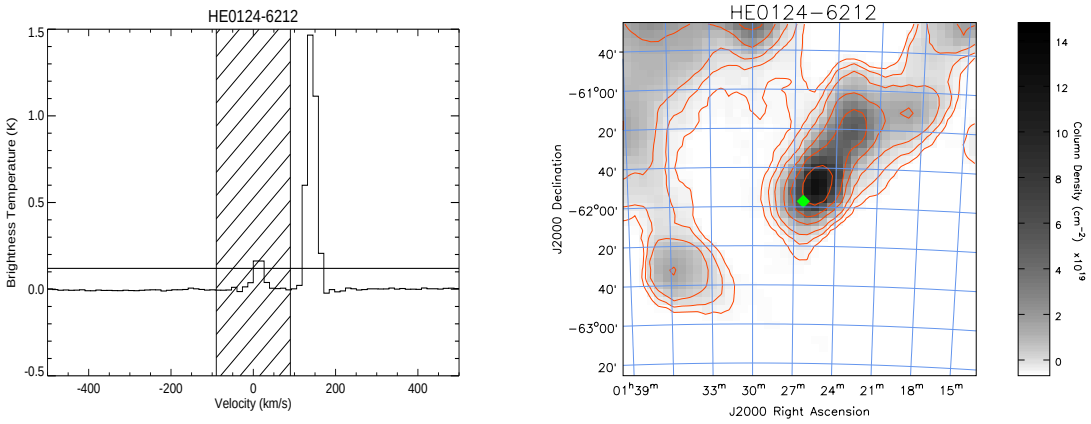


Figure B.133: HE 0124−6212

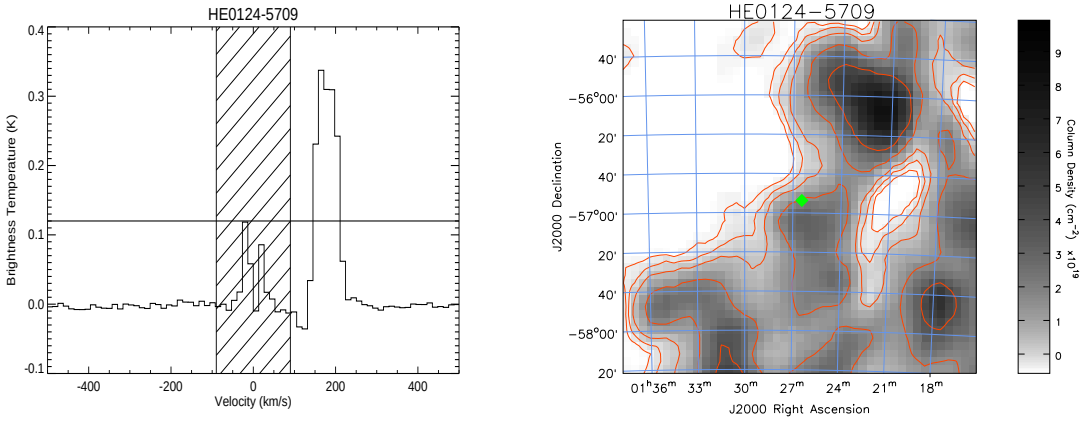


Figure B.134: HE 0124−5709

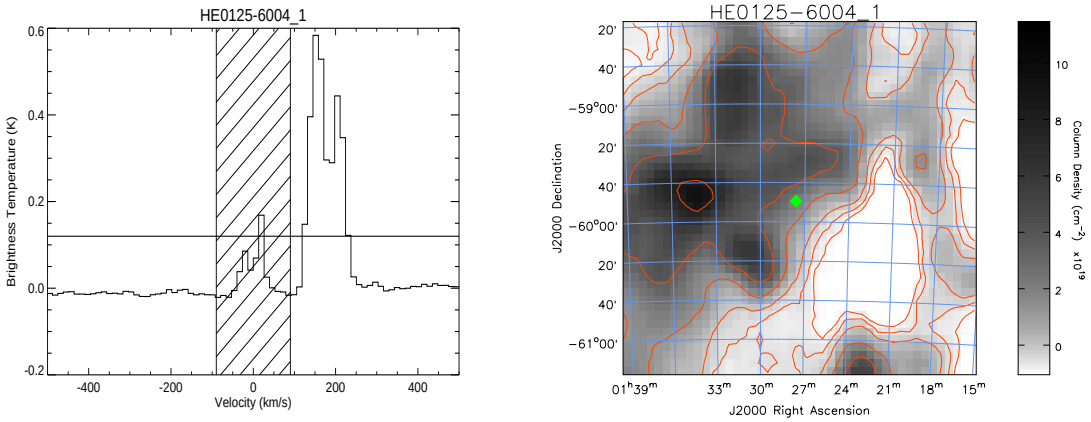


Figure B.135: HE 0125−6004_1

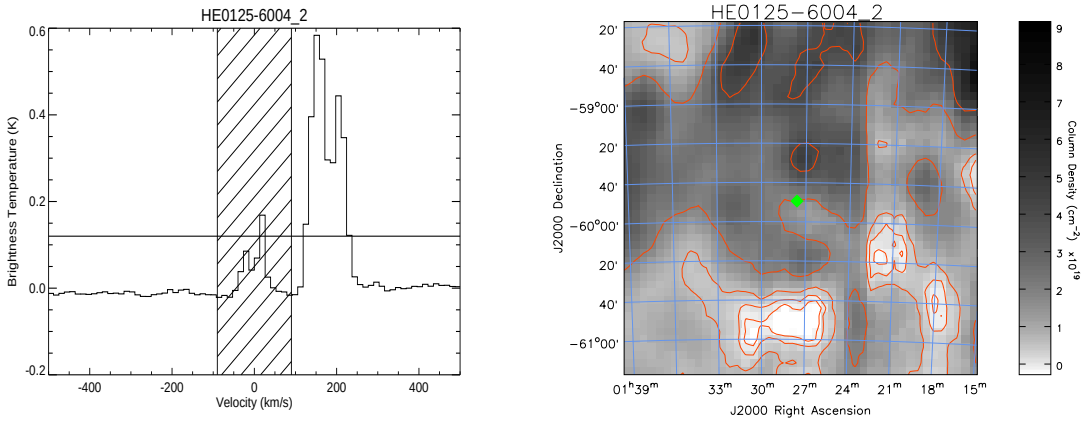


Figure B.136: HE 0125−6004_2

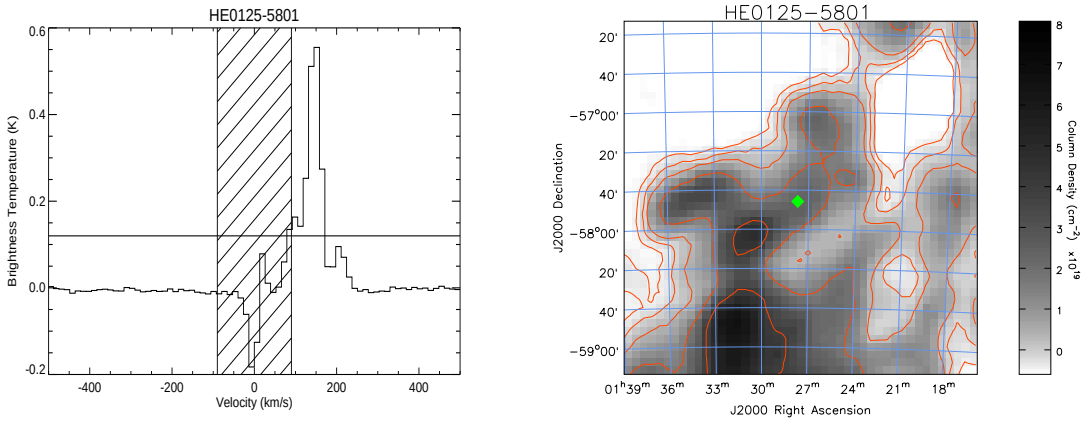


Figure B.137: HE 0125−5801

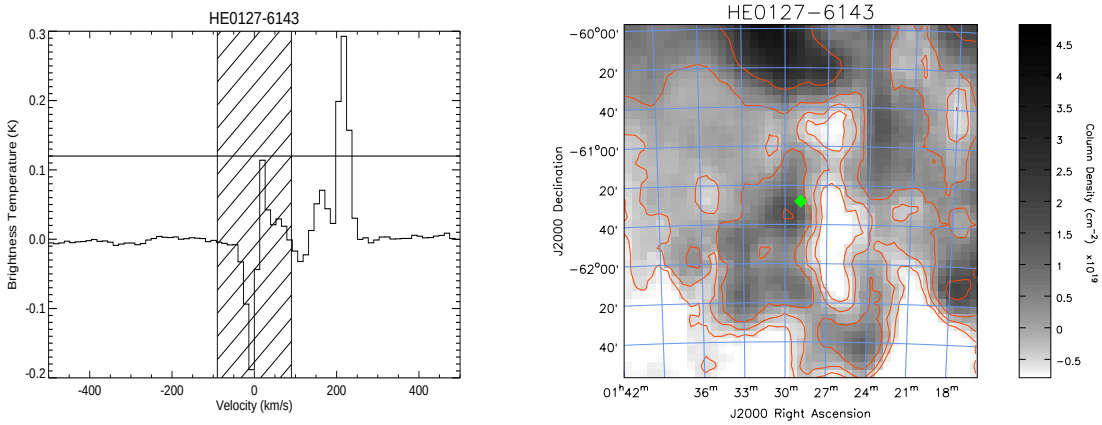


Figure B.138: HE 0127−6143

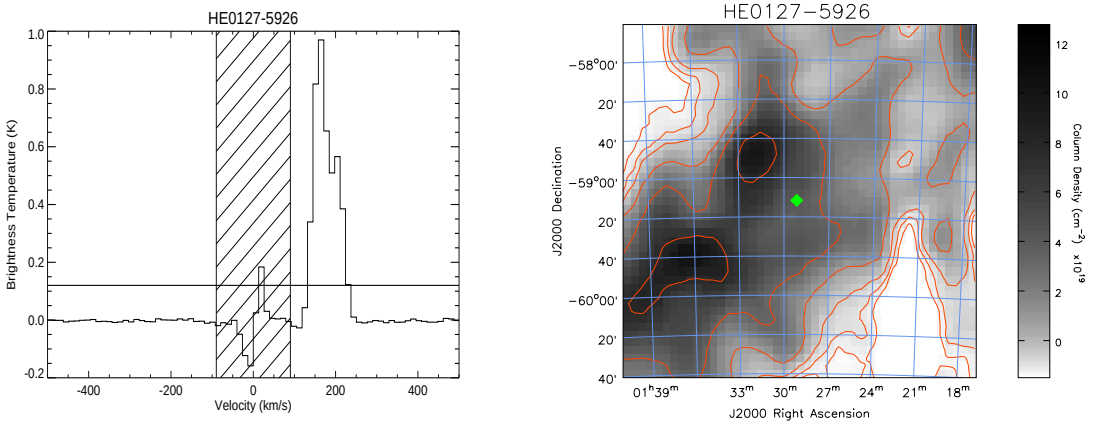


Figure B.139: HE 0127−5926

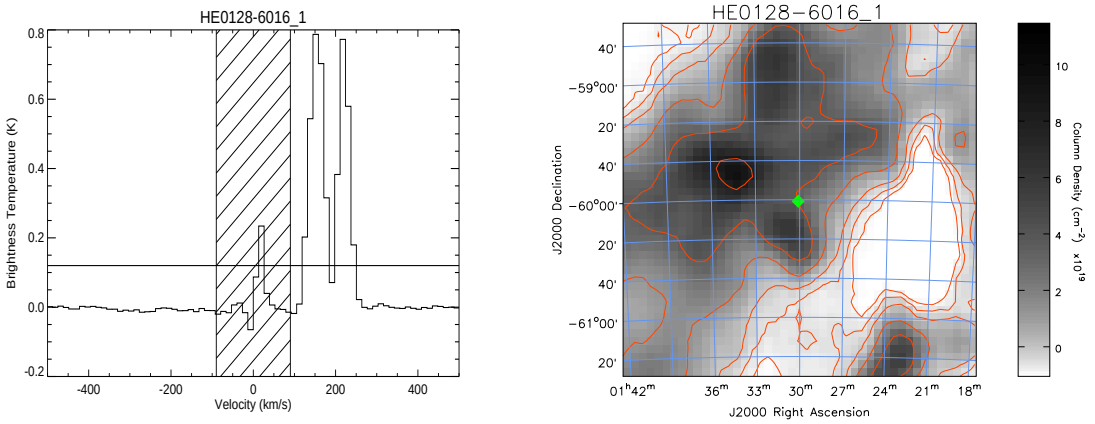


Figure B.140: HE 0128−6016_1

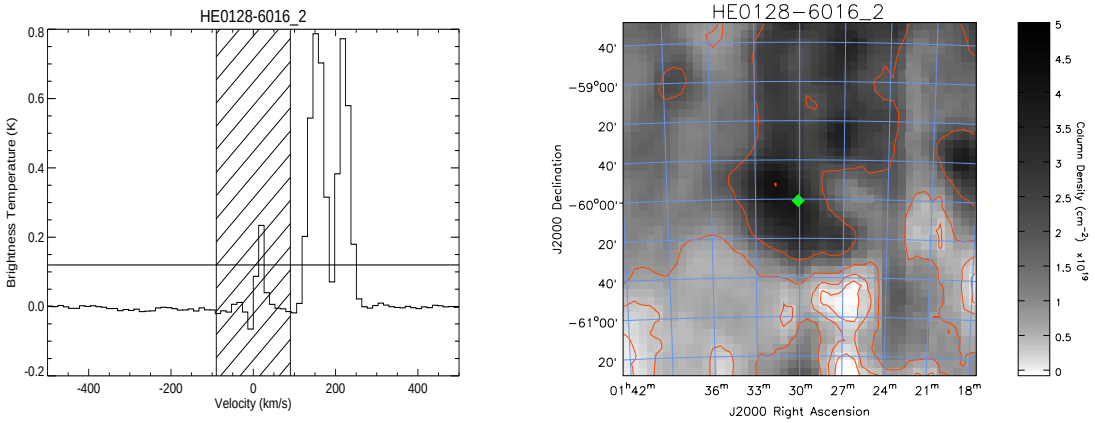


Figure B.141: HE 0128−6016_2

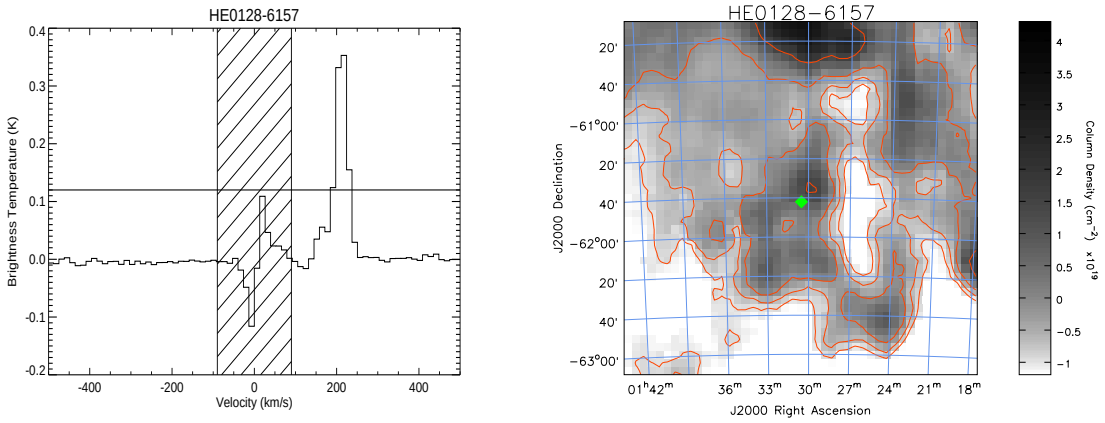


Figure B.142: HE 0128−6157

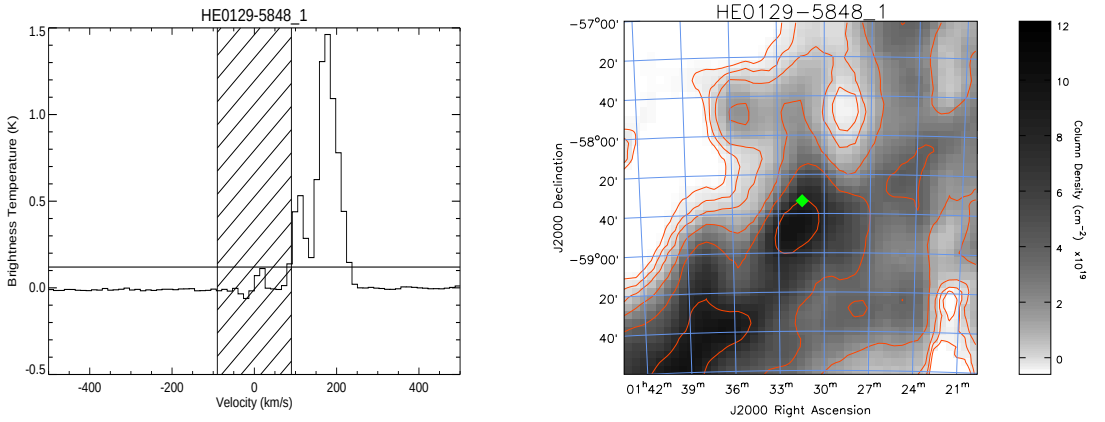


Figure B.143: HE 0129−5848_1

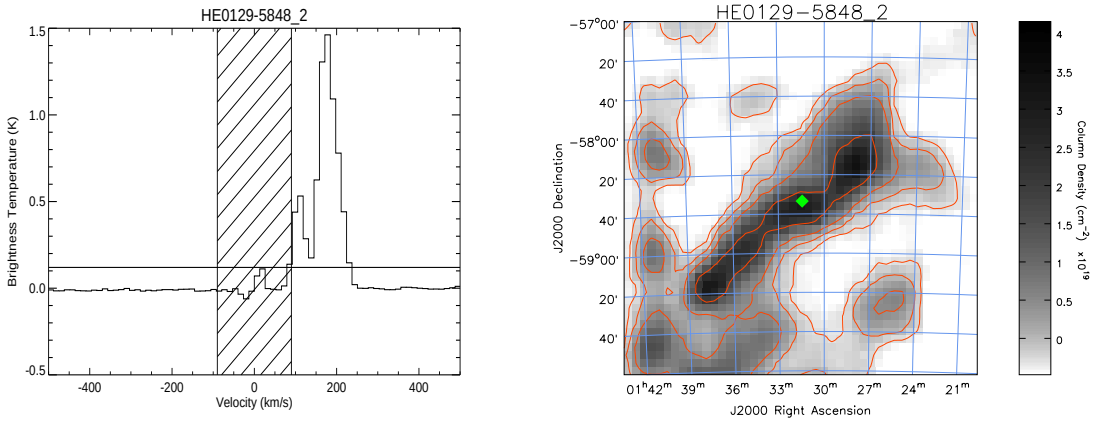
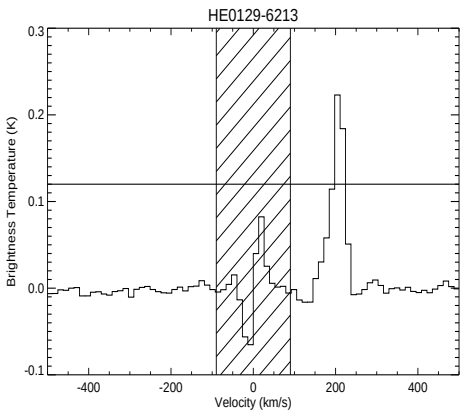


Figure B.144: HE 0129−5848_2



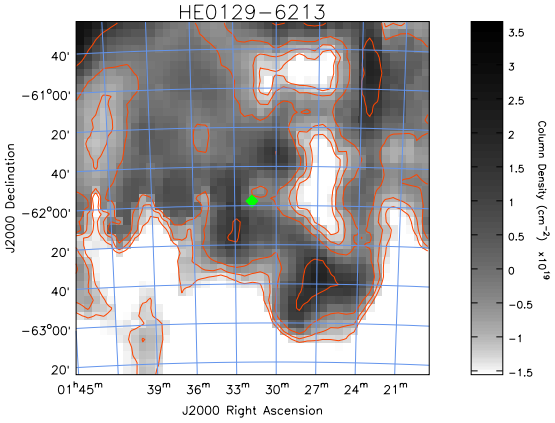
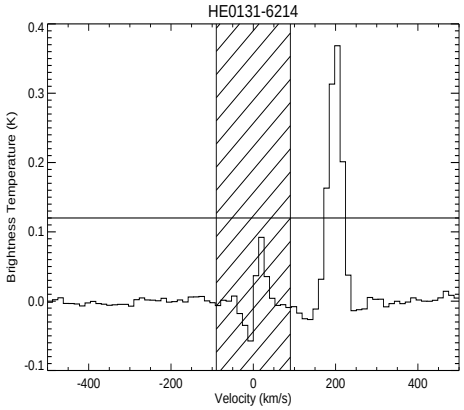


Figure B.145: HE 0129−6213



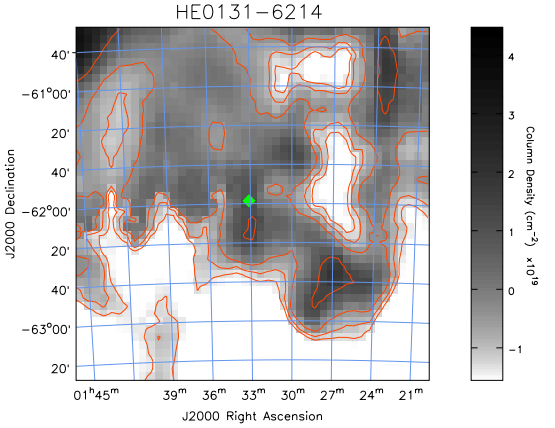
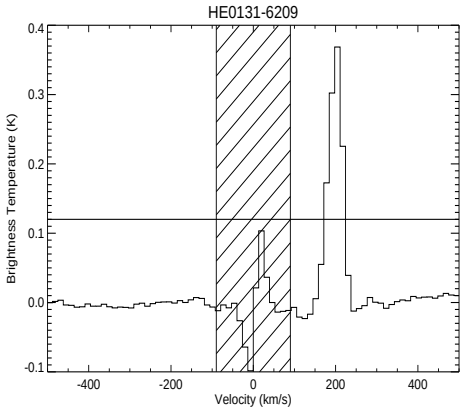


Figure B.146: HE 0131−6214



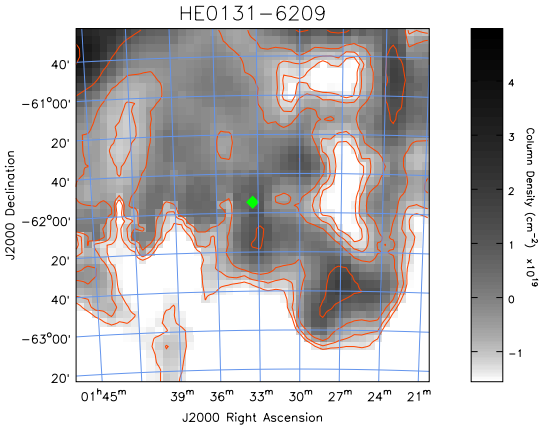


Figure B.147: HE 0131−6209

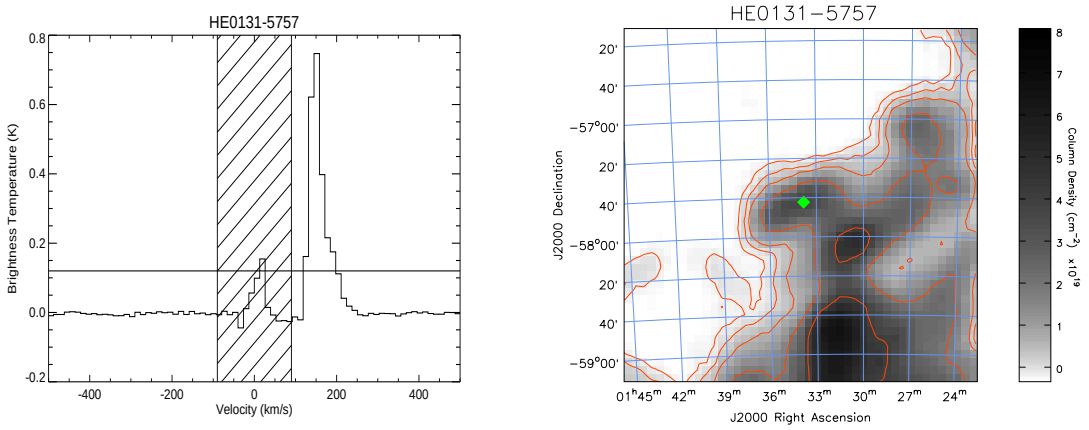


Figure B.148: HE 0131−5757

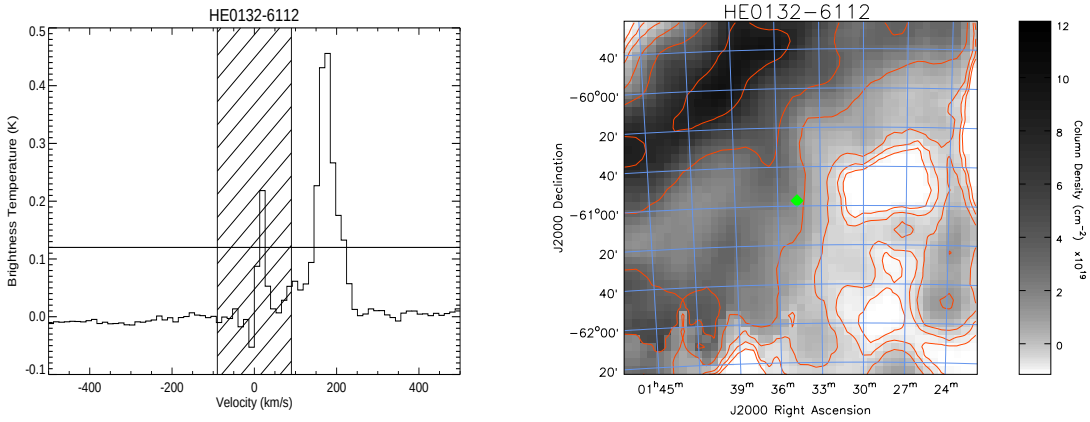


Figure B.149: HE 0132−6112

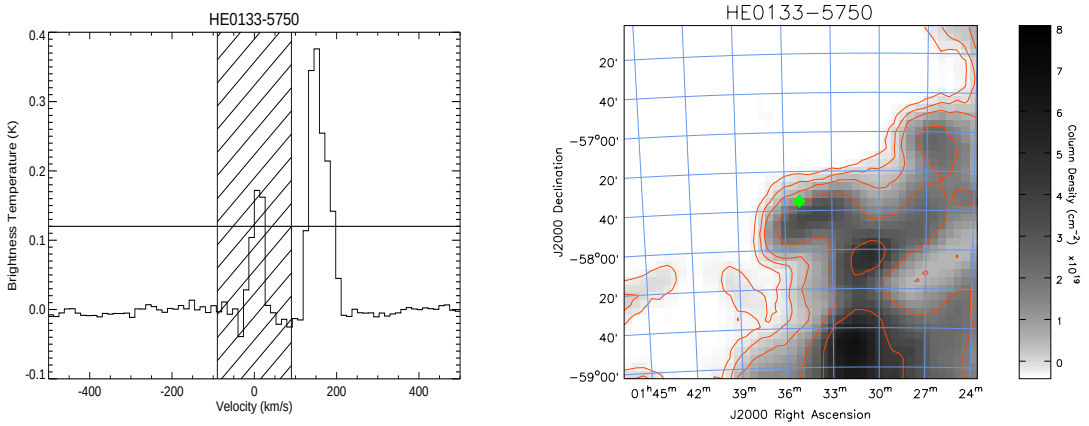


Figure B.150: HE 0133−5750

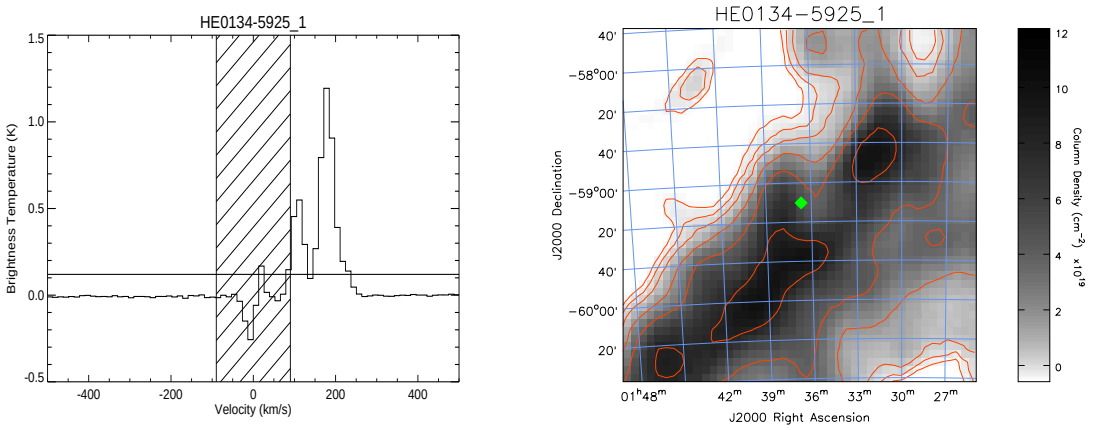


Figure B.151: HE 0134−5925_1

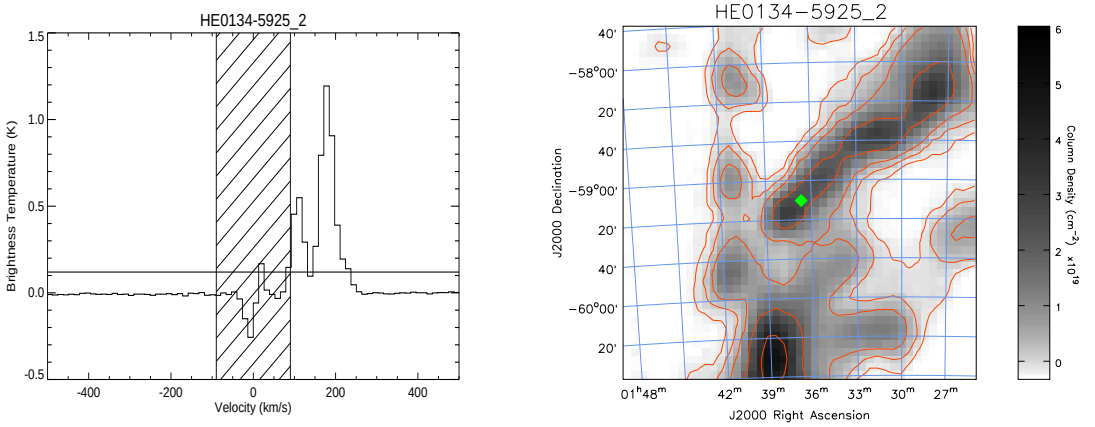


Figure B.152: HE 0134−5925_2

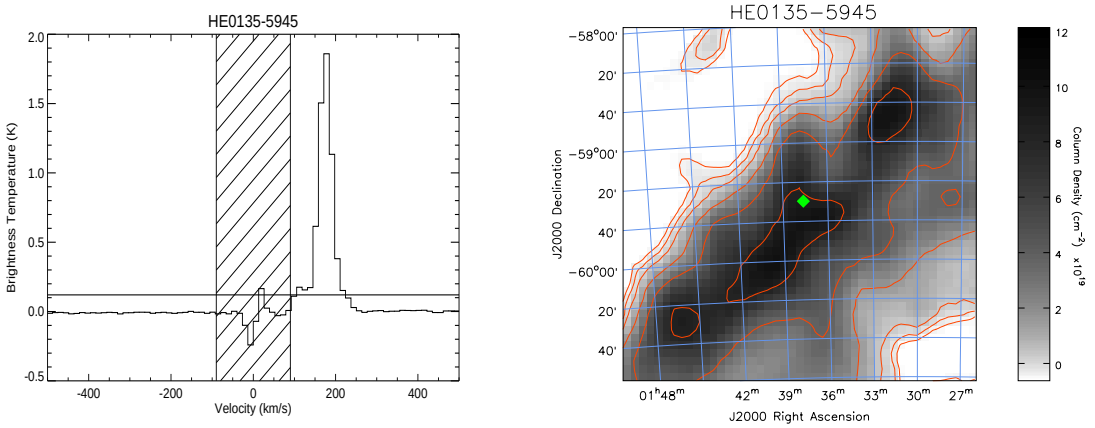


Figure B.153: HE 0135−5945

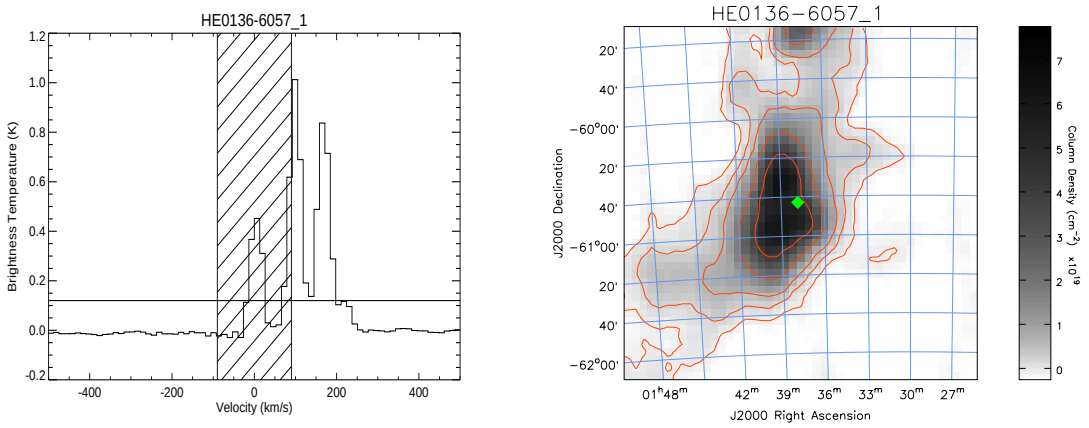


Figure B.154: HE 0136−6057_1

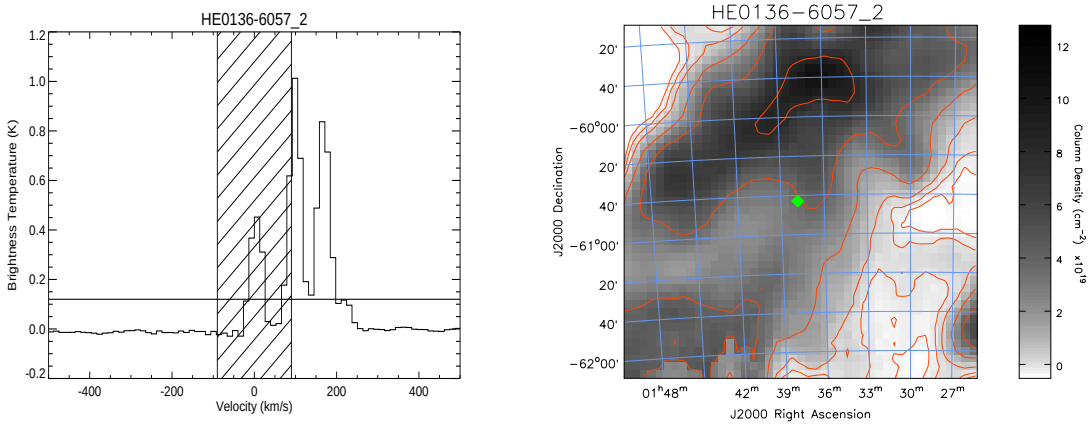


Figure B.155: HE 0136−6057_2

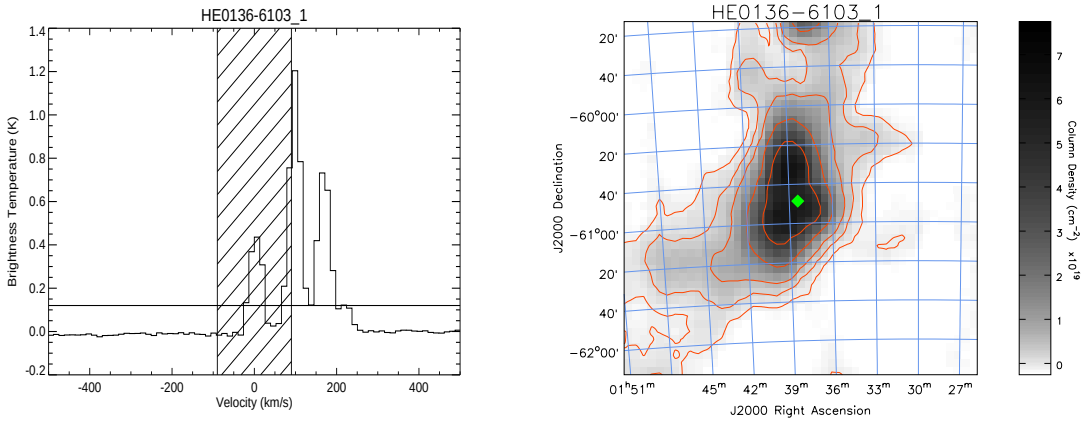
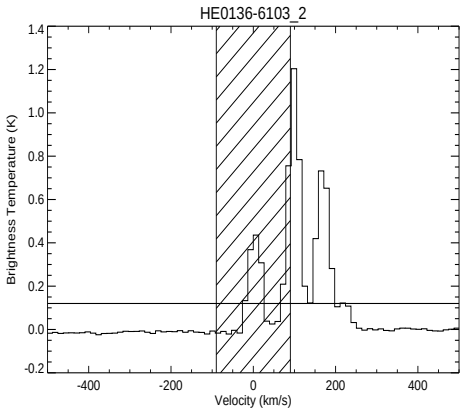


Figure B.156: HE 0136−6103_1



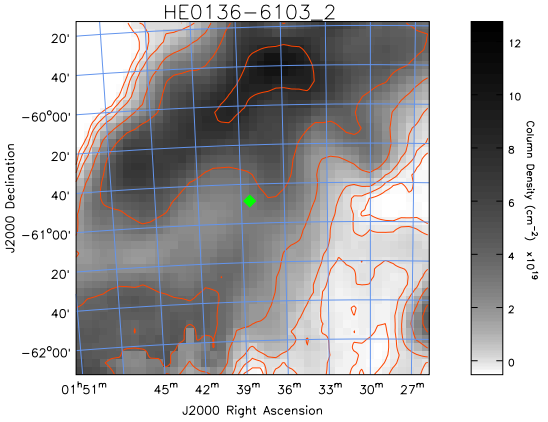
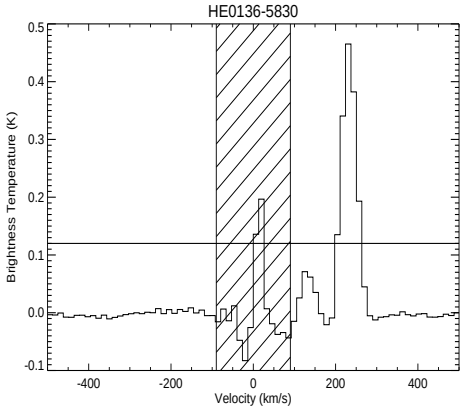


Figure B.157: HE 0136−6103_2



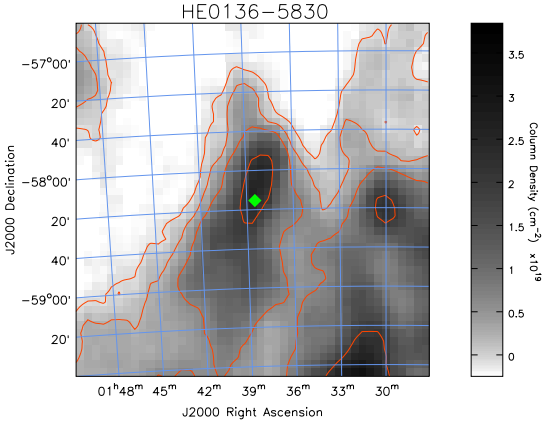
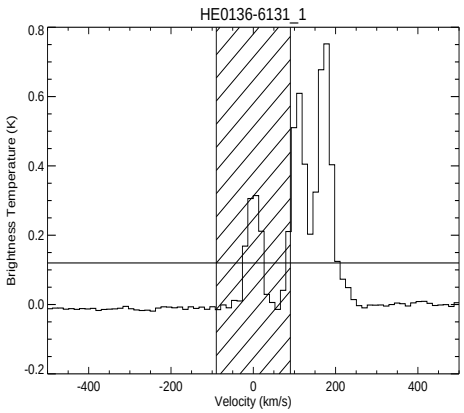


Figure B.158: HE 0136−5830



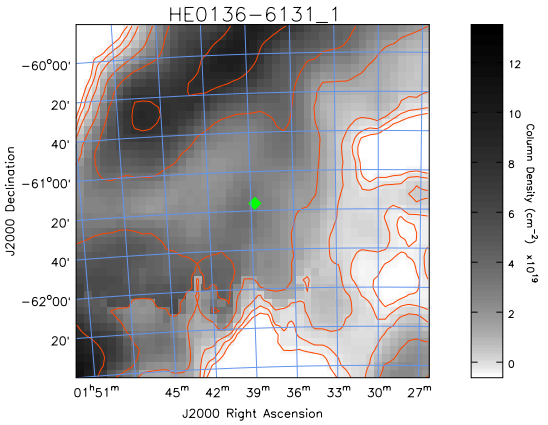


Figure B.159: HE 0136−6131_1

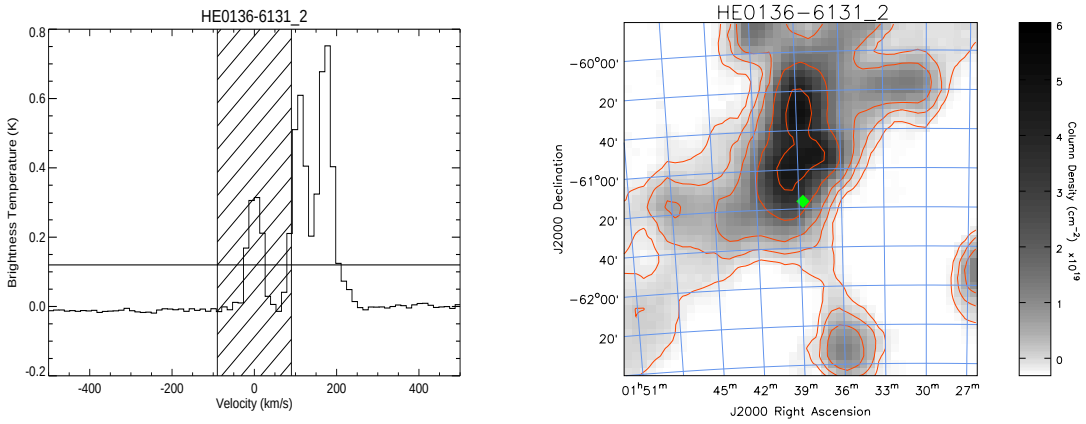


Figure B.160: HE 0136−6131_2

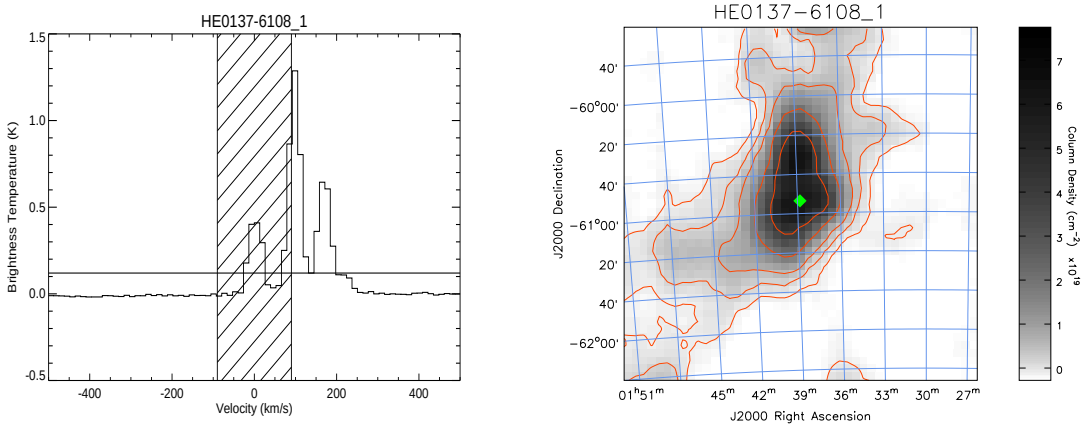


Figure B.161: HE 0137−6108_1

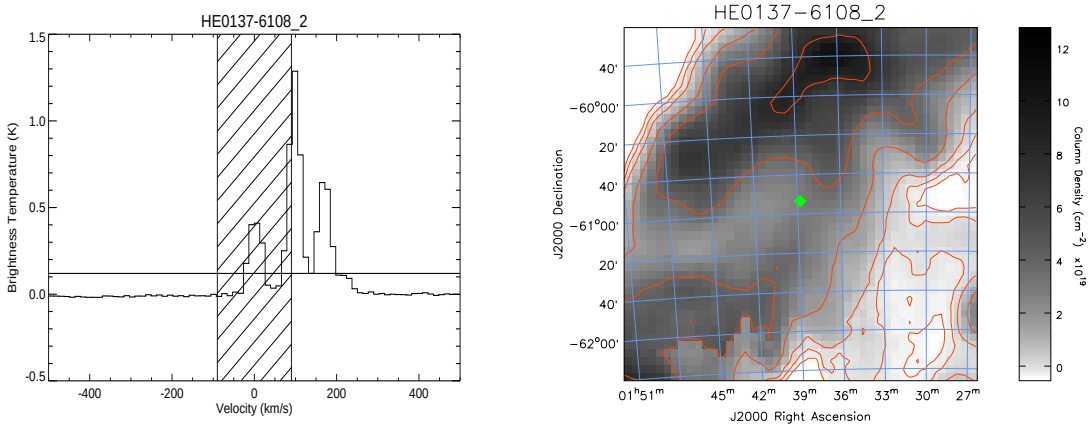


Figure B.162: HE 0137−6108_2

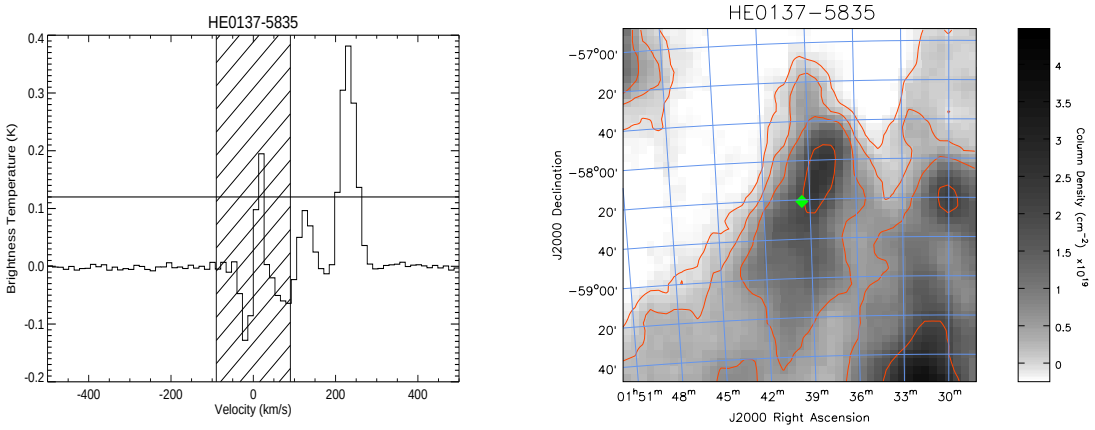


Figure B.163: HE 0137−5835

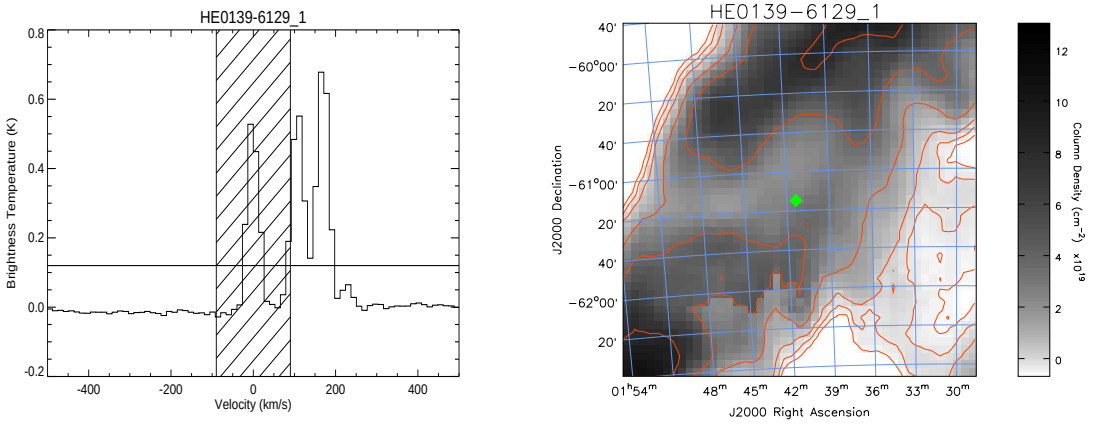


Figure B.164: HE 0139−6129_1

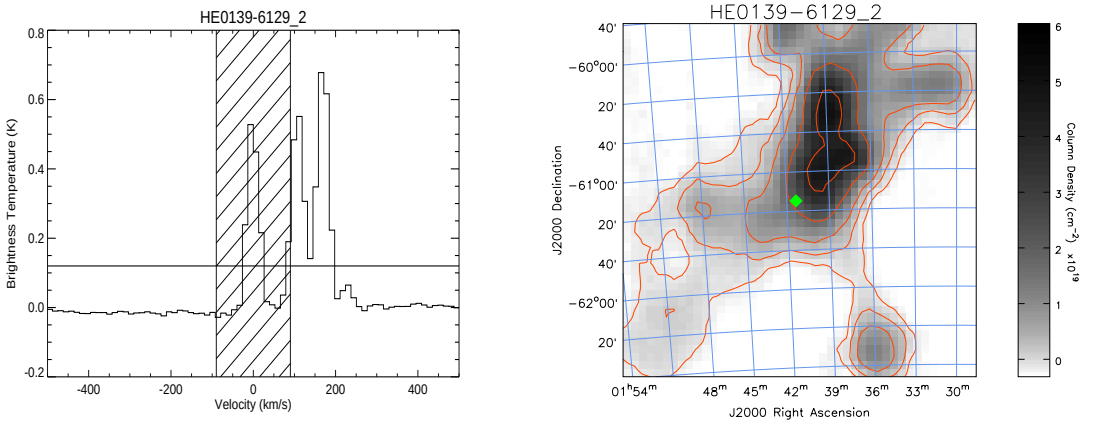


Figure B.165: HE 0139−6129_2

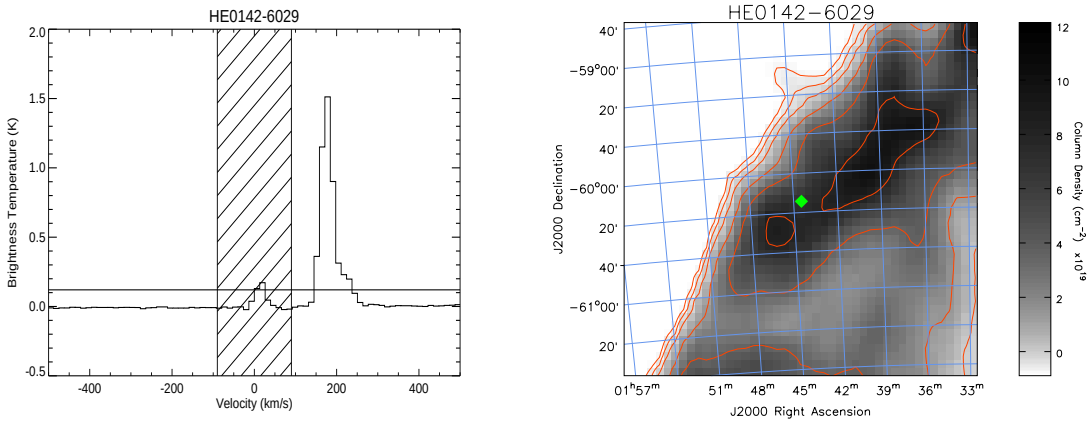


Figure B.166: HE 0142−6029

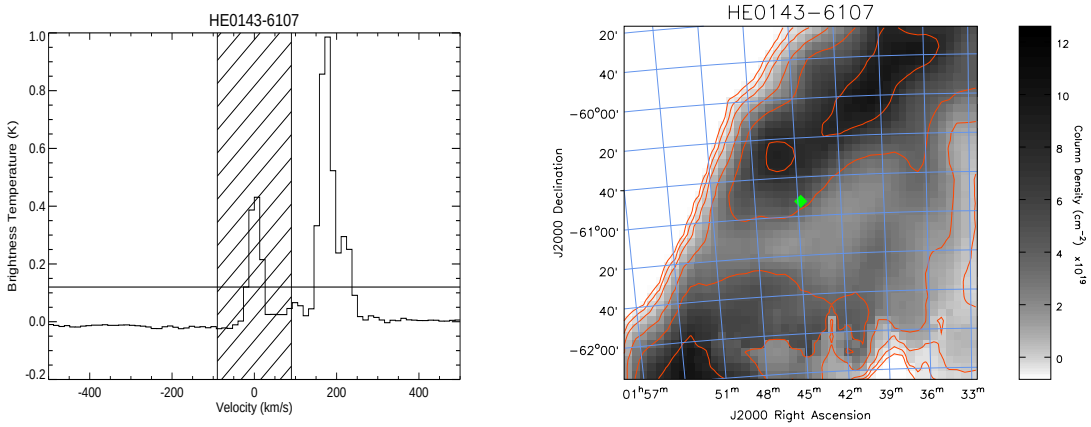


Figure B.167: HE 0143−6107

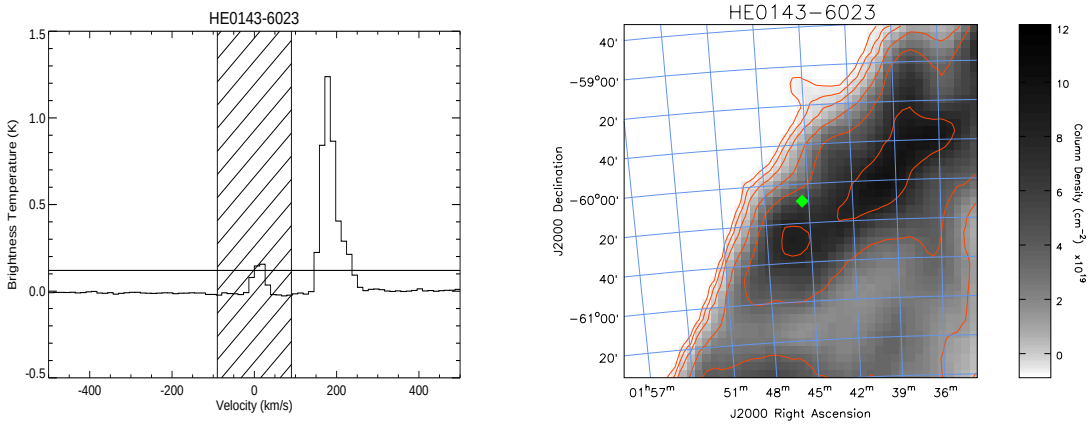


Figure B.168: HE 0143−6023

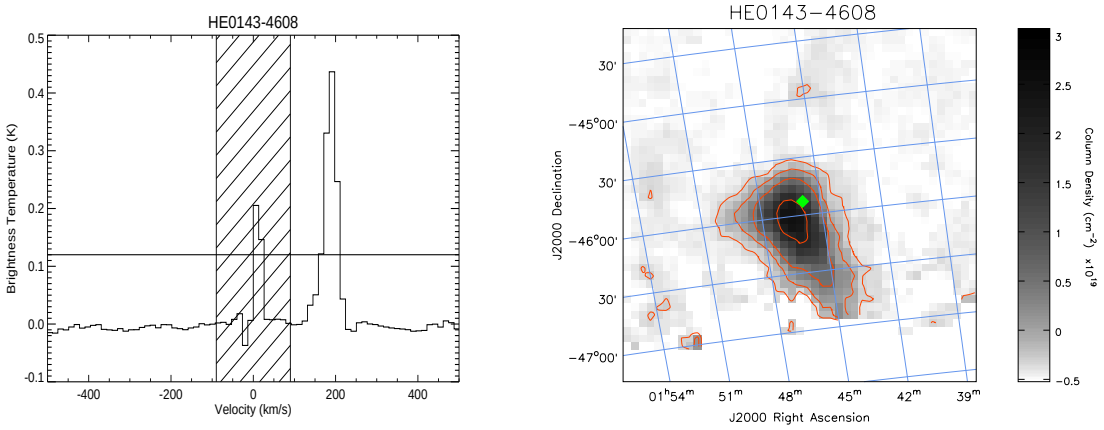


Figure B.169: HE 0143−4608

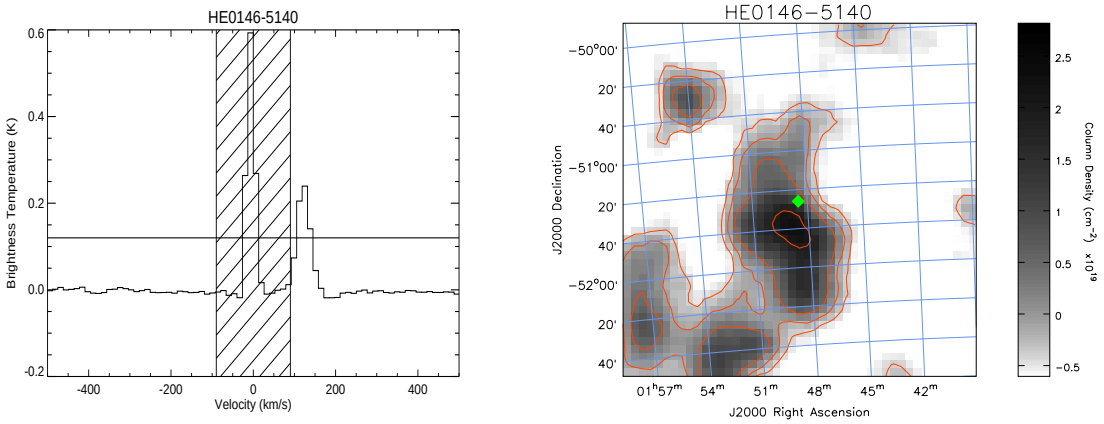


Figure B.170: HE 0146−5140

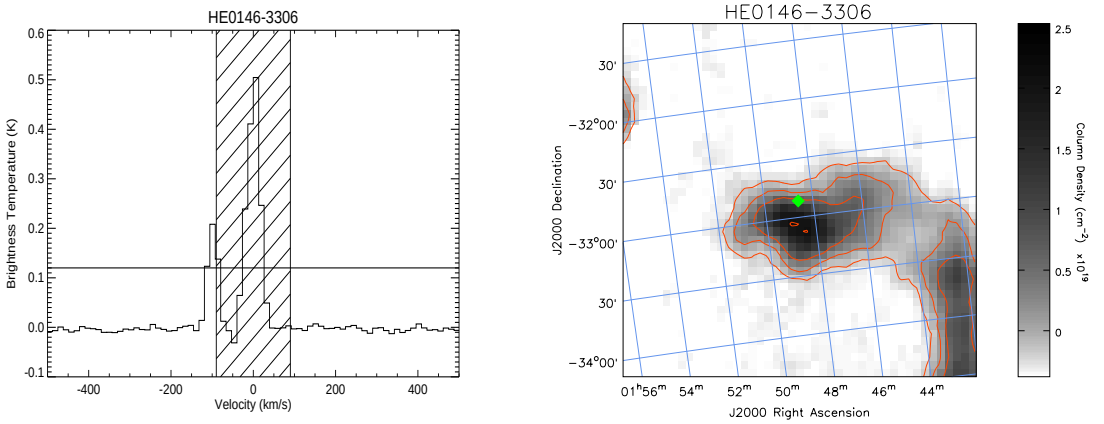


Figure B.171: HE 0146−3306

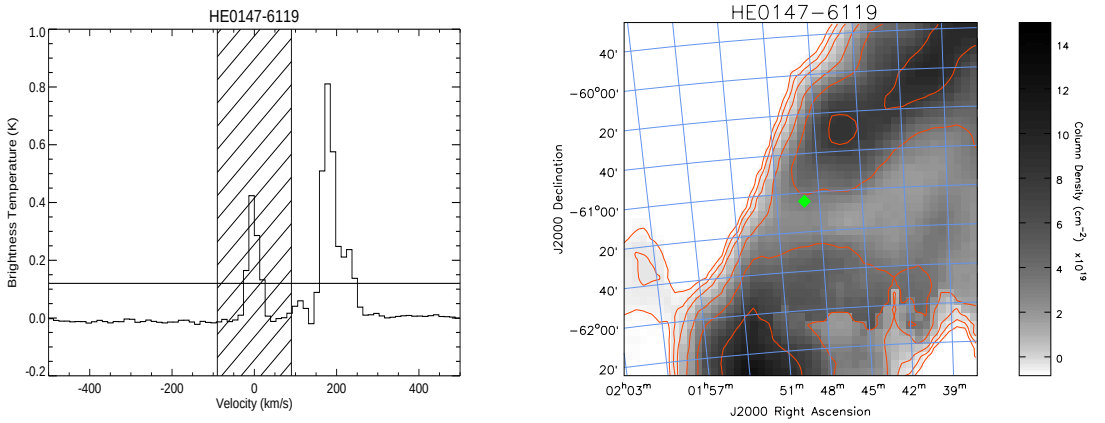


Figure B.172: HE 0147−6119

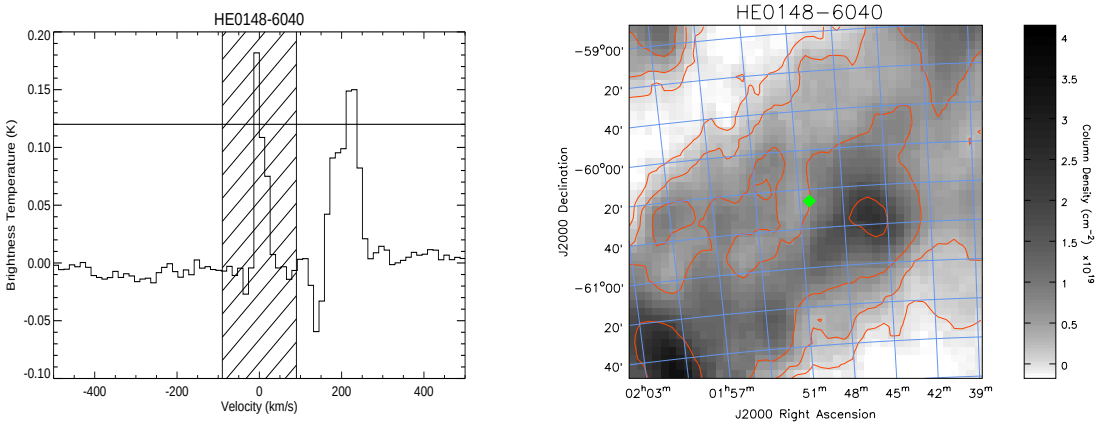


Figure B.173: HE 0148−6040

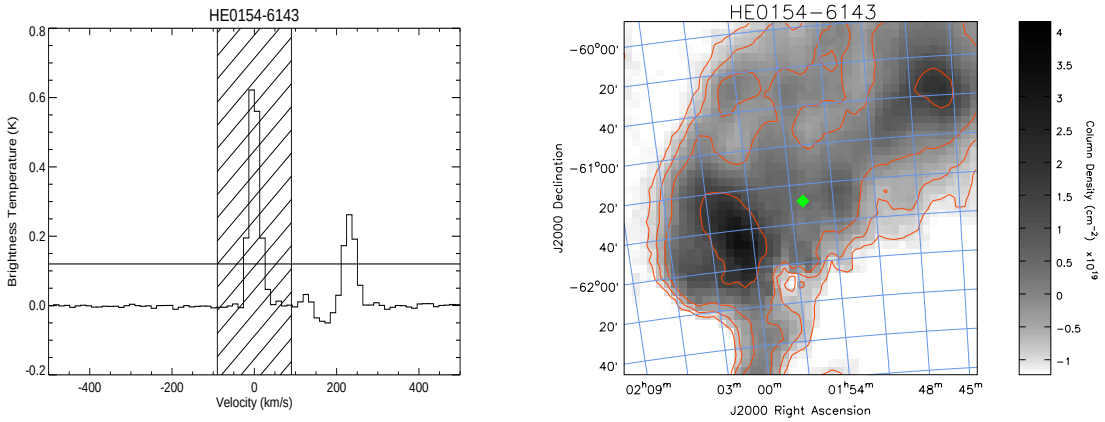


Figure B.174: HE 0154−6143

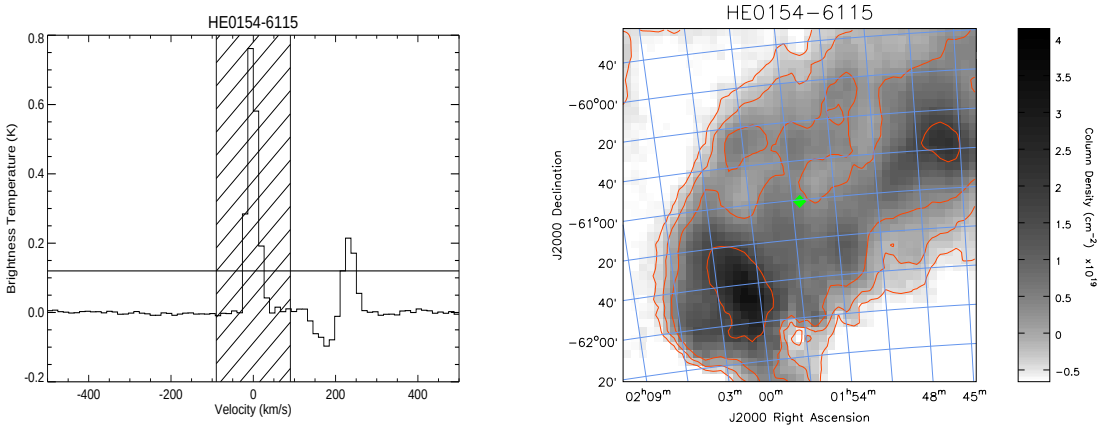


Figure B.175: HE 0154−6115

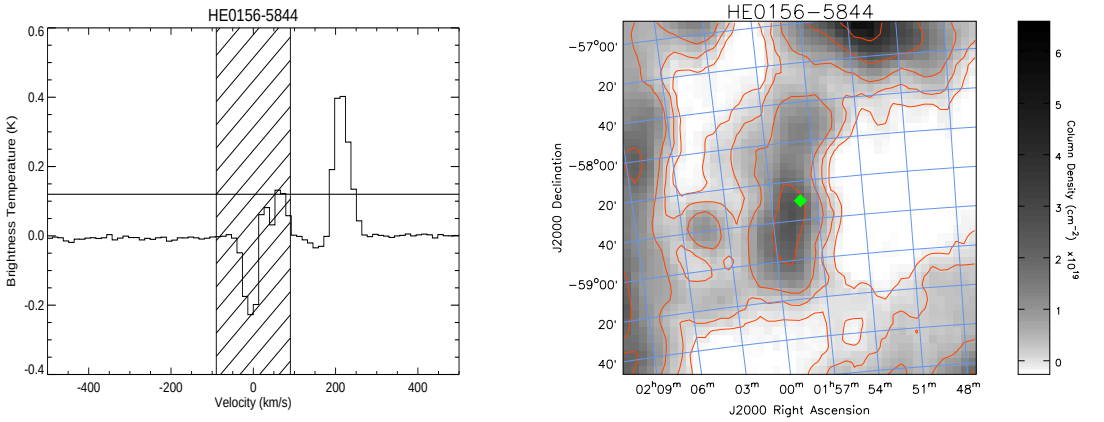


Figure B.176: HE 0156−5844

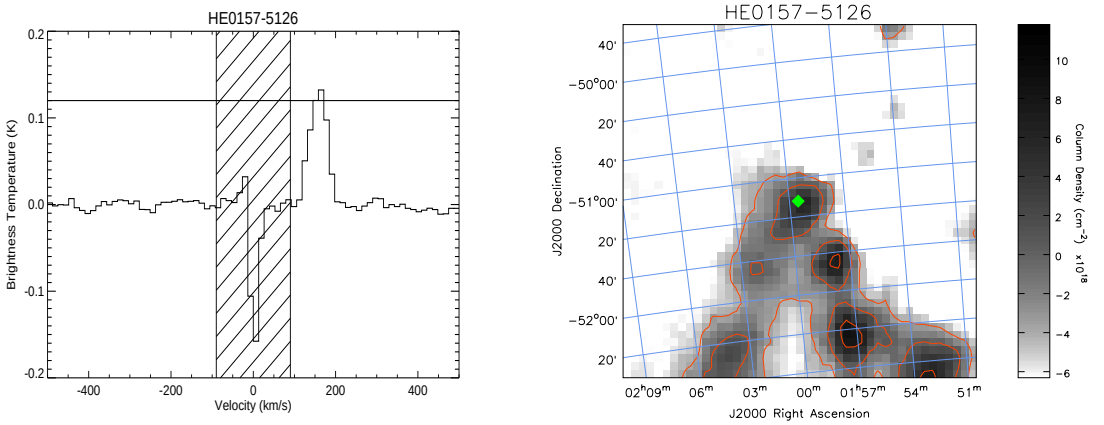


Figure B.177: HE 0157−5126

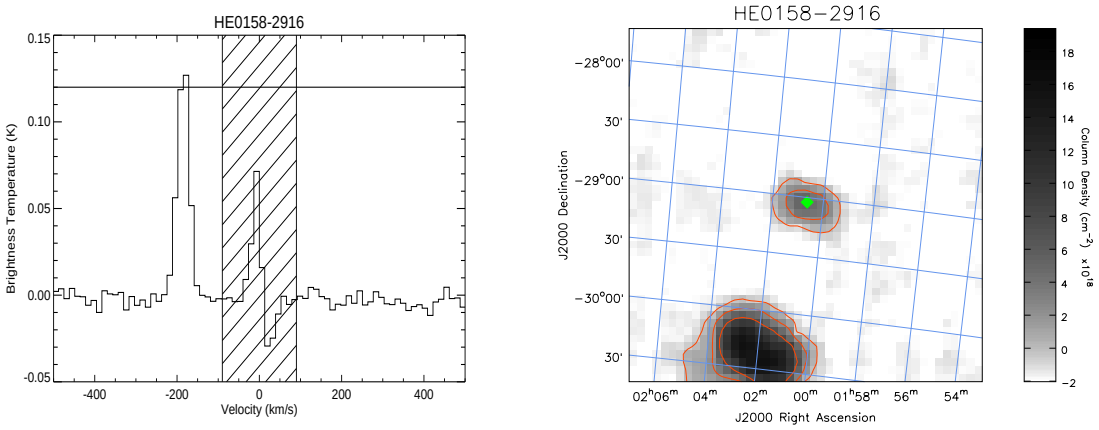


Figure B.178: HE 0158−2916

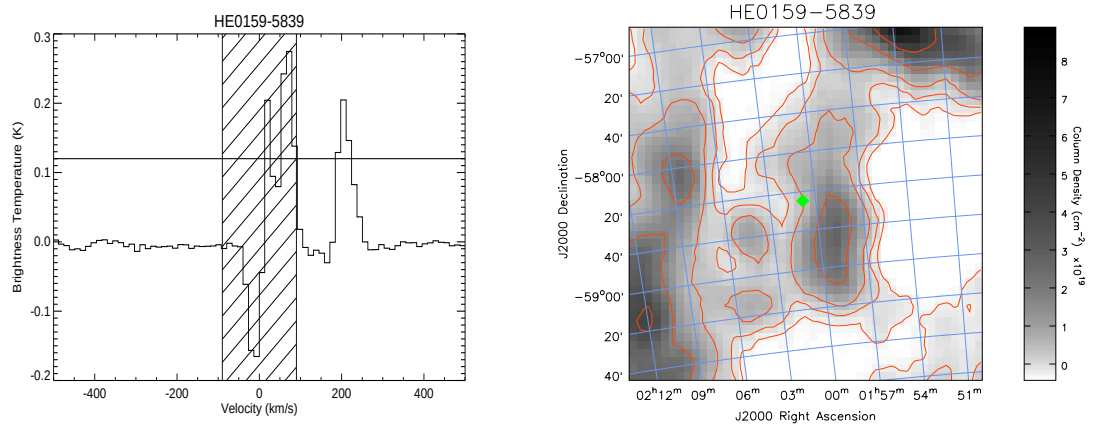


Figure B.179: HE 0159−5839

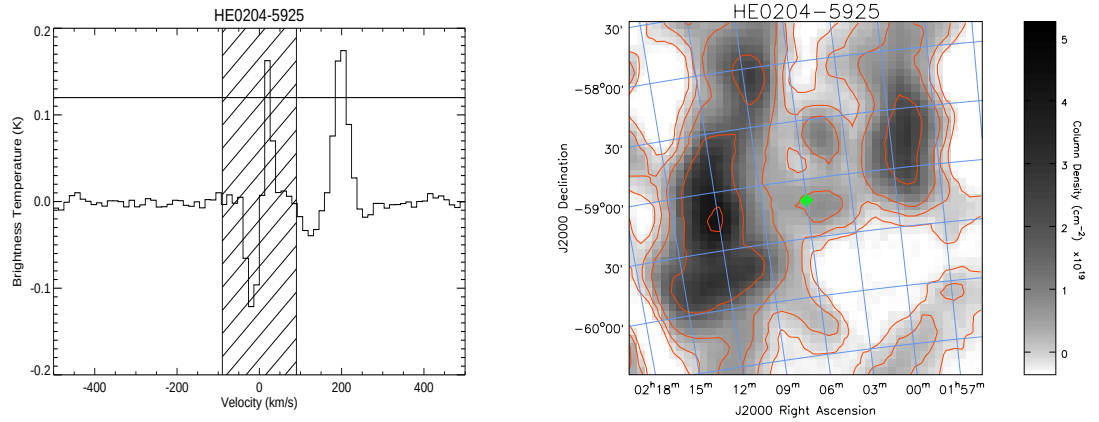
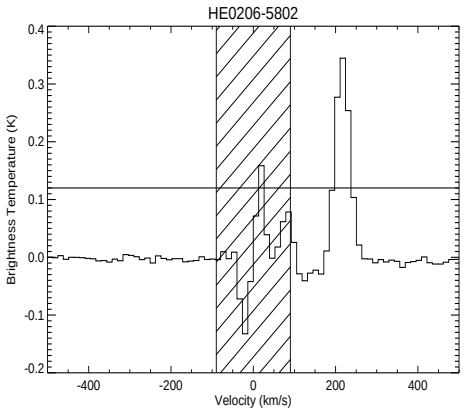


Figure B.180: HE 0204−5925



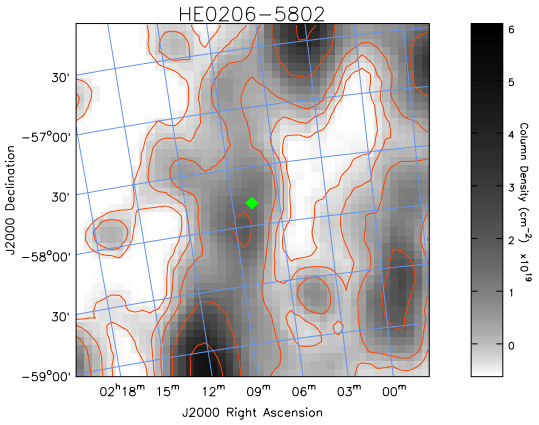
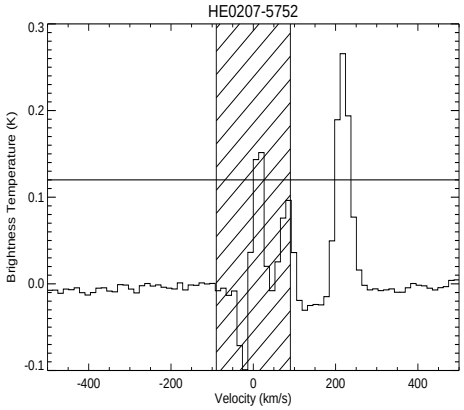


Figure B.181: HE 0206−5802



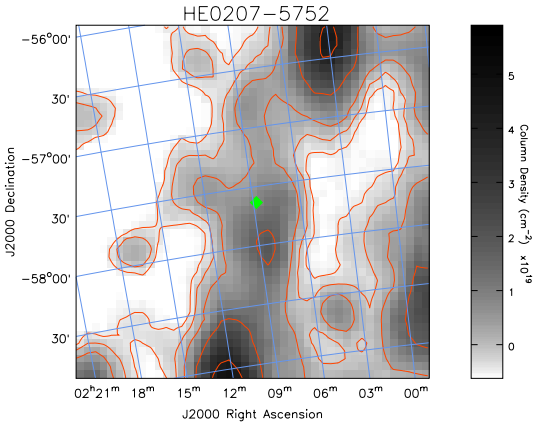
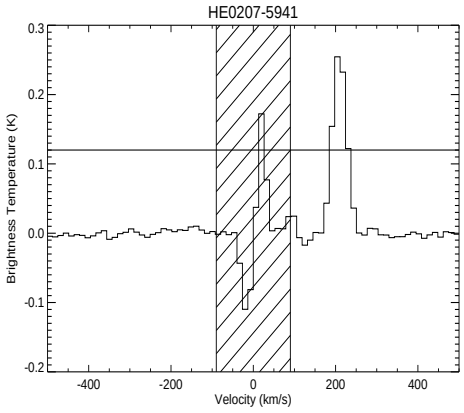


Figure B.182: HE 0207−5752



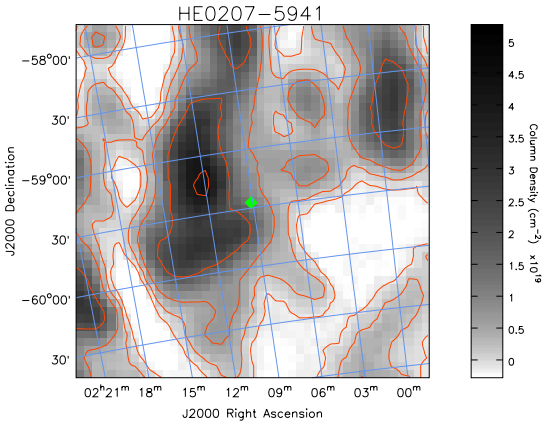


Figure B.183: HE 0207−5941

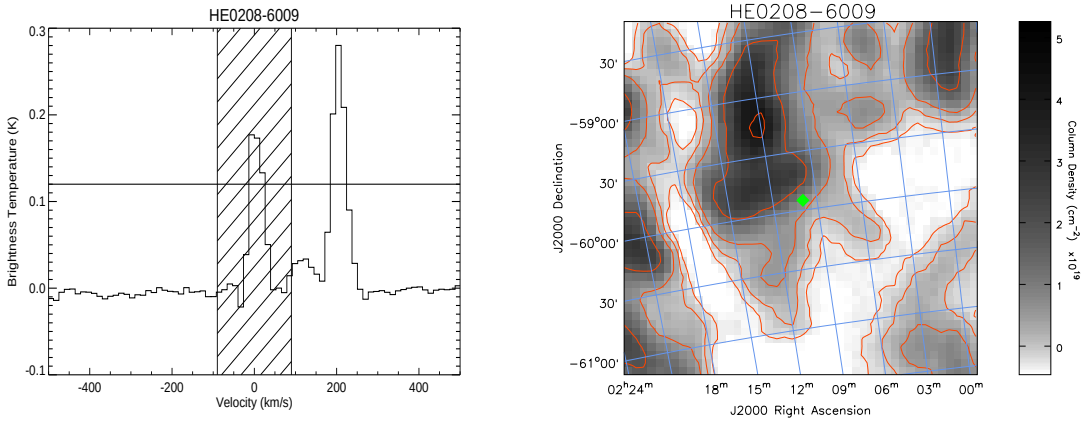


Figure B.184: HE 0208−6009

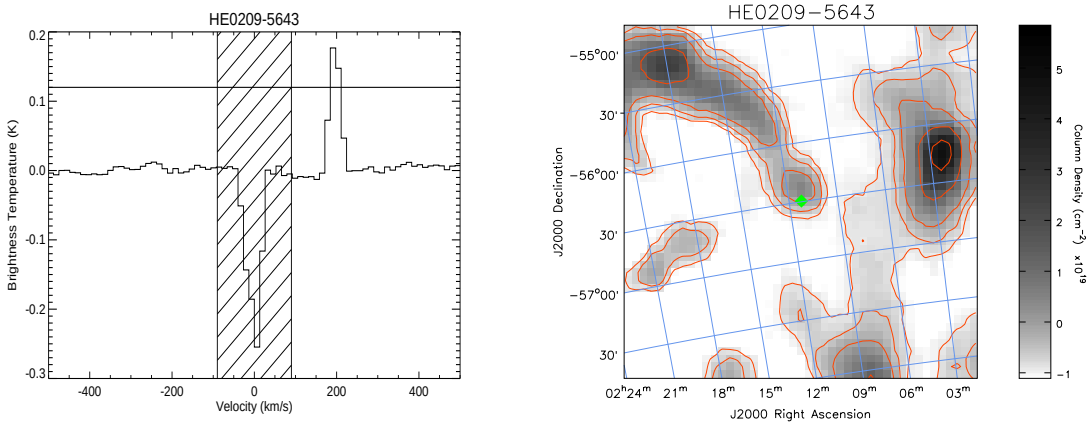


Figure B.185: HE 0209−5643

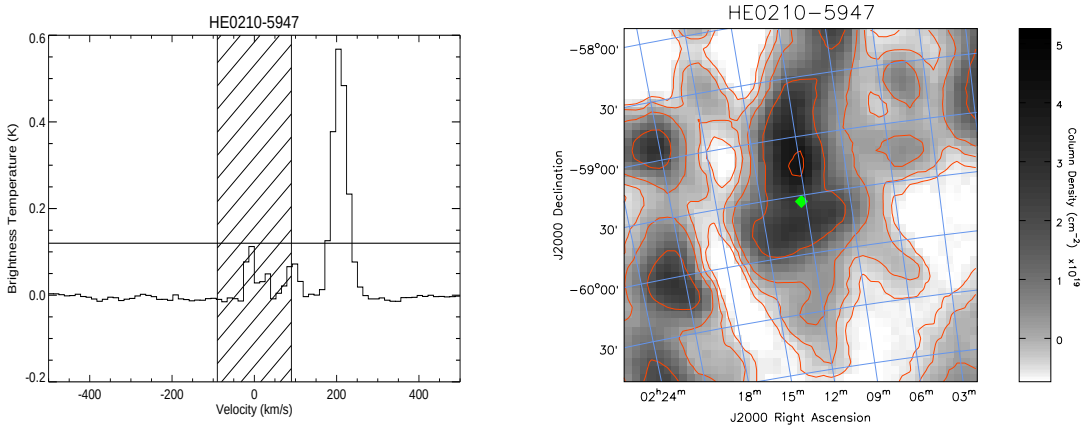
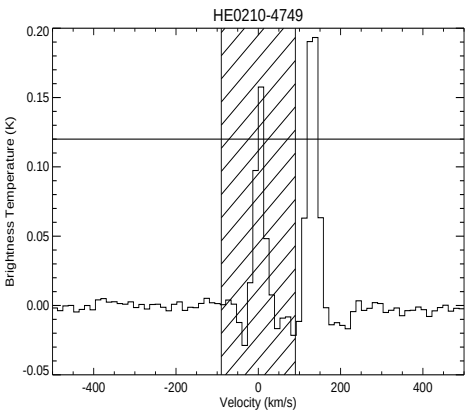


Figure B.186: HE 0210−5947



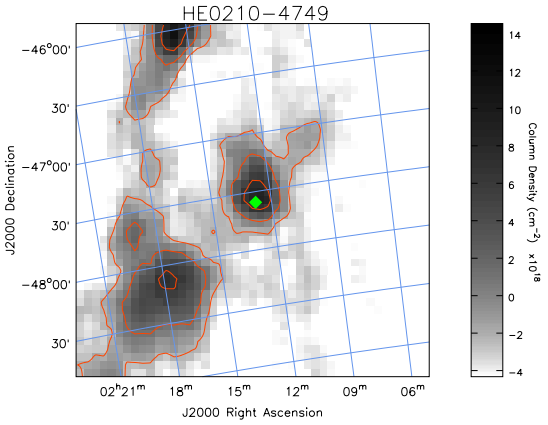
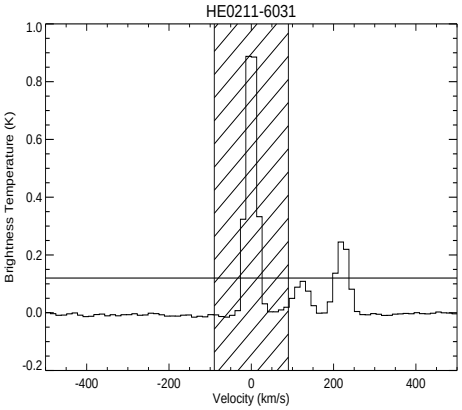


Figure B.187: HE 0210−4749



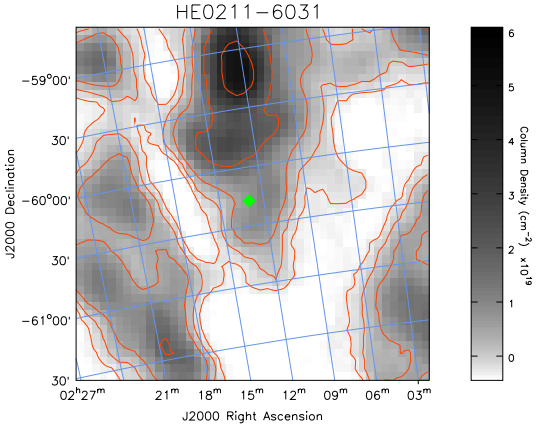
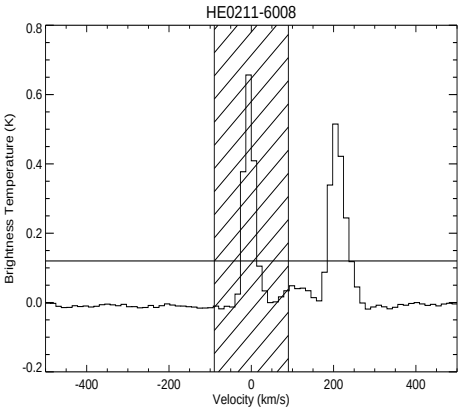


Figure B.188: HE 0211−6031



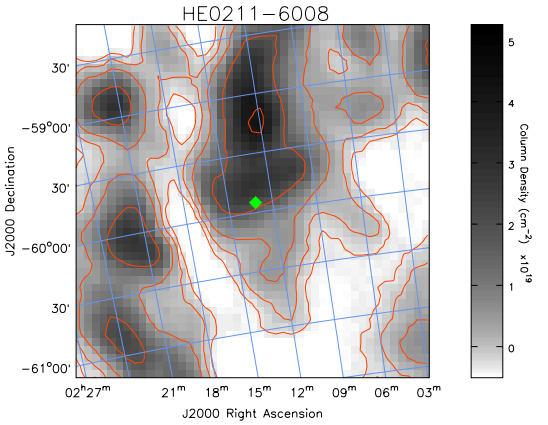


Figure B.189: HE 0211−6008

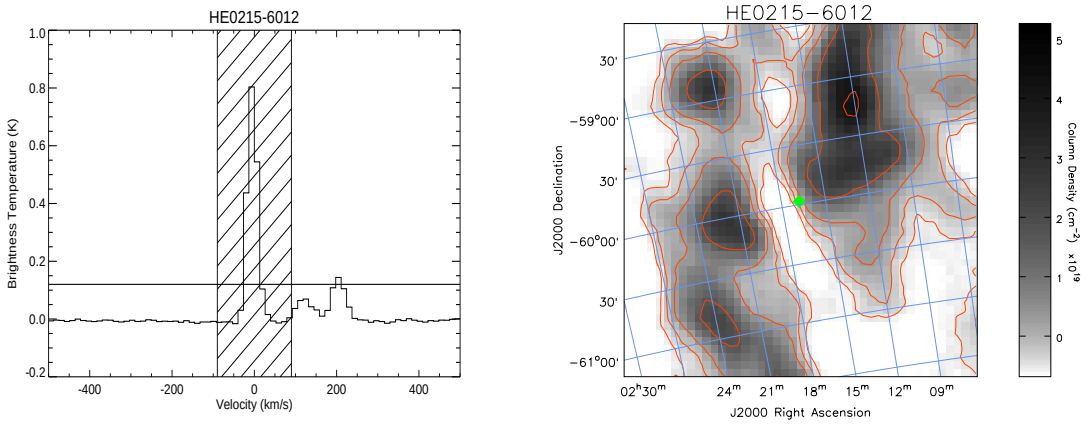


Figure B.190: HE 0215−6012

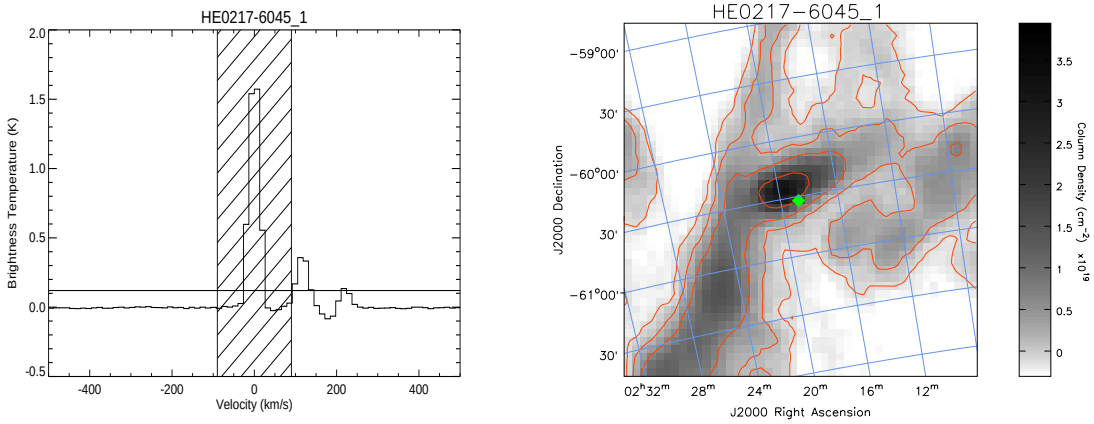


Figure B.191: HE 0217−6045_1

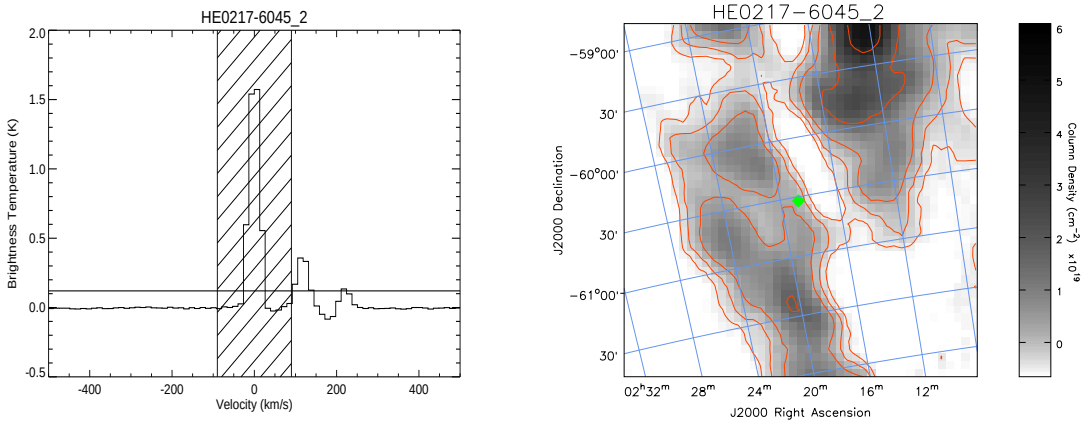


Figure B.192: HE 0217−6045_2

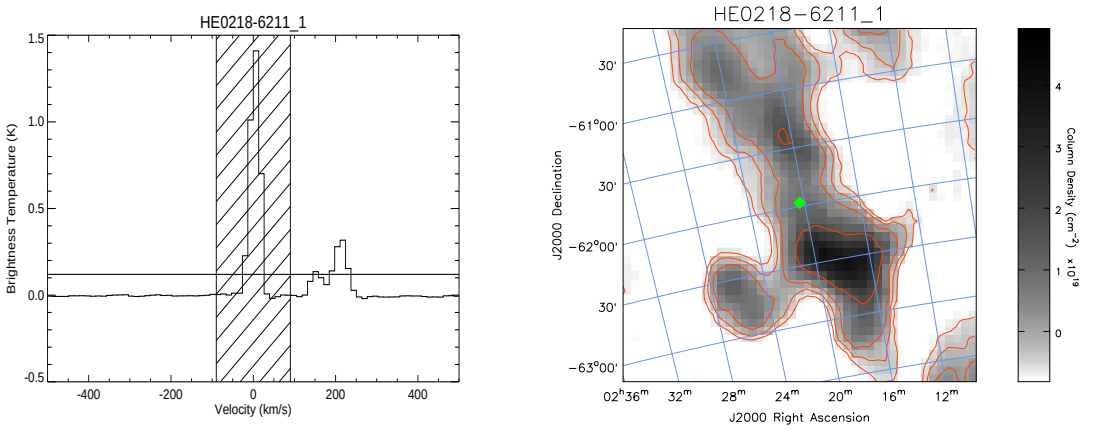


Figure B.193: HE 0218−6211_1

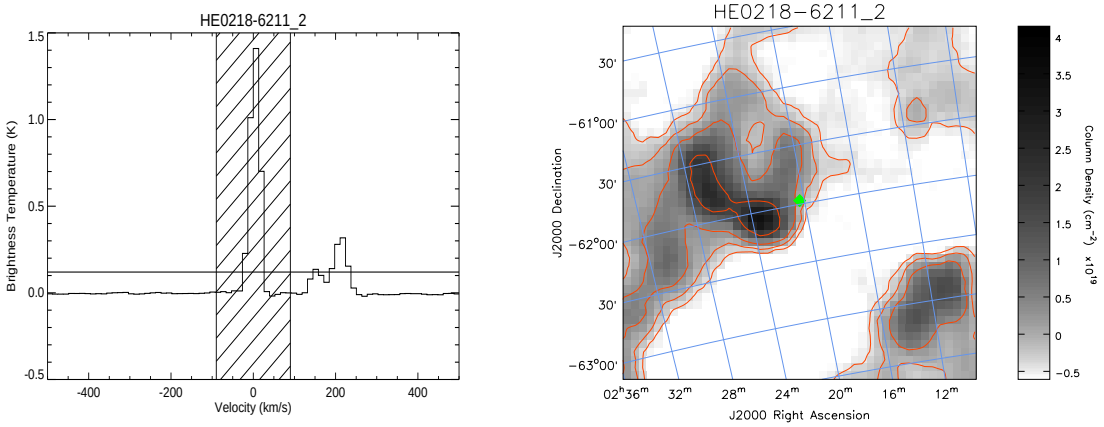


Figure B.194: HE 0218−6211_2

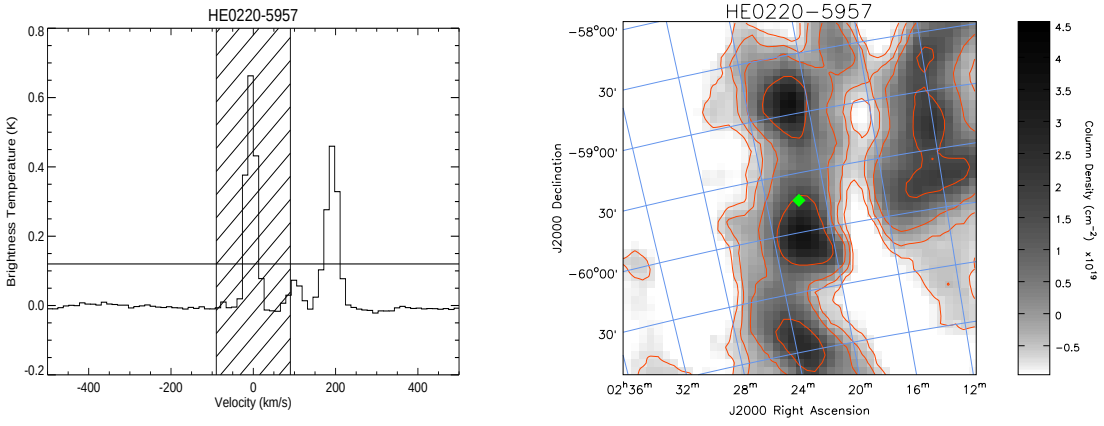


Figure B.195: HE 0220−5957

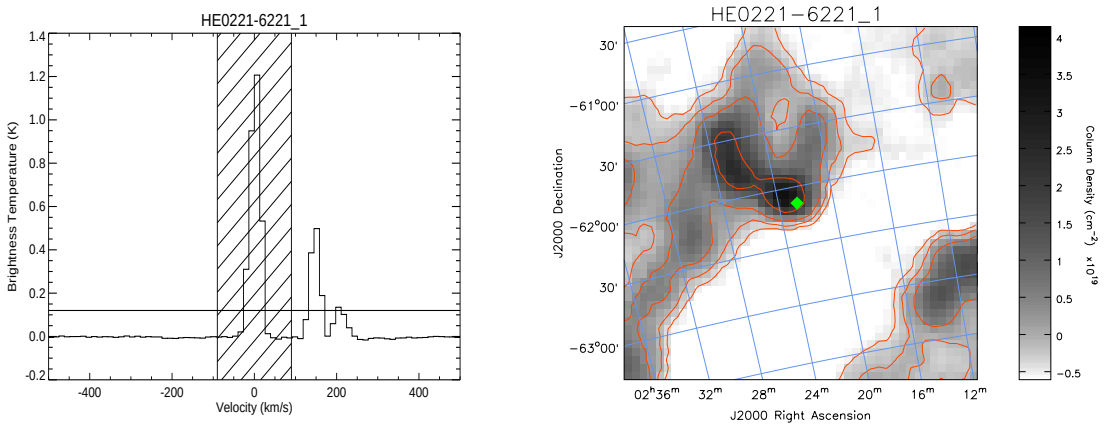


Figure B.196: HE 0221−6221_1

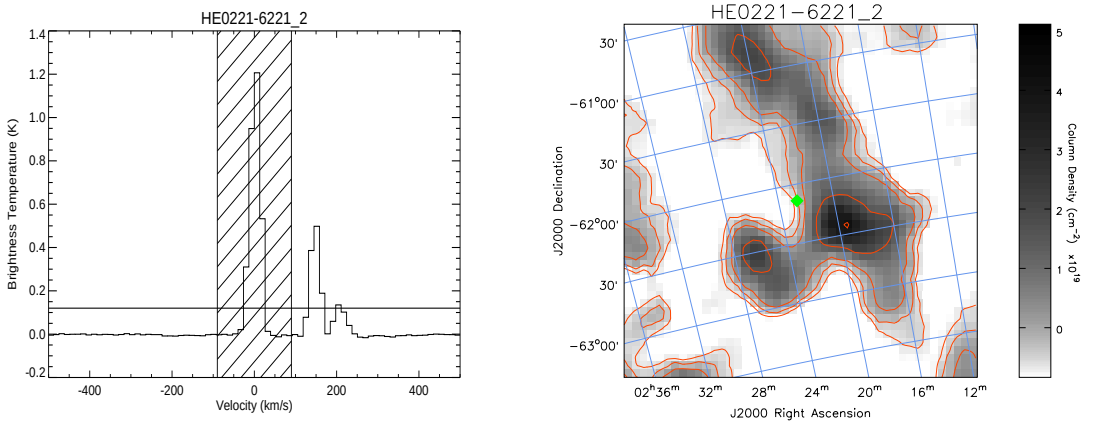


Figure B.197: HE 0221−6221_2

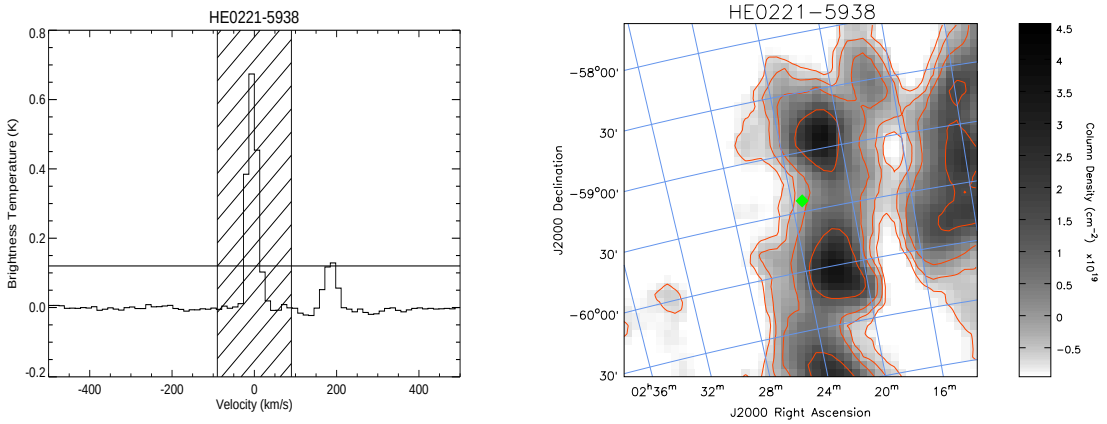
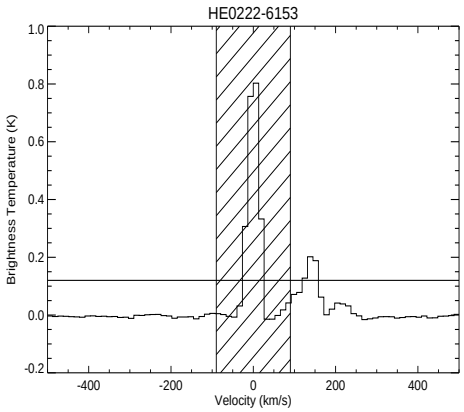


Figure B.198: HE 0221−5938



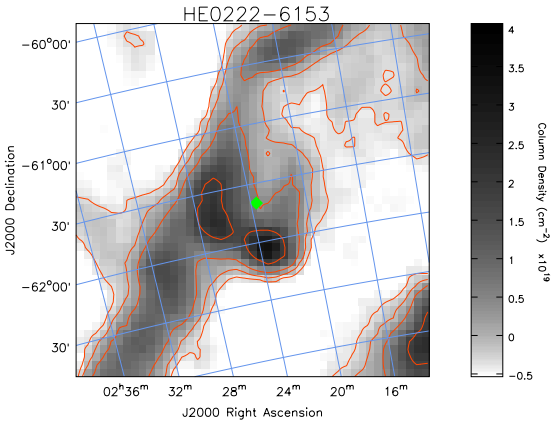
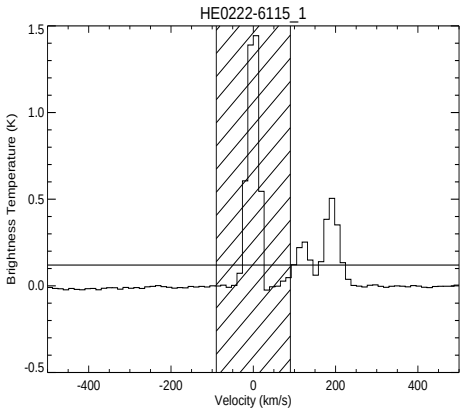


Figure B.199: HE 0222−6153



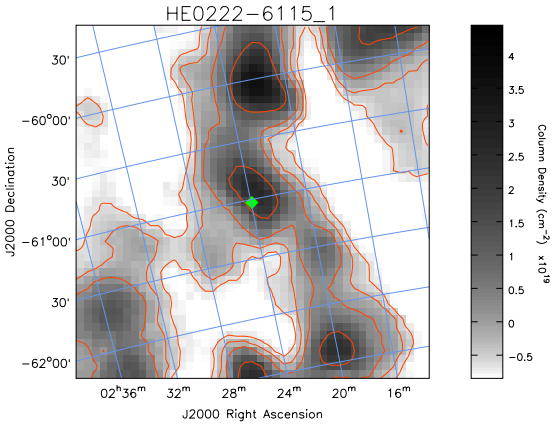
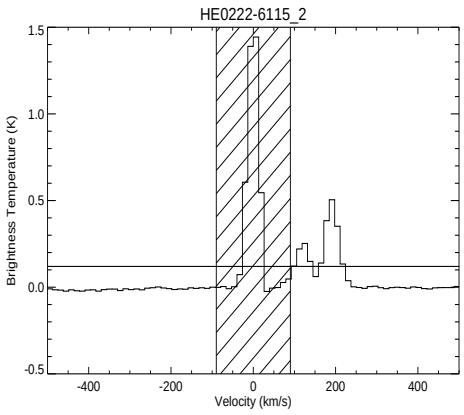


Figure B.200: HE 0222−6115_1



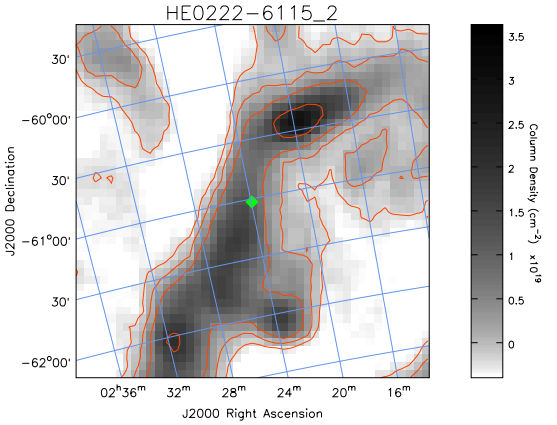


Figure B.201: HE 0222−6115_2

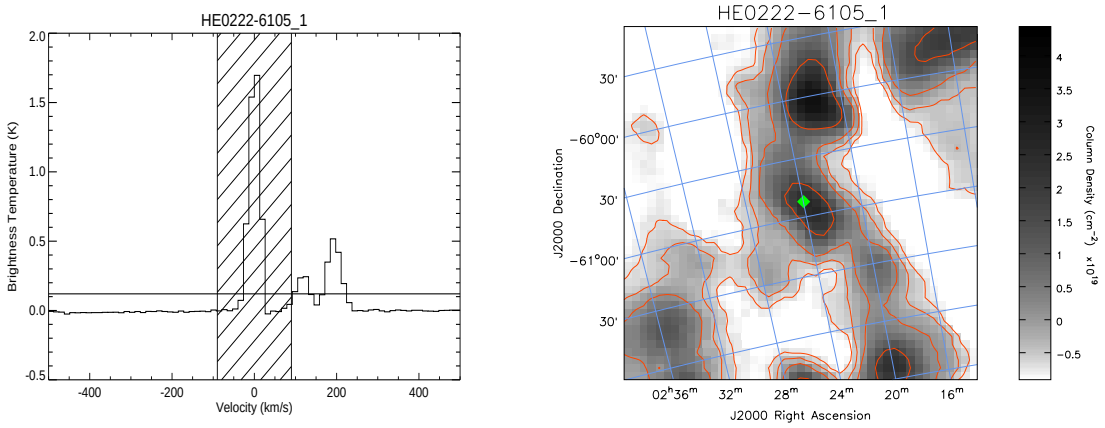


Figure B.202: HE 0222−6105_1

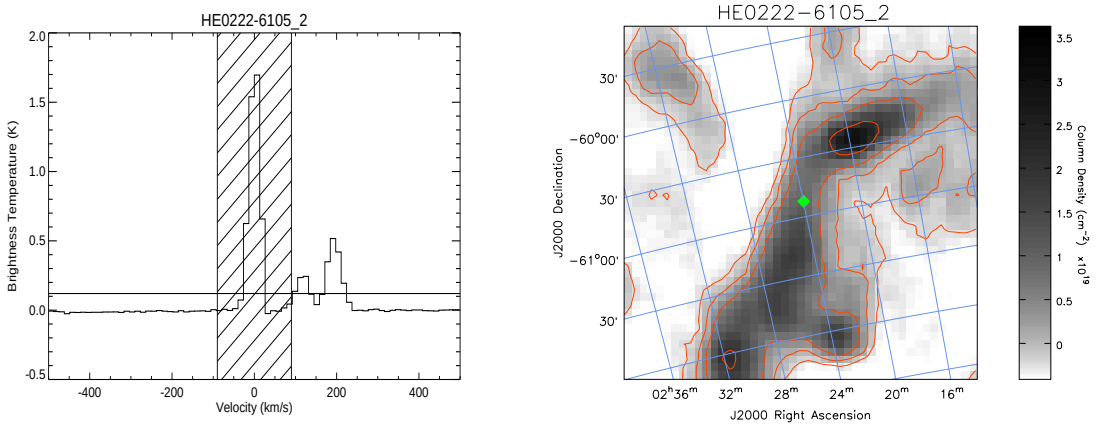


Figure B.203: HE 0222−6105_2

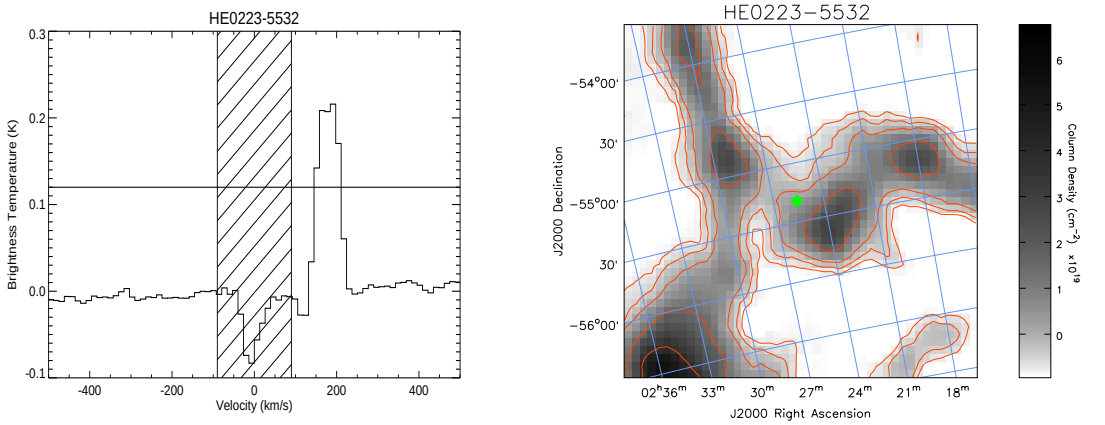
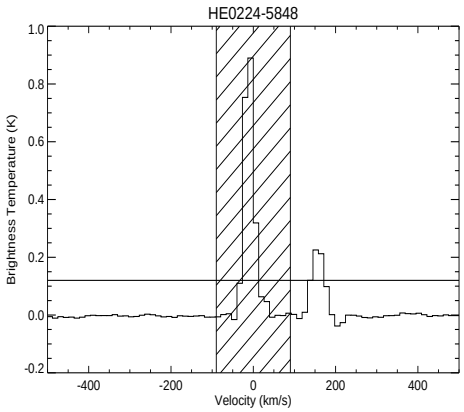


Figure B.204: HE 0223−5532



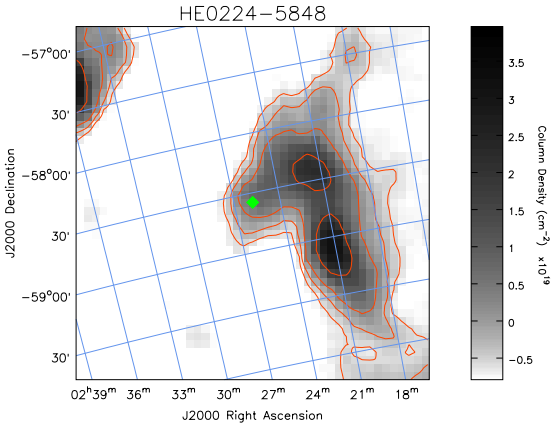
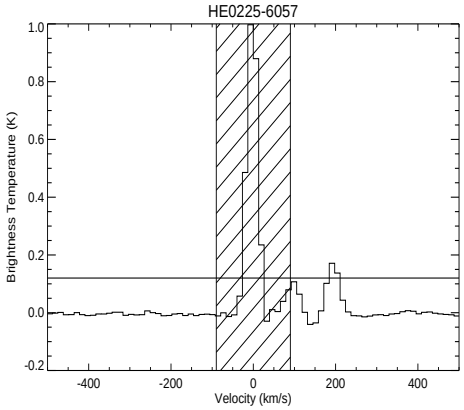


Figure B.205: HE 0224−5848



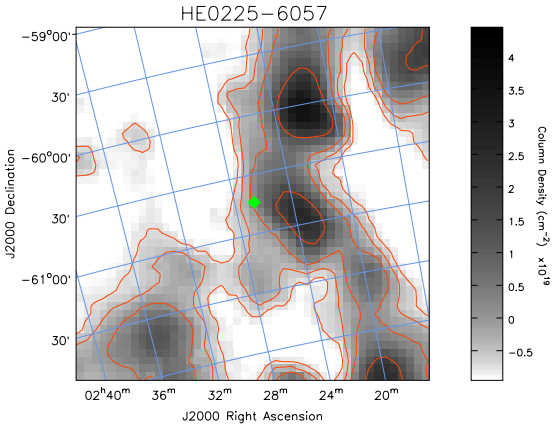
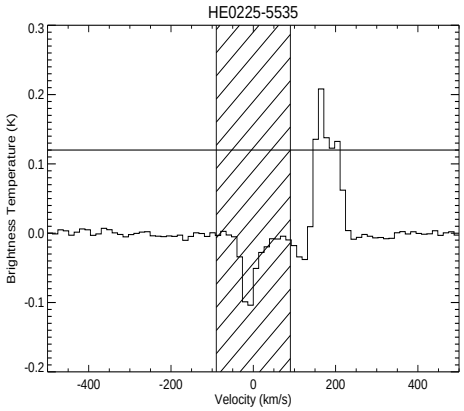


Figure B.206: HE 0225−6057



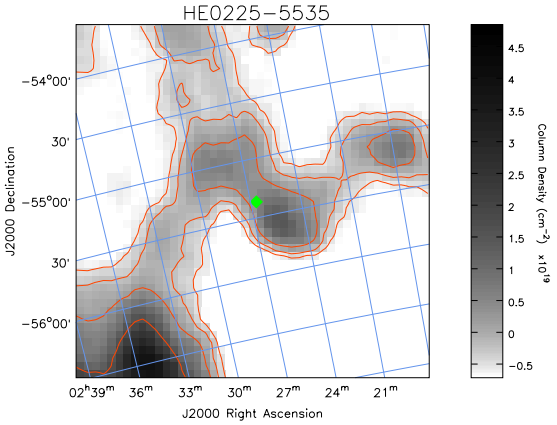


Figure B.207: HE 0225−5535

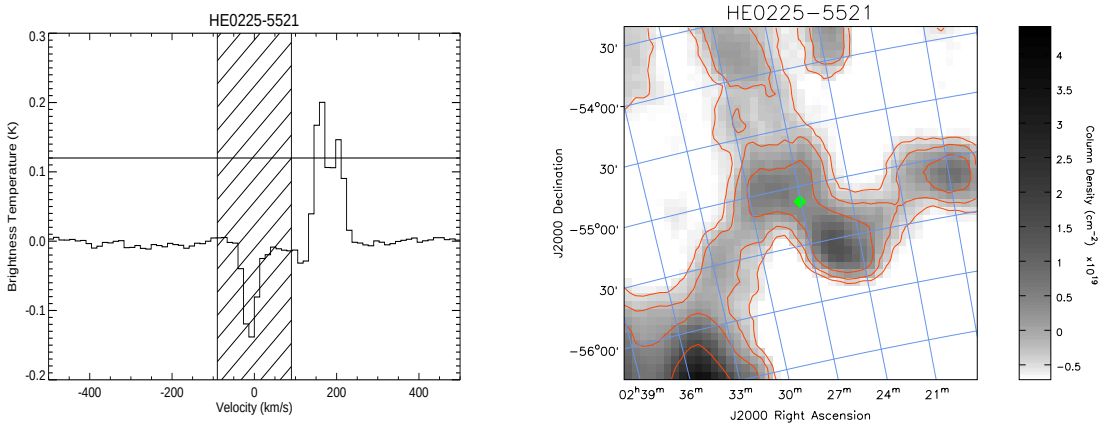


Figure B.208: HE 0225−5521

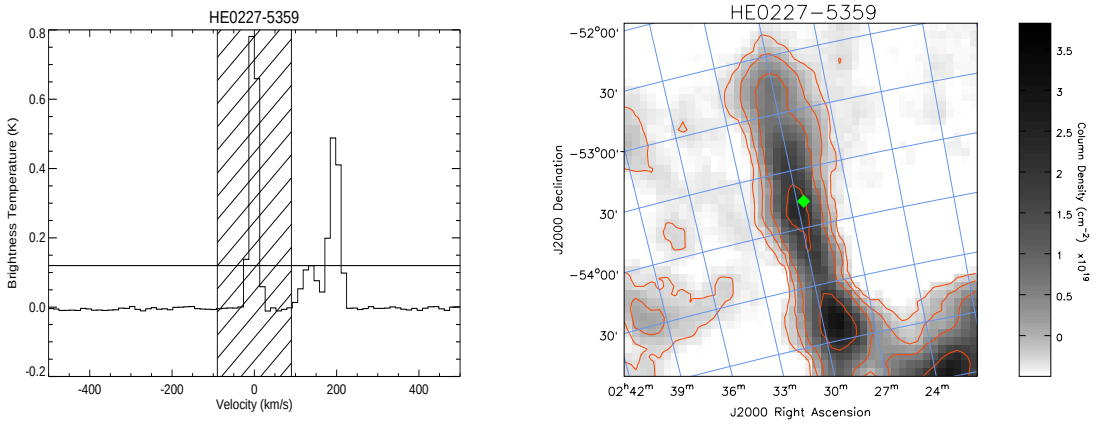


Figure B.209: HE 0227−5359

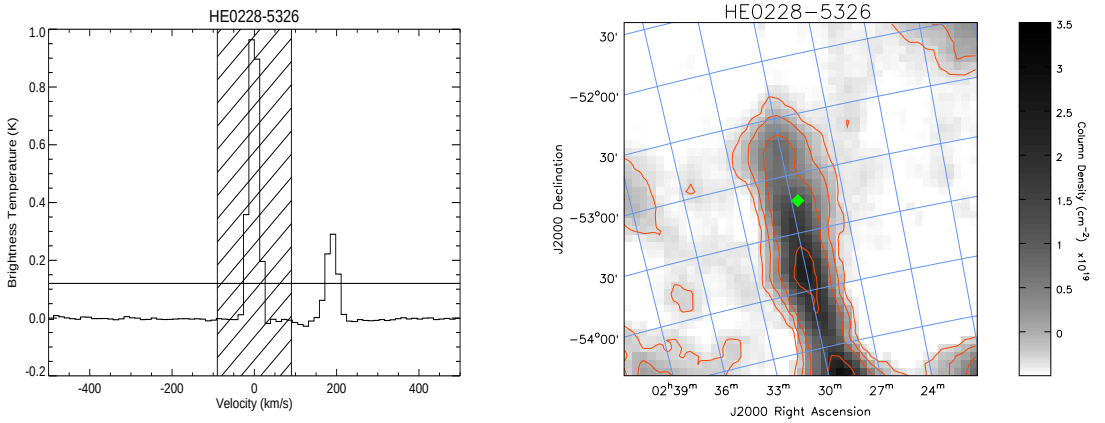


Figure B.210: HE 0228−5326

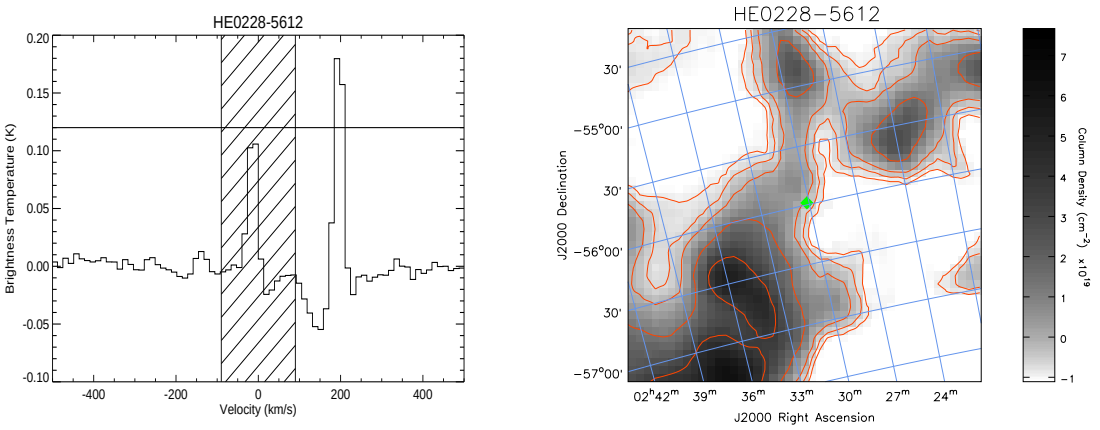


Figure B.211: HE 0228−5612

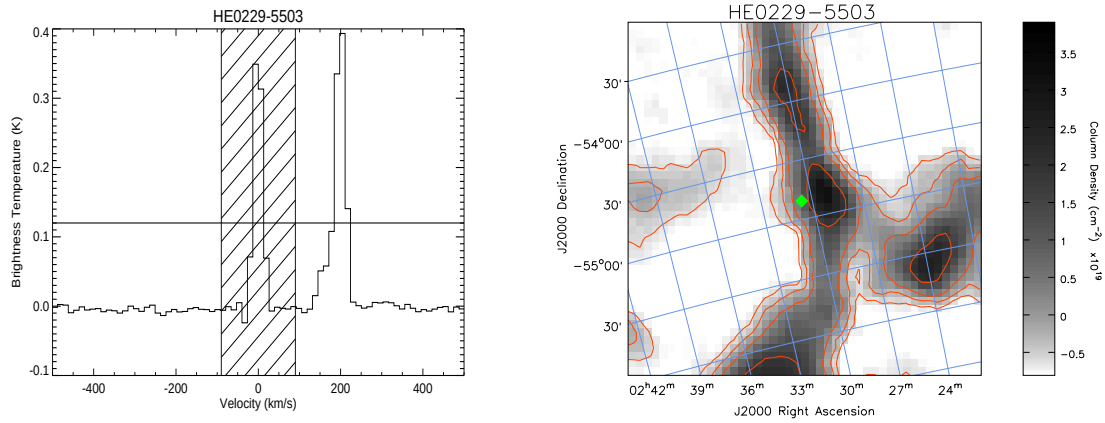


Figure B.212: HE 0229−5503

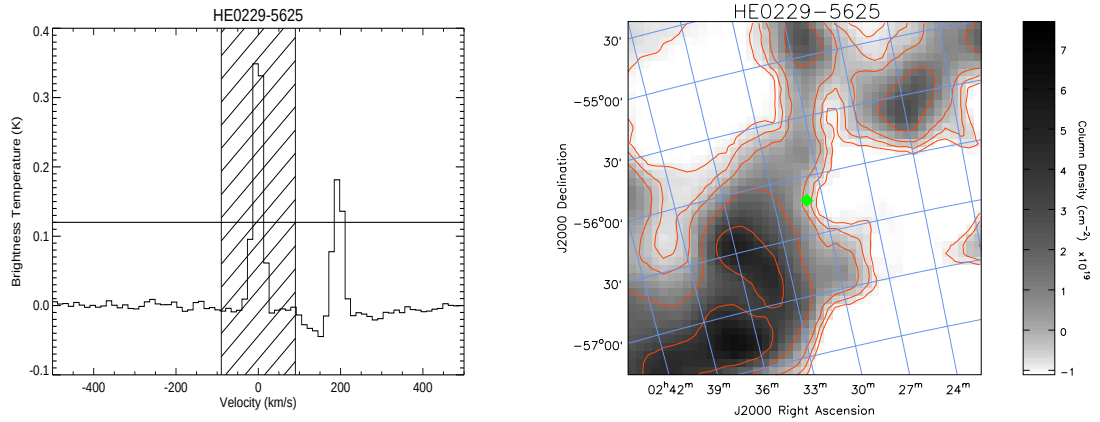


Figure B.213: HE 0229−5625

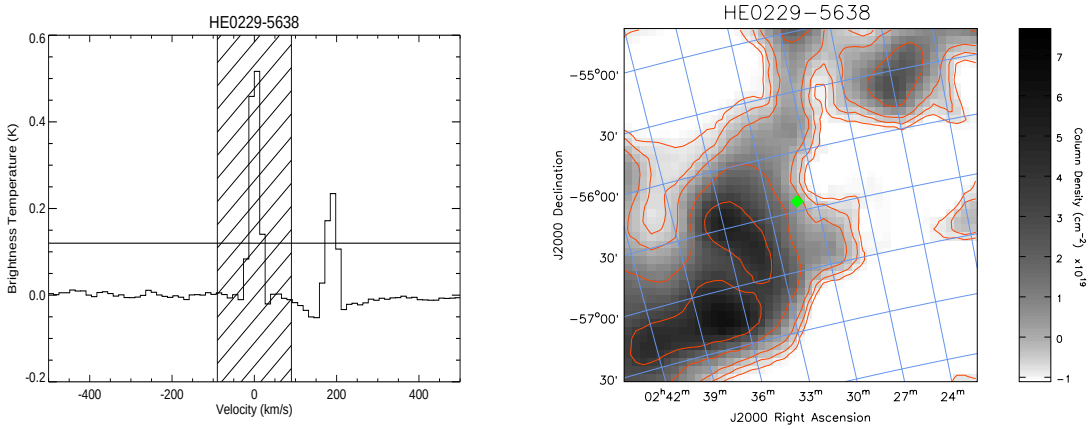


Figure B.214: HE 0229−5638

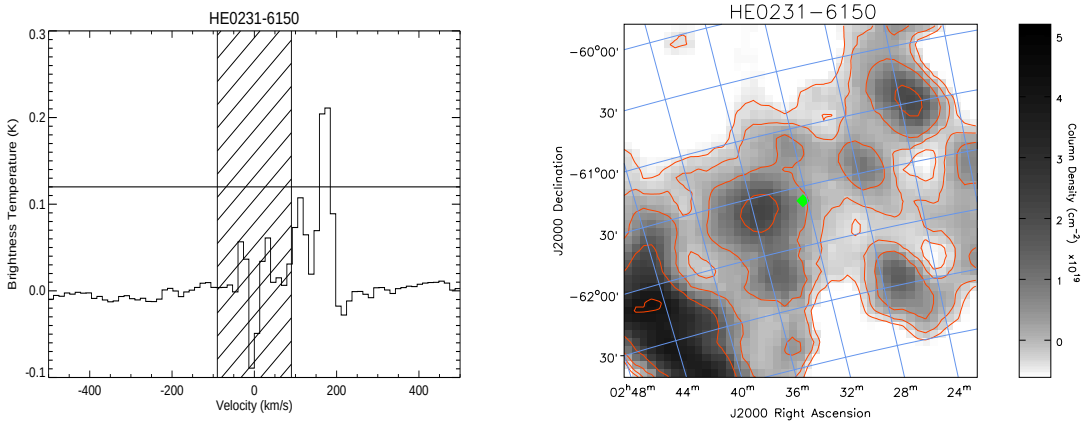


Figure B.215: HE 0231−6150

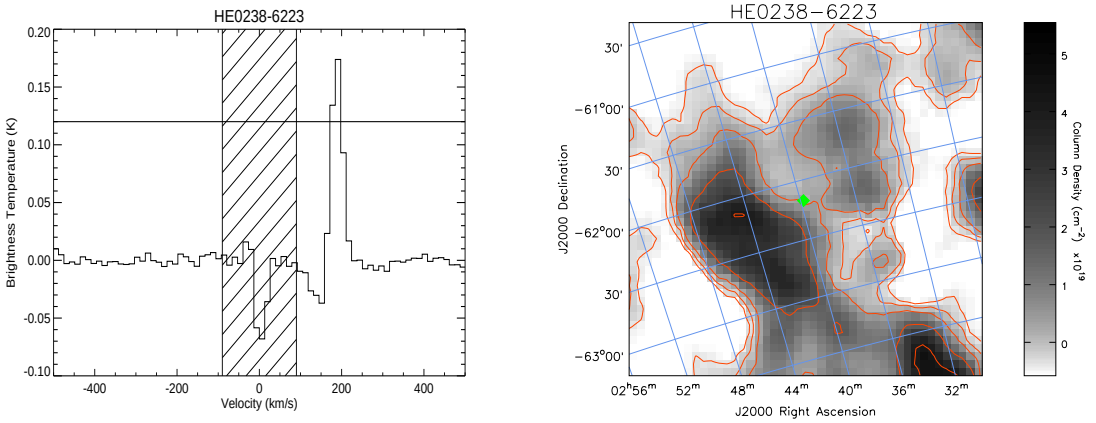


Figure B.216: HE 0238−6223

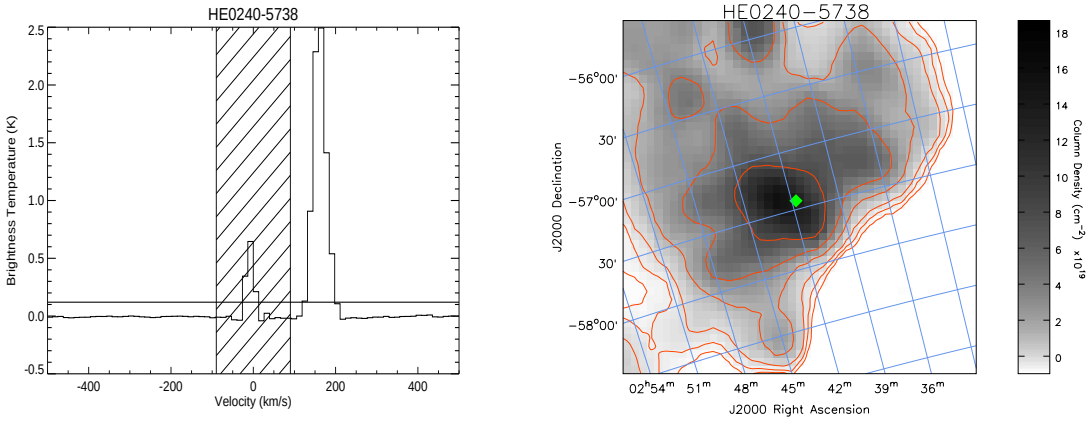


Figure B.217: HE 0240−5738

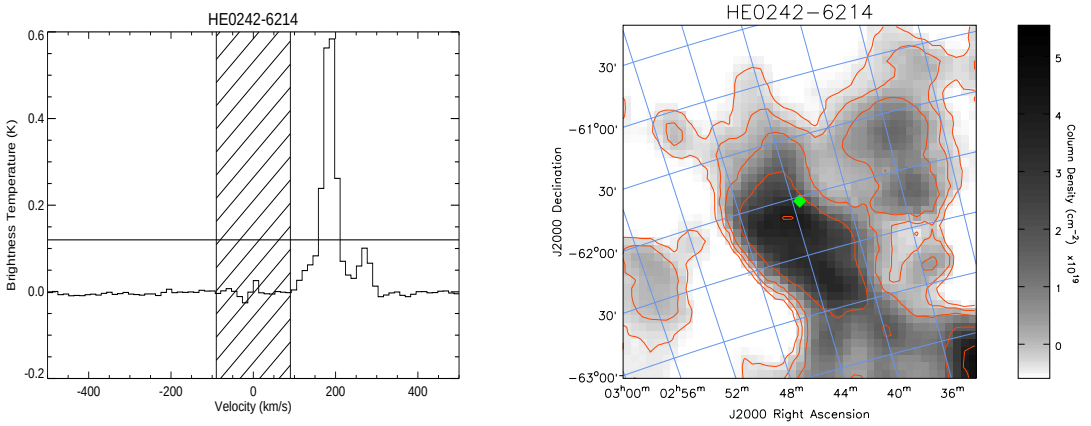


Figure B.218: HE 0242−6214

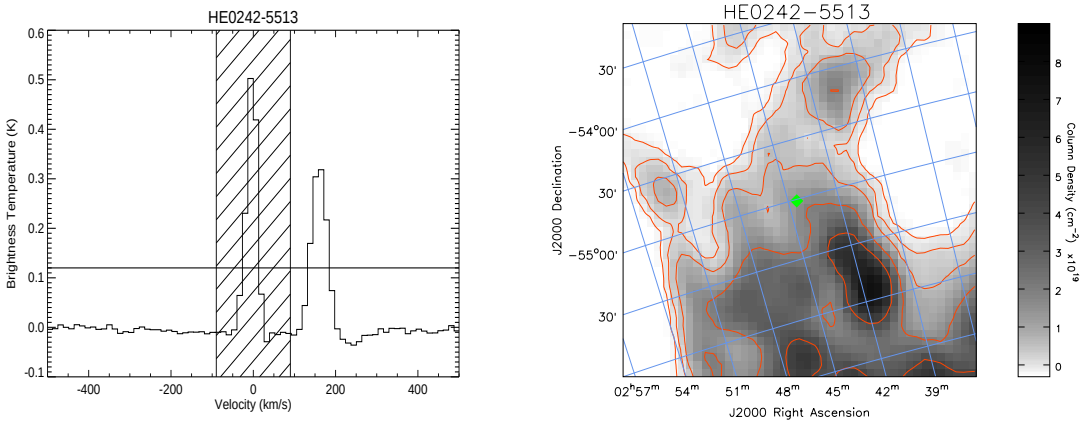


Figure B.219: HE 0242−5513

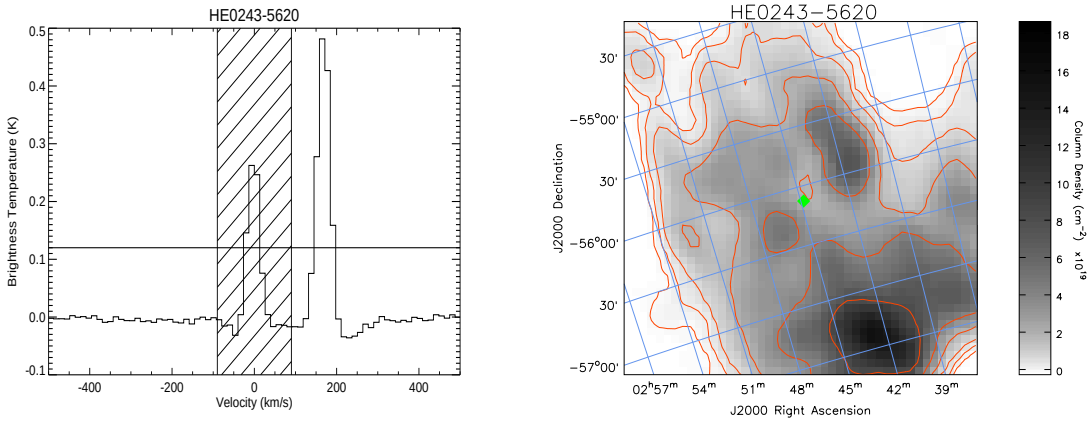


Figure B.220: HE 0243−5620

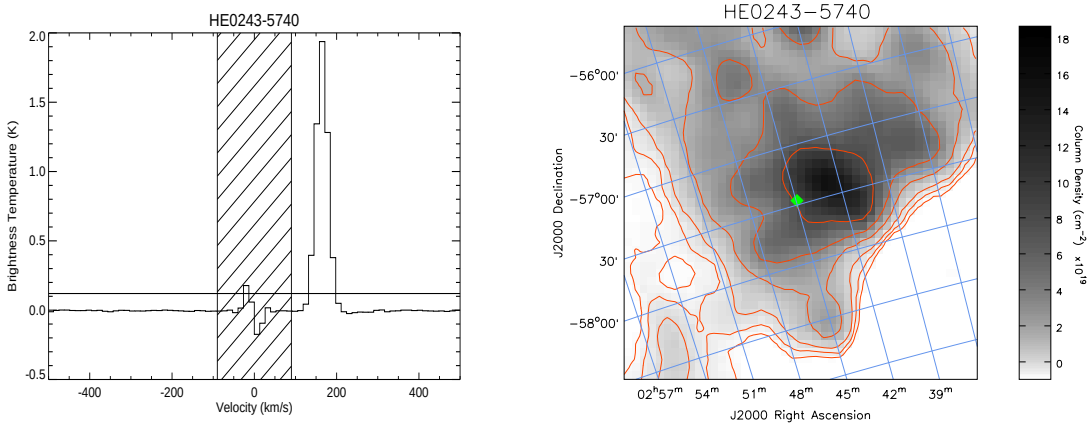


Figure B.221: HE 0243−5740

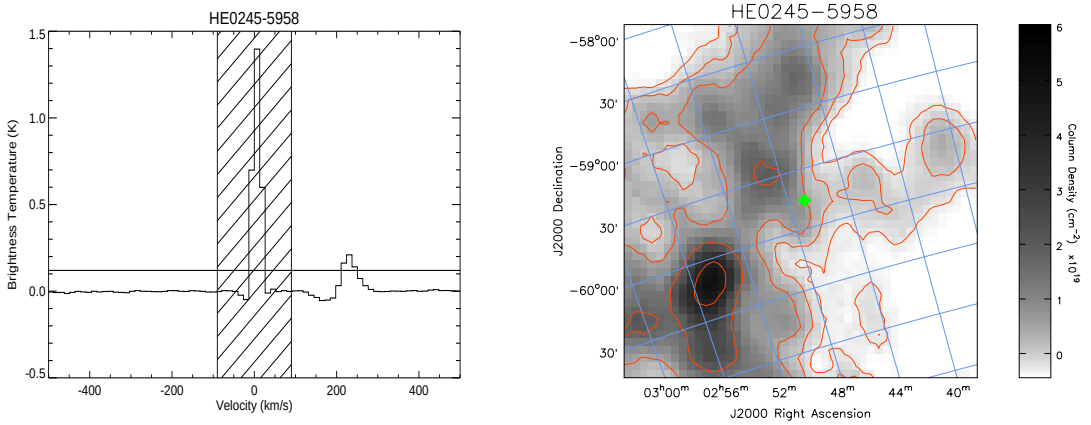


Figure B.222: HE 0245−5958

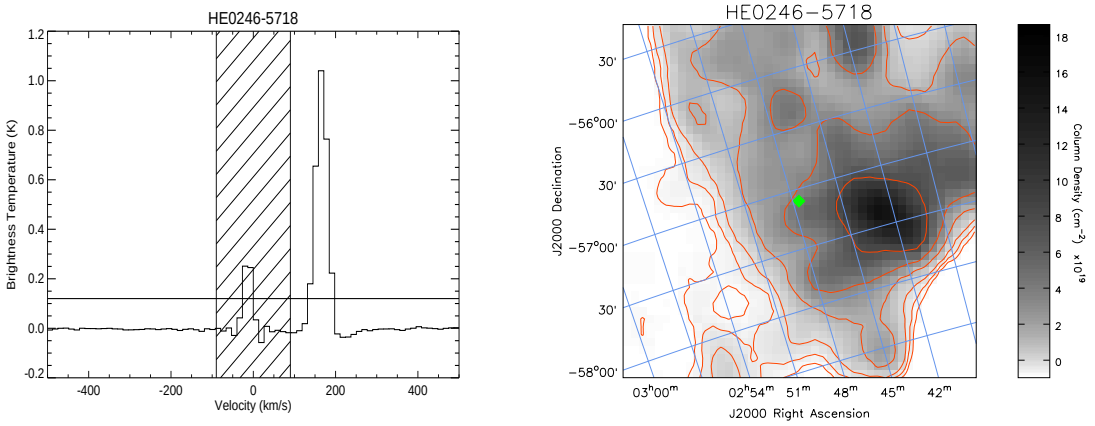


Figure B.223: HE 0246−5718

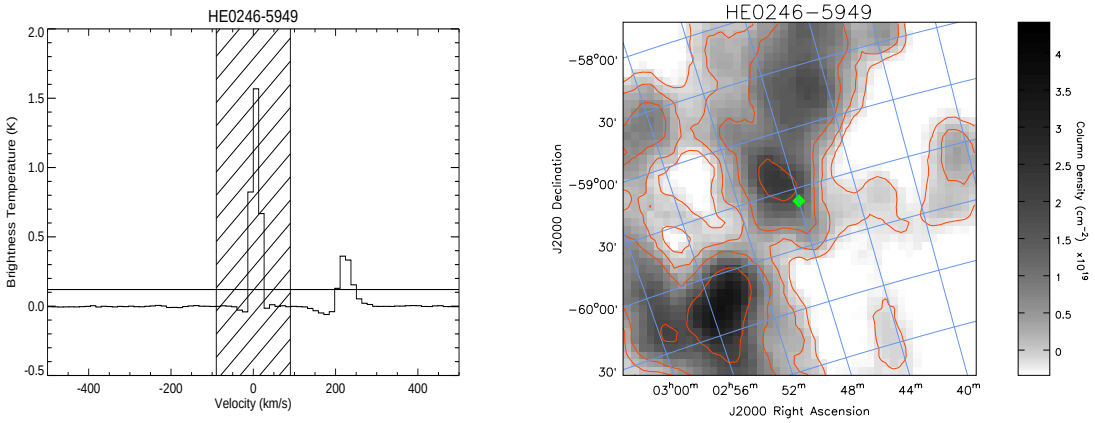


Figure B.224: HE 0246−5949

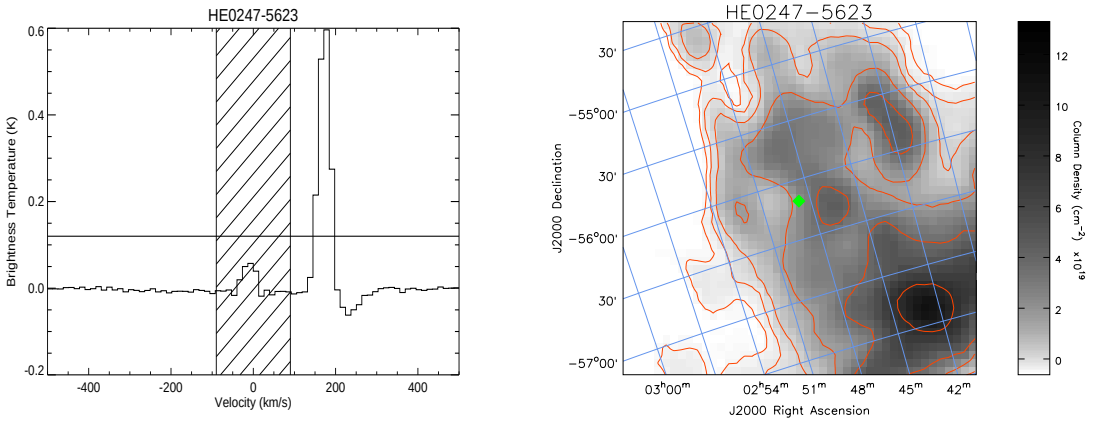


Figure B.225: HE 0247−5623

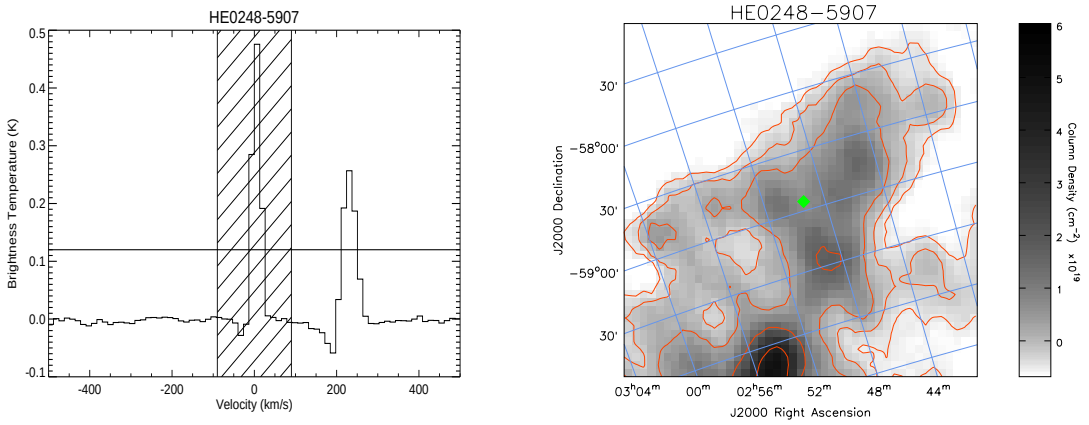


Figure B.226: HE 0248−5907

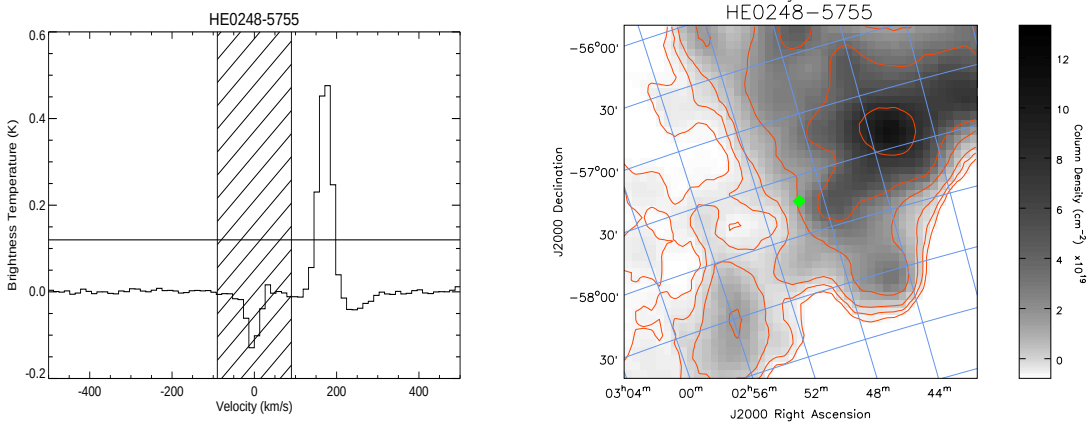


Figure B.227: HE 0248−5755

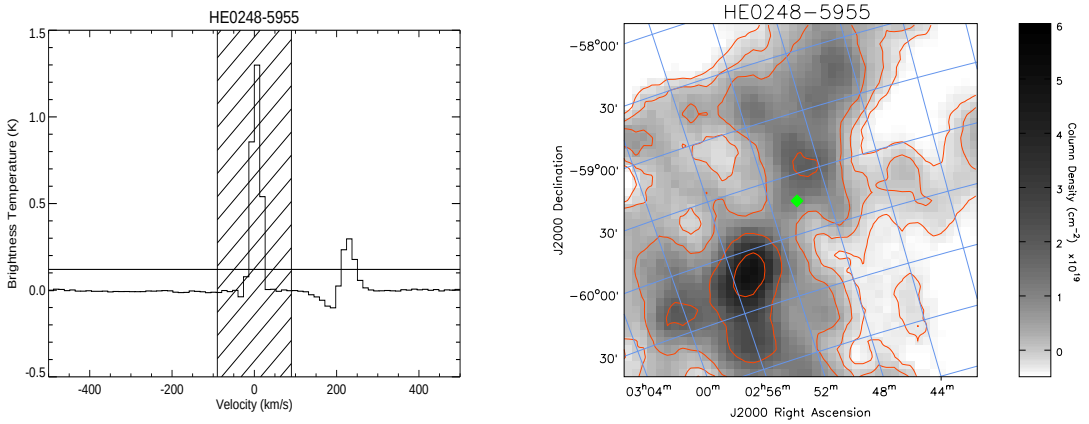


Figure B.228: HE 0248−5955

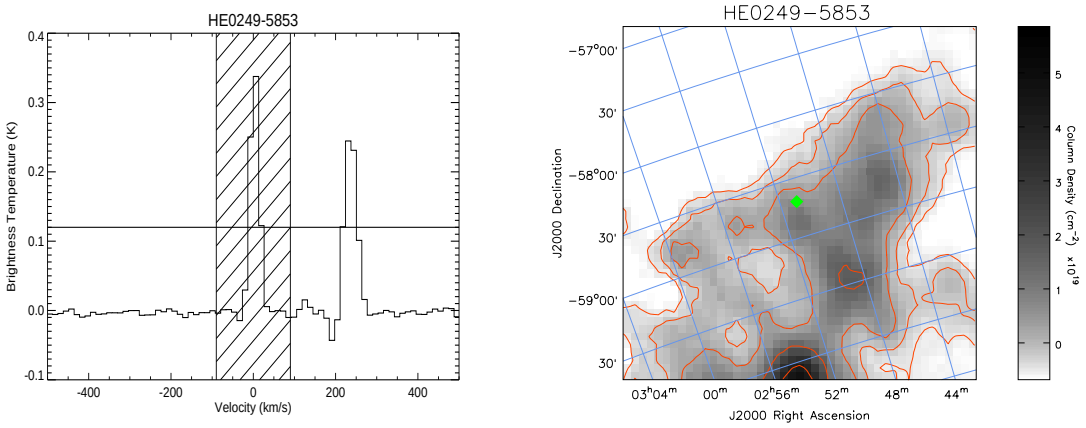


Figure B.229: HE 0249−5853

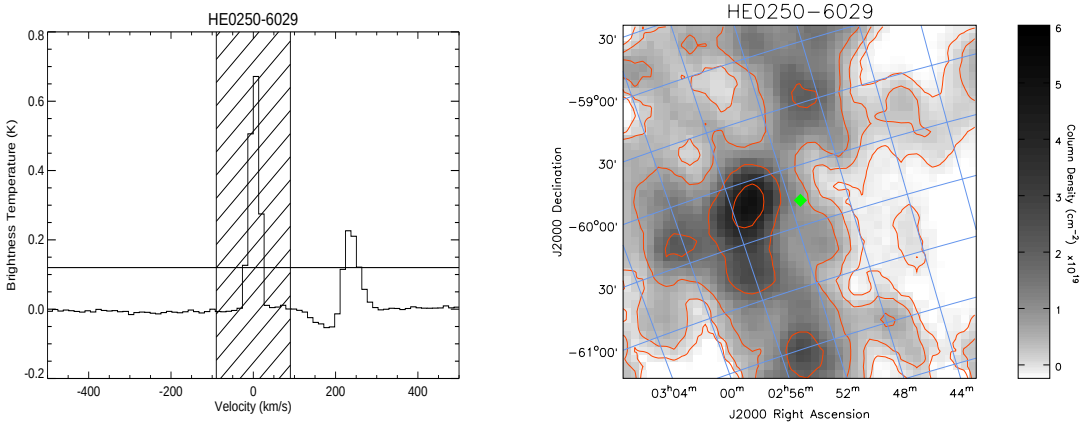


Figure B.230: HE 0250−6029

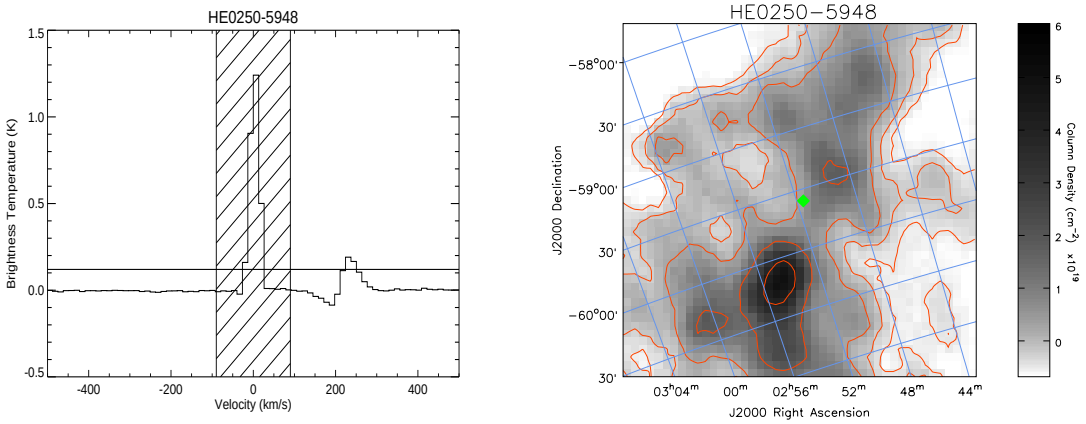


Figure B.231: HE 0250−5948

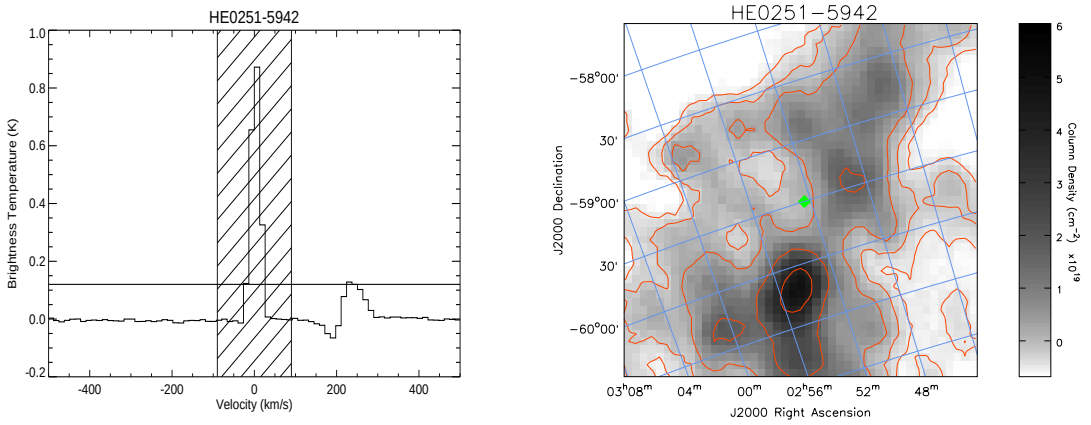


Figure B.232: HE 0251−5942

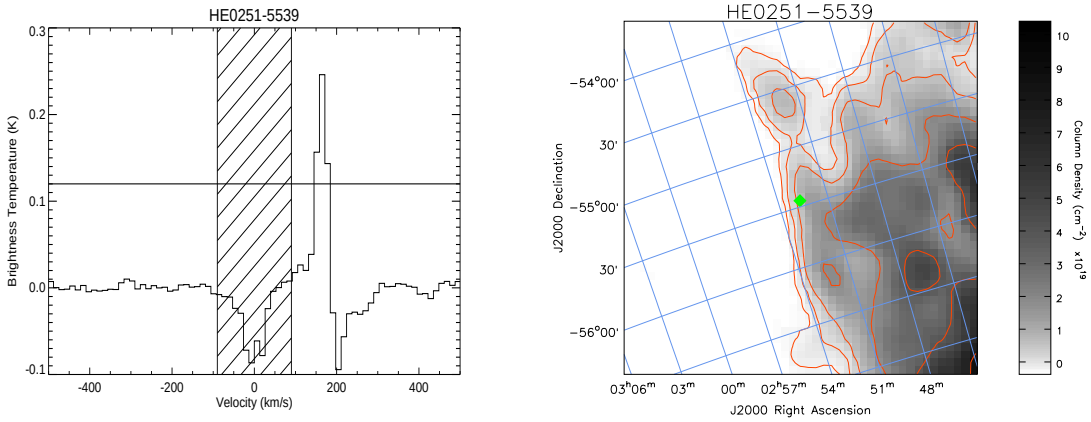


Figure B.233: HE 0251−5539

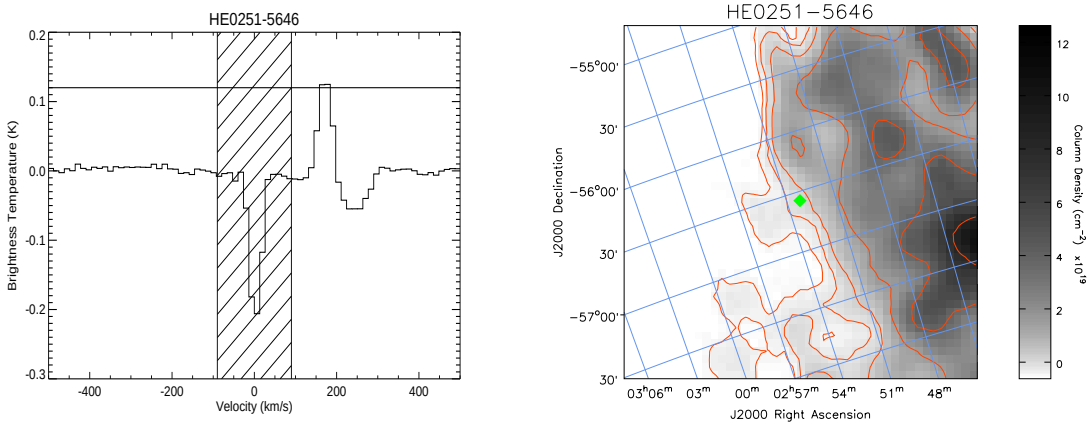


Figure B.234: HE 0251−5646

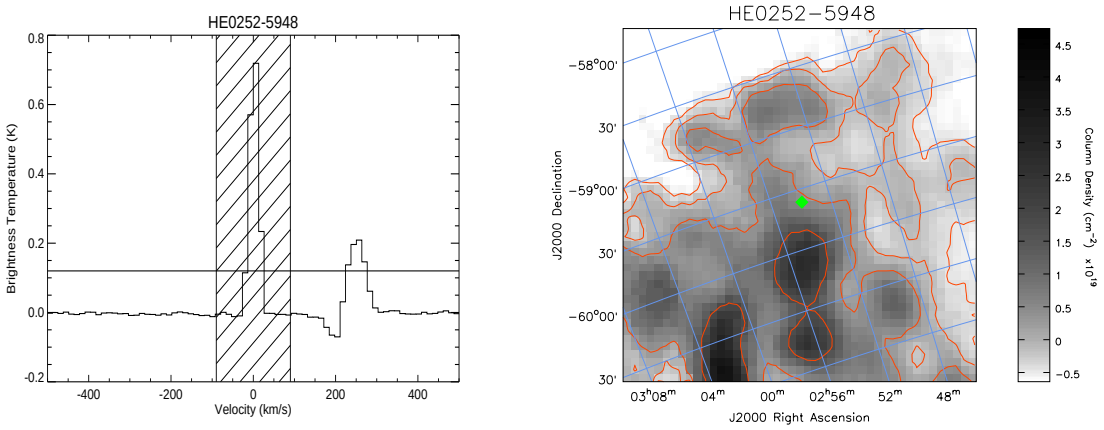


Figure B.235: HE 0252−5948

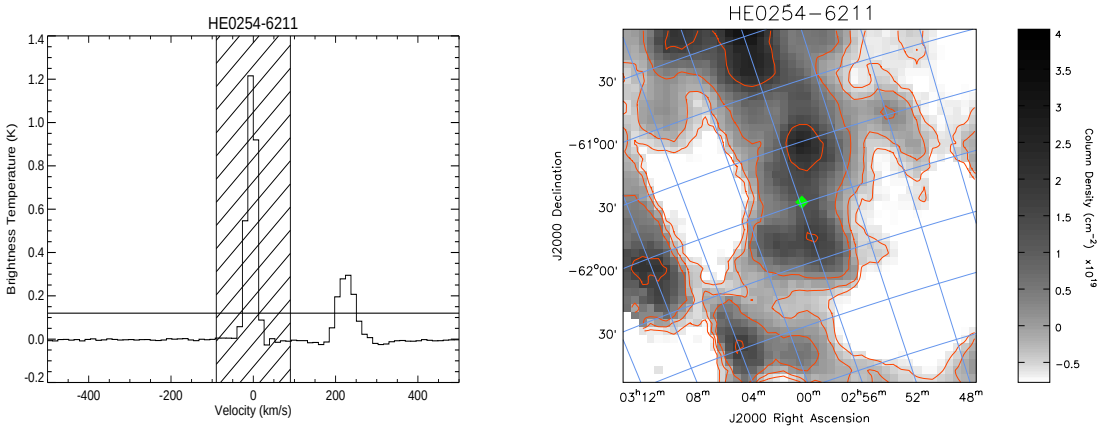


Figure B.236: HE 0254−6211

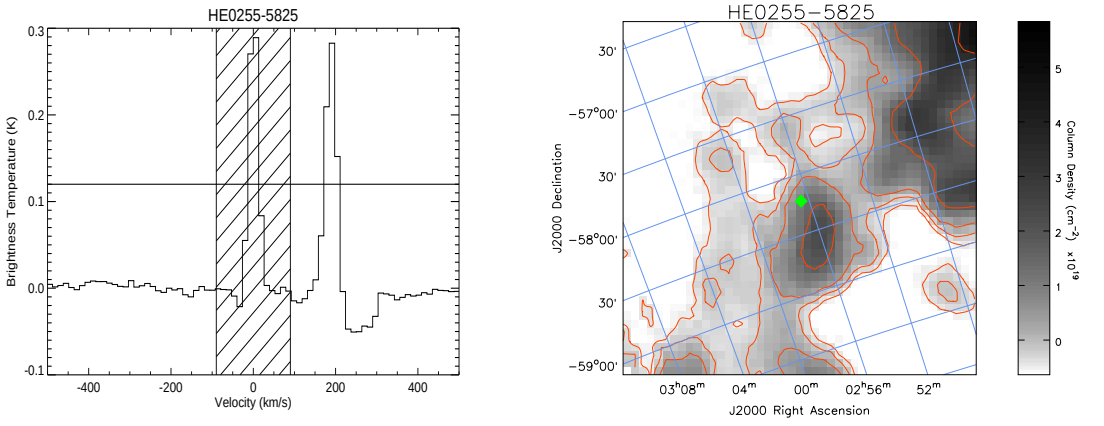


Figure B.237: HE 0255−5825

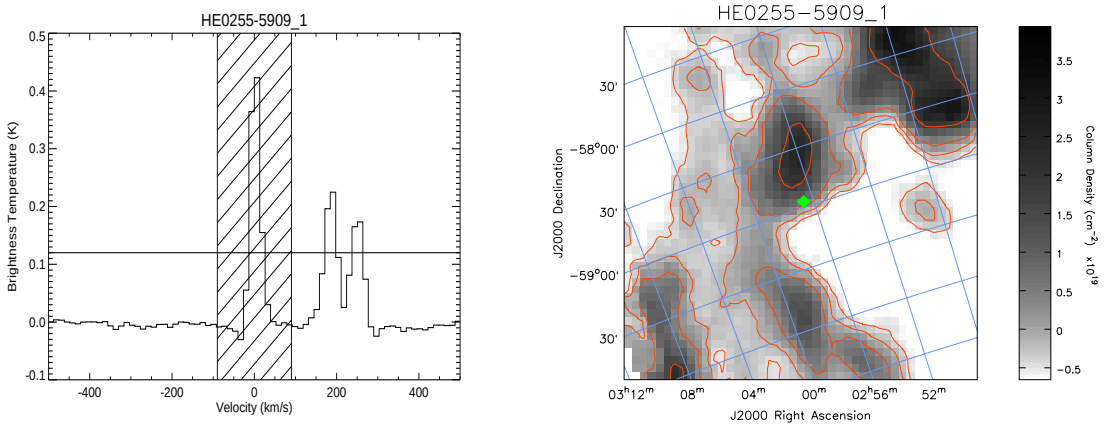


Figure B.238: HE 0255−5909_1

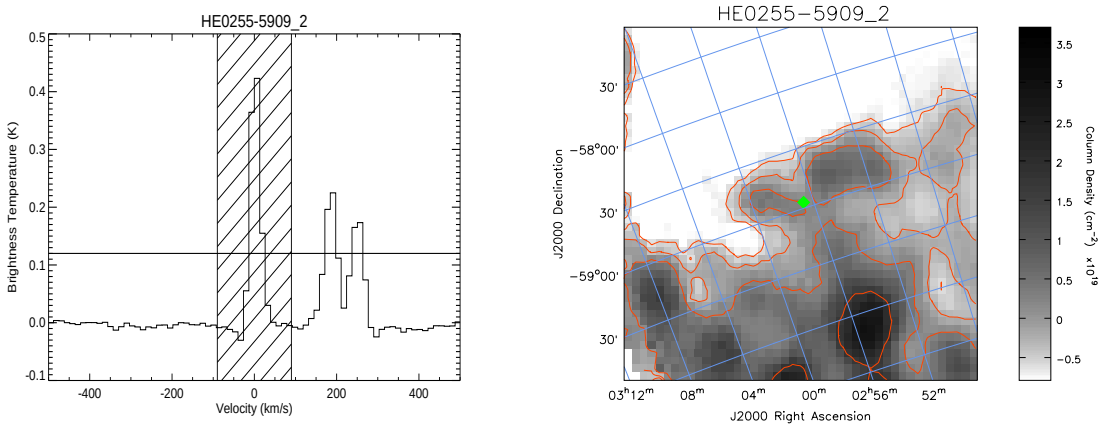


Figure B.239: HE 0255−5909_2

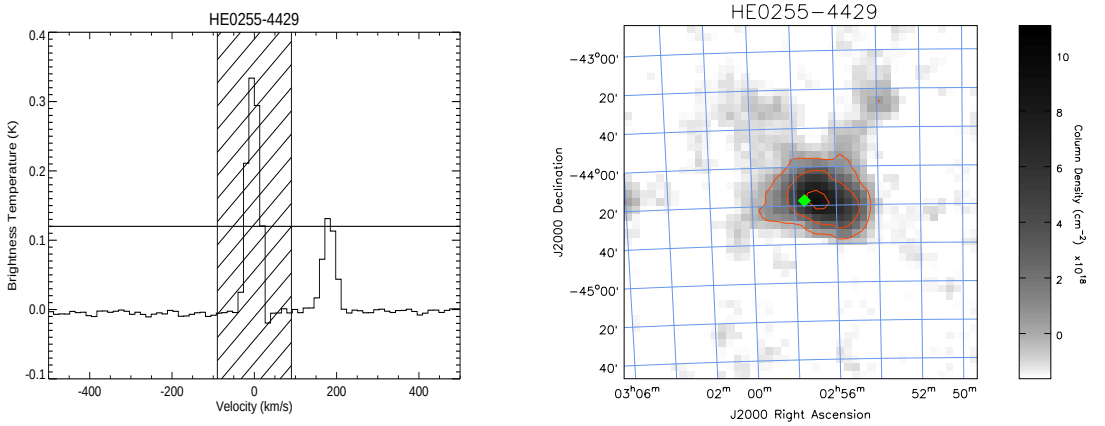


Figure B.240: HE 0255−4429

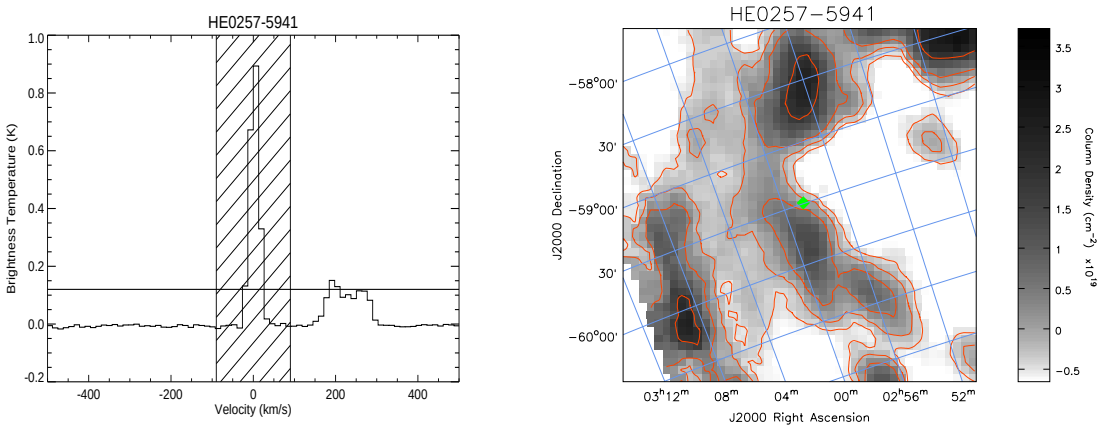


Figure B.241: HE 0257−5941

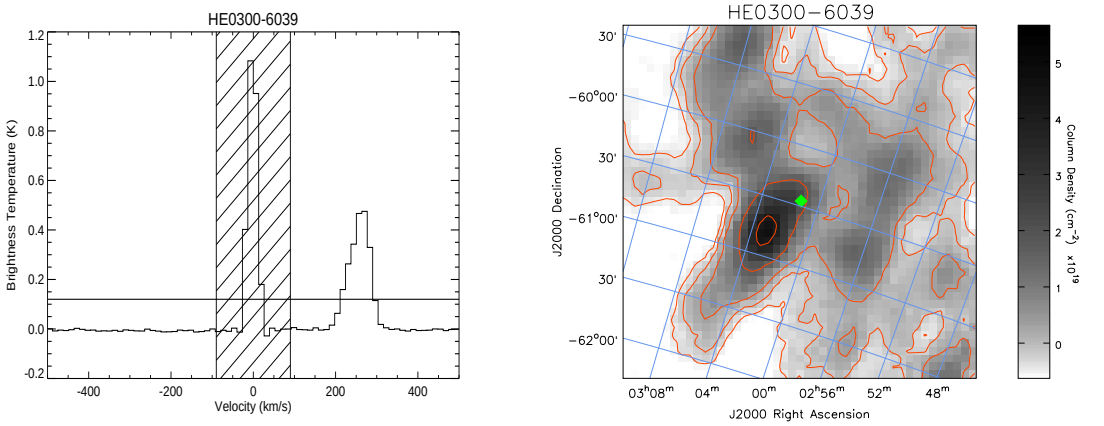


Figure B.242: HE 0300−6039

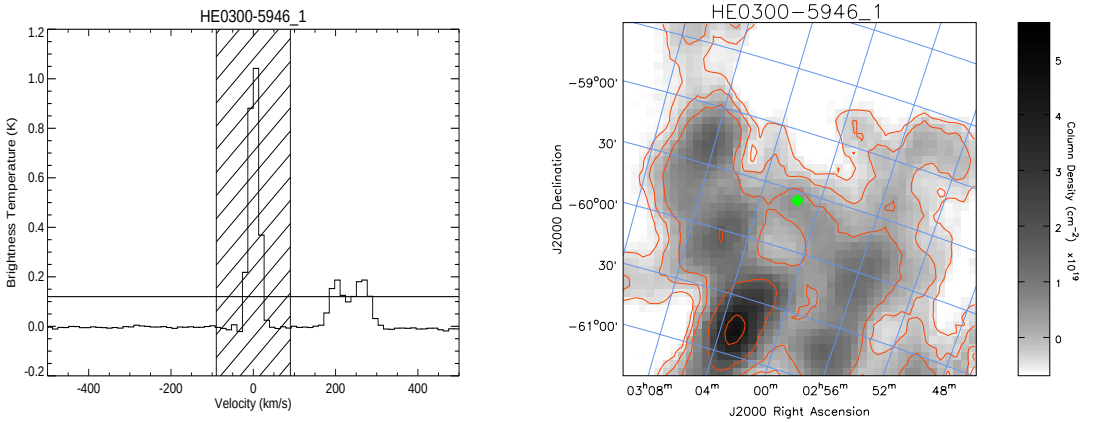


Figure B.243: HE 0300−5946_1

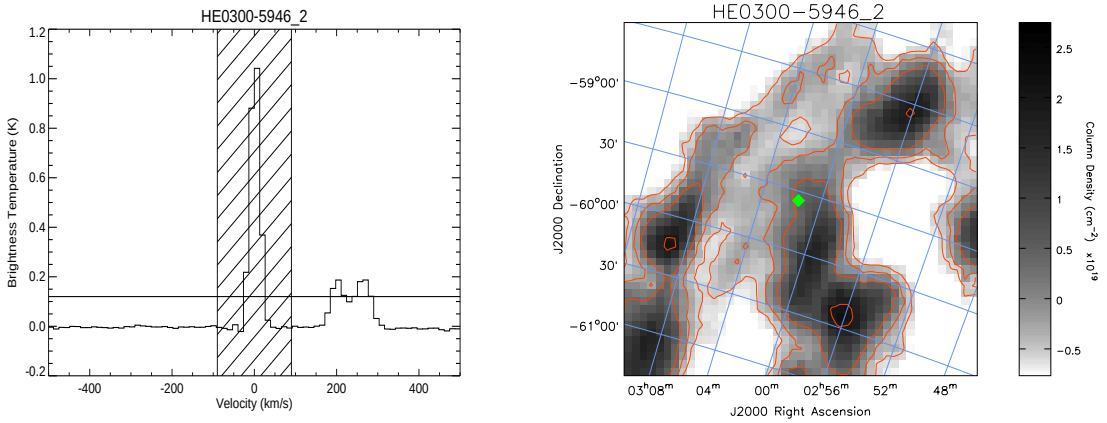


Figure B.244: HE 0300−5946_2

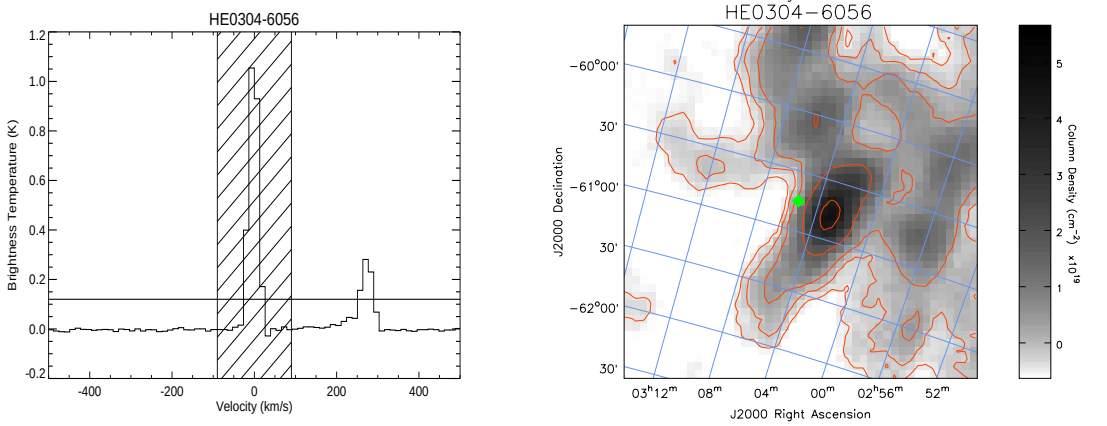


Figure B.245: HE 0304−6056

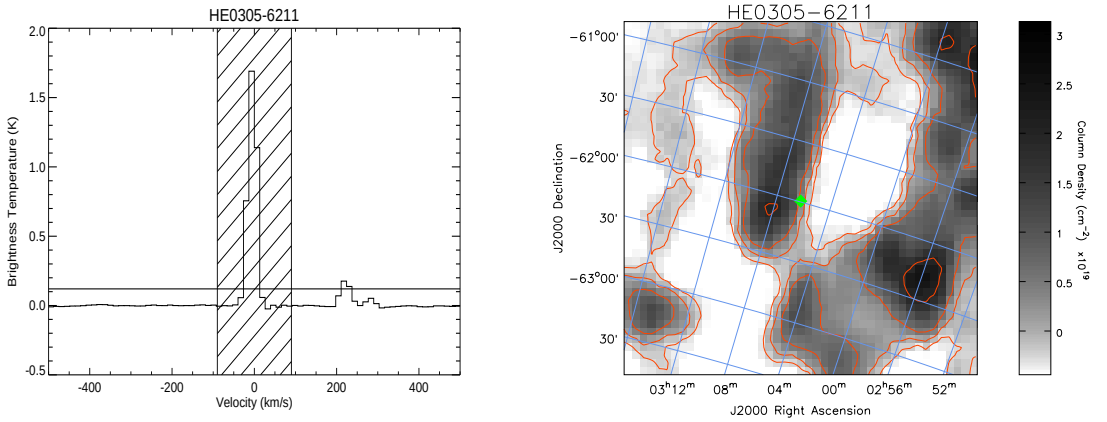
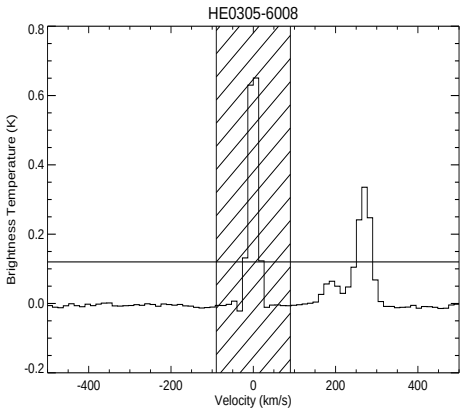


Figure B.246: HE 0305−6211



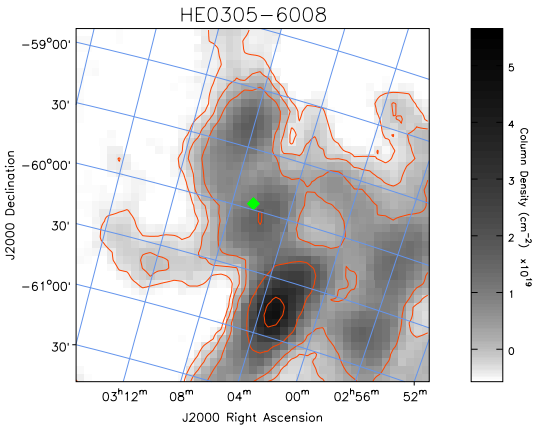
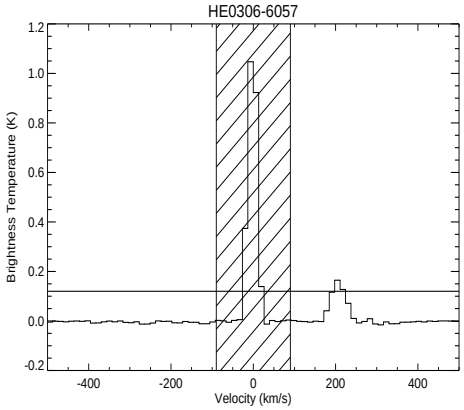


Figure B.247: HE 0305−6008



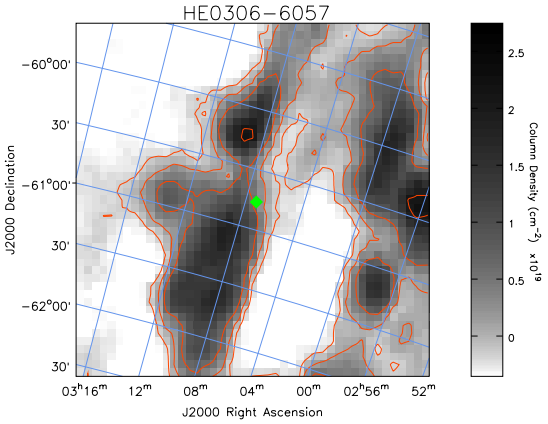
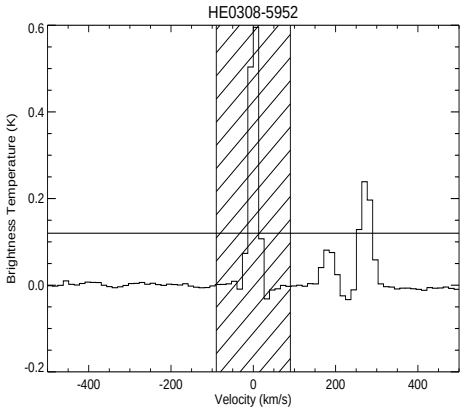


Figure B.248: HE 0306−6057



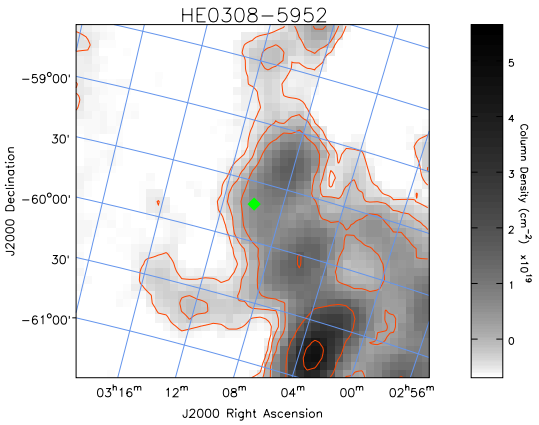


Figure B.249: HE 0308−5952

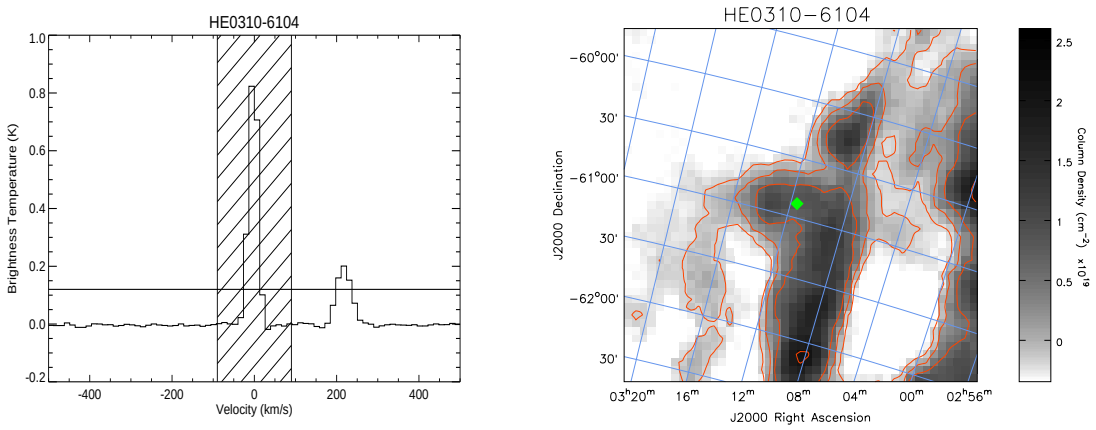


Figure B.250: HE 0310−6104

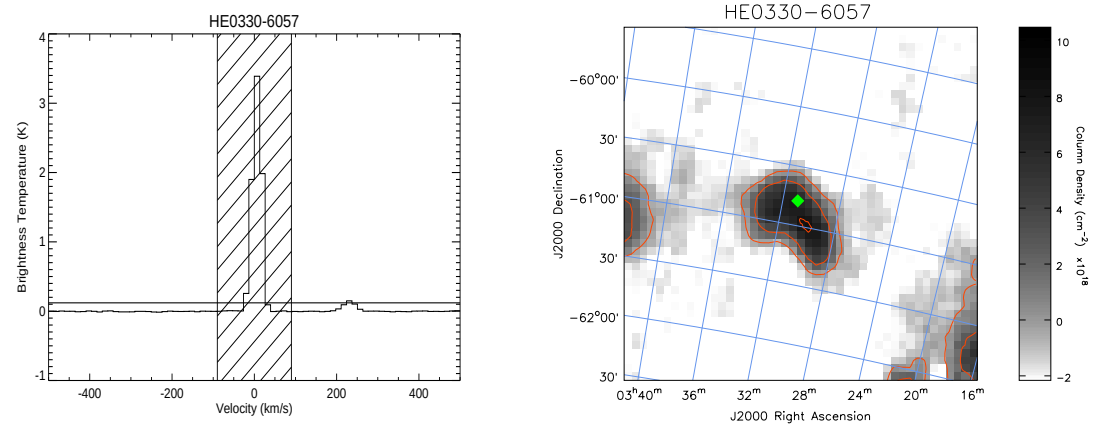


Figure B.251: HE 0330−6057

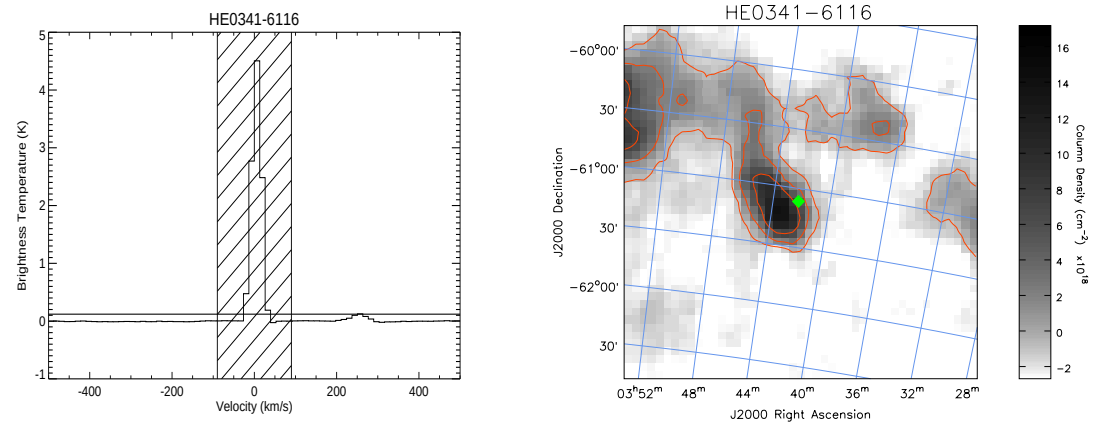


Figure B.252: HE 0341−6116

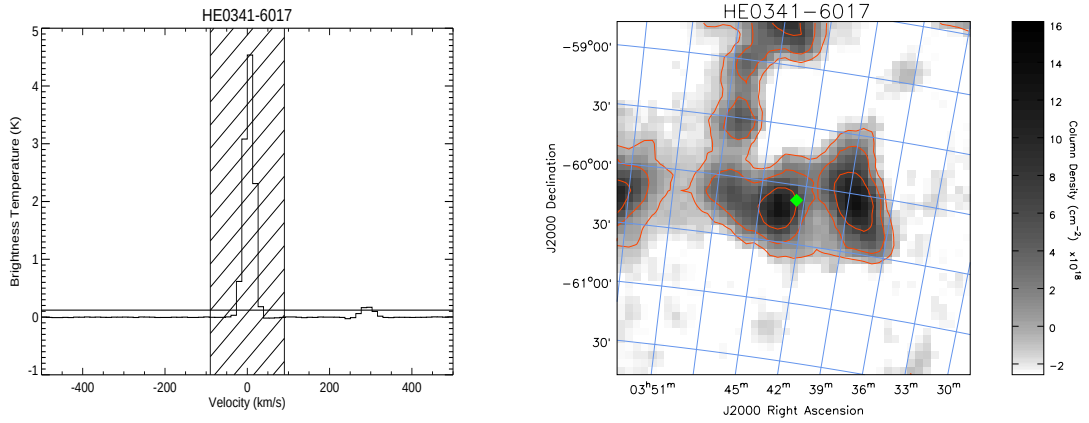


Figure B.253: HE 0341−6017

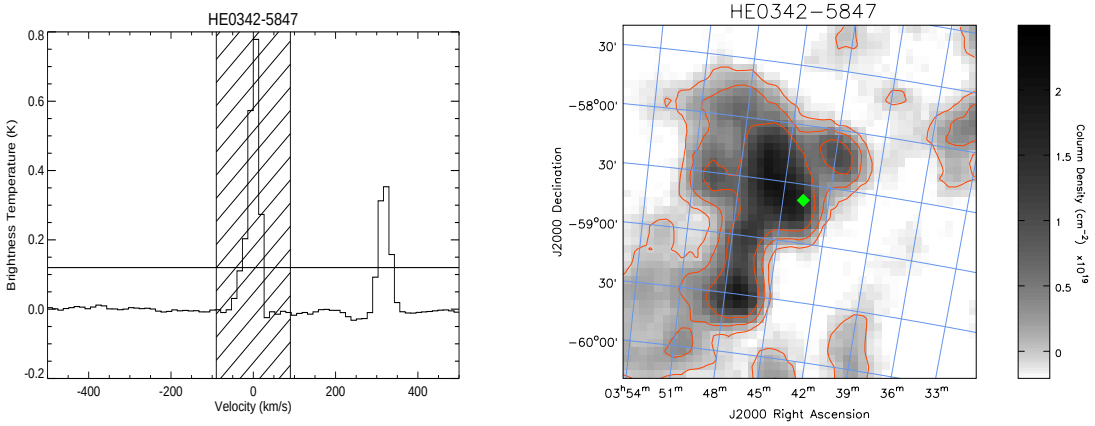


Figure B.254: HE 0342−5847

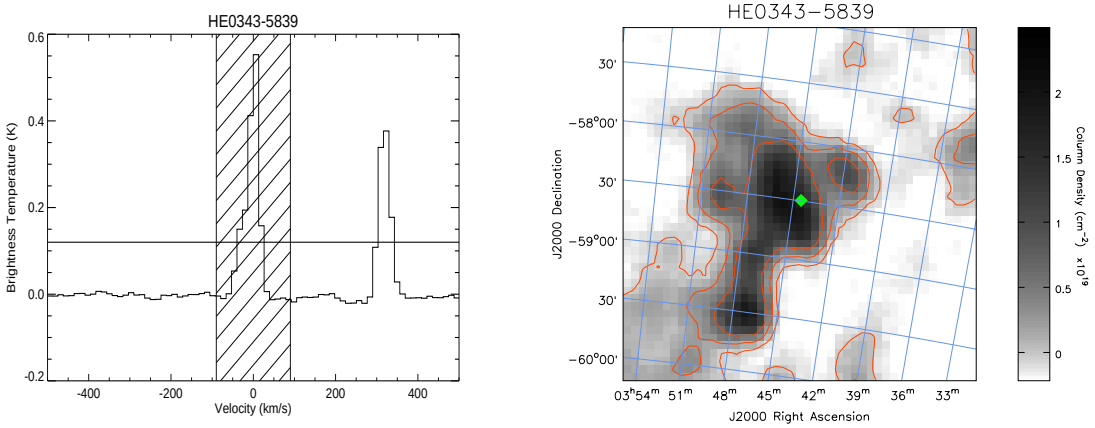


Figure B.255: HE 0343−5839

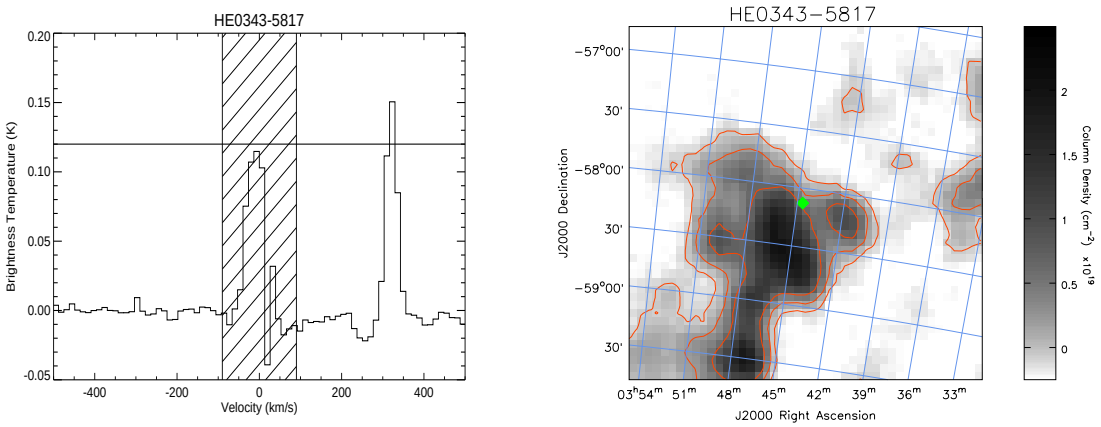


Figure B.256: HE 0343−5817

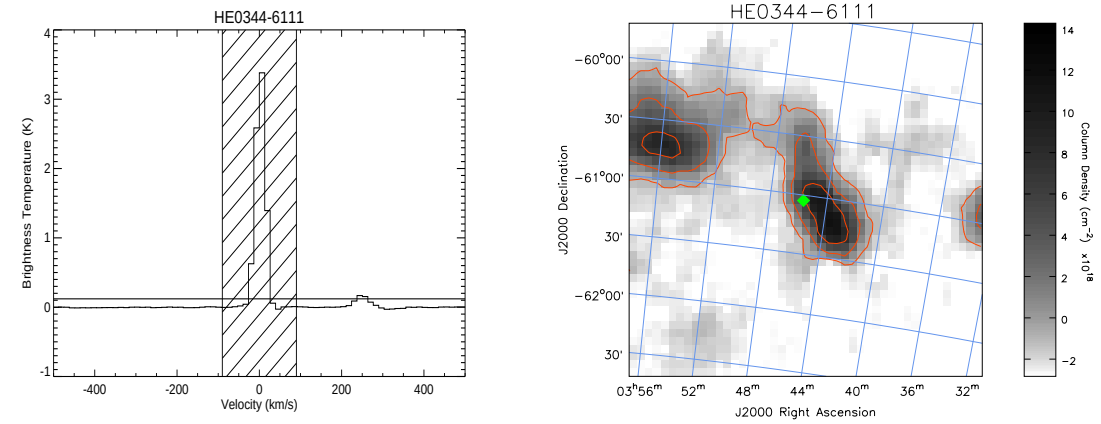


Figure B.257: HE 0344−6111

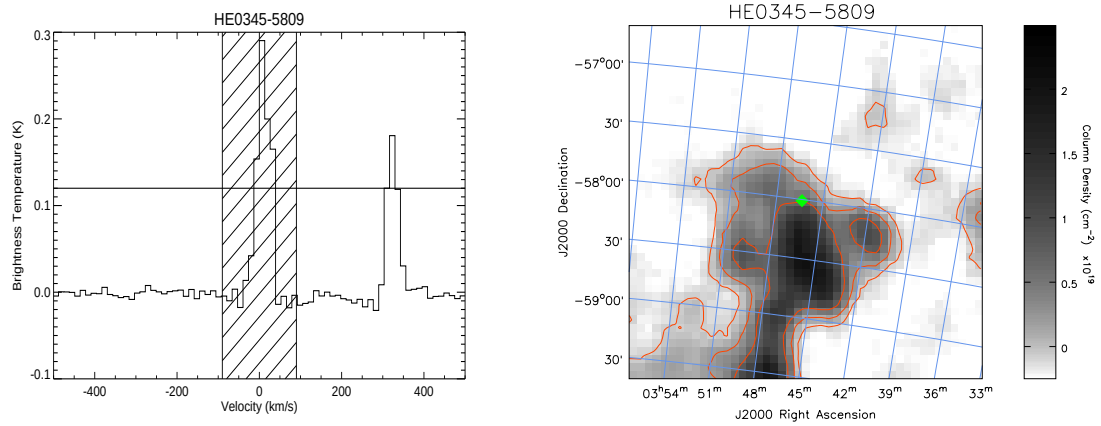


Figure B.258: HE 0345−5809

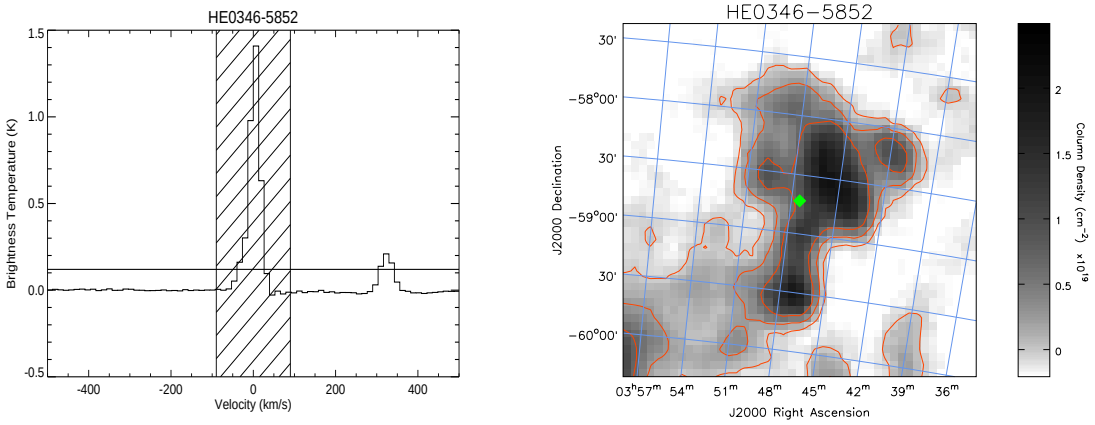


Figure B.259: HE 0346−5852

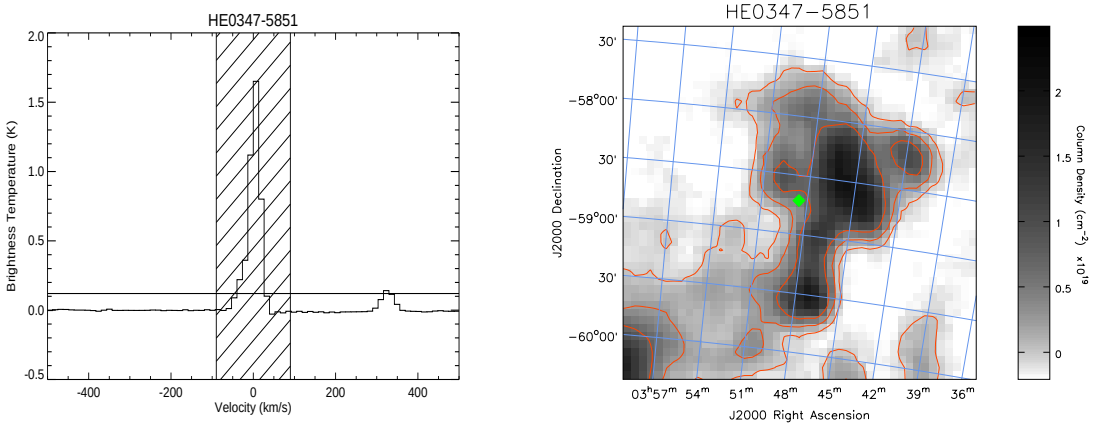


Figure B.260: HE 0347−5851

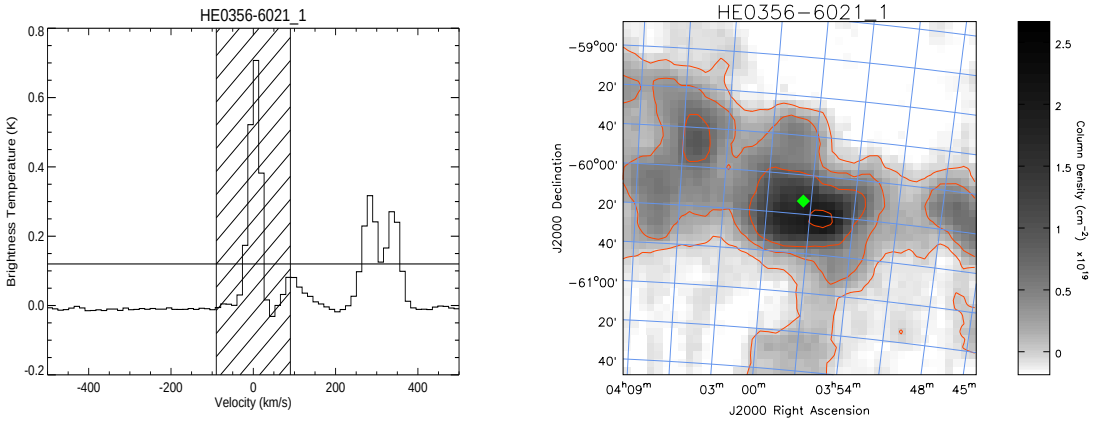


Figure B.261: HE 0356−6021_1

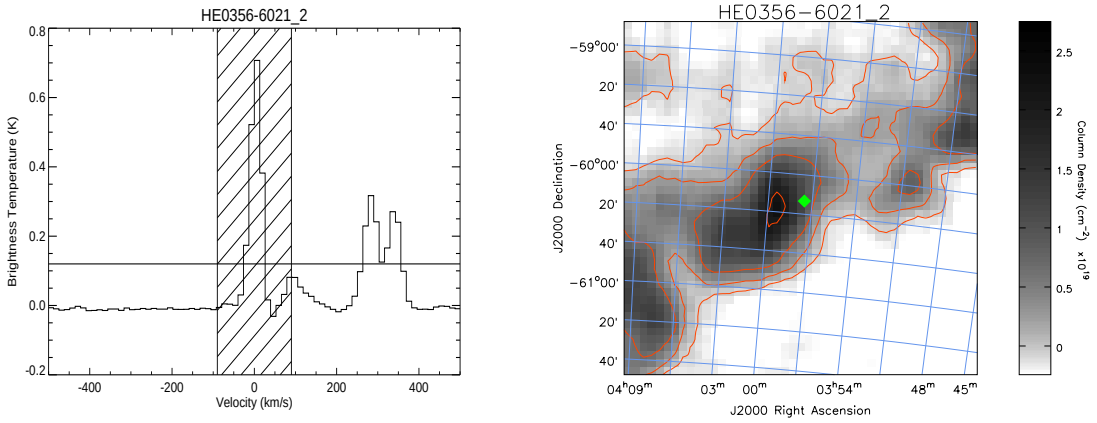


Figure B.262: HE 0356−6021_2

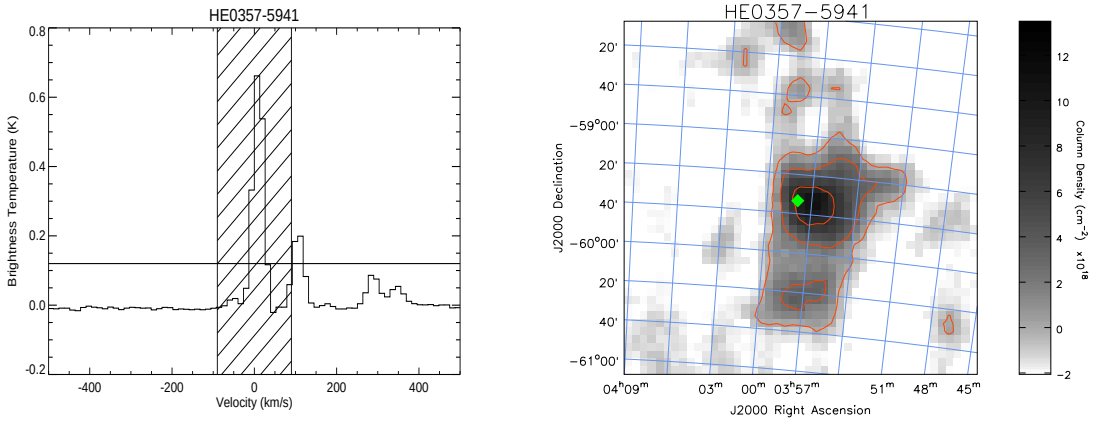


Figure B.263: HE 0357−5941

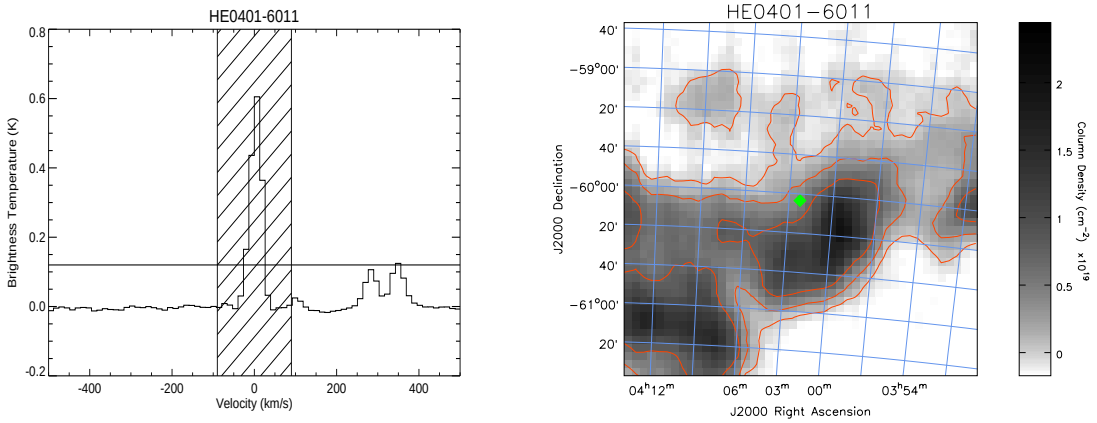


Figure B.264: HE 0401−6011

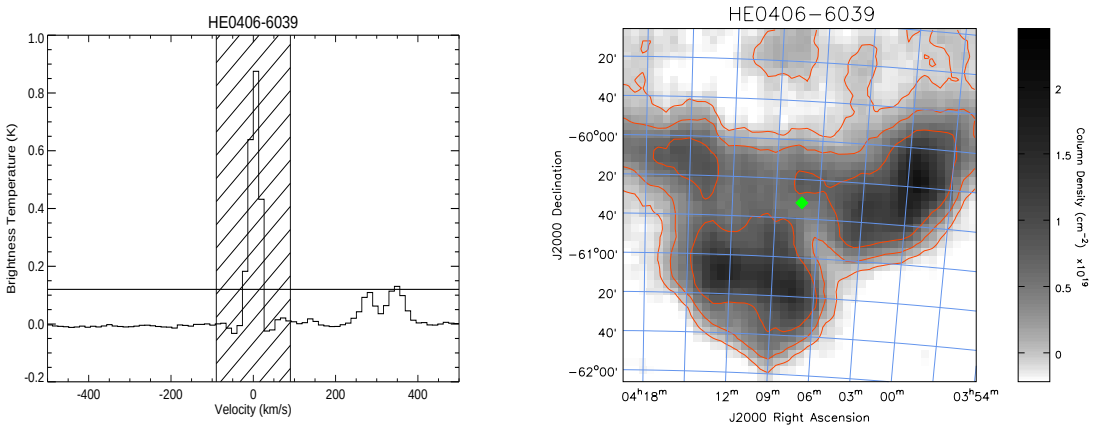


Figure B.265: HE 0406−6039

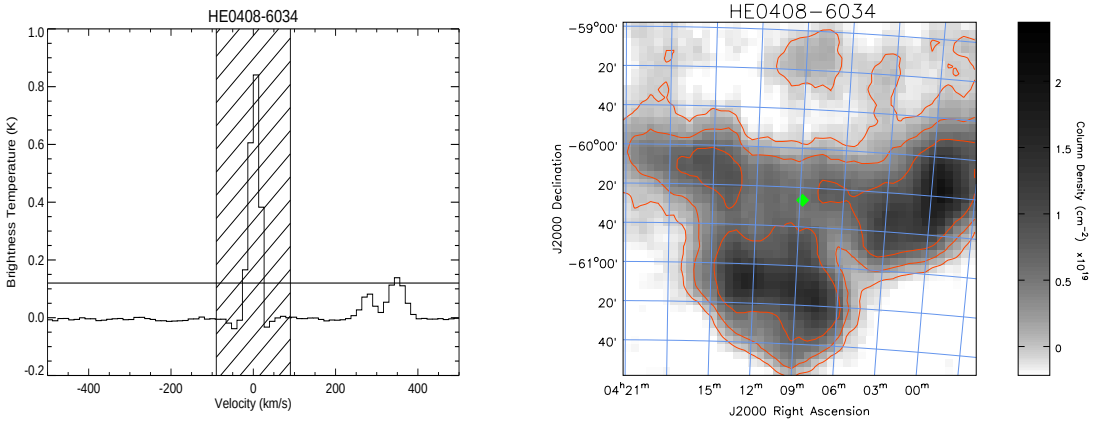


Figure B.266: HE 0408−6034

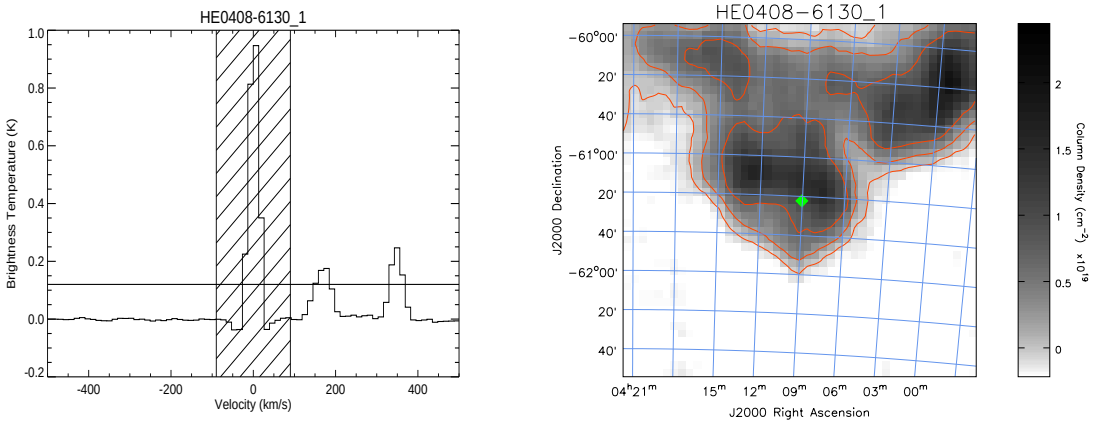


Figure B.267: HE 0408−6130_1

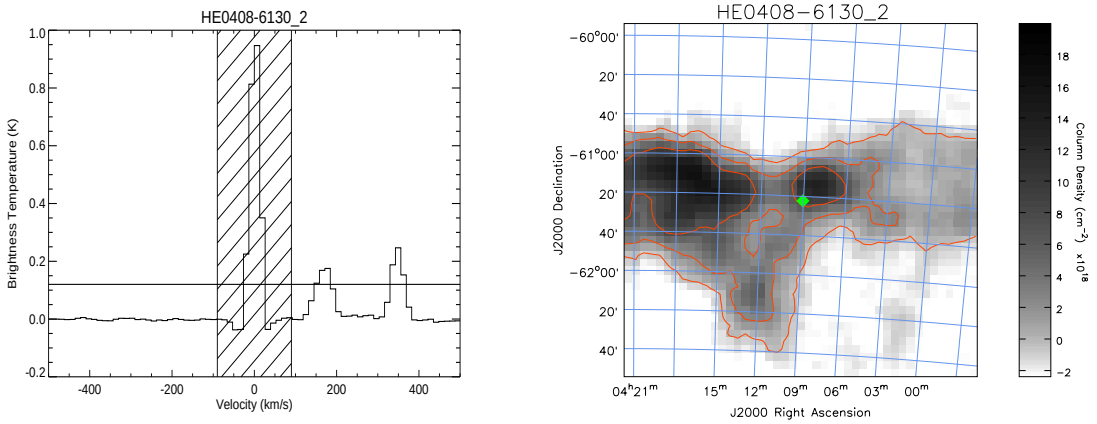


Figure B.268: HE 0408−6130_2

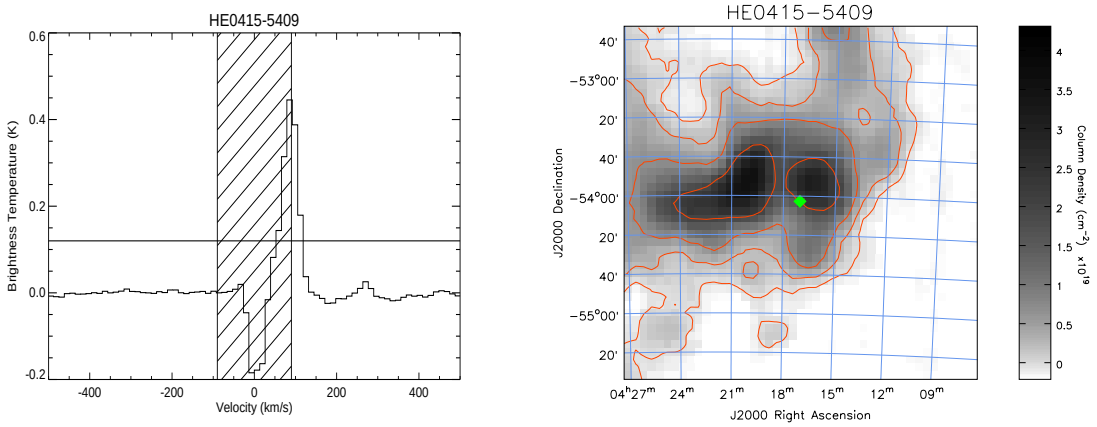


Figure B.269: HE 0415−5409

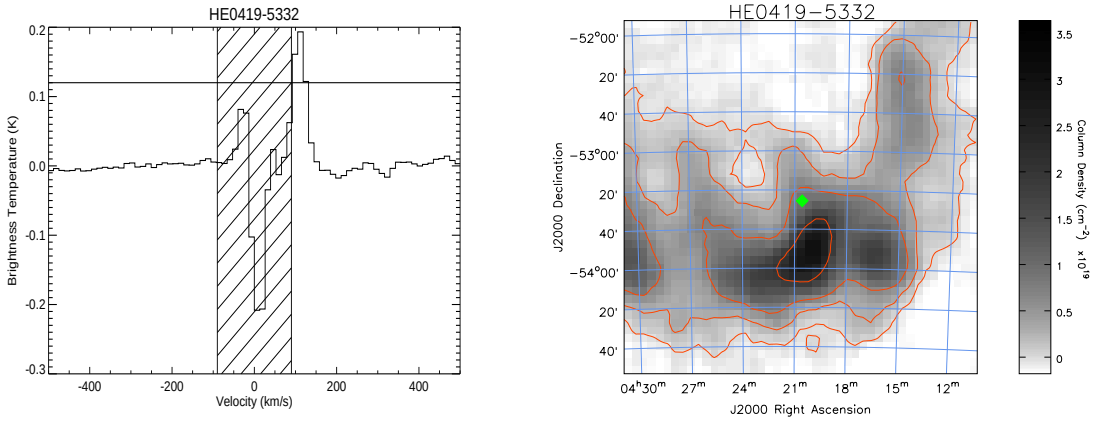


Figure B.270: HE 0419−5332

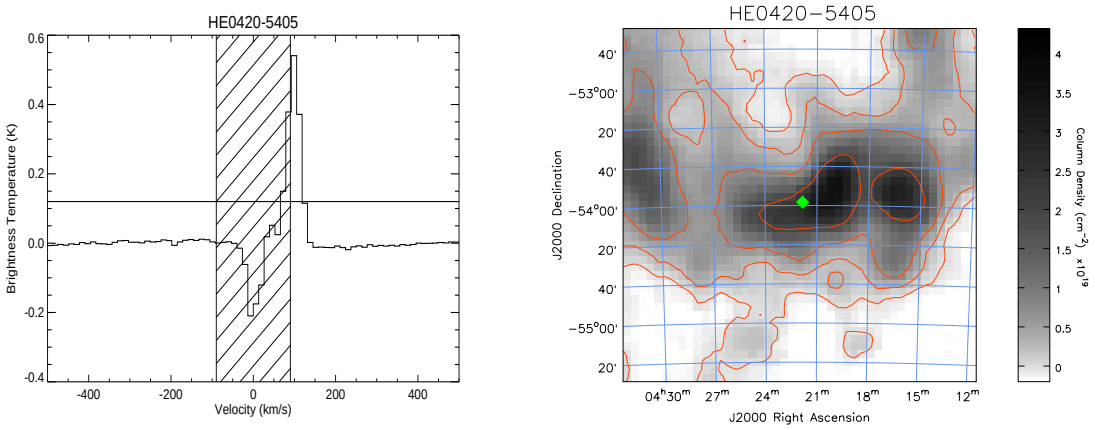


Figure B.271: HE 0420−5405

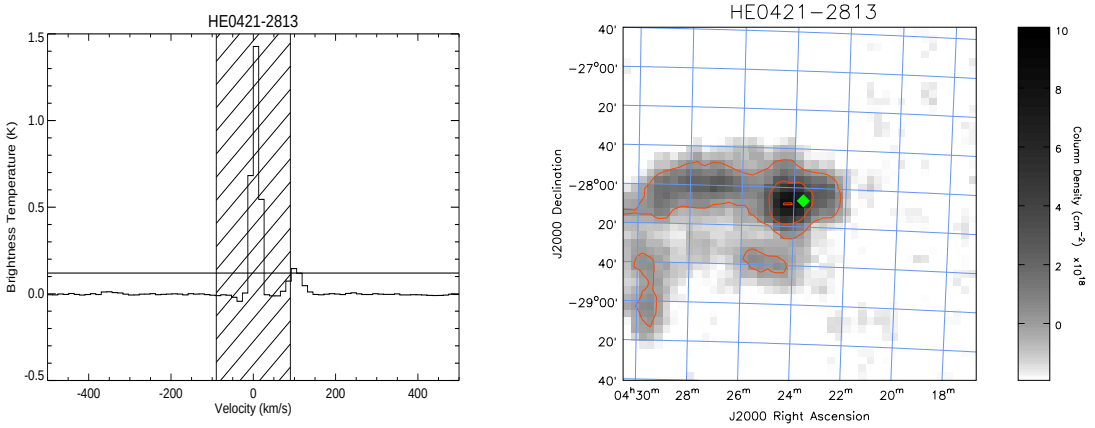


Figure B.272: HE 0421−2813

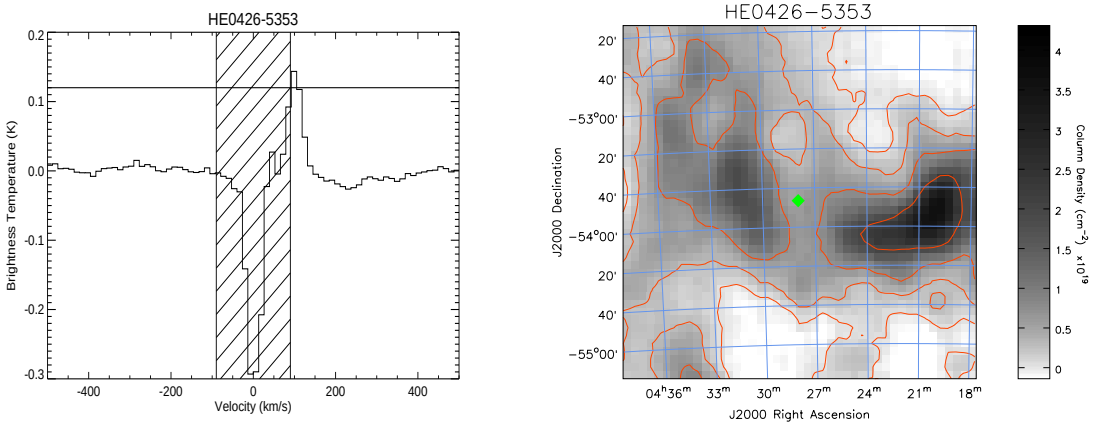


Figure B.273: HE 0426−5353

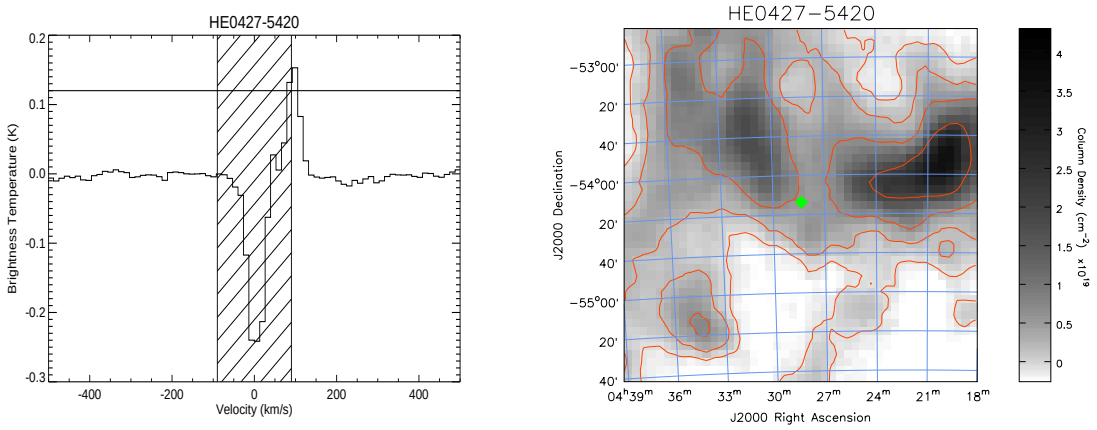


Figure B.274: HE 0427−5420

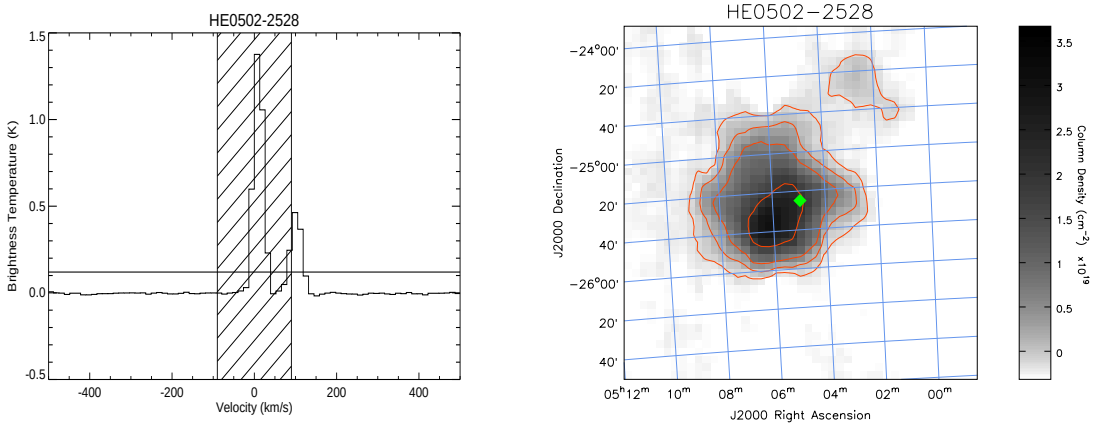


Figure B.275: HE 0502−2528

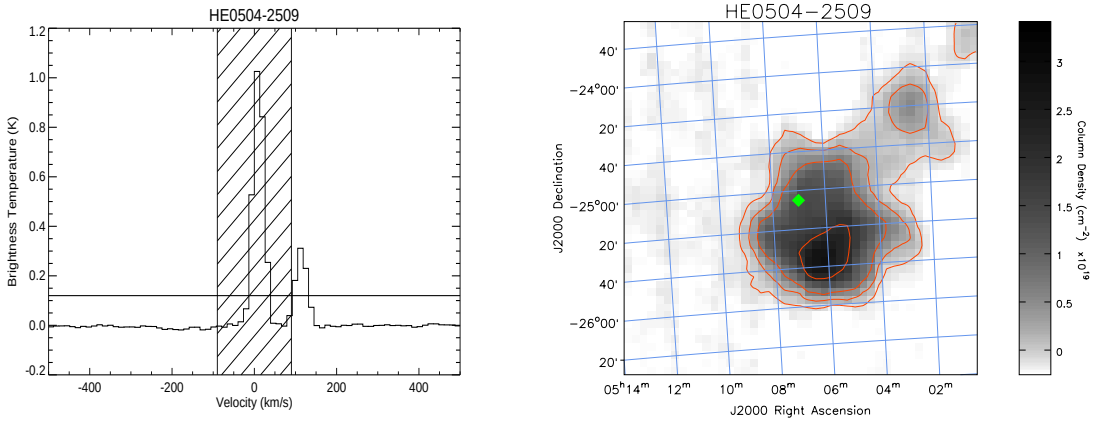


Figure B.276: HE 0504−2509

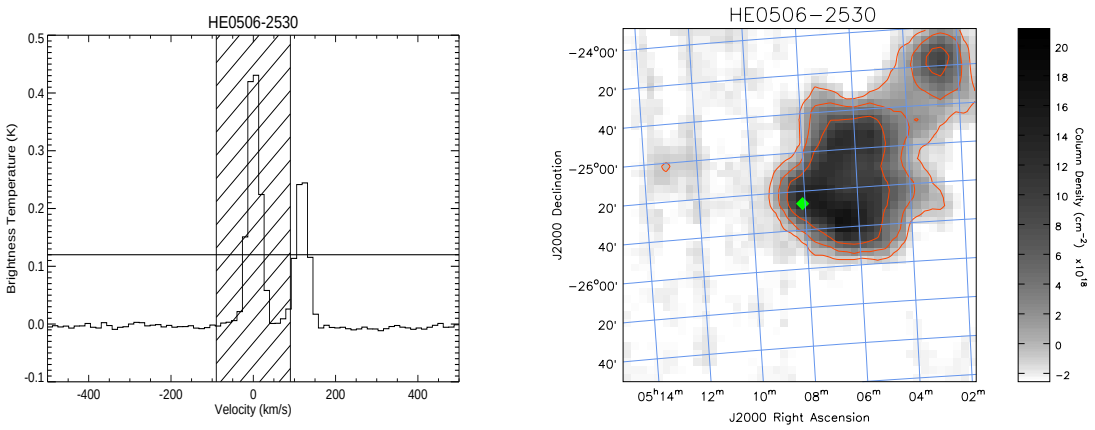


Figure B.277: HE 0506−2530

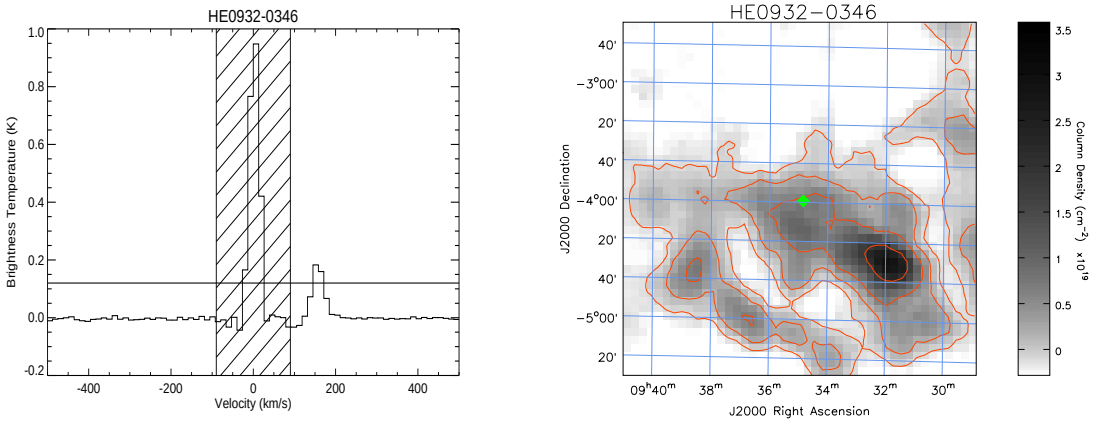


Figure B.278: HE 0932−0346

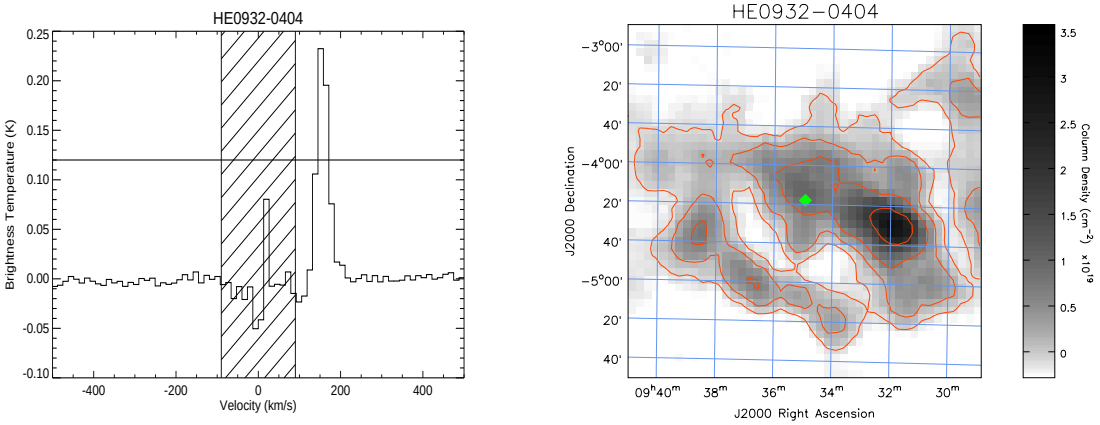


Figure B.279: HE 0932−0404

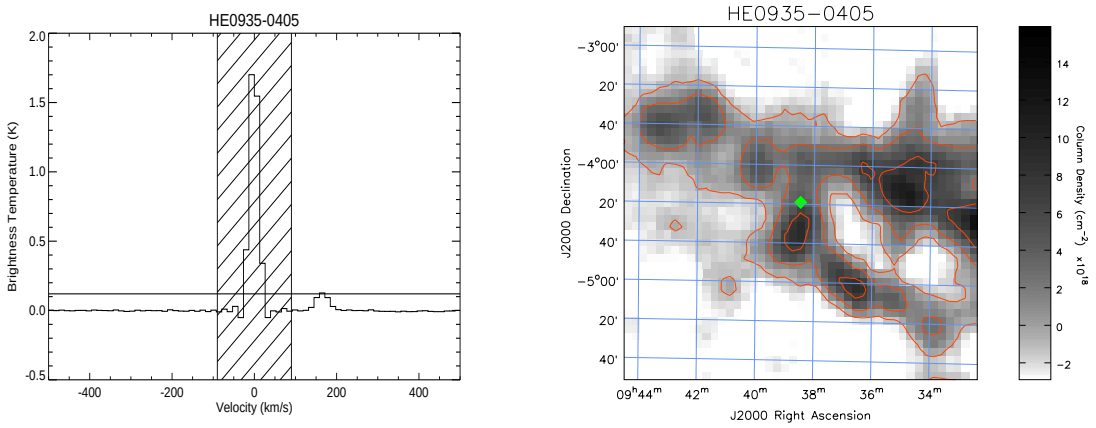


Figure B.280: HE 0935−0405

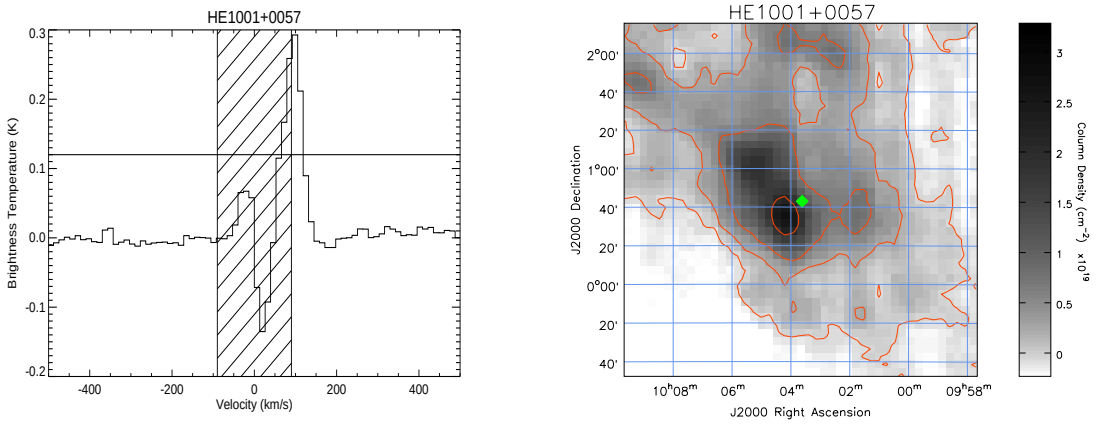


Figure B.281: HE 1001+0057

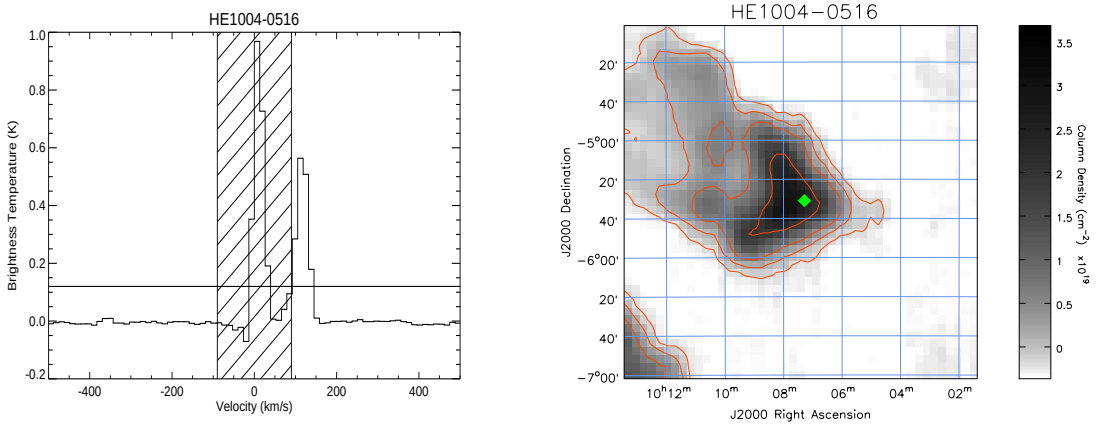


Figure B.282: HE 1004−0516

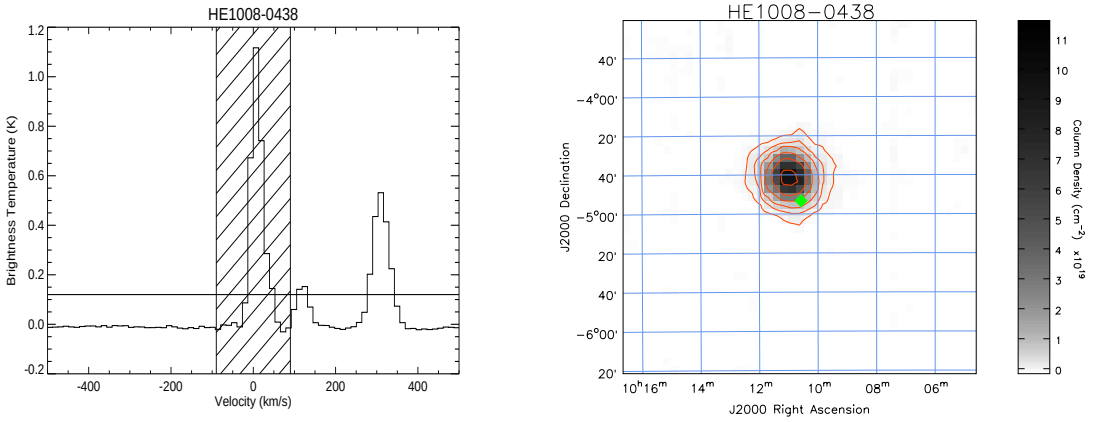


Figure B.283: HE 1008−0438

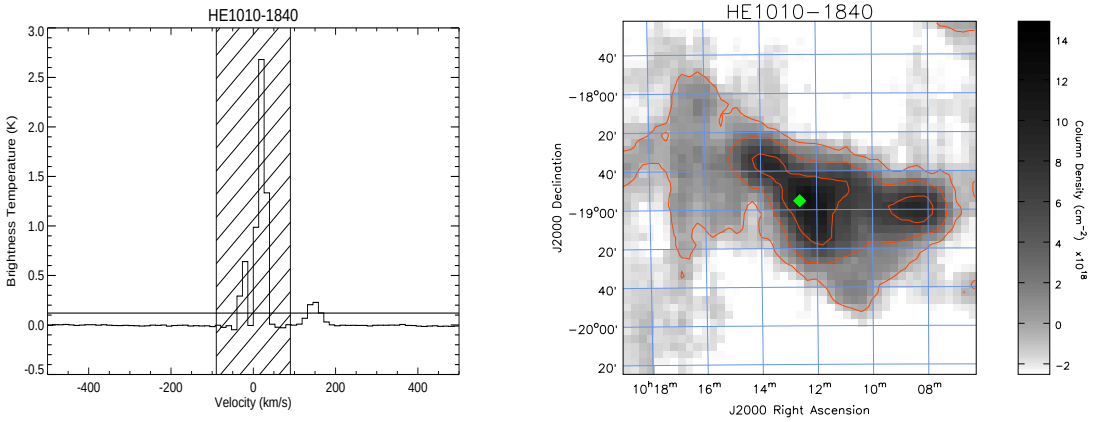


Figure B.284: HE 1010−1840

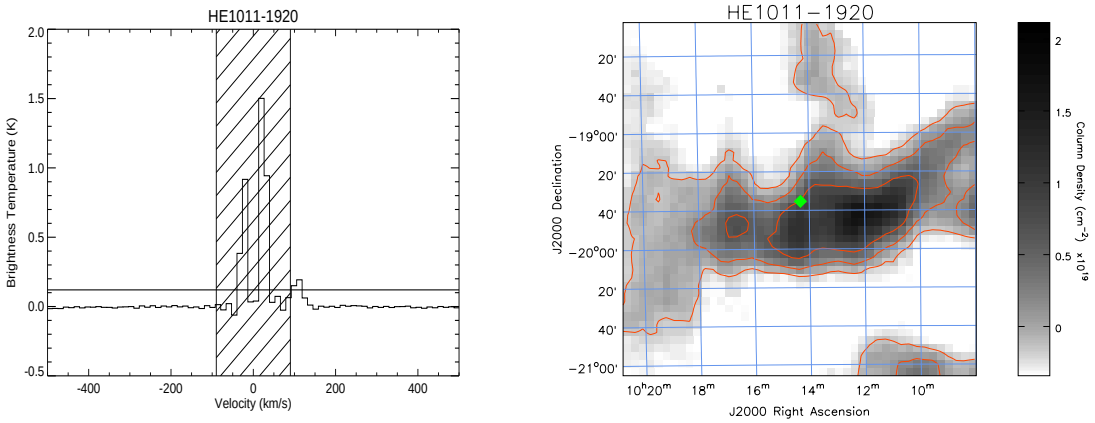


Figure B.285: HE 1011−1920

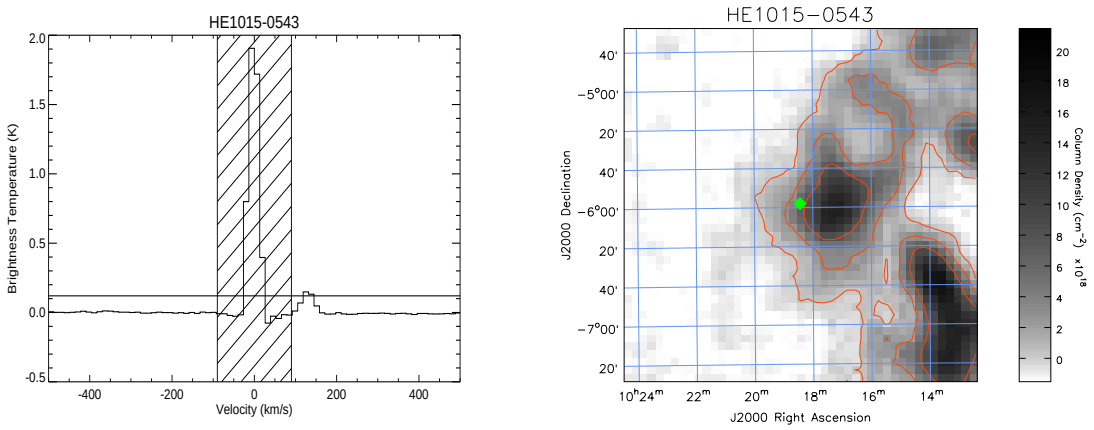


Figure B.286: HE 1015−0543

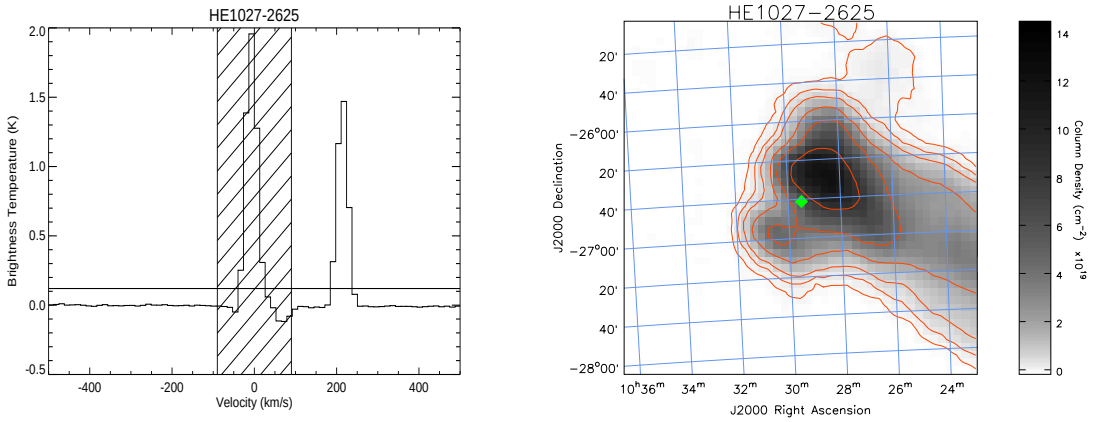


Figure B.287: HE 1027−2625

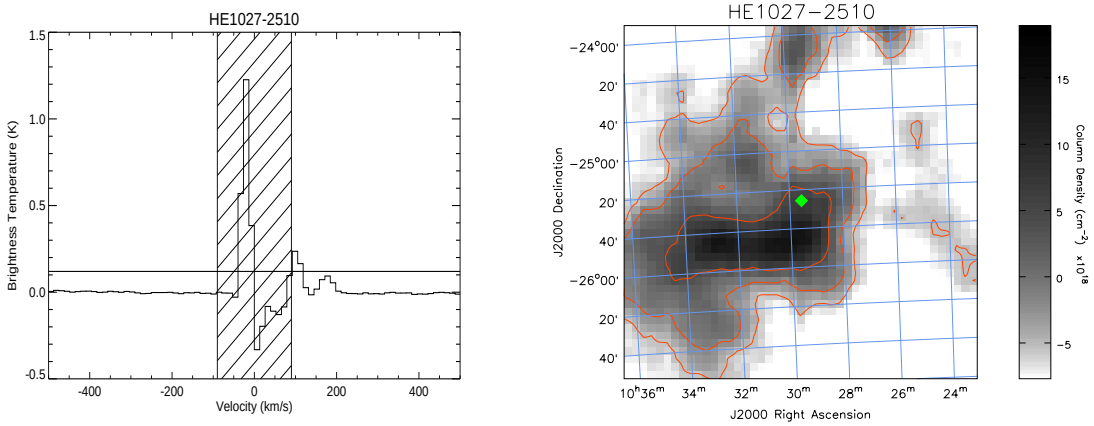


Figure B.288: HE 1027−2510

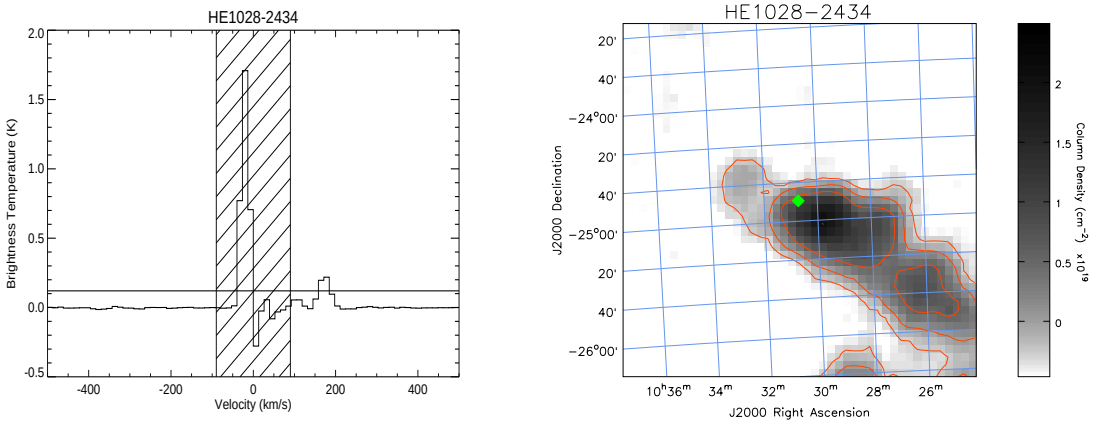


Figure B.289: HE 1028−2434

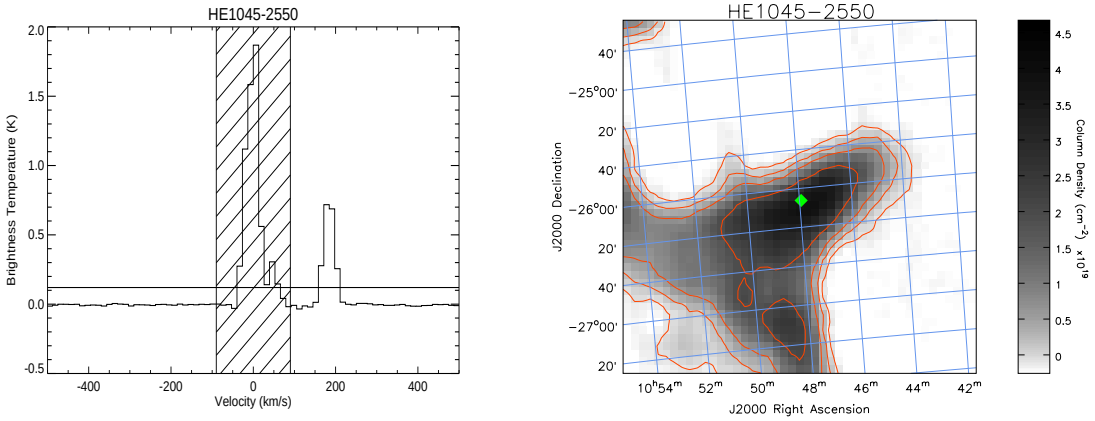


Figure B.290: HE 1045−2550

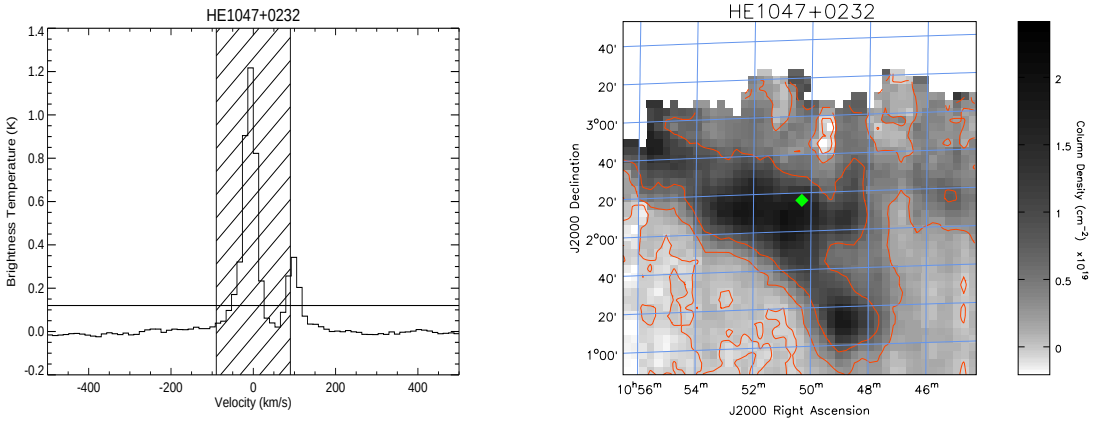
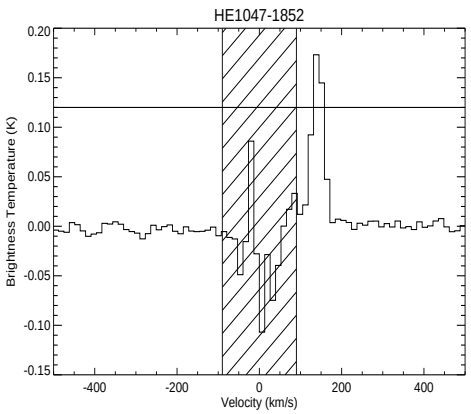


Figure B.291: HE 1047+0232



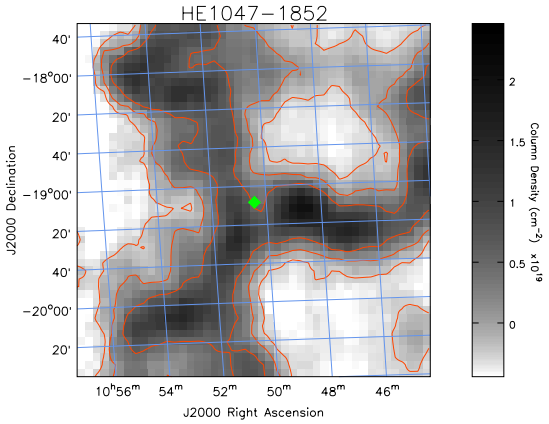
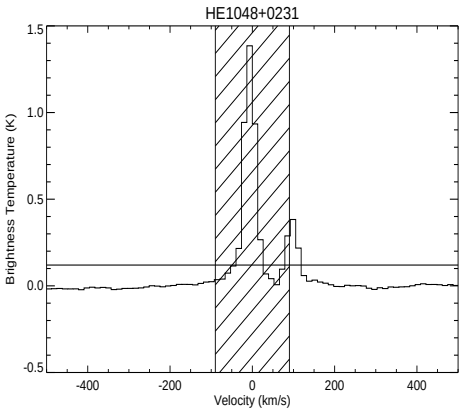


Figure B.292: HE 1047−1852



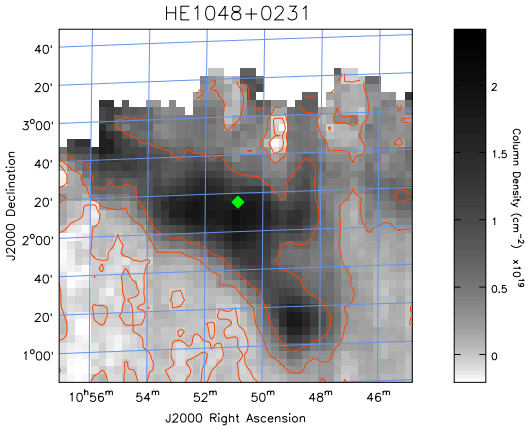
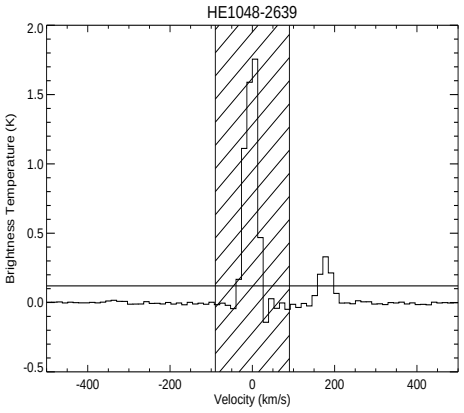


Figure B.293: HE 1048+0231



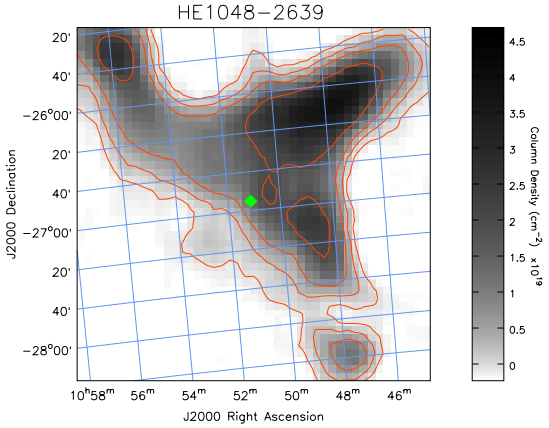


Figure B.294: HE 1048−2639

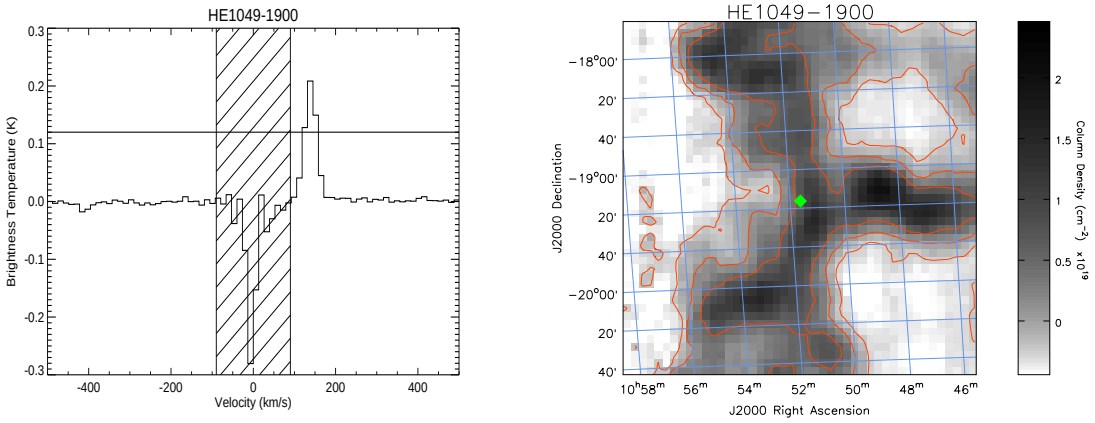


Figure B.295: HE 1049−1900

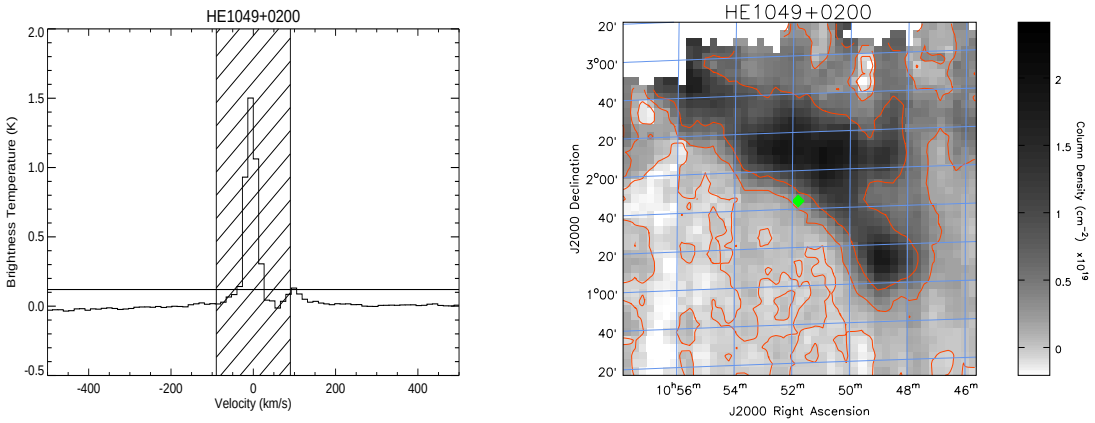


Figure B.296: HE 1049+0200

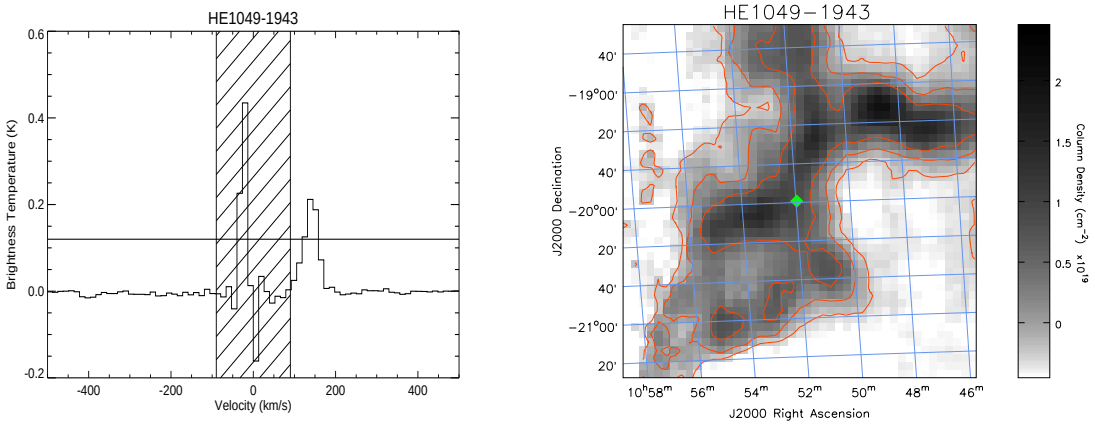


Figure B.297: HE 1049−1943

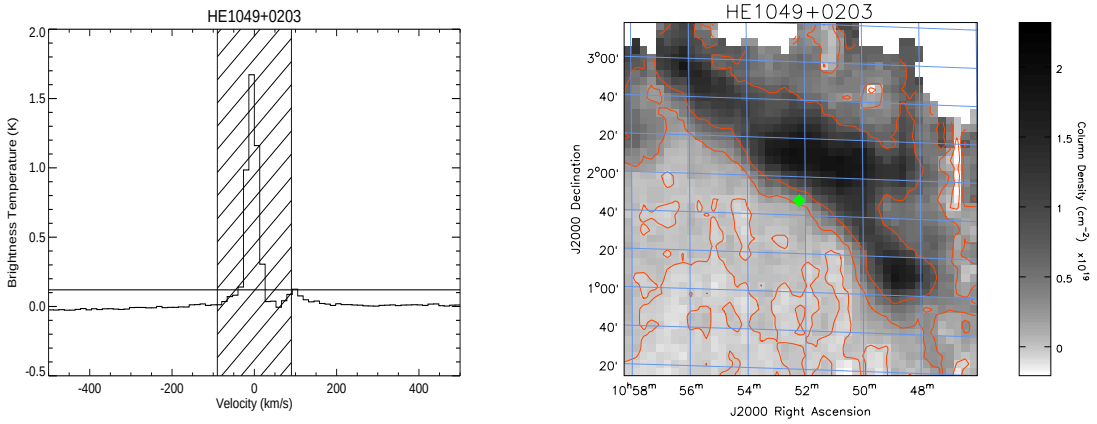


Figure B.298: HE 1049+0203

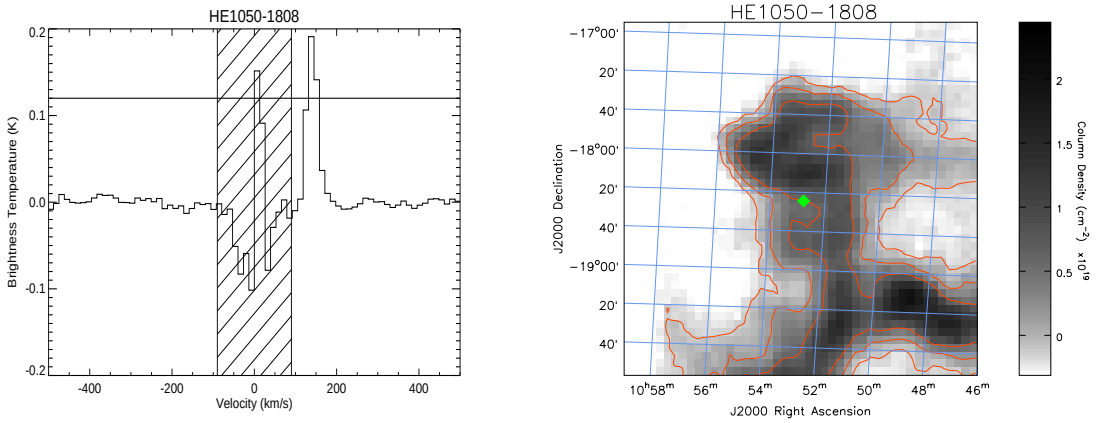


Figure B.299: HE 1050−1808

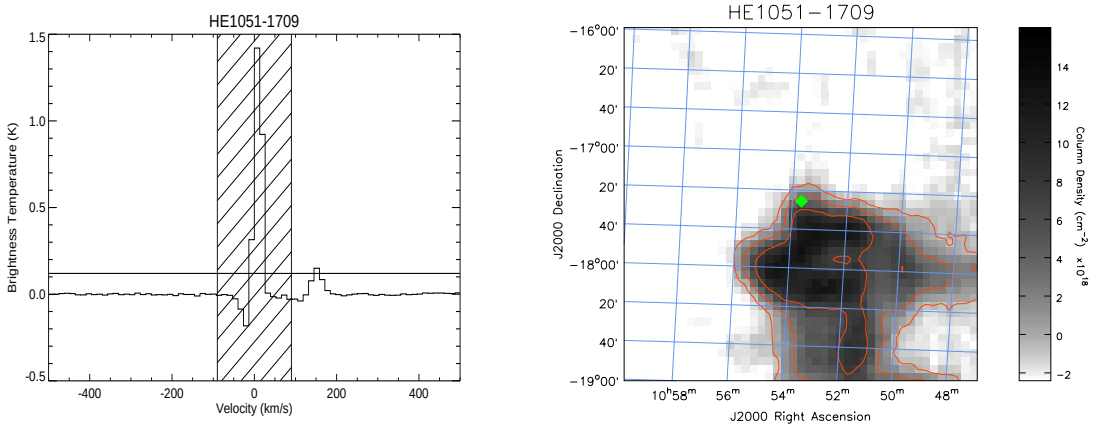


Figure B.300: HE 1051−1709

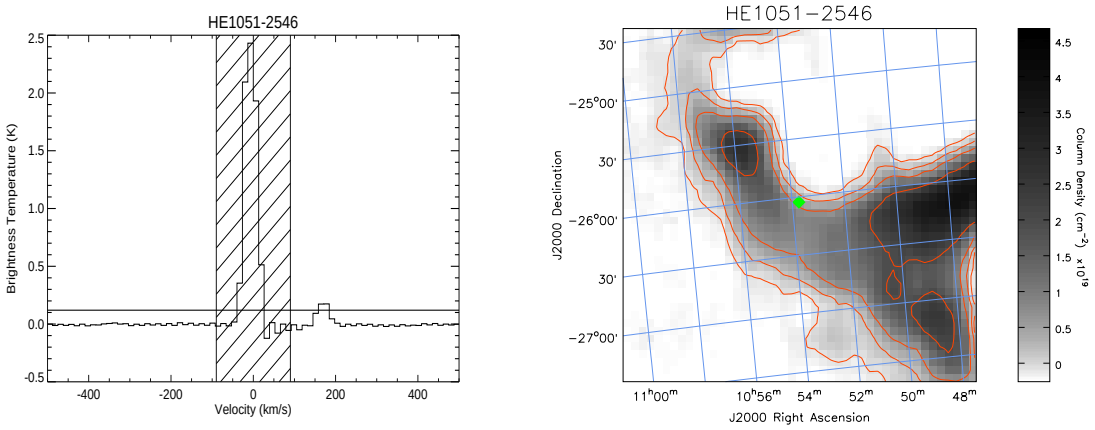


Figure B.301: HE 1051−2546

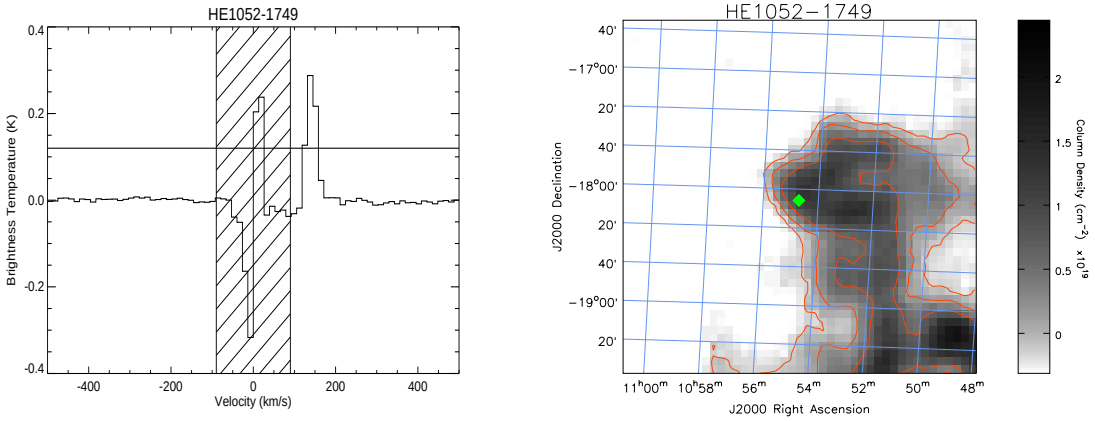


Figure B.302: HE 1052−1749

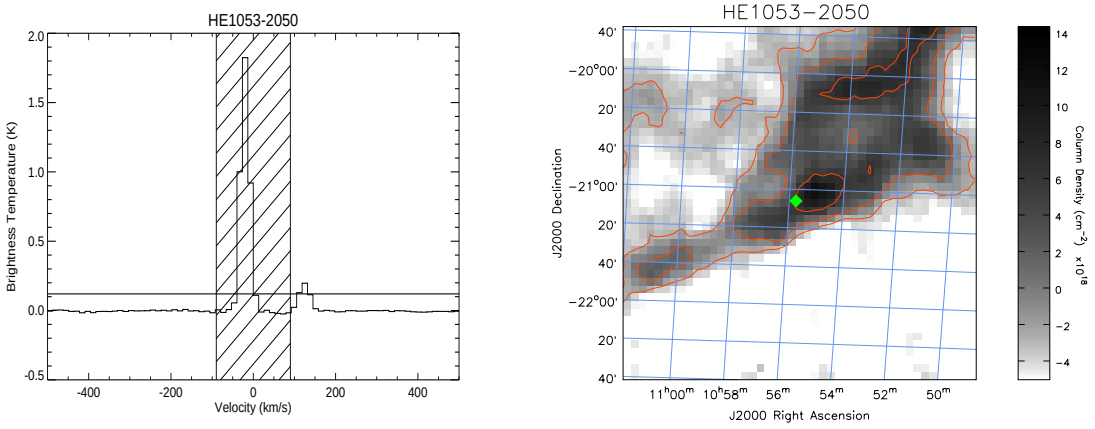


Figure B.303: HE 1053−2050

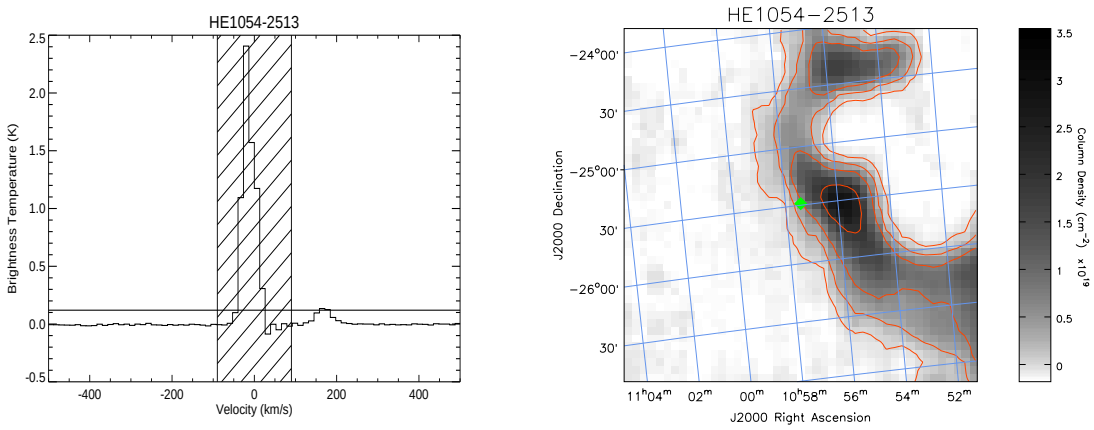


Figure B.304: HE 1054−2513

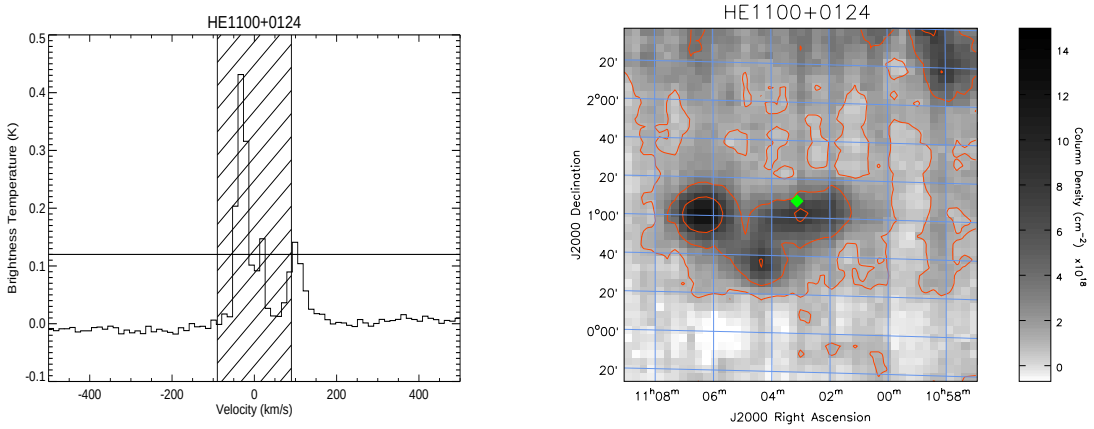


Figure B.305: HE 1100+0124

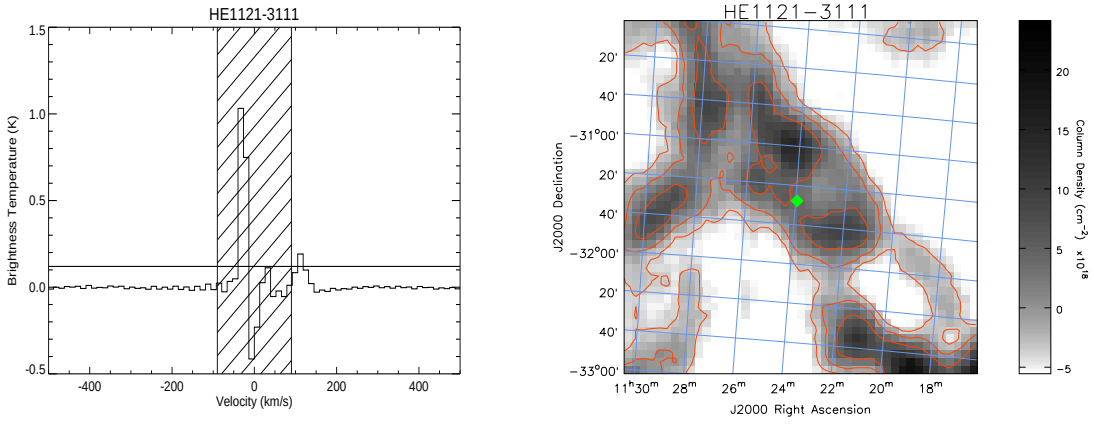


Figure B.306: HE 1121−3111

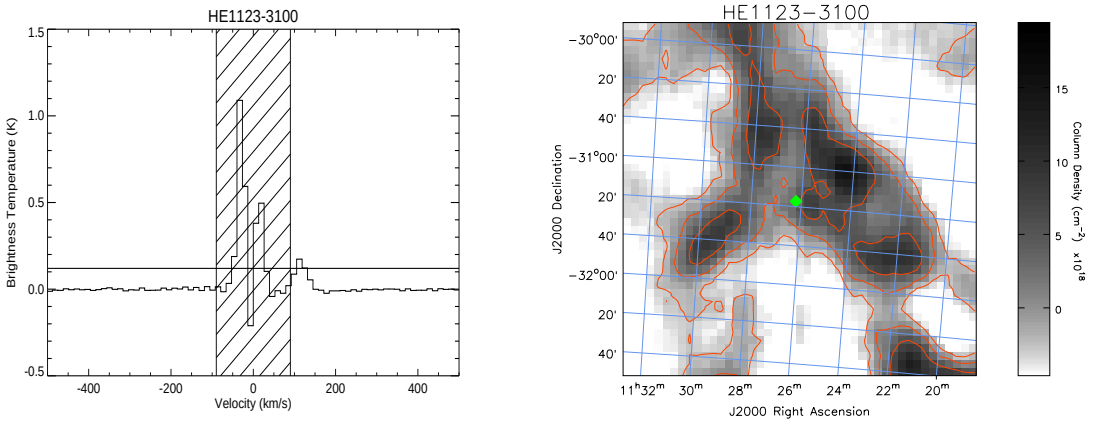


Figure B.307: HE 1123−3100

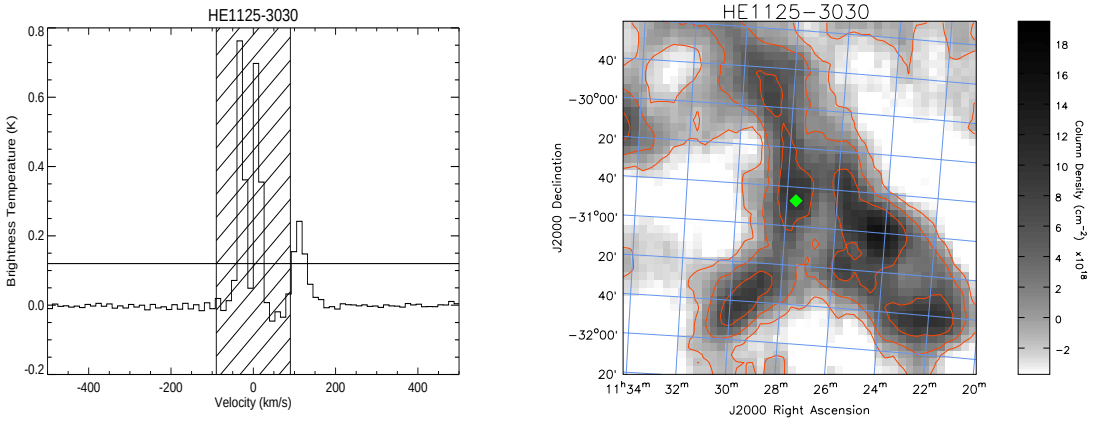


Figure B.308: HE 1125−3030

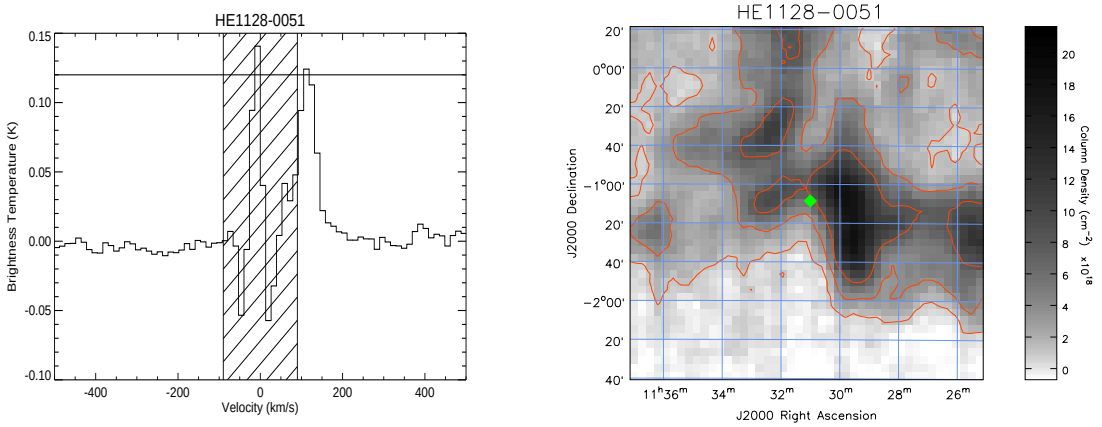


Figure B.309: HE 1128−0051

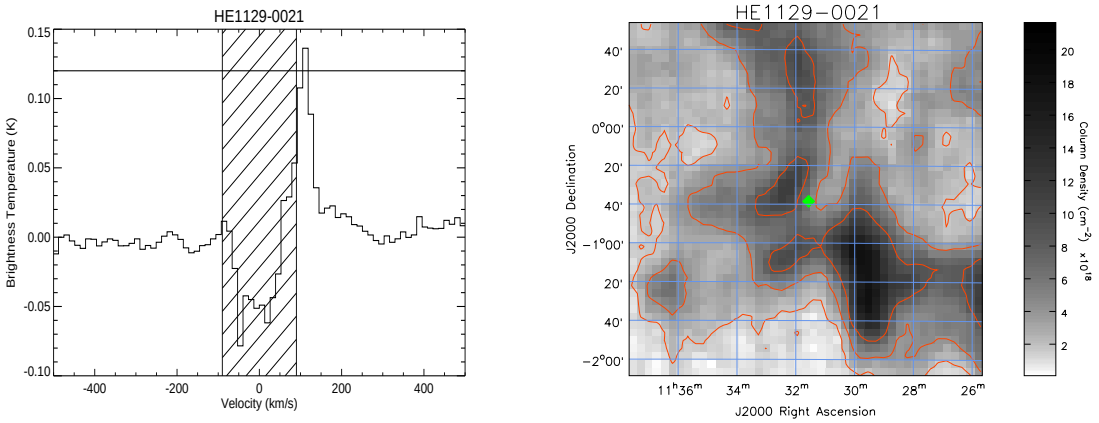


Figure B.310: HE 1129−0021

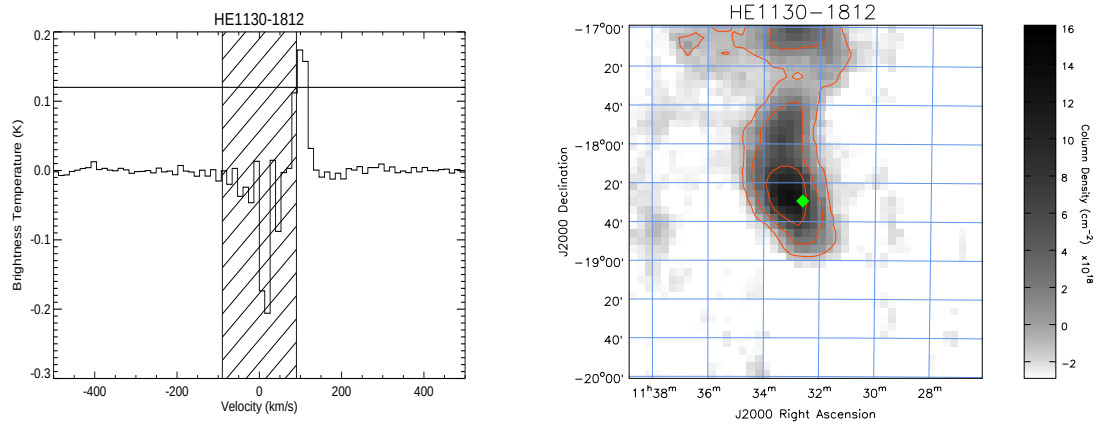


Figure B.311: HE 1130−1812

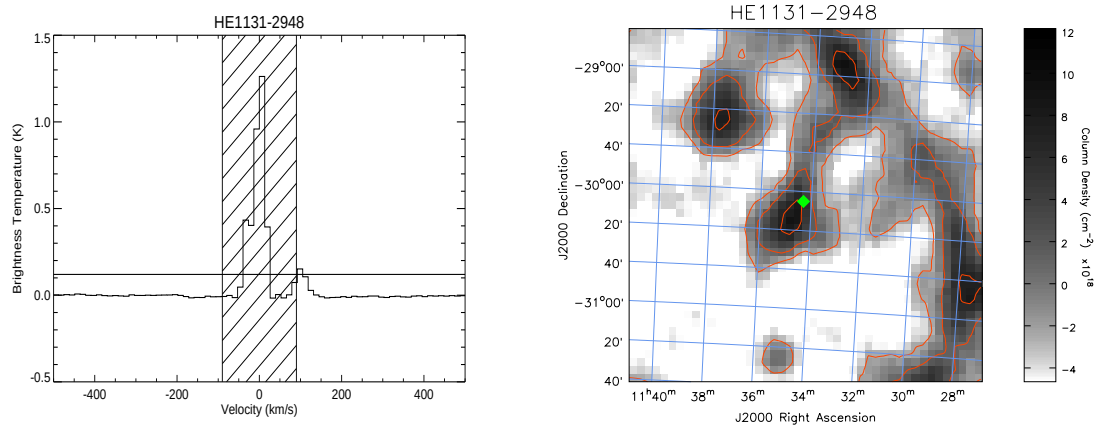


Figure B.312: HE 1131−2948

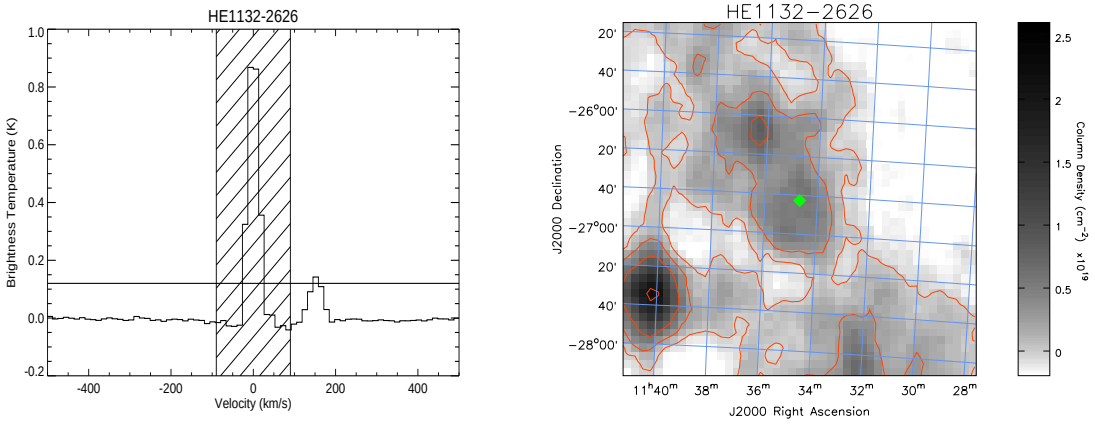


Figure B.313: HE 1132−2626

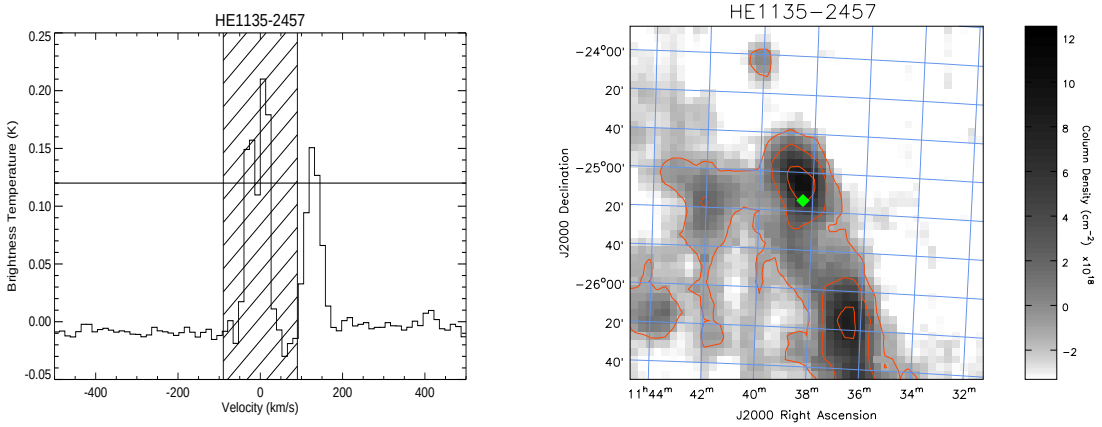


Figure B.314: HE 1135−2457

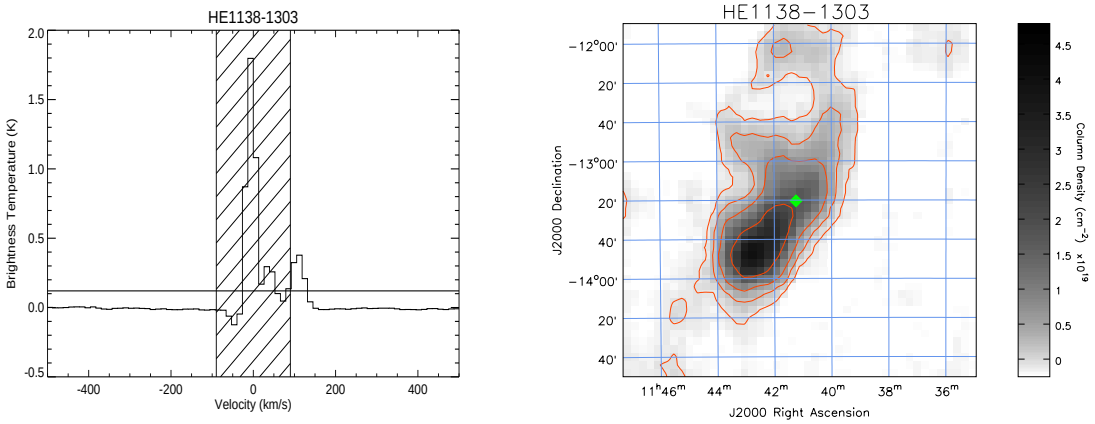


Figure B.315: HE 1138−1303

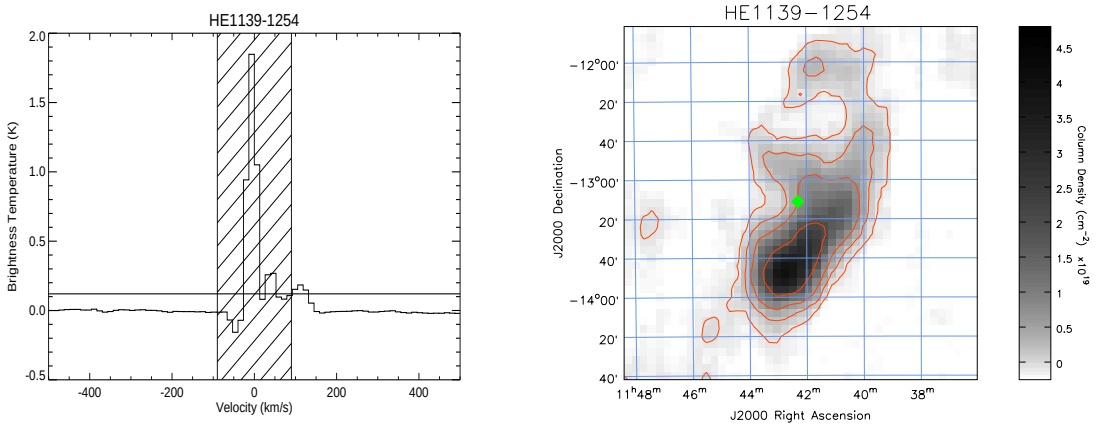


Figure B.316: HE 1139−1254

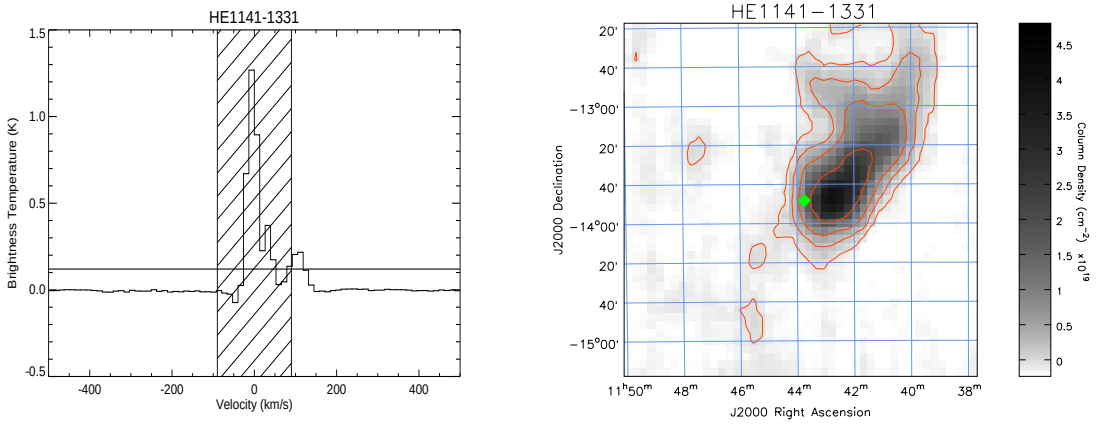


Figure B.317: HE 1141−1331

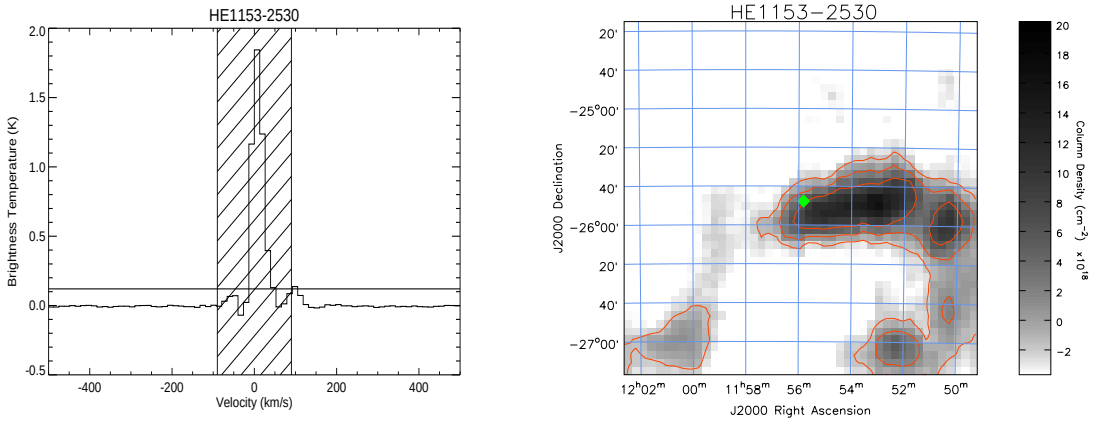


Figure B.318: HE 1153−2530

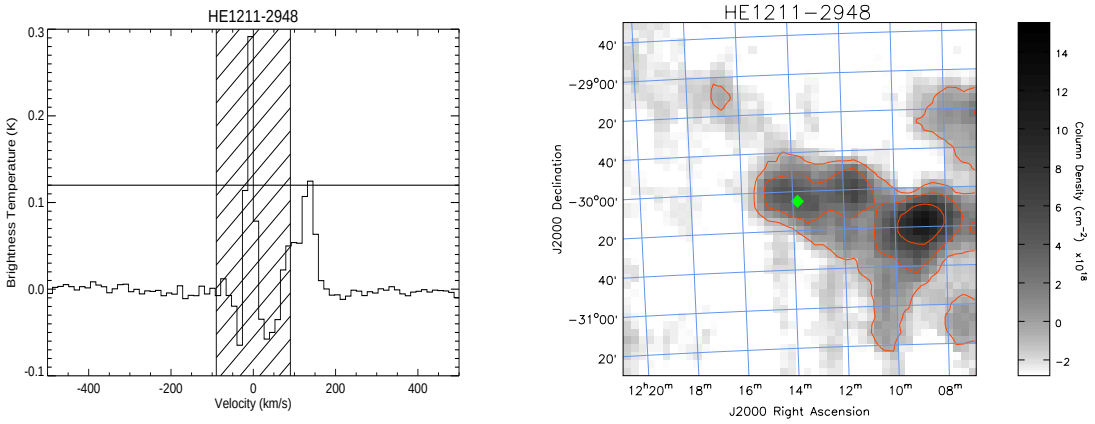


Figure B.319: HE 1211−2948

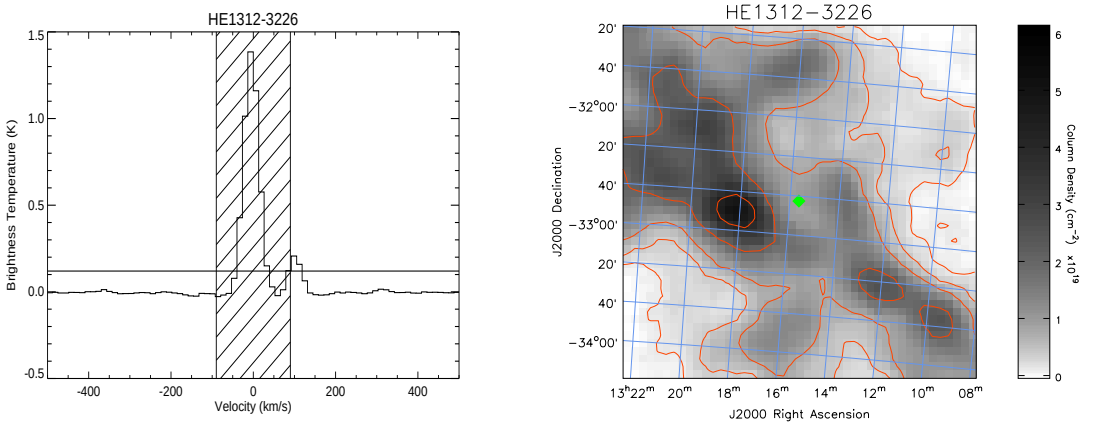


Figure B.320: HE 1312−3226

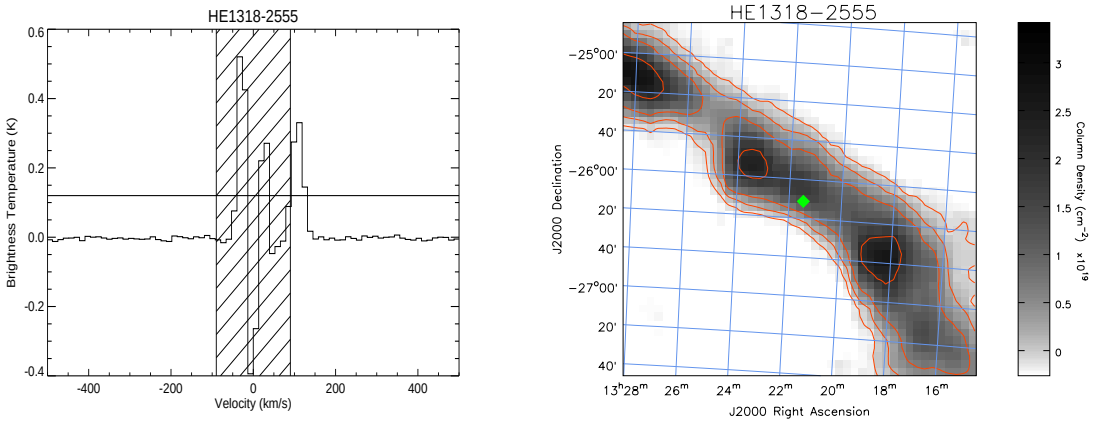
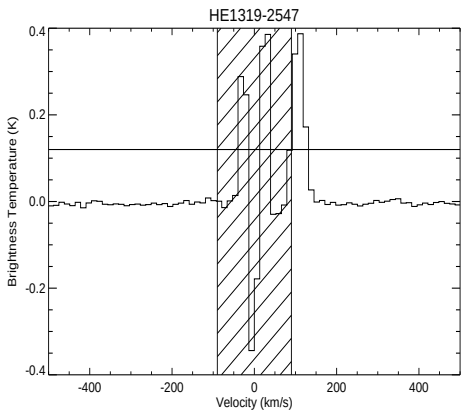


Figure B.321: HE 1318−2555



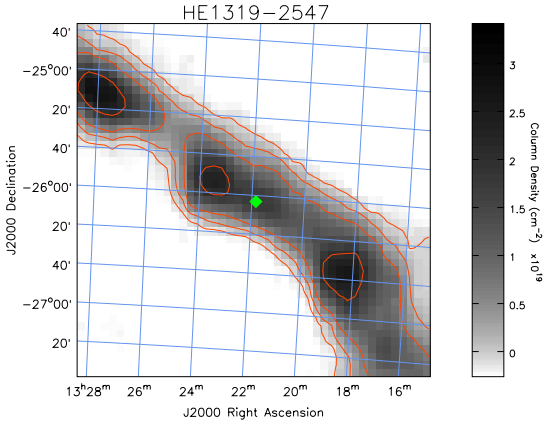
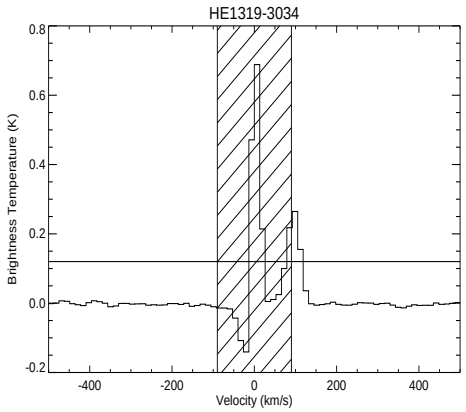


Figure B.322: HE 1319−2547



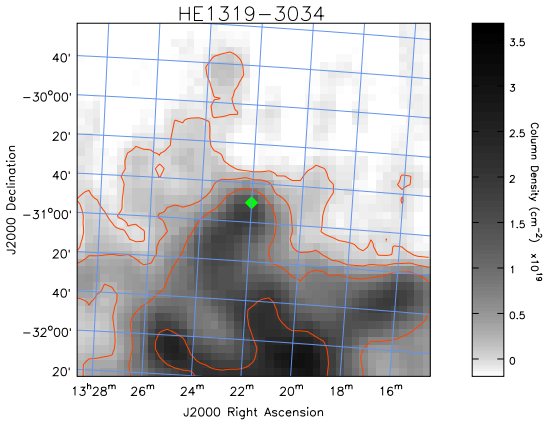
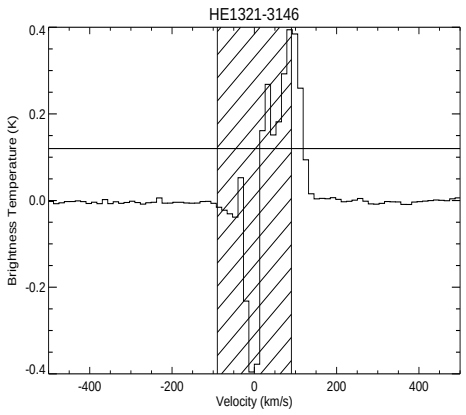


Figure B.323: HE 1319−3034



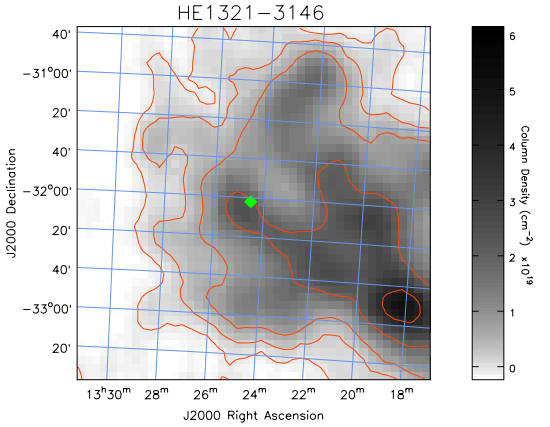


Figure B.324: HE 1321−3146

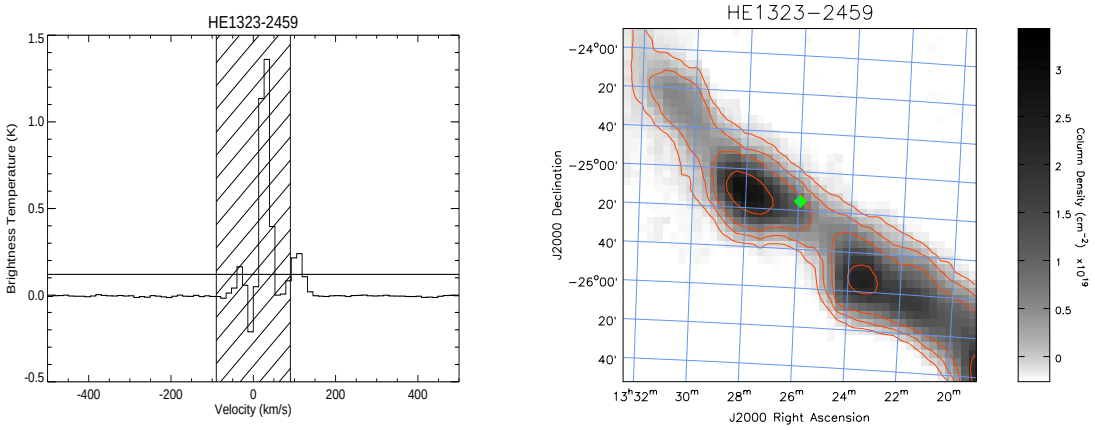


Figure B.325: HE 1323−2459

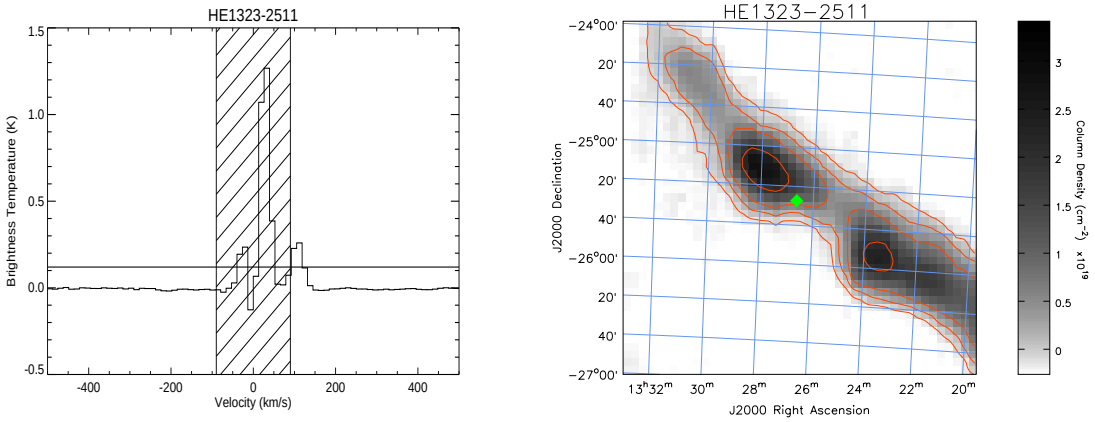


Figure B.326: HE 1323−2511

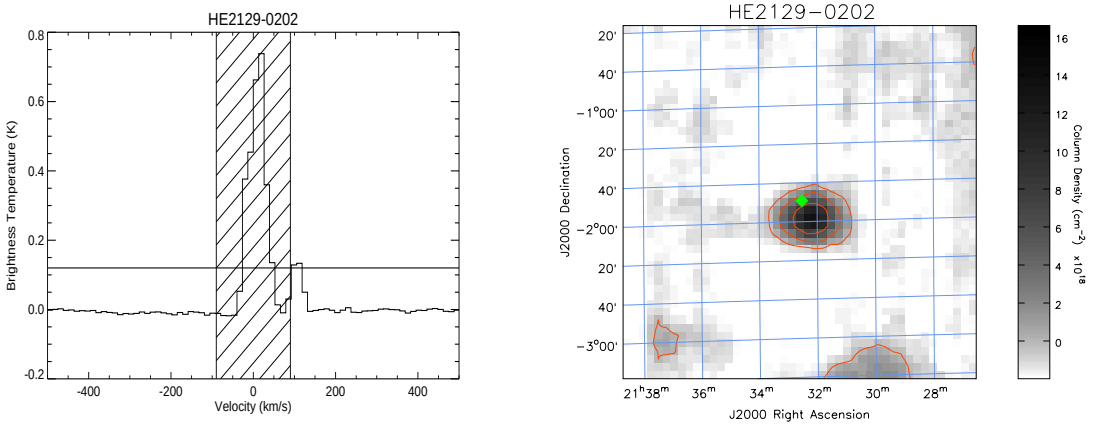


Figure B.327: HE 2129−0202

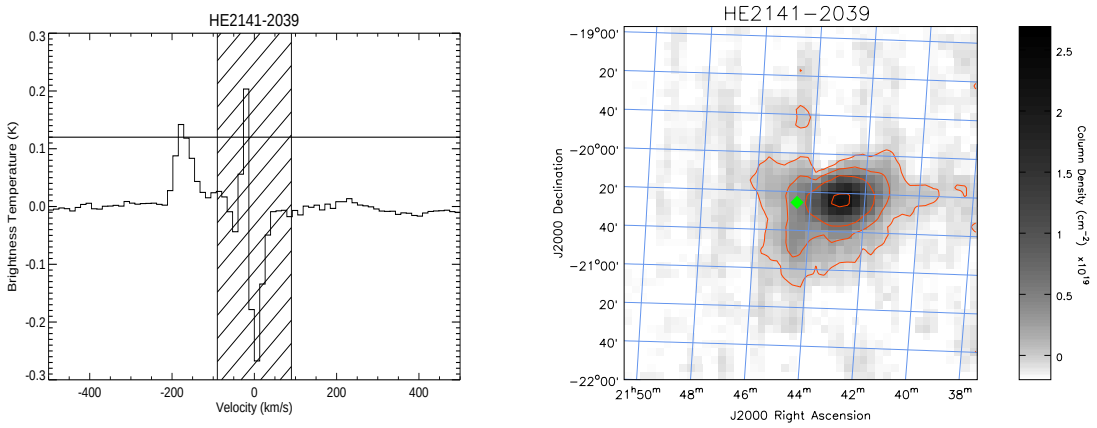


Figure B.328: HE 2141−2039

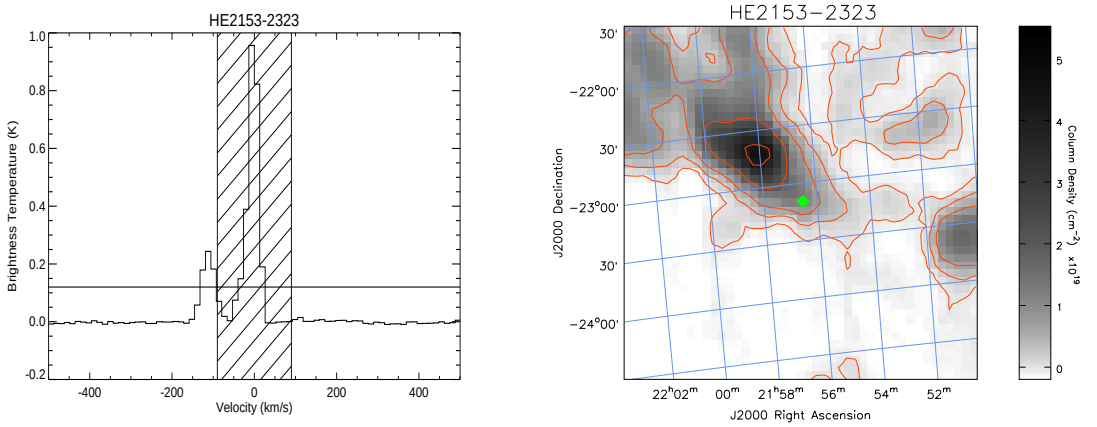


Figure B.329: HE 2153−2323

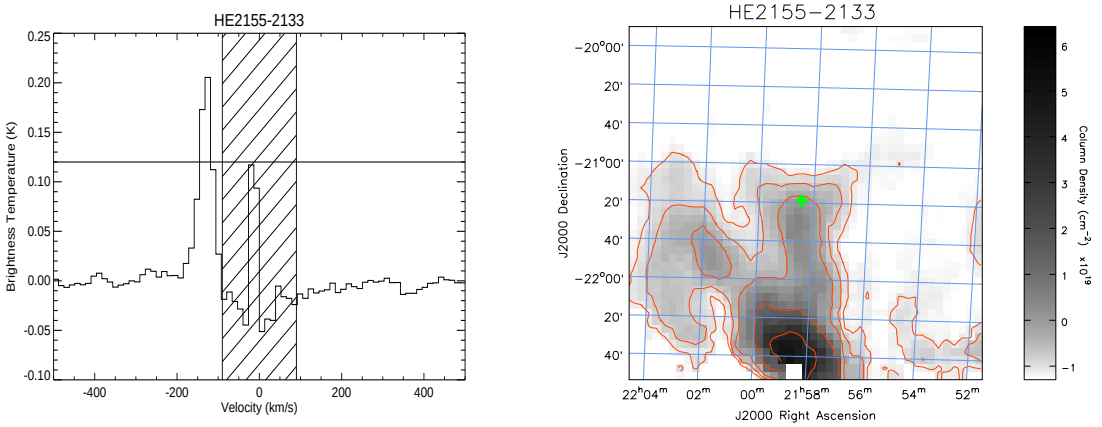


Figure B.330: HE 2155−2133

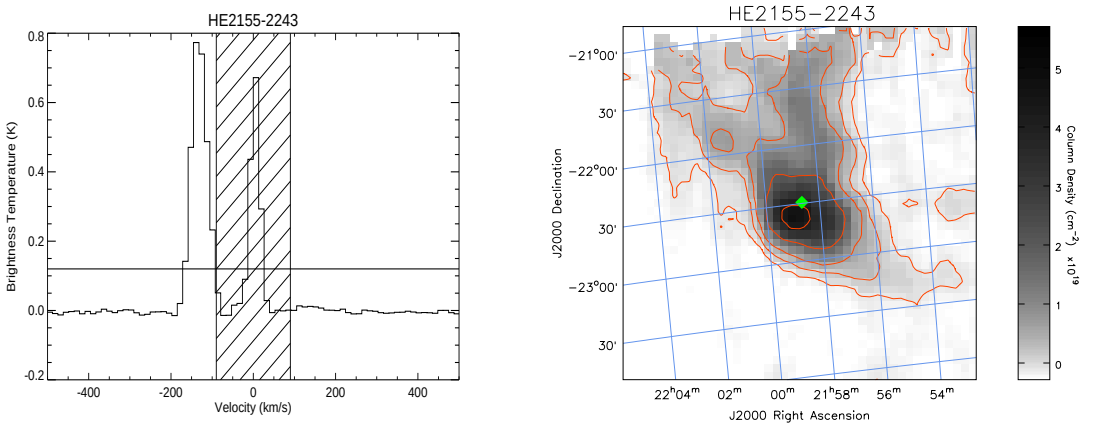


Figure B.331: HE 2155−2243

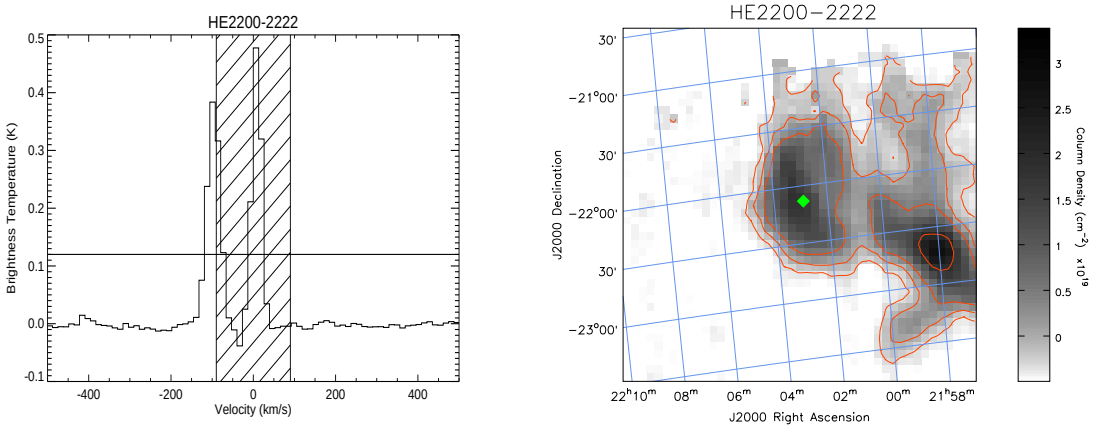


Figure B.332: HE 2200−2222

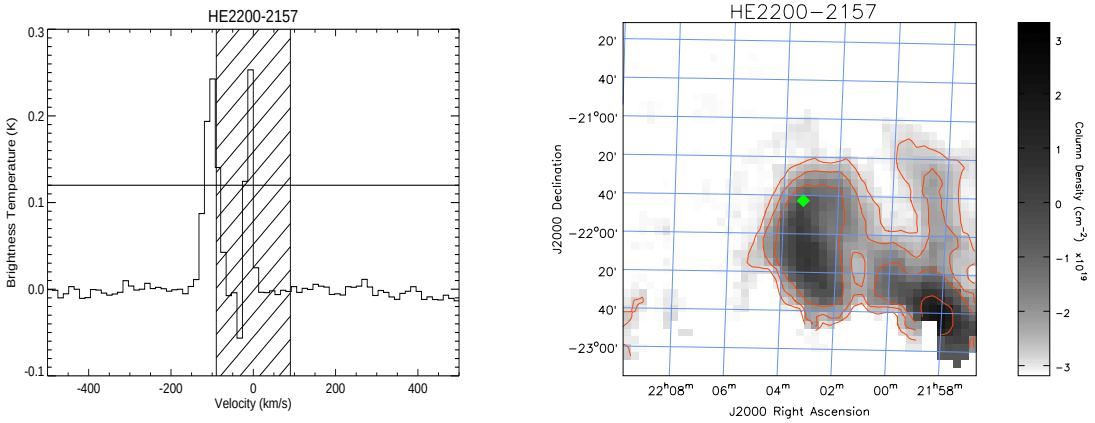


Figure B.333: HE 2200−2157

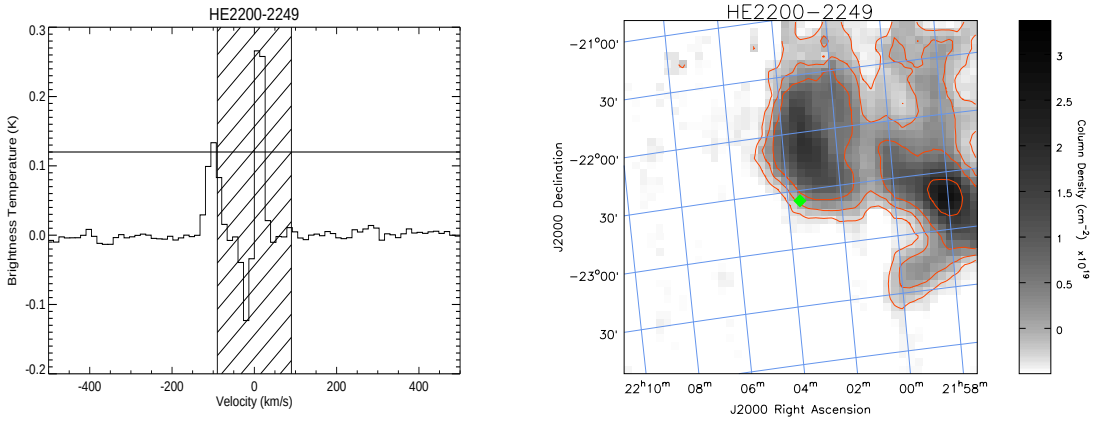


Figure B.334: HE 2200−2249

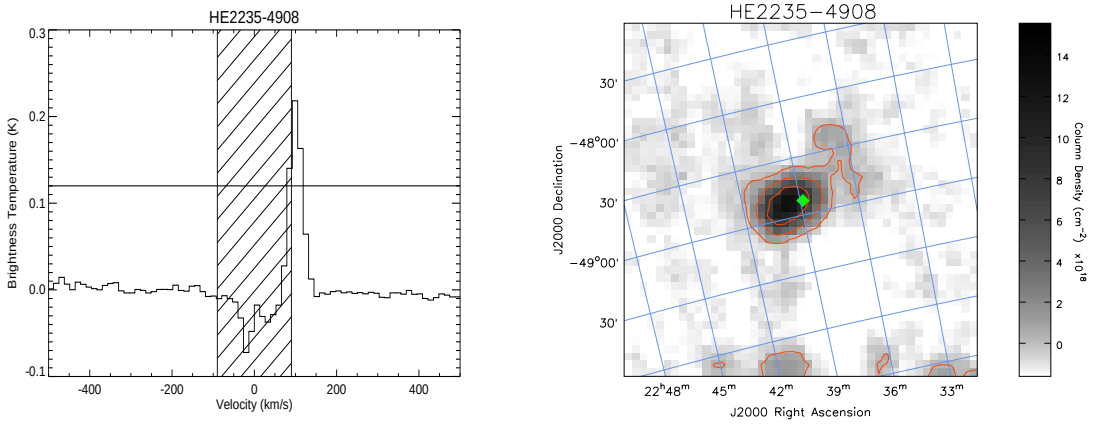


Figure B.335: HE 2235−4908

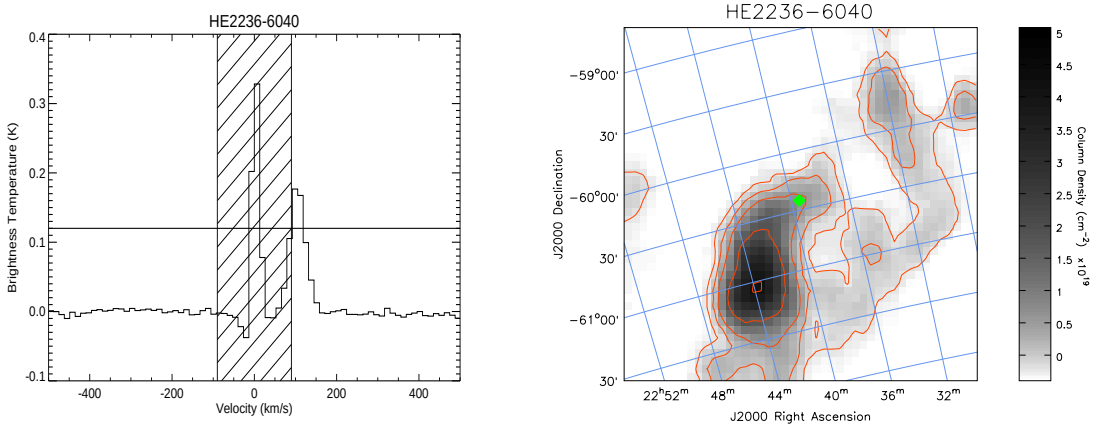


Figure B.336: HE 2236−6040

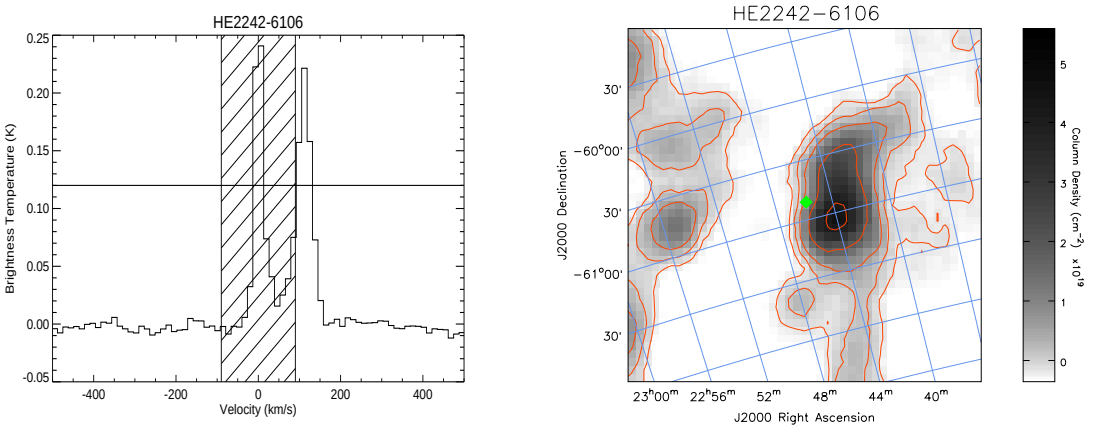


Figure B.337: HE 2242−6106

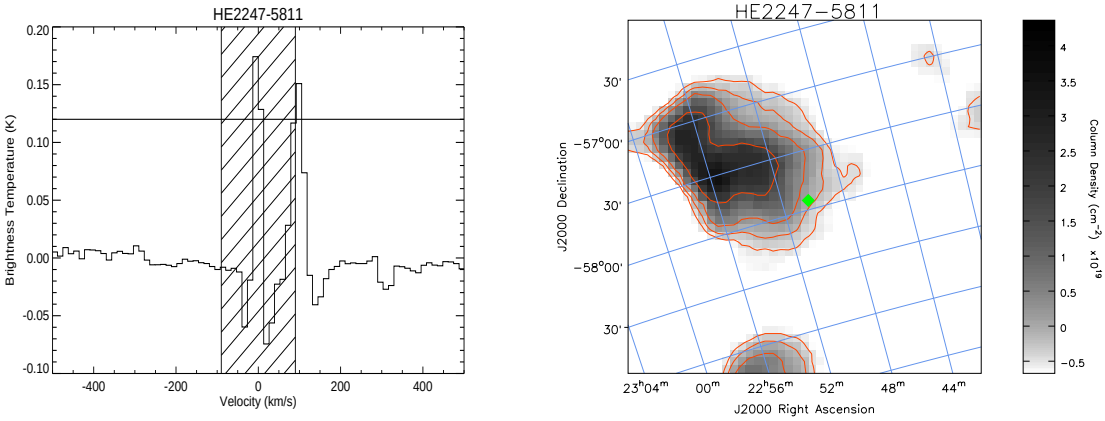


Figure B.338: HE 2247−5811

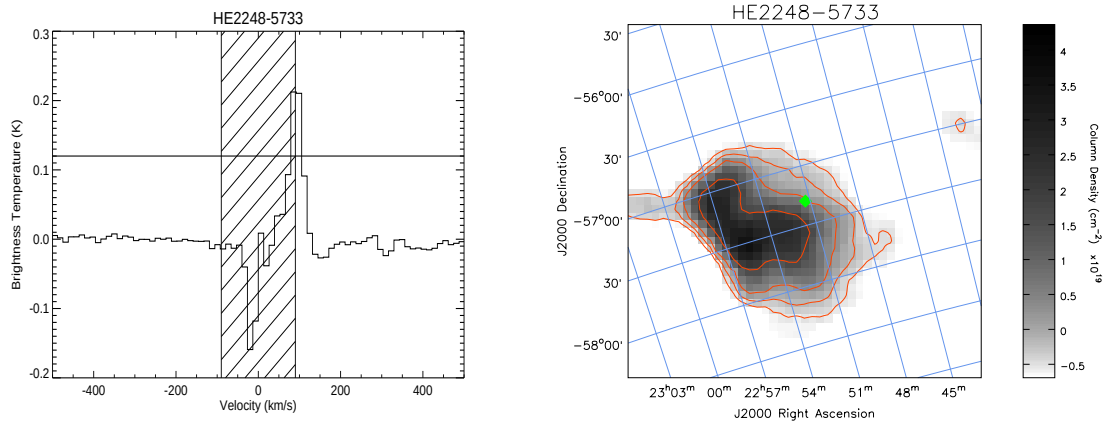


Figure B.339: HE 2248−5733

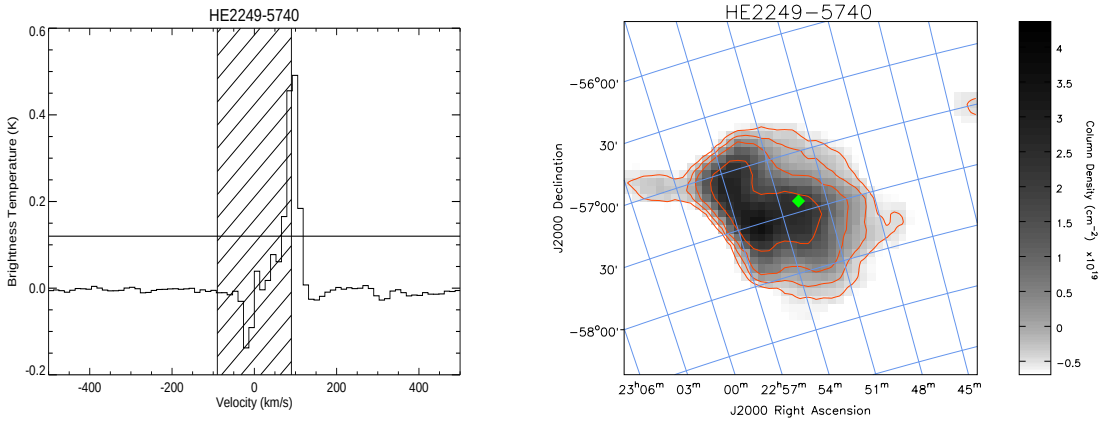


Figure B.340: HE 2249−5740

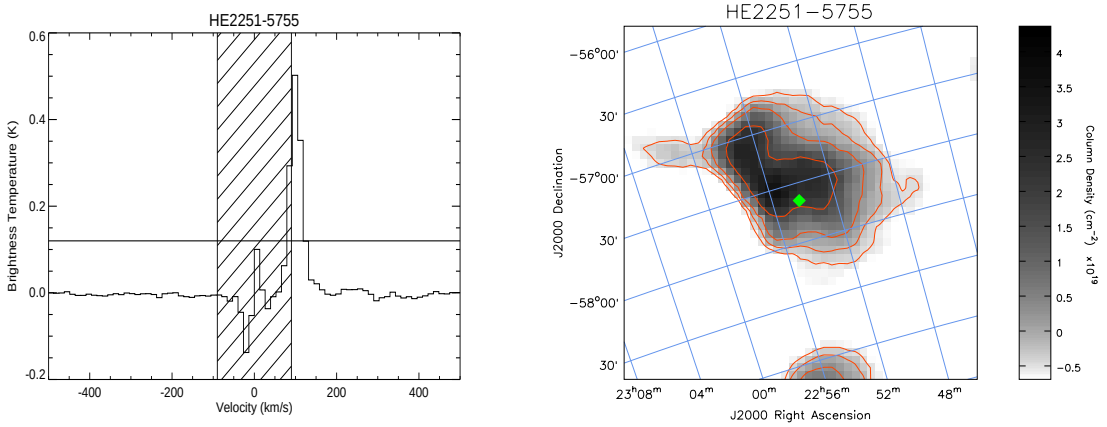


Figure B.341: HE 2251−5755

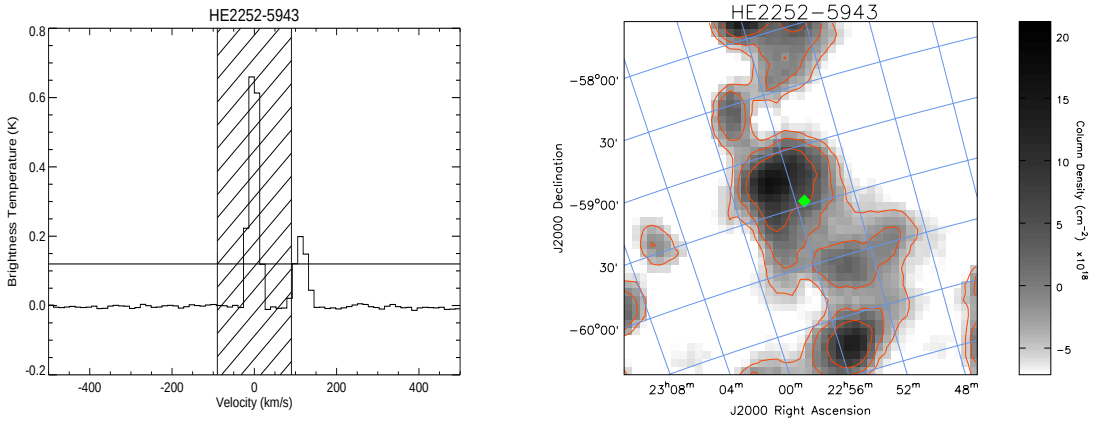


Figure B.342: HE 2252−5943

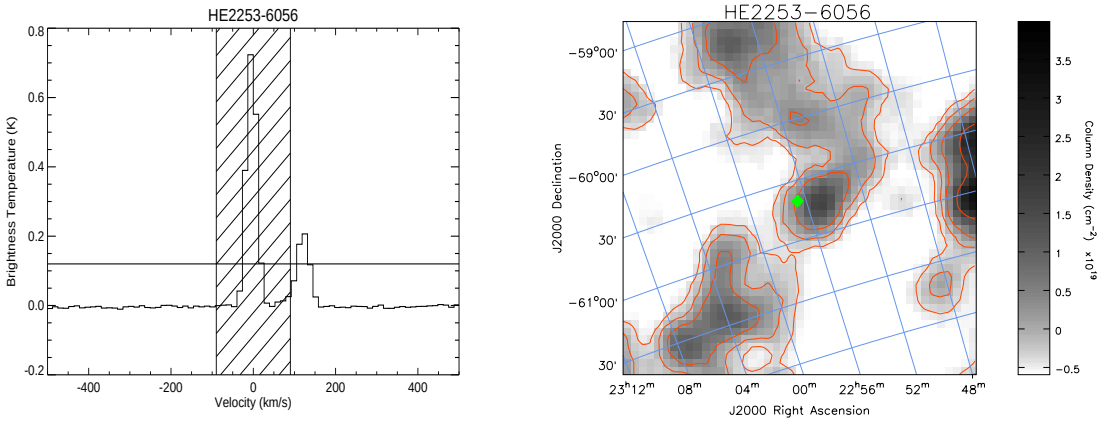


Figure B.343: HE 2253−6056

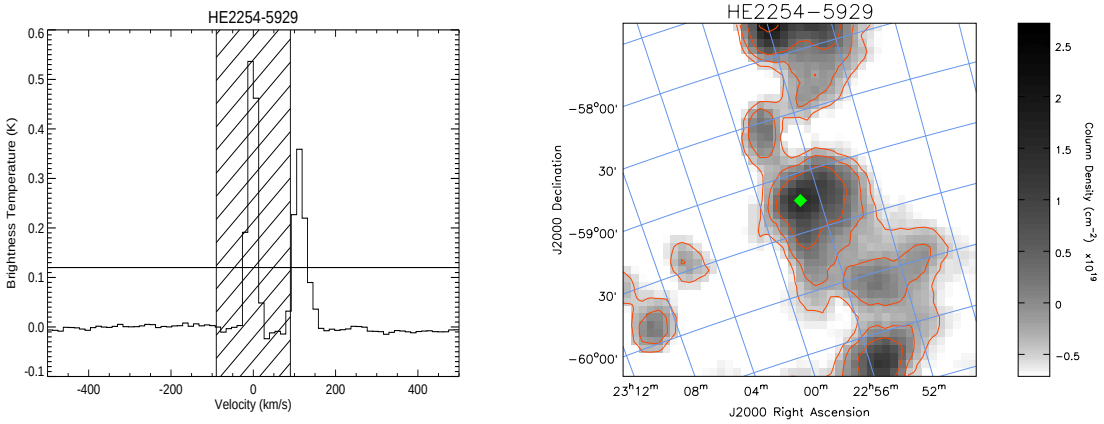


Figure B.344: HE 2254−5929

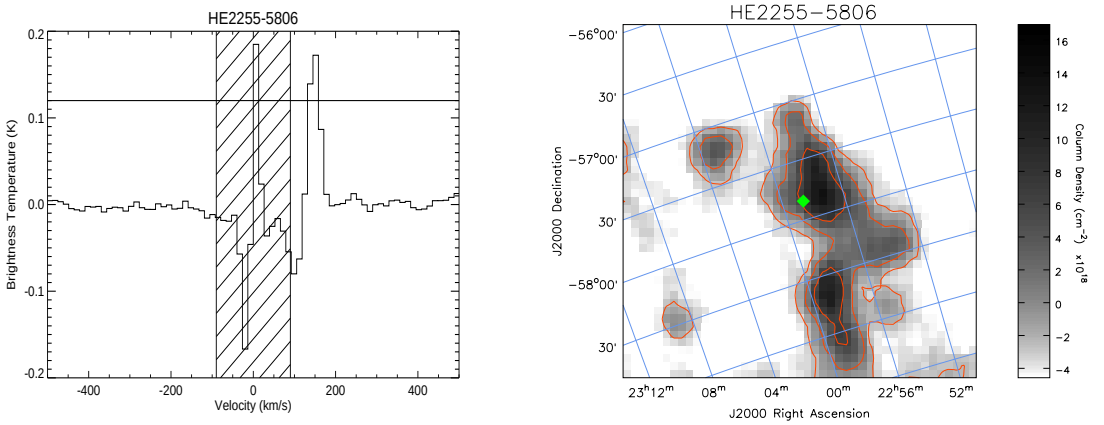


Figure B.345: HE 2255−5806

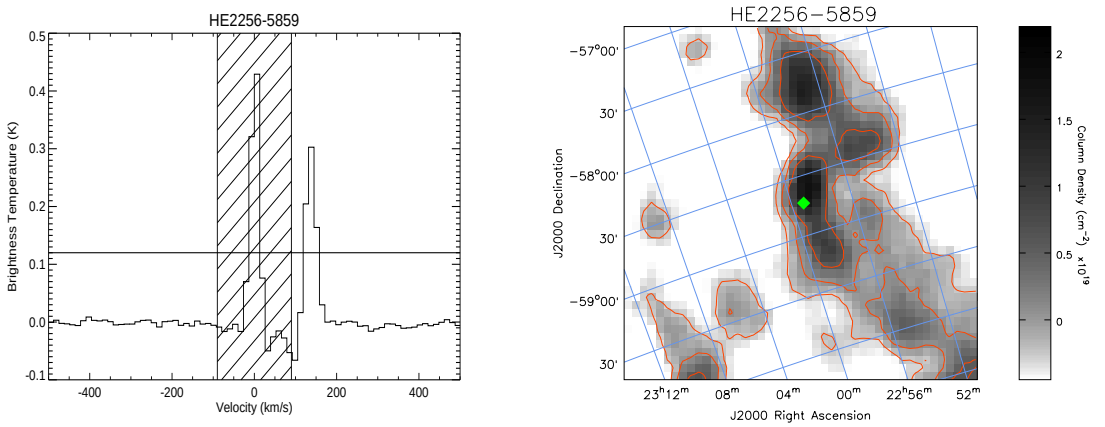


Figure B.346: HE 2256−5859

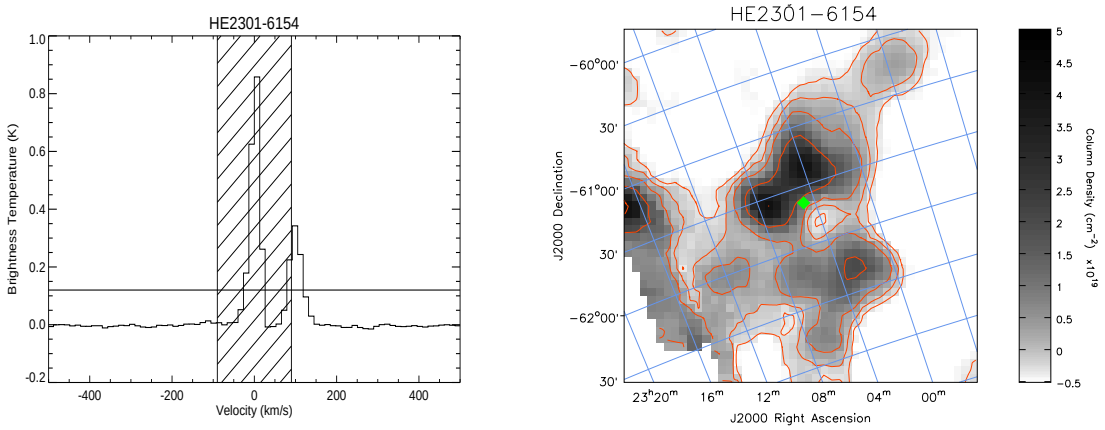


Figure B.347: HE 2301−6154

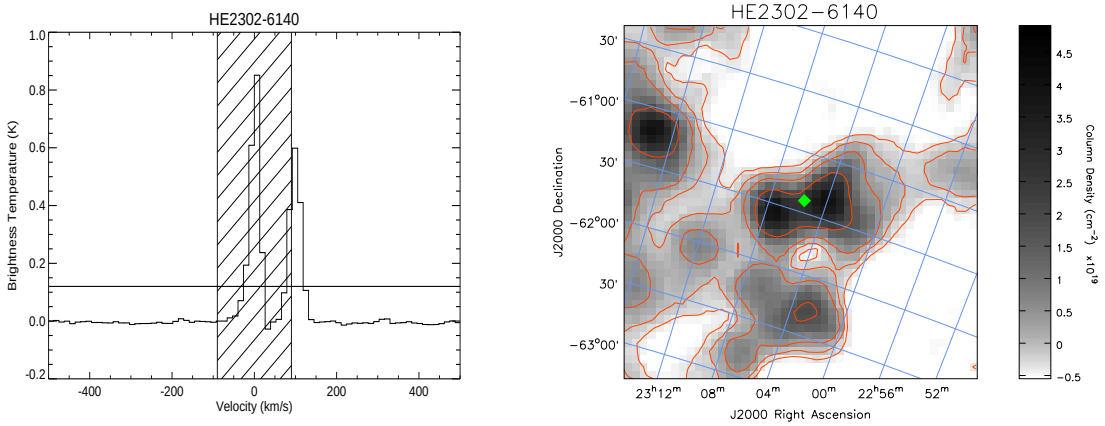


Figure B.348: HE 2302−6140

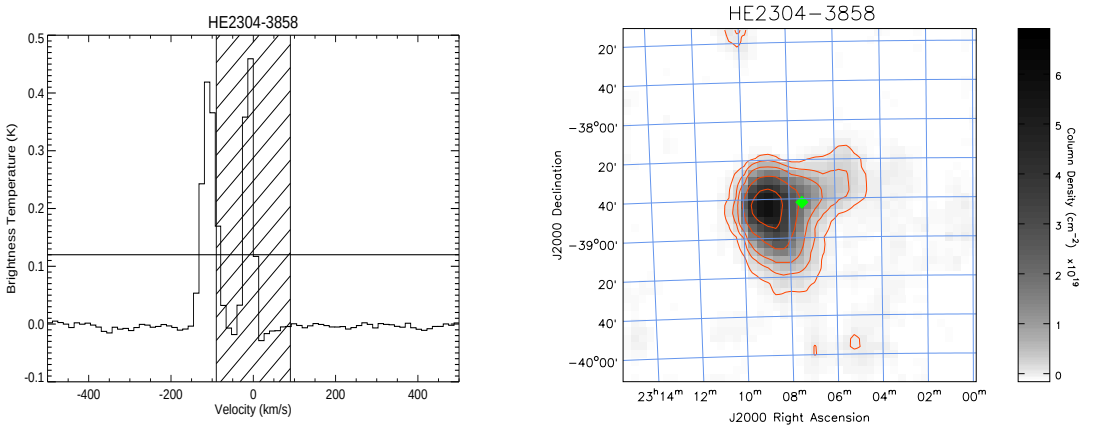


Figure B.349: HE 2304−3858

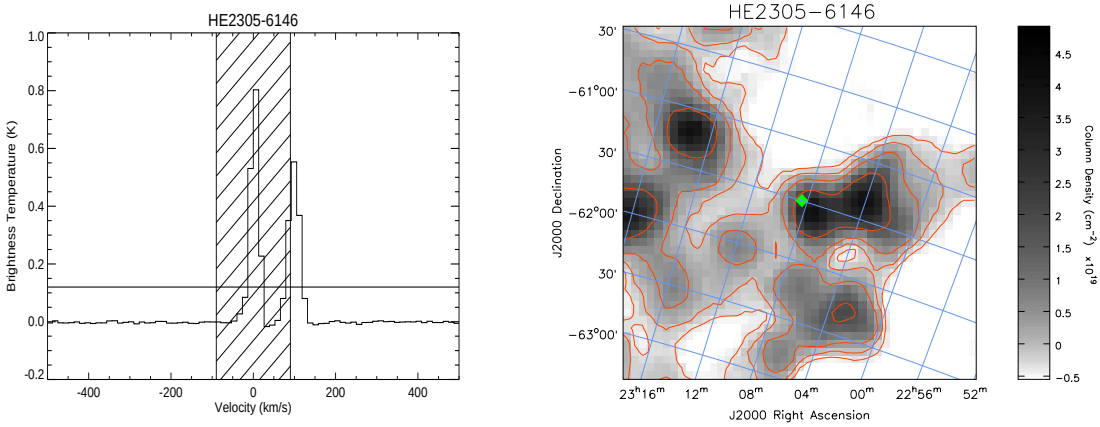


Figure B.350: HE 2305−6146

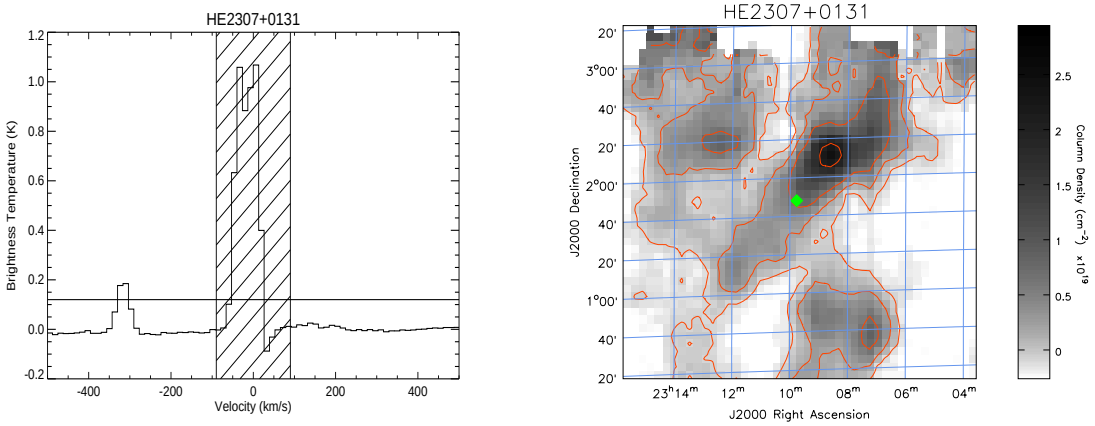


Figure B.351: HE 2307+0131

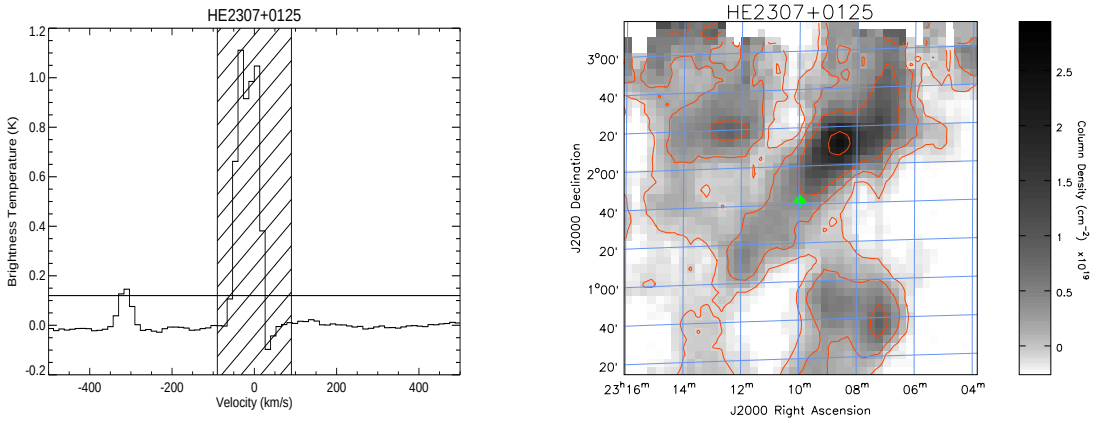


Figure B.352: HE 2307+0125

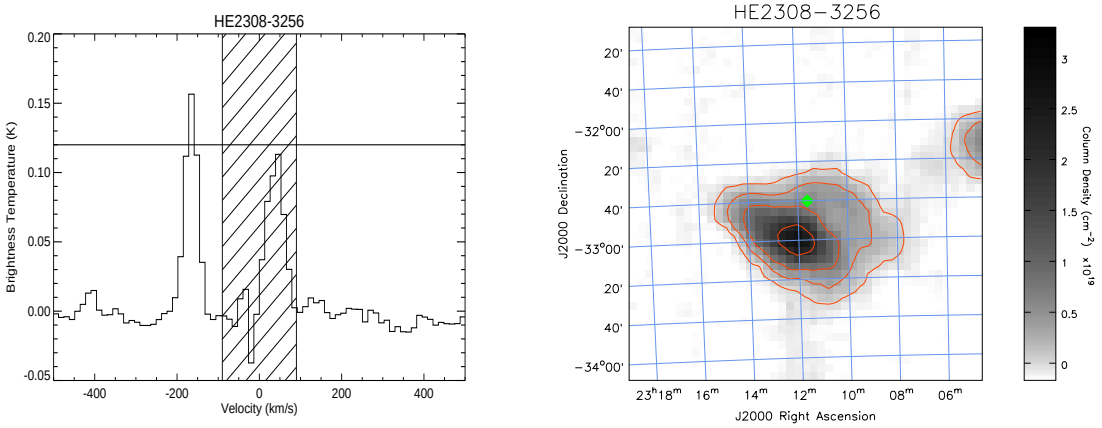


Figure B.353: HE 2308−3256

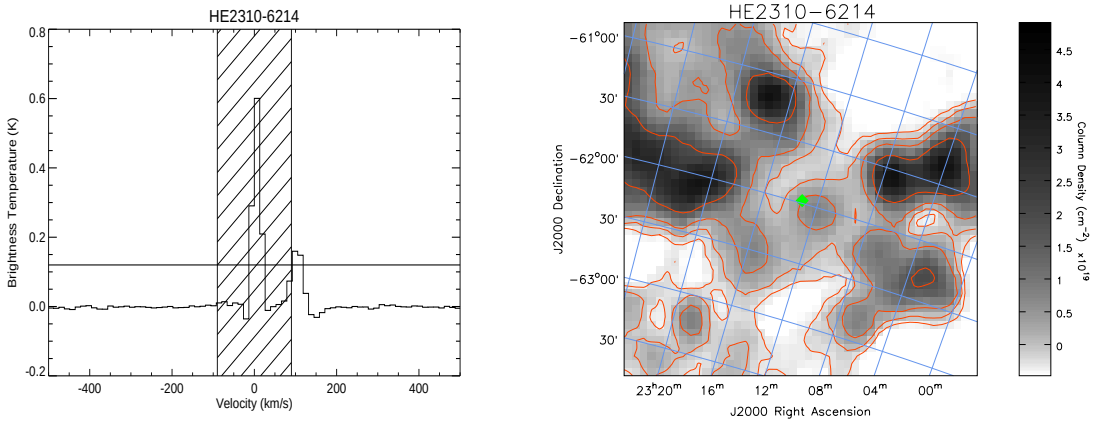


Figure B.354: HE 2310−6214

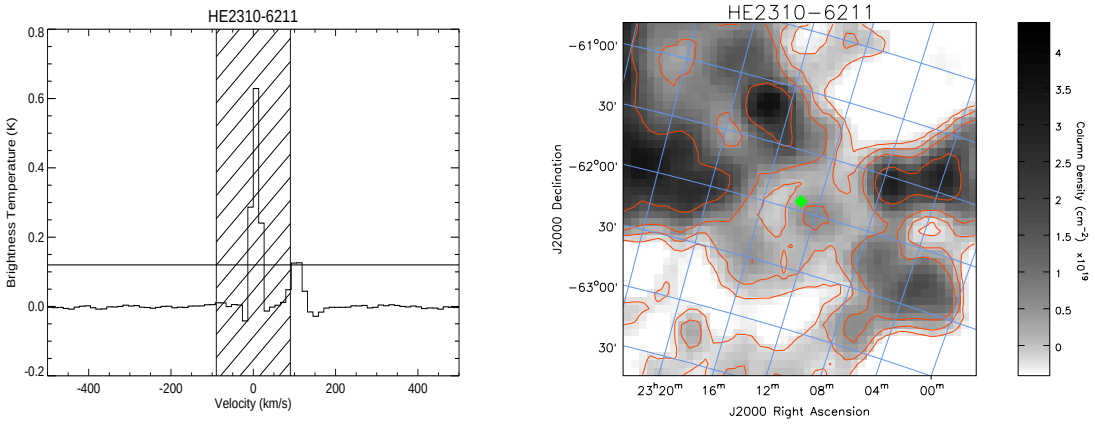


Figure B.355: HE 2310−6211

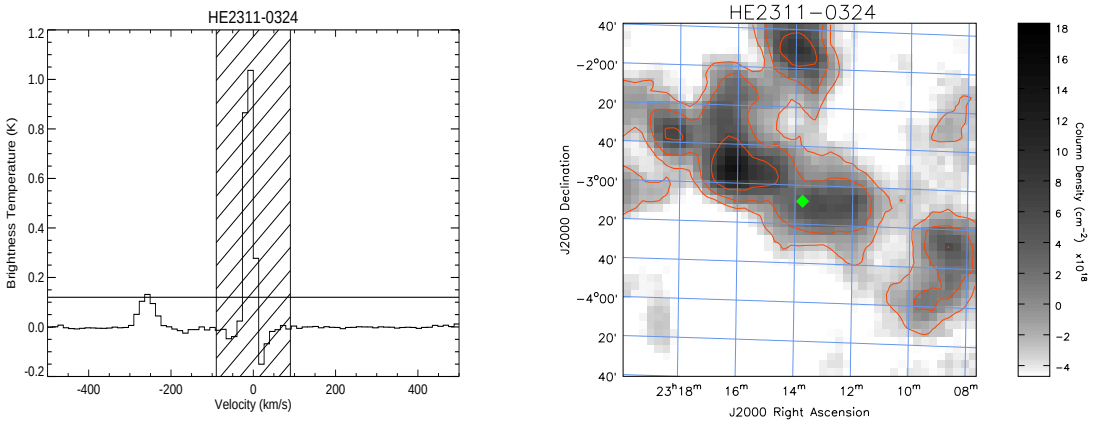


Figure B.356: HE 2311−0324

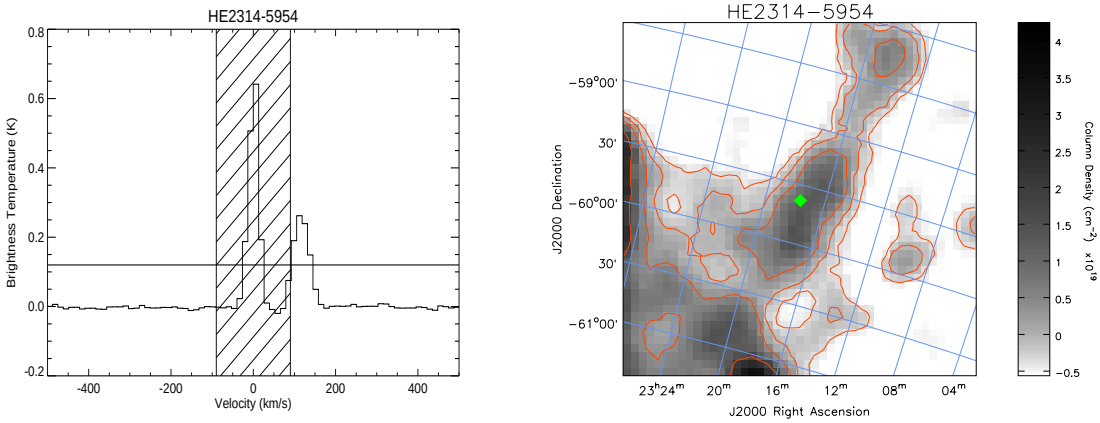
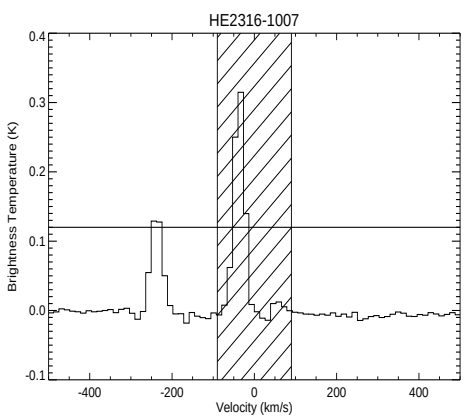


Figure B.357: HE 2314−5954



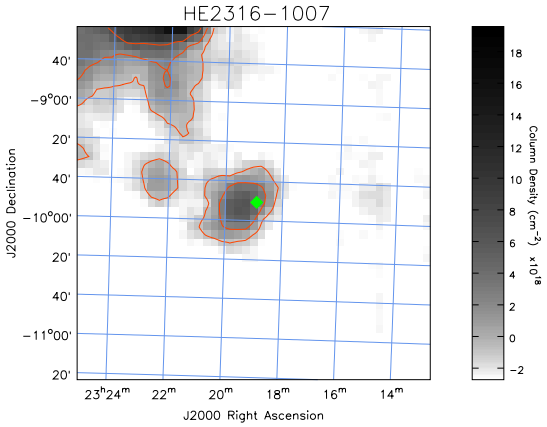
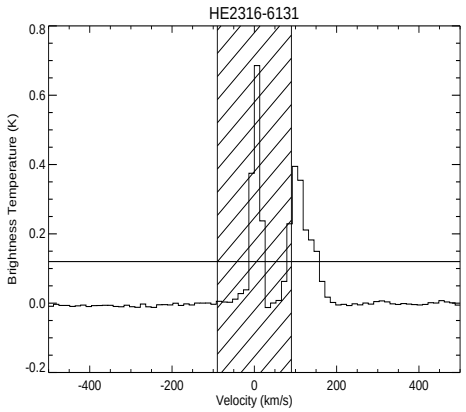


Figure B.358: HE 2316−1007



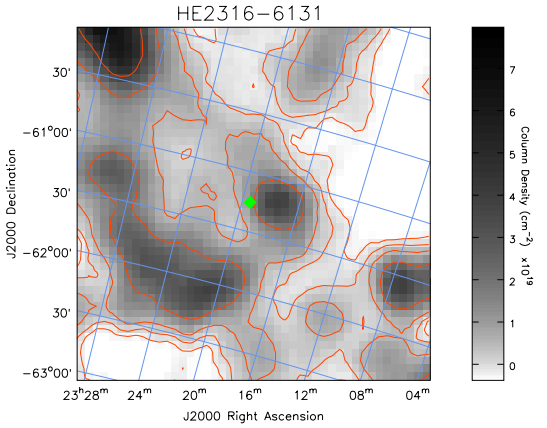
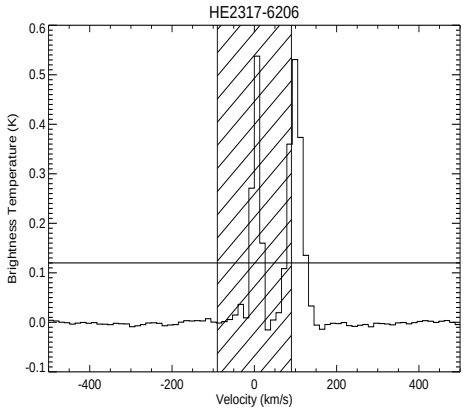


Figure B.359: HE 2316−6131



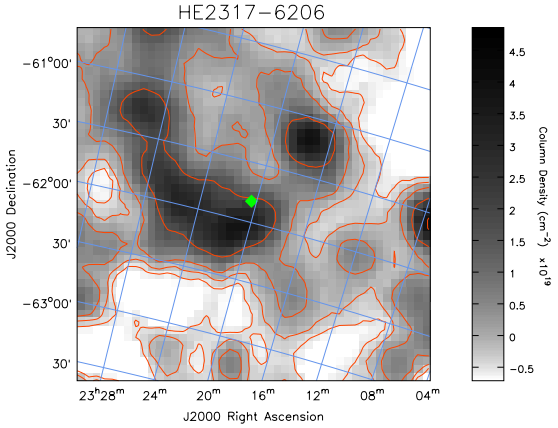
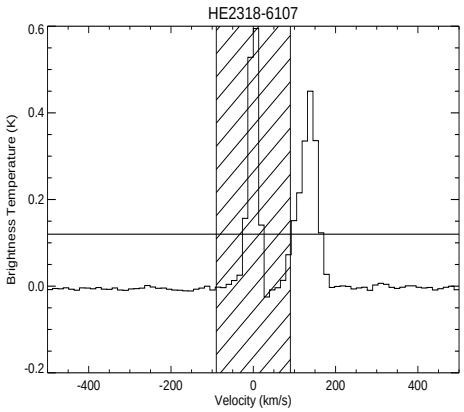


Figure B.360: HE 2317−6206



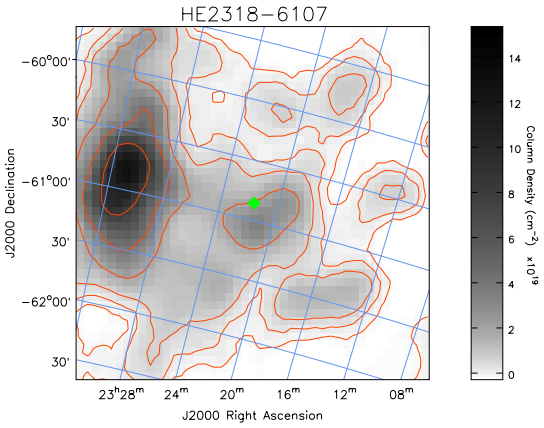
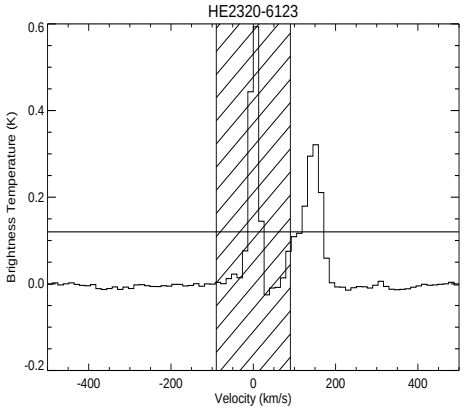


Figure B.361: HE 2318−6107



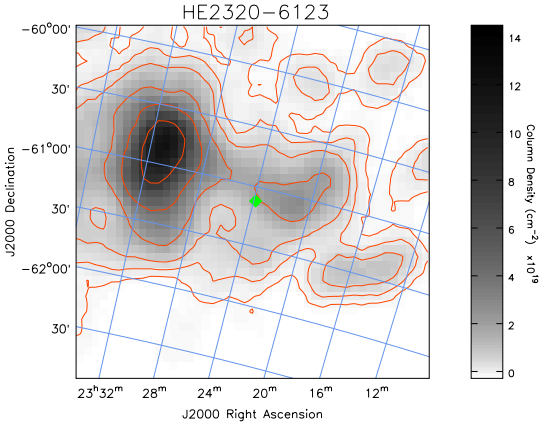
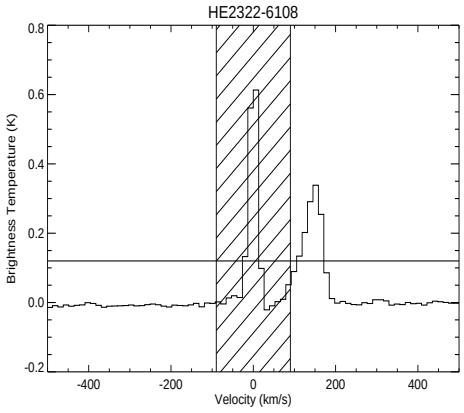


Figure B.362: HE 2320−6123



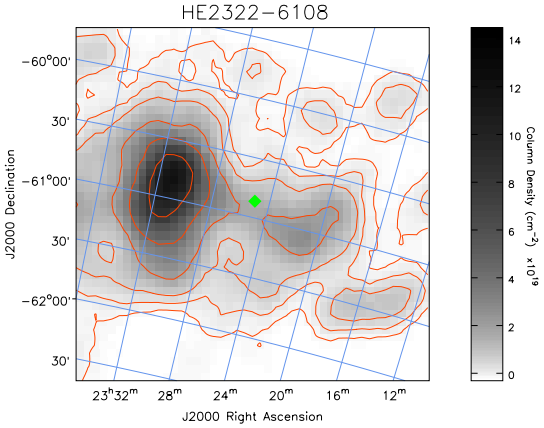


Figure B.363: HE 2322−6108

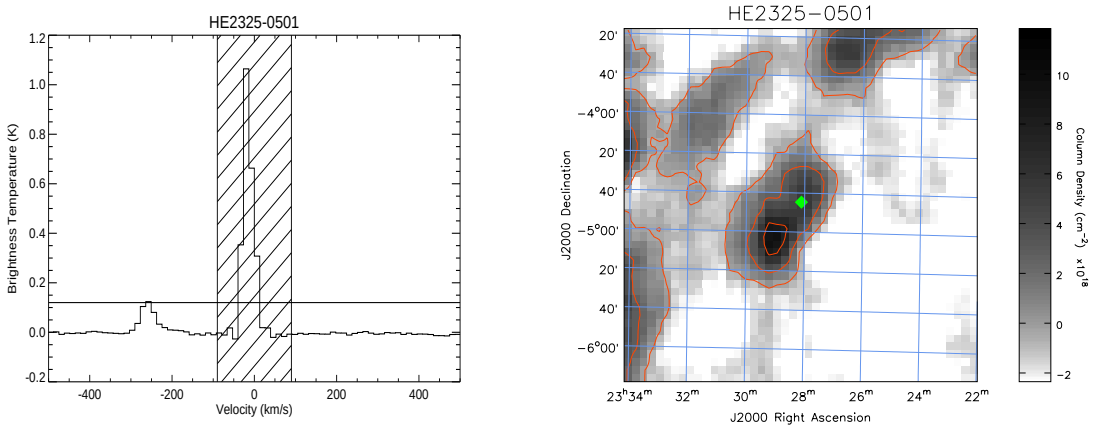


Figure B.364: HE 2325−0501

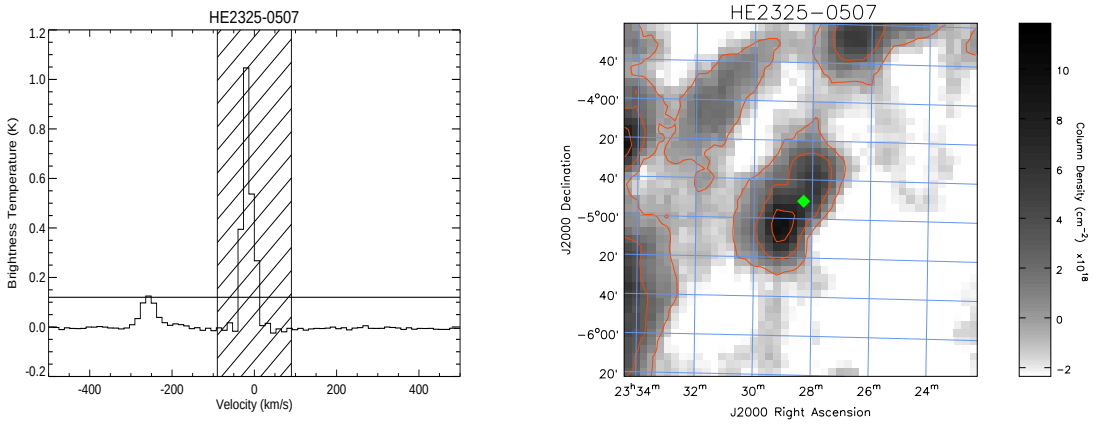


Figure B.365: HE 2325−0507

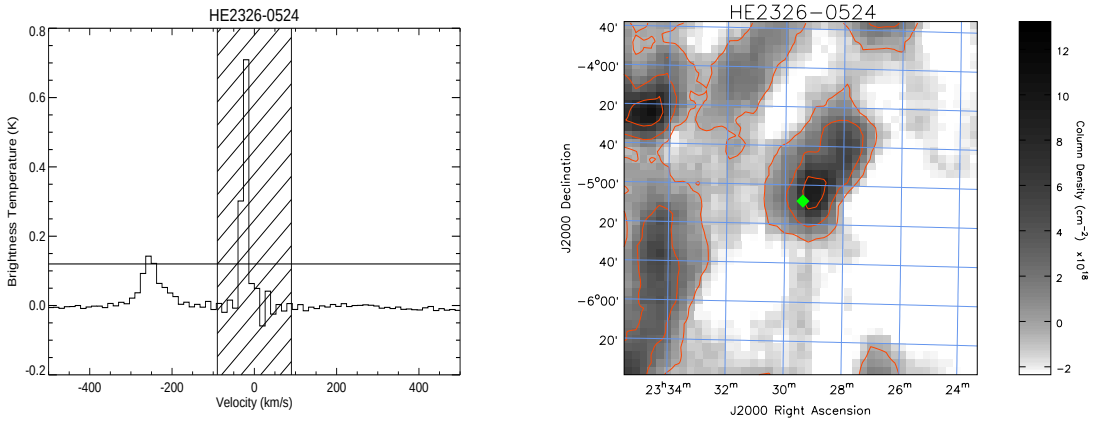


Figure B.366: HE 2326−0524

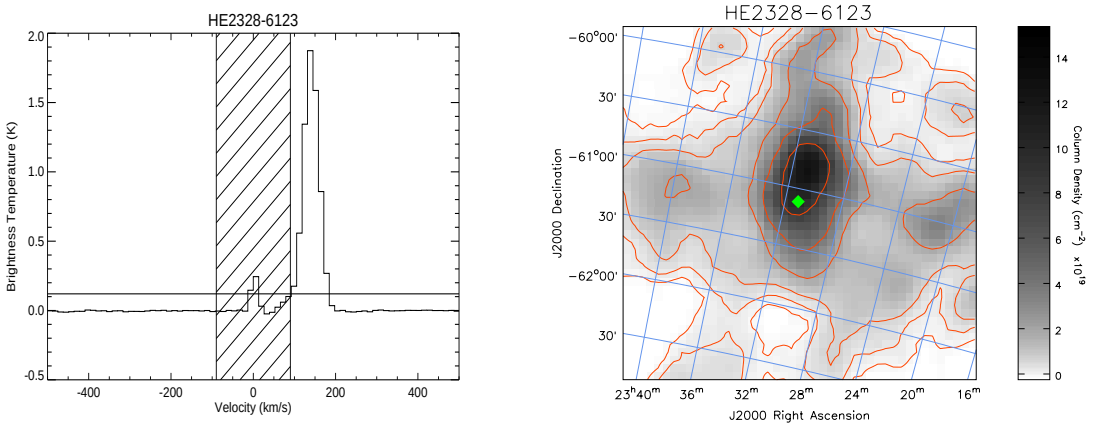


Figure B.367: HE 2328−6123

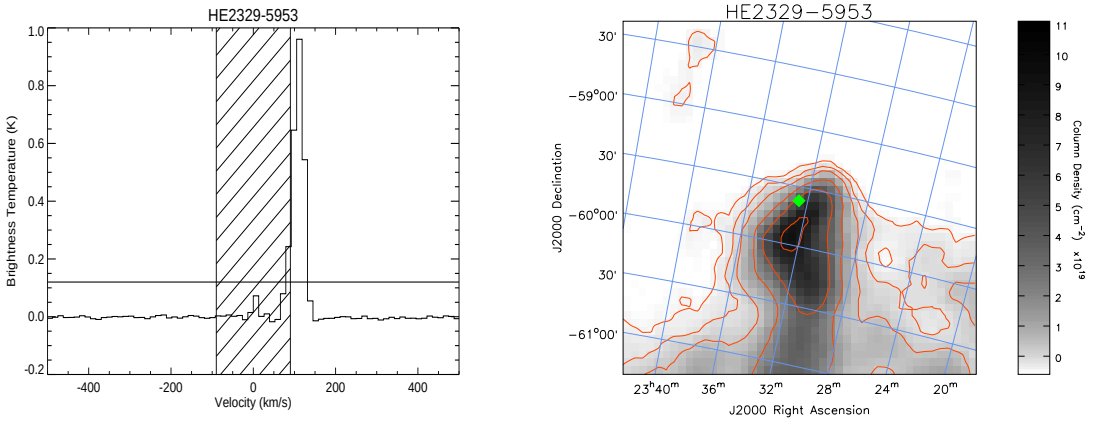


Figure B.368: HE 2329−5953

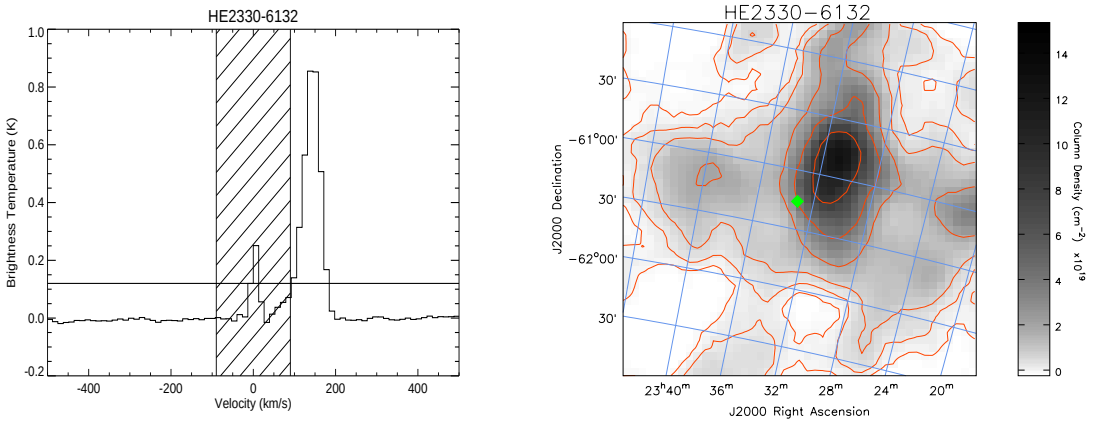


Figure B.369: HE 2330−6132

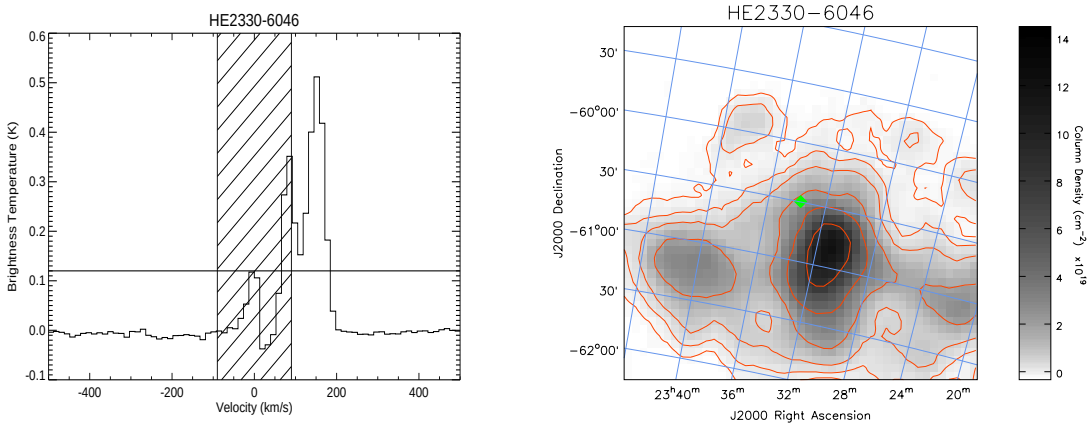


Figure B.370: HE 2330−6046

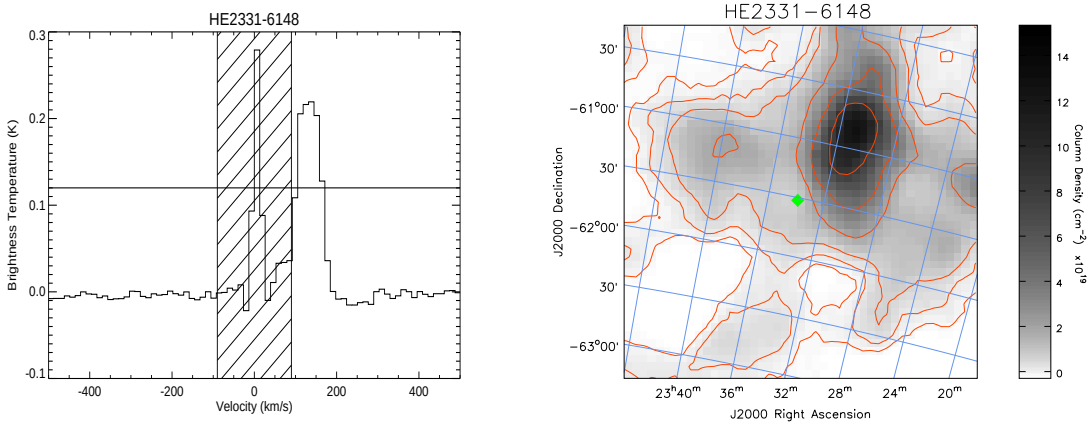


Figure B.371: HE 2331−6148

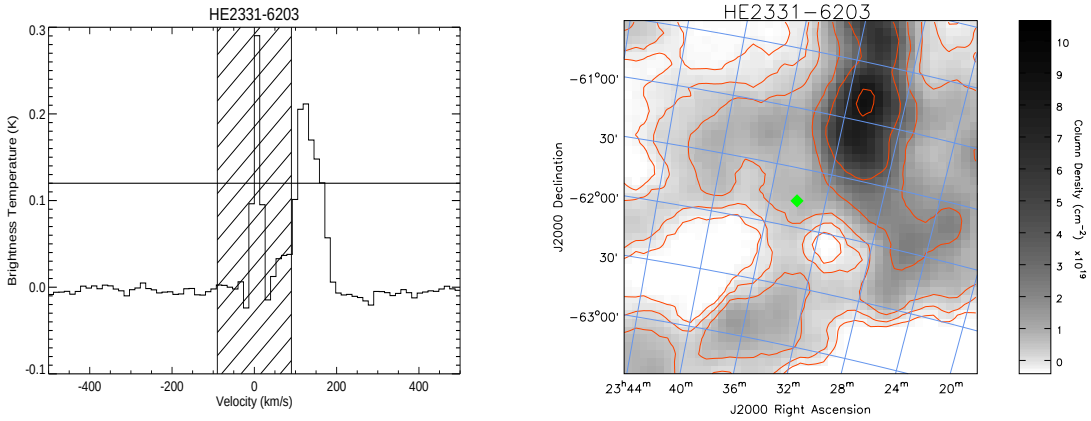


Figure B.372: HE 2331−6203

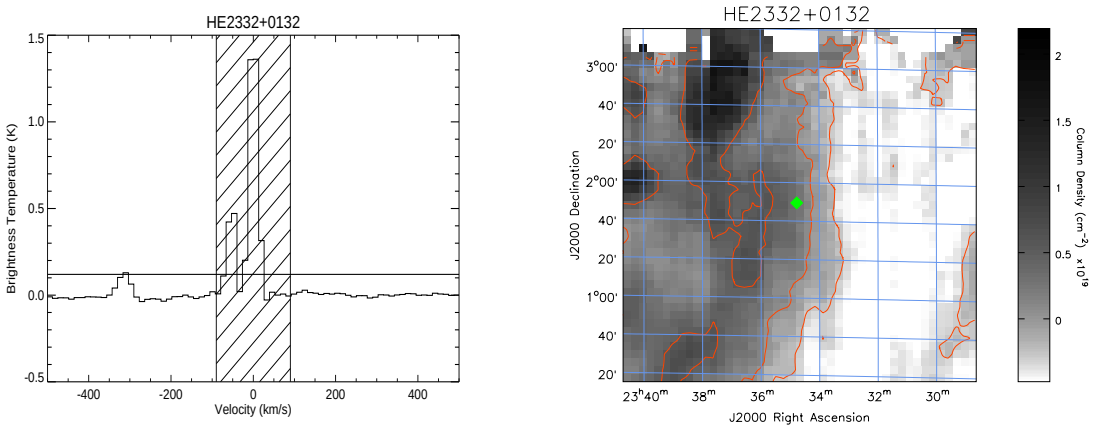


Figure B.373: HE 2332+0132

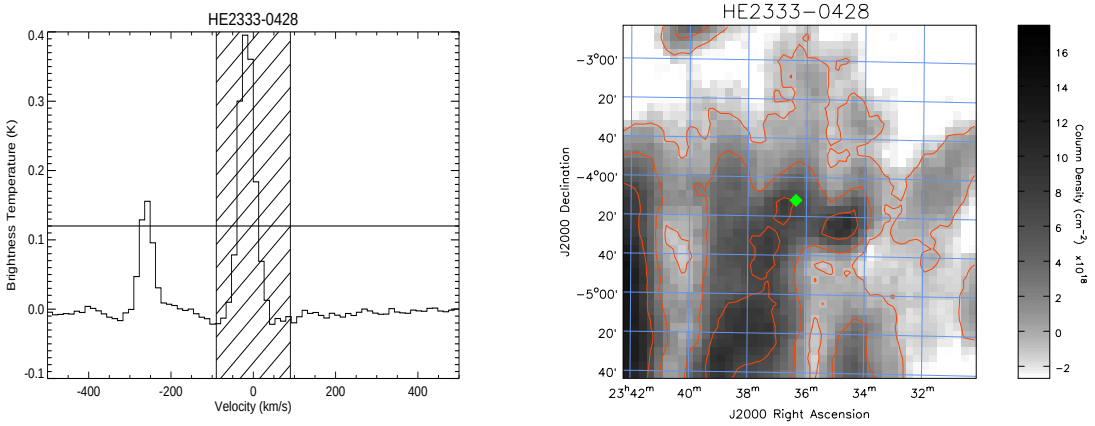


Figure B.374: HE 2333−0428

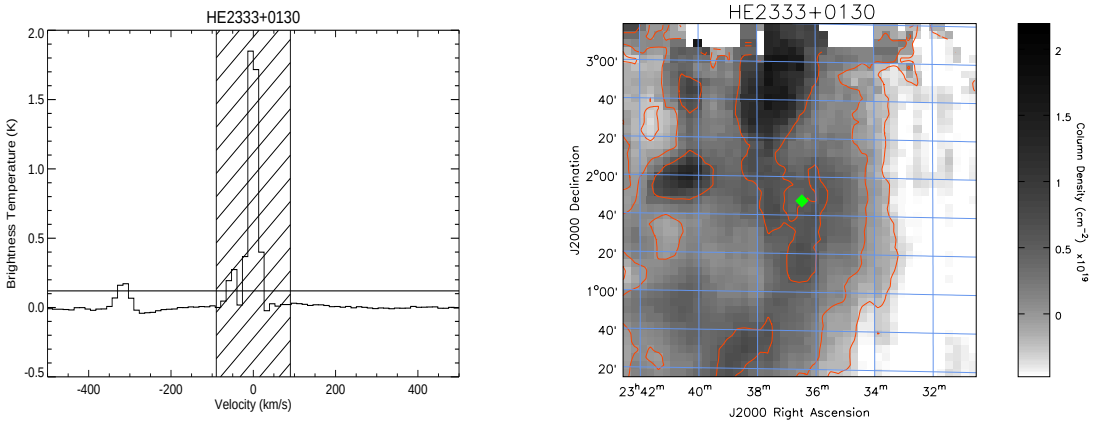


Figure B.375: HE 2333+0130

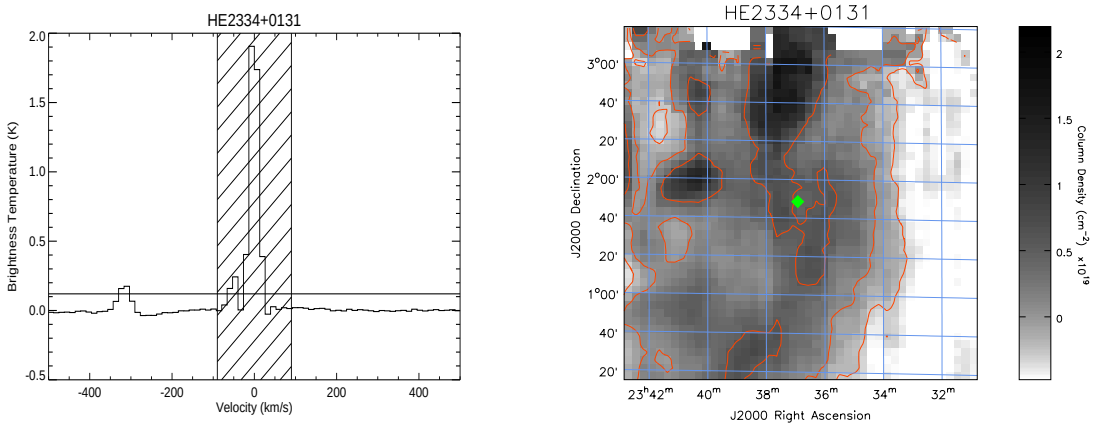


Figure B.376: HE 2334+0131

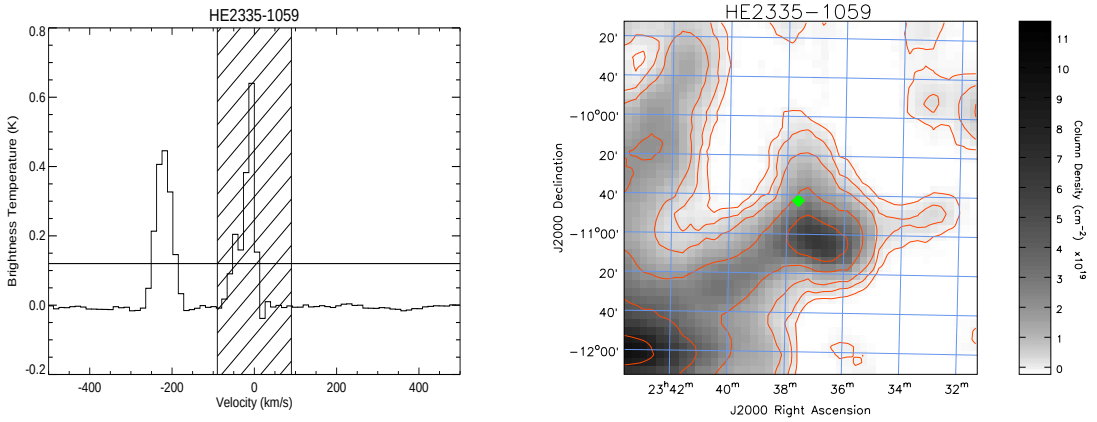


Figure B.377: HE 2335−1059

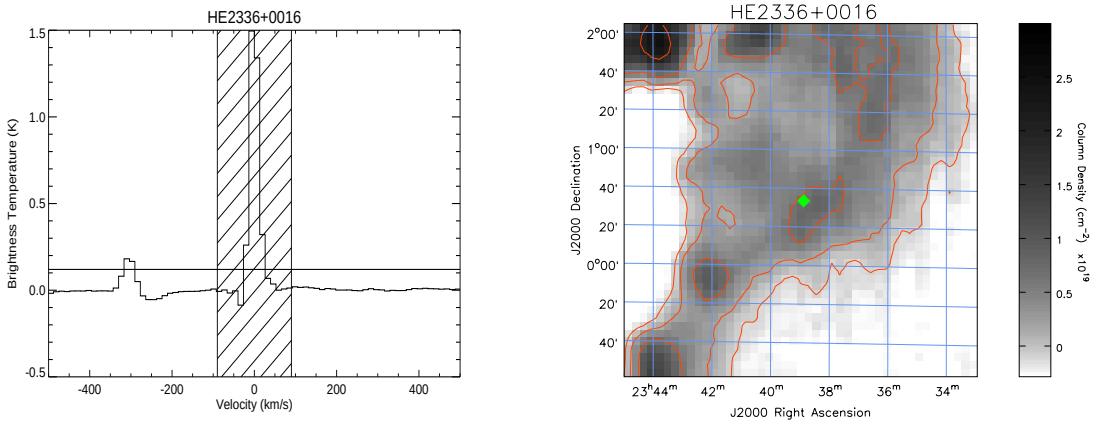


Figure B.378: HE 2336+0016

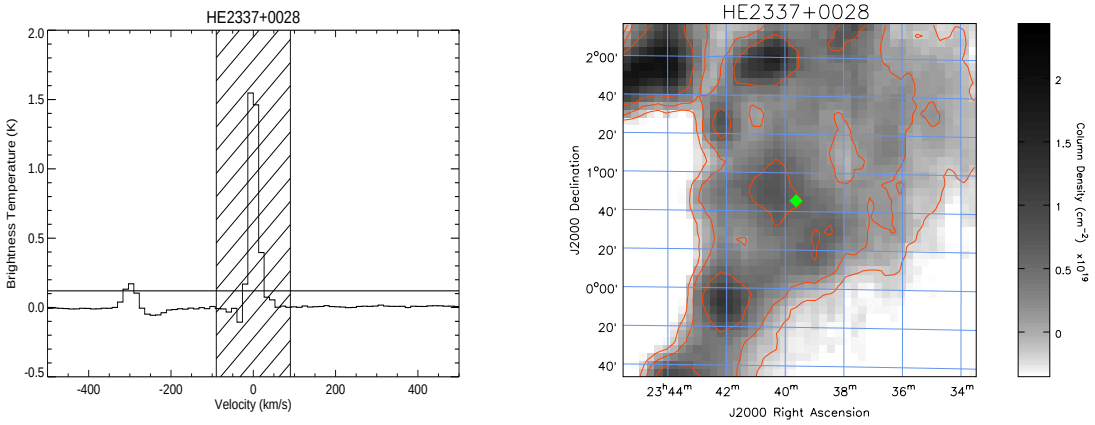


Figure B.379: HE 2337+0028

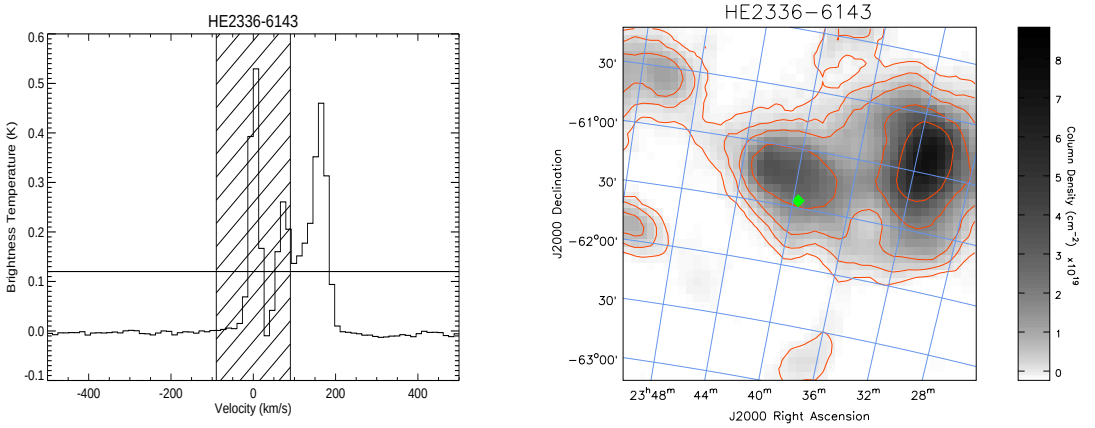


Figure B.380: HE 2336−6143

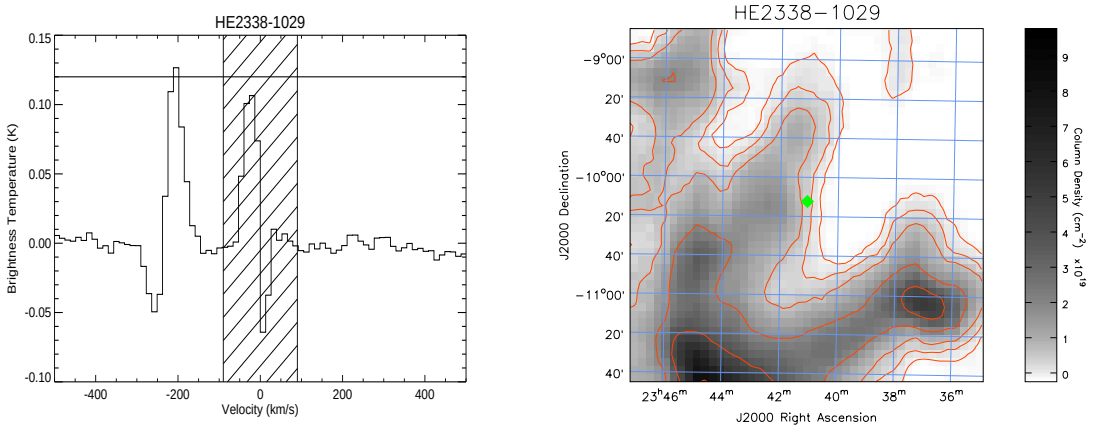


Figure B.381: HE 2338−1029

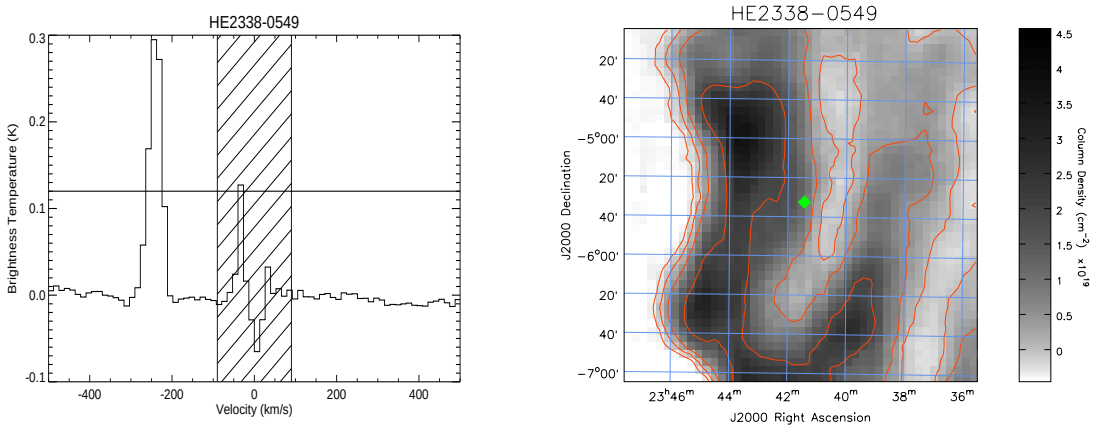


Figure B.382: HE 2338−0549

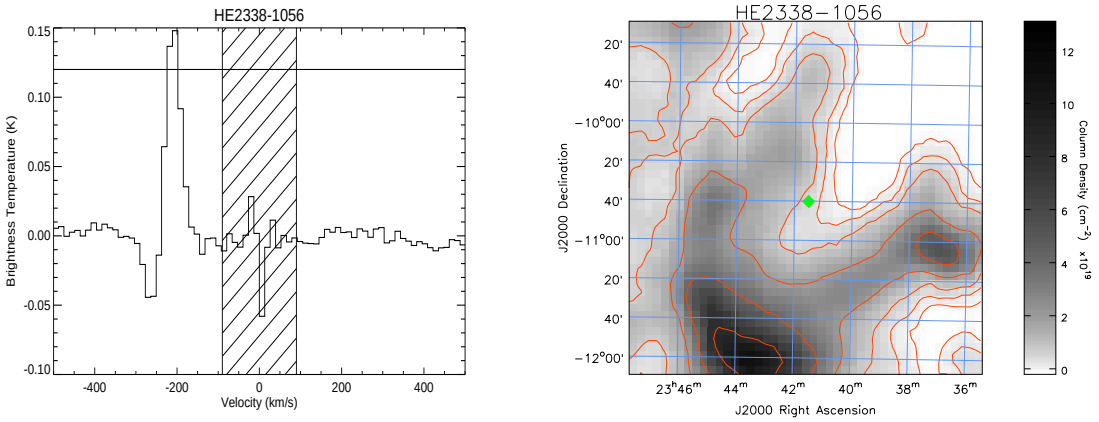


Figure B.383: HE 2338−1056

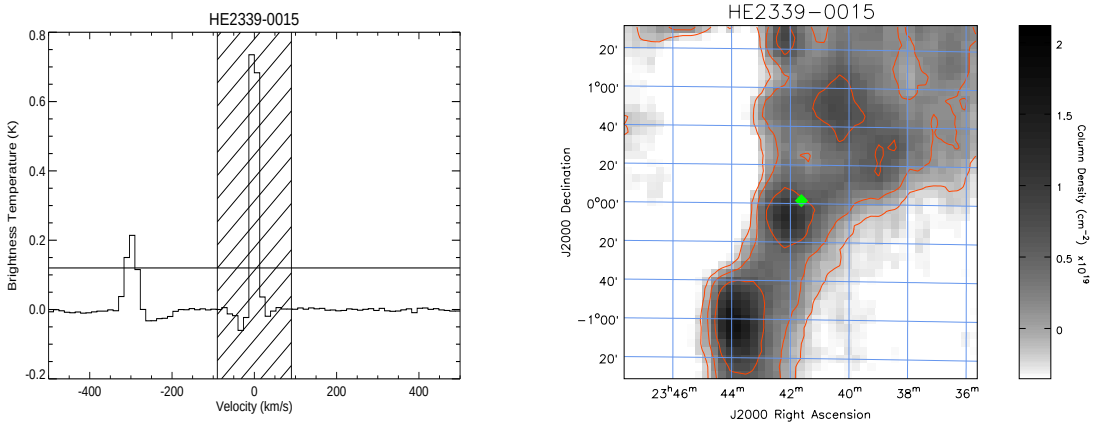


Figure B.384: HE 2339−0015

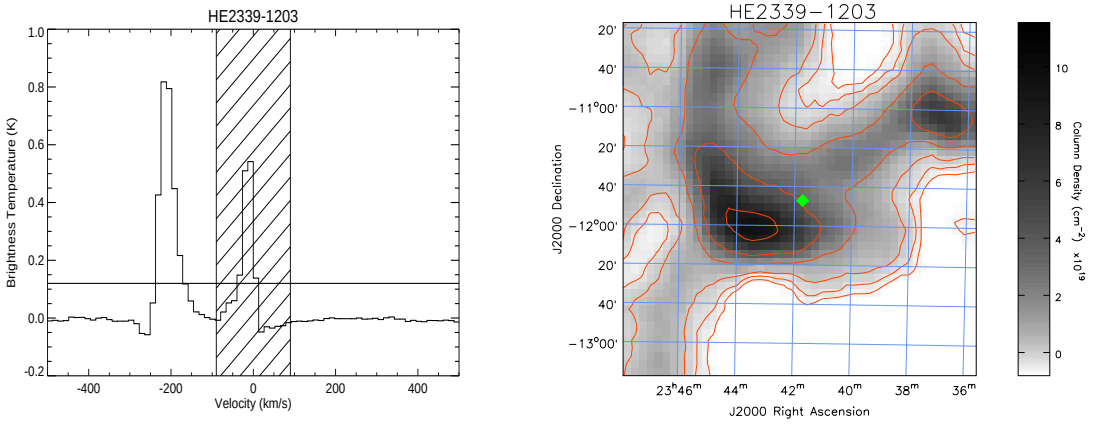


Figure B.385: HE 2339−1203

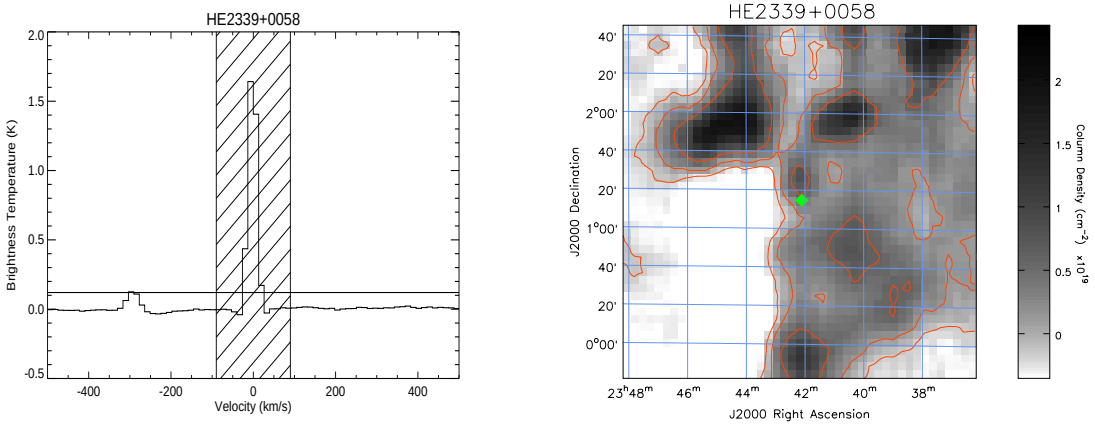


Figure B.386: HE 2339+0058

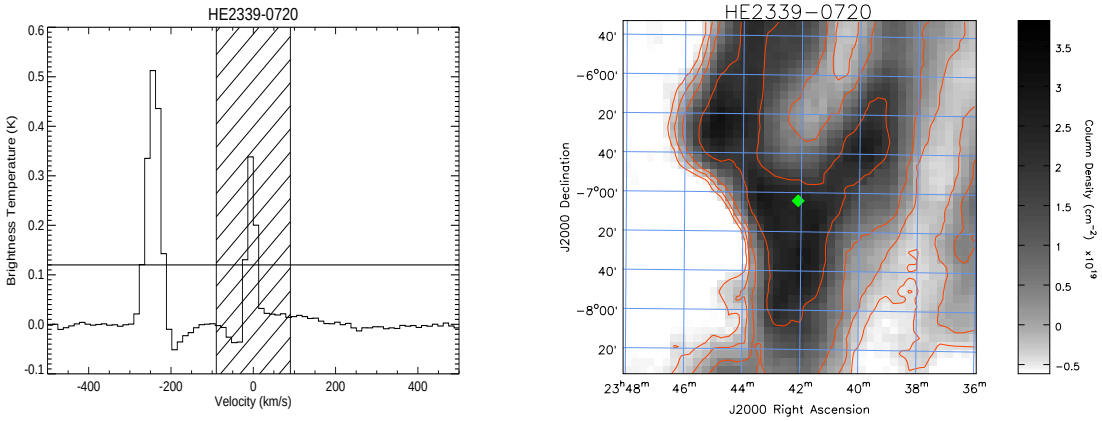


Figure B.387: HE 2339−0720

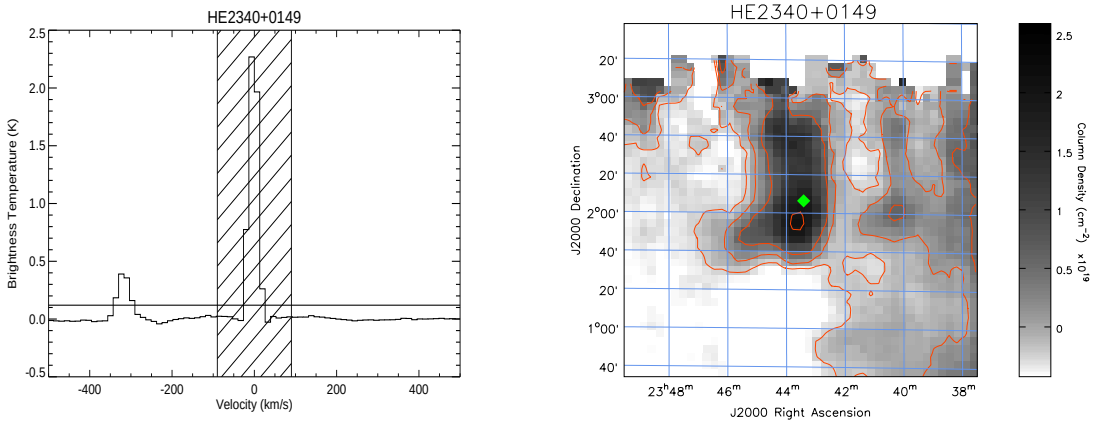


Figure B.388: HE 2340+0149

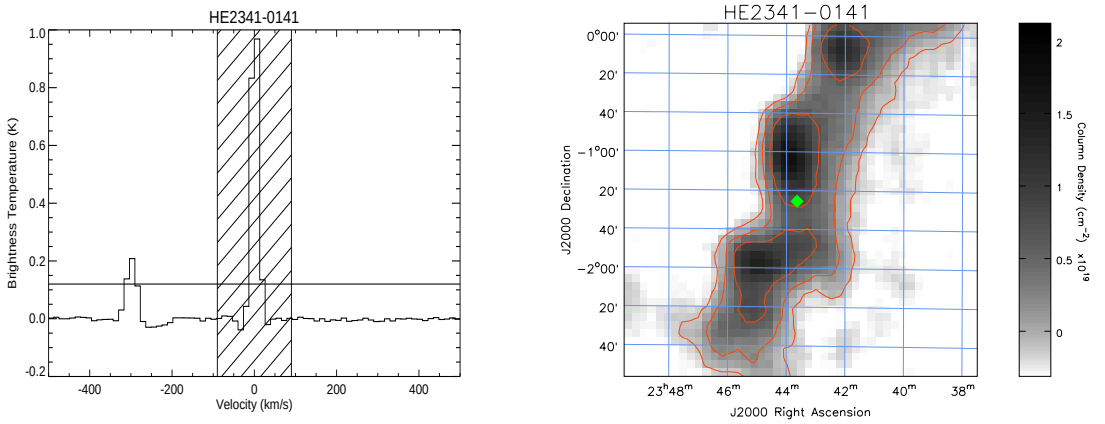


Figure B.389: HE 2341−0141

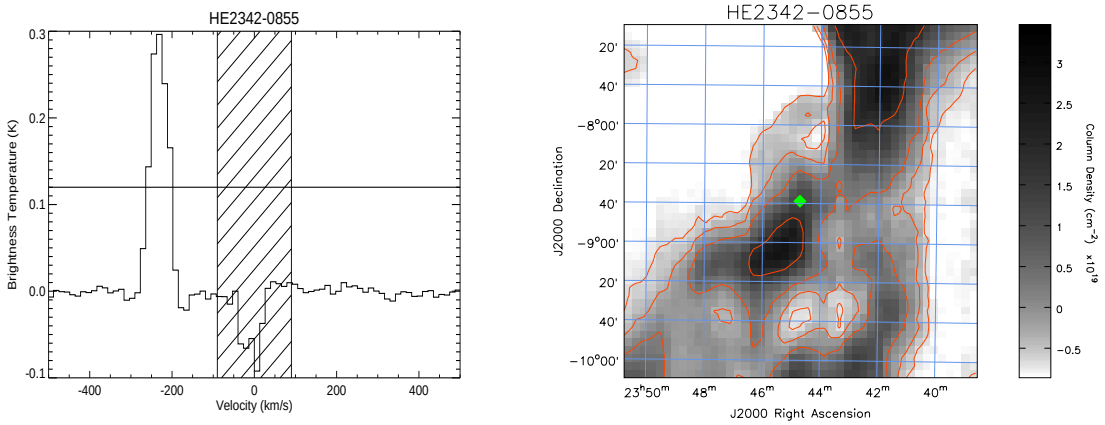


Figure B.390: HE 2342−0855

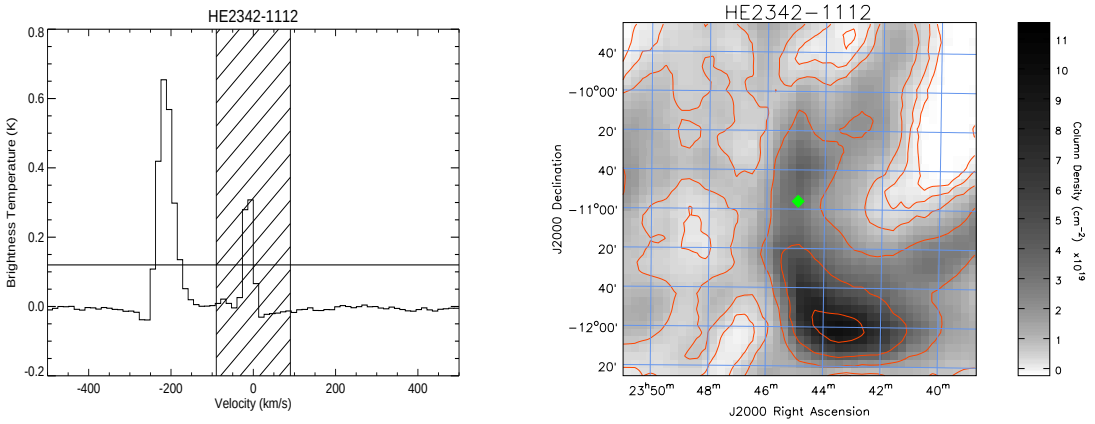


Figure B.391: HE 2342−1112

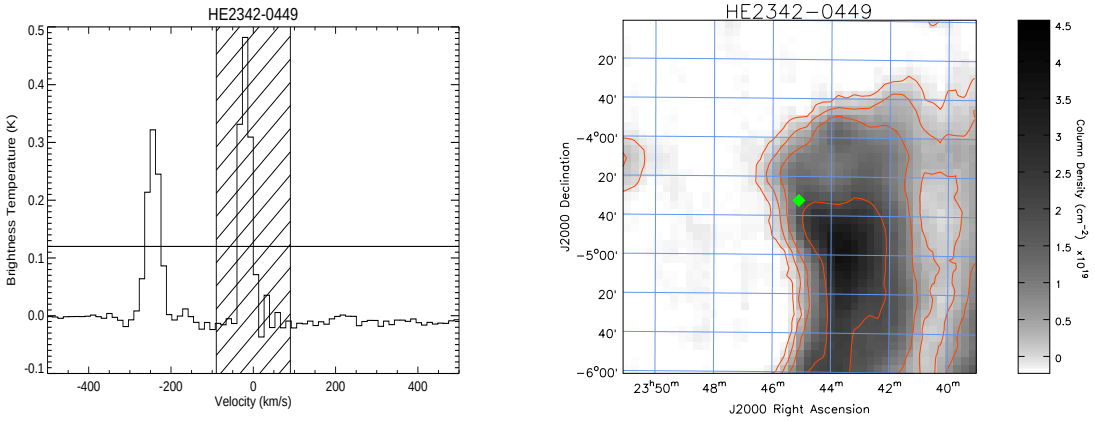


Figure B.392: HE 2342−0449

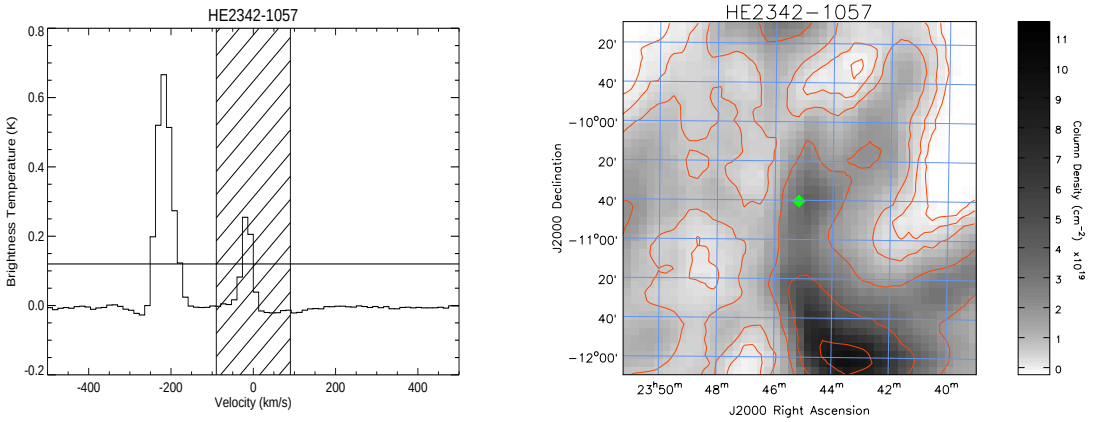


Figure B.393: HE 2342−1057

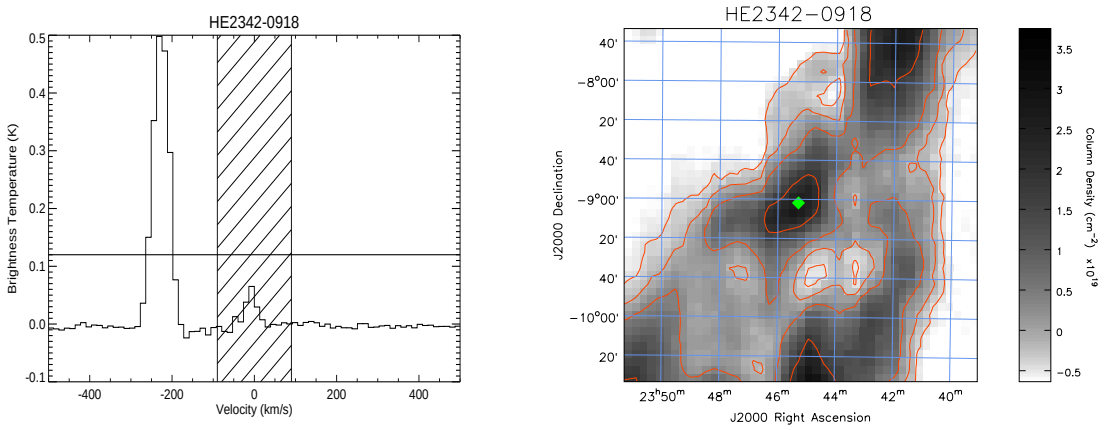


Figure B.394: HE 2342−0918

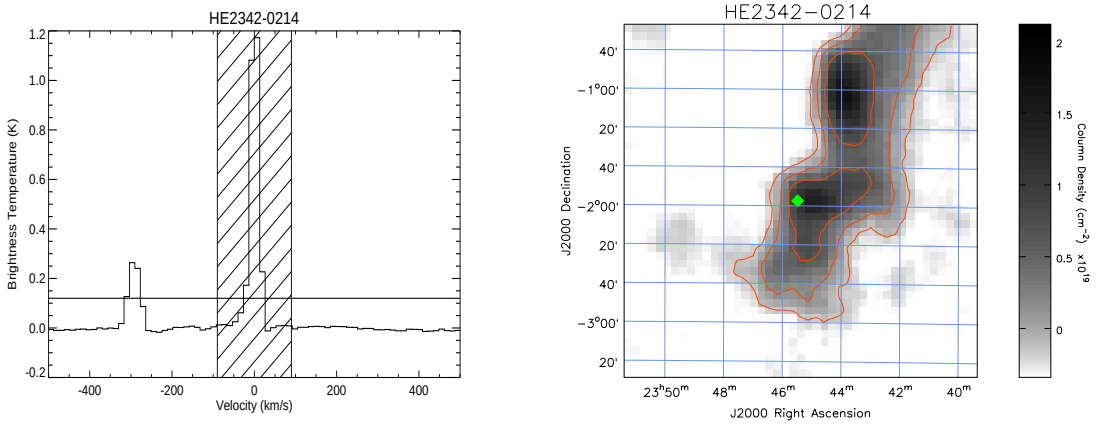


Figure B.395: HE 2342−0214

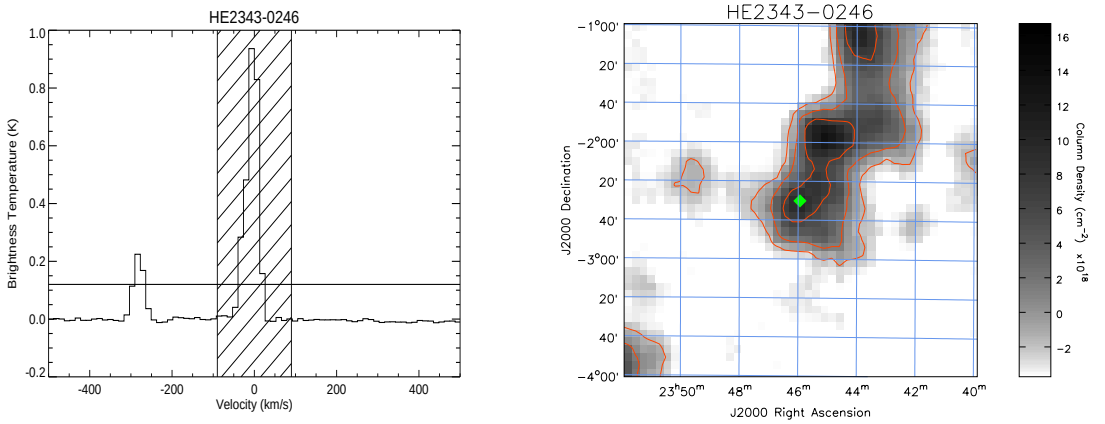


Figure B.396: HE 2343−0246

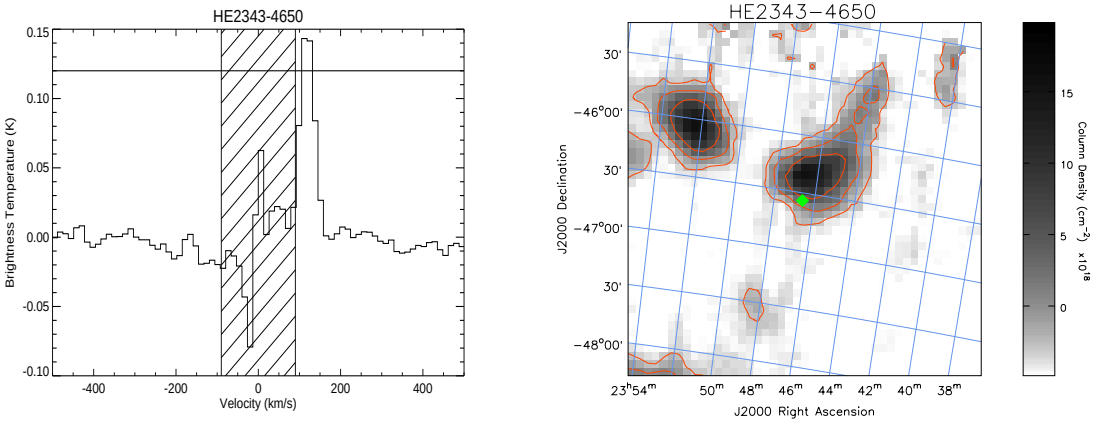


Figure B.397: HE 2343−4650

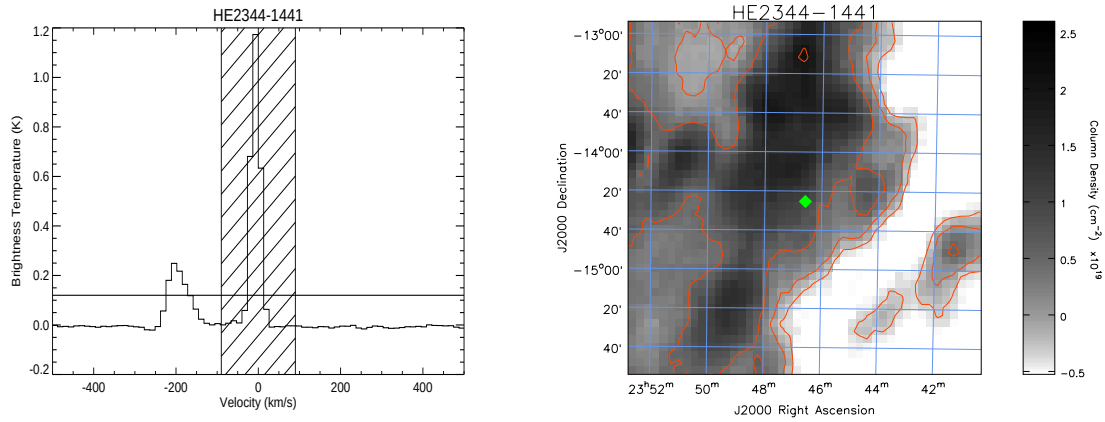


Figure B.398: HE 2344−1441

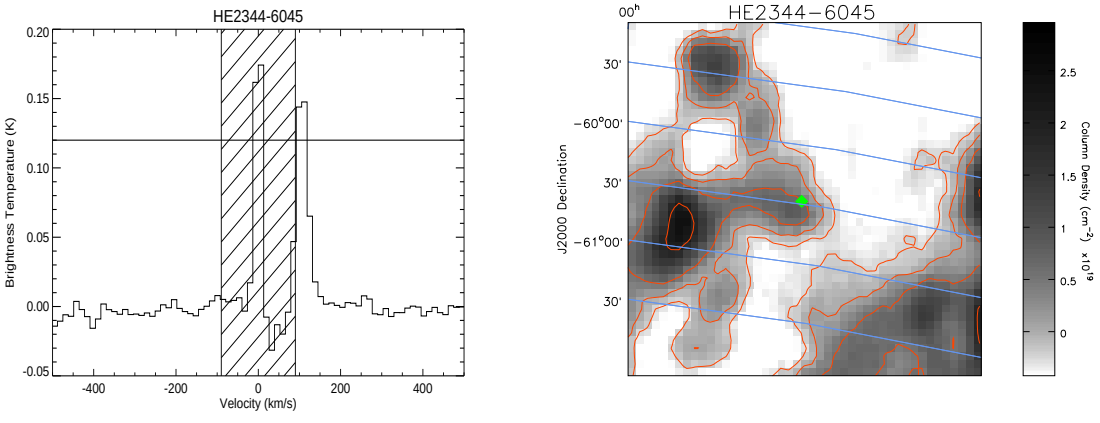
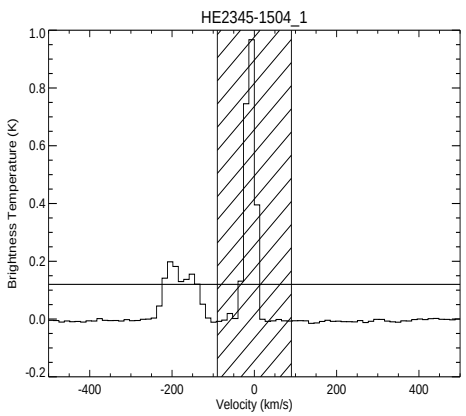


Figure B.399: HE 2344−6045



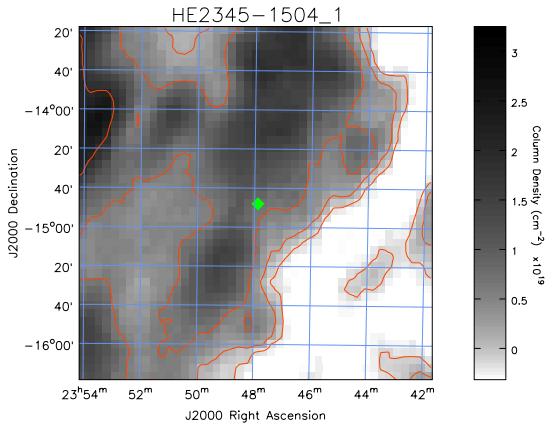
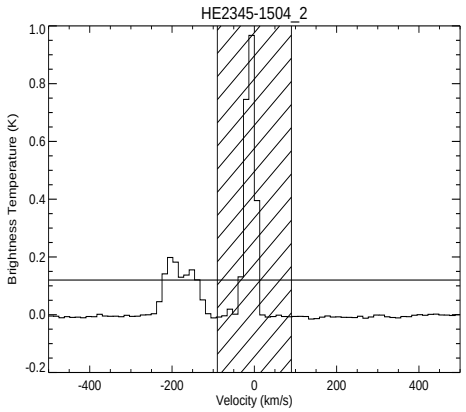


Figure B.400: HE 2345−1504_1



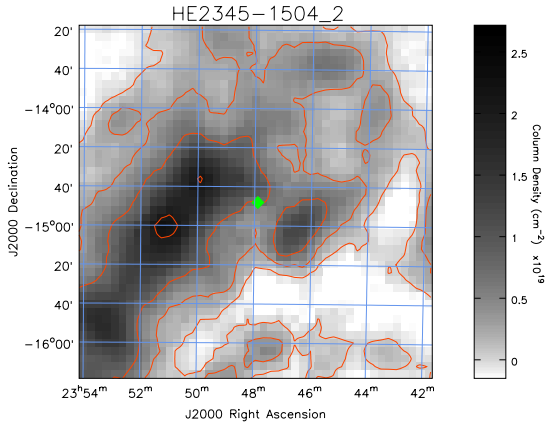
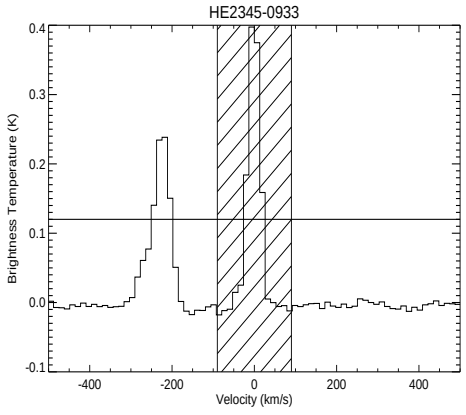


Figure B.401: HE 2345−1504_2



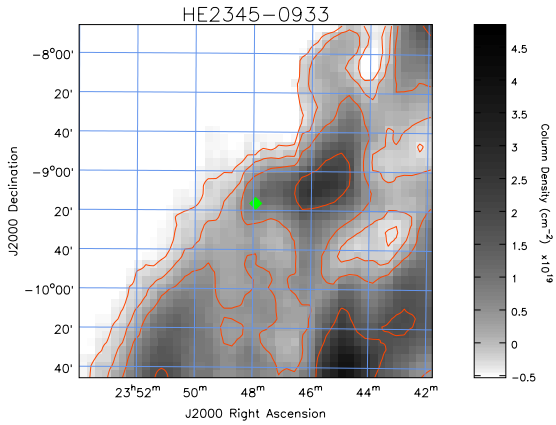


Figure B.402: HE 2345−0933

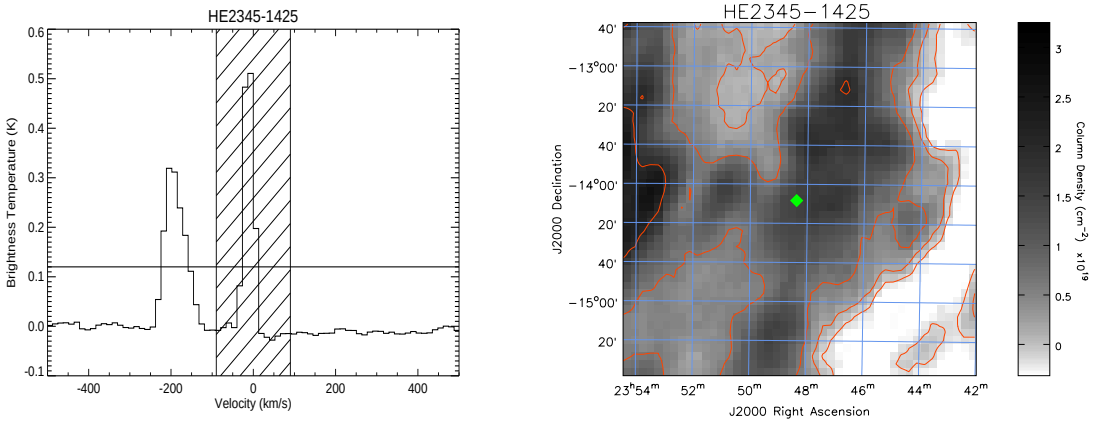


Figure B.403: HE 2345−1425

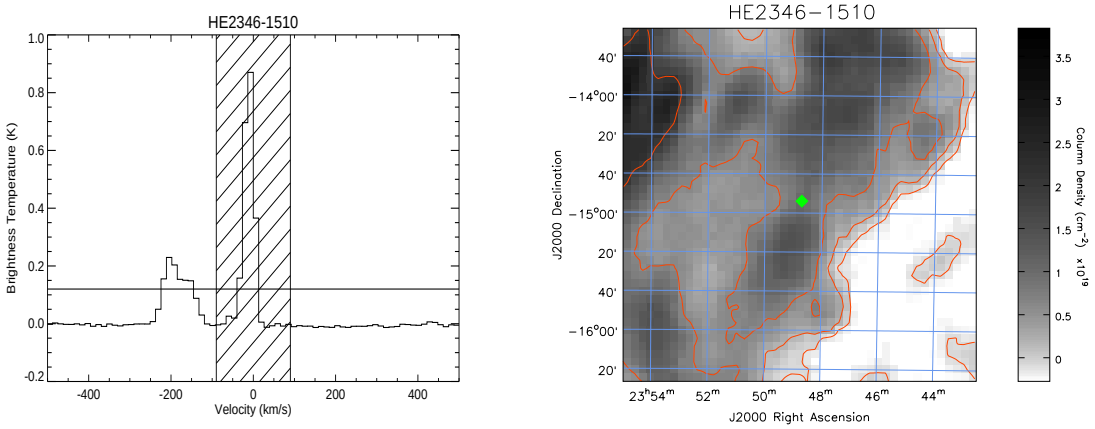


Figure B.404: HE 2346−1510

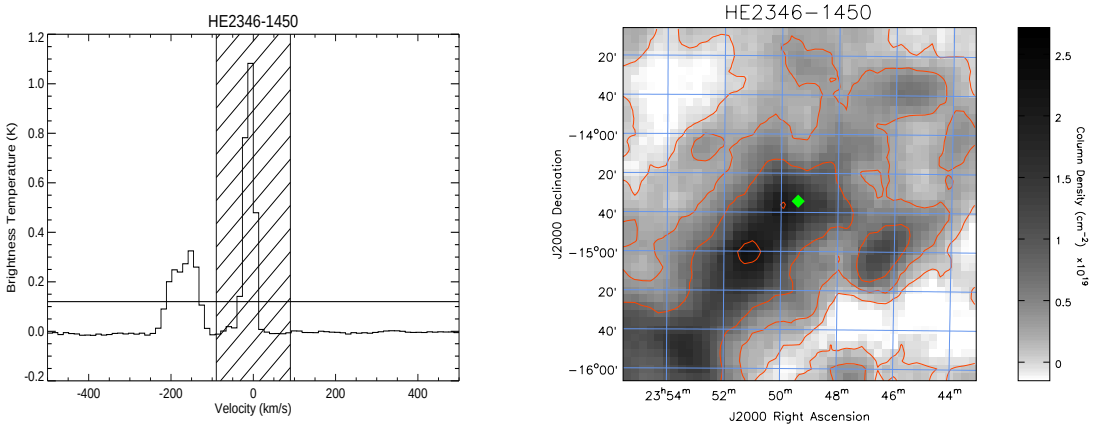


Figure B.405: HE 2346−1450

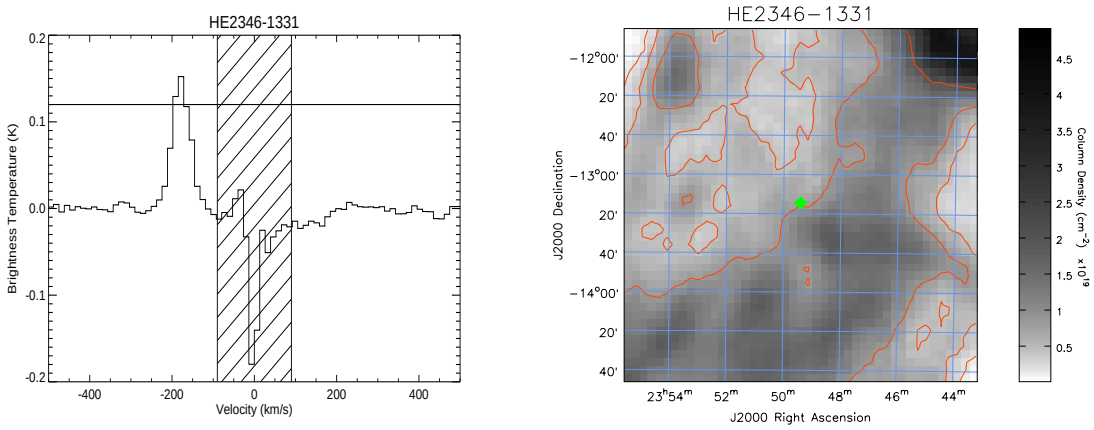


Figure B.406: HE 2346−1331

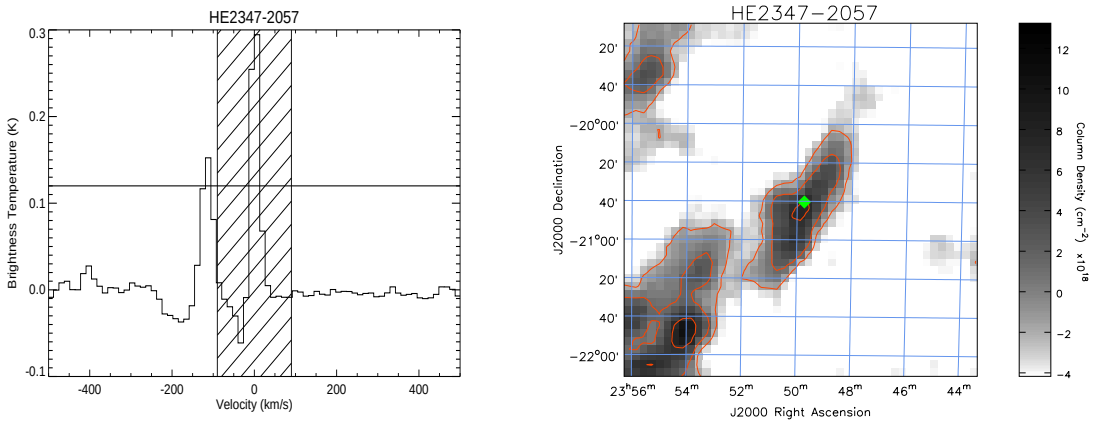


Figure B.407: HE 2347−2057

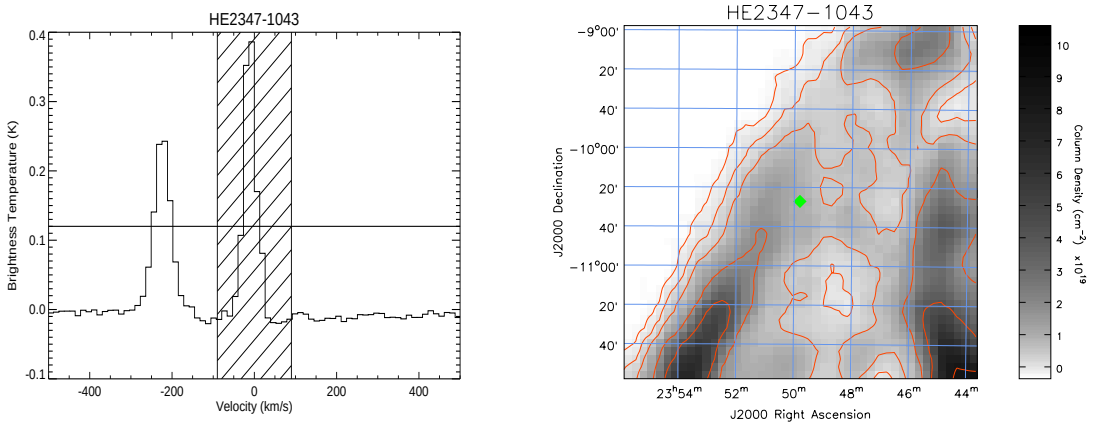


Figure B.408: HE 2347−1043

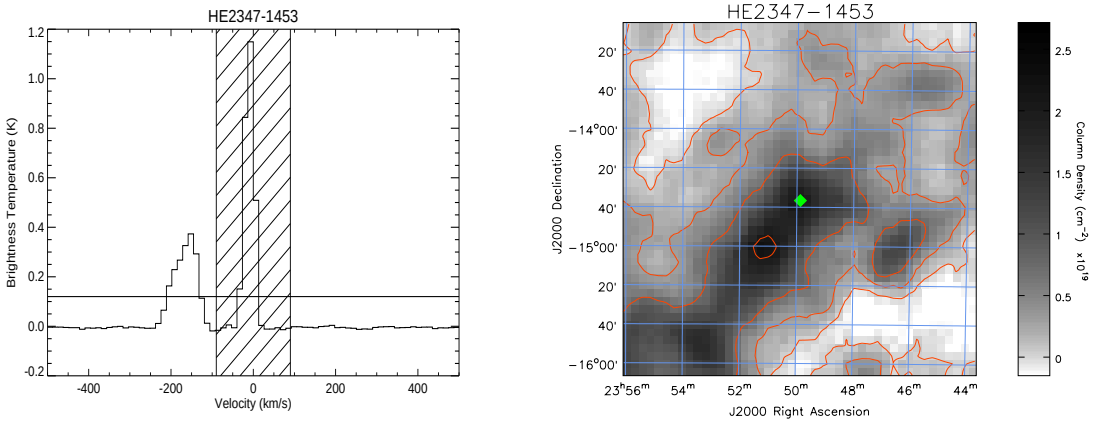


Figure B.409: HE 2347−1453

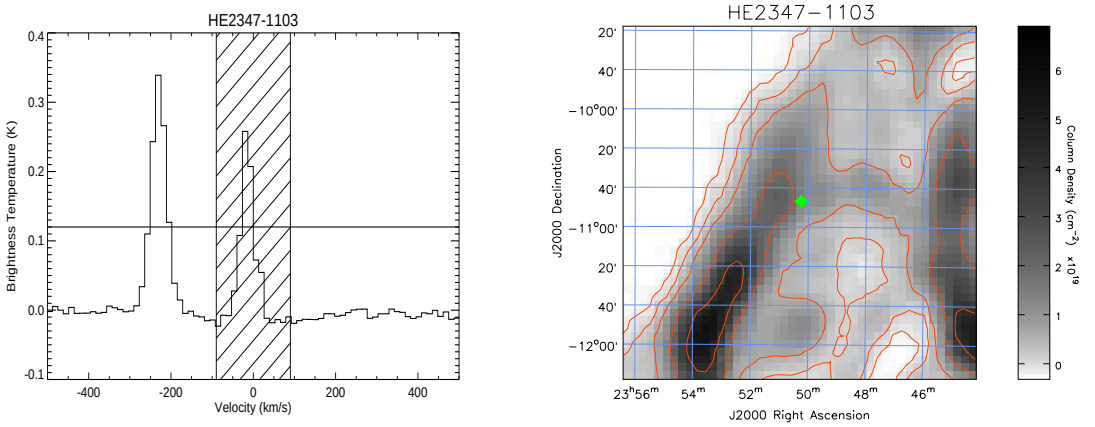


Figure B.410: HE 2347−1103

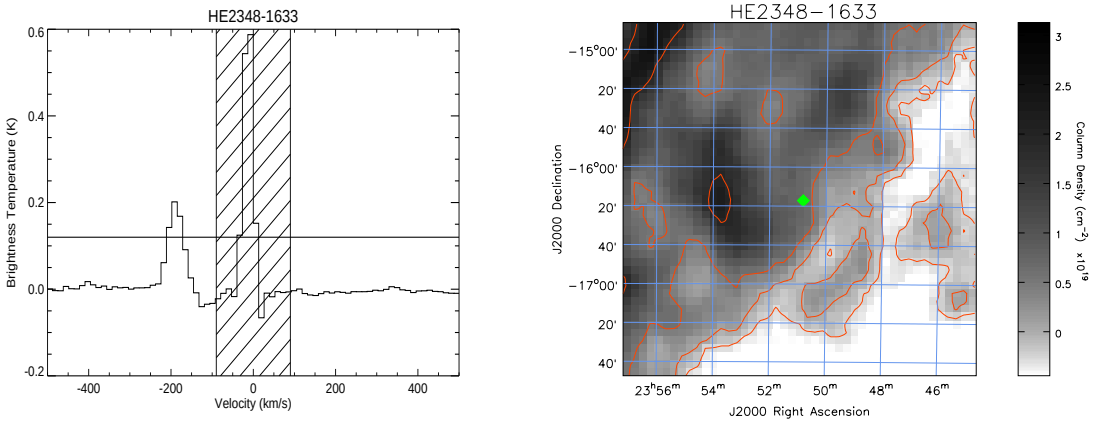


Figure B.411: HE 2348−1633

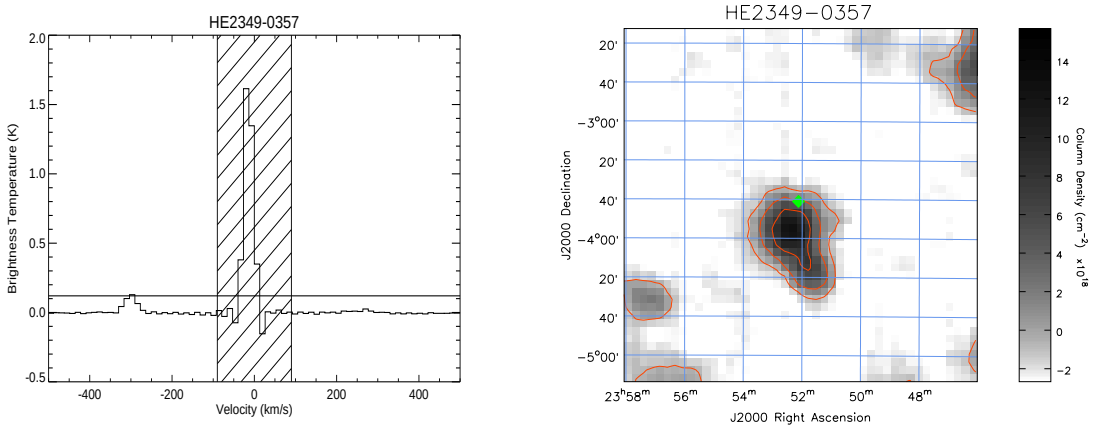


Figure B.412: HE 2349−0357

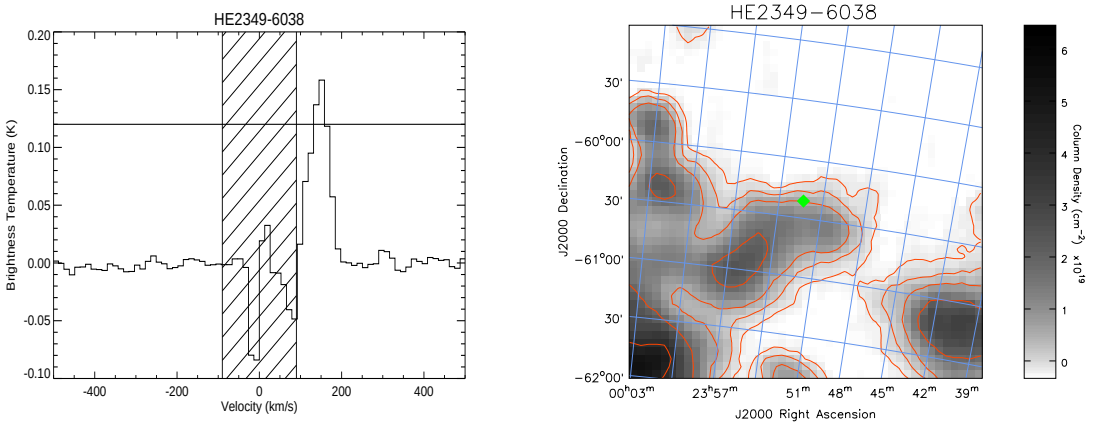


Figure B.413: HE 2349−6038

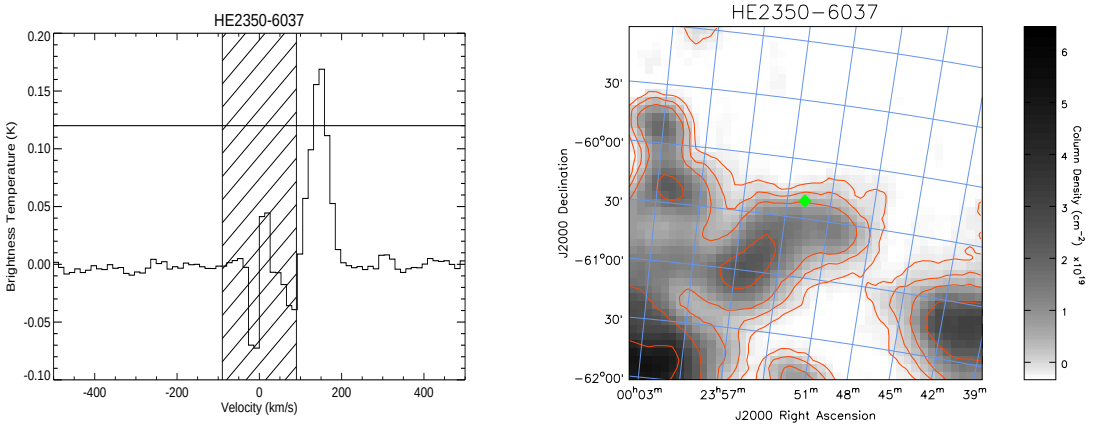
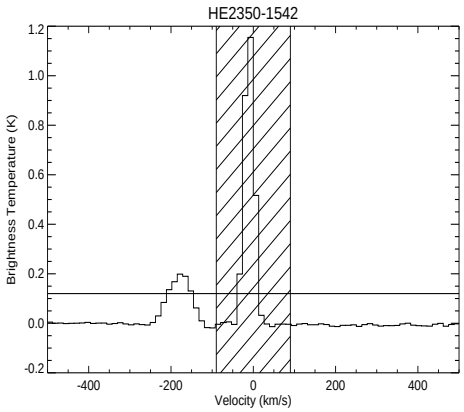


Figure B.414: HE 2350−6037



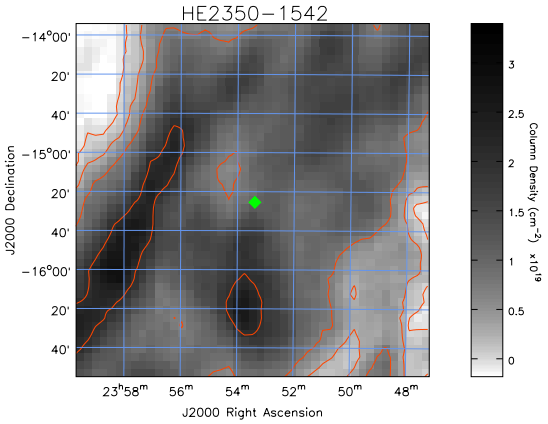
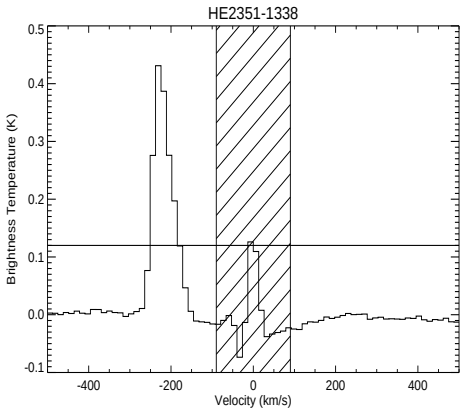


Figure B.415: HE 2350−1542



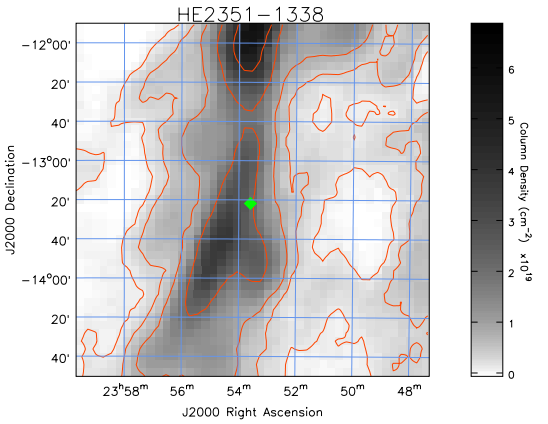
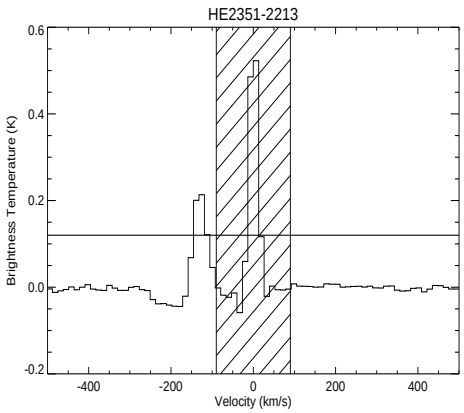


Figure B.416: HE 2351−1338



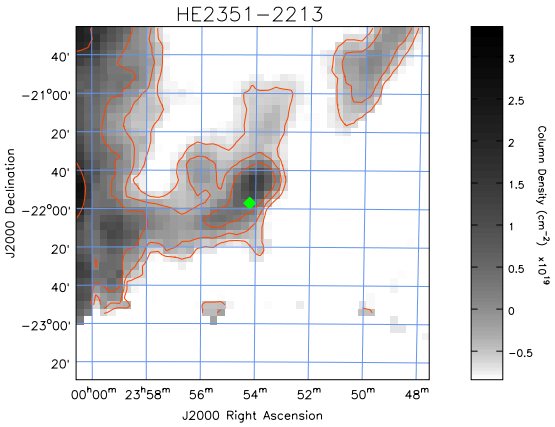


Figure B.417: HE 2351−2213

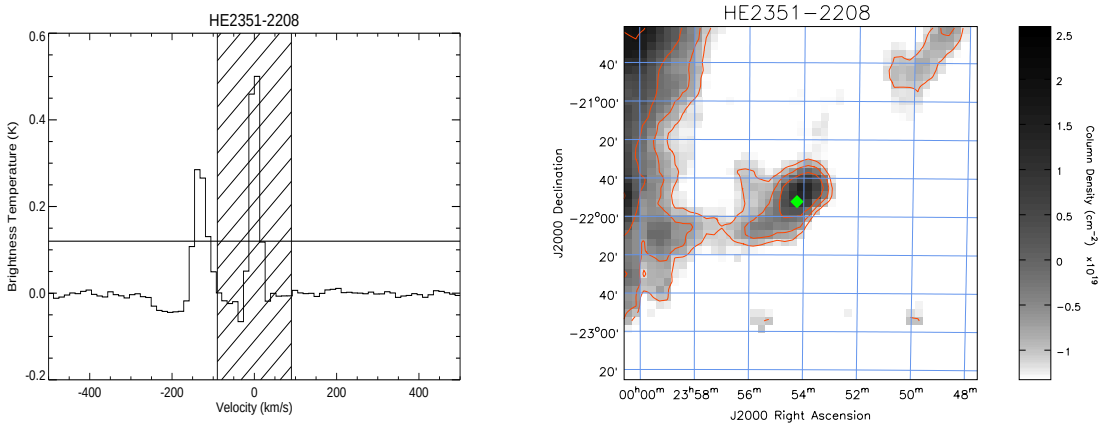


Figure B.418: HE 2351−2208

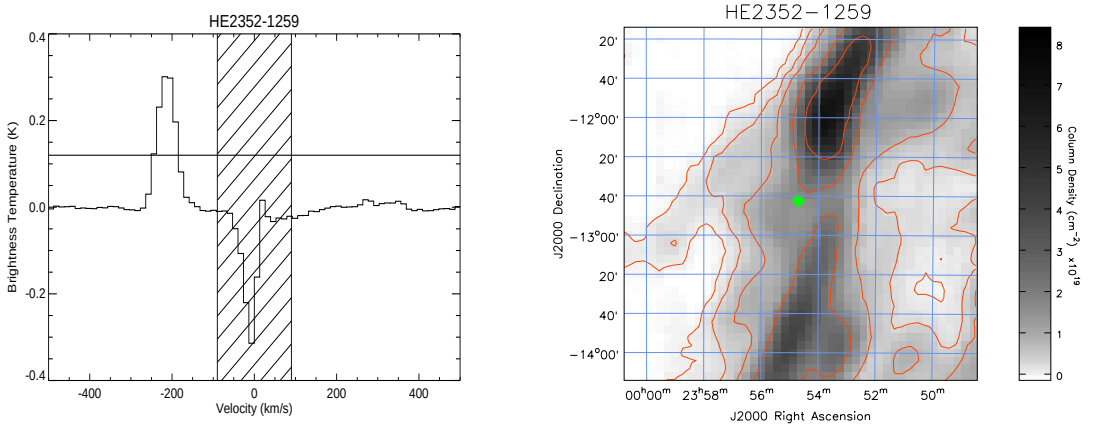


Figure B.419: HE 2352−1259

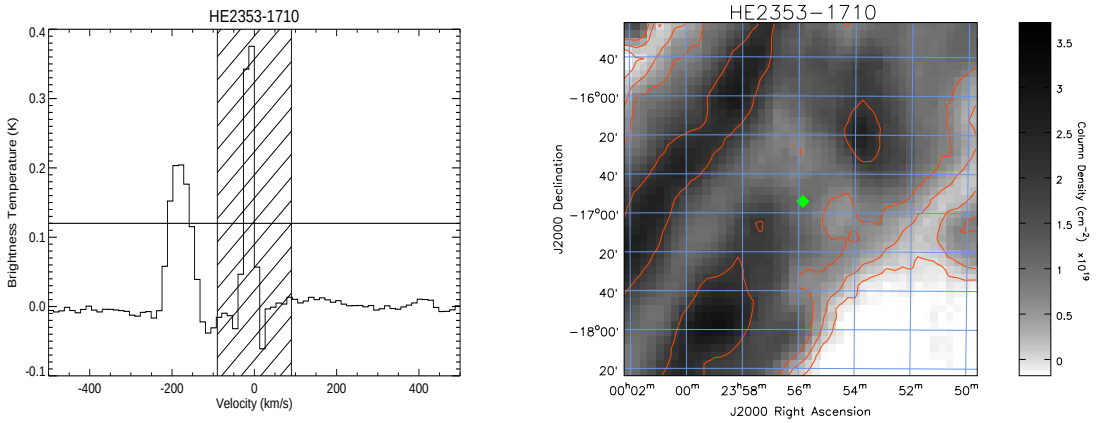


Figure B.420: HE 2353−1710

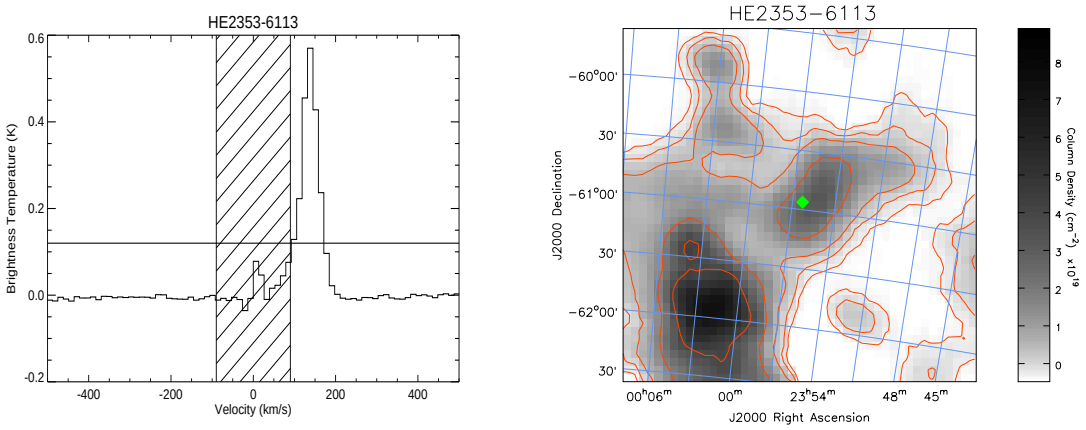


Figure B.421: HE 2353−6113

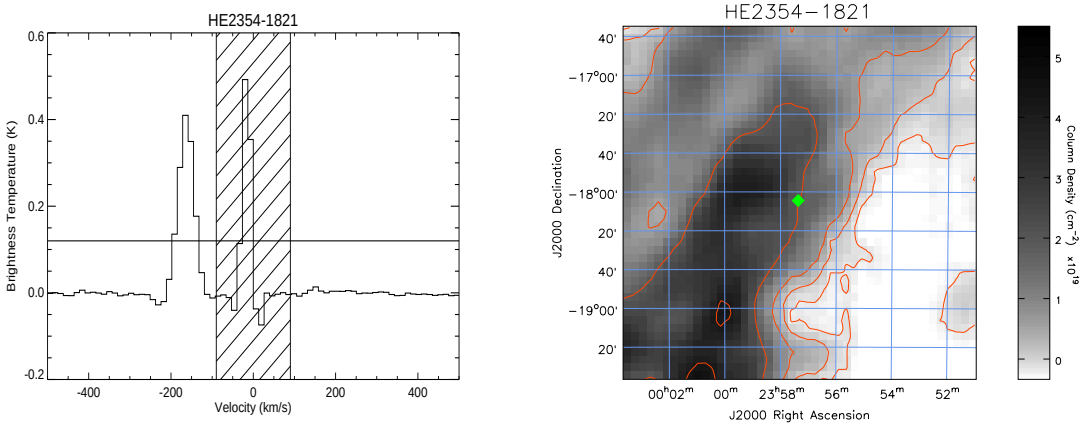


Figure B.422: HE 2354−1821

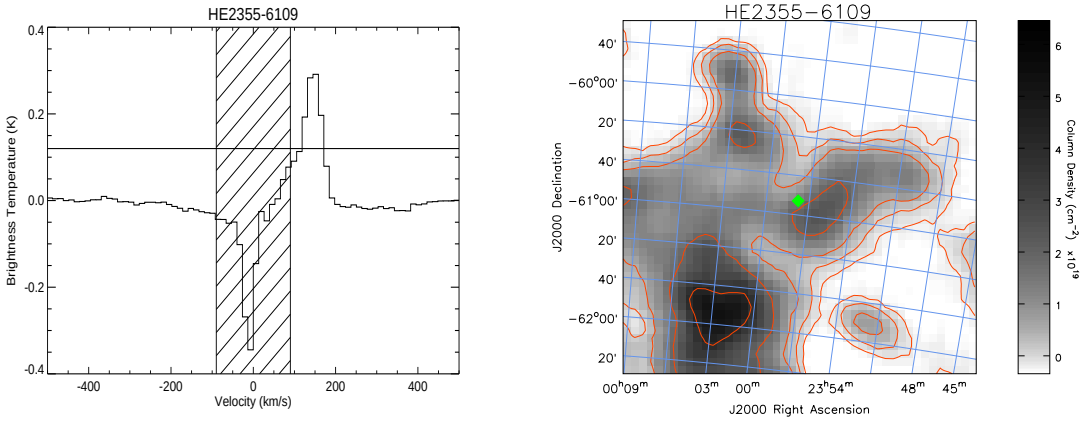


Figure B.423: HE 2355−6109

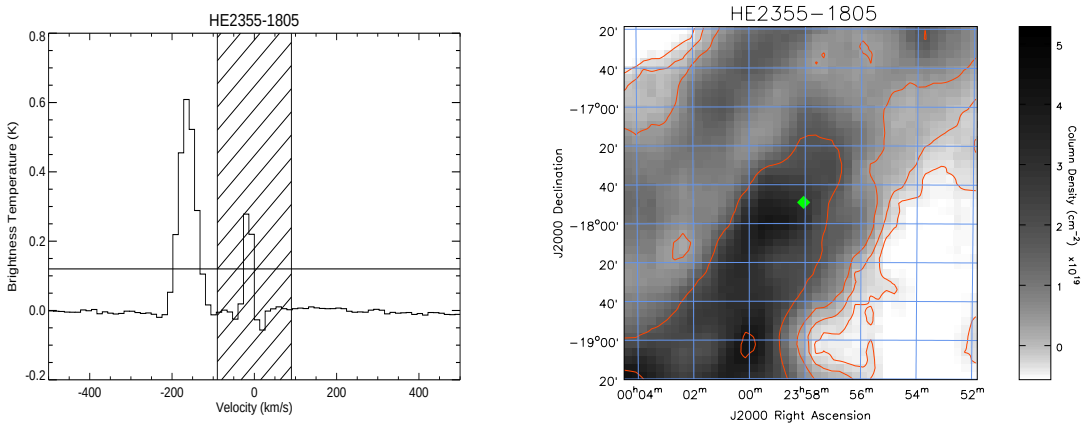


Figure B.424: HE 2355−1805

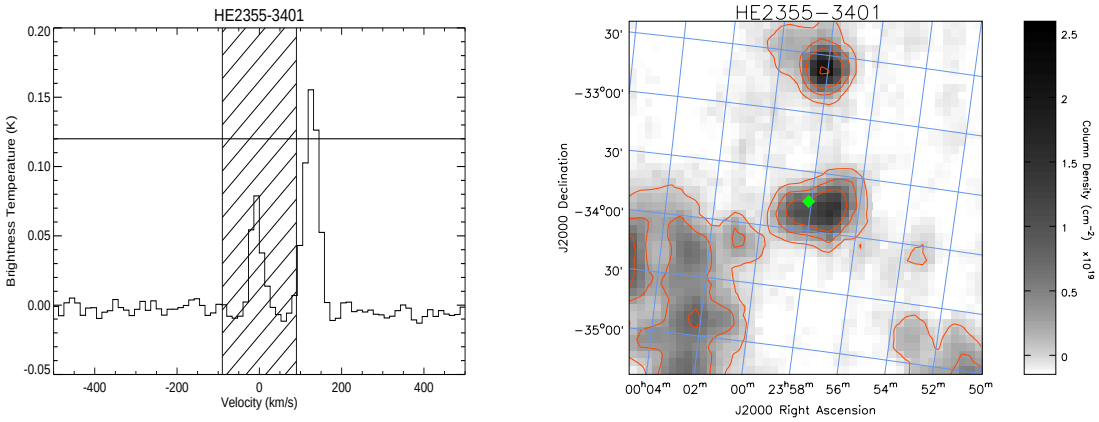


Figure B.425: HE 2355−3401

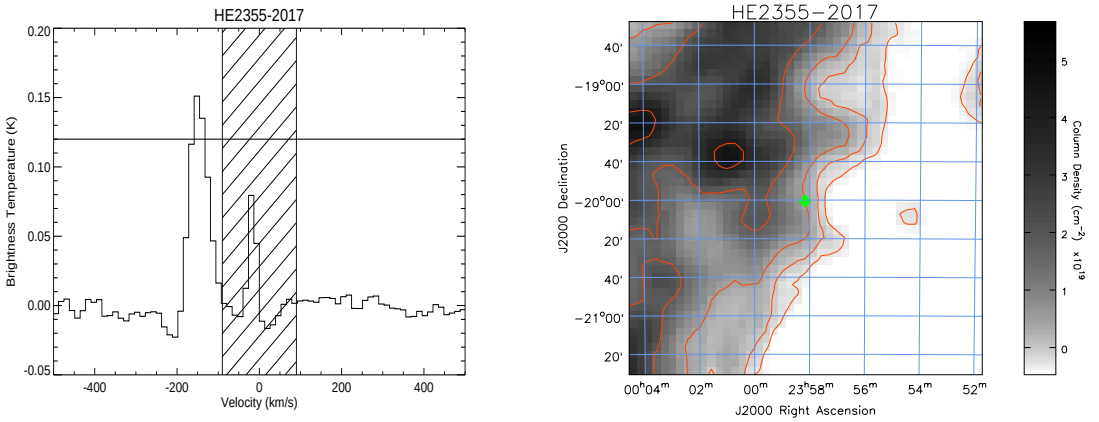


Figure B.426: HE 2355−2017

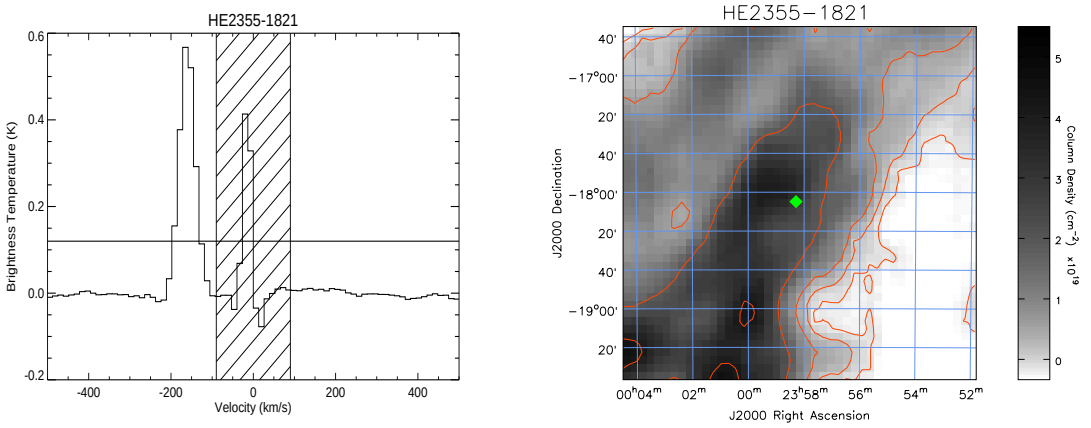


Figure B.427: HE 2355−1821

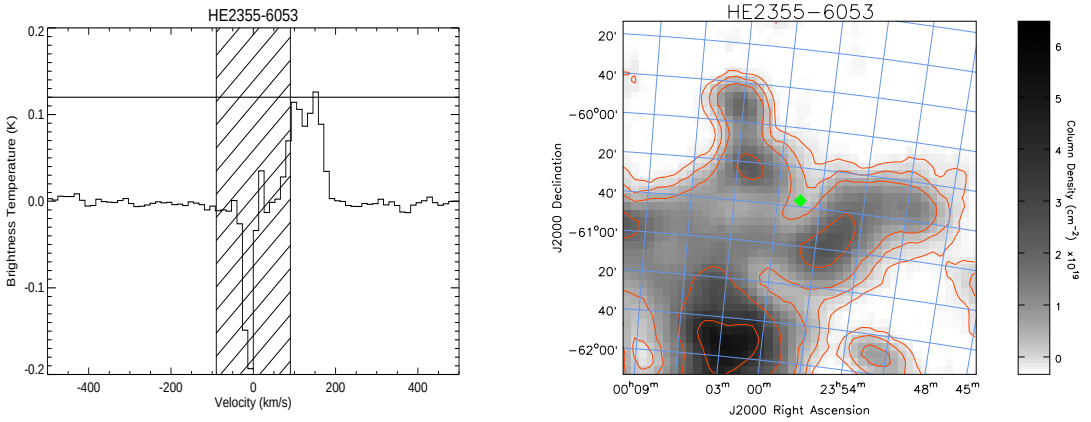


Figure B.428: HE 2355−6053

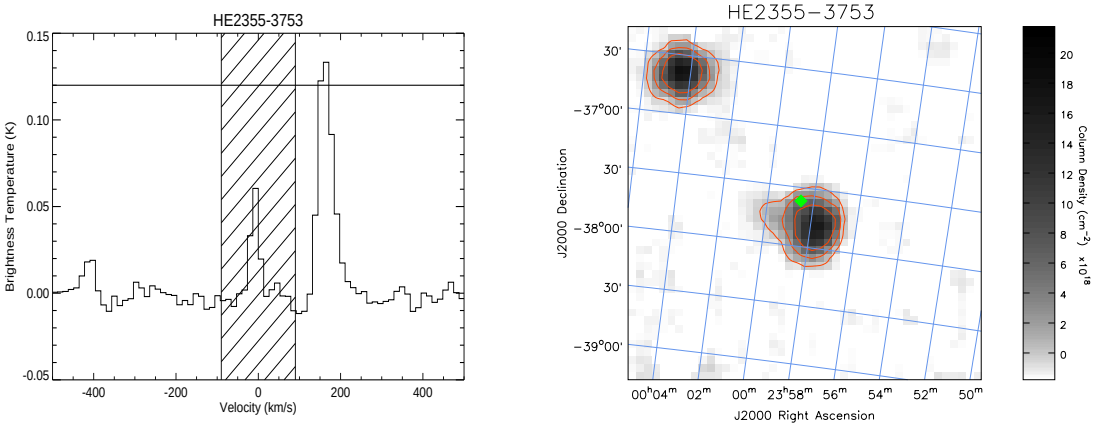


Figure B.429: HE 2355−3753

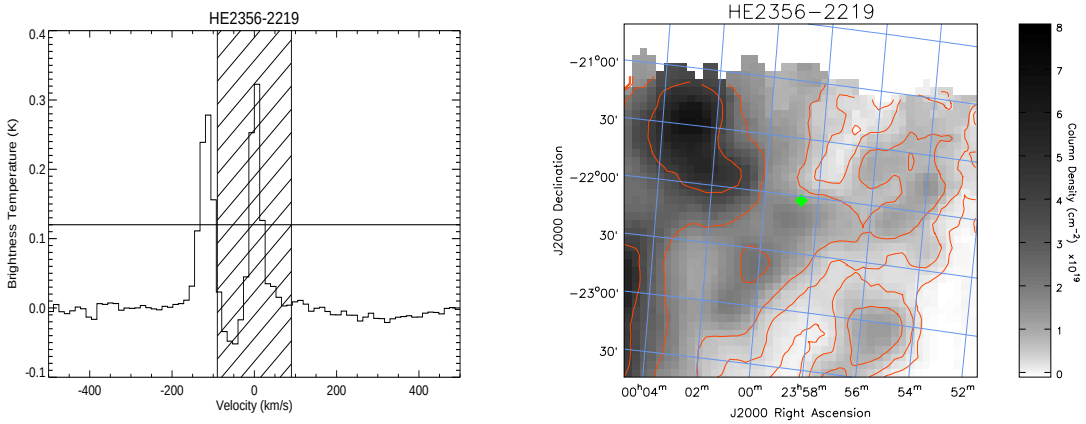


Figure B.430: HE 2356−2219